Maynooth University
National University of Ireland Maynooth

Experimental and Numerical Modelling of a Multiple Oscillating Water Column Structure

Supervisor:
Professor John V. Ringwood

Co-supervisor:
Dr Thomas Dooley

Author:
Mr Thomas Kelly

A thesis submitted in partial fulfilment of the requirements for the degree of Doctor of Philosophy

Faculty of Science and Engineering
Department of Electronic Engineering

November 2018

Declaration of Authorship

I, Mr Thomas Kelly, declare that this thesis titled 'Experimental and Numerical Modelling of a Multiple Oscillating Water Column Structure' and the work presented in it are my own. I confirm that:

- This work was done wholly or mainly while in candidature for a research degree at this University.
- Where any part of this thesis has previously been submitted for a degree or any other qualification at this University or any other institution, this has been clearly stated.
- Where I have consulted the published work of others, this is always clearly attributed.
- Where I have quoted from the work of others, the source is always given. With the exception of such quotations, this thesis is entirely my own work.
- I have acknowledged all main sources of help.
- Where the thesis is based on work done by myself jointly with others, I have made clear exactly what was done by others and what I have contributed myself.

Signed: _____

Date: _____

"Can ye fathom the ocean, dark and deep, where the mighty waves and the grandeur sweep?"

Fanny Crosby

MAYNOOTH UNIVERSITY, IRELAND

Abstract

Faculty of Science and Engineering
Department of Electronic Engineering

Doctor of Philosophy

Experimental and Numerical Modelling of a Multiple Oscillating Water Column Structure

by Mr Thomas Kelly

The potential exists for ocean energy from waves to meet a large fraction of future global energy needs. Furthermore, synergies between the existing offshore wind industry, and the future offshore wave energy industry, can be exploited. This thesis is concerned with the physical and numerical modelling of an offshore floating platform, as proposed by a commercial developer. It is envisaged that the platform will capture both wave and wind energy, using an array of oscillating water columns (OWC) and conventional wind energy technology. The focus of this thesis is on the wave energy-capturing aspects of the proposed platform.

A 1:50, physical scale model of the proposed platform is described, and a tank testing programme for the model, in a variety of configurations, is outlined. A frequency domain, numerical model of the physical scale model is developed. Predictions from the numerical model are compared to the tank testing results. Based on the results of tank testing, and predictions from the numerical model, a number of useful tools for future design work have been created, and some fundamental changes to the design of the platform are proposed. On completion of the tank testing, the platform progressed to Technical Readiness Level 3.

Due to the complexities of studying and numerically modelling the hydrodynamic and thermodynamic interactions within the array of OWCs in the model platform, a non-linear, time domain, numerical model, at a scale of 1:50, of a single OWC from the proposed platform, with control components, is developed. Predictions from the numerical model are compared to the results of testing on a physical model of the single OWC. An investigation to quantify the effect of air compression in the single-OWC model, not captured using Froude scaling, is conducted. The investigation leads to a proposed novel method for measuring the hydrodynamic parameters of a water column.

The key conclusions from this thesis are:

- A non-linear, time-domain numerical model has been developed for a single-OWC with novel cross section and control components. The numerical model has been extensively validated using the rests obtained from narrow tank testing.
- A new method for determining hydrodynamic parameters has been developed and demonstrated numerically. The method has been implemented for an OWC, but requires further validation.
- It has been demonstrated through the analysis of data obtained from tank testing that the airflow from the chambers of a V-shaped, 32-OWC wave energy converter (WEC) can absorb power from the wave front with an efficiency of up to 37 % at a wave period of 1.13 s.
- A frequency domain model of the multiple degree-of-freedom WEC, predictions from which compare well with results obtained from tank testing, has been developed.

Acknowledgements

The author would like to express his sincere gratitude to a number of people, without whom the work described in the thesis could not have been carried out. Firstly I would like to thank my supervisor, Professor John Ringwood, for his guidance, patience and encouragement throughout the processes. Secondly, I would like to express my gratitude to my co-supervisor, Dr Thomas Dooley, for initially sparking my interest in wave energy, for suggesting I pursue the work described herein, and for his support throughout.
I would also like to thank all the staff at Wave Energy Ireland Ltd., particularly John Campbell, Emmett Farrell and Marcus Wallace, for giving me the opportunity to become involved in a commercial wave energy venture. I owe a debt to all the administrative and technical staff at both Maynooth University, and the Dundalk Institute of Technology, notably the team in the Carpentry and Joinery department, whose assistance in model building was invaluable.
The author would further like to thank the Irish Research Council (formerly the Irish Research Council for Science, Engineering and Technology) for part-funding this PhD.
Over the years, many people have come and gone from the wave energy group in Maynooth University, and while they are too numerous to mention individually, the conversations, discussions and cups of coffee over the years have been both grounding and invigorating, and I wish each and everyone well in the future.
Finally, I would like to thank my family, not only for their love, patience and support throughout this process, but also throughout the years.

Contents

List of Figures

List of Tables

Abbreviations

AMETS	**A**tlantic **M**arine **E**nergy **T**est **S**ite
BEM	**B**oundary **E**lement **M**ethod
BVP	**B**oundary **V**alue **P**roblem
CAPEX	**CAP**ital **EX**penditure
CFD	**C**omputational **F**luid **D**ynamics
CREDIT	**C**entre for **R**enewable **E**nergy at **D**undalk IT
CSA	**C**ross for **S**ectional **A**rea
DAQ	**D**ata **A**quistion system
DkIT	**D**undalk **I**nstitute of **T**echnology
DNV	**D**et **N**orske **V**eritas
EWEA	**E**uropean **W**ind **E**nergy **A**ssociation
FDI	**F**requency **D**omain **I**dentification
FEA	**F**inite **E**lement **A**nalysis
FPSO	**F**loating **P**roduction **S**torage and **O**ffloading
FFT	**F**ast **F**ourier **T**ransform
GRP	**G**lass-**R**einforced **P**lastic
HMRC	**H**ydraulic and **M**aritime **R**esearch **C**entre
IRCSET	**I**rish **R**esearch **C**ouncil for **S**cience, **E**ngineering and **T**echnology
IRF	**I**mpulse **R**esponse **F**unction
IRR	**I**nternal **R**ate of **Return**
IWEDA	**I**rish **W**ave **E**nergy **D**evelopers **A**ssociation
JAMSTEC	**J**apan **A**gency for **M**arine-Earth **S**cience and **TEC**hnology
MSS	**M**arine **S**ystems **S**imulator
Mtoe	**M**ega **t**onnes of **o**il **e**quivalent
MUFOW	**M**ultiple **U**nit **F**loating **O**ffshore **W**ind farm

NEL	**N**ational **E**ngineering **L**aboratory
NPV	**N**ett **P**resent **V**alue
OEDU	**O**cean **E**nergy **D**evelopment **U**nit
O&M	**O**perational and **M**aintenance
OPEX	**OP**erational **EX**penditure
OWC	**O**scillating **W**ater **C**olumn
PS	**P**ressure **S**ensor
PTO	**P**ower **T**ake-**O**ff
QUB	**Q**ueen's **U**niversity **B**elfast
RAO	**R**esponse **A**mplitude **O**perator
RMS	**R**oot **M**ean **S**quare
SEAI	**S**ustainable **E**nergy **A**uthority of **I**reland
SME	**S**mall to **M**edium-sized **E**nterprise
SWL	**S**till **W**ater **L**evel
TRL	**T**echnical **R**eadiness-**L**evel
WEC	**W**ave **E**nergy-**C**onverter
WEI	**W**ave **E**nergy-**I**reland Ltd.
WP	**W**ave **P**robe

Symbols

Greek Symbols

Symbol	Name	Unit
α	scaling factor	
β	phase angle between two time series	rad
γ	heat capacity ratio or adiabatic index	
δ	density ratio between a fluid at model and at full scale	
ζ	instantaneous free surface elevation	m
η	wave energy conversion efficiency	%
μ	dynamic viscosity of a fluid	$\mathrm{Pa\,s}$
ρ	density of a fluid	$\mathrm{kg^3\,m^{-3}}$
ϕ	scalar velocity potential function	$\mathrm{m^2\,s^{-1}}$
φ_r	radiation potential proportionality coefficient	$\mathrm{m^3}$
$\vec{\omega}$	water particle rotation vector	$\mathrm{rad\,s^{-1}}$
ω	angular frequency	$\mathrm{rad\,s^{-1}}$
λ	wave length	m

Roman Symbols

Symbol	Name	Unit
A_j	added mass in the j^{th} mode	kg
A_{wp}	waterplane area	$\mathrm{m^2}$
A_{owc}	cross-sectional area of a water column	$\mathrm{m^2}$
A_{vent}	cross-sectional area of the throat of a Venturi	$\mathrm{m^2}$
A_o	cross-sectional area of an orifice water column	$\mathrm{m^2}$
B_j	radiation damping in the j^{th} mode	$\mathrm{N\,s\,m^{-1}}$
Cd	coefficient of discharge	

C_j	coefficient of buoyancy in the j^{th} mode	$\mathrm{kg\,s^{-2}}$
C_v	specific heat capacity at constant volume	$\mathrm{J\,K}$
C_p	specific heat capacity at constant presure	$\mathrm{J\,K}$
D_j	linear damping due to PTO in the j^{th} mode	$\mathrm{N\,m\,s^{-1}}$
E	energy	J
E	expected value of a function	
Fh	hydrostatic force in the j^{th} mode	N
Fe	exciting force in the j^{th} mode	N
Fr	radiation force in the j^{th} mode	N
Fr	Froude number	
Fu	force due to PTO in the j^{th} mode	N
G	one-sided power spectral density	
H	wave height	m
$H(f)$	Fourier transform between the input and output of a linear system	
I	moment of inertia	$\mathrm{kg\,m^2}$
$\Im$	imaginary part of a complex number	
J	power flux	$\mathrm{W\,m^{-1}}$
L	length of a leg of the proposed WEI platform	m
L_g	edge distance of an air admittance valve	m
L_p	the length of the wave crest presented to the model	m
N	number of compounding periods	
Pow	power	W
Q	volumetric flow rate	$\mathrm{m^3\,s^{-1}}$
Q	heat transferred to or from the system	J
R	gas constant of the fluid	$\mathrm{J\,kg^{-1}\,K}$
$R_{yy}(\tau)$	autocorrelation function	
Re	Reynolds number	
$\Re$	real part of a complex number	
S	wetted surface of a object in a fluid	
$S\,(f)$	spectral energy density function	$\mathrm{m^2\,Hz^{-1}}$
T	wave period	s
T	fluid temperature	K

U	internal energy of a system	J
$\vec{V}$	fluid particle velocity vector	$\mathrm{m\,s^{-1}}$
V	velocity vector	$\mathrm{m\,s^{-1}}$
V	volume occupied by a fluid	$\mathrm{m^3}$
W	work done on or by a system	J
$X(f)$	Fourier transform of the input to a linear system	
$Y(f)$	Fourier transform of the output from a linear system	
Z_j	complex impedance in the j^{th}, $j = 1, 2, 3$	$\mathrm{N\,s\,m^{-1}}$
Z_j	complex impedance in the j^{th}, $j = 4, 5, 6$	$\mathrm{N\,s\,m\,rad^{-1}}$
amp	amplitude of a wave	m
c_s	speed of sound in a fluid	$\mathrm{m\,s^{-1}}$
d	water depth	m
g	acceleration due to gravity	$\mathrm{m\,s^{-2}}$
$g(x)$	a single-valued function	
h_{max}	opening height of the diaphragm for the valve	m
h_o	initial height of an air volume	m
$h(\tau)$	impulse response of a system	
$\vec{i}$	unit vectors in the in the x-direction	
$\vec{j}$	unit vectors in the in the y-direction	
$\vec{k}$	unit vectors in the in the z-direction	
k	wave number $= 2\pi/\lambda$	$\mathrm{rad\,m^{-1}}$
kr	kernel of the radiation forces	$\mathrm{kg\,m^{-1}}$
ks	linearised for the air spring effect coefficient	$\mathrm{N\,m^{-1}}$
m	mass	kg
m_n	n^{th} spectral moment	
n	unit normal at the point on surface S	
p	pressure in a fluid	$\mathrm{N\,m^{-2}}$
$p(x)$	the probability density function	
t	time	s
u	component of the fluid particle velocity in x	$\mathrm{m\,s^{-1}}$
u_i	body displacement in the t^{th} mode	m
v	component of the fluid particle velocity in y	$\mathrm{m\,s^{-1}}$
$\vec{v}$	velocity of a body moving due to an incident wave	$\mathrm{m\,s^{-1}}$

w	component of the fluid particle velocity in z	$\mathrm{m\,s^{-1}}$
x	positive direction of wave propagation	m
$x\,(t)$	time series input to a linear system	
y	upwards positive direction	m
z	direction forming a right-hand system with x and y	m
$y\,(t)$	time series output from a linear system	

Miscellaneous

Symbol	Name	Unit
$\varnothing$	diameter	m

Subscripts

I	incident
R	reflected
ab	absorbed
$atmos$	atmosphere
av	average
d	diffraction
d	discharge
f	full scale
g	center of gravity
hp	high pressure
lp	low pressure
m	model scale
nl	non-linear
o	original
ori	orifice
owc	oscillating water column
p	peak period
pl	plenum
r	radiation
s	significant wave
$vent$	venturi
w	wave
wp	water plane
z	zero-crossing period

Chapter 1

Introduction

The increasing global demand for energy, and associated environmental issues, is one of the greatest problems facing society today. In 2015, the International Energy Agency (IEA) estimated the total global energy usage at 13,647 Mtoe, equivalent to 158,714,610 GWh. Of this, 11,263.5 Mtoe, or ~82.5%, was provided by fossil fuels. The total energy demand for Ireland in 2015 was estimated at 1.91 Mtoe, or 22.2 TWh, of which ~86% was derived from fossil fuels [1]. The IEA predicts that the global energy demand will continue to grow, and estimates that the global requirement will reach 17,866 Mtoe, or 207,781,580 GWh, by 2040 [2]. The high energy density of fossil fuels makes the use of such fuels attractive, and has helped to bring about the modern era. However, fossil fuels are polluting, generating carbon monoxide (CO_2), sulphur oxides (SOx) and nitrogen oxides (NOx), amongst other pollutants. The CO_2 released when fossil fuels are combusted is the major contributor to climate change [3]. Ireland emitted 37,946 kt of energy-related CO_2 in 2015, a figure which had shown some decline during the recession, but which has begun to increase in line with the economic recovery [4]. Fossil fuels are, by their nature, finite, and while energy prices have been relatively low in recent times, the cost of fossil fuels is likely to grow as such fuels become more scarce. While nuclear energy based on uranium-235 (^{235}U) fission technology may provide a short-term solution to global energy needs, leaving aside concerns regarding the safety of such technology, energy so derived, again, depends on a finite resource. The Nuclear Energy Agency and International Atomic Energy Agency estimate that, at current rates of consumption, there remain sufficient ^{235}U resources for 200 years [5]. However, nuclear power currently provides only 5% of the total primary global energy demand [1]

and, if this percentage increases, clearly the available ^{235}U resource will deplete faster. At best, such technology can only provide a stopgap solution.

In response to the challenges faced to meet future global energy requirements, interest in alternative, renewable, energy sources has grown. Between 2008 and 2017, the global installed capacity of renewable energy plants approximately doubled [6], with renewable energy sources providing 22.8% of global energy needs in 2015 [1]. While interest in wave energy specifically has waxed and waned in line with raising and falling oil prices, showing a notable increase during the oil crisis of the 1970s [7], for instance, enthusiasm for wave energy has increased significantly in recent years. From an Irish perspective, renewable forms of energy generation are especially attractive. Ireland has few indigenous fossil fuel sources, with an energy import dependency of ~88% in 2015 [4]. Historically, the primary indigenous fuel source has been peat, which is burned to generate heat and electrical power; however, Bord na Móna (the semi-state company with responsibility for managing Ireland's peatlands) has announced its intention to end the harvesting of peat by 2030 [8]. What Ireland does have in abundance, however, is renewable energy sources, suitable for generating wind, bio and ocean energy. For example, the Sustainable Energy Authority of Ireland (SEAI) has estimated that a wave energy resource of 525 TWh exists in Irish territorial waters, although the estimated accessible resource is significantly lower at 21 TWh [9]. As well as the potential to provide a significant contribution to energy needs, an ocean energy industry could generate employment, with a 2010 study suggesting a potential for up to 52,000 jobs in wave energy in Ireland alone by the year 2030 [10], a figure which encouraged the development of the Offshore Renewable Energy Plan (OREDP) [11] in 2014, which aimed to set out a path to the sustainable development of offshore renewable energy in Ireland.

The heavy reliance on fossil fuels within the generation mix in Ireland, and the associated CO_2 emissions, has a further potential economic consequence. Under the EU 2020 Climate and Energy package [12], Ireland committed to reducing CO_2 emissions by 20% of 2005 levels by 2020. It now seems certain this target will be missed [13], which will result in the imposition of heavy fines. Energy generation is responsible for 20.4% of greenhouse gas emissions in Ireland, with transport contributing a further 20% [14]. Thus, renewable energy has the potential to significantly reduce Ireland's energy- and transport-related CO_2 emissions.

In summary, the development of a sustainable offshore renewable energy industry would bring energy security and independence, economic benefits and environmental benefits.

1.1 Motivation

At this time, a large number of wave energy converters (WECs) are under development worldwide, and a number of prototype devices have been deployed, see, for example, [15]. It is clear that it is technically feasible to deploy a WEC to extract wave energy; however, to date, no company has managed a commercially-viable deployment. A number of researchers have proposed combining offshore wind and wave energy converting devices [16]. The capital costs associated with a wave energy project may potentially be reduced by sharing infrastructure (for example, substations and cabling to shore), with offshore wind projects. A further benefit of combining the two energy generation methods is that there is relatively poor correlation between wind and wave resources, giving a degree of energy resilience. [17]. Thus, by combining offshore wind and wave energy converting devices, aggregation of resources may be achieved. Further, the relatively low correlation of environmental conditions suitable for the respective energy generation methods allows the same infrastructure be used by one generation method when conditions do not suit energy generation by the second method, making more efficient use of expensive infrastructure.

This thesis is concerned with the physical and numerical modelling of a prospective wind/wave energy-converting platform, which has been proposed by Wave Energy Ireland Ltd. (WEI), and some of the work described herein has been carried out in a commercial context. The commercial nature of the project is reflected in the 3-year funding granted to the author by the Irish Research Council (formerly known as the Irish Research Council for Science, Engineering and Technology) under the Enterprise Partnership Scheme. The proposed wind/wave platform, and the operation concept of the wave energy components of the platform, are described in Chapter 3. While some work has been carried out on the combined effect of wind and wave action on the proposed platform [18], the physical and numerical modelling of the proposed platform described herein focusses primarily on the hydrodynamic behaviour, and the capture of wave energy.

The primary motivation of the work herein is to progress the development of the proposed WEI platform to Technical Readiness Level (TRL) 3, and develop suitable design tools to facilitate technical development of the platform. For a description of the TRL levels as applied to wave energy concepts, see, for example, [19]. Both tank testing of a 1:50 physical scale model of the proposed WEI platform, and narrow tank testing

of a configurable single-oscillating water column (OWC) model were undertaken. The tank testing of the 1:50 physical scale model was motivated by the need to validate the operational concept of the wave energy absorbing components of the platform. Data obtained from such testing is also required in order to examine the behaviour, and performance, of a full-scale platform to identify any operational issues that may exist. As a commercial project, the gathering of performance data was motivated by the need to establish not only the technical feasibility, but also the financial feasibility of the concept. Furthermore, data obtained from the tank testing of a physical model may be used to validate and inform a frequency domain numerical model of the platform, which may subsequently be used as a design tool to improve future iterations of the platform.

A large number of non-linear processes and interactions occur within the model platform during operation, and the difficulty of examining, and numerically modelling, the individual processes within the platform provided the motivation for the narrow tank testing of a configurable single-OWC model. Data obtained from this testing may be used to validate numerical models, which may then be used as tools to aid in component design. Both the 1:50 physical model of the proposed platform, and the single-OWC configurable model, are described in Chapter 8.

It is well known that geometric scaling of the air volumes in physical models of OWC-based WECs does not accurately scale the effect of air compression on the WEC. The secondary motivation underpinning the work described herein, therefore, is to investigate the scaling issue and its effect on the behaviour and performance of the single-OWC model. Further, while not an initial motivation, following on from the investigation into air compressibility, the opportunity was taken to investigate a proposed novel means by which the hydrodynamics of an OWC may be measured using spectral methods.

1.2 Background

Chapter 3 describes in detail the concept and operating principles of the wave energy-converting aspects of the proposed WEI platform. In the current section, the platform is introduced, and the background to the research described in this thesis is presented. The proposed floating platform is V-shaped in plan, with an internal angle of 90 degrees. It is intended that the platform would be moored using single-point floating production storage and offloading unit (FPSO)-style mooring, located at the apex of the V. Each leg of the V comprises 16 OWCs, hence the platform comprises 32 OWCs in total. The airflows generated by the OWCs in each leg are rectified and manifolded using air admittance valves to generate uni-directional airflow. The airflows within each leg of the platform operate in a closed system, and no airflow takes place between the two legs. It is proposed that one, or more, offshore wind turbines be mounted on the platform, and share power transmission infrastructure with the wave-energy converting elements of the platform.

The research described in this thesis builds on previous work conducted by the engineers at WEI, and by the author. WEI was founded as a subsidiary of J. J. Campbell and Associates, a civil and structural engineering consultancy. Prior to the founding of WEI, J. J. Campbell and Associates had, in 2001, proposed a breakwater design which incorporated multiple OWCs, however, the breakwater was not constructed. The design work on the breakwater was the first foray in the field of wave energy by the team which would become WEI. In 2008, the WEI platform, which is the focus of this thesis, was first conceived, and, following the identification of funding mechanisms, WEI was formed. An initial feasibility study, funded by Enterprise Ireland, was undertaken by the Centre for Renewable Energy at Dundalk Institute of Technology (CREDIT) on behalf of WEI [18]. WEI subsequently secured funding from the Ocean Energy Development Unit within the Sustainable Energy Authority of Ireland (SEAI) for 1:50 scale model tank testing.

The first phase of the 1:50 scale model testing investigated the effect on the power absorbed by an array of OWCs of varying both the OWC chamber geometry and the orientation of the chamber walls relative to the incident wave direction, and was carried out in a flume. A number of **1:50 scale three-chamber OWC models** were constructed, and tested at the Hydraulic and Maritime Research Centre (HMRC), Co.

Cork. The airflows from the OWC chambers in the three-chamber models were not manifolded, and during the testing, the three-chamber OWC models were fixed to one side of the flume at a 45-degree angle to the incident wave. The models were tested for different damping conditions, and the data gathered was analysed to assess which model geometry absorbed the greatest level of wave power. A report on the testing of the three-chamber devices was delivered to SEAI in 2010 [20].

WEI secured further funding from Enterprise Ireland to allow the development, by the author on behalf of CREDIT, of **frequency domain numerical models, based on BEM codes** [21]**, of the three-chamber OWC models with varying geometries**. Based on the results from both the flume testing and numerical modelling of the three-chamber OWC models, a preferred design for the OWC chambers of the 32-OWC, 1:50 scale model platform was conceived. The chamber design comprised a curved cross section, and the walls between the chambers were set at 90 degrees to the back wall of the platform. The curved profile of the chamber was, in part, inspired by the work described in [22]. A **1:50 scale, 32-OWC model platform** was subsequently constructed from stainless steel, and was tested under a range of conditions at the ocean basin located at the HMRC. In addition, a **frequency domain numerical model of the scale model platform** was developed by the author. The 32-OWC scale model platform is the first major subject of this thesis. A report on the tank testing, and numerical modelling in the frequency domain, of the scale model platform was delivered to SEAI in 2013 [23].

However, the complex hydrodynamic, thermodynamic and mechanical processes and interactions which take place in the 32-OWC model platform result in significant difficulties in determining the influence of individual components in the system, and also in using tank test results to validate numerical models. Consequently, a single-chamber OWC device was modelled to facilitate investigations into, and modelling of, the individual processes and interactions taking place within the 32-OWC model platform, and is the second major subject of this thesis. The research on the single-chamber OWC links the commercial work performed with academia. The cross section of the single-chamber OWC is similar to one chamber of the 32-OWC device. A **non-linear time domain numerical model of the single-chamber OWC** was developed by the author. Rigorous scale model testing in the narrow tank at DkIT of a **1:50 scale single-chamber OWC physical model, with control components**, in multiple configurations, was used to validate the non-linear, time-variant numerical model.

1.3 Objectives

A commercial project will only succeed in securing investors if it can be demonstrated to have a reasonable chance of generating a return on investment through technical viability. One of the main objective of this thesis is to assess the technical viability of the proposed wind/wave energy offshore platform, while developing tools to further the design of the platform. The technical viability is assessed via data obtained from the 3-dimensional tank testing of the 1:50 physical scale model of the platform, which was constructed, instrumented and commissioned for that purpose. The physical scale model was tested while subject to a range of frequencies of incident, monochromatic waves in order to assess the frequency response of the motions of the model and the water columns. The frequency response of the wave power absorbed by the model, which operates a closed, thermodynamic system, driven by multiple OWCs, as described in Chapter 3, is determined using measurements of air pressure throughout the system. The 1:50 physical scale model of the platform was then tested while subject to a number of polychromatic waves. A numerical model of the physical model of the platform is developed in the frequency domain and validated using data from tank tests. The numerical model is used to draw conclusions as to the efficiency of the current proposed configuration of the platform.

In order to examine the behaviour of individual components in the proposed platform, the configurable single-chamber physical OWC model was to be constructed and tested in a 2-dimensional tank with, and without, a number of control components installed. The data thus obtained is used to validate time domain numerical models of the single-chamber physical model.

A secondary objective of this thesis is to investigate the effect of geometrically scaling air volumes in the tank testing of OWCs, and investigate a proposed new method of measuring the hydrodynamic parameters of an OWC.

1.4 Contributions

The main contributions of this thesis are:

1. The proposed WEI wind/wave energy platform has, through the work in this thesis, been progressed through TRL 3. This has been accomplished by:

    - The construction, instrumentation and deployment of a 1:50 physical scale model of the platform.
    - An extensive testing campaign during which the response of the platform, and the wave energy converting OWCs, was analysed, and the wave power absorbed determined, for regular waves of varying frequency under a number of platform configurations and with varying levels of applied damping simulating power take-off (PTO) systems.
    - The creation of a frequency domain numerical model of a 1:50 physical scale model of a multiple OWC device incorporating latching based on a time-averaged PTO damping applied to each OWC chamber obtained from tank test data. This numerical model has been implemented using a number of software tools, and, with some caveats, the predictions made by the numerical model compare favourably with the corresponding results from tank testing of the physical model.
    - A number of improvements that may be made to the general physical layout of the platform have been identified.

2. A numerical, time domain model of a single-chamber OWC, accounting for hydrodynamic and thermodynamic interactions, has been developed and implemented. This numerical model allows for the inclusion/exclusion of a number of control components which mey lead to latching of the water column. A means by which a limitation in the results obtained from commercial boundary element method (BEM) solvers may be overcome has been developed and implemented. The approach to numerically modelling a fixed, single-chamber OWC can be extended to model a floating OWC, or a set of interacting OWCs, such as that which the WEI platform comprises. The numerical model has been extensively validated against physical tank tests, both with and without control components.

3. An investigation into the effect of neglecting the compressibility of air in geometric scaling has been performed and has generated a data set for use in future investigations into means by which the effect of air compression may be accounted for in physical scale modelling.

4. A novel means by which the frequency-dependent hydrodynamic parameters of an OWC may be measured has been proposed. The use of spectral methods to measure such parameters for a range of frequencies from two tank tests, using polychromatic waves, has been proposed and investigated.

5. A narrow tank has been installed, calibrated, instrumented and commissioned at the Dundalk Institute of Technology (DkIT).

1.5 Organisation of thesis

This thesis is divided into twelve chapters. The content of each chapter is summaried below:

- Chapter 1
  - Chapter 1 comprises the Introduction.
- Chapter 2
  - Chapter 2 describes the context in which the proposed WEI platform has been devised by presenting an overview of wave energy conversion before the concept of the oscillating water column device is described. Next a literature survey covering the use of OWCs to extract energy from ocean waves is given and a review into the current state of combined wind/wave energy capture technologies is presented. Finally, in order to give a background to the theory presented later in this thesis, relevant works on numerical modelling are reviewed.
- Chapter 3
  - The first part of Chapter 3 gives a brief history of the involvement of WEI in wave energy. In order to familiarise the reader with the proposed WEI wind/wave energy platform, the general layout and operation of the platform is next described, before the preliminary work carried out on the platform, prior to the work described herein, is outlined. The proposed future development steps of the platform are then discussed.

- Chapter 4
  - Chapter 4 describes the theory that was used to create a frequency domain, numerical model of a physical scale model of the 32-OWC WEI platform which was tested in a large wave tank. Next, the software tools used to populate the parameters required to use the frequency domain numerical model to simulate the behaviour of the physical scale model are described. Results from the frequency domain numerical model of the proposed platform provide insight into future design considerations.
- Chapter 5
  - In Chapter 5, a numerical, time domain model of a single-chamber OWC is developed. A time domain model is developed in order to capture the effect of a number of non-linear processes which take place in the OWC chamber which cannot be adequately captured by a frequency domain model. The geometry of this model is such as to match one chamber of the physical scale model of the WEI platform. The numerical model is developed to include a number of control components. Non-linear terms are included in the numerical model, and the software tools required to populate the numerical model are described. An issue with the high-frequency added mass results for an OWC obtained from boundary element methods is discussed, and a means by which the issue may be overcome is outlined.
- Chapter 6
  - Chapter 6 begins by describing the design of, and rationale for, the experiments that were performed on the 1:50 physical scale model of the 32-OWC proposed wind/wave platform in the large wave tank then located in the Hydraulic and Maritime Research Centre (HMRC). The second part of Chapter 6 outlines the testing performed on the physical scale model of the single-chamber OWC, in various configurations, using the narrow tank at DkIT, and the rationale behind the tests.
- Chapter 7
  - In Chapter 7, the test facilities used in the physical tank tests described in Chapter 6 are discussed. Particular attention is paid to the narrow tank

facility in DkIT, which was commissioned as part of the work undertaken for this thesis.

- Chapter 8
  - Chapter 8 first describes the techniques used to construct the stainless steel 1:50 physical scale model of the proposed wind/wave platform. The second part of Chapter 8 outlines the techniques and materials used to build the single-chamber OWC physical model, which were inspired by 3-D printing methods. Sufficient design detail is provided so as to allow the reader to recreate the models.
- Chapter 9
  - Chapter 9 comprises two parts. The first part presents a comparison between the results obtained from the tank testing of the 32-OWC 1:50 physical scale model, and the corresponding estimates from the numerical model of the scale model in the frequency domain. A number of observations on the behaviour and performance of the platform are discussed. The second part of Chapter 9 presents a comparison between the results from the narrow tank testing and numerical modelling of the single-chamber OWC in the time domain.
- Chapter 10
  - Scaling of the compressibility of air is a well-known issue when physical OWC models are tested. In Chapter 10, the effect of this issue is investigated using two physical models, one where the volume of air in the OWC chamber is scaled according to geometric scaling, and the second where a larger volume of air is included in the physical model to better capture the effect of air compressibility.
- Chapter 11
  - Arising from the investigation into air compressibility, in Chapter 11, a novel approach to measuring the frequency-dependent hydrodynamic parameters for an OWC is proposed and implemented using monochromatic, and poly-chromatic, waves. Initial results for the process are presented, along with suggestions to improve the technique.

- Chapter 12
  - The final chapter presents a summary of the main conclusions arising from this work, and suggests some future work arising from this thesis.

1.6 List of publications

Journal article

- Kelly, T., Dooley, T., Campbell, J. and Ringwood, J. V., "Frequency Domain Testing and Simulation of a 32-OWC Floating Wave Energy Converter," *Energies*, Vol.6, pp 4045-4077, Aug. 2013.

Conference articles

- Kelly, T., Dooley, T., Ringwood, J. V. and Campbell, J., "Modelling and results for an array of 32 oscillating water columns" In *Proc. 10th European Wave and Tidal Energy Conf.* EWTEC2013, Aalborg, DK, Sept. 2013.
- Kelly, T., Dooley, T. and Ringwood, J. V., "Efforts towards a validated time-domain model of an oscillating water column with control components" In *Proc. 11th European Wave and Tidal Energy Conf.* EWTEC2015, Nantes, FR, Sept. 2015.
- Kelly, T., Dooley, T. and Ringwood, J. V., "Experimental determination of the hydrodynamic parameters of an OWC" In *Proc. 12th European Wave and Tidal Energy Conf.* EWTEC2017, Cork, IE, Sept. 2017.
- Penalba, M., Kelly, T., and Ringwood, J. V. "Using NEMOH for Modelling Wave Energy Converters: A Comparative Study with WAMIT" In *Proc. 12th European Wave and Tidal Energy Conf.* EWTEC2017, Cork, IE, Sept. 2017.

Technical Reports

- Kelly T. et al., "Analysis of Testing of Cúnamara Model in Ocean Basin," Technical report for Wave Energy Ireland produced under grant OC-09-19681164, May 2012.
- Kelly T. et al., "Report for JJ Campbell & Associates," Technical report for Wave Energy Ireland produced under grant OCN-00031, June 2014.[1]

[1]This report related to four separate objectives, the author was actively involved in objective 2, which comprised a desktop study into construction techniques and locations for a full-scale platform, and performed all the work pursuant to objectives 3 and 4, which relate to numerical modelling in the frequency and time domains. Objective 1 concerned considerations of a novel mooring design.

- "Case Studies with Companies - Case B5," Marine Investment for the Blue Economy (MARIBE), June, 2016. Available: http://maribe.eu/download/2710/.[2]
- Kelly, T., "A Technical Report on Oscillating Water Column Scale Model Testing - Results," Centre for Ocean Energy Research, May 2018.

[2]The author contributed technical and financial estimates to this report.

Chapter 2

Introduction to Wave Energy and Literature Review

2.1 Introduction

The extraction of energy from ocean waves relies on the interaction between a wave energy convertor (WEC) and the waves. A range of wave energy conversion technologies and devices are under development worldwide. In this chapter, a brief description of the most common technologies is presented. This is followed by a more detailed discussion of the specific concept and operating principle of an oscillating water column (OWC), and the advantages associated with it. A literature review of the historical development of WECs which are based on the OWC concept is then presented. Consideration is then given to a variety of PTO arrangements for use with OWCs. A summary of current and proposed combined wind/wave technologies follows. Subsequently, the mathematical theory which describes linear waves, and the hydrodynamic interaction of linear waves with physical bodies, is outlined. Next, a synopsis of existing techniques to numerically model OWCs is presented. Wave spectra, used to interpret and model realistic seastates, are then briefly described. Finally, the wave regime in the North Atlantic, the proposed deployment location for the full-scale WEI platform, is presented.

2.2 Conversion technologies

The absorption of wave energy by a WEC arises from the interaction of the WEC with ocean waves. The interaction gives rise to motion of some part of the WEC, which is dependent on the WEC geometry, and on the frequency components and the amplitude of the incident wave. The development of WECs has a long history. The patent issued to Pierre-Simon Girard and son, in 1799, is often cited as the earliest wave-energy related patent [24]. Since that time, a large variety of approaches to converting the power in ocean waves into useful energy have been investigated. Descriptions of the different technologies may be found in a number of books on wave energy, including [25–27] while review papers containing comparative studies between conversion technologies are also found in the literature, for example [7, 15, 28–30]. WECs may be classified based on:

1. location relative to shore
2. directional characteristics relative to an incident wave
3. operating principle.

Under the first classification system, a WEC may be onshore, near-shore or offshore. The proposed WEI platform, described in Chapter 3, belongs to the offshore category. While commonly used at one time, the classification of a WEC based on location relative to shore has fallen out of use in recent times.

When classified based on directional characteristics, WECs are divided into three categories: point absorbers, attenuators and terminators. These terms have been borrowed from acoustic and radio technology. A point absorber is a device where the primary dimension is significantly smaller than the expected wave lengths at a given location. Such WECs typically comprise an axisymmetric floater, and are capable of capturing energy from a wave interacting with the floater which has come from any direction, see Figure 2.1. Point absorbers are likely to be deployed in numbers in farms. The farm should be laid out so that the wave radiated by each floater constructively interacts with the incident wave to improve overall power absorbed by the farm, as described in [31]. Examples of point absorbers under development at the present time include the CorPower wave energy converter [32] and the PowerBuoy [33]. An attenuator is a WEC which has its principal axis placed parallel to the direction of the incident wave travel,

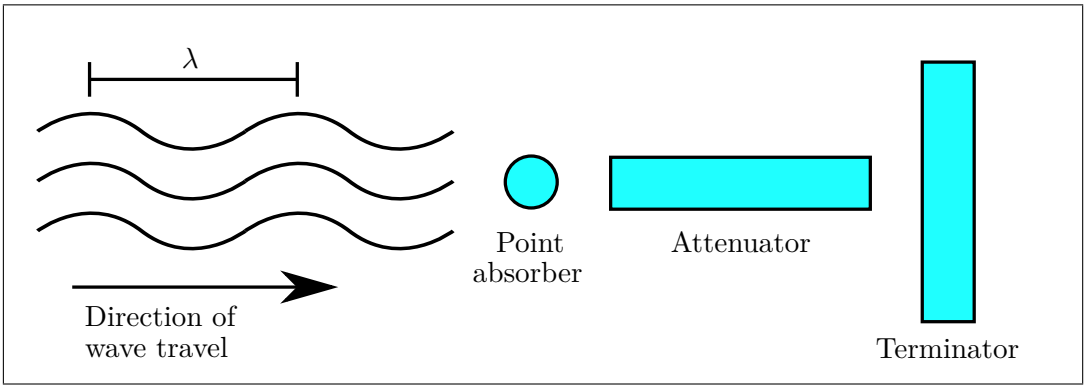

FIGURE 2.1: Schematic illustrating the classification of WECs based on orientation to incident wave.

see Figure 2.1. An attenuating device converts wave energy through the relative motion of the parts of the device as the wave propagates along the length of the device. Examples of proposed attenuating devices include the Pelamis [34], the McCabe Wave Pump [35] and the Wave Energy Conversion Corporation of America (WECCA) hinged barge [36]. A terminator is a WEC which has a principal axis perpendicular to the direction of incident wave travel, see Figure 2.1. Such devices attempt to prevent the incident wave from passing, and will absorb or reflect the energy in the wave. Examples include OWCs such as the Pico [37], Mitruku [38] and LIMPET [39], and overtopping devices such as Wave Dragon [40] and the Sea-wave Slot-cone Generator [41]. The concept and operating principle of OWC-type devices are discussed in greater detail in Section 2.3 and a literature review of existing OWC technology is presented in Section 2.3.1. The proposed WEI platform would be predominantly considered a terminator, as it comprises a plurality of OWCs, but the platform also exhibits some characteristics of an attenuator.

WECs may also be classified by operating principle. A large number of conversion concepts exist; however, the majority of proposed devices fall into one of three categories: oscillating body systems, overtopping systems and oscillating water column systems. Oscillating body systems absorb energy due to the motion of some part of the WEC, known as a prime mover, resulting from the interaction between the WEC and the incident wave. However, motion alone is not sufficient to extract power. The moving element of the WEC must react against something, for example, the seabed (as is the case for the Lysekil device [42]), a mass that is another part of the WEC (as was the case for the WaveBob device [43]) or the sea itself (for example, by using heave damping plates, as for the PowerBuoy device [33]). Oscillating body systems can be further

subdivided based on the degree of freedom used to absorb wave energy. The examples above operate primarily in heave, but another common approach is the hinged-flap type device, which operates in a pitching mode. Such flap-type devices include the Oyster device [44] and the Resolute Marine device [45]. Thus, energy is absorbed when a power take-off (PTO) mechanism is acted on by the relative motion between the prime mover and the reacting element, which converts the motion to usable energy. A brief summary of the most common PTO arrangements used in wave energy conversion is presented in Section 2.2.1.

Overtopping devices comprise a structure designed to channel the water in an incident wave to an elevated reservoir. The elevated water is allowed to return to sea level, in the process driving one or more low head turbines [46]. Perhaps the most well-known, floating overtopping device is the Wavedragon [40]. A number of onshore, fixed, overtopping installations have been proposed, and one was completed at Toftestallen, Norway in 1985, but the facility suffered extensive storm damage in 1988 and ceased operation [47].

Oscillating water columns are partially submerged, hollow structures which are open below the water surface, inside which air is trapped above the water free surface. In the most straight-forward realisation of the OWC concept, the heave motion of the sea surface alternately pressurises and depressurises the air inside the structure, generating airflow through a turbine installed in the device. The proposed WEI platform comprises a plurality of OWC chambers.

While the majority of WECs under development fall into one of the categories above, other concepts do exist, including, but not limited to, differential pressure devices (for example, the original Archimedes Wave Swing device [48]), bulging devices (for example, the Anaconda [49]) and rotating mass devices (for example, the Wello Penguin device [50]).

2.2.1 Power take-off

The transformation of the power in ocean waves to useful electrical (or other) energy is a multi stage process. In an oscillating body-type WEC, the hydrodynamic power in the wave is first captured and converted into mechanical energy, that is to say, work is

done by the wave on the prime mover. Due to the motion of the prime mover, some energy is returned to the surrounding water in the form of the radiated wave. The remaining energy, neglecting losses, is absorbed by the PTO. The reciprocating nature of the motion of a prime mover presents challenges to wave energy conversion, which are not a feature of, for example, wind energy conversion. Significantly, the level of energy absorbed by a WEC varies continuously with time in accordance with the energy variability in the incident waves. Electrical power may be generated by the coupling of the prime mover to a linear generator. Alternatively, the prime mover may be coupled to a pneumatic or hydraulic piston, which then generates a high-pressure fluid, which can be used to drive an impulse turbine, such as a Pelton wheel, which is, in turn, coupled to a generator. Such an arrangement was used by the Oyster device [51]. The high-pressure fluid may also be used to drive a reverse osmosis system to produce fresh water. PTO systems based on hydraulic or pneumatic arrangements may make use of accumulators to smooth the delivery of power over time.

The first stage of energy conversion in overtopping devices is the conversion of the kinetic energy in the wave into potential energy of the water stored in the reservoir. The potential energy is then reconverted into uni-directional kinetic energy flux as the stored water is allowed to return to the sea, and the kinetic energy is absorbed by low-head turbines coupled to electrical generators, to convert the kinetic energy into useable electrical energy.

The water column in an OWC device can be viewed as a prime mover. Energy in the incident wave causes the water column to oscillate, and this energy is converted into pneumatic energy as the air in the chamber is alternately pressurised and depressurised. The resultant airflow is used to drive a pneumatic turbine coupled to a generator to produce electricity. The reciprocating nature of the airflow requires either the use of a self-rectifying turbine, such as a Wells turbine or an impulse turbine, or that the airflow be rectified before it passes through a turbine suitable for uni-directional airflow, using check valves. The latter approach has been adopted for the proposed WEI device.

A number of control strategies have been investigated in order to improve the efficiency of wave energy devices. One approach, initially developed by Budal and Falnes for use on a point absorber [52], and later adapted for use with OWCs [22], is the concept of 'latching'. It can be shown that, for a passive PTO, the optimum level of absorbed power will occur at the resonant frequency of the prime mover of a device [25]. Resonance occurs when the velocity of the prime mover and the exciting force due to the incident

wave are in phase. The aim of latching is to mimic resonant conditions for incident waves not occurring at the resonant frequency of the prime mover by holding the prime mover stationary (known as 'latching the prime mover') so as to delay any movement until the wave force has built up to a threshold level. The prime mover is then released so that the velocity is in phase with the exciting force of the wave. Latching may be used to improve the performance of a WEC, when the incident wave frequency is less than the resonant frequency of the prime mover. If the frequency of the incident wave is greater than the resonant frequency of the prime mover, 'declutching' may be used. Declutching is effectively the reverse of latching, that is to say, under declutching, the prime mover is disconnected from the PTO and allowed to move freely for part of the cycle. The PTO mechanism is then engaged at the desired velocity. A form of passive latching is implemented on the WEI platform. A review of PTO strategies and hardware may be found in [53].

2.3 The oscillating water column concept

The OWC is one of the oldest and most investigated mechanisms for the conversion of wave energy. In its simplest form, an OWC comprises a chamber with an opening below the minimum level of the sea. As a wave propagates across this opening, the column of water within the chamber rises and falls, analogous to how waves interact with naturally-occurring blow holes [54]. The variation in water height within the column in turn pressurises and depressurises the air above the water. A turbine is located above the water column, and the airflow resulting from the pressure difference between the ambient air and that within the chamber is used to drive the turbine. The turbine is coupled to an electrical generator, which, for a large-scale device, would be grid-connected. OWCs may be fixed, such as the LIMPET [39] or the Mutriku breakwater [38], or floating, such as the OWC Spar Buoy [55] or the Backward Bent Duct Buoy [56]. Figure 2.2 illustrates a typical, fixed, OWC arrangement.

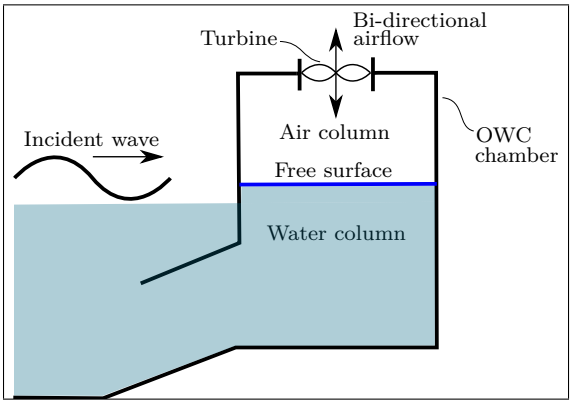

FIGURE 2.2: Schematic illustrating the major features of a typical, fixed OWC device.

The block diagram shown in Figure 2.3 illustrates the stages involved in the conversion of wave energy into electricity in an OWC system, and the flows of information between the stages.

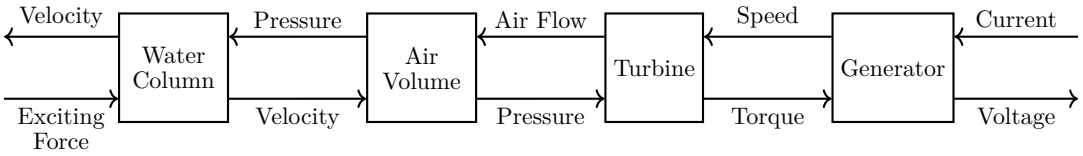

FIGURE 2.3: Stages in the transformation of wave energy into electrical energy and information flow for an OWC (modified from [57]).

As with other WECs, under monochromatic waves, an OWC will optimally absorb power when the frequency of the incident wave matches the resonant frequency of the water column. While other factors also effect the resonant frequency of a water column, the draft of the column is the primary parameter effecting the resonant frequency [58].

There are a number of advantages to the OWC concept over other WEC systems which made the OWC concept attractive to WEI at the initial design stages for the proposed platform. Firstly, the OWC is one of the most established approaches to wave energy conversion and there is a considerable volume of literature and research available on the subject. From the perspective of maintenance, there are fewer moving parts in an OWC device, when compared to other WEC designs, which could, potentially, reduce system downtime. In addition, there are no moving parts in the water, as the turbine, generator and associated electrical equipment are all located above the water level, making these components less susceptible to water damage, and easier to access for maintenance, when required. Furthermore, one of the main infrastructural elements of an OWC device is the collector/chamber. The staff at WEI have a background in civil and structural engineering. The chamber of an OWC device can be designed and constructed using

materials and techniques used elsewhere in these fields of engineering (for example, using reinforced concrete construction), techniques already familiar to the team at WEI. A further advantage to adopting an OWC device over other WEC systems is that, clearly, not all locations experience the same wave regimes, and the shape of an OWC collector may be adjusted to suit different locations, and withstand different loading conditions.

2.3.1 Historical development of OWCs

A number of reviews have been published in the literature (beyond those reviews which survey wave energy conversion in general) which focus specifically on the development of OWC technology, for example, [54, 59]. The phrase 'oscillating water column' was first used by Evans, in 1978, in a paper in which closed form solutions for the hydrodynamic parameters of a water column in a thin-walled vertical pipe were obtained [60]. Since that time, any entrapped volume of water which oscillates in response to an incident wave resulting in an airflow which may be converted into useful power, has been referred to as an OWC. However, the use of OWCs predates that designation by almost a century. Perhaps the earliest application of OWC technology was in the manufacture of navigation aids. As far back as the 1880s, numerous buoys were deployed off the coast of the USA with air-driven whistles. The whistles were powered by airflow generated by OWCs, and the buoys were designed to aid night time navigation [61]. One of the earliest recorded uses of an OWC to generate electrical power was installed near Bordeaux, in France, by M. Bochaux-Praceique in 1910. In Bochaux-Praceique arrangement, a bore hole in a cliff formed the body of the OWC, the airflow from which was used to drive a 1 kW turbine to provide power to light a domestic dwelling [62]. However, the systematic development of the OWC device began in Japan, in 1964, when Masuda, who had previously investigated a number of other approaches to wave energy conversion, began working with the Japan Research and Development Corporation [63]. The aim of this research was to construct wave-powered navigation buoys. Two buoys were developed, one based on a pendulum mechanism, and the second based on a tail-tube buoy which incorporates a vertical tube through the centre of the buoy which is open to the water at the bottom. In the second buoy, the airflow resulting from the relative motion of the water column to the rest of the buoy was rectified using check valves and used to drive an impulse turbine. The OWC-based buoy proved the most successful, and was widely deployed, with some buoys having in excess of 30 years' operation [64]. The

subsequent development of the self-rectifying Wells turbine allowed researchers to design buoys without the need for check valves [65]. A variant of the OWC-based navigation buoy using a Wells turbine may still be purchased from the Ryokuseisha Corporation [66].

The initial success of the OWC-powered buoy, coupled with the oil crisis of the 1970s, encouraged further research into OWCs in Japan. In 1978, under the direction of Masuda, and operating under the auspices of the International Energy Agency (with contributions from a number of countries including Ireland, the UK, Canada and the USA), the Japan Agency for Marine-Earth Science and Technology (JAMSTEC) deployed the Kaimei. The Kaimei was an experimental ship-like floating device with a displacement of 820 t, which comprised a number of OWC chambers, each rated at 125 kW. The reported number of OWC chambers varies (reported as 8 [54], 11 [63, 67], or 13 [59]). The Kaimei was initially deployed between 1978 and 1980 with eight turbines of various designs installed, incorporating different air rectification arrangements. Subsequently, the Kaimei was retrofitted and redeployed in 1985. On this occasion, two self-rectifying turbines were installed, in the form of one Wells turbine and one McCormick turbine [54, 59]. Three standard air turbines were also installed during the second deployment. Research into OWC technologies was also taking place at this time in other parts of the world, notably in the UK. A wave energy conference in 1978 included a number of papers on OWCs [67–69]. A UK government-sponsored programme funded investigations into a number of proposed WECs, including the multi-OWC chamber National Engineering Laboratory (NEL) shoreline device, which would also function as a breakwater [70]. The dimensions of the OWC chambers proposed in the NEL device are similar to those of the chambers in the proposed WEI device. However, as the oil crisis abated, funding for such projects in the UK ceased.

At the same time, in South Africa, a multi-chamber, onshore device was under development at the University of Stellenbosch [71]. The Stellenbosch device proposed to manifold and rectify airflow from multiple OWC chambers to produce uni-directional airflow. A similar idea to manifold the airflow from multiple OWC chambers was patented by Bolding in the USA in 1974, although, as presented in the patent, the OWC chambers were stacked vertically [72].

Ultimately, the power output from the JAMSTEC Kaimei device was below that expected [63]. This was in part due to the parasitic motion of the hull of the device with respect to the moonpools [73]. However, the hydrodynamic response of the water

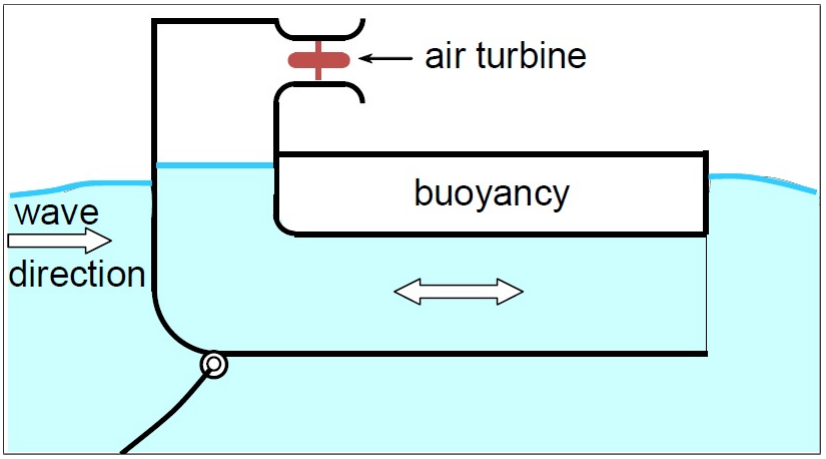

FIGURE 2.4: Schematic of the bent backward duct floating OWC device, (source: [59]).

columns was also poor [59]. As mentioned previously, the parameter which most influences the natural frequency of a water column is the draft of the column. In order to increase the draft of a water column for use in shallow water, and improve the absorption characteristics of the WEC, the concept of creating a floating bent duct was devised. Such a device is illustrated in Figure 2.4. While initially envisaged that the opening of the OWC chamber would face the incident wave, it was discovered by accident that the performance of the WEC improved if orientated so that the back of the device faced the on-coming waves [59]. A device, based on the bent duct concept, is currently being developed by Ocean Energy [74], who intend to test a full-scale prototype in a Hawaiian test site in 2018 [75]. In order to increase the effective draft of a fixed onshore OWC (as distinct from a floating OWC), a number of researchers have investigated the J-tube concept, both numerically [22], and experimentally [76]. The original profile of the chambers of the proposed WEI platform owe much to this previous research on J-tube OWCs.

In the 1980s, the development of onshore OWCs was to the fore. In 1984, Masuda oversaw the installation of a 40 kW onshore OWC device at Sanze, with the Japan Research and Development Corporation. Elsewhere, an OWC device was built in Norway at Toftestallen in 1985, near to the location of the overtopping device, with the intention of comparing the performance of the two devices, but the OWC was also destroyed by a storm in 1988. In 1989, a five-chamber, 60 kW OWC was built as part of the harbour wall at Sakata Port in Japan, and a 125 kW bottom-standing OWC device was installed at Trivandrum, India in 1990 [77]. An OWC with a rating of 75 kW was constructed on the island of Islay, Scotland and was commissioned in 1991 [78]. Development of onshore

OWC devices in Europe accelerated in the 1990s when the EEC Commissioner for Research allocated research funding into the JOULE 2 programme [79]. This programme led to the construction of two demonstration OWC power plants, one on the island of Pico on the Portuguese Azores, and the other on the island of Islay, close to the location of the earlier onshore OWC. Construction of the Pico plant commenced in 1996 and the plant was commissioned in 1999, although a further delay arose due to flood damage. The Pico OWC was equipped with a Wells turbine coupled to a 400 kW generator [80]. The Pico plant operated intermittently until the decision was made to dismantle the site as sufficient funds to maintain the project could not be obtained. Following a partial collapse of the facility in April 2017, all connections to the facility were removed, and the site was made safe [81]. The Land Installed Marine Pneumatic Energy Transformer, or LIMPET, OWC was built into the shoreline on Islay, with construction beginning in 1998. The plant was commissioned in 2000. The LIMPET featured two back-to-back, contra-rotating Wells turbines with a generator rated at 500 kW, although the rating was later reduced to 250 kW [39]. The LIMPET plant ran until 2013, when the operator of the plant, Wavegen Ltd., was closed. Both the Pico plant and the LIMPET provided useful knowledge and have been the subject of numerous publications, for example, [37, 82, 83]. The historical development of the Pico and Islay installations are described in detail in [84], and detailed technical specifications for the installations may be found in [85].

The Osprey device, which was backed by the Irish and UK governments, was a 2 MW-rated, bottom-mounted, near-shore OWC. Four 500 kW turbines were installed to be driven by back-to-back pairs of Wells turbines. While the device was constructed and deployment had begun in 1995, it was irreparably damaged during a storm before final deployment could be completed [85]. In 2010, the Australian company Oceanlinx deployed the grid-connected MK3 device. The MK3 comprised eight OWC chambers and was equipped with two types of turbine, a Denniss-Auld turbine, which is a variable-pitch, self-rectifying turbine developed by Oceanlinx, and which is described in [86], and a HydroAir turbine, designed by Dresser-Rand. In 2014, Oceanlinx attempted to deploy a 1 MW bottom-mounted, offshore device called the greenWAVE. However, in an incident reminiscent of the fate of the Osprey device, the greenWAVE device was lost during deployment. A similar, bottom-mounted, near-shore South Korean device, located at Jeju and rated at 500 kW, was successfully deployed in 2015 [59].

The Sakata OWC in Japan was one of the first instances of the inclusion of an onshore

OWC into a breakwater. However, a number of developers have explored the possible benefits of including wave energy conversion into breakwater structures, not least of which are the economic benefits of the shared construction costs. Indeed, the first wave energy design developed by WEI was the inclusion of OWCs into a proposed breakwater at Rossaveal harbour in Co. Galway, Ireland, see Chapter 3. A number of other breakwaters in Japan have also incorporated OWC technology. A 30 kW installation, comprising 10 OWC chambers, was constructed in Kujukuri in Japan in 1987, and a 40 kW OWC was operated in the Niigata breakwater between 1986 and 1988 [85]. A 130 kW-rated OWC, which uses rectification valves, was installed into a breakwater in Fukushima in 1996 [87]. Some research into OWCs has also taken place in China, where a 100 kW OWC was commissioned in 2001 [88]. In Europe, the Mutriku breakwater, in the Basque region of Spain, was commissioned in 2011. This breakwater incorporates 16 OWCs with multiple turbines and is rated at 300 kW, and, despite some operational issues, this plant continues to function [38]. The primary purpose of the Mutriku installation is to serve as a test bed for turbine and control design, see, for example, [89]. A number of other breakwaters incorporating OWCs are under consideration, such as the U-OWC at Civitavecchia in Italy. The cross-sectional profile of the OWC chambers in this installation are U-shaped, which increases the length of the water column. A review of breakwaters incorporating wave energy conversion may be found in [90].

During the 1990s and into the 2000s, research into floating OWC technology continued. Following on from the Kaimei, the Mighty Whale was deployed in Japan in 1998 [91]. This large, ship-like, floating device, the shape of which was designed to improve energy absorption and resembled the shape of a whale, displaced 4,400 t. The Mighty Whale comprised three OWC chambers using Wells turbines, and had a total rating of 110 kW [59]. While both the Kaimei and the Mighty Whale were large-scale, multiple-chamber devices, other researchers have considered the benefits of the so-called 'spar-buoy' concept. A spar-buoy comprises a long axi-symmetric OWC, and would be suitable for deep water locations, and such devices have been investigated through numerical, physical and economic modelling [92–94].

A number of variations on the concept of the OWC have also been developed. One variant was used in the Aquabuoy 2.0 device, where the motion of the water column is used to drive a piston which operates a rubber hose-based pump [95]. Another variant on the OWC concept can be seen in the PolyWEC device, where the pressure in the air above the water column is used to flex a dielectric elastomer, which creates a potential

difference across the elastomer [96]. The U-Gen device represents another realisation of the OWC concept [97]. The device comprises a closed, partially water-filled u-shaped vessel. The two legs of the u-shaped vessel are connected near the top via a duct through which air may flow between the two legs. As the vessel rotates, the water transfers between the legs of the vessel, and air is drawn through the duct at the top of the u-shape, and rotates a Wells turbine.

2.3.2 OWC power take-off

Air will flow from the OWC chamber to atmosphere through an aperture, which, in operation, would house a turbine, when the air pressure in the chamber is higher than atmosphere. The direction of airflow will reverse when the air pressure in the chamber is lower than atmosphere, and the reciprocating nature of the airflow poses a unique problem for the design of the PTO mechanism. Traditional air turbines are designed to operate in a uni-directional flow regime. In order to deal with the reciprocating nature of the airflow generated by an OWC, a number of approaches have been devised, including self-rectifying turbines, airflow rectification and the use of two uni-directional turbines, in the absence of rectifying valves.

Self-rectifying turbines

A self-rectifying turbine, is one which will rotate in the same direction irrespective of the direction of airflow. Two types of self-rectifying turbine dominate OWC research, namely, the Wells turbine, and impulse turbines, which may either operate in axial or radial flow regimes. The Wells turbine, named after its inventor, Prof. Alan Wells, comprises fixed symmetrical airfoil blades located around an axis perpendicular to the direction of axial airflow [98]. Wells turbines have been extensively tested and modelled, for example in [99–101], and are one of the few wave energy conversion technologies for which a large amount of real-world data exists against which full-scale numerical models may be validated [102]. and through the use of non-dimensional analysis, may be optimally designed to suit airflow and pressure conditions [103, 104]. Wells turbines may be used with, or without, guide vanes and a variant using radial airflow has been proposed in [59]. While providing uni-directional rotation for reciprocating airflow, the Wells turbine does have a number of disadvantages, notably lower efficiency, poorer self-starting

characteristics and higher operational noise levels when compared to conventional air turbines. A variation on the Wells turbine, which allows the airfoil blades to pitch over a range of angles as the direction of airflow changes, attempts to address the first two of these disadvantages. An advantage of the Wells turbine is that, unlike conventional turbines, the Wells turbine does not act as a pump [98]. Thus, any inertia the turbine possesses is not lost to air pumping under conditions of variable flow.

Axial impulse turbines use guide vanes on both sides of the runner to direct the airflow into radially mounted buckets. The buckets lie in a plane perpendicular to the axial airflow. The guide vanes may be either fixed or self-pitching. Axial impulse turbines have also been designed with two, contra-rotating, runners [105]. Self-rectifying impulse turbines may also operate using radial flow, as was proposed by McCormick [106], and have been studied both experimentally [107] and theoretically [108]. A numerical method by which a radial impulse turbine in a spar buoy may be optimally designed for different wave regimes is given in [109]. In general, impulse turbines are reported as having improved conversion efficiencies over a larger range of operating conditions when compared to Wells turbines [110]. A review of impulse turbine technology may be found in [111].

A third self-rectifying option is the Sevonius turbine, which might offer a low-cost alternative for low-energy sites [112]. A review of self-rectifying turbines may be found in [113], in which efficiencies for such turbines are reported between 0.3 and 0.56. A description of self-rectifying turbines and turbine topologies, including variants on the Wells turbine, such as the Denniss-Auld turbine, can be found in [86].

Airflow rectification

If conventional turbines are to be used to convert the airflow generated by an OWC into rotational motion, the airflow must be rectified. This is achieved using non-return (or check) valves. Non-return valves have two ports, an inlet and an outlet, and allow a fluid, in this instance air, to flow from the inlet to the outlet, but not in the opposite direction. A discussion on the design and operation of non-return valves may be found in [114]. The use of non-return valves to rectify airflow can be considered analogous to the use of diodes to rectify alternating electrical current. One of the earliest implementations of non-return valves in the context of an OWC can be found in the design of the navigation buoy initially proposed by Masuda [59]. While most OWCs using valves to

date have used automatic non-return valves, the possibility of using controlled valves to implement OWC latching has also been investigated [115]. Non-return valves are used in the proposed WEI platform to manifold and rectify the airflow generated by multiple OWC chambers operating out of phase with each other, as described in Chapter 3. By manifolding the airflow from multiple OWC chambers, the number of turbines required is reduced, which offsets the extra capital costs of the non-return valves. Other proposed multi-OWC chamber devices, such as the Seabreath [116], the Leancon [117] and the Tupperware device [118], use a similar approach to manifolding the airflow.

Two uni-directional turbines

A third, less common, solution that has been proposed in the literature is the use of two uni-directional turbines in the absence of non-return valves [105]. In this arrangement, each turbine works for half a cycle. When air flows from atmosphere into the OWC, the first turbine is driven, and when the airflow is reversed, the second turbine is driven. Through the use of properly-designed guide vanes, airflow through the non-driven turbine at each stage of the cycle is effectively choked. Each turbine has only one set of guide vanes, resembling the arrangement typical of a de Laval steam turbine, the concept from which the impulse turbine for wave energy was developed. An experimental investigation into the use of two impulse turbines in the absence of check valves is described in [119]. Figure 2.5 illustrates the turbine arrangement.

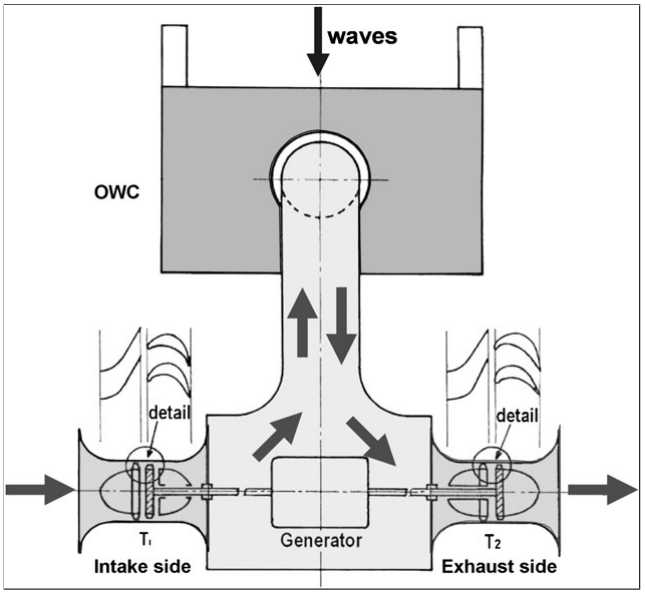

FIGURE 2.5: Schematic of a two-impulse turbines in the absence of check valves arrangements for OWCs. Source: [119]

2.4 Multi-use wave energy converting platforms

The potential benefits of the synergies between offshore wind and wave energy conversion are both legislative and economic. The European Union funded the ORECCA (Offshore Renewable Energy Conversion Platforms Coordination Action) programme under the Seventh Framework Programme (FP7) to investigate joint renewable energy sources, and focussed particularly on the combined wave and offshore wind resource [120]. The ORECCA project collaborated closely with the MARINA Project, which was also funded under FP7. The MARINA project specifically explored the technologies required to bring combined wind and wave platforms to a reality [121]. Testing on the scale model of the proposed WEI wind/wave platform formed part of the MARINA project [122].

Early wave energy pioneers wishing to exploit the larger wave energy resource located in the offshore environment proposed a number of large, floating structures. In 1977, a UK patent was granted to Masuda [123] who proposed a large ring-like polygon of a size larger than the longest wave from which the device would capture energy. The polygon was to comprise multiple OWC chambers and use check valves with impulse turbines. This patent also made reference to a V-shaped platform comparable to the form of the proposed WEI device. The airflow from multiple chambers was not manifolded in Masuda's patent. Likewise, wind energy engineers, aware of the increasing levels of

onshore wind saturation, began to consider floating offshore wind. One early concept was the Multiple Unit Floating Offshore Wind Farm (MUFOW) platform. MUFOW was envisaged as a floating, V-shaped platform supporting multiple wind turbines [124]. Other inventors proposed technologies to combine wind and wave energy, including an OWC-based structure to support a Darius-type wind turbine [125], an over-topping device including wind turbines and based on the Wave Dragon device [126] and [127], and a number of other concepts which use OWCs as the wave energy converting apparatus [128], [129] and [130]. The Australian Sustainable Energy and Desalination on Vessel (SEADOV) project [129] is of interest as the focus of the developers is on the desalination of water via reverse osmosis, rather than on the generation of electrical energy. Floating Power Plant A/S have developed a combined floating wind/wave platform called the Poseidon [131]. A 1:2.5 scale, grid-connected, demonstration unit of this device was sea trialled at Lolland in the Baltic Sea between 2008 and 2014. The demonstration unit, which supported three 2-bladed wind turbines, was rated at 33 kW of wind and 50 kW of wave power. The company envisages the full-scale device would be rated at 5 MW to 8 MW wind and 2 MW to 2.6 MW of wave power. A review of combined offshore wind and wave energy technologies can be found in [16].

A number of proposed wave energy platforms have converged on a V-shaped hull as a preferred configuration. One example is the Weptos device [132], which comprises two legs of multiple nodding floaters. The individual floaters are reminiscent of the Salter Duck device [15]. The angle between the legs of the Weptos may be varied to aid survivability in extreme weather. While the Weptos has progressed to tank testing, it appears the designers do not envisage the inclusion of wind energy on the platform at this time. Another V-shaped wave energy platform is the Leancon device [117], which shares a number of traits with the proposed WEI device. The Leancon, which has progressed to 1:10 scale sea trials, manifolds and rectifies airflow from a plurality of downward-facing OWCs. The Seabreath [116] is another floating, multiple-OWC device. Seabreath has been designed for deployment in the Mediterranean. Similarly to the proposed WEI device and the Leancon, the Seabreath would manifold and rectify the airflow from multiple OWC chambers using valves .

Many of the proposed combined wind/wave energy solutions essentially add one or more wind turbines to a platform that could otherwise function as a stand alone wave energy converting system, for example, the WindWaveFloat [133] being developed by Principle

Power. The WindFloat is a pre-existing floating wind concept based on a tripod arrangement, which uses large damping plates and water ballast which may be re-distributed between the legs of the tripod to stabilise the wind turbine. Principle Power have investigated incorporating different types of WEC into the existing float design, including OWCs, oscillating wave surge converters and point absorbers. A similar concept has been explored by Pelagic Power, who investigated a wind/wave tripod with two, rather than one, wind turbines installed [134].

2.5 Linear wave theory

In order to predict the behaviour of WECs in response to incident waves, numerical models of the pressures and velocities in the fluid through which the wave is propagating have been developed. The force acting on a body in a fluid due to an incident wave depends on the pressure exerted on the body by the wave. In the present section, a brief description of linear wave theory is presented. In the treatment that follows, water is assumed to be incompressible, that is to say, the density cannot change. In addition, continuity is assumed, in other words, that the mass of the fluid is conserved. Under the assumption of incompressibility, continuity of mass implies continuity of volume, which gives rise to Equation (2.1):

$$\frac{\partial u}{\partial x} + \frac{\partial v}{\partial y} + \frac{\partial w}{\partial z} = 0 \tag{2.1}$$

where x, y and z are the directions in a Cartesian coordinate system such that:

$$\begin{aligned} x &= \text{the positive direction of wave propagation} \\ z &= \text{the upwards positive direction} \\ y &= \text{a direction which forms a right-hand system with } x \text{ and } z. \end{aligned}$$

Further, u, v and w are the components of the fluid particle velocities in the x, y and z directions, respectively. Note that the origin of the coordinate system lies at the still water surface. Equation (2.1) may be re-written in vector form as:

$$\nabla \cdot \vec{V} = 0 \tag{2.2}$$

where the velocity vector, $\vec{V}$, is given by:

$$\vec{V} = u\vec{i} + v\vec{j} + w\vec{k} \tag{2.3}$$

and the operator, ∇, is defined as:

$$\nabla = \frac{\partial}{\partial x}\vec{i} + \frac{\partial}{\partial y}\vec{j} + \frac{\partial}{\partial z}\vec{k} \tag{2.4}$$

where $\vec{i}$, $\vec{j}$ and $\vec{k}$ are the unit vectors in the x, y and z directions. In general, flow is rotational if the fluid particle undergoes rotational motion in addition to translational motion. A rotational vector, $\vec{\omega}$, can be defined such that:

$$\vec{\omega} = \frac{1}{2}\nabla \times \vec{V} \tag{2.5}$$

The three components of the vector $\vec{\omega}$, around the Cartesian axes, are given by:

$$\omega_1 = \frac{1}{2}\left(\frac{\partial u}{\partial z} - \frac{\partial w}{\partial x}\right),\ \omega_2 = \frac{1}{2}\left(\frac{\partial v}{\partial x} - \frac{\partial u}{\partial y}\right) \text{ and } \omega_3 = \frac{1}{2}\left(\frac{\partial w}{\partial y} - \frac{\partial v}{\partial z}\right) \tag{2.6}$$

A function, ϕ, is now defined, such that:

$$u = \frac{\partial \phi}{\partial x},\ v = \frac{\partial \phi}{\partial y} \text{ and } w = \frac{\partial \phi}{\partial z} \tag{2.7}$$

ϕ is termed the velocity potential, and the velocity vector may be re-written in terms of ϕ as:

$$\vec{V} = -\nabla\phi \tag{2.8}$$

By substituting the expressions in Equation (2.7) into Equation (2.8), it can be shown that, if the velocity potential exists, $\omega_1 = \omega_2 = \omega_3 = 0$, showing that irrotational flow can be described using the velocity potential function. Substituting the expression in Equation (2.7) into Equation (2.1) results in the Laplace wave equation:

$$\nabla^2\phi = \frac{\partial^2\phi}{\partial x^2} + \frac{\partial^2\phi}{\partial y^2} + \frac{\partial^2\phi}{\partial z^2} = 0 \tag{2.9}$$

The Laplace Equation can be solved as a boundary value problem (BVP), subject to certain boundary conditions and subject to a number of approximations. It can be shown that the complete BVP cannot be solved in general.

2.5.1 Bernoulli equation

In order to solve the Laplace Equation BVP, boundary conditions must be established. Under certain conditions, the Bernoulli Equation can be obtained from the Navier-Stokes Equation. The Navier-Stokes Equation is given by:

$$\rho\frac{\partial\vec{V}}{\partial t}+\rho\left(\nabla\times\vec{V}\right)\times\vec{V}-\mu\nabla^2\vec{V}+\nabla\left(p+\rho gz+\rho\frac{\vec{V}^2}{2}\right)=0 \tag{2.10}$$

where:

$$\begin{aligned}\rho &= \text{density of the fluid in } kg/m^3\\ \mu &= \text{dynamic viscosity of the fluid in } Pa.s\\ g &= \text{acceleration due to gravity in } m/s^2\\ p &= \text{pressure in the fluid in } Pa.\end{aligned}$$

By rewriting $\vec{V}$ in terms of ϕ, assuming irrotational flow and that the wave is propagating through an ideal fluid (thus, $\mu=0$), Equation (2.10) may be written as:

$$\rho\frac{\partial\phi}{\partial t}+p+\rho gz+\frac{1}{2}\rho\left[\left(\frac{\partial\phi}{\partial x}\right)^2+\left(\frac{\partial\phi}{\partial y}\right)^2+\left(\frac{\partial\phi}{\partial z}\right)^2\right]=f\left(t\right) \tag{2.11}$$

where $f(t)$ is a function of time. For steady flow, where $^{\partial\phi}/_{\partial t}=0$,

$$p+\rho gz+\frac{1}{2}\rho\left(u^2+v^2+w^2\right)=\text{constant} \tag{2.12}$$

Equation (2.12) represents the familiar form of the Bernoulli Equation.

2.5.2 Boundary conditions

Three boundary conditions are commonly applied in the solution of the BVP in the derivation of wave theories, namely, the bottom boundary condition, the free surface kinematic condition and the free surface dynamic condition. The bottom boundary condition states that the seabed is impermeable and hence the vertical water particle velocity at the seabed is zero. This is expressed mathematically as:

$$\frac{\partial\phi}{\partial z}=0 \text{ at } z=-d \tag{2.13}$$

where d is the water depth. The free surface kinematic condition, which implies that a water particle on the free surface remains on the free surface, is given by:

$$\frac{\partial \phi}{\partial z} = \frac{\partial \zeta}{\partial t} + u\frac{\partial \zeta}{\partial x} + v\frac{\partial \zeta}{\partial y} = 0 \text{ at } z = \zeta \tag{2.14}$$

where ζ is the instantaneous free surface elevation at a point. The free surface dynamic condition is an application of the Bernoulli Equation to the free surface, in the form given in Equation (2.11) and yields:

$$\rho\frac{\partial \phi}{\partial t} + \frac{1}{2}\rho\left[\left(\frac{\partial \phi}{\partial x}\right)^2 + \left(\frac{\partial \phi}{\partial y}\right)^2 + \left(\frac{\partial \phi}{\partial z}\right)^2\right] + \rho g\zeta = f(t) \text{ at } z = \zeta \tag{2.15}$$

2.5.3 Small amplitude waves

The simplest, and most commonly used, wave theory based on potential flow was first developed by George Airy in the 19$^{\text{th}}$ century [135]. Airy's theory was developed for long-crested, sinusoidal waves in two dimensions which are periodic in time and in space. The instantaneous free surface elevation is given by:

$$\zeta = \frac{H}{2}cos\left[kx - \omega t\right] \tag{2.16}$$

where:

H = the wave height m

ω = the wave frequency rad/s

k = the spacial wave frequency, or wave number rad/m.

The wave number is related to the wave length, λ, by $k = {}^{2\pi}/_{\lambda}$. Airy theory makes a number of assumptions beyond those already discussed in order that a closed form solution for the velocity potential may be obtained from the Laplace Equation. One assumption is that the amplitude of the wave is small, thus any conditions that may be applied at $z = \zeta$ may be applied at $z = 0$. A further assumption is that the free surface boundary conditions may be linearised. In two dimensions, Equation (2.9) reduces to:

$$\frac{\partial^2 \phi}{\partial x^2} + \frac{\partial^2 \phi}{\partial z^2} = 0 \tag{2.17}$$

and the kinematic and dynamic free surface boundary conditions reduce to:

$$\frac{\partial \zeta}{\partial t} - \frac{\partial \phi}{\partial z} = 0 \text{ at } z = 0 \tag{2.18}$$

and

$$\frac{\partial \phi}{\partial t} g\zeta = 0 \text{ at } z = 0. \tag{2.19}$$

By applying the boundary conditions and using the separation of variables technique, solving Equation (2.17) for ϕ yields:

$$\phi = \frac{gH}{2\omega} \frac{\cosh k\,(z+d)}{\cosh kd} sin\,[kx - \omega t] \tag{2.20}$$

From the expression for ϕ in Equation (2.20), and by combining the two free surface conditions, the so-called dispersion relation, which relates wave frequency to wave length, can be obtained:

$$\omega^2 = gk \tanh\,(kd) \tag{2.21}$$

Expressions for the water particle velocity components can be obtained by combining Equation (2.7) and Equation (2.20) to give:

$$u = \frac{gkH}{2\omega} \frac{\cosh k\,(z+d)}{\cosh kd} cos\,[kx - \omega t] \tag{2.22}$$

and

$$w = \frac{gkH}{2\omega} \frac{\sinh k\,(z+d)}{\cosh kd} sin\,[kx - \omega t] \tag{2.23}$$

The water particle acceleration components may be obtained by differentiating the expressions in Equation (2.22) and Equation (2.23) with respect to time, while the displacements may be obtained by integrating the expressions in Equation (2.22) and Equation (2.23) with respect to time. The linearised Bernoulli Equation is given by:

$$p = -\rho \frac{\partial \phi}{\partial t} - \rho g z. \tag{2.24}$$

The expression for ϕ may now be substituted into Equation (2.24) to obtain an expression for the hydrodynamic pressure due to the wave:

$$p - p_{atm} = -\rho g z + \frac{\rho g H}{2} \frac{\cosh k\,(z+d)}{\cosh kd} cos\,[kx - \omega t] \tag{2.25}$$

where p_{atm} denotes atmospheric pressure. The first term on the right-hand side in Equation (2.25) is due to the hydrostatic pressure, and the second term is due to the action of the wave.

The total energy, per unit area, in a wave can be found by calculating the sum of the kinetic and potential energy. The potential energy can be found by considering the weight per unit area of the water column and multiplying by the height of the water mass centre. The time-averaged value of the potential energy, per unit area, is given by:

$$E_{pot} = \frac{\rho g H^2}{16} \tag{2.26}$$

The kinetic energy per unit area in a wave may be found by considering the part of the term $\frac{1}{2}\rho\left[u^2 + w^2\right]$ which is travelling in the positive x-direction. The water particle velocities, u and w, vary through the water column. The total kinetic energy can be found by integration from the water surface to the seabed, and yields:

$$E_{kin} = \frac{\rho g H^2}{16} \tag{2.27}$$

Thus, the total energy per metre in the wave is given by:

$$E_{tot} = E_{pot} + E_{kin} = \frac{\rho g H^2}{8} \tag{2.28}$$

The power transported by an Airy wave may be determined from the integral of the pressure in the wave multiplied by the velocity in the x-direction from the surface to the seabed. It can be shown (see, for example, [25]) that the energy transport is given by:

$$J = \frac{\rho g^2}{32\pi} T H^2 \tag{2.29}$$

The results obtained above pertain to Airy's theory. Other wave theories, including Stokes' finite amplitude and Cnoidal wave theories exist. A full treatment of the derivation of the velocity potential, using Airy's theory, can be found in, for example, [136], and a full treatment of the energy and power in a monochromatic wave can be found in [25]. A review of the historical development of wave theories can be found in [137].

2.6 Wave-body interactions

The modelling of the interaction between ocean waves and WECs, and the resultant behaviour of a WEC, based on an equation of motion, has been developed from hydrodynamic modelling from other marine applications such as ship design and the design of offshore structures. The history of numerically predicting the behaviour of floating bodies, subject to incident waves, can be traced back to the Mulberry harbours used during the Second World War [138]. Initial mathematical models failed to accurately predict the behaviour of the harbours and considerable efforts were subsequently made to devise more accurate models, leading to the equation of motion in common use [139, 140]. A rigid body moving under the action of an incident wave can operate in three translational and three rotational modes of motion, or degrees of freedom. Under the Cartesian coordinate system, described in Section 2.5, the translational modes in the x, y and z-directions are termed surge, sway and heave, and properties of the modes are assigned the subscripts 1, 2 and 3 respectively. The rotational modes around the x, y and z axes are termed roll, pitch and yaw, and these modes are assigned the subscripts 4, 5 and 6, respectively, see Figure 2.6.

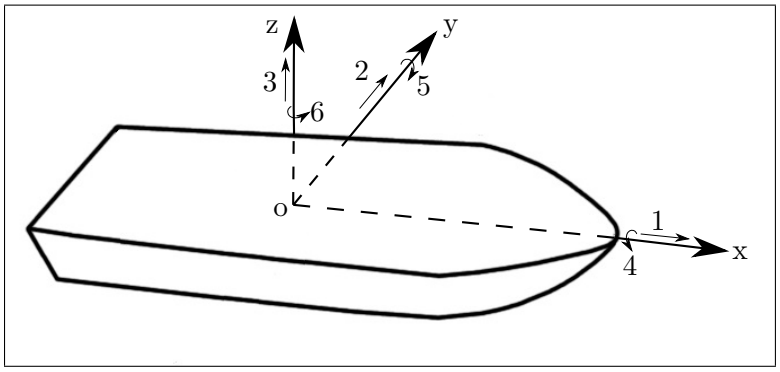

FIGURE 2.6: The six degrees of freedom of a rigid body (after [25]).

A body partially or fully immersed in a fluid, which is subject to an incident wave, will experience oscillatory forces and moments due to the hydrodynamic pressure acting on the wetted surface of the body due to the wave. The undisturbed incident wave will have some velocity potential, denoted ϕ_I. The wave will diffract around the body, resulting in a diffracted potential, denoted ϕ_d. If the body is free to move, the force acting on the body will cause it to oscillate, and the motion of the body will generate a radiated wave, with an associated radiated potential, denoted ϕ_r. All three potentials will effect the motion of the body. A hydrostatic force will act on a displaced, surface-piercing body

due to the change in the volume of water displaced by the body in modes 3, 4 and 5 (note, no change in the displaced water volume takes place in the remaining modes of motion). A further force will act on the body, if a PTO is used to extract wave energy. The linear hydrodynamic approach, classically taken to predict the behaviour of such a body, is based on a number of assumptions. The motion of the body is assumed to be small. As a consequence, it is assumed that the wetted surface of the body does not change with time. A further consequence is that the cross-sectional area of the body at the water surface, to which the hydrostatic forces and moments are related, does not change with time. In addition, the principle of superposition is assumed, meaning that the individual forces acting on the body may be evaluated separately, and linearly combined.

2.6.1 Exciting force

A number of theories have been devised to estimate the force acting on a body operating in a translational mode (or the moment acting on the body in a rotational mode) subject to incident waves, including Froude-Krylov theory, the Morison equation and diffraction theory. In the current work, diffraction theory is used to numerically model the behaviour of the proposed WEI platform. Under diffraction theory, the force acting on the body due to the incident wave in a translational mode is known as the exciting force, and arises due to the incident and diffracted wave potentials. For rotational modes, an incident wave acting on a body results in an exciting moment. As a consequence of the assumptions applied to linear hydrodynamics, the exciting force may be determined by assuming the body is held fixed and no radiated wave occurs. The approach is applied both theoretically and experimentally (where a fixed-body test may be used to measure the exciting force, see Chapter 11). Figure 2.7 shows a semi-submerged body in water, illustrating the vector, $\vec{s}$, which is the position of a point on the wetted surface, S, of the body and the unit normal, $\vec{n}$, at that point.

In diffraction theory, the exciting force (or, for $j = 4, 5$ or 6 the exciting moment), due to the incident and diffracted potentials in the j^{th} mode, Fe_j, is given by:

$$Fe_j = i\omega\rho \iint_S (\phi_I + \phi_d)\, n_j dS \tag{2.30}$$

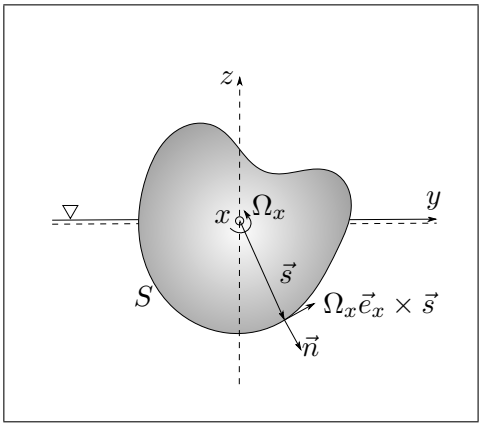

FIGURE 2.7: Schematic of a body oscillating in water due to the action of an incident wave. The vector, $\vec{s}$, is the position of a point on the wetted surface, S, while the vector, $\vec{n}$, is the unit normal at the point (after [25]).

Equation (2.30) has units of N for $j = 1, 2$ and 3 and N.m for $j = 4, 5$ and 6. Determining ϕ_d is known as 'solving the diffraction problem'. The diffraction problem is a BVP which may be solved using the boundary conditions used for ϕ_I and the wetted surface boundary condition given by:

$$\frac{-\partial\phi_d}{\partial n} = \frac{\partial\phi_I}{\partial n} \text{ on } S \tag{2.31}$$

The exciting force acting on a body is a frequency-dependent parameter. Note that, if the diffracted potential is neglected in Equation (2.30), the expression for the exciting force reduces to the exciting force predicted using Froude-Krylov theory. Froude-Krylov theory estimates the exciting force by integrating the undisturbed hydrodynamic pressure over the wetted surface of the body. Froude-Krylov theory assumes that the body does not interfere with the wave field, and hence no diffraction takes place.

2.6.2 Radiation force

The assumption of linear superposition allows the force required to generate the wave which radiates from a moving, semi-submerged body to be analysed in the absence of an incident wave. Experimentally, this process is known as a forced-oscillation test. In diffraction theory, the radiation force, which opposes motion of the body, is estimated by considering the velocity potential of the radiated wave, ϕ_r. Under linear conditions, ϕ_r may be expressed in terms of the velocity of the body, v, in terms of a proportionality

coefficient, φ. For a single degree of freedom:

$$\phi_r = \varphi_j v_j \tag{2.32}$$

and the radiation force for a single degree of freedom may be written as:

$$fr_j = i\omega\rho \iint_S \varphi_j v_j n_j dS \tag{2.33}$$

For a rigid body, the velocity is constant under the integration, and thus Equation (2.33) may be written as:

$$fr_j = -z_j u_j \tag{2.34}$$

where z_j is the radiation impedance in the j^{th} mode. Determining φ is another BVP, which is subject to boundary conditions, and is known as 'solving the radiation problem'. Using complex notation, z_j may be written as:

$$z_j = b_j + i\omega a_j \tag{2.35}$$

In Equation (2.35), b_j is known as the radiation damping and a_j as the added mass, both of which are frequency-dependent parameters.

2.6.3 Hydrostatic and PTO force

The hydrostatic force arises from the change in the mass of water displaced by the body as it moves. For a displacement, u, this force is given by:

$$fh_j = c_j u_j \tag{2.36}$$

where c_j is a proportionality constant known as the coefficient of buoyancy. That c_j is assumed constant is a result of the assumption that the motion of the body is small. In the heave mode, c_j is proportional to the cross-sectional area at the water plane, which may change with heave displacement. It is often possible to establish a relationship between c_j and the displacement of the body, which may then be used when the body is numerically modelled in the time domain to vary c_j with body displacement. Such a scheme is implemented in the time domain model of an OWC, described in Chapter

5. The force exerted by the PTO will depend on the nature of the system used. If the device is to be numerically modelled in the frequency domain, some form of linear force which is a function of a system variable must be used. It is common to model the PTO force as a function of velocity, in the manner of a linear damper.

Obtaining closed form solutions for the velocity potentials, and hence exciting and radiation forces, is infeasible for all but very basic geometries. However, numerical techniques have been developed to estimate the frequency-dependent parameters of arbitrary geometries based on the so-called 'panel method'. For an explanation of the panel method, see, for example, [25]. Both commercial and open-source software packages are available to estimate the frequency-dependent parameters for arbitrary geometries. The frequency domain equation of motion for the proposed WEI platform is derived in Chapter 4, and the time domain equation of motion for a single OWC, similar to those in the WEI platform, is derived in Chapter 5. In the current work, frequency-dependent parameters for a scale model of the proposed WEI platform, and for a single, fixed, OWC, are obtained using the commercial software package, WAMIT [141].

2.7 OWC hydrodynamic modelling

A number of approaches have been used in the numerical modelling of the behaviour of, and fluid flows in, an OWC. Computational fluid dynamics (CFD) and finite element analysis (FEA) have been used by some researchers [142] and [143]. While such approaches may incorporate non-linear effects, neglected in other approaches, these techniques are computationally expensive and, as the number of interacting elements increases, so does the computational expense. The approach used to numerically model OWCs in the current work is based on the linear theory presented in Sections 2.5 and 2.6. This approach assumes that the motion of the free surface of the water column matches that of an infinitely-thin, massless plate located on the free surface, and was first proposed by Evans [60]. The frequency-dependent exciting force, added mass and radiation damping, for the massless plate, are calculated numerically by solving the diffraction and radiation problems for the plate, and the equation of motion for the plate can then be solved. Evans also obtained closed form solutions for the hydrodynamic parameters of simple OWC geometries [144]. This approach assumes that the free surface of the water column remains plane, which may be considered reasonable when the wave length

is greater than one third the length of the OWC chamber, in the direction of wave propagation [145]. The commercial BEM solver, WAMIT [141], includes a routine to model the behaviour of an OWC modelled as an infinitely-thin plate on the free surface. This routine was modified, as described in Chapter 4, in order to numerically model the 32-OWC proposed WEI platform.

A related approach to modelling OWC behaviour is to assume that the pressure on the free surface of the water column remains constant [146]. The volume flux produced by the oscillating of the internal water surface and the so-called radiation admittance (comprising of the radiation conductance and the radiation susceptance) are analogous to the exciting force and the radiation impedance of the massless plate approach. A full treatment of the admittance approach may be found in [25].

2.8 Polychromatic waves

The waves described in Section 2.5 are monochromatic and harmonic in nature and are often described as monochromatic waves. Real ocean waves, which are stochastic in nature, and which are often referred to as irregular waves, may be approximated by a linear superposition of harmonic waves of different amplitudes and frequencies [147]. Note that this approximation has greater fidelity for swell waves than for locally-generated wind waves. Normally, only statistical information for a sea state comprising irregular waves is available for a given location. Such information describes the spectral characteristics of the sea state, in terms of displacement and frequency parameters. The displacement parameters include:

- one third significant wave height, H_s (also known as $H_{1/3}$) or H_{m0}, defined as the average of the one-third highest waves in a wave record
- average wave height, H_{av}, defined as the average height of the waves in a wave record

The frequency parameters include:

- zero crossing wave period, T_z, defined as the average time interval between similar direction crossings of mean water level for a wave record

- significant wave period, T_s, defined as the average period of the one-third highest waves in a wave record
- energy period, T_e, defined as the wave period corresponding to the weighted average of the wave energy in a spectrum
- peak period, T_p, defined as the period in a spectrum with the maximum energy.

Wave spectra represent a sea state by illustrating the distribution of wave energy in the sea state as a function of frequency. The spectral energy density function, S, may be calculated in terms of cyclic ($S(f)$) or circular frequency ($S(\omega)$), and the two forms are related by:

$$S(f) = 2\pi S(\omega) \tag{2.37}$$

Many wave spectral parameters may be described in terms of spectral moments. The n^{th} spectral moment may be determined from the integral of the spectral energy density function by:

$$m_n = \int_0^\infty \omega^n S(\omega)\, d\omega \tag{2.38}$$

In terms of spectral moments:

$$H_s = 4\sqrt{m_0} \tag{2.39}$$

$$T_s = \sqrt{\frac{m_0}{m_1}} \tag{2.40}$$

$$T_z = \sqrt{\frac{m_0}{m_2}} \tag{2.41}$$

$$T_e = \frac{m_{-1}}{m_0} \tag{2.42}$$

The time-averaged power per metre of wave in an polychromatic wave is given [27] by :

$$J = \frac{\rho g^2}{64\pi} H_s^2 T_e \tag{2.43}$$

Most of the energy in real ocean waves occurs in periods between 5 s and 15 s [25]. Table 2.1 shows the frequency occurrence of pairings of significant wave height and zero-crossing period for the North Atlantic. For a full treatment of the description and modelling of irregular ocean waves, as well as the techniques of estimating wave spectra from measurements, see, for example, [148].

Probability of sea-states in the North Atlantic described as occurrence per 100000 observations.
Derived from BMT's Global Wave Statistics

Hs/Tz	1.5	2.5	3.5	4.5	5.5	6.5	7.5	8.5	9.5	10.5	11.5	12.5	13.5	14.5	15.5	16.5	17.5	18.5	SUM
0.5	0.0	0.0	1.3	1337	866.6	1186.0	634.2	186.3	36.9	5.6	0.7	0.1	0.0	0.0	0.0	0.0	0.0	0.0	3050
1.5	0.0	0.0	0.0	293	906.0	4976.0	7738.0	5569.7	2375.7	703.5	160.7	30.5	5.1	0.8	0.1	0.0	0.0	0.0	22575
2.5	0.0	0.0	0.0	22	197.5	2158.8	6230.0	7449.5	4860.4	2066.0	644.5	160.2	33.7	6.3	1.1	0.2	0.0	0.0	23810
3.5	0.0	0.0	0.0	0.2	34.9	696.5	3226.5	5675.0	5099.1	2838.0	1114.1	337.7	84.3	18.2	3.5	0.6	0.1	0.0	19128
4.5	0.0	0.0	0.0	0.0	6.0	196.1	1354.3	3288.5	3857.5	2685.5	1275.2	456.1	130.9	31.9	6.9	1.3	0.2	0.0	13289
5.5	0.0	0.0	0.0	0.0	1.0	51.0	498.4	1602.9	2372.7	2008.3	1126.0	463.6	150.9	41.0	9.7	2.1	0.4	0.1	8328
6.5	0.0	0.0	0.0	0.0	0.2	12.6	167.0	690.3	1257.9	1268.6	825.9	386.8	140.8	42.2	10.9	2.5	0.5	0.1	4806
7.5	0.0	0.0	0.0	0.0	0.0	3.0	52.1	270.1	594.4	703.2	524.9	276.7	111.7	36.7	10.2	2.5	0.6	0.1	2596
8.5	0.0	0.0	0.0	0.0	0.0	0.7	15.4	97.9	255.9	350.6	296.9	174.6	77.6	27.7	8.4	2.2	0.5	0.1	1309
9.5	0.0	0.0	0.0	0.0	0.0	0.2	4.3	33.2	101.9	159.9	152.2	99.2	48.3	18.7	6.1	1.7	0.4	0.1	626
10.5	0.0	0.0	0.0	0.0	0.0	0.0	1.2	10.7	37.9	67.5	71.7	51.5	27.3	11.4	4.0	1.2	0.3	0.1	285
11.5	0.0	0.0	0.0	0.0	0.0	0.0	0.3	3.3	13.3	26.6	31.4	24.7	14.2	6.4	2.4	0.7	0.2	0.1	124
12.5	0.0	0.0	0.0	0.0	0.0	0.0	0.1	1.0	4.4	9.9	12.8	11.0	6.8	3.3	1.3	0.4	0.1	0.0	51
13.5	0.0	0.0	0.0	0.0	0.0	0.0	0.0	0.3	1.4	3.5	5.0	4.6	3.1	1.6	0.7	0.2	0.1	0.0	21
14.5	0.0	0.0	0.0	0.0	0.0	0.0	0.0	0.1	0.4	1.2	1.8	1.8	1.3	0.7	0.3	0.1	0.0	0.0	8
15.5	0.0	0.0	0.0	0.0	0.0	0.0	0.0	0.0	0.1	0.4	0.6	0.7	0.5	0.3	0.1	0.1	0.0	0.0	3
16.5	0.0	0.0	0.0	0.0	0.0	0.0	0.0	0.0	0.0	0.1	0.2	0.2	0.2	0.1	0.1	0.0	0.0	0.0	1
SUM:	0	0	1	165	2091	9280	19922	24879	20970	12898	6245	2479	837	247	66	16	3	1	100000

The Hs and Tz values are class midpoints.

TABLE 2.1: Frequency occurrence of pairings of significant wave height and zero-crossing period for the North Atlantic (source: [149]).

Chapter 3

The WEI Floating Wind/Wave Platform

3.1 Introduction

In this chapter, WEI is introduced, and a history of the company to date, and its involvement in wave energy conversion research, is presented. The proposed wind and wave energy converting platform is then described. Finally, the plan for the future development of the project is outlined.

3.2 Wave Energy Ireland Ltd.

WEI was incorporated in 2009 with the aim of developing a large-scale, floating platform that would be capable of harnessing both wind and wave energy, and converting this energy into usable electricity. WEI is a subsidiary of J.J. Campbell and Associates, which is a structural and civil engineering consultancy. J.J. Campbell and Associates' interest in wave energy began in 2001, when the company submitted a proposal for a breakwater incorporating OWC technology to an open competition to design a breakwater for Rossaveal port in Co. Galway, Ireland. The primary objective of incorporating OWC technology into the breakwater proposed by J.J. Campbell and Associates was not to generate significant electrical power, but rather to provide a learning opportunity to promote an indigenous wave energy industry, and to provide a test bed for future wave

energy engineers. In this regard, the proposal preceded the Mutriku breakwater wave power plant, that was constructed in the Bay of Biscay off the north coast of Spain, and which began construction in 2006 [150]. J.J. Campbell and Associates' proposal failed to win the competition, and was cited as 'too futuristic' by the selection panel. Furthermore, construction of a breakwater at Rossaveal did not proceed at that time. J.J. Campbell and Associates did not subsequently actively pursue wave energy development until the economic downturn that occurred in the construction industry in Ireland from 2008 onwards.

In 2008, the floating energy platform was first conceived and christened the 'Cú na Mara', which translates from Irish as 'Hound of the Sea'. Shortly after this, in 2009, the Ocean Energy Development Unit (OEDU) was established within the Sustainable Energy Authority of Ireland (SEAI).[1] The OEDU made grant funding available to small to medium size enterprises (SMEs) for wave energy device development through the Prototype Development Fund. The Prototype Development Fund has subsequently part-funded the model construction and tank testing described in this work.

3.3 The WEI floating wind/wave platform

A schematic of the WEI platform can be seen in Figure 3.1. The platform is designed to harness both wave and wind energy. The large surface area of the platform may also be utilised to mount photo-voltaic solar panels and, depending on the conditions at the deployment site, the platform may also serve as a suitable location to instal tidal turbines. However, neither the solar nor the tidal energy possibilities are considered in this thesis. As with all design projects, the WEI platform has progressed through a number of design iterations, in part as a result of the work described herein. However, in all of the design iterations, wind power is harnessed using one or more horizontal axis wind turbines, and wave energy is harnessed using multiple OWCs.

The proposed platform consists of a large floating hull, comprising two legs joined at a 90-degree angle in a V-configuration. Each leg of the platform is approximately 245 m long. The device presents a total front of approximately 346 m to the incident wave. Cross trusses between the two legs of the platform provide the necessary structural

[1] Note, Sustainable Energy Ireland was founded in 2002 under the Sustainable Energy Act [151]. This body was rebranded the Sustainable Energy Authority of Ireland in 2010. For convenience, the Authority is referred to as SEAI throughout this thesis.

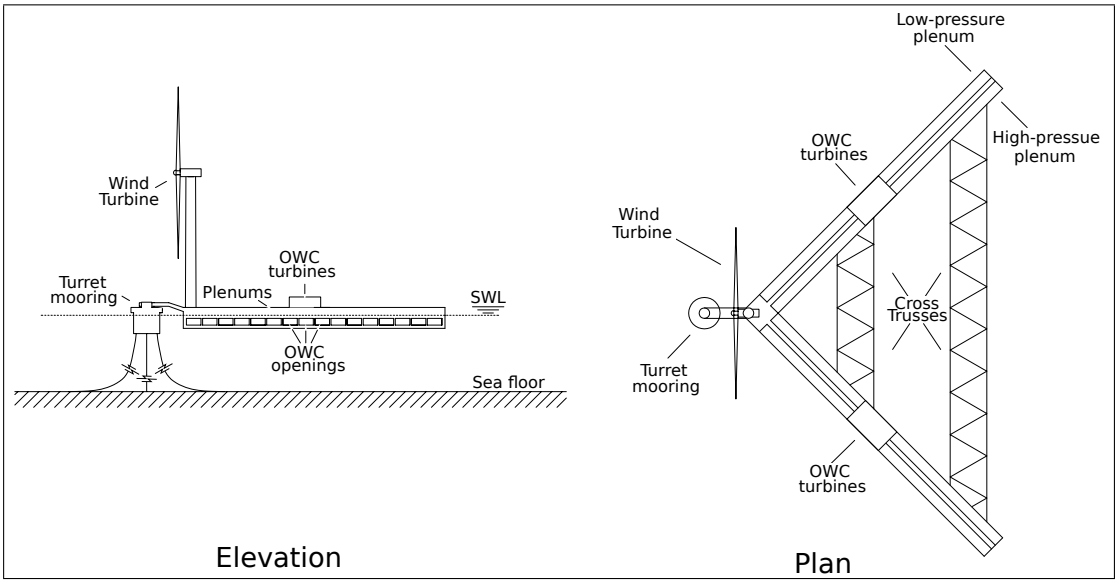

FIGURE 3.1: Schematics of the proposed WEI wind/wave platform.

strength to enable the platform to survive adverse sea conditions, and the platform has been designed in accordance with the relevant Det Norske Veritas (DNV) codes [152–155]. The overall footprint of the WEI platform bears similarities to that proposed by Masuda in [123], although the designs of the mooring arrangement are quite different. For the WEI platform, it is proposed to use a single-point floating production storage and offloading unit (FPSO)-style mooring located at the nose of the structure. Such a mooring would allow the platform to weather-vane into the direction of the incident waves. In this regard, the platform is similar to the Leancon device discussed in Chapter 2 [117]. However, as mentioned in Chapter 2, unlike the WEI platform, the Leancon device does not harness wind energy and, while of a comparable size, the Leancon device is smaller than the WEI platform.

In the design iteration shown in Figure 3.1, both legs of the platform incorporate a number of chambers with side openings. The chamber openings are located on the outside of the platform and below the water level to allow ingress of seawater to create a column of water within the chambers. While the exact number of chambers in each leg may vary depending on the prevailing conditions at a deployment site, each leg of the scale model platform, described in Chapter 8, comprises 16 OWCs. The geometry of the OWCs has been designed so that the resonant frequency of the pumping mode of the water column lies within the incident wave spectrum which the platform would experience in the North Atlantic, where it is envisaged the platform will be deployed.

Along the length of each leg of the platform, and above water level, high- and low-pressure plenums are situated. Each OWC chamber is connected to the two plenums on the corresponding leg via airflow conduits. Passive air admittance valves allow for air to flow in one direction only between each chamber and the plenums. The high-pressure plenum collects air that is generated by the upward movement of the water column in a chamber. Air will only flow into this plenum from a chamber if the air pressure within the chamber is greater than that within the plenum. Air from the low-pressure plenum will flow into a chamber, due to the downward motion of the water column in the chamber, if the air pressure within the chamber is lower than that within the plenum. Should the air pressure within a chamber at any time be less than that within the high-pressure plenum while also being greater than that within the low-pressure plenum, no flow of air between the chamber and the plenums will take place. Under this condition, the water column will become virtually locked, though some movement will take place, due to the compressibility of the air within the chamber. In this case, a 'latching' effect occurs, which can align the phase of the exciting force due to the incident wave and the phase of the velocity of the water column motion. This passive latching is based on a force threshold method, the theory of which is discussed in [156, 157].

Air is allowed to flow between the high-pressure and low-pressure plenums through a pneumatic turbine, which converts the pneumatic power to electric power. Each leg of the platform, and the associated chambers and plenums, form a closed system. By this means, the reciprocating flow of air from each OWC chamber is rectified, and the flows from all the chambers in one leg are manifolded together with the aim of providing a more uniform and smooth flow of air across the turbine.

As mentioned above, the WEI device will also serve as a stable, floating platform to allow for the installation of one or more offshore wind turbines. According to the European Wind Energy Association (EWEA), economic deployment of fixed, offshore wind turbines using monopiles or gravity-based foundations is limited to water depths of up to 40-50 m [158]. At this time, it is envisaged that a single, large, offshore horizontal axis wind turbine would be located at the nose of the WEI platform, ensuring that the turning moments acting on the platform due to the reaction of the wind force on the turbine will be minimised. This will eliminate the danger of such moments turning the platform beam-on to the incident waves when the wind and wave headings are not identical. WEI have also considered installing a number of wind turbines on the platform in an arrangement similar to the MUFOW discussed in Chapter 2. However,

at the time the MUFOW was proposed, the typical rating for offshore wind turbines, and hence the rotor diameter, was significantly lower than the current state-of-the-art wind turbines. The MUFOW was designed to accommodate wind turbines with rotor diameters less than 40 m. Modern offshore turbines can have blade diameters up to 180 m [159]. Turbine spacing wake effects limit the number of large turbines that may be installed on the WEI platform. At this time, WEI are concentrating on a single wind turbine design.

3.4 The current platform

The WEI floating platform was conceived in 2008. An initial feasibility study on the platform, funded by an Enterprise Ireland Innovation Voucher (IV–2009-1388), was completed [18]. On the back of this study, WEI secured funding from the ODEU of SEAI under the Prototype Development Fund (grant no. OC/OC/2009/19681164). This funding was phased to align to three milestones proposed by WEI:

- Milestone 1 - design and build a number of 1:50 scale devices to be tested in the flume located at the then Hydraulic and Maritime Research Centre (HMRC) in Co. Cork, Ireland.[2] These models, each of which comprised three OWC chambers, were used to investigate the effect on both the motion of the water columns and the power absorbed by the columns, of changing the chamber geometry, changing the angle of the incident wave and changing the damping level applied to the water columns. Frequency domain, numerical models of the physical scale models were also to be created.

- Milestone 2 - using the most efficient chamber geometry identified during Milestone 1, design and build a 1:50 scale model of a 32-OWC platform to be tested at the HMRC, to establish proof-of-concept of the wave energy converting element of the proposed platform. The scale model of the 32-OWC platform was to be tested in a number of configurations, as described in Chapter 6.

- Milestone 3 - develop a frequency domain, numerical model of the 1:50 scale 32-OWC model informed by the results of the testing obtained during Milestone 2.

[2]The HMRC has since relocated and been renamed the Lir Centre.

Concurrent with the work relating to the physical models carried out as part of Milestone 1, WEI engaged the Centre for Renewable Energy at Dundalk IT (CREDIT) to perform numerical modelling of the devices tested in the flume at the HMRC during Milestone 1. This numerical modelling, which was performed by the author, but does not form part of this thesis, was funded through another Enterprise Ireland Voucher (IV-2010-1069), and was completed in 2010 [21]. The final report on Milestone 1 was submitted to SEAI in 2010 [20]. Upon completion of Milestone 1, for efficiency, Milestones 2 and 3 were combined into a single milestone. WEI, in conjunction with the author, worked on Milestone 2 between mid-2010 and late-2011, designing and constructing the 1:50 scale model of the proposed platform from stainless steel. At that time, the concept envisaged stainless steel as the primary construction material. Note that the planned primary construction material has since changed to post-tensioned concrete, due primarily to cost concerns which have arisen in the intervening period. A complete set of drawings, which were required to cut, roll and weld the hull of the model, were drafted, and a number of subcontractors were engaged to perform these tasks. Once the hull of the model was built, WEI, in conjunction with the author, installed the ancillary components required to rectify airflow, and also a large number of sensors to be used to monitor air pressures, air flows, water column motion and platform motion during the extensive testing campaign. This 32-chamber testing piece is described in detail in Chapter 8.

In December 2011, the stainless steel test model was installed in the ocean basin test facility at the HMRC. Due to the complexity of calibrating the sensors and setting up the required data acquisition system, testing proper did not being until late January 2012. At that time, the author was awarded funding by the Irish Research Council for Science, Engineering and Technology (IRCSET), through the Enterprise Partnership Scheme, to continue work on this project pursuant to a PhD. The testing programme carried out at the HMRC, and the results generated, are the subject of Chapter 9. In brief, the testing programme investigated the feasibility of the platform both from the perspective of wave energy capture and also the suitability of using the platform as a location for offshore wind turbine installations. A number of important lessons were learned during this testing which have resulted in the modification of the original design to address potential issues, notably the tendency of the original platform to enter into a pitch resonance under certain wave conditions. Further, it was clear that the power

take-off associated with the OWCs was not optimised, and could be significantly improved. In addition, the author developed a frequency domain numerical model of the platform, which is tuned using the results obtained from the tank tests.

WEI delivered a final report to conclude the work associated with SEAI grant OC/OC/2009/19681164 in mid-2013 [23]. This report was largely written by the current author. During this time, WEI became a member of the Irish Wave Energy Developers Association (IWEDA). At the start of 2014, the company was awarded a further grant by the ODEU to conduct a number of desktop studies (grant no. OC/OC/2014/201414903). This allowed WEI to investigate a number of possible mooring solutions, including performing finite element analysis of the current proposed mooring solution. A number of possible construction sites and techniques were also explored. Numerical modelling was extended during this phase, notably to introduce a non-linear time domain model of a single-chamber OWC system, which is described in Chapter 5. The final report associated with OC/OC/2014/201414903 was delivered in June 2014 [160].

In 2015, a third-party marine consultant, Black and Veatch, was engaged to independently assess the report resulting from grant OC/OC/2009/19681164 relating to the 32-chamber model testing. This assessment [161] confirmed the validity of the testing techniques and data processing, and was broadly positive about the device. It did highlight a number of issues arising from the testing, notably those already identified by the author and the WEI team. Following the completion of the SEAI-funded projects, WEI considers that it has demonstrated proof of concept and proceeded through Technical Readiness Levels (TRL) 1 and 2, and into TRL 3 [162].

In late 2015, and following extensive discussions with SEAI, a third grant was awarded by SEAI to WEI (grant no. OCN/00031) to facilitate work to investigate the optimisation of chamber geometry from the perspective of energy capture. This work, which incorporates advice from Black and Veatch, was carried out at the narrow tank test facility at the Dundalk Institute of Technology (DkIT), but does not form part of this thesis. Further work to use finite element analysis to examine the structural integrity of the platform in response to extreme loads has also been carried out under this grant. The work associated with this grant is now complete [163]. A timeline showing the development of the platform to date is illustrated in Figure 3.2.

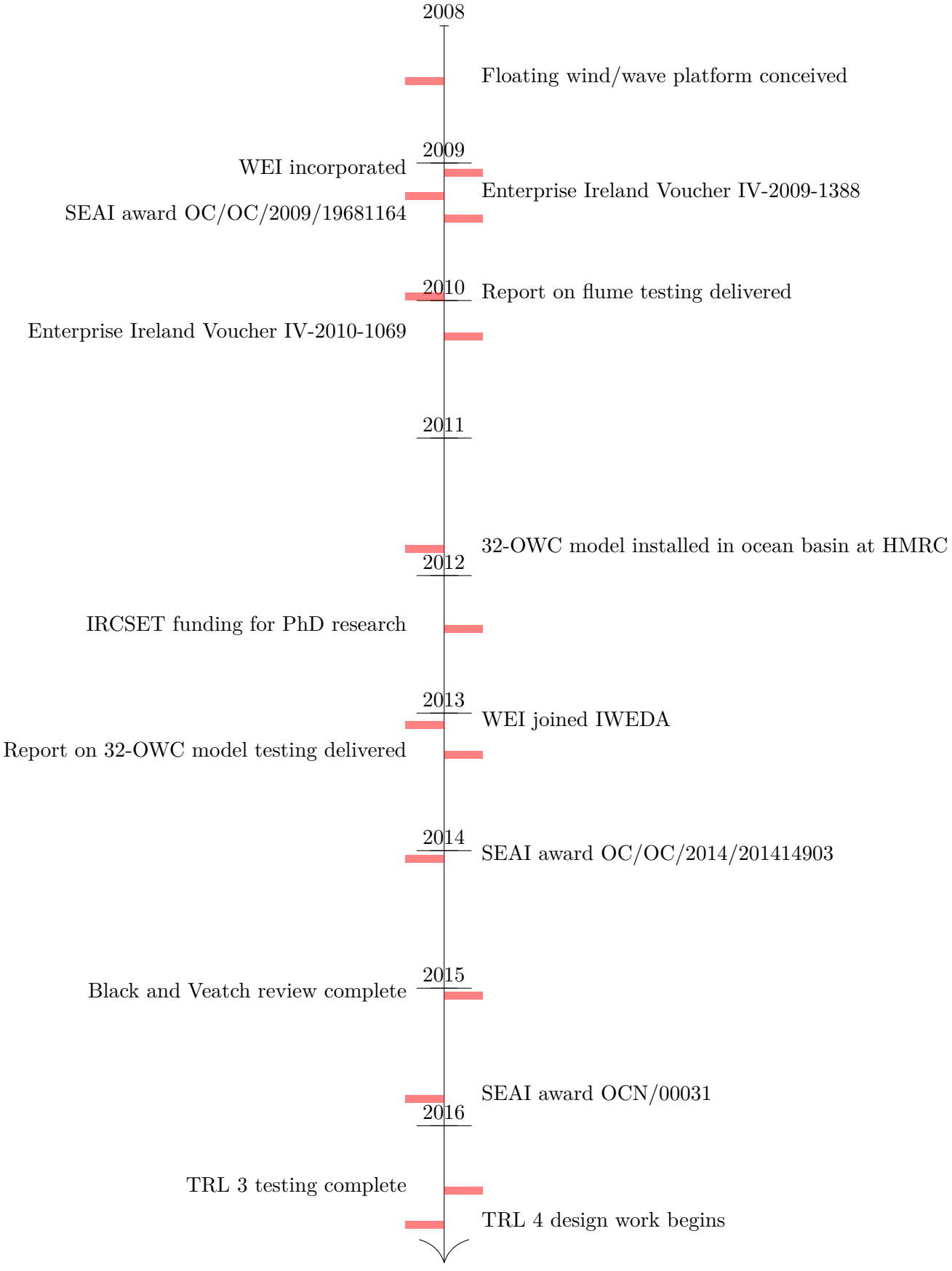

FIGURE 3.2: Timeline of the development of the proposed WEI wind/wave platform to date.

3.5 Future development of the WEI platform

WEI have laid out a development path for the proposed wind and wave energy platform. By following this path, it is intended that the proposed platform will progress along the TRL levels to the point where a commercial project, comprising a farm of multiple platforms, may be achieved. This development path is outlined below.

3.5.1 TRL 4 testing

The next step in the development path, leading to TRL 4, will see tank testing of a multi-chamber, modular platform, in a 3-dimensional wave tank, at a scale of 1:50. Based on the results of the rounds of tank testing that are the subject of this thesis, WEI has made a number of fundamental design changes to the floating platform as first proposed which relate to the primary construction material, the mooring arrangement and the hydrostatic stiffness of the platform in the pitch mode.

As previously mentioned, the primary construction material for the hull of the proposed platform has changed from stainless steel to reinforced concrete. The hull will be constructed from units comprising up to 5 OWC chambers, with each leg of the platform comprising up to 5 units. Bending moments and wave loadings will be sustained by a large superstructure constructed from space trusses.

As discussed in Chapter 9, at certain incident wave frequencies, the scale model tested under grant OC/OC/2009/19681164 underwent large pitch motion which, on a full-scale platform, would result in unacceptably large accelerations on a wind turbine at hub height. Two actions have been taken to reduce the pitch motion. Firstly, the mooring has been redesigned, and secondly, the pitch stiffness of the platform has been increased by increasing the moment of inertia of the water plane area.

The first objective of the tests, leading to TRL 4, is to determine experimentally if the efforts to address pitch stability have been successful. The second objective of the tests leading to TRL 4 is to measure, experimentally, the power absorbed by the model with manifolded OWC chambers, from known incident waves. The cross-sectional profile of the water column chambers in future multi-chamber models will be based on the optimum shape as determined from the 2-dimensional tests carried out under SEAI grant OCN/00031, referred to in Section 3.4. It is also intended to test a number of other power take-off arrangements, including manifolding groups of chambers on each leg, with

and without airflow rectification, and removing all manifolding from the system so that the airflow from each chamber is independent of all others. The results will be used, in conjunction with financial modelling, to determine the most cost efficient power take-off arrangement over the course of the lifetime of the proposed platform.

The final stage of TRL 4 testing requires that all but the two 5-OWC chamber units at the prow of the platform be removed from the model. This will result in a much shorter V-shaped platform, which may be thought of as the 'nose-piece' of the full platform and will comprise 10 OWC chambers. The purpose of this arrangement is to obtain data that may be used to correlate the behaviour of the nose-piece with the behaviour of the full platform to facilitate further testing. As the project proceeds along the TRL levels, the scale at which test pieces will be constructed increases, and the cost of the test pieces, and all associated costs, will increase concomitantly. Furthermore, at scales such as 1:10, few commercially available tank facilities are large enough to accommodate a complete model of the platform. Thus, once the correlation between the behaviour of the nose-piece with the behaviour of the full platform is known, it is intended to conduct larger-scale testing using only a nose-piece and extrapolate full platform results from nose-piece testing. It is estimated that this stage of the development plan will take approximately 2 years to complete and would be funded by WEI, with the support of the OEDU at SEAI.

3.5.2 TRL 5 testing

In order to progress the project to TRL 5, the next step of the development plan envisages the building of a 1:10 nose-piece model to be tank tested. This model will only be tested for one power take-off arrangement. The results from this testing will be used to verify estimates for the absorbed power and the forces acting on the mooring, hull and superstructure of the platform. These estimates will be based on the scaled up results from the testing associated with TRL 4. It is estimated that this step of the development plan will take 1.5 years and would be funded by WEI with the support of the OEDU at SEAI. Further funding under European programmes similar to MaRINET2 [164] may also be available. In this regard, relationships established under the MARIBE programme, a Horizon 2020 project in which WEI were invited to partake, may be useful. Upon completion of the testing associated with TRL 5, a 1:4 scale, nose-piece model will be designed.

3.5.3 TRL 6 testing

In order for the project to reach TRL 6, a 1:4 scale nose-piece model is to be constructed. This will be a substantial model, larger indeed than many full-scale prototype WECs, with each leg of the nose-piece platform currently envisaged as having a length of 10 m. This test piece would have a realistic power take-off and would generate electrical power. It is intended that such a test piece would be deployed in an ocean-based test facility, such as the SmartBay facility located off the west coast of Ireland where, due to shadowing of the Atlantic swell, the wave regime is close to a 1:4 scale representation of the typical North Atlantic regime [165]. This model would take up to 2 years to build, and would include a suitably-scaled wind turbine analogue. At that point, it is intended that the platform would remain deployed for up to 3 years in order that it may experience a wide range of wave and weather conditions. Once this testing is complete, the scale model has the potential to be re-located and re-used to generate useful electrical power for a niche location, for example, an island community or a fish farm. Due to the large costs associated with constructing and testing of this test piece, it is unlikely that WEI and SEAI alone could fund this step of the development plan. Either European funding, through a programme such as the Horizon 2020 programme, or a source of private funding, would be required at that point.

3.5.4 TRL 7 and 8 testing

Should the project successfully progress to TRL 6, it is envisaged that a full-scale prototype of the floating wind/wave platform, leading to TRL 7 and 8, would be constructed. The platform required for this testing would need the construction facilities of a custom-built fabrication yard. Precedent exists for the establishment of a facility that would be suitable for the construction of the platform in the form of Kishorn Port [166] on the northwest coast of Scotland, which was developed as a manufacturing and fabrication yard for oil platforms in the 1970s. This port included a circular dry dock of diameter 150 m, and was used to construct the Ninian Central oil platform which, upon completion, was the largest man-made moveable object in history. Kishorn dry dock is not currently in use, but could be recommissioned. As currently envisaged, the first full-scale prototype of the WEI wind/wave platform would be deployed at a suitable

full-scale wave energy test site, such as the Atlantic Marine Energy Test Site (AMETS), located off the west coast of Ireland [167].

3.5.5 TRL 9 deployment

TRL 9 would comprise a farm of platforms, located at a suitably energetic site in the North Atlantic. WEI are also exploring other opportunities for combining OWC and wind turbine technology.

Chapter 4

Frequency Domain Modelling

4.1 Introduction

Numerical models of WECs are useful design tools to further the development of the wave energy industry. Such models may be used to predict the behaviour of a WEC in response to incident waves, including the motions experienced by, and the forces acting on, and power output from, a WEC. The output from numerical models may be used to optimise WEC design from a cost, power production and survivability perspective. Numerical models may be further used in the design of suitable control strategies. The predicted energy production may be used as input to financial models. Numerical models may typically be developed for a significantly lower cost when compared to physical scale model equivalents. In order for a proposed WEC to advance through the technical readiness levels, numerical models must be developed, and validated against tank testing [168]. Furthermore, the development of numerical models of a WEC is a requirement for the awarding of funding by the OEDU within SEAI under the Prototype Development Fund [169]. In this chapter, a frequency-domain numerical model of the physical scale model of the 32-OWC WEI platform, described in Chapter 8, which was used for tank testing as discussed in Chapter 6, is presented. The theory underpinning the numerical model is first outlined. The software tools used to create the numerical model are introduced, and the use of the software tools is outlined.

4.2 Numerical model development

In this section, the theory which leads to the standard frequency domain equation of motion for a semi-submersible rigid body oscillating in a single degree of freedom in response to the action of an incident wave is briefly described. The frequency domain equation of motion is then extended to describe the motion in the six rigid body modes and the 32 pumping modes of the OWCs of the physical model of the WEI platform. The process of identifying the parameters of this equation to model the behaviour of the physical model of the platform is described.

A semi-submersible rigid body will oscillate in response to the action of an incident wave acting upon it. Several forces act on the body, and the total force acting on the body is the sum of all these forces. The force due to the incident wave, termed the exciting force, is denoted as Fe. The force due to the hydrostatic stiffness of the body (the buoyancy force) is denoted as Fh. As the body oscillates, it generates a radiated wave. The force required to generate this radiated wave is denoted Fr, and can be resolved into components in phase with the body acceleration and the body velocity. This gives rise to the concepts of the added mass and added damping. An external power take-off (PTO) device, or other external damping mechanism generates a force, Fu. Non-linear forces, F_{nl}, which are mainly due to viscous effects and vortex formation, also act on the body. If mooring lines are present, such lines will also result in forces which act on the body, which are typically non-linear and time variant and can be included in F_{nl}.

$$F_{total} = Fe + Fh + Fr + Fu + F_{nl} \tag{4.1}$$

For harmonic motion in a single degree of freedom in the i^{th} mode, the body will have a displacement, u_i, given by:

$$u_i = |u_i|\, e^{j\omega t} \tag{4.2}$$

where $|u_i|$ is the amplitude of the motion of the body, ω is the angular frequency of the motion of the body, and t is time. Under harmonic motion:

$$\begin{aligned}
&\text{Displacement} = u_i = |u_i|\, e^{j\omega t} \\
&\text{Velocity} = \dot{u}_i = j\omega\, |u_i|\, e^{j\omega t} = j\omega u_i \\
&\text{Acceleration} = \ddot{u}_i = j\omega j\omega\, |u_i|\, e^{j\omega t} = -\omega^2 u_i
\end{aligned}$$

Taking, for example, the heave mode of the body, denoted mode 3, the hydrostatic restoring force, F_h, is equal to the mass of the water displaced by the body multiplied by the acceleration due to gravity. Where CSA is the cross-sectional area of the body at the waterplane, the following expression for F_h is obtained.

$$F_h = -CSA \times \rho_{water} \times g \times u_3 \tag{4.3}$$

Equation (4.3) has the same form as a spring equation, that is to say, the force is proportional to the displacement by a constant. This constant, termed the coefficient of buoyancy, or the hydrostatic stiffness, c_{33}, is given by:

$$c_{33} = -CSA \times \rho_{water} \times g \tag{4.4}$$

and hence, Equation (4.3) may be re-written as:

$$F_h = -c_{33}u_3 \tag{4.5}$$

The force required to generate the radiated wave is resolved into two orthogonal components. The component of the force in phase with the body acceleration is considered to be due to an 'added mass' (denoted a_{33} for the heave mode). The added mass is thus the component of the force required to generate the radiated wave in phase with the acceleration of the body, divided by that acceleration. The component in phase with the body velocity is considered to be due to a 'radiation damping' (denoted b_{33} for the heave mode), and, similarly, that added damping is the force required to generate the radiated wave in phase with the velocity of the body, divided by that velocity. As the velocity and acceleration are 90 degrees out of phase due to the harmonic nature of the motion, these two components can be used to describe the total force required to generate the radiated wave. This force is in the opposite direction to the motion of the body. This leads to the following expression for the radiation forces for the heave mode:

$$F_r = -\left[-\omega^2 a_{33} + j\omega b_{33}\right] u_3 \tag{4.6}$$

In the frequency domain, the force due to a PTO system is typically represented by a linear damping term proportional to the velocity of the body. This leads to the following

expression for the radiation forces for the heave mode:

$$F_u = -j\omega d_3 u_3 \tag{4.7}$$

By combining the above terms, neglecting non-linear forces and noting that Newton's second law states that the total force acting on the body is the product of the body mass and body acceleration, the frequency domain equation of motion for a semi-submersible rigid body, operating in a single degree of freedom in the i^{th} mode, is given in [148] and others by:

$$fe_i(\omega) = \left[c_{ii} - \omega^2 (m_{ii} + a_{ii}(\omega)) + j\omega (b_{ii}(\omega) + di)\right] u_i \tag{4.8}$$

Equation (4.8) may be extended to multiple degrees of freedom where the linear coefficients are replaced by matrix equivalents, including any cross coupling terms, to yield:

$$Fe(\omega) = \left[C - \omega^2 (M + A(\omega)) + j\omega (B(\omega) + D)\right] U \tag{4.9}$$

It is convenient when performing power calculations to define the complex velocity vector, V, in terms of the displacement vector, U. The complex velocity vector is given by:

$$V = j\omega U \tag{4.10}$$

In terms of the complex velocity, Equation (4.9) may be rewritten as:

$$Fe(\omega) = \left[B(\omega) + D + j\left(\omega (M + A(\omega)) - \frac{C}{\omega}\right)\right] V \tag{4.11}$$

The use of the equation of motion may be extended to model OWCs using the approach first proposed by Evans [60], whereby the water column is modelled as a column of water with a massless, infinitely-thin disc located on the free surface of the water column. In the numerical modelling which follows, initially the platform is assumed to be free to operate in the six rigid body modes of motion (surge, sway, heave, roll, pitch and yaw), and that each of the 32 OWCs operate in the pumping mode only, where the surface of the OWC will move in the vertical direction, in a manor analogous to a piston. The assumption that the OWCs operate in the pumping mode only is based on the fact that, when subjected to waves with wavelengths which are long when compared to the OWC chamber dimensions, the water surface remains plane. In shorter wave lengths, sloshing

within the chamber will take place. The pumping mode of the water column is modelled as the heave mode of the massless disc. The first sloshing mode may be modelled as the pitch of the massless disc. However, the principle power mode will remain the pumping mode [144, 145]. Physically, the added mass of the massless disc in the heave mode may be thought of as the mass of the water in the chamber, as well as the added mass of the water which moves outside the chamber when the OWC is in motion. The motions of the platform and the water columns predicted by the numerical model are compared to those obtained from tank testing outlined in Chapter 9. As described in Chapter 8, the wave probes for the water columns are located at the centroid of the water column surface. Due to the location of the probes along the vertical centre line of the chambers, no rotational motion of the water columns is assumed nor was recorded. The numerical model thus considers a total of 38 degrees of freedom, the six rigid body modes of the platform and the 32 pumping modes of the OWCs. The remainder of the current chapter describes how the matrices and vectors in Equation (4.9) were determined.

4.2.1 Mass matrix

The matrix M in Equation (4.9) contains the inertia terms for the platform. For six rigid modes of motion, the mass matrix, (see, for example Chapter 3 [141]), is given by:

$$M_{6\times6} = \begin{bmatrix} m & 0 & 0 & 0 & mz_g & -my_g \\ 0 & m & 0 & -mz_g & 0 & mx_g \\ 0 & 0 & m & my_g & -mx_g & 0 \\ 0 & -mz_g & my_g & I_{11} & I_{12} & I_{13} \\ mz_g & 0 & -mx_g & I_{21} & I_{22} & I_{23} \\ -my_g & mx_g & 0 & I_{31} & I_{32} & I_{33} \end{bmatrix} \tag{4.12}$$

where:

m	=	the mass of the platform
(x_g, y_g, z_g)	=	the coordinates of the centre of gravity of the platform
I_{ij}	=	are the moments of inertia of the platform.

During tank testing, the physical model is positioned such that the incident waves are perpendicular to the prow of the platform, as described in Chapter 6. Due to the symmetric nature of the platform, while the heave and pitch rigid body modes are excited by the incident wave, the surge, sway, roll and yaw modes are not significantly excited. The surge, sway, roll and yaw coefficients are thus not considered by the numerical model, and the number of modes of operation is reduced from 38 (as was the case under the initial assumption) to 34. Hence, the rigid body mass matrix reduces to:

$$M_{2\times 2} = \begin{bmatrix} m & -mx_g \\ -mx_g & I_{22} \end{bmatrix} \tag{4.13}$$

Using the massless disc approach, this matrix is expanded to include the pumping modes of the OWCs as follows:

$$M = \begin{bmatrix} M_{2\times 2} & 0 & \cdots & 0 \\ 0 & 0 & \cdots & 0 \\ \vdots & \vdots & \ddots & \vdots \\ 0 & 0 & \cdots & 0 \end{bmatrix} \tag{4.14}$$

Note that all terms in the mass matrix in Equation (4.14) relating to the OWCs are zero as a consequence of the massless disc approach. Due to the large size and weight of the WEI platform, it was not possible to measure the mass or moments of inertia of the platform directly. Thus, a dimensionally-accurate computer aided design (CAD) model of the physical scale model of the platform was generated using AutoCAD, and the coefficients of the mass matrix in Equation (4.14) were determined using results obtained from the CAD model. While the use of dimensionally-accurate CAD models to determine parameters is not without some precedence [170], no validation for the use of AutoCAD in this context could be found in the literature. Thus, a validation process was undertaken to demonstrate the reliability of using CAD models to determine the mass and moments of inertia of a 3-dimensional semi-submerged body. During this process, a square box section of similar dimensions to the model platform was developed in stages. The volume (and hence the mass) and moments of inertia for the box sections, for which analytical solutions exist, where calculated by hand for each stage. These were then compared to the corresponding values calculated by AutoCAD, which may be obtained

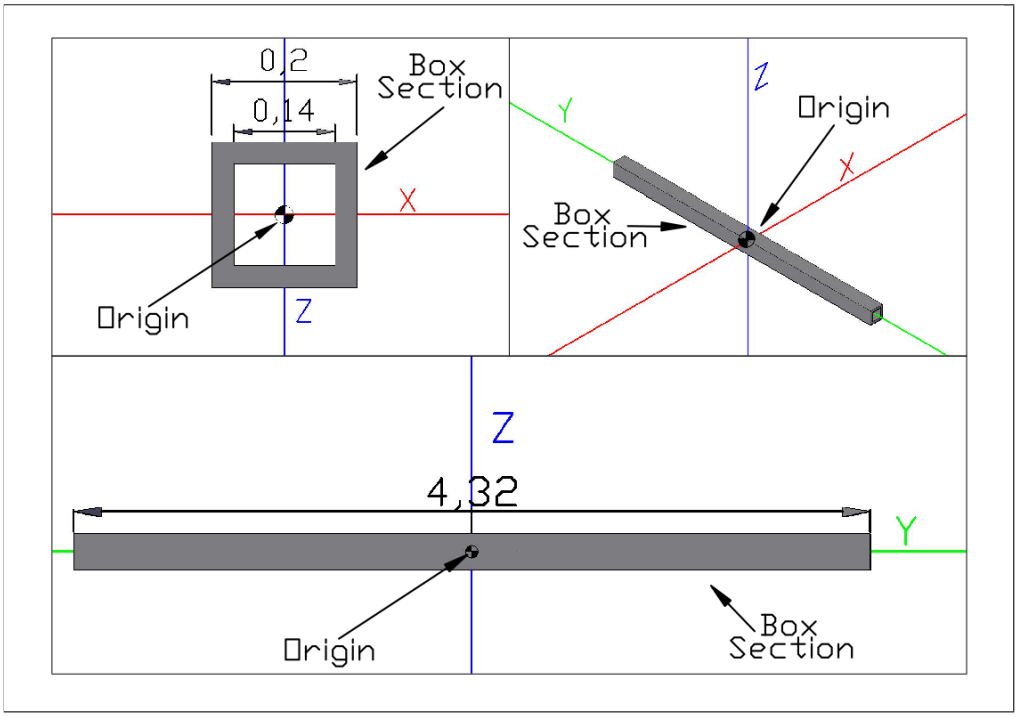

FIGURE 4.1: Elevation, isometric and plan view of a hollow square section of dimensions similar to one leg of the scale model platform.

using the *massprop* command [171]. The first stage of the validation process consisted of creating a CAD model in AutoCAD of a hollow box section of outer dimensions 0.2 × 0.2 m, inner dimensions 0.14 × 0.14 m, and length 4.32 m. These dimensions are similar to those of one leg of the physical scale model described in Chapter 8. The box section is assumed to have a draft of half its height, i.e., 0.1 m. The origin of this section is placed at the centre of gravity as shown in Figure 4.1, which illustrates an elevation, isometric and plan view of the box section.

The output from the *massprop* command for the box section shown in Figure 4.1 is:

```
---------------   SOLIDS   ----------------

Mass:                  0.0881
Volume:                0.0881
Bounding box:          X: -0.1000  --  0.1000
                       Y: -0.1000  --  0.1000
                       Z: -2.1600  --  2.1600
Centroid:              X: 0.0000
                       Y: 0.0000
                       Z: 0.0000
Moments of inertia:     X: 0.1375
                       Y: 0.0009
                       Z: 0.1375
Products of inertia: XY: 0.0000
                     YZ: 0.0000
                     ZX: 0.0000
Radii of gyration:     X: 1.2491
                       Y: 1.2491
                       Z: 0.0997
Principal moments and X-Y-Z directions about centroid:
                       I: 0.1375 along [1.0000 0.0000 0.0000]
                       J: 0.1375 along [0.0000 1.0000 0.0000]
                       K: 0.0009 along [0.0000 0.0000 1.0000]
```

As is highlighted in the output of the *massprop* command, the volume of the box section has been calculated by AutoCAD to be 0.0881 m^3. Note that the mass and volume figures given are equal, since AutoCAD assumes a default density of 1 kg/m^3 for the material from which the solid is constructed. The actual mass of the body can be determined by multiplying the mass by the density of the material in question. In order to verify that AutoCAD has correctly calculated the volume of the solid, the volume is determined analytically by subtracting the volume of the smaller inner rectangular region from the volume of the larger region:

$$\text{Volume of box section} = (0.22 \times 4.32) - (0.142 \times 4.32) = 0.0881 \text{ m}^3$$

As can be seen, agreement for the volume as calculated by AutoCAD, and analytically, is achieved to four decimal places. The moment of inertia for the section shown in Figure 4.1 can be found by firstly determining the moment of inertia for a solid section with

dimension equal to the outer dimensions of the section in Figure 4.1. The moment of inertia for a solid section with dimensions equal to the inner dimensions of the section in Figure 4.1 is next calculated. The moment of inertia for the actual section in Figure 4.1 may then be found by subtracting the moment for the smaller solid section from the moment of the larger solid section. For a cuboid of length d and width, w, equal to the height, h, the moments of inertia about the x, y and z-axes, I_{xx}, I_{yy} and I_{zz}, as shown in Figure 4.1, are given by, (see for example [172]):

$$\begin{aligned} I_{xx} &= \frac{1}{12} m \left(h^2 + d^2\right) \\ I_{yy} &= \frac{1}{12} m \left(w^2 + h^2\right) \\ I_{zz} &= \frac{1}{12} m \left(w^2 + d^2\right) \end{aligned} \tag{4.15}$$

As in the case for the mass, the results for the moments calculated by AutoCAD assume a material density of 1 kg/m^3, and the actual mass moments can be determined by multiplying these values by the density of the material in question. From Equation (4.15), and assuming a density of 1 kg/m^3, I_{xx} for the section shown in Figure 4.1 can be determined as follows:

$$\begin{aligned} I_{xx} &= \frac{1}{12} \times \left(0.2^2 \times 4.32\right) \times \left(0.2^2 + 4.32^2\right) - \frac{1}{12} \times \left(0.14^2 \times 4.32\right) \times \left(0.14^2 + 4.32^2\right) \\ &= 0.1375 \text{kgm}^2 \end{aligned}$$

For a body of uniform cross-section, such as that shown in Figure 4.1, $I_{xx} = I_{zz}$.
I_{yy} is determined from Equation (4.15) as follows:

$$\begin{aligned} I_{yy} &= \frac{1}{12} \times (0.2^2 \times 4.32) \times (0.2^2 + 0.2^2) - \frac{1}{12} \times (0.14^2 \times 4.32) \times (0.14^2 + 0.14^2) \\ &= 0.0009 \text{kgm}^2 \end{aligned}$$

As was the case for the volume calculation, agreement can be seen between the moments of inertia as determined analytically and those calculated by AutoCAD as highlighted in the output from the *massprop* command.

For the second stage of the process of validating inertia properties, as calculated by AutoCAD, the box section shown in Figure 4.1 is rotated round the Z-axis by 45 degrees, as shown in Figure 4.2.

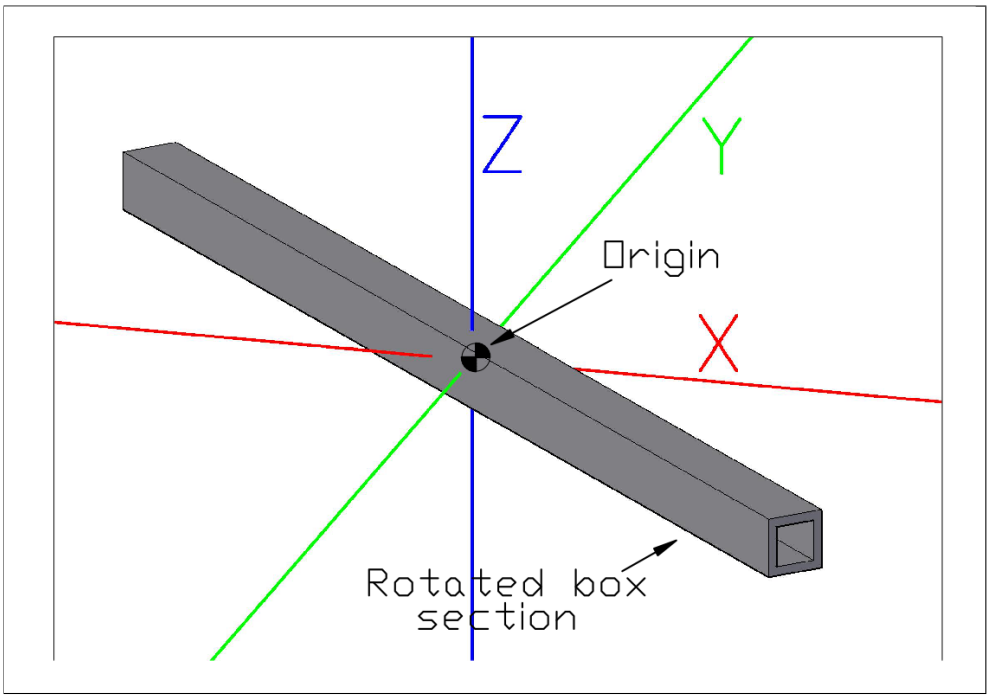

FIGURE 4.2: Box section rotated 45 degrees about the Z-axis during the second step in the process of validating inertia values calculated by AutoCAD.

As expected, the highlighted results from the *massprop* command, for the body in Figure 4.2, show a change in the moments of inertia about the X, Y and Z-axes compared to the body in Figure 4.1, while the volume of the body remains the same.

```
 ----------------   SOLIDS    ----------------

Mass:                    0.0881
Volume:                  0.0881
Bounding box:         X: -1.5981  --  1.5981
                      Y: -1.5981  --  1.5981
                      Z: -0.1000  --  0.1000
Centroid:             X: 0.0000
                      Y: 0.0000
                      Z: 0.0000
Moments of inertia:    X: 0.0692
                      Y: 0.0692
                      Z: 0.1375
Products of inertia: XY: -0.0683
```

```
                    YZ: 0.0000
                    ZX: 0.0000
Radii of gyration:   X: 0.8860
                     Y: 0.8860
                     Z: 1.2491
Principal moments and X-Y-Z directions about centroid:
                     I: 0.1375 along [0.7071 0.7071 0.0000]
                     J: 0.0009 along [-0.7071 0.7071 0.0000]
                     K: 0.1375 along [0.0000 0.0000 1.0000]
```

Analytically, the moments of inertia of the new body about the x, y and z-axes may be related to those of the original body, prior to rotation, by considering that, in general, for any inclined axis OA ([172]):

$$I_{OA} = I_{xx}u_x^2 + I_{yy}u_y^2 + I_{zz}u_z^2 \tag{4.16}$$

where u_x, u_y and u_z are the directional cosines. Terming the moments of inertia for the rotated box section in Figure 4.2 $\hat{I}_{xx}$, $\hat{I}_{yy}$ and $\hat{I}_{zz}$, and using Equation (4.16) with the results obtained for the box section before rotation:

$$\begin{aligned}\hat{I}_{yy} &= I_{yy}\cos(45)^2 + I_{zz}\cos(45)^2 \\ &= 0.00089 \times 0.70712 + 0.1375 \times 0.70712 \\ &= 0.0692\text{kgm}^2\end{aligned}$$

In the arrangement in Figure 4.2, it is clear that $I_{yy} = I_{xx}$, and that I_{zz} will not change. This is reflected in the highlighted output from the *massprop* command from AutoCAD. At this stage, agreement between the results obtained analytically and those calculated by AutoCAD has been achieved.

The final step of this validation process involves mirroring the box section shown in Figure 4.2 about the YZ plane to produce two legs arranged in a V-shaped configuration that is similar in form to the physical scale model of the WEI platfrom. The two sections are joined to form a single body using the *union* command, and the origin of the universal coordinate system (UCS) is placed at the centroid of this shape. This arrangement is illustrated in Figure 4.3.

The results from the *massprop* command for the V-shaped box section shown in Figure 4.3 are:

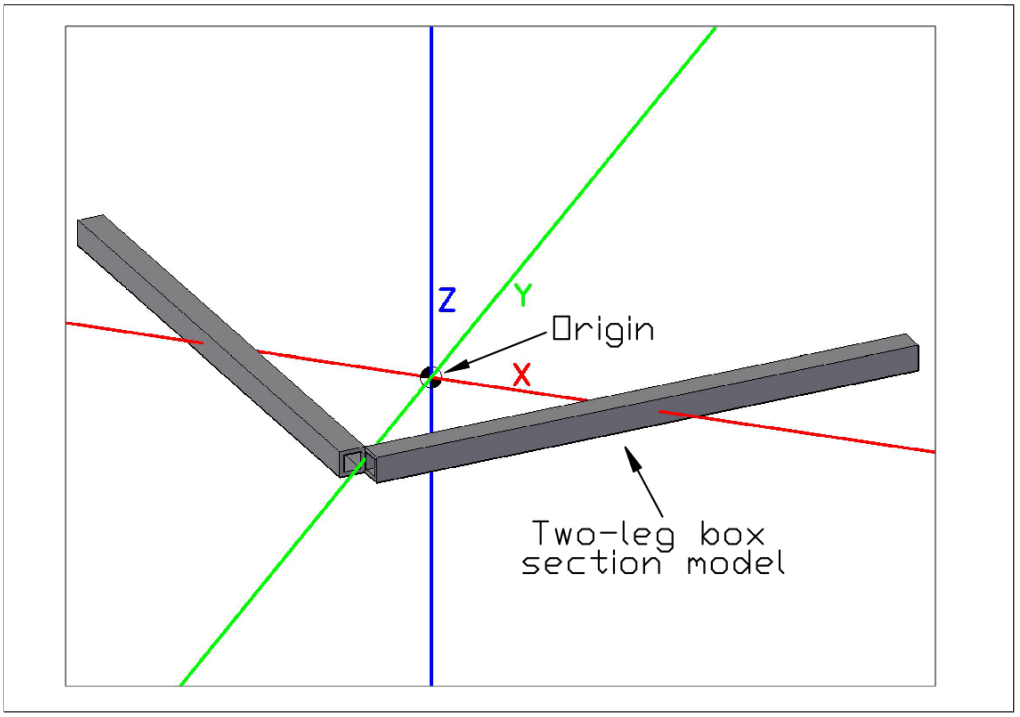

FIGURE 4.3: V-shaped box section model for use in the final stage of the process of validating inertia values calculated by AutoCAD.

```
  ----------------   SOLIDS    ----------------

Mass:                 0.1763
Volume:               0.1763
Bounding box:         X: -3.1962  --  3.1961
                      Y: -1.5981  --  1.5981
                      Z: -0.1000  --  0.1000
Centroid:             X: 0.0000
                      Y: 0.0000
                      Z: 0.0000
Moments of inertia:    X: 0.1384
                      Y: 0.5885
                      Z: 0.7251
Products of inertia: XY: 0.0000
                     YZ: 0.0000
                     ZX: 0.0000
Radii of gyration:    X: 0.8860
                      Y: 1.8273
                      Z: 2.0283
Principal moments and X-Y-Z directions about centroid:
                      I: 0.1384 along [1.0000 0.0000 0.0000]
                      J: 0.5885 along [0.0000 1.0000 0.0000]
                      K: 0.7251 along [0.0000 0.0000 1.0000]
```

The moments of inertia of the new solid, $\hat{\hat{I}}_{xx}$, $\hat{\hat{I}}_{yy}$ and $\hat{\hat{I}}_{zz}$, can be determined as follows:

$$\hat{\hat{I}}_{xx} = 2 \times \hat{I}_{xx} \text{from the rotated leg shown in Figure 4.2}$$
$$\hat{\hat{I}}_{yy} = 2 \times \hat{I}_{yy} \text{from the rotated leg shown in Figure 4.2} + \mathrm{ML}^2$$
$$\hat{\hat{I}}_{zz} = 2 \times \hat{I}_{zz} \text{from the rotated leg shown in Figure 4.2} + \mathrm{ML}^2$$

where:

M = mass of the body

L = distance between inclined leg centre of gravity and device centre of gravity.

The expressions for $\hat{\hat{I}}_{xx}$ and $\hat{\hat{I}}_{yy}$ arise from the Parallel Axis Theorem [172]. Thus:

$$\hat{\hat{I}}_{xx} = 2 \times 0.0692 = 0.1384 \mathrm{kgm}^2$$
$$\hat{\hat{I}}_{yy} = 2 \times 0.0692 + 2 \times 0.0881 \times (1.5981)2 = 0.5885 \mathrm{kgm}^2$$
$$\hat{\hat{I}}_{zz} = 2 \times 0.1375 + 2 \times 0.0881 \times (1.5981)2 = 0.7251 \mathrm{kgm}^2$$

Again, the agreement between the values obtained from the analytical solution, and those calculated by AutoCAD, and highlighted in the output from the *massprop* command, has been achieved. It has thus been demonstrated that AutoCAD can be effectively used to determine the volume, and hence the mass, and the moments of inertia of a 3-dimensional solid. Two AutoCAD models of the physical scale model of the WEI platform were developed. The first CAD model was drawn dimensionally accurate so that the wall thicknesses used matched those of the physical model made from rolled steel. The density of the rolled steel used to construct the model is known to be 7480 kg/m^3. Note that the windows which allow visual inspection of the water column chambers are made from PERSPEX cast acrylic, the density of which is 1.18 kg/m^3, which is significantly less than the density of stainless steel. As it was not possible to assign different density values to different elements of an AutoCAD model, the thickness of the windows in the CAD model has been reduced by the ratio of the density of PERSPEX to the density

of stainless steel, so that the mass of the windows is correct when the volume of each window as determined from the CAD model is multiplied by the density of steel. A similar approach was used to include the effects of ballast used to set the model draft. This ballast took the form of sand bags of known mass.

The second CAD model is a solid model of the volume of water displaced by the platform when set to the desired draft in the wave tank using ballast. The mass of the platform may be determined by multiplying the volume of this solid by the density of water, 1000 kg/m^3. As described in Chapter 8, concern was raised by WEI that the hull of the platform may be susceptible to leaks, and, for this reason, additional buoyancy was added to the physical model in the form of 120 mm diameter, sealed WAVIN pipes, located fully below the water level, and running the full 4.9 m length of both platform legs. The additional mass of water displaced by these may be calculated easily by determining the volume of water displaced by the cylindrical pipes. The location of the centre of gravity, the mass including appropriate ballast, and the moments of inertia of the physical scale model of the WEI platform were estimated from the CAD model of the full platform, with the effect of ballast included. The purpose of the AutoCAD model based on the mass of displaced water density was to verify the estimate of the mass of the physical platform calculated using the first CAD model. This was done since, while the density of steel used to make the physical model is known, some variation in the material density is possible. Variation in the density of water is unlikely. Note that it is not possible to estimate the location of the centre of gravity or the moments of inertia of the physical model of the WEI platform from the second AutoCAD model. Good agreement between the two estimates of the platform mass, one based on the density of steel of which the model comprises, and the second based on the density of the water displaced by the model, was achieved. The CAD model of the full physical model of the platform is shown in Figure 4.4, and the CAD model of the displaced volume of water, with the buoyancy pipes omitted for clarity, is shown in Figure 4.5.

4.2.2 Hydrodynamic matrices

The frequency-dependent hydrodynamic quantities, that is to say, the values in the added mass matrix, A, the radiation damping matrix, B, and the wave-induced exciting force vector, F_e, were determined using the numerical Boundary Element Solver,

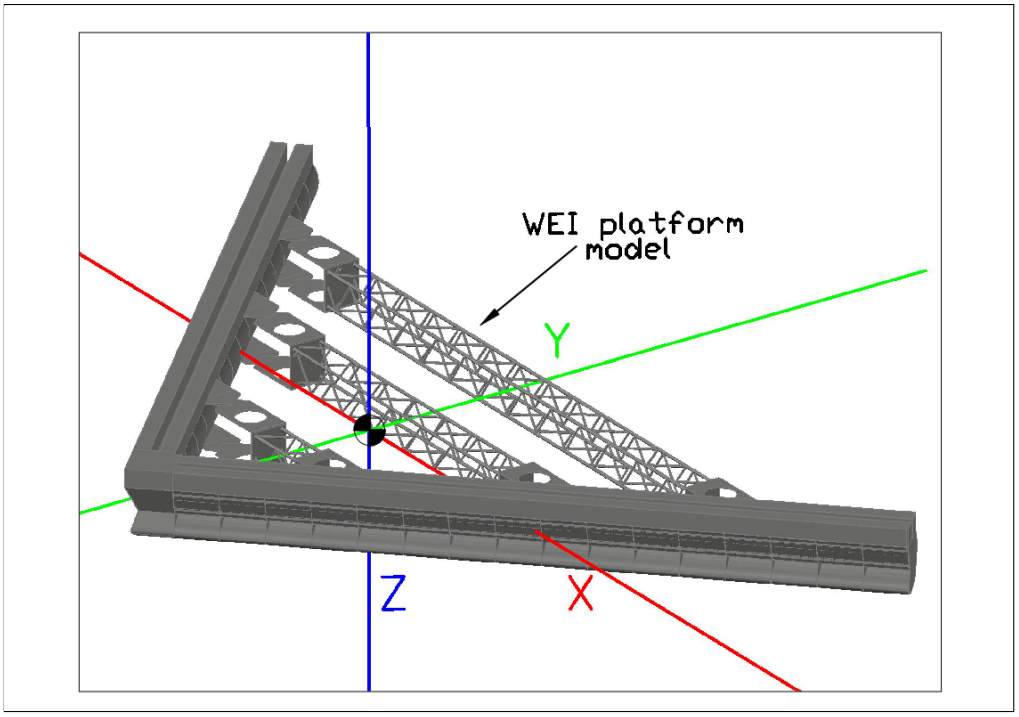

FIGURE 4.4: Dimensionally-accurate AutoCAD model of the physical scale model of the WEI platform used to calculate the mass, moments of inertia and centre of gravity of the physical scale model.

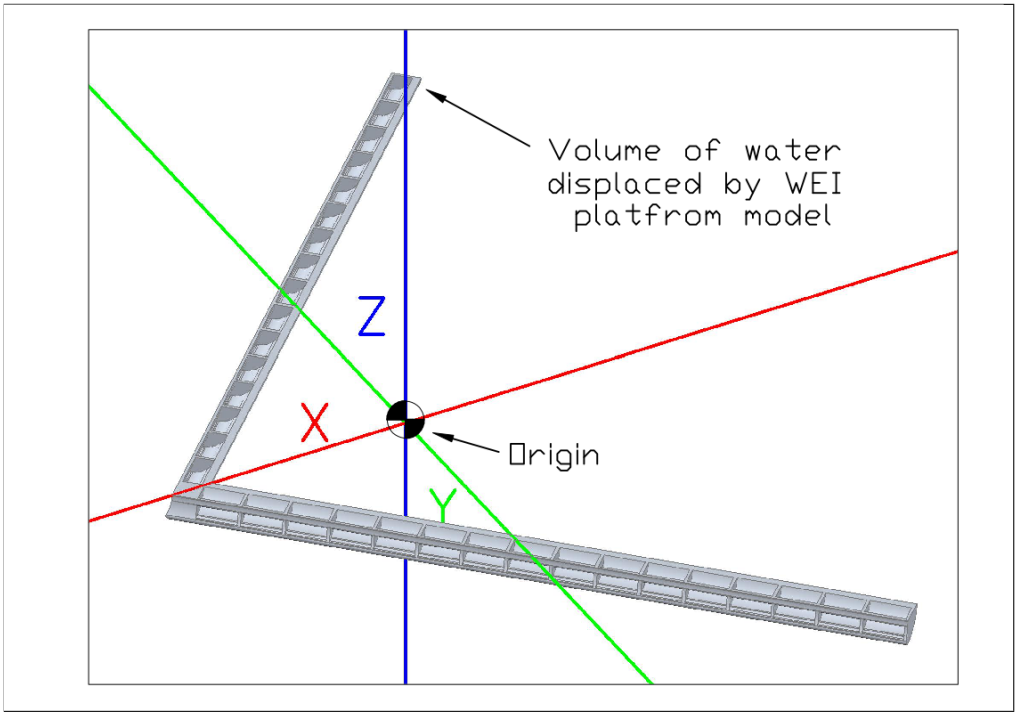

FIGURE 4.5: Solid AutoCAD model of the volume of water displaced by the physical platform model used to verify the mass of the physical model as calculated by AutoCAD.

WAMIT [141]. WAMIT uses the so-called 'panel method' described in, for example, [25]. When the panel method is used, the surface of a body, subject to an incident wave, is divided into small areas known as 'panels' and the effect of the incident wave on the body is determined by numerically calculating potentials and the resulting forces at the centroid of each panel, and summing the results. MultiSurf is a surface CAD modeller (as opposed to a solid modeller), where an object is represented by drawing the exterior surfaces of the object. Such a modelling technique lends itself readily to the creation of geometric representations of objects to be analysed using the panel method. Indeed, a close relationship exists between MultiSurf and WAMIT, and a drawing produced in MultiSurf may be exported in a format that can be directly interpreted by WAMIT [173]. A CAD model is created in MultiSurf from surfaces. The surfaces are formed from curves, and the curves are in turn defined by points in a Cartesian coordinate system. This coordinate system is known as the body coordinate system or body frame. WAMIT also employs a separate, global coordinate system, or global frame. The relationship between the body frame and the global frame is controlled by the input parameter *XBODY*, which the user must specify when performing a WAMIT analysis. When a model of a body geometry is being created for use in a WAMIT analysis, only that part of the body below the still water level should be drawn, that is to say, only the mean wetted surface of the body is included. The centre of gravity of the body should be located at the origin of the body frame, as WAMIT will assume the body rotates about the origin of the body frame, and calculate moments based on rotations around this point. The still water level is located on the z=0 plane of the global frame. The *XBODY* parameter is used to align the two frames so that the body is located correctly in the global system. For example, the centre of gravity of the surface CAD model of the WEI platform is located above the still water level. When drawn in MultiSurf, placing the origin of the body frame at the centre of gravity places some of the surfaces of the MultiSurf model above the Z=0 plane of the body frame. Therefore, a negative Z value equal in magnitude to the height of the centre of gravity of the platform above the still water level is required for use in *XBODY* to position the body correctly in the global frame. No model surfaces should exist on the still water level in the global frame unless they have a specific purpose. Thus, for the modelling performed herein, surfaces are drawn at the free surface level of each moonpool so as to indicate to WAMIT that an additional mode of motion is required to represent the moonpool. Figure 4.6 illustrates

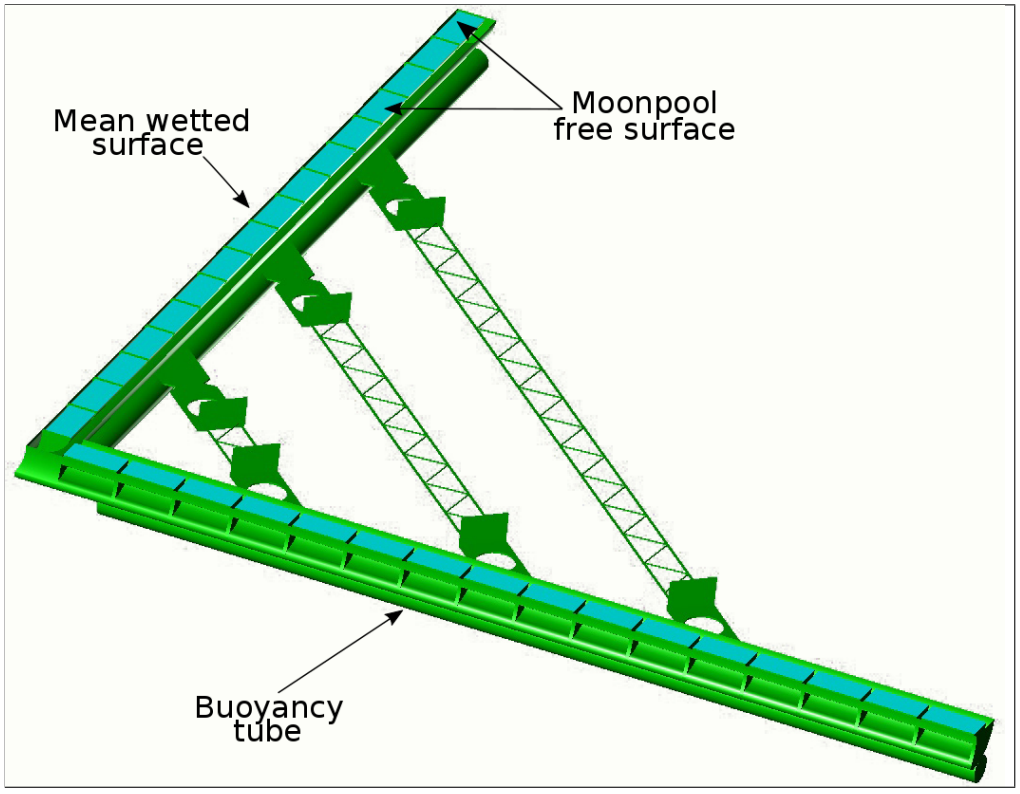

FIGURE 4.6: MultiSurf representation of model. Note surface patches corresponding to the free surfaces of the water columns.

the MultiSurf model of the 32-chamber physical model in the same configuration as illustrated in Figure 4.5.

The water columns are represented in the MultiSurf model by surface patches, which can be seen as the cyan patches in Figure 4.6. (Note the patches representing the moonpools are shown in cyan for clarity. In practice, the colour of a patch can affect how it is treated by WAMIT. In WAMIT, cyan is reserved to indicate dipole patches, and thus the patches were left the default green colour during the actual analysis.) Each patch is assigned a unique number by MultiSurf. By default, WAMIT solves for the frequency-dependent properties of the six rigid body modes of motion of the object being analysed. However, additional modes of motion may be included in the WAMIT solution through the use of the 'Generalized Body Modes' function. A custom routine was written in FORTRAN (compiled using the Intel Visual FORTRAN compiler) to incorporate the heave modes of each of massless surfaces which represent the 32 OWCs based on the patch numbers assigned by MultiSurf. WAMIT includes a number of test cases which demonstrate the use of generalised modes. One such test case is based on the oil exploration and drillship, the Navis Explorer I [174]. This vessel includes three moonpools, and the pumping mode

for each moonpool (and associated coupling terms) are modelled. The routine used to analyse the Navis Explorer I was adapted to model the pumping mode of the 32 OWCs of the WEI platform. Further details on user-generated input files required for use with WAMIT may be found in the user manual.

4.2.3 Hydrostatic stiffness matrix

WAMIT was also used to calculate the values for the hydrostatic stiffness matrix, C. As for the mass matrix case, the stiffness matrix results from WAMIT were verified using AutoCAD. As no detailed discussion could be found in the literature on the use of AutoCAD to validate hydrostatic stiffness values, this technique is described below using the same box section model shown in Figure 4.3. The box section was examined to verify first that the outputs from AutoCAD are valid, and once confidence in the AutoCAD results was established, AutoCAD results for the scale model platform were used to validate the WAMIT results.

The waterplane area and second moment of area are required to populate the hydrostatic stiffness matrix in Equation (4.9). Both of these quantities can be obtained from AutoCAD. First, a region is created from a 'polyline' drawn along the perimeter of the waterplane area, and this was done for the V-shaped box section model in Figure 4.3. The waterplane area, shown in red for clarity, is indicated in Figure 4.7.

Using the *massprop* command again, the area of the region is obtained. Furthermore, as the region is 2-dimensional, the moment of inertia of this area is, in fact, the second moment of area. The second moment of area can be thought of as the mass moment of inertia of an infinitely-thin solid. The results of the *massprop* command for this region are:

```
---------------   REGIONS   ----------------

Area:                      1.7280
Perimeter:                 18.0800
Bounding box:          X: -3.1961  --  3.1961
                       Y: -1.5981  --  1.5981
Centroid:              X: 0.0000
                       Y: 0.0000
Moments of inertia:    X: 1.3466
                       Y: 5.7595
```

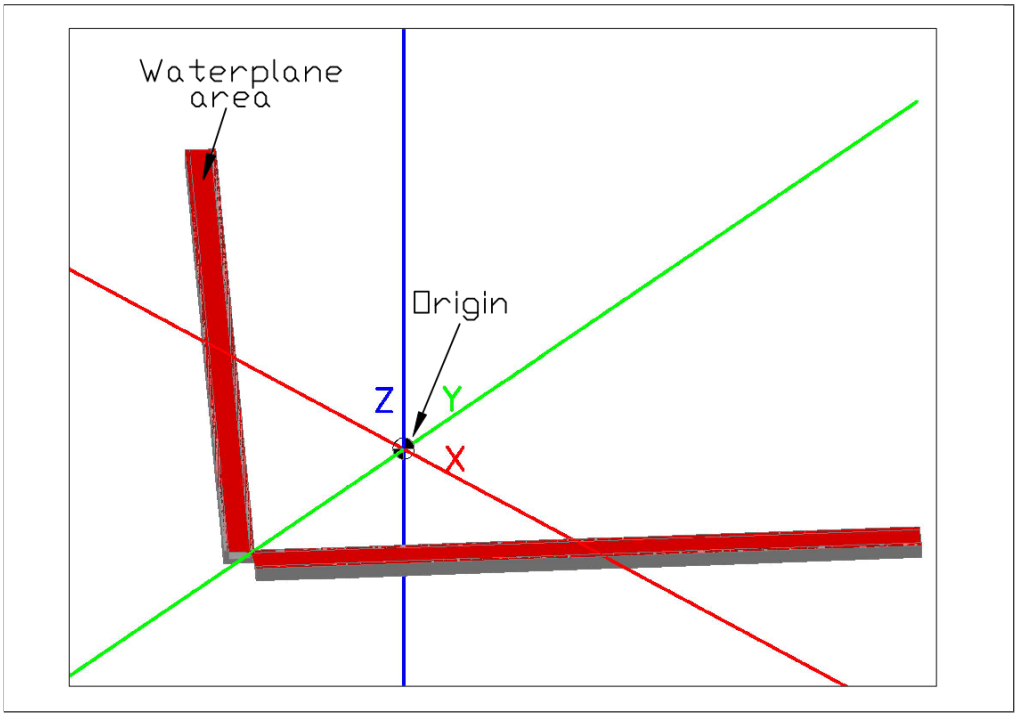

FIGURE 4.7: V-shaped box section model as drawn in AutoCAD with the waterplane area shown in red.

```
Product of inertia:  XY: 0.0000
Radii of gyration:    X: 0.8828
                      Y: 1.8257
Principal moments and X-Y directions about centroid:
                      I: 1.3466 along [1.0000 0.0000]
                      J: 5.7595 along [0.0000 1.0000]
```

The waterplane area, A_{wp}, can be verified easily by the following calculation:

$$A_{wp} = 0.2X4.32X2 = 1.728\text{m}^2$$

The ability of AutoCAD to accurately calculate the moment of inertia, and hence the second moment of area, has been demonstrated in Section 4.2.1. The waterplane area of the physical model is estimated from the AutoCAD model. Figure 4.8 illustrates a region created in AutoCAD corresponding to the waterplane area of the physical model when set to the desired draft.

The results from the *massprop* command, for the waterplane region in Figure 4.8, when the centroid is located at the origin are:

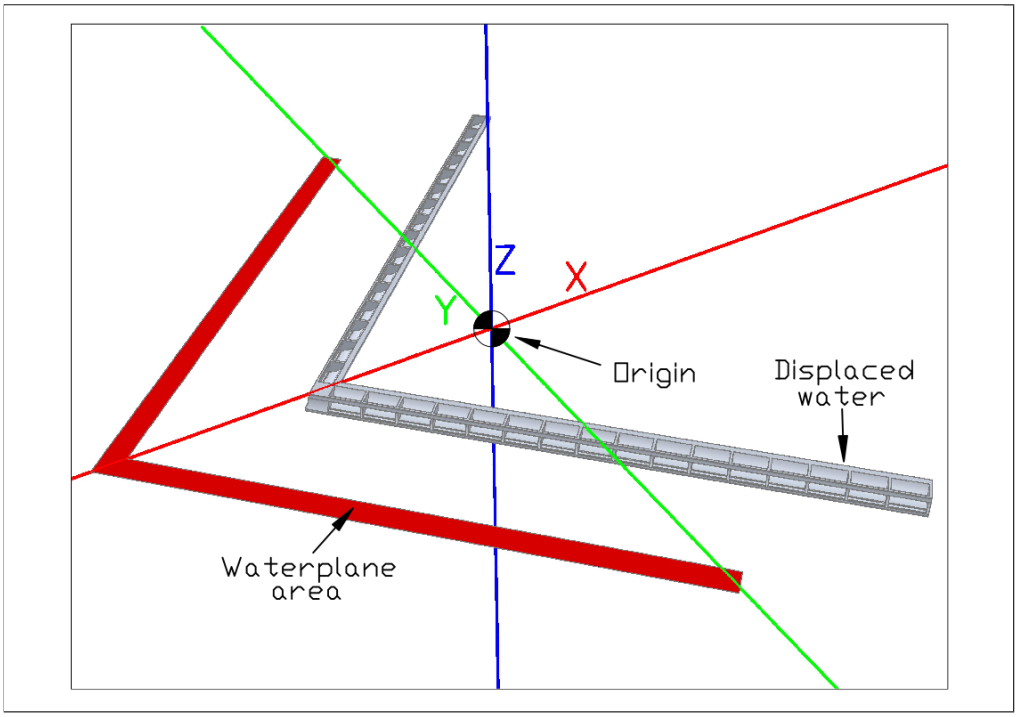

FIGURE 4.8: Waterplane area of the physical scale model, as drawn in AutoCAD, used to estimate the coefficient of hydrostatic stiffness.

```
----------------   REGIONS   ----------------

Area:                      2.2836
Perimeter:                 21.2000
Bounding box:          X: -3.7476  --  3.7477
                       Y: -1.9896  --  1.9136
Centroid:              X: 0.0000
                       Y: 0.0000
Moments of inertia:     X: 2.5745
                       Y: 10.2565
Product of inertia:   XY: 0.0000
Radii of gyration:     X: 1.0618
                       Y: 2.1193
Principal moments and X-Y directions about centroid:
                       I: 2.5745 along [1.0000 0.0000]
                       J: 10.2565 along [0.0000 1.0000]
```

The area at the waterplane is calculated by AutoCAD, and is highlighted in the output of the *massprop* command. This area was calculated to be 2.2836 m^2. The second moment of area about the roll axis is calculated to be 10.2565 m^4 and the second moment of area about the pitch axis is calculated to be 2.5745 m^4. For comparison, as determined by WAMIT, the corresponding values are 2.291 m^2 for the water plane area, 10.229 m^4

for the second moment of area about the roll axis and 2.521 m^4 for the second moment of area about the pitch axis. The hydrostatic coefficients for the heave, pitch and roll modes can be found by multiplying the above results by the density of water and by the acceleration due to gravity.

4.2.4 Power take-off matrix

As mentioned earlier, the effect of the roll, sway, surge and yaw motions on the vertical displacement of the platform will be negligible in head seas. Consequently, when the PTO damping matrix is constructed, only the heave and pitch motions of the platform, and the relative vertical motion of the water columns, need be considered. This leads to a damping matrix of the following form:

$$D = \begin{bmatrix} \sum d_i & \sum d_i x_i & -d_1 & -d_2 & \cdots & -d_{32} \\ \sum d_i x_i & \sum d_i x_i^2 & -d_1 x_1 & -d_2 x_2 & \cdots & -d_{32} x_{32} \\ -d_1 & -d_1 x_2 & d_1 & 0 & \cdots & 0 \\ -d_2 & -d_2 x_2 & 0 & d_2 & \cdots & 0 \\ \vdots & \vdots & \vdots & \vdots & \vdots & \vdots \\ -d_{32} & -d_{32} x_{32} & 0 & 0 & \cdots & d_{32} \end{bmatrix} \tag{4.17}$$

where:

d_i = the linear damping for the i^{th} chamber

x_i = is the perpendicular distance of the centre of the i^{th} chamber from the axis of rotation for the pitch mode.

The platform will pitch about an axis which runs through the centre of gravity of the platform. The location of the centre of gravity is determined using AutoCAD, and the perpendicular distance, x_i, from the centre of each chamber to the axis of pitch rotation may be measured from the CAD model. During the tank tests, the air flow into, and out of, the OWC chambers and plenums is controlled by non-return air flow valves as described in Chapter 8, resulting in latching of the water columns. Such air flow is not time invariant, and, in general, it is not possible to numerically simulate the effects of latching, as manifested in the physical model, directly in the frequency domain. The

approach used here, to include in the numerical model the effects of the latching of the water columns, is to determine a time-averaged linear value of the apparent PTO damping as experienced for each OWC chamber. This is performed by considering the power absorbed by each OWC as determined experimentally, see Chapter 9. The pressure drop per unit flow from an OWC chamber through an outlet, d_η, for each chamber, is given by [175]:

$$d_\eta = \frac{Pow_i^{av}}{(Q_i^{rms})^2} \tag{4.18}$$

In Equation (4.18), Pow_i^{av} is the time-averaged power absorbed by the i^{th} water column, Q_i^{rms} is the root mean square of the air flow into, or out of, the i^{th} OWC chamber. The root mean square of the air flow into or out of an OWC chamber is given by:

$$Q_I^{rms} = Aowc_i v_i^{rms} \tag{4.19}$$

where v_i^{rms} is the root mean square of the velocity of the i^{th} water column under the assumption that the water column is operating in the pumping mode only, and $Aowc_i$ is the cross-sectional area of the i^{th} water column. Equation (4.18) may now be re-written as:

$$d_\eta = \frac{Pow_i^{av}}{Aowc_i^2 \, |v_i^{rms}|^2} \tag{4.20}$$

and hence:

$$Pow_i^{av} = d_\eta Aowc_i^2 \, |v_i^{rms}|^2 \tag{4.21}$$

This allows the power absorbed to be defined in terms of a time-averaged linear damping and the square of the water column velocity, where the time-averaged damping is given by:

$$d_i = d_\eta \times Aowc_i^2 \tag{4.22}$$

Equation (9.8) in Chapter 9 may be used to determine the power absorbed by each chamber of the physical model during testing. The velocity of the water column is

found by differentiating the time series of the displacement of the water columns during tests. As the cross-sectional area of each water column is known, d_i may then be found. In practice, d_i is averaged over the frequency range of the physical test so that one damping value for each of the 32 OWCs is obtained. The frequency domain model may then be used to predict the power absorbed by the physical scale model under monochromatic wave conditions by noting that, in terms of the PTO matrix, D, and the complex velocity vector V, the wave power absorbed for the entire platform is given by:

$$Pow = \frac{1}{2} V^H D V \tag{4.23}$$

The platform and water column motions, the calculated values for the time-averaged PTO damping, as well as the absorbed power estimates from the frequency domain numerical model may be found in Chapter 9.

Chapter 5

Time Domain Modelling

5.1 Introduction

In Chapter 4, a frequency domain numerical model of the physical scale model of the hydrodynamic aspects of the proposed WEI platform was developed. This model was based on frequency domain coefficients, and linearised, time-averaged PTO damping. A comparison between the prediction of the behaviour of the platform and the OWCs, of which the hull comprises, and the wave power absorbed by the platform when subject to monochromatic incident waves, are presented in Chapter 9. The frequency domain numerical model has provided some significant insights into the WEI concept as discussed in Chapter 9; however, it is not capable of capturing the effect of time variant characteristics, such as the latching of a water column, as described in Chapter 3. In the current chapter, state equations describing the interaction between the motion of the platform, the motion of the water columns and the mass flow of air through the closed system of the platform, in the time domain, are developed.

However, the large number of interacting components in the multi-chamber model results in difficulty in studying the behaviour of individual processes in the system due to the large number of hydrodynamic, thermodynamic and mechanical interactions. To further investigate these processes, the state equations are then developed for a single-chamber OWC, the geometry of the wetted surface of which is similar in form to that of the wetted surfaces of a single chamber of the multi-chamber model. A time domain numerical model of the single-chamber OWC, in a number of configurations, is implemented. The

predictions from the numerical model may then be compared to the results from narrow tank testing of the physical model of a single chamber, while investigating the effects of individual components of the system.

5.2 Equation of motion of the water column

A time domain numerical model of the WEI platform must take account of the hydrodynamic interactions between the platform, the OWCs and the incident wave, as well as the thermodynamic processes which take place within the closed air flow system of the platform. The closed air flow system is considered to comprise a number of volumes in which the air pressure is assumed to be constant throughout, at any instant in time, and which varies with respect to time. The volumes comprise 1) the air trapped above the water column in each chamber, 2), the air within the high-pressure plenum and the section of conduit leading from the high-pressure plenum to the Venturi and, finally, 3) the air within the section of conduit from the Venturi to the low-pressure plenum combined with the air in the low-pressure plenum. The theory described herein assumes that the instantaneous pressure in a plenum and its associated conduit can be considered constant throughout the plenum. As described in Chapter 9, experiment has shown that, at model scale, this assumption is valid. At full scale, the compressibility of air, which does not scale according to Froude scaling, will likely render this assumption invalid. The effects of air compressibility on scale models is discussed in Chapter 10. Figure 5.1 illustrates a schematic of one of the OWC chambers of the platform connected to a high- and a low-pressure plenum via air admittance valves. The high- and a low-pressure plenums are connected via a length of conduit containing a Venturi. The OWC chamber, which may represent any one of the OWC chambers in the platform, is henceforth referred to as the i^{th} chamber, and the subscript i is used to denote any property relating to the i^{th} chamber.

At this point in the thesis, the chamber is considered to be fixed in all rigid body modes and the water column is assumed to operate in a pumping mode only (analogous to the heave mode of a massless disc located at the free surface of the water column), while interacting with a high- and low-pressure plenum. When subject to an incident ocean wave, the water column may operate in one of three modes:

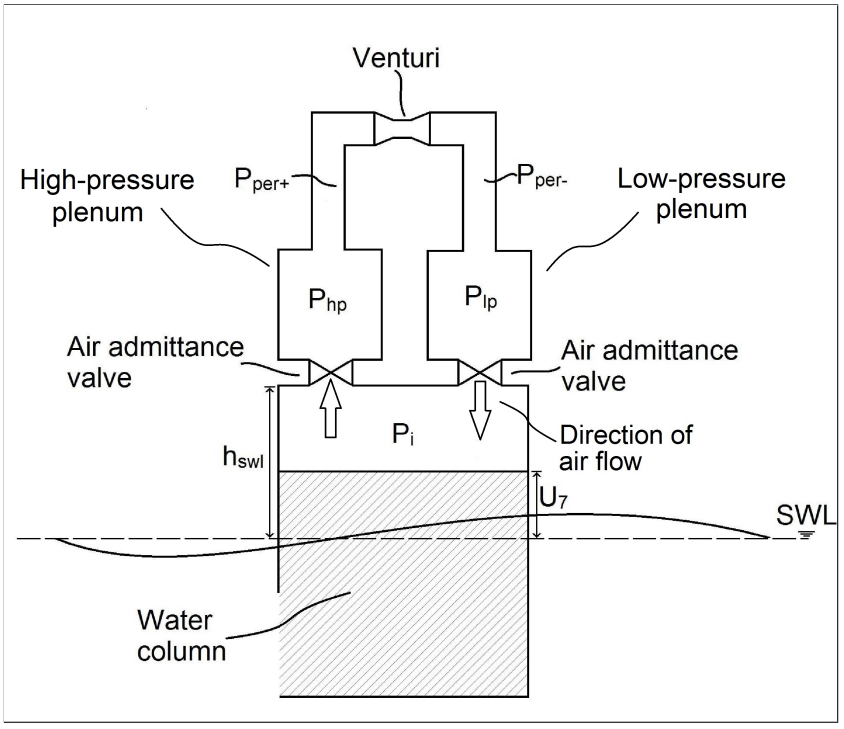

FIGURE 5.1: Schematic of one OWC chamber, the high- and low-pressure plenum and the conduit including Venturi.

1. If the pressure within the OWC chamber is greater than that in the high-pressure plenum, air will flow from the OWC chamber into the high-pressure plenum.

2. If the pressure within the OWC chamber is lower than that in the low-pressure plenum, air will flow from the low-pressure plenum into the OWC chamber.

3. If the pressure within the OWC chamber is less than that in the high-pressure plenum and greater than that in the low-pressure plenum, no air will flow between the OWC chamber and either plenum,effectively latching the water column.

Under the assumption that the water column acts in the pumping mode only, as discussed in Chapter 4, and terming the pumping mode as mode 7, the equation of motion of the water column in the time domain is given by:

$$a_{77}(\infty)\ddot{u}_7(t) + \int_{-\infty}^{t} kr_7(t-\tau)\dot{u}_7(\tau)d\tau + F_{nl}(t) + c_{77}u_7(t) + (p_i(t) - p_{atmos})A_{owc} = fe_7(t) \quad (5.1)$$

Equation (5.1) is a modified version of Cummins' Equation [140]. The term $(p_i - p_{atmos})A_{owc}$ is the force which acts on the water column due to the variation in the pressure of the air trapped in the OWC chamber above the water column, and atmospheric pressure, which acts on the surface of the water outside the chamber. The pressure given by $(p_i - p_{atmos})$ is assumed to act uniformly over the surface of the water column. In Equation (5.1), $a_{77}(\infty)$ is the infinite frequency added mass, the convolution integral $\int_{-\infty}^{t} kr_7(t-\tau)\dot{u}_7(\tau)d\tau$ incorporates the memory effects of the fluid from minus infinity to the current instant in time. Assuming zero initial conditions at a time $t = 0$, the convolution integral may be performed from $t = 0$ to the current instant in time, i.e., the memory effects of the fluid may be captured by the integral $\int_{0}^{t} kr_7(t-\tau)\dot{u}_7(\tau)d\tau$. $F_{nl}(t)$ denotes the non-linear viscous force, and is analogous to F_{nl} in Equation (4.1). When the water column is latched, some small oscillation of the water column will occur due to the compressibility of air within the OWC chamber. An investigation into latching control algorithms for an OWC in [176] found that the frequency of the small oscillations of the latched OWC, ω_L, is given by:

$$\omega_L^2 \approx \frac{\gamma A_{owc}^2 p_{atm}}{V_L(t)(a_{77}(\infty) + u_L A_{owc}\rho_w)} \tag{5.2}$$

where:

γ = the heat capacity ratio or adiabatic index for air

u_L = the latched position of the surface of the water column, m

$V_L(t)$ = the volume of air in the OWC chamber, m^3

and:

$$V_L(t) = (V_o - A_{owc}u_L) \tag{5.3}$$

where:

V_o = the initial volume of air in the OWC chamber, m^3

5.2.1 Variation of pressure within a chamber

An expression to describe the coupling of the variation of the air pressure within the volume above the water column in each chamber with respect to the mass flow of air into or out of the chamber, and the variation in the water column height within the

chamber, can be obtained by considering the First Law of Thermodynamics. The First Law states that, for a closed system [177]:

$$U = Q - W \tag{5.4}$$

where:

U = the change in the internal energy of a thermodynamic system, J
Q = the heat transferred to or from the system, J
W = the work done by the system on the surroundings, J

Where mass flow can take place into or out of the system, the internal energy associated with the additional (or lost) mass must be included, when considering the change in internal energy. For an open system such as an OWC, the rate of change of internal energy of the air in the chamber is given [178] by:

$$\dot{U} = \dot{Q}_{in} - \dot{Q}_{out} + \gamma \left[C_v \dot{m}_{in} T_{in} - C_v \dot{m}_{out} T_{out} \right] - \dot{W} \tag{5.5}$$

where:

C_v = the specific heat capacity of air at constant volume, $J/kg.K$
$\dot{m}_{in}$ = the mass flow rate of air into the OWC chamber, kg/s
T_{in} = the temperature of air flow into the chamber, K
$\dot{m}_{out}$ = the mass flow rate of air out of the OWC chamber, kg/s
T_{out} = the temperature of air flow out of the chamber, K

For a diatomic gas at room temperature, $\gamma = \frac{C_p}{C_v} = 1.4$. As approximately 99% of air is composed of diatomic gases (≈78% nitrogen and ≈21% oxygen), the value of γ for air may be approximated by 1.4.

The internal energy, U, of a system is given by:

$$U = C_v m T \tag{5.6}$$

where:

m = the mass of fluid in the system, kg
T = the temperature of the fluid in the system, K

thus:

$$\dot{U} = \frac{d}{dt}\left[C_v m T\right] \tag{5.7}$$

The ideal gas law states:

$$p = \rho R T \tag{5.8}$$

where:

p = the absolute pressure of the fluid in the system, Pa

R = is the gas constant, $J/kg.K$.

Hence:

$$T = \frac{p}{\rho R} \tag{5.9}$$

and:

$$R = \frac{p}{\rho T} \tag{5.10}$$

For air, $R = 286.9\ J/kg.K$. In the case of an ideal gas, the specific heat capacities at constant volume and constant pressure, C_v and C_p, are related to the gas constant, R, by:

$$C_v = \frac{R}{\gamma - 1} \tag{5.11}$$

$$C_p = \frac{\gamma R}{\gamma - 1} \tag{5.12}$$

By substituting Equations (5.9) and (5.11) into Equation (5.7), the rate of change of internal energy is given by:

$$\dot{U} = \frac{d}{dt}\left[\frac{R}{\gamma - 1} m \frac{p}{\rho R}\right] \tag{5.13}$$

Noting that:

$$V = \frac{m}{\rho}$$

where V is the volume of a material in m^3,

Equation (5.13) becomes:

$$\dot{U} = \left[\frac{1}{\gamma - 1}\right] \frac{d}{dt} \left[pV\right] \tag{5.14}$$

Applying the product rule to Equation (5.14) yields:

$$\dot{U} = \left[\frac{1}{\gamma - 1}\right] \left[p\dot{V} + \dot{p}V\right] \tag{5.15}$$

If no heat energy transfer takes place between the surroundings of the OWC chamber and the system within the chamber through the walls of the OWC chamber, the thermodynamic processes within the chamber are adiabatic. This assumption is often applied to processes which take place sufficiently rapidly that there is not enough time for heat energy to transfer between the system and the surroundings [177]. The assumption that the processes within an OWC chamber are adiabatic is common, [178], [179], [180], [176]. Under the assumption of adiabatic conditions:

$$\dot{Q}_{in} - \dot{Q}_{out} = 0 \tag{5.16}$$

The rate of change of work done by a system is given by:

$$\dot{W} = p\dot{V} \tag{5.17}$$

By substituting Equations (5.15), (5.16) and (5.17) into Equation (5.5), the follow expression is obtained:

$$\left[\frac{1}{\gamma - 1}\right] \left[p\dot{V} + \dot{p}V\right] = \gamma C_v \left[\dot{m}_{in} T_{in} - \dot{m}_{out} T_{out}\right] - p\dot{V} \tag{5.18}$$

Rearranging Equation (5.18), and noting that:

$$\left[\frac{1}{\gamma - 1} + 1\right] = \left[\frac{\gamma}{\gamma - 1}\right]$$

yields:

$$\left[\frac{\gamma}{\gamma - 1}\right] p\dot{V} + \left[\frac{1}{\gamma - 1}\right] \dot{p}V = \gamma C_v \left[\dot{m}_{in} T_{in} - \dot{m}_{out} T_{out}\right] \tag{5.19}$$

From Equation (5.11), it is apparent that:

$$\gamma C_v = \frac{\gamma R}{\gamma - 1} \tag{5.20}$$

Substituting Equation (5.10) into Equation (5.20) yields:

$$\gamma C_v = \left[\frac{\gamma}{\gamma - 1}\right] \frac{p}{\rho T} \tag{5.21}$$

Equation (5.21) is now substituted into Equation (5.19) with some rearranging to give:

$$\left[\frac{1}{\gamma - 1}\right] \dot{p}V = \left[\frac{\gamma}{\gamma - 1}\right] \frac{p}{\rho T} \left[\dot{m}_{in} T_{in} - \dot{m}_{out} T_{out}\right] - \left[\frac{\gamma}{\gamma - 1}\right] p\dot{V} \tag{5.22}$$

If the temperature inside the OWC chamber and the surroundings is equal, then $T_{in} = T_{out} = T$. Terming the total mass flow into or out of the system $\dot{m}$, Equation (5.22) becomes:

$$\left[\frac{1}{\gamma - 1}\right] \dot{p}V = \left[\frac{\gamma}{\gamma - 1}\right] \frac{p}{\rho} \dot{m} - \left[\frac{\gamma}{\gamma - 1}\right] p\dot{V} \tag{5.23}$$

Hence:

$$\left[\frac{1}{\gamma - 1}\right] \dot{p}V = \left[\frac{\gamma}{\gamma - 1}\right] \left[\frac{p}{\rho} \dot{m} - p\dot{V}\right] \tag{5.24}$$

Multiplying both sides of Equation (5.24) by $\left[\frac{\gamma - 1}{V}\right]$ yields:

$$\dot{p} = \frac{\gamma p}{V\rho} \dot{m} - \frac{\gamma}{V} p\dot{V} \tag{5.25}$$

The speed of sound, c_s, in an ideal gas is given by:

$$c_s^2 = \gamma R T \tag{5.26}$$

Given that, from the ideal gas law,

$$RT = \frac{p}{\rho}$$

Equation (5.26) becomes:

$$c_s^2 = \frac{\gamma p}{\rho} \tag{5.27}$$

Substituting Equation (5.27) into Equation (5.25) gives the following expression for the rate of change of pressure in the volume of air trapped in the OWC chamber above the water column, in terms of the mass flow of air into or out of the chamber and the changing volume of the air:

$$\dot{p} = \frac{c_s^2}{V}\dot{m} - \frac{\gamma p}{V}\dot{V} \tag{5.28}$$

A similar result was obtained for a pneumatically-actuated system based on the Energy Equation in [181]. Since the water column is modelled as a piston, the two systems can be considered analogous. The same analysis can be performed to obtain expressions for the rate of change of pressure in the high- and low-pressure plenums. Where the subscript hp denotes a property of the high-pressure plenum and the subscript lp denotes a property of the low-pressure plenum, as the volume of both plenums remains constant, $\dot{V}_{hp} = \dot{V}_{lp} = 0$. Thus:

$$\dot{p}_{hp} = \frac{c_s^2}{V_{hp}}\dot{m}_{hp} \tag{5.29}$$

$$\dot{p}_{lp} = \frac{c_s^2}{V_{lp}}\dot{m}_{lp} \tag{5.30}$$

5.2.2 Mass flow rates

The variation in air pressure within the OWC chamber depends on the mass flow rate of air into and out of the chamber. Further mass flows take place into the high-pressure plenum from the OWC chambers, between the high- and low-pressure plenums and from the low-pressure plenum into the OWC chambers. Terming the mass flow from a chamber in discharge to the high-pressure plenum $m_i^{discharge}$, the mass flow rate of air for the high-pressure plenum, $\dot{m}_{hp}$, is the sum of flows into the plenum from all chambers operating in discharge mode, minus the flow out of the plenum through the Venturi,

$\dot{m}^{vent}$, thus:

$$\dot{m}_{hp} = \sum \dot{m}_i^{discharge} - \dot{m}^{vent} \tag{5.31}$$

Note that any chambers operating in suction mode do not contribute to this mass flow rate. $\dot{m}^{vent}$ is, in turn, given by [182]:

$$\dot{m}_{vent} = Cd_{vent} A_{vent} \sqrt{2\rho \left(p_{hp} - p_{lp}\right)} \tag{5.32}$$

where:

$$\begin{aligned} Cd_{vent} &= \text{the coefficient of discharge for the Venturi} \\ A_{vent} &= \text{the cross-sectional area of the Venturi throat, } m^2 \end{aligned}$$

The pressure drop across the Venturi is the difference between the pressures in the high- and low-pressure sides of the PTO arrangement. Similarly, the mass flow rate across a air admittance valve can be expressed in terms of the pressure difference Δp, across it as [183]:

$$\dot{m}_i = Cd_V L_g h_{max} \sqrt{2\rho_{air} \Delta p} \tag{5.33}$$

where:

$$\begin{aligned} Cd_V &= \text{the coefficient of discharge for the valve} \\ L_g &= \text{the edge distance,} m \\ h_{max} &= \text{is the opening height of the diaphragm for the valve, } m. \end{aligned}$$

When air is flowing across a valve from an OWC chamber into the high-pressure plenum, $\Delta p = p_{hp} - p_i$. The mass flow rate for the low-pressure plenum, $\dot{m}_{lp}$, is likewise the mass flow into the low-pressure side from the Venturi minus the flow out of the plenum into those OWC chambers operating in suction mode:

$$\dot{m}_{lp} = \dot{m}^{vent} - \sum \dot{m}_i^{suction} \tag{5.34}$$

The mass flow rate into chambers in the suction mode, $m_i^{suction}$, from the low-pressure plenum may be expressed mathematically as in Equation (5.33), where $\Delta p = p_i - p_{lp}$. Note that when an OWC chamber is operating in suction, the mass flow rate, $\dot{m}_i$, will be into the OWC chamber and hence will have the opposite sign to when a chamber is

operating in discharge. For a chamber that is latched, the change in pressure is equal to the change in exciting force divided by the water column area, and $\dot{m}_i = 0$. This theory may be extended to include the six rigid body motions of the platform. The final equation required is derived on the basis that the total mass of air in one leg, m_T, is constant at all times as the system is closed, and thus the sum of all airflows is equal to zero, thus:

$$\dot{m}_T = \sum \dot{m}_i^{discharge} - \sum \dot{m}_i^{suction} - \dot{m}_{vent} = 0 \tag{5.35}$$

Under the assumption that the water column operates in a pumping mode only, the rate of change of the volume of air trapped above the water column in the OWC chamber is a function of the velocity of the water column. In the model shown in Figure 5.1, for which the cross-section of the air chamber does not vary with height, the volume of air is given by:

$$V_i = A_{owc}\,[h_o - u_7] \tag{5.36}$$

where:

V_i = the volume of air in the OWC chamber, m^3

A_{owc} = the cross-sectional area of the water column, m^2.

By differentiating Equation (5.36) with respect to time, the rate of change of the air volume is given by:

$$\dot{V}_i = -A_{owc}\dot{u}_7 \tag{5.37}$$

While Equations (5.36) and (5.37) apply to an air volume with uniform cross section with respect to height, once the variation in cross section can be described by a polynomial of height, the same approach can be used to determine an expression for $\dot{V}_i$ for an OWC chamber for which the cross-sectional area varies with height.

5.3 System equations for a single chamber

Due to the complexity of the physical scale model of the proposed WEI 32-OWC platform, which gives rise to a large number of interacting thermodynamic, hydrodynamic and mechanical systems, it is difficult to characterise or examine the influence of specific components within the system. Thus, in order to examine individual components within

the system, a set of tests, to be performed on a single-OWC chamber model in the narrow wave tank located at DkIT, was devised. During the tests, the single chamber model was reconfigured and retested for a range of monochromatic wave conditions. Numerical time domain models, based on the Equations in Section 5.2 (above), were developed and implemented for each arrangement of the single-OWC model. In the following section, the numerical time domain models for each configuration of the single-OWC model are described.

5.3.0.1 State-space modelling

A state-space approach is used to describe the models of each configuration of the single-chamber OWC. State-space modelling, which has been widely applied in numerous engineering applications, uses state variables to describe a system by a set of first-order differential equations. Linear state-space models take the form:

$$\begin{aligned} \dot{x}(t) &= A\ x(t) + B\ u(t) \\ y(t) &= C\ x(t) + D\ u(t) \end{aligned} \qquad x(t_0) = x_0 \tag{5.38}$$

In Equation (5.38), $x(t)$ is the state vector, comprises state variables, and is of dimension equal to the number of states of the system. For an n^{th}-dimensional system, $x(t)$ has the form:

$$x(t) = \begin{bmatrix} x_1(t) \\ x_2(t) \\ \vdots \\ x_n(t) \end{bmatrix}$$

The n-dimensional vector $\dot{x}(t)$ has the form:

$$\dot{x}(t) = \begin{bmatrix} \dot{x}_1(t) \\ \dot{x}_2(t) \\ \vdots \\ \dot{x}_n(t) \end{bmatrix}$$

The m-dimensional input vector, $u(t)$, and p-dimensional output vector, $y(t)$, have the forms:

$$u(t) = \begin{bmatrix} u_1(t) \\ u_2(t) \\ \vdots \\ u_n(t) \end{bmatrix} \qquad y(t) = \begin{bmatrix} y_1(t) \\ y_2(t) \\ \vdots \\ y_n(t) \end{bmatrix}$$

The matrix $A \in \mathbb{R}^{n \times n}$ in Equation (5.38). Matrix $B \in \mathbb{R}^{n \times m}$ is termed the input matrix, while matrix $C \in \mathbb{R}^{p \times n}$ is the output matrix. Matrix $D \in \mathbb{R}^{p \times m}$ is the feedback matrix. At time t_0, the state vector comprises the initial conditions of the system. Higher-order differential equations may be rewritten as a set of coupled first-order differential equations, with the number of coupled equations equal to the order of the higher-order differential equation. Thus, a system described by higher-order differential equations may be reduced to a system of first-order differential equations through the choice of appropriate state variables. The state-space approach may be adapted to implement the time domain numerical models described herein, and it is particularly convenient to replace the convolution term in Equation (5.1) with a computationally-efficient approximation when using the state-space approach as described in Section 5.4.2.3. A full description of the state-space approach to modelling linear systems may be found in, for example, [184].

5.3.0.2 Single sealed OWC

Consider first a system, as shown by the schematic of a physical model in Figure 5.2, where a volume of air is contained above a water column in a sealed chamber. Equation (5.1) applies to the water column in the chamber. The only motion of the water column which can take place is due to the compressibility of air. The mass flow rate of air into and out of this chamber is clearly zero. The force acting on the surface of the water column due to the change in pressure within the air volume arises as the air is compressed due to the force of the incident wave on the water column. Note that throughout this section, all pressures are absolute pressures.

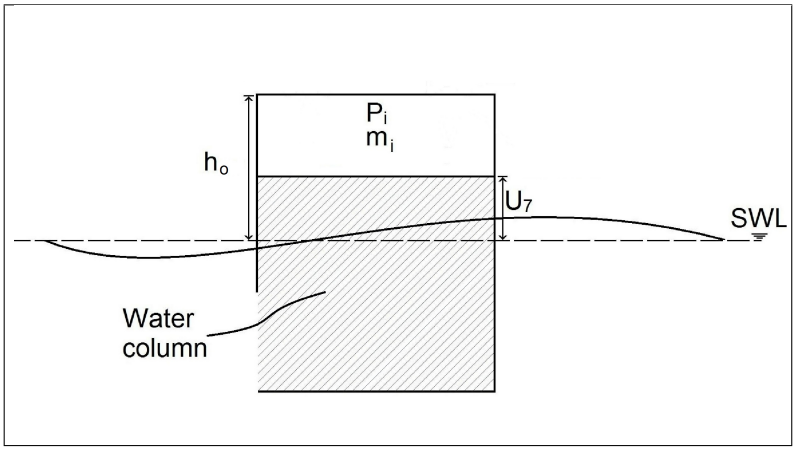

FIGURE 5.2: Schematic of sealed system.

The first step in this numerical modelling approach is to choose appropriate state variables. The state variables chosen here have been selected so as to prevent the formation of ill-conditioned matrices, which can result in mathematical instability. Three state variables are used to model the single chamber sealed system. Denoting the vector of state variables as X, and the i^{th} entry of X as x_i, the chosen state variables are:

$$\begin{aligned} x_1 &= u_7 \\ x_2 &= \dot{u}_7 \\ x_3 &= \Delta p = (p_i - p_{atmos}). \end{aligned}$$

All other variables can be derived from these state variables. The next step is to set out the expression for the derivative of each of the state variables, before assembling these expressions in matrix form. $\dot{x}_1$ is the first derivative with respect to time of u_7, and is equal to x_2. $\dot{x}_2$ is equal to $\ddot{u}_7$, and can be isolated from the equation of motion of the water column, Equation (5.1). $\dot{x}_3$, equal to $\dot{\Delta p}$ is equal to $\dot{p}_i$ if p_{atmos} is assumed constant as is the case in this thesis. Hence:

$$\dot{x}_1 = \dot{u}_7 = x_2 \tag{5.39}$$

$$\dot{x}_2 = \ddot{u}_7 = \frac{fe_7}{a_{77\infty}} - \frac{\int_0^t kr_7(t-\tau)\dot{u}_7(\tau)dt}{a_{77\infty}} - \frac{c_{77}}{a_{77\infty}}x_1 - \frac{A_{owc}}{a_{77\infty}}x_3 \tag{5.40}$$

$$\dot{x}_3 = \dot{\Delta p} = \dot{p}_i = \frac{c_s^2}{V_i}\dot{m}_i - \gamma\frac{p_i}{V_i}\dot{V}_i \tag{5.41}$$

For clarity, the convolution integral is replaced in Equation (5.43) (and future equations) with the notation *conv*, hence $conv = \int_0^t kr_7(t-\tau)\dot{u}_7(\tau)dt$. Equation (5.41) can be further developed by noting that $\dot{m}_i = 0$, and substituting for $\dot{V}_i$, to yield:

$$\dot{x}_3 = \frac{\gamma p_i}{[h_o - x_1]} x_2 \tag{5.42}$$

Noting that $p_i = x_3 + p_{atmos}$, Equations (5.39), (5.40) and (5.42) may be assembled into matrix form as follows:

$$\begin{pmatrix} \dot{x}_1 \\ \dot{x}_2 \\ \dot{x}_3 \end{pmatrix} = \begin{pmatrix} 0 & 1 & 0 \\ -\frac{c_{77}}{a_{77\infty}} & 0 & -\frac{A_{owc}}{a_{77\infty}} \\ 0 & \frac{\gamma(x_3+p_{atmos})}{[h_o-x_1]} & 0 \end{pmatrix} \begin{pmatrix} x_1 \\ x_2 \\ x_3 \end{pmatrix} + \begin{pmatrix} 0 \\ (fe_7 - conv) \\ 0 \end{pmatrix} \left(\frac{1}{a_{77\infty}} \right) \tag{5.43}$$

This is a highly non-linear system, as some elements of the state vector appear in elements of the state matrix, and elements of the input vector include mass flow rates that depend on the state vector, as per Equation (5.43). This state-space system has been implemented in MATLAB using inputs from WAMIT and Multisurf as described in Section 5.4.

5.3.1 Model with an orifice

The numerical model is now developed to include the effect of a single orifice through which air can flow freely between the air volume above the water column and atmosphere. Figure 5.3 illustrates a schematic of a physical model of this configuration.

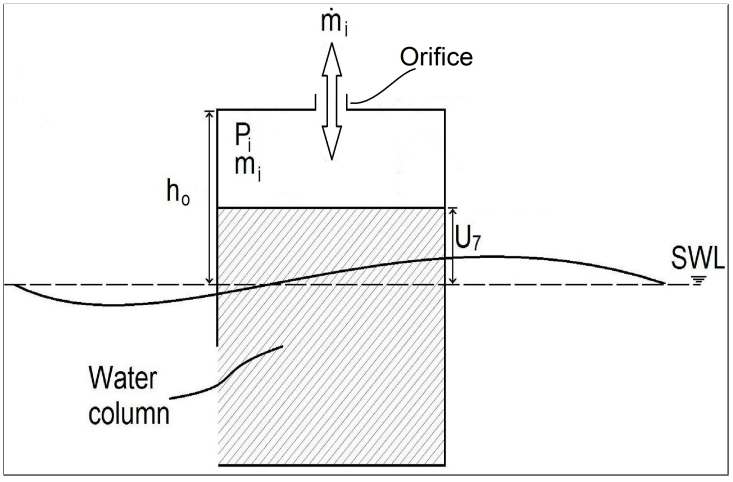

FIGURE 5.3: Schematic of OWC model with an orifice.

The development of the state-space system to model this configuration numerically proceeds along similar lines to that for the single chamber sealed system except that $\dot{m}_i \neq 0$, and the direction of the flow, either into or out of the chamber is dependent on the value of $p_i - p_{atmos}$. If $p_i > p_{atmos}$, then air flows from the chamber to atmosphere, whereas if $p_i < p_{atmos}$ the reverse is the case. If $p_i = p_{atmos}$, then no airflow takes place. Table 5.1 lists the required equations to describe the rate of change of mass within the air chamber for these three scenarios. The equation for mass flow rate through an orifice under the assumption of incompressibility, is identical to Equation (5.32) for a Venturi, the difference arising from the value of the coefficient of discharge [185]. The coefficient of discharge of the orifice is termed Cd_O, where the cross-sectional area of the orifice is A_{ori}. A conditional statement is included in the MATLAB code to model the system shown in Figure 5.3. At each time step, the code interrogates the state variables to determine the direction of air flow, and uses the appropriate mass flow rate equation in Table 5.1 for the time step. Note that mass flow into the air chamber is considered positive.

TABLE 5.1: Mass flow equations for system with single orifice

Case	Mass flow
$p_i > p_{atmos}$	$\dot{m}_i = -Cd_O A_{ori}\sqrt{2\rho_{air}\left\|p_i - p_{atmos}\right\|}$
$p_i < p_{atmos}$	$\dot{m}_i = Cd_O A_{ori}\sqrt{2\rho_{air}\left\|p_{atmos} - p_i\right\|}$
$p_i = p_{atmos}$	$\dot{m}_i = 0$

Upon investigation, it was found that the most appropriate choice of state variables for the model with a single orifice was identical to the choice of state variables applied to the sealed single chamber configuration, that is: $x_1 = u_7$, $x_2 = \dot{u}_7$ and $x_3 = \Delta p = (p_i - p_{atmos})$. As a consequence, Equations (5.39), (5.40) and (5.41) are valid here, and it is only the development of Equation (5.41) that needs to be revisited as $\dot{m}_i$ is no longer equal to 0. The corresponding equation to Equation (5.41) for the single chamber with an orifice setup is:

$$\dot{\Delta p} = \dot{x}_3 = \frac{c_s^2}{A_{owc}[h_o - x_1]}\dot{m}_i + \frac{\gamma\left(x_3 + p_{atmos}\right)}{[h_o - x_1]}x_2 \tag{5.44}$$

These equations are assembled into a state-space form to yield:

$$\begin{pmatrix} \dot{x}_1 \\ \dot{x}_2 \\ \dot{x}_3 \end{pmatrix} = \begin{pmatrix} 0 & 1 & 0 \\ -\frac{c_{77}}{a_{77\infty}} & 0 & -\frac{A_{owc}}{a_{77\infty}} \\ 0 & \frac{\gamma(x_3+p_{atmos})}{[h_o-x_1]} & 0 \end{pmatrix} \begin{pmatrix} x_1 \\ x_2 \\ x_3 \end{pmatrix} + \begin{pmatrix} 0 & 0 \\ (fe_7 - conv) & 0 \\ 0 & \frac{c_s^2}{A_{owc}[h_o-x_1]} \end{pmatrix} \begin{pmatrix} \frac{1}{a_{77\infty}} \\ \dot{m}_i \end{pmatrix} \quad (5.45)$$

Physical tank testing can be used to both calibrate the coefficient of discharge of the orifice and also validate the numerical model.

5.3.2 Model with suction and discharge valves

At this point, the numerical model may be developed further to describe a single-chamber OWC with two air admittance valves. A schematic of a physical model of this arrangement is illustrated in Figure 5.4. While, at first glance, the arrangement in Figure 5.4 is very similar to the model-with-orifice case illustrated in Figure 5.3, a number of key differences exist between how the numerical models of the two systems are implemented. Firstly, the system in Figure 5.4 is not time-invariant. The system may operate in one of three modes: 1) a discharge mode, 2) a suction mode or a 3) latched mode. Each mode is described by a different set of system equations. At each time step, the system states are interrogated to determine which mode the system is operating in at that time step, and the appropriate system equations applied for that time step. The numerical model assumes that the system with two air admittance valves continues to operate in one mode only for the duration of a time step. Secondly, the air admittance valves are assumed to operate in either a fully open or fully closed state, and switches instantaneously between these two control states, known as a bang-bang regime [186]. Finally, the results of narrow tank testing presented in Chapter 9 has shown that so-called 'valve stiction' [187] affects the operation of the air admittance valves. In order for a valve to overcome stiction and open, the pressure difference across the valve must reach a certain value, otherwise the valve will remain closed, even if a pressure difference exists across the valve. The pressure difference required to overcome stiction is greater than the pressure difference required to keep the valve open, once the valve has opened. The

pressure difference required to overcome stiction can be determined experimentally. If the pressure within the OWC chamber is greater that atmosphere, and hence the suction valve is closed, but the pressure difference is insufficient to open a closed discharge valve, the chamber operates in a latched mode until the pressure in the chamber is sufficient to overcome stiction. A similar process operates in reverse if the chamber pressure is below atmospheric, but not sufficiently low to overcome the stiction on a closed suction valve. In the numerical code, the open/closed status of a valve is monitored using a dedicated variable which is set equal to 1 when a valve is opened, and 0 when a valve is closed.

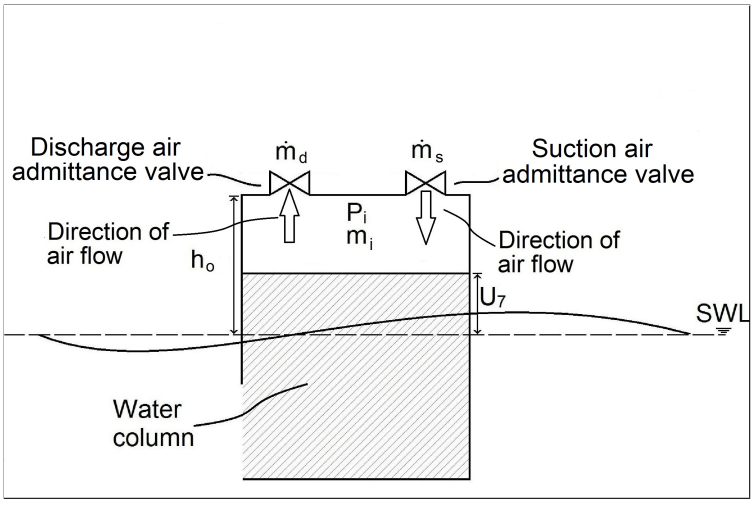

FIGURE 5.4: Schematic of a physical OWC model with discharge and suction air admittance valves.

The mass flow rates which take place in the system in Figure 5.4 for each mode of operation are given in Table 5.2.

TABLE 5.2: Mass flow equations for system with two air admittance valves

Case	Mass flow
$p_i > p_{atmos}$	$\dot{m}_i = -\dot{m}_d = -Cd_V L_g h_{max} \sqrt{2\rho_{air} \lvert p_i - p_{atmos} \rvert}$
$p_i < p_{atmos}$	$\dot{m}_i = -\dot{m}_s = Cd_V L_g h_{max} \sqrt{2\rho_{air} \lvert p_{atmos} - p_i \rvert}$
$p_i = p_{atmos}$	$\dot{m}_i = 0$

The same state variables as were used for the numerical model of the OWC with an orifice are appropriate for use with the numerical model of the OWC with two air admittance valves. The state-space formulation for the three modes in which the OWC illustrated in Figure 5.4 may operate, namely, discharge, suction and latched, are described below.

5.3.2.1 Discharge mode

If $p_i > p_{atmos}$, and valve stiction has been overcome, the chamber will operate in the discharge mode, and mass flow of air will take place from the OWC chamber to atmosphere via the discharge valve. The mass flow rate of air for the chamber, $\dot{m}_i$, will be equal to the mass flow through the discharge valve, $\dot{m}_d$. The state-space formulation matches that for the OWC with an orifice case, except that $\dot{m}_i = \dot{m}_d$:

$$\begin{pmatrix} \dot{x}_1 \\ \dot{x}_2 \\ \dot{x}_3 \end{pmatrix} = \begin{pmatrix} 0 & 1 & 0 \\ -\frac{c_{77}}{a_{77\infty}} & 0 & -\frac{A_{owc}}{a_{77\infty}} \\ 0 & \frac{\gamma(x_3+p_{atmos})}{[h_o-x-1]} & 0 \end{pmatrix} \begin{pmatrix} x_1 \\ x_2 \\ x_3 \end{pmatrix} + \begin{pmatrix} 0 & 0 \\ (fe_7 - conv) & 0 \\ 0 & \frac{c_s^2}{A_{owc}[h_o-x_1]} \end{pmatrix} \begin{pmatrix} \frac{1}{a_{77\infty}} \\ \dot{m}_i \end{pmatrix} \quad (5.46)$$

5.3.2.2 Suction mode

If $p_i < p_{atmos}$, and valve stiction has been overcome, the chamber will operate in the suction mode, and mass flow of air will take place from the atmosphere into the OWC chamber via the suction valve. The mass flow rate of air for the chamber, $\dot{m}_i$, will be equal to the mass flow through the suction valve $\dot{m}_s$. The state-space formulation matches that for the discharge mode case, except that $\dot{m}_i = \dot{m}_s$:

$$\begin{pmatrix} \dot{x}_1 \\ \dot{x}_2 \\ \dot{x}_3 \end{pmatrix} = \begin{pmatrix} 0 & 1 & 0 \\ -\frac{c_{77}}{a_{77\infty}} & 0 & -\frac{A_{owc}}{a_{77\infty}} \\ 0 & \frac{\gamma(x_3+p_{atmos})}{[h_o-x_1]} & 0 \end{pmatrix} \begin{pmatrix} x_1 \\ x_2 \\ x_3 \end{pmatrix} + \begin{pmatrix} 0 & 0 \\ (fe_7 - conv) & 0 \\ 0 & \frac{c_s^2}{A_{owc}[h_o-x_1]} \end{pmatrix} \begin{pmatrix} \frac{1}{a_{77\infty}} \\ \dot{m}_s \end{pmatrix} \quad (5.47)$$

If the suction and discharge valves share the same characteristics, then the system of equations in Equations (5.46) will match those in Equations (5.47) except for the sign of the mass flow of air, $\dot{m}_i$.

5.3.2.3 Latched mode

When the system is latched, which occurs if $p_i = p_{atmos}$, or if stiction has not yet been overcome, $\dot{m}_i = 0$. Hence the state-space formulation becomes:

$$\begin{pmatrix} \dot{x}_1 \\ \dot{x}_2 \\ \dot{x}_3 \end{pmatrix} = \begin{pmatrix} 0 & 1 & 0 \\ -\frac{c_{77}}{a_{77\infty}} & 0 & -\frac{A_{owc}}{a_{77\infty}} \\ 0 & \frac{\gamma(x_3+p_{atmos})}{[h_o-x_1]} & 0 \end{pmatrix} \begin{pmatrix} x_1 \\ x_2 \\ x_3 \end{pmatrix} + \begin{pmatrix} 0 & 0 \\ (fe_7 - conv) & 0 \\ 0 & \frac{c_s^2}{A_{owc}[h_o-x_1]} \end{pmatrix} \begin{pmatrix} \frac{1}{a_{77\infty}} \\ 0 \end{pmatrix} \quad (5.48)$$

In practice, when the water column is latched, due to valve stiction, the pressure within the chamber will rise or drop rapidly until the appropriate valve overcomes stiction. The results of tank testing, presented in Chapter 9, show the process of a valve overcoming stiction takes place over a time period which is in the order of milliseconds.

5.3.3 Model with high-pressure discharge plenum

The next step is to include in the numerical model the effect of the incorporation into the system of a single, high-pressure plenum to which the air in the chamber discharges via an air admittance valve once the pressure within the chamber is greater than that in the plenum. Air can flow via an orifice from the high-pressure discharge plenum to atmosphere. A second air admittance valve allows air to flow from atmosphere directly into the chamber once the chamber pressure is below atmospheric pressure. In both cases, air flow takes place once valve stiction has been overcome. This setup is illustrated in Figure 5.5 below.

Under all conditions, air may flow through the orifice between the high-pressure discharge plenum and atmosphere. While, in reality, air flow through the orifice will only take place in one direction, to prevent mathematical instability, the MATLAB simulation allows for bidirectional flow to take place should small rounding errors allow a scenario to arise where a very small negative pressure arises in this plenum. The mass flow rate, from

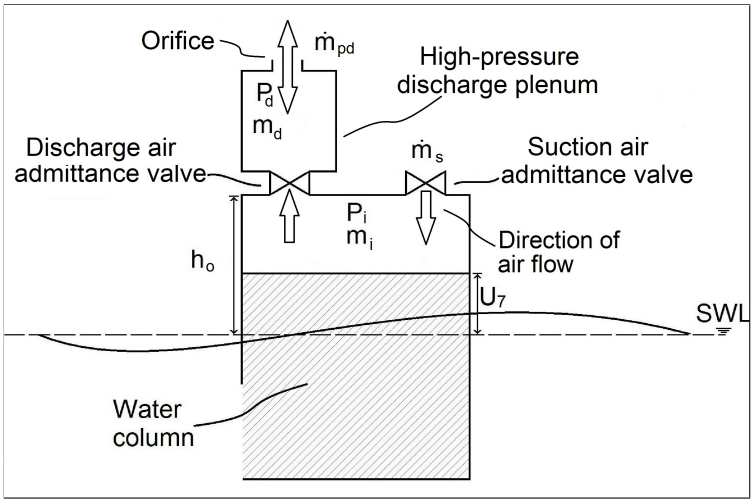

FIGURE 5.5: Schematic of model with single, high-pressure discharge plenum and air admittance valves.

the plenum to atmosphere through the orifice, $\dot{m}_{pd}$ is given by:

$$\dot{m}_{pd} = Cd_O A_{ori} \sqrt{2\rho_{air}|p_d - p_{atmos}|} \tag{5.49}$$

As for the model with two air admittance valves (Figure 5.4), if valve stiction has not been overcome, the system is assumed to be operating in the latched mode. A number of possible options exist, and have been explored successfully, as to the most suitable choice of state variables for this system. For the derivation below, the state variables used were:

$$\begin{aligned} x_1 &= u_7 \\ x_2 &= \dot{u}_7 \\ x_3 &= \Delta p = (p_i - p_{atmos}) \\ x_4 &= \Delta p_2 = (p_d - p_{atmos}). \end{aligned}$$

where p_d is the absolute pressure in the discharge plenum in Pa.

Note that the additional pressure term, compared to the OWC-with-two-air-admittance-valves model, results in an additional state variable, x_4. At each time step, the MATLAB simulation checks the relative pressure in each volume and, based on the pressures, uses the appropriate set of differential equations for that time step. The state-space formulations for the discharge, suction and latched modes for the OWC with single, high-pressure discharge plenum, are outlined below.

5.3.3.1 Discharge mode

Consider first when the pressure in the chamber, p_i, is greater than that in the plenum, p_d, and stiction on the discharge valve has been overcome. In discharge mode, the mass flow rate equations for the system illustrated in Figure 5.5 are given in Table 5.3.

TABLE 5.3: Mass flow equations for system with a high-pressure discharge plenum in the discharge mode.

Mass flow rate into chamber via suction valve	$\dot{m}_s = 0$
Mass flow rate from discharge plenum to atmosphere	$\dot{m}_{pd} = Cd_O A_O \sqrt{2\rho \left\lvert p_d - p_{atmos} \right\rvert}$
Mass flow rate from chamber to discharge plenum	$\dot{m}_i = Cd_V L_g h_{max} \sqrt{2\rho \left\lvert p_i - p_d \right\rvert} = \dot{m}_d$
Net Mass rate flow into discharge plenum	$\dot{m}_d = \dot{m}_i - \dot{m}_{pd}$

Following the same process as for the OWC-with-orifice example, the derivatives of each of the state variables for the discharge mode can be expressed as follows:

$$\dot{x}_1 = \dot{u}_7 = x_2 \tag{5.50}$$

$$\dot{x}_2 = \ddot{u}_7 = \frac{fe_7}{a_{77\infty}} - \frac{conv}{a_{77\infty}} - \frac{c_{77}}{a_{77\infty}} x_1 - \frac{A_{owc}}{a_{77\infty}} x_3 \tag{5.51}$$

$$\dot{x}_3 = \dot{\Delta p_i} = \dot{p}_i = \frac{c_s^2}{A_{owc}[h_o - x_1]} \dot{m}_i - \frac{\gamma \left[x_3 - p_{atmos}\right]}{[h_o - x_1]} x_2 \tag{5.52}$$

$$\dot{x}_4 = [p_d - \dot{p}_{atmos}] = \dot{p}_d = \frac{c_s^2}{V_d} \left[\dot{m}_i - \dot{m}_d\right] \tag{5.53}$$

As before, Equations (5.50), (5.51), (5.52) and (5.53) are now assembled into matrix form to yield:

$$\begin{pmatrix}\dot{x}_1\\ \dot{x}_2\\ \dot{x}_3\\ \dot{x}_4\end{pmatrix} = \begin{pmatrix}0 & 1 & 0 & 0\\ -\frac{c_{77}}{a_{77\infty}} & 0 & -\frac{A_{owc}}{a_{77\infty}} & 0\\ 0 & -\frac{\gamma[x_3+p_{atmos}]}{[h_o-x_1]} & 0 & 0\\ 0 & 0 & 0 & 0\end{pmatrix}\begin{pmatrix}x_1\\ x_2\\ x_3\\ x_4\end{pmatrix} + \begin{pmatrix}0 & 0 & 0\\ (fe_7 - conv) & 0 & 0\\ 0 & 0 & \frac{c_s^2}{A_{owc}[h_o-x_1]}\\ 0 & -\frac{c_s^2}{V_d} & -\frac{c_s^2}{V_d}\end{pmatrix}\begin{pmatrix}\frac{1}{a_{77\infty}}\\ \dot{m}_d\\ \dot{m}_i\end{pmatrix} \tag{5.54}$$

5.3.3.2 Suction mode

If p_i is less than atmospheric pressure, air will be drawn into the chamber via the suction valve (once stiction has been overcome), while any pressure difference between the high-pressure plenum and atmosphere will also result in a flow of air from the high-pressure plenum to atmosphere. The mass flow rates of air in the system in the suction mode are given by:

TABLE 5.4: Mass flow equations for system with a high-pressure discharge plenum in the suction mode.

Mass flow into chamber via suction valve	$\dot{m}_s = Cd_V L_g h_{max}\sqrt{2\rho\,\lvert p_{atmos} - p_i\rvert}$
Mass flow from rate discharge plenum to atmosphere	$\dot{m}_{pd} = Cd_O A_O\sqrt{2\rho\,\lvert p_d - p_{atmos}\rvert}$
Mass flow from rate suction plenum into chamber	$\dot{m}_i = \dot{m}_s = Cd_V L_g h_{max}\sqrt{2\rho\,\lvert p_{atmos} - p_i\rvert}$
Net mass flow rate into discharge plenum	$\dot{m}_d = -\dot{m}_{pd}$

Using the same state variables as used in the discharge case, the governing equations for this scenario are given by:

$$\dot{x}_1 = \dot{u}_7 = x_2 \tag{5.55}$$

$$\dot{x}_2 = \ddot{u}_7 = \frac{fe_7}{a_{77\infty}} - \frac{conv}{a_{77\infty}} - \frac{c_{77}}{a_{77\infty}}x_1 - \frac{A_{owc}}{a_{77\infty}}x_3 \tag{5.56}$$

$$\dot{x}_3 = \dot{\Delta p} = -\dot{p}_i = \frac{c_s^2}{A_{owc}[h_o - x_1]}\dot{m}_i - \frac{\gamma x_3 + p_{atmos}}{[h_o - x_1]}x_2 \tag{5.57}$$

$$\dot{x}_4 = -p_d - \dot{p}_{atmos} = \dot{p}_i - \dot{p}_d = \frac{c_s^2}{V_d}\dot{m}_d \tag{5.58}$$

In matrix form this yields:

$$\begin{pmatrix} \dot{x}_1 \\ \dot{x}_2 \\ \dot{x}_3 \\ \dot{x}_4 \end{pmatrix} = \begin{pmatrix} 0 & 1 & 0 & 0 \\ -\frac{c_{77}}{a_{77\infty}} & 0 & -\frac{A_{owc}}{a_{77\infty}} & 0 \\ 0 & -\frac{\gamma(x_3+p_{atmos})}{[h_o-x_1]} & 0 & 0 \\ 0 & 0 & 0 & 0 \end{pmatrix} \begin{pmatrix} x_1 \\ x_2 \\ x_3 \\ x_4 \end{pmatrix} + \begin{pmatrix} 0 & 0 & 0 \\ (fe_7 - conv) & 0 & 0 \\ 0 & 0 & \frac{c_s^2}{A_{owc}[h_o-x_1]} \\ 0 & \frac{c_s^2}{V_d} & 0 \end{pmatrix} \begin{pmatrix} \frac{1}{a_{77\infty}} \\ \dot{m}_d \\ \dot{m}_i \end{pmatrix} \tag{5.59}$$

5.3.3.3 Latched mode

If $p_i < p_d$ while, at the same time $p_i > p_s$, the system is latched, neither air admittance valve will be open and $\dot{m}_i = 0$. Mass flow out of the high-pressure plenum to atmosphere may still take place. The system of equations used for the suction configuration may be modified to model this scenario. The set of ODEs in matrix form below results:

$$\begin{pmatrix} \dot{x}_1 \\ \dot{x}_2 \\ \dot{x}_3 \\ \dot{x}_4 \end{pmatrix} = \begin{pmatrix} 0 & 1 & 0 & 0 \\ -\frac{c_{77}}{a_{77\infty}} & 0 & -\frac{A_{owc}}{a_{77\infty}} & 0 \\ 0 & -\frac{\gamma(x_3+p_{atmos})}{[h_o-x_1]} & 0 & 0 \\ 0 & 0 & 0 & 0 \end{pmatrix} \begin{pmatrix} x_1 \\ x_2 \\ x_3 \\ x_4 \end{pmatrix} + \begin{pmatrix} 0 & 0 & 0 \\ (fe_7 - conv) & 0 & 0 \\ 0 & 0 & 0 \\ 0 & 0 & 0 \end{pmatrix} \begin{pmatrix} \frac{1}{a_{77\infty}} \\ \dot{m}_d \\ 0 \end{pmatrix} \tag{5.60}$$

5.3.4 Model with high-pressure discharge plenum and low-pressure suction plenum

The next step is to include, in the numerical model, the effect of incorporating a second, low-pressure plenum, from which air may flow into the OWC chamber via an air admittance valve, once the pressure within the chamber is less than that in the low-pressure plenum. Figure 5.6 illustrates this arrangement. The mass flow rate from atmosphere

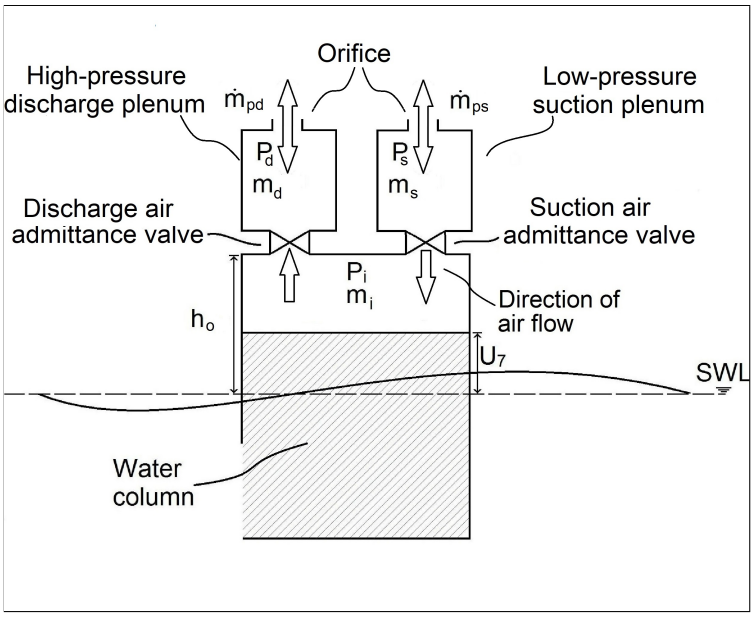

FIGURE 5.6: Schematic of model with high-pressure discharge and low-pressure suction plenums.

to the low-pressure suction plenum through the orifice, $\dot{m}_{ps}$ is given by:

$$\dot{m}_{pd} = Cd_O A_{ori} \sqrt{2\rho_{air}|p_{atmos} - p_d|} \tag{5.61}$$

The additional air volume, and associated air pressure and air mass, require a further state variable to be included. The state variables chosen for the arrangement in Figure 5.6 are:

$$\begin{aligned} x_1 &= u_7 \\ x_2 &= \dot{u}_7 \\ x_3 &= \Delta p = (p_i - p_{atmos}) \\ x_4 &= \Delta p_2 = (p_d - p_{atmos}) \\ x_5 &= \Delta p_2 = (p_{atmos} - P_s) \end{aligned}$$

where p_s is the absolute pressure in the low-pressure suction plenum in Pa.

As for the single-plenum model, the arrangement in Figure 5.6 can operate in three modes, a discharge mode, a suction mode and a latched mode, and state-space formulations for the three modes of the OWC with two plenums are outlined below.

5.3.4.1 Discharge mode

If $p_i > p_d$, and the discharge valve stiction has been overcome, the model will operate in the discharge mode. The mass flow rates of air through the system when operating in the discharge mode are outlined in Table 5.5:

TABLE 5.5: Mass flow equations for system with a high-pressure discharge plenum and a low-pressure suction plenum in the discharge mode.

Mass flow into suction plenum from atmosphere	$\dot{m}_{ps} = Cd_O A_{ori}\sqrt{2\rho\left\|p_{atmos} - p_s\right\|}$
Mass flow rate from discharge plenum to atmosphere	$\dot{m}_{pd} = Cd_O A_{ori}\sqrt{2\rho\left\|p_d - p_{atmos}\right\|}$
Mass flow rate from chamber to discharge plenum	$\dot{m}_i = Cd_V L_g h_{max}\sqrt{2\rho\left\|p_i - p_d\right\|}$
Net mass flow rate into discharge plenum	$\dot{m}_d = \dot{m}_i - \dot{m}_{pd}$
Mass flow rate from suction plenum	$\dot{m}_s = \dot{m}_{ps}$

Note that, in the discharge mode, the net mass flow rate into the discharge plenum is $\dot{m}_i - \dot{m}_{pd}$, and that $p_i - p_d = x_3 - x_4$. The derivatives of each of the state variables for the discharge mode can be expressed as follows:

$$\dot{x}_1 = \dot{u}_7 = x_2 \tag{5.62}$$

$$\dot{x}_2 = \ddot{u}_7 = \frac{fe_7}{a_{77\infty}} - \frac{conv}{a_{77\infty}} - \frac{c_{77}}{a_{77\infty}}x_1 - \frac{A_{owc}}{a_{77\infty}}x_3 \tag{5.63}$$

$$\dot{x}_3 = \dot{\Delta p_i} = \dot{p}_i = \frac{c_s^2}{A_{owc}[h_o - x_1]}\dot{m}_i - \frac{\gamma\left[x_3 + p_{atmos}\right]}{[h_o - x_1]}x_2 \tag{5.64}$$

$$\dot{x}_4 = [p_d - \dot{p}_{atmos}] = \dot{p}_d = \frac{c_s^2}{V_d}\left[-\dot{m}_i - \dot{m}_d\right] \tag{5.65}$$

$$\dot{x}_5 = [\dot{p_{atmos}} - \dot{p_s}] = -\dot{p}_s = -\frac{c_s^2}{V_s}\dot{m}_s \tag{5.66}$$

In matrix form this yields:

$$\begin{pmatrix} \dot{x}_1 \\ \dot{x}_2 \\ \dot{x}_3 \\ \dot{x}_4 \\ \dot{x}_5 \end{pmatrix} = \begin{pmatrix} 0 & 1 & 0 & 0 & 0 \\ -\frac{c_{77}}{a_{77\infty}} & 0 & -\frac{A_{owc}}{a_{77\infty}} & 0 & 0 \\ 0 & -\frac{\gamma(x_3+p_{atmos})}{[h_o-x_1]} & 0 & 0 & 0 \\ 0 & 0 & 0 & 0 & 0 \\ 0 & 0 & 0 & 0 & 0 \end{pmatrix} \begin{pmatrix} x_1 \\ x_2 \\ x_3 \\ x_4 \\ x_5 \end{pmatrix} + \begin{pmatrix} 0 & 0 & 0 & 0 \\ (fe_7 - conv) & 0 & 0 & 0 \\ 0 & 0 & 0 & -\frac{c_s^2}{A_{owc}[h_o-x_1]} \\ 0 & -\frac{c_s^2}{V_d} & 0 & \frac{c_s^2}{V_d} \\ 0 & 0 & -\frac{c_s^2}{V_s} & 0 \end{pmatrix} \begin{pmatrix} \frac{1}{a_{77\infty}} \\ \dot{m}_d \\ \dot{m}_s \\ \dot{m}_i \end{pmatrix} \tag{5.67}$$

5.3.4.2 Suction mode

If $p_i < p_s$, and the suction valve stiction has been overcome, the model will operate in the suction mode. The mass flow rates of air through the system when operating in the suction mode are outlined in Table 5.6.

TABLE 5.6: Mass flow equations for system with a high-pressure discharge plenum and a low-pressure suction plenum in the discharge mode.

Mass flow into suction plenum from atmosphere	$\dot{m}_{ps} = Cd_O A_{ori}\sqrt{2\rho\,\lvert p_{atmos} - p_s\rvert}$
Mass flow from discharge plenum to atmosphere	$\dot{m}_{pd} = Cd_O A_{ori}\sqrt{2\rho\,\lvert p_d - p_{atmos}\rvert}$
Mass flow from suction plenum to chamber	$\dot{m}_i = Cd_V L_g h_{max}\sqrt{2\rho\,\lvert p_i - p_s\rvert}$
Net mass flow rate into discharge plenum	$\dot{m}_d = -\dot{m}_{pd}$
Net mass flow rate from suction plenum	$\dot{m}_s = \dot{m}_{ps} - \dot{m}_i$

Note that, in suction mode, net mass flow rate into the suction plenum is $\dot{m}_{ps} - \dot{m}_i$, and that $p_s - p_i = -x_3 - x_4$. Using the same state variables as for the discharge mode, the

derivatives of each of the state variables in the suction mode can be expressed as follows:

$$\dot{x}_1 = \dot{u}_7 = x_2 \tag{5.68}$$

$$\dot{x}_2 = \ddot{u}_7 = \frac{fe_7}{a_{77\infty}} - \frac{conv}{a_{77\infty}} - \frac{c_{77}}{a_{77\infty}} x_1 - \frac{A_{owc}}{a_{77\infty}} x_3 \tag{5.69}$$

$$\dot{x}_3 = \dot{\Delta p_i} = \dot{p}_i = \frac{c_s^2}{A_{owc}[h_o - x_1]} \dot{m}_i - \frac{\gamma \left[x_3 + p_{atmos}\right]}{[h_o - x_1]} x_2 \tag{5.70}$$

$$\dot{x}_4 = [p_d - \dot{p}_{atmos}] = \dot{p}_d = -\frac{c_s^2}{V_d} \dot{m}_d \tag{5.71}$$

$$\dot{x}_5 = [\dot{p_{atmos}} - p_s] = -\dot{p}_s = -\frac{c_s^2}{V_s} \left[\dot{m}_s - \dot{m}_i\right] \tag{5.72}$$

In matrix form this yields:

$$\begin{pmatrix} \dot{x}_1 \\ \dot{x}_2 \\ \dot{x}_3 \\ \dot{x}_4 \\ \dot{x}_5 \end{pmatrix} = \begin{pmatrix} 0 & 1 & 0 & 0 & 0 \\ -\frac{c_{77}}{a_{77\infty}} & 0 & -\frac{A_{owc}}{a_{77\infty}} & 0 & 0 \\ 0 & -\frac{\gamma(x_3 + p_{atmos})}{[h_o - x_1]} & 0 & 0 & 0 \\ 0 & 0 & 0 & 0 & 0 \\ 0 & 0 & 0 & 0 & 0 \end{pmatrix} \begin{pmatrix} x_1 \\ x_2 \\ x_3 \\ x_4 \\ x_5 \end{pmatrix} + \begin{pmatrix} 0 & 0 & 0 & 0 \\ (fe_7 - conv) & 0 & 0 & 0 \\ 0 & 0 & 0 & -\frac{c_s^2}{A_{owc}[h_o - x_1]} \\ 0 & -\frac{c_s^2}{V_d} & 0 & 0 \\ 0 & 0 & -\frac{c_s^2}{V_s} & \frac{c_s^2}{V_s} \end{pmatrix} \begin{pmatrix} \frac{1}{a_{77\infty}} \\ \dot{m}_d \\ \dot{m}_s \\ \dot{m}_i \end{pmatrix} \tag{5.73}$$

5.3.4.3 Latched mode

If $p_i = p_{atmos}$, and both air admittance valves are closed, or if the pressure drop across either valve is insufficient to overcome valve stiction, the OWC chamber will be latched.

Under such circumstances, $\dot{m}_i = 0$, and the mass flow rates for the system are given in Table 5.7.

TABLE 5.7: Mass flow equations for system with a high-pressure discharge plenum and a low-pressure suction plenum in the latched mode.

Mass flow into suction plenum from atmosphere	$\dot{m}_{ps} = Cd_O A_{ori}\sqrt{2\rho\left\|p_{atmos} - p_s\right\|}$
Mass flow from discharge plenum to atmosphere	$\dot{m}_{pd} = Cd_O A_{ori}\sqrt{2\rho\left\|p_d - p_{atmos}\right\|}$
Mass flow to/from chamber	$\dot{m}_i = 0$
Net mass flow rate into discharge plenum	$\dot{m}_d = -\dot{m}_{pd}$
Net mass flow rate from suction plenum	$\dot{m}_s = \dot{m}_{ps}$

The derivatives of the state variables become:

$$\dot{x}_1 = \dot{u}_7 = x_2 \tag{5.74}$$

$$\dot{x}_2 = \ddot{u}_7 = \frac{fe_7}{a_{77\infty}} - \frac{conv}{a_{77\infty}} - \frac{c_{77}}{a_{77\infty}}x_1 - \frac{A_{owc}}{a_{77\infty}}x_3 \tag{5.75}$$

$$\dot{x}_3 = \dot{\Delta p_i} = \dot{p}_i = \frac{c_s^2}{A_{owc}[h_o - x_1]}\dot{m}_i - \frac{\gamma\left[x_3 + p_{atmos}\right]}{[h_o - x_1]}x_2 \tag{5.76}$$

$$\dot{x}_4 = [p_d - \dot{p}_{atmos}] = \dot{p}_d = -\frac{c_s^2}{V_d}\dot{m}_d \tag{5.77}$$

$$\dot{x}_5 = [\dot{p_{atmos}} - p_s] = -\dot{p}_s = -\frac{c_s^2}{V_s}\dot{m}_s \tag{5.78}$$

In matrix form this yields:

$$\begin{pmatrix}\dot{x}_1\\ \dot{x}_2\\ \dot{x}_3\\ \dot{x}_4\\ \dot{x}_5\end{pmatrix} = \begin{pmatrix} 0 & 1 & 0 & 0 & 0\\ -\frac{c_{77}}{a_{77\infty}} & 0 & -\frac{A_{owc}}{a_{77\infty}} & 0 & 0\\ 0 & -\frac{\gamma(x_3+p_{atmos})}{[h_o-x_1]} & 0 & 0 & 0\\ 0 & 0 & 0 & 0 & 0\\ 0 & 0 & 0 & 0 & 0\end{pmatrix}\begin{pmatrix}x_1\\ x_2\\ x_3\\ x_4\\ x_5\end{pmatrix} + \begin{pmatrix} 0 & 0 & 0 & 0\\ (fe_7 - conv) & 0 & 0 & 0\\ 0 & 0 & 0 & -\frac{c_s^2}{A_{owc}[h_o-x_1]}\\ 0 & -\frac{c_s^2}{V_d} & 0 & 0\\ 0 & 0 & -\frac{c_s^2}{V_s} & 0\end{pmatrix}\begin{pmatrix}\frac{1}{a_{77\infty}}\\ \dot{m}_d\\ \dot{m}_s\\ \dot{m}_i\end{pmatrix} \quad (5.79)$$

5.4 Implementation of time domain numerical models

In this section, the process by which the numerical models described in Section 5.3 are implemented is described. The process of implementation follows a similar methodology to that used for the frequency domain model of the multi-chamber platform described in Chapter 4. This process is summarised in the flowchart presented in Figure 5.7. Multi-

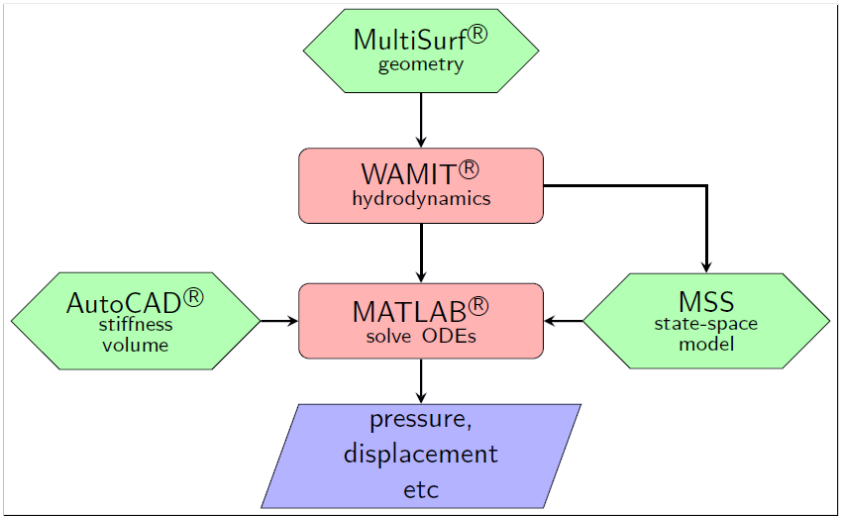

FIGURE 5.7: Flowchart of software used to create time domain models.

Surf is used to create the input geometry, describing the wetted surface of the single-cell OWC. The geometry is then processed by WAMIT to determine the hydrodynamic quantities required to create the impulse response of the radiation forces. AutoCAD

is used to determine the volume of the air trapped within the water column, and how this volume varies with water column displacement. AutoCAD is also used to find the area of the free surface, and hence the hydrostatic stiffness, of the water column. The coefficients of discharge for the valves and orifices of the system are determined experimentally. MATLAB is then used to solve the coupled set of state space equations. This was first performed using a discrete convolution method for the radiation forces, before the convolution term in the equation of motion for each model was replaced with a state-space approximation as described in [188]. The Marine Systems Simulator (MSS) Frequency Domain Identification (FDI) toolbox, created at the Norwegian University of Science and Technology (NTNU) [189], is used to create a state-space approximation of the convolution term. An issue with the hydrodynamic quantities calculated by WAMIT for the water column at high frequencies, and how the issue effects the FDI toolbox, is described. A technique for overcoming this issue is also presented and implemented.

5.4.1 Modelling of hydrodynamic quantities

Figure 5.8 illustrates the geometry initially produced in MultiSurf to be used as input to WAMIT. Note that, for clarity, the free surface of the water column is shown in blue in Figure 5.8.

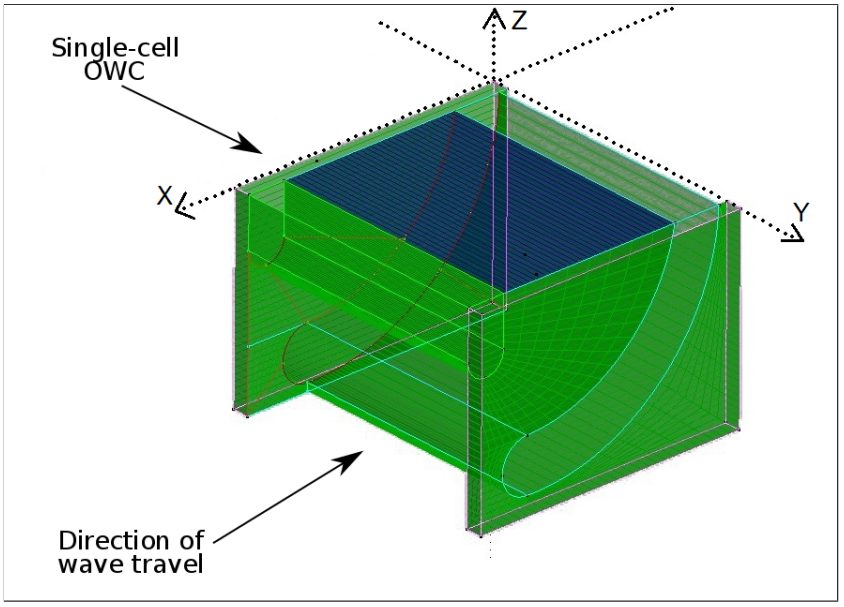

FIGURE 5.8: MultiSurf model of the mean wetted surface of the single-OWC model.

The input files for test run 17a, which is one of a number of sample runs which are supplied with the WAMIT software, and which analyses a circular, floating OWC, were modified to perform the hydrodynamic analysis on the model shown in Figure 5.8. WAMIT is a 3-dimensional solver, whereas the physical tank testing of the single-chamber OWC described herein took place in a 2-dimensional tank. In order to replicate 2-dimensional conditions, the MultiSurf model is extended in the cross-wave direction, labelled the y-axis in Figure 5.8. The resultant hydrodynamic parameters are then divided by the width of the extended OWC to obtain 'per unit' values. The per unit values are multiplied by the actual width of the water column. The model is extended in the cross-wave direction and re-analysed in this fashion until convergence on 2-dimensional results is obtained. The model is analysed for a sufficiently large range of frequencies, so that the complete range of non-zero radiation damping values are captured, in order to calculate the impulse response of the radiation forces as outlined in Section 5.4.2 below.

5.4.2 The convolution integral

Equation (5.1), the modified Cummins integro-differential equation, contains a convolution term upon which the radiation potential arising from the motion of the water column depends, taking into account the so-called 'memory effect' of the radiation potential. The convolution term takes into consideration the transient effects of the motion of the object in water from $t = 0$ to the present instant, and must be recalculated at each time step. A relationship between the kernel, $kr(t)$, of the convolution integral and the frequency-dependent added mass and radiation damping hydrodynamics of an object which is in motion in the fluid was established in [139]. Typically, the convolution integral is truncated to begin from time $t = 0$, and the kernel is convolved with the velocity vector of the object to obtain the memory function.

5.4.2.1 The kernel

Before the equations governing the motion of the water column can be solved, it is necessary to obtain the kernel for the radiation forces. The kernel takes the form of the impulse response function (IRF) of the radiation forces of the water column in the mode of motion of interest, in this case the pumping mode of the water column. The required frequency-dependent hydrodynamic values can be obtained using WAMIT [141]. It is

then possible to use WAMIT to obtain the IRF using the 'F2T' utility supplied by WAMIT. However, for ease of integration, the IRF of the radiation forces is calculated within the MATLAB code developed herein, as required. The IRF can be formed from either of the following two formulations, where a_{ij} and b_{ij} are the frequency-dependent added mass and radiation damping coefficients respectively, of the ij^{th} mode of motion:

$$kr_{ij}(t) = \frac{2}{\pi}\int_0^\infty b_{ij}(\omega)cos(\omega t)d\omega \tag{5.80}$$

$$kr_{ij}(t) = \frac{2}{\pi}\int_0^\infty \frac{[a_{ij}(\omega) - a_{ij}(\infty)]}{\omega} sin(\omega t)d\omega \tag{5.81}$$

The impulse response thus obtained may then be used in the convolution integral. In both Equations (5.80) and (5.81) an integration to infinity over frequency is required. In practice, the integration must be truncated at some sensible point. As it is typically the case that the frequency-dependent radiation damping begins at zero, for low frequencies, before returning to zero for high frequencies, and once a sufficiently large range of frequencies to capture the non-zero region of radiation damping is included in the integration, the frequency range may be truncated on the higher end. The radiation damping, b_{ij}, tends to converge faster than the added mass, a_{ij}, and thus Equation (5.80) was used to construct the IRF in MATLAB from the radiation damping. However, calculating the convolution integral at each time step of a time domain simulation is computationally expensive [190], [191]. Since the IRF decays to zero after a relatively short time, at any time step during a time domain simulation it is possible to limit the number of previous time steps in the convolution to a number equal to that required for the IRF to decay, and this would reduce the computational expense. However, when the numerical model of the WEI platform is developed to include multiple, interacting OWCs incorporated into a floating platform each with a memory term (and coupled memory terms), the computation cost of the convolution terms would dramatically increase. At that time it will be essential to replace the convolution terms. A number of techniques can be used to replace a convolution term with a computationally more efficient approximation. The two most common techniques are to replace the convolution integral with a linear, state-space system [192], or to replace the kernel with a function as in Prony's technique [193]. In order to approximate the convolution term in the Cummins equation given in Equation (5.1), the MSS toolbox is used. This creates a

state-space model, based on user-defined parameters, in conjunction with vectors of the frequency, the frequency-dependent added mass and the frequency-dependent damping, such as those determined by WAMIT. The success or otherwise of the process can be determined by comparing the impulse response of the resulting state-space system to the impulse response obtained from Equation (5.80).

5.4.2.2 Impulse response function

Figure 5.9 illustrates the frequency-dependent radiation damping for the pumping mode of the water column of the model illustrated in Figure 5.8. Note that the full range of non-zero radiation damping is included in the plot.

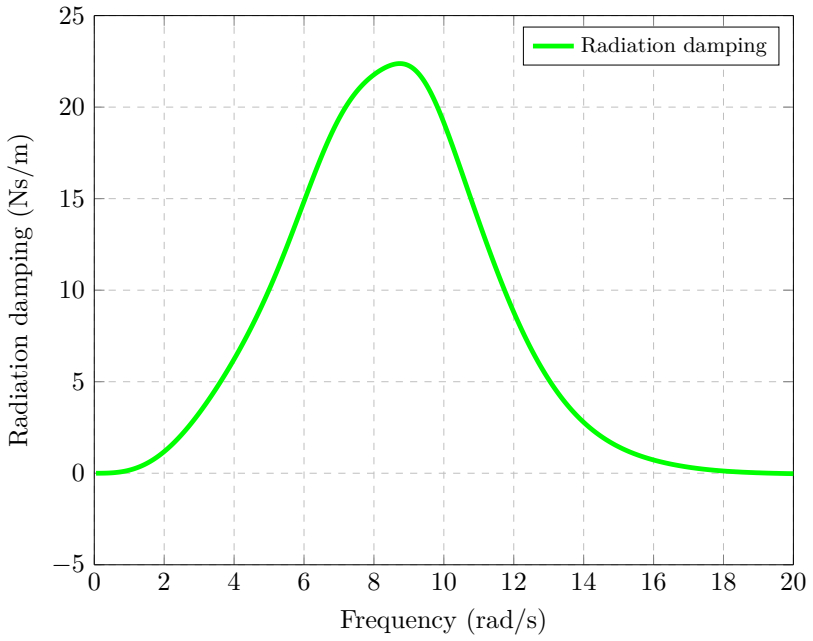

FIGURE 5.9: Radiation damping calculated by WAMIT V7 for the OWC shown in Figure 5.8.

The impulse response of the radiation forces for the pumping mode is found using Equation (5.80), and the results are shown in Figure 5.10.

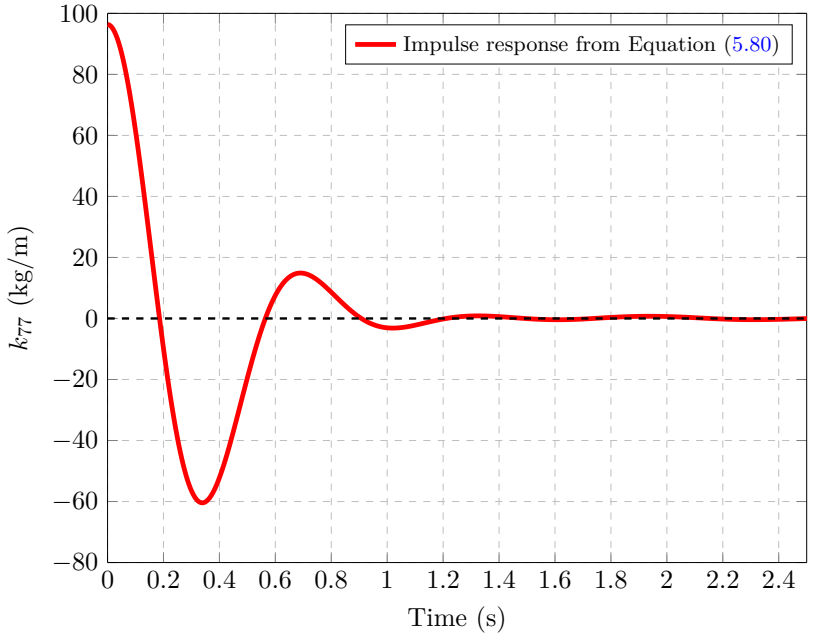

FIGURE 5.10: The impulse response of the pumping mode of the OWC shown in Figure 5.8 as constructed from Equation (5.80).

While it is possible to use the impulse response, shown in Figure 5.10, to calculate the convolution term in the Cummins Equation at each time step using a discrete convolution technique [194], the primary purpose of creating the IRF using the Ogilvie relations [139] is so that the impulse response of the state-space system used to replace the convolution term may be compared to the IRF in Figure 5.10.

5.4.2.3 State-space approximation of the convolution integral

The approach to the state-space approximation of the convolution term in the Cummins equation given in Equation (5.1) follows that first proposed in [188]. This process approximates the convolution integral with a state-space system, with zero initial conditions, as follows:

$$\dot{X}_P(t) = A_p X p(t) + B_p u_p(t)$$

$$y_p(t) = C_p X_p(t) \approx \int_0^t kr(t-\tau)\dot{u}_7(\tau)dt \tag{5.82}$$

The ease with which the state-space model of the radiation forces may be integrated with the state-space approach, used to model the systems described in Section 5.3, provides the rationale for using the state-space approach to model the systems. The order

of the coupled ODEs, in a system modelling one of the arrangements in Section 5.3, increases by the order of the system in Equation (5.82). So, for example, using an nth order state-space model to approximate the convolution term, the matrices A and B in the system of ODEs modelling the single-chamber OWC with an orifice, shown in Equation (5.45), become:

$$A = \begin{bmatrix} & & & 0 & & 0 \\ & A_p & & \vdots & B_p & \vdots \\ & & & 0 & & 0 \\ 0 & \dots & 0 & 0 & 1 & 0 \\ & -\frac{Cp}{a_{77\infty}} & & -\frac{c_{77}}{a_{77\infty}} & 0 & -\frac{A_{owc}}{a_{77\infty}} \\ 0 & \dots & & 0 & \frac{\gamma(x_{3+n}+p_{atmos})}{(h_o - x_{1+n})} & 0 \end{bmatrix}$$

$$B = \begin{bmatrix} 0 & 0 \\ \vdots & \vdots \\ 0 & 0 \\ fe_7 & 0 \\ 0 & \frac{c_s^2}{A_{owc}[h_o - x_{1+n}]} \end{bmatrix}$$

In order to populate and determine the order of the matrices A_p, B_p and C_p in Equation (5.82), the FDI MATLAB toolbox [189] was used. This toolbox requires vectors comprising the frequency-dependent radiation damping, added mass and corresponding frequencies, and, optionally, the infinite frequency added mass, for the mode of motion for which the convolution term is to be approximated. However, it was found that when the parameters determined by WAMIT for the pumping mode of the single chamber OWC in Figure 5.8 were passed to the FDI toolbox, the resultant state-space system was unstable, irrespective of system order selected. This problem would appear to relate to the values calculated by WAMIT for the added mass at higher frequencies and for the infinite frequency added mass. A plot of the added mass versus frequency, as calculated by WAMIT, and dimensioned according to the WAMIT manual [141], can be seen in Figure 5.11.

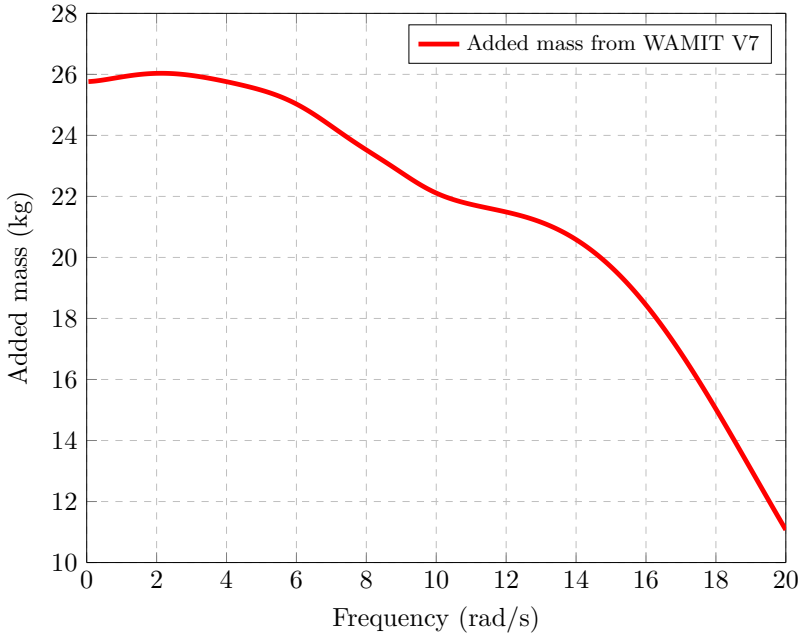

FIGURE 5.11: Dimensionalised frequency-dependent added mass from WAMIT V7.

The dimensionalised infinite frequency added mass, $a_{77\infty}$, returned by WAMIT V7 is given as 26.4 kg. It would be expected that the added mass curve should be asymptotic to the infinite frequency added mass at higher frequency. However, clearly, the added mass curve is not asymptotic to the value calculated by WAMIT. The added mass versus frequency curve exhibits atypical behaviour at higher frequencies, seemingly tending towards a value of $-\infty$, when compared to the equivalent curve that would be obtained for, for example, a floating cylinder [25], [195]. During execution, the FDI toolbox recreates the added mass and damping curves from the approximation of the impulse response function (along with plots of the magnitude and phase of the frequency domain representation of the kernel) and displays the results overlaid with the original values used as input. At this point, the user may change the order of the approximation and re-run the process. Figure 5.12 illustrates the plot for the data set generated for the geometry in Figure 5.8, for a transfer function of order 6, as determined by the FDI toolbox. Clearly, a good fit has not been achieved for the hydrodynamics, and hence a good fit has also not been achieved for the frequency domain impulse response.

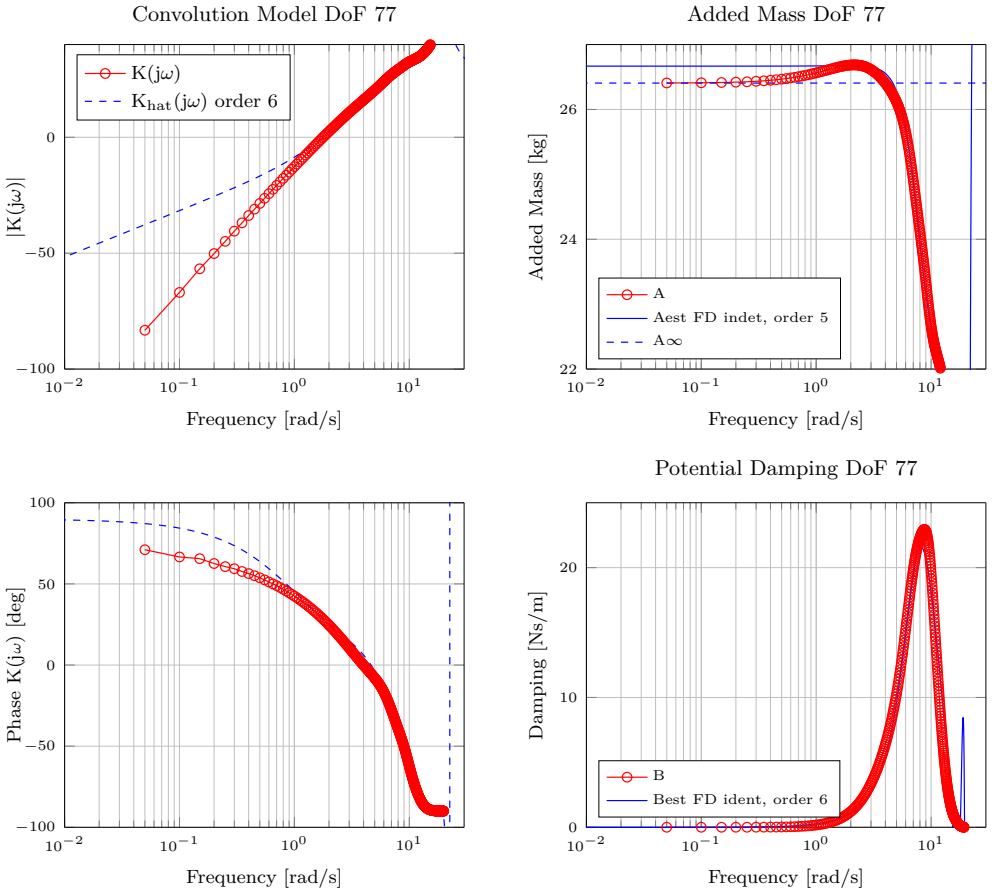

FIGURE 5.12: Figure from FDI toolbox showing original and recreated added mass, radiation damping and impulse response for the pumping mode of the single-cell OWC.

Despite the issues that are apparent in Figure 5.11, the FDI toolbox will execute to completion and output a transfer function using this data, which may easily be converted to a state-space system in MATLAB. The impulse response of this state-space system should then approximate that shown in Figure 5.10. Figure 5.13 shows the impulse response of the state-space approximation, created using the FDI toolbox, in conjunction with the WAMIT results for the modified test run 17a case. As can be seen, not only does this system fail to approximate the curve shown in Figure 5.13, but the system is unstable, as confirmed by the presence of complex conjugate poles with positive real parts in the transfer function used to create the state-space system.

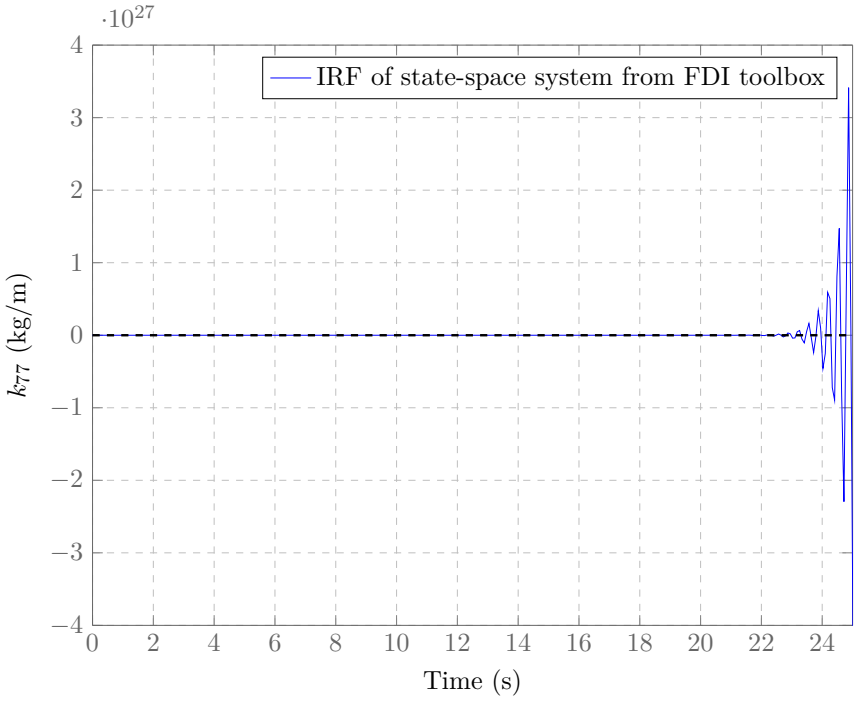

FIGURE 5.13: Impulse response of the state-space approximation to the kernel of the convolution integral generated by MSS toolbox using WAMIT data generated for the geometry shown in Figure 5.8.

In order to verify that the FDI toolbox was being used correctly, a WAMIT analysis of the cylinder used in [188] was performed, and the results from WAMIT used with the FDI toolbox to create a state-space approximation of the radiation kernel. While the state-space model realised by the FDI toolbox was not identical to that presented in [188], the IRF of the approximation from the FDI toolbox compared favourably with that in [188]. While the absolute values of the hydrodynamic parameters differ between the cylinder in [188] and the OWC in Figure 5.8, the main difference in form between the two is the shape of the added mass.

5.4.3 Reconstructing the added mass

The added mass and damping are related to each other through the Kramers-Kronig [196] or Ogilvie [139] relations, which may also be considered expressions of the Hilbert transformation, and are given by:

$$a(\omega) = a_{77\infty} - \frac{1}{\omega}\int_0^\infty kr(t)\sin(\omega t)\,dt \tag{5.83}$$

and

$$b(\omega) = \int_0^\infty kr(t) \cos(\omega t)\, dt \tag{5.84}$$

This suggests that, once values for $b_{77}(\omega)$ are known, and the appropriate value of $a_{77\infty}$ has been determined, $a_{77}(\omega)$ can be 'reconstructed' from the radiation damping values by creating '$kr(t)$' from the $b(\omega)$ vector, once confidence in the radiation damping values has been established. While the use of WAMIT to estimate the hydrodynamic quantities for proposed WECs is common [197], in the light of the concerns raised with respect to the added mass values shown in Figure 5.11, a short investigation was undertaken to compare the results for the radiation damping, for a generic water column with analytical results presented in the existing literature. An analytical solution for the radiation damping of a water column contained within a thin-walled narrow pipe is presented in [60] and given by:

$$b_{77}(\omega) = m_{77}\omega\frac{\pi}{2}\left(\frac{d}{a}\right)^2 Lae^{-2La} \tag{5.85}$$

where:

$$\begin{aligned} m_{77} &= \text{the mass of the water column, } kg \\ a &= \text{the draft of the pipe, } m \\ d &= \text{the radius of the pipe, } m \\ L &= \tfrac{\omega^2}{g}. \end{aligned}$$

A thin-walled narrow pipe of draft 0.18 m and radius 0.0225 m was modelled in MultiSurf as a single dipole patch, with a second patch representing the water column surface. This arrangement, which can be seen in Figure 5.14, was then analysed using WAMIT.

The comparison between the results for the radiation damping obtained for the narrow pipe using WAMIT and those obtained using Equation (5.85) is shown in Figure 5.15. It can be seen that there is good agreement between the two sets of results.

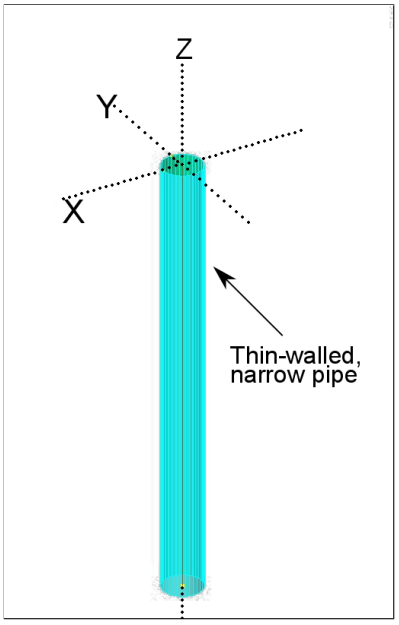

FIGURE 5.14: MultiSurf model of an OWC comprising a thin-walled narrow pipe.

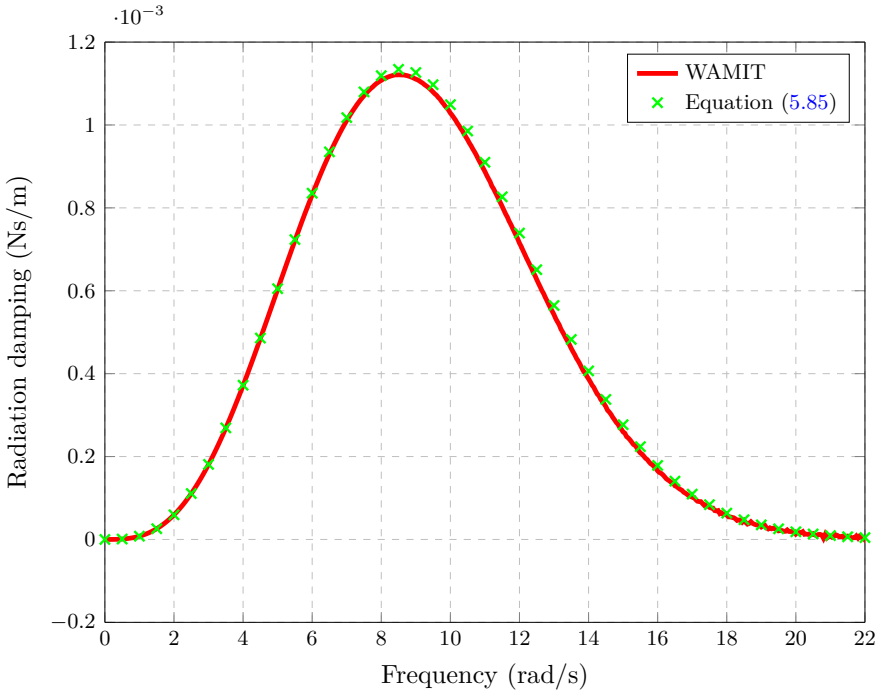

FIGURE 5.15: Comparison of radiation damping calculated from WAMIT V7 and closed form solution for a thin-walled narrow pipe obtained by solving Equation (5.85).

The results presented in Figure 5.85 demonstrate the capability of WAMIT to calculate the radiation damping of a water column in agreement with analytical theory, and thus the process of reconstructing the added mass from the radiation damping values, obtained from WAMIT for the water column shown in Figure 5.8, was continued. The

shape of a curve of the added mass versus frequency, that would result from implementing Equation (5.83), is determined by the term:

$$\frac{1}{\omega}\int_0^\infty kr\left(t\right)\sin\left(\omega t\right)dt$$

in Equation (5.83). The position of the added mass curve with respect to the y-axis is determined by $a_{77\infty}$. To clarify the concept, consider the equation of a line in the form:

$$y = mx + c \tag{5.86}$$

The slope of the line in Equation (5.86) is analogous to the term $\frac{1}{\omega}\int_0^\infty kr\left(t\right)\sin\left(\omega t\right)dt$ in Equation (5.83). The y-intercept, c, changes the vertical offset of the line, and is thus analogous to $a_{77\infty}$. Initially, Equation (5.83) was implemented in MATLAB, using the infinite frequency added mass, and the impulse response $kr(t)$ was found using the damping values calculated by WAMIT for the single chamber OWC model shown in Figure 5.8. Figure 5.16 illustrates a comparison between the added mass versus frequency curves for the added mass values calculated directly by WAMIT, and the analogous curve found from solving Equation (5.83) using $a_{77\infty}$, as calculated by WAMIT.

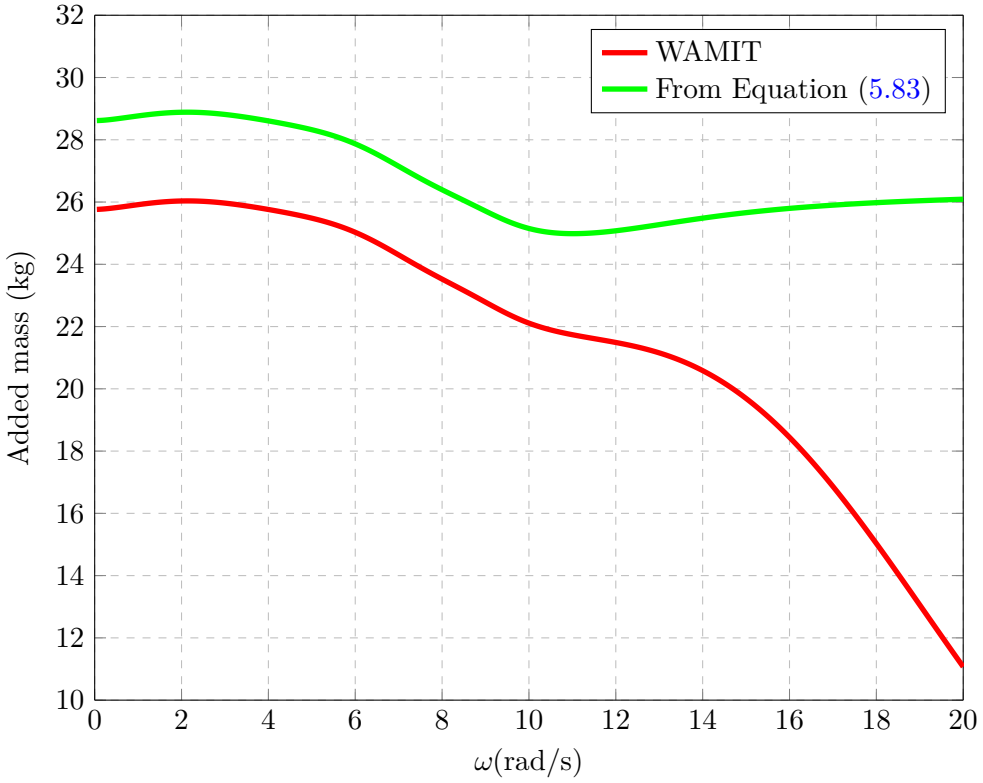

FIGURE 5.16: Added mass versus frequency results calculated directly by WAMIT, and as reconstructed using Equation (5.83) with $a_{77\infty}$ calculated directly by WAMIT for the single chamber OWC shown in Figure 5.8.

A number of features in the plot of the reconstructed added mass presented in Figure 5.16 are worth noting. Firstly, the shape of the curve is as might be expected, and is in keeping with that presented elsewhere for regular shapes, [25] and [195]. Secondly, between zero and approximately 4.5 rad/s, the shape of the two curves match closely, and subsequent investigation demonstrated that this fit improves as the time step used to solve Equation (5.83) is decreased. However, even at lower frequencies, a significant vertical offset exists between the two set of results. It is worth noting that the single chamber OWC geometry had previously been analysed using WAMIT V6.2, and that WAMIT V6.2 and WAMIT V7 produced two significantly different values of $a_{77\infty}$. After 4.5 rad/s, the shapes of the two curves diverge. In order to remove the y-axis offset between the reconstructed added mass and the added mass calculated by WAMIT at frequencies below 4.5 rad/s, the value of $a_{77\infty}$, used to solve Equation (5.83), is chosen so that the two added mass values for the lowest, non-zero frequency are equal. This value for $a_{77\infty}$ of 23.55 kg (as compared to the value of 26.4 kg calculated by WAMIT V7) is then used to solve Equation (5.83) for the remaining frequencies. Figure 5.17

illustrates the added mass calculated using Equation (5.83) with a value for $a_{77\infty}$, equal to 23.55 kg, overlaid upon the original values calculated by WAMIT. As can be seen, the two curves match closely up to 4 rad/s.

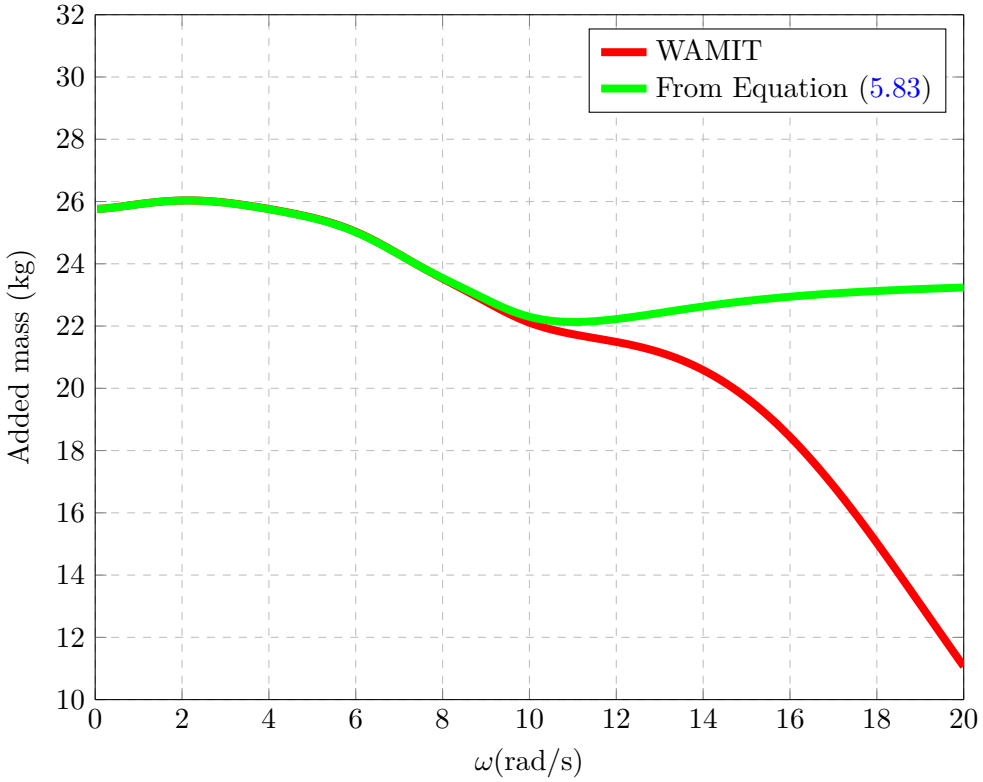

FIGURE 5.17: Added mass versus frequency results calculated directly by WAMIT, and as reconstructed using Equation (5.83) using a value of $a_{77\infty} = 23.55\ kg$ for the single chamber OWC shown in Figure 5.8.

The reconstructed added mass curve illustrated in Figure 5.17 is now passed to the FDI toolbox, along with the value of $a_{77\infty}$ used to produce them, 23.55 kg. The frequency vector and radiation damping vector remain unchanged from those used previously. Figure 5.18 is analogous to Figure 5.12, but uses the reconstructed added mass vector in place of the original. Figure 5.18 shows none of the irregularities associated with Figure 5.12.

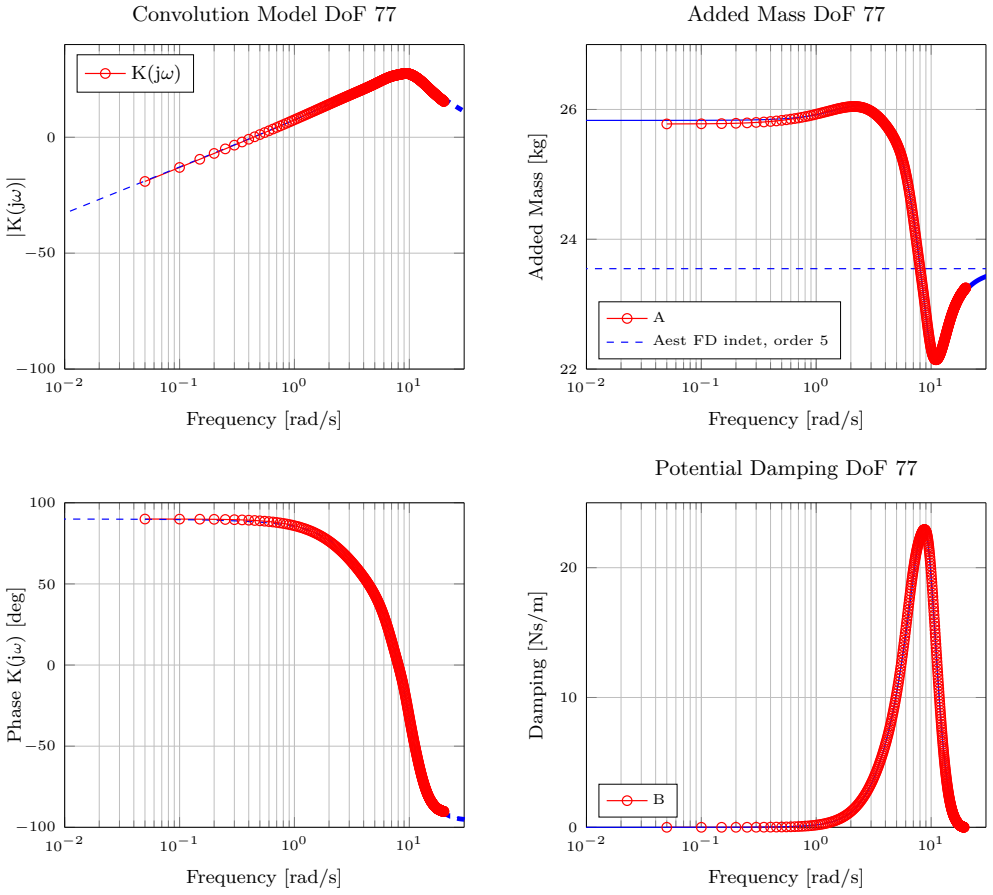

FIGURE 5.18: Figure from FDI toolbox showing added mass and damping used as input to FDI toolbox, and corresponding values recreated by the toolbox for the single chamber OWC shown in Figure 5.8.

The FDI toolbox generates a selected fourth order transfer function, which is converted to a state-space system. Figure 5.19 shows the impulse response of this state-space system overlaid with the results found from implementing Equation (5.81). As can been seen, the state-space model now closely matches the desired behaviour. For clarity, a large time step has been used to generate Figure 5.19. The state-space approximation of $kr(t)$, used to generate the results in Chapter 9, uses a finer time step than that shown in Figure 5.19.

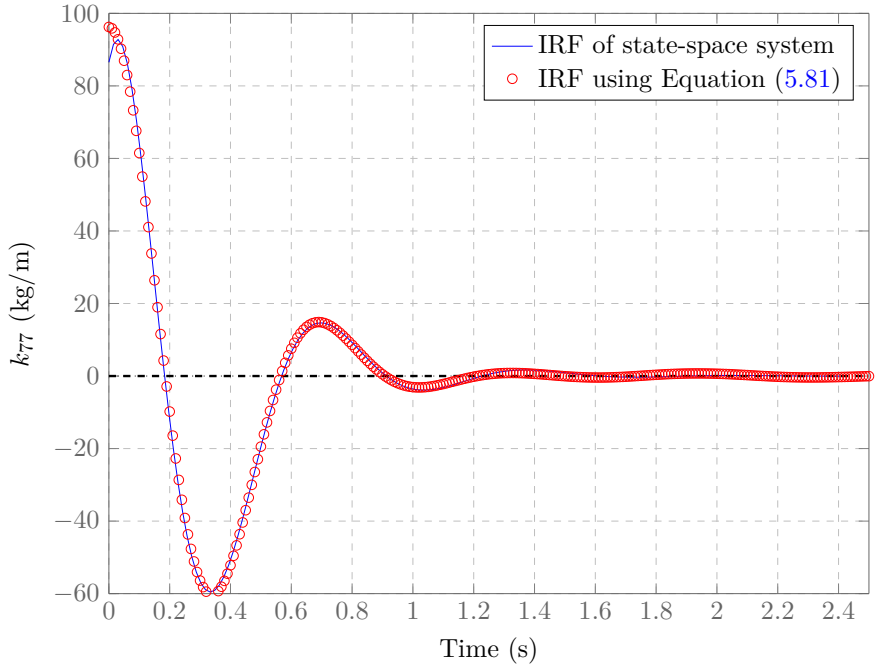

FIGURE 5.19: Impulse response of the state-space model found using reconstructed added mass overlaid with k from Equation (5.81) for the single chamber OWC shown in Figure 5.8.

The impulse response of the state-space system is stable, and approximates well the impulse response, based on the radiation damping values using Equation (5.81). While the cause of the unexpected values for the high frequency added mass and $a_{77\infty}$ is unknown at this time, it may relate to how WAMIT solves for the radiation potential, and the tendency for Green's integral equations to become singular as the thickness of the body analysed decreases [141].

Note that, while the results here relate to the geometry presented in Figure 5.8, in order to ensure the issue relating to the added mass at higher frequencies was not unique to that geometry, an analysis of the WAMIT-supplied geometry for test run 17a in the WAMIT manual was conducted. The identical issue arose for the geometry supplied for test run 17a. The author sent the results of that analysis to WAMIT Inc. with a request for any information; however, no response was forthcoming.

5.4.4 MATLAB implementation

The state-space models presented in Section 5.3 are implemented in MATLAB as a set of ODEs in matrix form which are solved using the built in 'ODE45' solver, which is

based on an explicit Runge-Kutta formulation [198]. The choice of ODE solver was based on MATLAB documented advice on the topic, which recommends first trying ODE45. Should ODE45 fail to solve for the system of differential equations, or take an excessively long time to produce a solution, this is an indication of a highly stiff system, and MATLAB have a range of solvers for stiff problems. ODE45 was used successfully to implement the time domain simulations outlined in Section 5.3. While other built-in MATLAB solvers were explored, no improvement in performance was found.

5.4.5 Non linear parameters

A number of refinements were made to the time domain model to include the effect of the variation in the cross-sectional area (and hence the hydrostatic stiffness) of the water column, and the non-linear variation in the air volume trapped above the water column in the chamber, as the water column height varies. In the state-space systems presented in Section 5.3, the hydrostatic stiffness is assumed constant, and the air volume is assumed to vary linearly with respect to water column displacement. However, due to the curved nature of the single OWC chamber in Figure 5.8, the hydrostatic stiffness varies with water column displacement. Likewise, the air volume varies in a non-linear fashion with variation in water column height. In order to derive a polynomial to express both these quantities, in terms of the water column displacement over the range of likely displacements, the AutoCAD model shown in Figure 8.12 was used. A set of regions, representing the free surface of the water column as the displacement of the water column moves from the still water position, in increments of 1 mm over a range of $\pm$ 55 mm, was created. The *massprop* command was used to find the area of the regions, and hence the hydrostatic stiffness, of the water column in each position, and a second order polynomial was fitted to the results. The R^2 value of the fitted polynomial is 0.9998. Figure 5.20 illustrates the variation in the hydrostatic stiffness with water column height, and the second order polynomial fitted to the data points obtained from AutoCAD. During a time domain simulation, at each time step, the current height of the water column is used to determine the appropriate value of hydrostatic stiffness, for that time step.

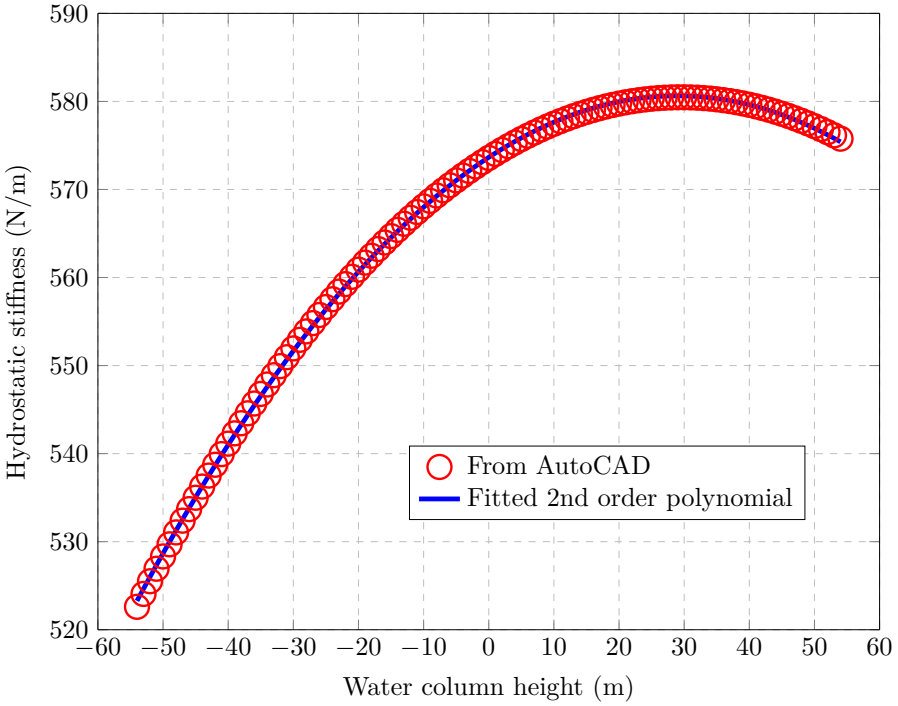

FIGURE 5.20: Variation in water column hydrostatic stiffness with water column displacement for the single chamber OWC shown in Figure 5.8.

A similar process was performed to determine the variation in the air chamber volume with respect to water column height. A set of 3-dimensional solids representing the air in the chamber for various water column displacements was created, and AutoCAD was used to find the volume of these solids, again using the *massprop* command. In this case, however, the variation in the air chamber volume with respect to water column height is virtually linear, and a straight line was fitted to the AutoCAD data. Figure 5.21 illustrates the variation in the volume found using AutoCAD, the fitted straight line (which has a R^2 value equal to 0.9998), and also the variation in air volume with respect to water column height using Equation (5.36), which was used to create the state-space systems in Section 5.3. As can be seen, the three data sets are virtually indistinguishable.

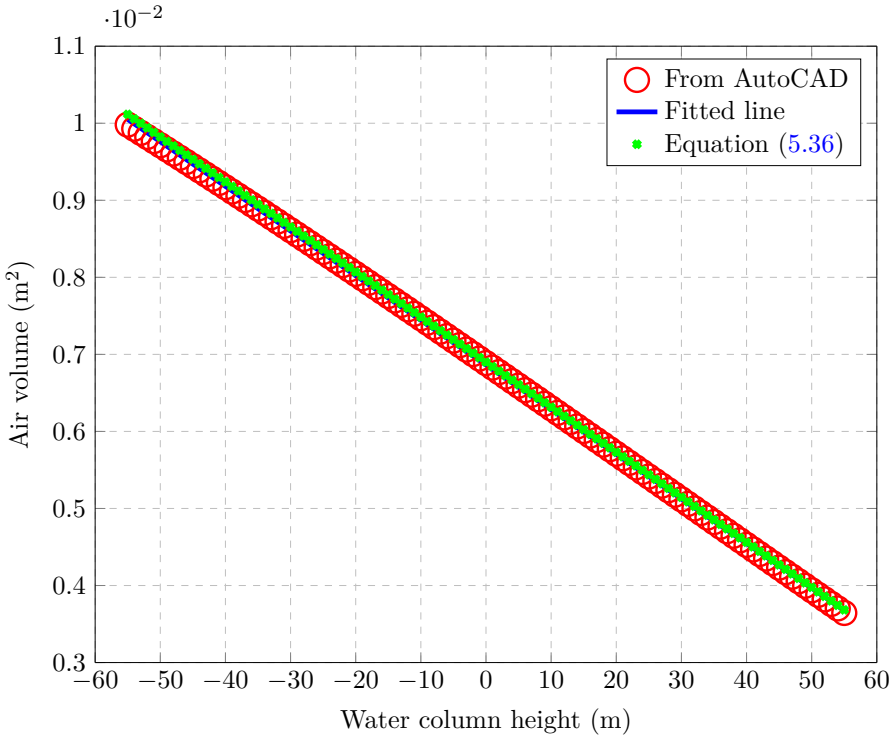

FIGURE 5.21: Variation in trapped air volume in the OWC chamber with water column displacement for the single chamber OWC shown in Figure 5.8.

The mass flow rate through the valves and orifices of the physical systems described in Section 5.3 depends on the density of air, and the density of air within the chamber will vary due to the compressibility of air, as the pressure within the chamber varies. As shown in [179], for an adiabatic process, the linearised relationship between air density and pressure is given by:

$$\rho_{air} = \rho_{atmos}\left(1 + \frac{p}{\gamma \rho_{atmos}}\right) \tag{5.87}$$

At each time step, the pressure of the air in the OWC chamber and the plenums, where appropriate, are interrogated, and the density of air within the chamber and plenums is set in accordance with Equation (5.87). The predictions made by the time domain simulations are presented and compared to the results of narrow tank testing in Chapter 9.

Chapter 6

Experimental Design

6.1 Introduction

In this chapter, the design of the tank tests performed on the physical models, and the rationale for the tests, is presented. The scaling of both the physical models and the wave regime is first described. Next, the tests conducted in the ocean basin tank located at the HMRC on the 32-OWC, physical 1:50 scale model of the proposed WEI platform, in various configurations, using monochromatic waves, are outlined. Tests, using polychromatic wave conditions for the 32-OWC physical model in one configuration are presented, before some demonstration tests that were performed are also described. Finally, the testing performed on the 1:50 scale model of the single-chamber OWC, in various configurations, using the narrow tank at DkIT, and the rationale behind the tests, are outlined.

6.2 Scaling

The objective of tank testing scale physical models is to use the results obtained from tests, performed on the physical model of an object, under one set of conditions to predict the behaviour of the object in a different set of conditions. Typically, physical models are built to a scale smaller than full scale or prototype scale, and are tested in wave conditions that are scaled by the same factor as the physical models. In order for a comparison between a scale model and a large-scale prototype to be valid, the conditions associated

with both must be physically similar. The term 'physical similarity' encompasses a number of different kinds of similarity. In general, two sets of conditions are considered physically similar with respect to a specific physical quantity if the ratio of the physical quantity between the two systems is constant throughout the systems. In the field of mechanics, there are three kinds of physical similarity:

- *Geometric similarity* is similarity of shape between two systems. Under conditions of geometric similarity, the ratio of a length in one system to the corresponding length in the second system is constant for all lengths in the system.
- *Kinematic similarity* is similarity of motion between two systems. Under conditions of kinematic similarity, length and time intervals of the two systems are kept similar, resulting in similarity of velocity and acceleration.
- *Dynamic similarity* is similarity of forces. Under conditions of dynamic similarity, the *ratio* of the magnitudes of forces at corresponding points in the two systems is constant.

A number of mechanisms may give rise to forces in systems which involve fluids, and such forces include gravitational forces, inertia forces, viscous forces, elastic forces and surface tension forces. It is not normally possible to maintain dynamic similarity for all forces, particularly if the same fluid is considered in both systems. However, in many instances, not all forces apply or are significant. For example, in wave energy modelling, it is common to neglect the effect of surface tension. Thus, it is possible to focus on the similarity of the most significant forces which, for wave propagation, are:

- Inertia forces $F_i \propto \rho u^2 l^2 \propto \rho \omega^2 l^4$
- Gravity forces $F_g \propto \rho g l^3$
- Viscosity forces $F_v \propto \mu u l$

where:

ρ = the density of the fluid, kg/m^3
u = the characteristic velocity of flow, m/s
l = the characteristic length, m
ω = is the characteristic frequency of flow, rad/s
μ = is the viscosity of the fluid, Ns/m^2

The study of similarity has given rise to standard dimensionless numbers. The two dimensionless indices which relate the inertial, gravitational and viscous forces are:

- Reynolds number, $\text{Re} = \dfrac{\text{Inertia Forces}}{\text{Viscous Forces}} = \dfrac{\rho\omega l^2}{\mu}$
- Froude number, $\text{Fr} = \sqrt{\dfrac{\text{Inertia Forces}}{\text{Gravitational Forces}}} = \omega\sqrt{\dfrac{l}{g}}$

Consider two systems, one geometrically scaled to the second by a factor α, such that $l_1 = \alpha l_2$. In order to preserve the Reynolds number between the two systems:

$$\frac{\rho_1\omega_1 l_1^2}{\mu_1} = \frac{\rho_2\omega_2 l_2^2}{\mu_2} \tag{6.1}$$

hence:

$$\frac{\rho_1\omega_1 l_1^2}{\mu_1} = \frac{\rho_2\omega_2 \left(\alpha l_1\right)^2}{\mu_2} \tag{6.2}$$

and thus:

$$\alpha^2 = \frac{\rho_1}{\rho_2}\frac{\omega_1}{\omega_2}\frac{\mu_2}{\mu_1} \tag{6.3}$$

A similar consideration for preserving the Froude number between two systems yields:

$$\omega_1\sqrt{\frac{l_1}{g_1}} = \omega_2 = \sqrt{\frac{l_2}{g_2}} \tag{6.4}$$

thus:

$$\frac{\omega_1}{\omega_2} = \sqrt{\alpha\frac{g_1}{g_2}} \tag{6.5}$$

In order to preserve both the Reynolds and Froude numbers, both Equation (6.3) and Equation (6.5) must be true, and hence:

$$\alpha^2 = \frac{\rho_1}{\rho_2}\sqrt{\alpha\frac{g_1}{g_2}}\frac{\mu_2}{\mu_1} \tag{6.6}$$

while:

$$\alpha^{1.5} = \frac{\rho_1}{\rho_2}\sqrt{\frac{g_1}{g_2}}\frac{\mu_2}{\mu_1} \tag{6.7}$$

Quantity	Scaling
Wave height	α
Wave length	α
Wave period	$\alpha^{0.5}$
Wave frequency	$\alpha^{-0.5}$
Linear displacement	α
Angular displacement	1
Mass	α^3
Force	α^3
Power	$\alpha^{3.5}$
Linear damping	$\alpha^{2.5}$

TABLE 6.1: Froude scaling for quantities of interest, where α is the scaling factor.

In order for Equation (6.7) to be true for any non-unity value of α, assuming the gravitation constant does not change between the locations of both systems, it would be necessary to use a different fluid in the two systems. Using water as one of the fluids, the second fluid would need to be 'designed' such that the density and viscosity varied appropriately to satisfy Equation (6.7), for the chosen value of α. Identifying a suitable second fluid is rarely practical. Of the three forces considered in the Reynolds and Froude numbers, the viscous force is the least significant. It is thus common to preserve the Froude number, which may be assumed to be satisfied using geometric scaling [199]. Under Froude scaling, viscous forces are relatively higher when compared to full scale, resulting in greater relative energy loss to viscous forces at model scale when compared to full scale. This, in turn, results in a conservative, under-estimation of the power absorbed by a full-scale device based on model-scale tank tests. A full discussion of physical similarity can be found in, for example, [200]. Under Froude scaling, for a scale factor of α, the scaling of the quantities of interest herein are given in Table 6.1. To obtain the full-scale equivalent of a model-scale parameter, the parameter is multiplied by the term in the 'Scaling' column of Table 6.1.

Both the physical model of the 32-OWC proposed WEI platform, and the wave regimes under which it was tested, were scaled in accordance with Froude scaling as given in Table 6.1.

6.3 32-OWC model tests

6.3.1 Monochromatic wave testing

The testing programme, undertaken on the 32-OWC physical model of the proposed WEI platform, described in Chapter 8, was developed by the author in conjunction with WEI and the technical staff at the HMRC. The testing plan was independently assessed by a third-party consultant (RPS Group plc.) engaged by the SEAI, who also assessed the suitability of the initial funding application by WEI, and the viability of the 32-OWC physical model constructed by WEI, in association with the author. In line with the approach and protocols outlined under the HMRC Development and Evaluation Protocol [201], and by EquiMar under the Seventh European Framework Programme [202], the purpose of the proposed testing was to:

1. Investigate the effect on the model of different physical configurations to identify and understand the critical parameters affecting the performance of the model.
2. Characterise the performance and behaviour of the model under controlled conditions.
3. Establish the technical feasibility of the proposed design.
4. Establish the survivability of the proposed design under extreme ocean conditions.
5. Validate and improve numerical models based on the analysis of the results. It is intended that, in the future, both the physical and numerical analysis streams would inform the development of each other.

6.3.2 Model configurations

The 32-OWC physical model of the proposed WEI platform was tested in a total of five physical configurations, through the removal and addition of a range of component parts. With reference to Chapter 8 on model construction, the five configurations are summarised in Table 6.2.

Configuration	Test Content
1	The platform is fitted with the buoyancy tubes/heave damping plates, and with the lower wave-guide 'shoes', see Figures 8.1 and 8.8.
2	The buoyancy tubes/heave damping plates are removed, and the platform is fitted with the lower wave-guide shoes.
3	The buoyancy tubes/heave damping plates and lower wave-guide shoes are removed.
4	The buoyancy tubes/heave damping plates are re-installed with the addition of larger heave damping plates made from a near neutrally-buoyant material (Perspex) of water plane area equal to that of the lower wave-guide shoes. These larger damping plates are installed using bolts to attach them to the existing base of the buoyancy tubes/heave damping plates.
5	As for Configuration 4, with the lid of the low-pressure plenums removed.

TABLE 6.2: Outline of the physical configurations of the 32-OWC model of the proposed WEI platform used during testing at the HMRC.

The objective of the testing programme, outlined in Table 6.2, was to examine the effect of removing components from the model on the model behaviour and the wave power absorbed by the platform. The heave damping plates were intended to provide stability to the platform by reducing platform motions, while the purpose of the wave-guide shoes was to channel waves into the opening of each water column to increase the motion of the water columns. During previous testing on fixed arrays of three OWCs, the inclusion of wave-guides increased the overall wave power absorbed. Testing of Configuration 2 was intended to establish how much of a stabilising effect the heave damping plates introduced, and the effect of this stabilisation on the power absorbed by the model platform. Testing of Configuration 3 was intended to establish the effect of the wave-guide shoes on the power absorbed by the platform, and also the degree to which pitch motions of the platform were reduced by the inclusion of the shoes. The decision to include larger heave damping plates for the testing on Configuration 4 was taken based on the analysis of the motions of the platform during the testing on Configurations 1 to 3.

Finally, Configuration 5, when the low-pressure plenum was open to atmosphere, was intended to investigate if the model platform was over-damped, and if the manifolding of airflows was advantageous or disadvantageous in terms of wave power absorbed. For each configuration of the physical model, pairs of Venturis of varying throat diameter were installed between the PTO pipes. Venturis of varying throat diameters were installed in order to introduce varying levels of PTO damping, and to identify the throat diameter which maximised the power absorbed by the platform. The tests for a given model configuration were repeated for each pair of Venturis. Each individual configuration/Venturi setup was tested for a total of 10 monochromatic wave periods, covering the range of typical wave periods experienced in the North Atlantic (scaled in accordance with Froude scaling). The wave periods used during the monochromatic-wave phase of this testing, the corresponding wave angular frequencies, and the equivalent full-scale wave periods are listed in Table 6.3.

Wave period (s)	Wave frequency ($rads^{-1}$)	Full-scale wave period (s)
0.71	8.85	5
0.85	7.39	6
0.99	6.35	7
1.13	5.56	8
1.27	4.95	9
1.41	4.46	10
1.56	4.03	11
1.70	3.70	12
1.84	3.41	13
1.98	3.17	14

TABLE 6.3: Wave periods, and full-scale equivalents, used during monochromatic wave tests of the physical model of the 32-OWC proposed WEI platform.

All monochromatic wave testing was carried out with a wave height of 60 mm, equivalent to a wave height of 3 m at full scale. For Configuration 1, the model was tested using Venturis of throat diameter equal to 15 mm, 20 mm, 22.5 mm, 25 mm, 27.5 mm and 30 mm. After transport to the HMRC, the 32-OWC physical model was installed in the tank, where it was then moored using a single-point catenary-style arrangement, where an anchored chain was connected to a floating buoy and, then, to the nose of the platform. The model was free to rotate about the point to which the mooring chain connected to the nose, simulating a single-point FPSO-style mooring. Figure 6.1 is a schematic showing a plan and elevation of the model moored in the ocean basin at the HMRC, and shows the main dimensions of the basin and model. Also illustrated is the

naming convention for the OWC chambers, with chambers 1 to 16 on the starboard leg and chambers 17 to 32 on the port leg, as indicated.

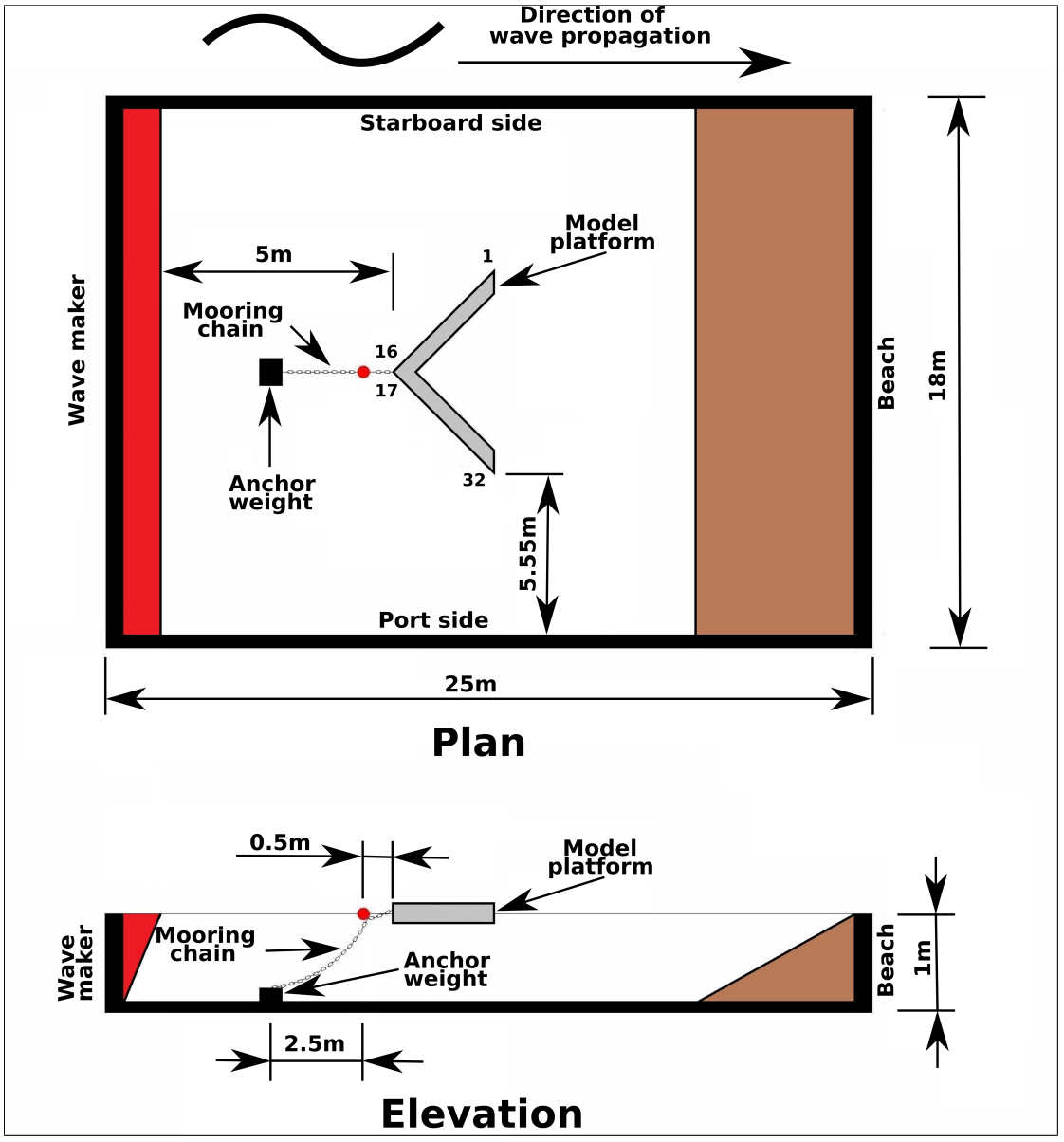

FIGURE 6.1: Plan (top) and elevation (bottom) of the physical model of the 32-OWC proposed WEI platform installed in the ocean basin at the HMRC.

Figure 6.2 shows a plan view of the 32-OWC platform model, illustrating the main dimensions of the model.

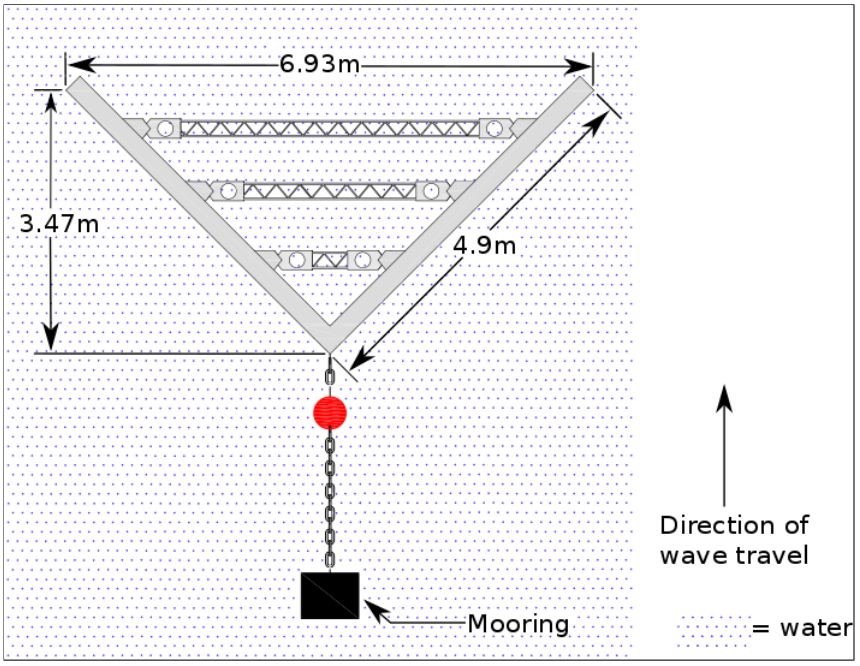

FIGURE 6.2: Plan view of the physical model of the 32-OWC proposed WEI platform, illustrating the main dimensions of the model

Figure 6.3 shows an elevation of the 32-OWC platform model. The draft of the model platform, and of the water columns within each OWC chamber are shown.

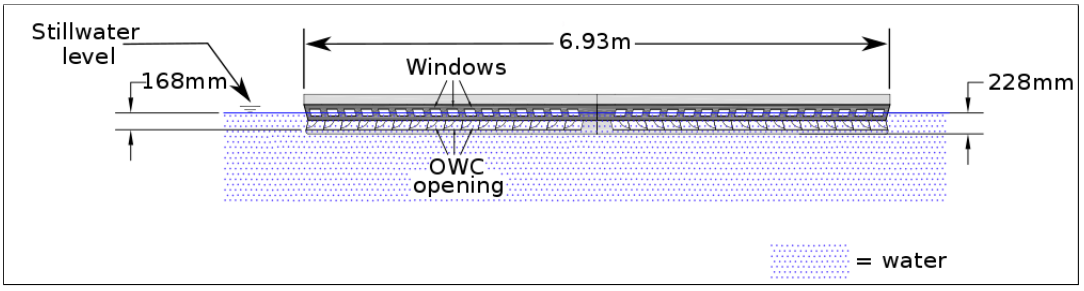

FIGURE 6.3: Plan view of the physical model of the 32-OWC proposed WEI platform, illustrating the draft of the model platform, and the OWC chambers

In order to illustrate the width of each water column, Figure 6.4 illustrates an abeam view of a number of chambers of one leg of the platform.

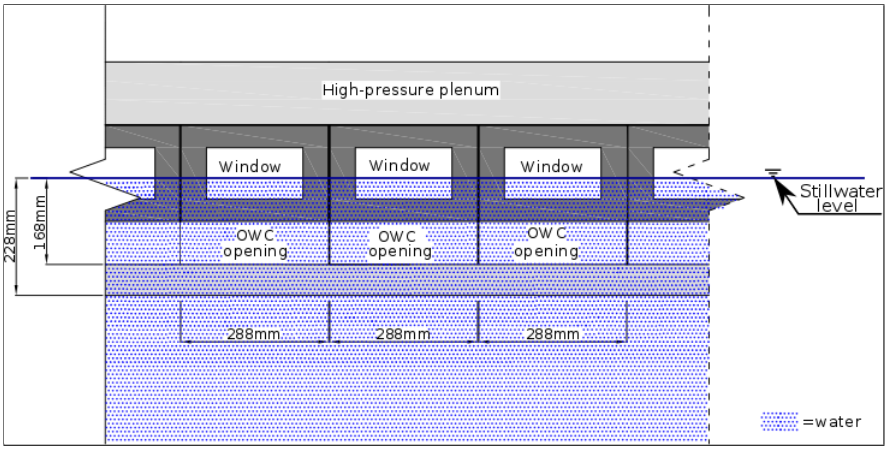

FIGURE 6.4: Abeam view of one leg of the platform showing a number of chambers and illustrating the width of the water columns

The final schematic of the 32-OWC model, Figure 6.5 is a cross section through one chamber of one leg, which shows the length of each water column, as well as the other main dimensions of the chamber.

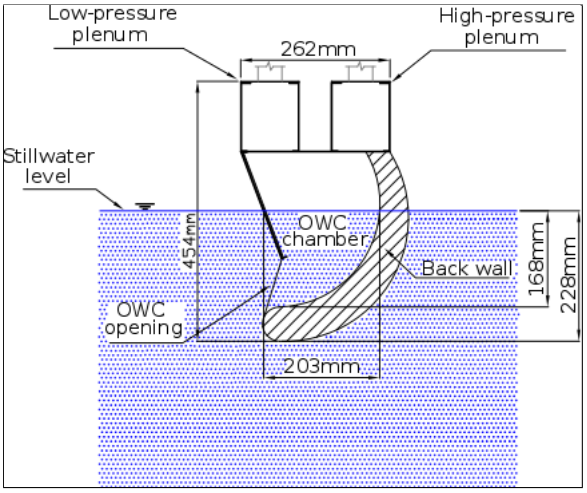

FIGURE 6.5: Abeam view of one leg of the platform showing a number of chambers and illustrating the width of the water columns

In addition to the sensing equipment installed on the model (described in Section 8.2.2), a Qualisys® motion capture system was used to track the movement of the platform during testing. For each set-up tested, the mass of ballast required to set the model to the desired draft varied, and thus the centre of gravity of the platform would change. In order for the motion capture system to correctly determine the rotational modes of the platform, a new centre of gravity was determined for each set-up and programmed into the motion capture system. In each case, the centre of gravity was determined using 3-D

models generated in AutoCAD®, as described in Section 4.2.1. All tests simulated head sea conditions, with waves impacting each OWC chamber at 45 degrees. For each test, data was recorded for 60 s once any transient effects had subsided. Wave probes, located in front of the model, were used to record the incident wave heights, and the time series data from these probes were used to ensure the incident wave height remained at 60 mm.

As well as characterising the 32-OWC model in the configuration described in Table 6.2, during the testing of Configuration 1, it was intended to identify which Venturi pairing optimised the power absorbed by the model. This was achieved by starting testing with pairs of Venturis of throat diameter smaller than that expected to produce the optimum level of power absorption, and increasing the throat diameter until diameters equal to, and greater than, that expected to produce the optimum power, were tested. The power absorbed for each level of applied damping tested was calculated, and the optimum Venturi throat diameter was then determined. The power absorbed at wave periods of 1.27 and 1.41 s, equivalent to 9 and 10 s at full scale, was used in the determination of the optimum Venturi pairing. These two wave periods were chosen so as to reflect the most common occurring zero crossing period in the North Atlantic, as shown in Table 2.1. It was found that the Venturi pairing with a throat diameter of 25 mm resulted in the optimum power absorbed for waves for the two chosen wave periods.

Following an analysis of the power absorbed by the model during this stage of the testing, the remaining configurations were tested for throat diameters of 20 mm, 22.5 mm, 25 mm and 30 mm only. The results of the testing of the 32-OWC model of the proposed WEI platform, performed in the ocean basin at the HMRC, are presented in Chapter 9.

6.3.3 Polychromatic waves

One aim of the testing of the 32-OWC physical model of the proposed WEI platform was to progress the concept through Technical Readiness Level (TRL) 2 and into TRL 3. In accordance with established TRL protocols for WECs [201], the focus of the testing was thus on monochromatic wave conditions. However, in order to gain some experience with polychromatic testing, a set of random wave tests was conducted, with the model in Configuration 4, with the 25 mm Venturi pairing installed. Each test run in this round of testing lasted 256 s, sufficient time for the representative range of wave heights

and frequencies within the polychromatic wave spectrum to develop [148]. A total of 10 such tests were performed. Table 6.4 lists the significant wave heights and mean wave periods used. The significant wave heights and mean wave periods were chosen based

Significant wave height (mm)	Mean wave period (s)	Full-scale mean period
60	1.08	7.64
60	1.52	10.75
60	2.03	14.35
60	2.50	17.67
60	2.72	19.23
90	1.08	7.64
90	1.52	10.75
90	2.03	14.35
90	2.50	17.67
90	2.72	19.23

TABLE 6.4: Range of significant wave heights and mean periods used in polychromatic tests on the 32-OWC model of the proposed WEI platform in Configuration 4 with the 25 mm Venturi pairing installed.

on typical conditions at the Atlantic Marine Energy Test Site (AMETS) at Belmullet off the west coast of Ireland [203].

6.3.4 Parameters measured

The parameters recorded during the tank testing of the 32-OWC physical model are given in Table 6.5. The numbering scheme of the OWC chambers can be seen in Figure 6.1. Plenum 1 refers to the high-pressure plenum, and Plenum 2 refers to the low-pressure plenum, which are both in communication with OWC chambers 1 to 16. Plenum 3 refers to the high-pressure plenum, and Plenum 4 refers to the low-pressure plenum, which are both in communication with OWC chambers 17 to 32.

All sensors were connected to the data acquisition system at the HMRC, and were calibrated by the HMRC technical staff. However, during the testing, a number of pressure transducer sensors failed. WEI considered the power absorbed by the model to be the single most important measurable output from the tests. Thus, it was ensured that the two pressure transducers required to make the power measurements, that is the two transducers either side of the Venturi on the starboard leg, were recording reliable data at all times.

Pressure	Free surface elevation
OWC Chambers 1-16	OWC Chambers 1-16
Stern Plenum 1	OWC 17
Middle Plenum 1	OWC 21
Prow Plenum 1	OWC 24
Stern Plenum 2	OWC 28
Middle Plenum 2	OWC 32
Prow Plenum 2	Located in tank
Prow Plenum 3	Located in tank
Middle Plenum 3	Located in tank
Stern Plenum 4	–
Middle Plenum 4	–
Prow side Venturi 4	–
Stern side Venturi 4	–
Pitot Tube	–

TABLE 6.5: Parameters measured and recorded during testing of the 32-OWC physical model of the proposed WEI platform at the HMRC.

6.3.5 Demonstration tests

As an extra day of testing was available at the test facility, three final sets of demonstration tests were performed on the 32-OWC model. During the first test, the model was returned to Configuration 4 and a simulated wind turbine located at the nose of the model. The wind turbine was simulated using a length of PVC pipe, with a mass located along its length in order to represent the scaled mass of a wind turbine tower and also to locate the centre of gravity of the tower appropriately. A second mass located at the top of the PVC pipe simulated the mass of a nacelle and turbine blades. No data was recorded during this test, and the purpose was simply to gain a visual idea of how the full-scale system might look and behave. The second demonstration test carried out with the model in Configuration 4 involved replacing the Venturi on the starboard leg with an arrangement consisting of two lengths of ducting between which was installed a modified 3 W PC cooling fan to simulate a turbine. The PC cooling fan was coupled to the PTO arrangement in Figure 8.1 using sealing tape, while a single 25 mm throat diameter Venturi was installed on the port leg. The fan had been modified to operate as an air-driven generator. Due to the design of the fan motor, when used as a generator,

AC current is created. Cabling was installed between the fan and a custom-made LED box containing a simple rectifier and eight LEDs. The model was then subjected to monochromatic waves of 60 mm height, at a period of 1.27 s (equivalent to a full-scale wave of 3 m height at a period of 9 s using Froude scaling). The model was then subjected to a Bretschneider spectrum Froude-scaled to resemble wave conditions typical of the AMETS. In both the mono- and poly-chromatic tests, the LEDs rapidly increased in brightness to their maximum intensity. During monochromatic wave testing, the LEDs remained at maximum intensity. Some variation in intensity occurred during the Bretschnieder tests, as would be expected. The staff at the HMRC stated that this was the first occasion when a WEC tested in the HMRC test facility had produced electricity of any kind.

6.4 Single-chamber model tests

The construction of the single-chamber OWC model is described in Chapter 8. The purpose of the single-chamber OWC tests is two-fold. The first objective is to characterise the behaviour of a single-chamber OWC of similar geometry to the chambers which make up of the 32-OWC physical model of the proposed WEI platform, as well as to characterise a number of control components, such as the air admittance valves, when the model is subject to monochromatic incident waves. The complex hydrodynamic, thermodynamic and mechanical interactions which took place within the 32-OWC model makes it impossible to study the behaviour of individual mechanisms and components in operation within the platform, or to validate numerical models of such mechanisms and components. The first motivation in the numerical and physical modelling of a signal-OWC chamber is to explore such mechanisms. The second motivation is to generate data that may be used to assess the validity of the numerical time domain models, described in Chapter 5. While the single-chamber OWC model has been tested in a number of configurations, the general test set-up remains the same, and this general layout is shown in Figure 6.6.

Figure 6.7 illustrates a cross section through (left), and an elevation of (right), the single-chamber OWC. The draft of the model, the draft of the water column, the width of the water column and the depth of the front lip of the model are illustrated. Note that the

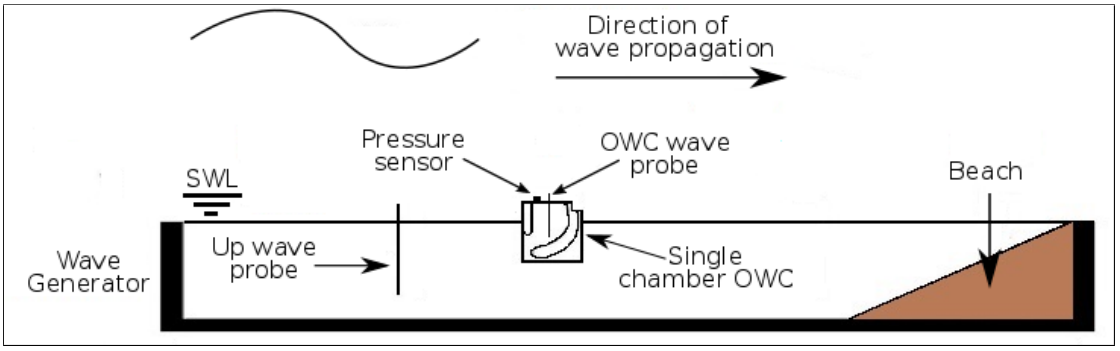

FIGURE 6.6: Schematic of single-chamber OWC model and narrow tank at DkIT.

width of the water column is equal to the width of the water column in a single chamber of the 32-OWC model platform.

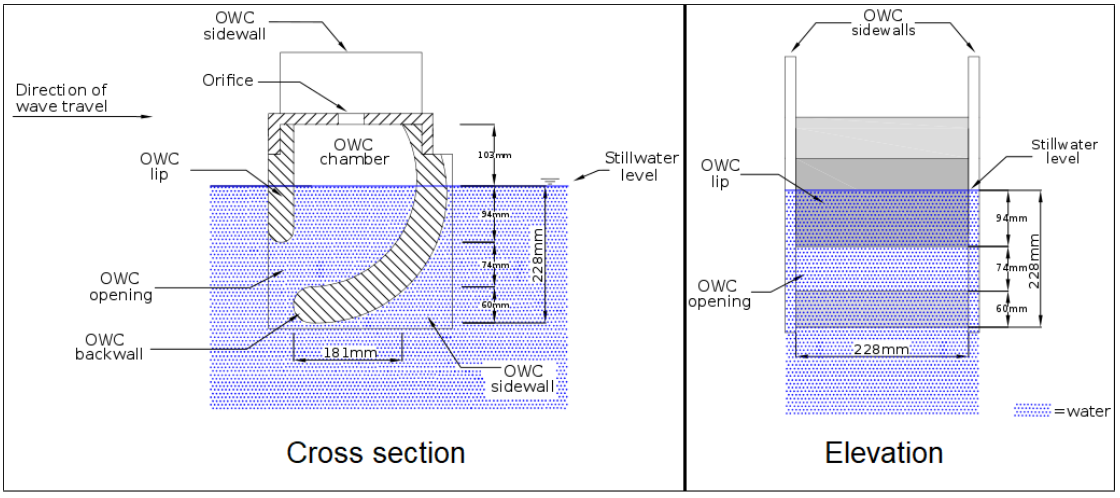

FIGURE 6.7: Cross section through (left), and elevation of (right), the single-chamber OWC illustrating the key dimensions of the single-OWC model and water column.

For all configurations, the displacement of the centroid of the free surface of the water column is measured and recorded using a resistive wave probe. The free surface displacement of the water in the narrow tank is recorded upwave and downwave from the model. The gauge pressure of the air within the chamber is recorded using a pressure transducer located at the top of the OWC chamber. One side wall of the single-chamber OWC model is made from Perspex® so that the motion of the water column can be observed. During testing, a digital camera was used to create a visual record of the behaviour of the water column. All monochromatic tests were run until steady-state conditions were achieved, after which time data was recorded for 60 s.

6.4.1 Test round 1 - Sealed system testing

For the first round of testing performed using the single-chamber OWC model, both of the 42 mm openings on top of the OWC, which can be seen in piece ⑤ in Figure 8.12, were completely sealed from atmosphere. An air-tight seal was verified by subjecting the model to large incident waves and using leak detection spray to locate any small air leaks, which were then stopped using silicone sealant. This process was repeated until no further leaks were detected. The model was then subjected to monochromatic incident waves of varying amplitude and frequency. Wave amplitudes, ranging from 5 mm to 30 mm, in increments of 5 mm, were used. The range of wave amplitudes, up to 1.5 m at full scale (corresponding to 30 mm amplitude at model scale), was chosen to correspond to the full-scale wave heights in which the WEI platform is intended to operate most efficiently. Wave frequencies ranging from 0.4 Hz to 1.4 Hz, in increments of 0.1 Hz were tested. The choice of wave frequencies was based on the typical range of wave periods experienced in the North Atlantic. At full scale, using Froude scaling, the chosen frequencies correspond to wave periods ranging from 5 s to 17.7 s. Furthermore, the wave frequency values employed range from the minimum to the maximum values which the narrow tank at DkIT is capable of generating. Following the advice of the technical staff at the HMRC, data was sampled and recorded at 32 Hz during the tests. Thus, a total of 66 tests were performed during the sealed system testing. The data obtained during Test round 1 of the single-chamber OWC model may be used to assess the validity of the numerical model of the sealed chamber described in Section 5.3.0.2, by examining the time series of the pressure signal and comparing the time series with the predictions of the numerical model. Furthermore, by assuming the small volume of air above the water column trapped in the OWC chamber is incompressible, the exciting force time series may be obtained from the pressure time series by multiplying the pressure time series by the cross-sectional area of the water column at the free surface. Table 6.6 lists the tested wave frequencies and amplitudes, as well as the full-scale equivalent wave frequencies and amplitudes during sealed system testing.

6.4.2 Test round 2 - Orifice testing

The second round of testing was performed using the single-chamber OWC model, in which one of the openings in the top of the OWC chamber was completely sealed, and

Test wave amplitude	Full-scale amplitude	Test wave frequency	Full-scale period
5 mm	0.25 m	0.4 hz	17.68 s
10 mm	0.50 m	0.5 hz	14.14 s
15 mm	0.75 m	0.6 hz	11.78 s
20 mm	1.00 m	0.7 hz	10.10 s
25 mm	1.25 m	0.8 hz	8.84 s
30 mm	1.50 m	0.9 hz	7.86 s
–	–	1.0 hz	7.07 s
–	–	1.1 hz	6.49 s
–	–	1.2 hz	5.89 s
–	–	1.3 hz	5.44 s
–	–	1.4 hz	5.05 s

TABLE 6.6: Wave frequencies and amplitudes tested during sealed system testing, and the full-scale equivalent wave frequencies and amplitudes.

an adjustable orifice installed into the second opening, using a custom-made coupler. The adjustable orifice can be seen in Figure 8.14. The objective of this testing was to characterise the orifice and the motions of the water column within the OWC chamber, and the effect of varying the orifice diameter, and hence the level of damping experienced by the water column, on the behaviour of the water column. Furthermore, through visual inspection of the water column (made possible by the Perspex® side wall), the presence of mechanisms, not included in the time-domain models, could be detected. During Test round 2, monochromatic tests, with wave amplitudes varying from 5 mm to 30 mm, in increments of 5 mm, for frequencies varying from 0.4 Hz to 1.4 Hz, in increments of 0.1 Hz, were performed. These tests were repeated for orifice diameters from 5 mm to 30 mm, in increments of 5 mm, which resulted in a total of 396 tests. The data obtained during Test round 2 may be used to determine the mass flow rate of air through the orifice, and calibrate the coefficient of discharge of the orifice. Further, the results may be used to assess the validity of the numerical model of the sealed chamber, described in Section 5.3.1, by examining the time series of the pressure signal and the water column displacement, and comparing both with the predictions of the numerical model. Table 6.6 lists the wave amplitudes and frequencies, and Table 6.7 lists the orifice diameters, used during the orifice testing.

Orifice diameter
5 mm
10 mm
15 mm
20 mm
25 mm
30 mm

TABLE 6.7: Orifice diameters used during the orifice testing.

6.4.3 Test round 3 - Air admittance valve testing

During the third round of testing, both the 42 mm openings in the top of the OWC were connected to air admittance valves in an arrangement similar to that used for each chamber of the 32-OWC scale model. One air admittance valve would allow air to flow from atmosphere into the OWC chamber when the pressure in the chamber was lower than that of atmosphere, while the second valve would allow air to flow from the chamber to atmosphere, once the pressure in the chamber exceeded that of atmosphere. During the testing of the 32-OWC physical model, 'OsmaVent 40' air admittance valves, made by WAVIN B.V., were used. However, at the time of the testing on the single-chamber OWC model in the narrow tank, these valves were no longer available. A number of alternative valves were trialled, and 'HypAir Balance' valves, manufactured by Capricorn S.A., were selected to replace the OsmaVent valves. HypAir Balance valves were chosen as the manufacturer-rated airflow through the HypAir Balance valves matches that for the OsmaVent valve. During Test round 3, the model was tested using monochromatic waves of amplitudes from 15 mm to 30 mm, in increments of 5 mm, and frequencies of 0.4 Hz to 1.4 Hz, in increments of 0.1 Hz. Note that, for waves of amplitude less than 15 mm, insufficient pressure differences between atmosphere and the OWC chamber rose to overcome valve stiction and allow air to flow either into, or out of, the OWC chamber. Initially, Test round 3 tests were performed with data sampled at a rate of 32 Hz. However, after an initial examination of the data, it was found that the duration of the valve stiction process was of the order of milliseconds (typically, pressure would spike within the chamber for approximately 4 ms before the valve would open). The sampling rate was, therefore, significantly increased up to 1 kHz, in order to capture this phenomenon. The data obtained during Test round 3 may be used to calibrate the mass flow rate of air through the valves, determine the stiction characteristics of the valves, and assess the validity of the numerical model of the sealed chamber, described

Test wave amplitude	Test wave frequency
15 mm	0.4 hz
20 mm	0.5 hz
25 mm	0.6 hz
30 mm	0.7 hz
–	0.8 hz
–	0.9 hz
–	1.0 hz
–	1.1 hz
–	1.2 hz
–	1.3 hz
–	1.4 hz

TABLE 6.8: Wave frequencies and amplitudes tested during the air admittance valve, the single plenum and the two plenum testing.

in Section 5.3.2, by examining the time series of the pressure signal and the water column displacement, and comparing both with the predictions of the numerical model. Table 6.8 lists the wave amplitudes and frequencies used during the air admittance valve testing.

6.4.4 Test round 4 - Single plenum testing

During Test round 4, an air box was installed on top of the OWC chamber over the discharge air admittance valve to represent the effect of a high-pressure discharge plenum. This volume is labelled (10) in Figure 8.12. Both air admittance valves used in Test round 3 remained installed on the model. An additional pressure transducer was used during Test round 4 to record the gauge pressure in the air box. As for Test round 3, data was recorded at 1 kHz during Test round 4, and the model was tested using monochromatic waves of amplitudes from 15 mm to 30 mm, in increments of 5 mm, and frequencies of 0.4 Hz to 1.4 Hz, in increments of 0.1 Hz. Table 6.8 lists the wave amplitudes and frequencies used during the single plenum testing. The data obtained during Test round 4 may be used to assess the validity of the numerical model of the sealed chamber, described in Section 5.3.3, by examining the time series of the pressure signals from inside the OWC chamber and the high-pressure air box, and the water column displacement, and comparing all three with the predictions of the numerical model.

6.4.5 Test round 5 - Two plenum testing

In Test round 5 of the single-chamber OWC model testing, a second air box was installed on the model, in addition to the air box installed during Test round 4. The second air box was installed over the suction air admittance valve, and was intended to represent the low-pressure suction plenum. A third pressure transducer was used to measure the gauge pressure in the second air box during the testing. As for Test rounds 3 and 4, data was recorded at 1 kHz during Test round 5, and the model was tested using monochromatic waves of amplitudes from 15 mm to 30 mm, in increments of 5 mm, and frequencies of 0.4 Hz to 1.4 Hz, in increments of 0.1 Hz. The data obtained during Test round 4 may be used to assess the validity of the numerical model of the sealed chamber, described in Section 5.3.4, by examining the time series of the pressure signals from inside the OWC chamber, the high-and low-pressure air boxes, and the water column displacement, and comparing the four time series with the predictions of the numerical model. Table 6.8 lists the wave amplitudes and frequencies used during the single plenum testing.

Chapter 7

Testing Facilities

7.1 Introduction

Two wave tank testing facilities were used to carry out the experimental work discussed in this thesis. The testing on a single-OWC model, described in Chapter 6, and the measurements of the hydrodynamic parameters of the single-OWC model, described in Chapter 11, were performed using the narrow tank facility at DkIT described in Section 7.2. The testing performed on the multiple-OWC, 1 : 50 scale model in conjunction with WEI, and described in Chapter 6, took place in the large ocean basin at University College Cork (UCC), which was, at that time, located at the HMRC in Pouladuff, Co. Cork. Both the DkIT test facility and the HMRC test facility are now described in Sections 7.2 and 7.3 respectively.

7.2 Narrow tank at DkIT

The testing of the single-OWC model using the DkIT narrow tank was the first time the narrow tank was used for testing, following the acquisition of the tank by DkIT. The tank, and the process of installing and calibrating the tank, are now presented. The measurement and data acquisition equipment used with the tank is also described. Finally, a number of technical issues that have arisen during the use of the narrow tank are discussed, with the aim that such information may prove useful to future users of the narrow tank.

7.2.1 Tank description

In 2008, DkIT purchased a narrow wave tank from Queens University Belfast (QUB). The tank was previously installed at QUB, where it had been used extensively in earlier model testing campaigns, [204, 205]. Following purchase, the tank was kept in storage until a suitable location was available at DkIT to install it. Such a location was found in 2012 when a dedicated hydraulics lab was established in the refurbished P.J. Carroll building, which was once a tobacco factory, and had been lately purchased by the college. The tank, which was originally designed and built by Edinburgh Designs, has a length of 18 m, a width of 350 mm, a depth of 1 m and a freeboard of 200 mm. The walls and floor of the tank are made primarily from glass-reinforced plastic (GRP). Two test sections, located at approximately 7.3 m and 10.1 m from the wave maker, are constructed from glass walls and floor pieces to allow for observation of models under test. Both of the glass sections have a length of 1.22 m. At one end of the tank, a single, wedge-shaped, flap-type wave maker is installed behind a water tight gusset. Figure 7.1 [206] illustrates the arrangement of the wavemaker. Water is present on only one side of the paddle. The paddle pivots about its tapered end, and is connected to the tank via a fabric hinge. A series of large springs are tensioned to counterbalance the weight of the water in the tank so that, in a neutral position, the face of the paddle is vertical. The paddle is controlled and driven using an 8 amp servomotor, and a force feedback system is employed to eliminate reflected waves. The DkIT narrow tank is two-dimensional, unlike the ocean basin facility at the HMRC described in Section 7.3, which is three-dimensional. It is therefore necessary that any model under test spans the entire width of the tank to prevent edge effects.

7.2.2 General tank installation and operation

The narrow tank was physically installed in the new DkIT hydraulics lab in the winter/spring of 2012/2013. With reference to Figure 7.2, which shows the narrow tank installed at DkIT, the external metal frame pieces, ①, which support the GRP and glass tank walls, were first positioned and the adjustable feet, ②, bolted to the concrete floor. The feet of the frame are slotted to allow the frame be levelled, and once the tank frame was levelled, the feet were locked into the floor. The glass panels, ③, and GRP panels, ④, were next installed, and the joints between panels sealed using Sikaflex, an

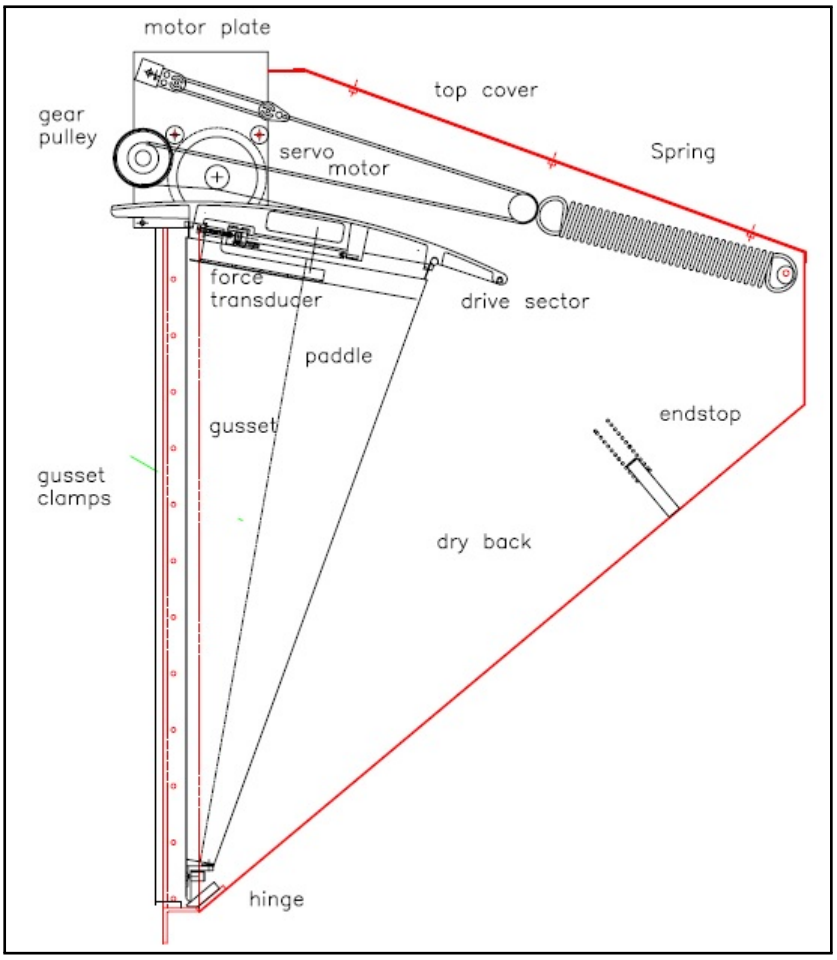

FIGURE 7.1: DkIT narrow tank wave maker arrangement [206].

elastic joint sealant. The wave maker, ⑤, comprises a separate stainless steel box, one side of which is open. The open side was mated to the rest of the tank, and a PVC gusset sealed in place between the GRP panels and the wave maker.

Within the stainless steel box is housed the wedge-shaped paddle, the force feedback sensor, the servomotor and the counterweight springs, see Figure 7.1. Figure 7.3 is a schematic of the setup between the wave maker servomotor and the equipment required to control the servomotor, which take the form of a PC, control box and interface box. The servomotor operates the paddle via a drive belt, and is controlled by a control box which houses a Copley Controls Corporation amplifier. The control box also houses circuitry for signal processing and for the force feedback control system, to absorb reflected waves. The position of the motor is monitored by the system using an encoder mounted on the motor itself. A separate interface box resides between the control box and the outside world. The interface box may be used as part of a data acquisition system, although the facility for data acquisition using the interface box was not employed during

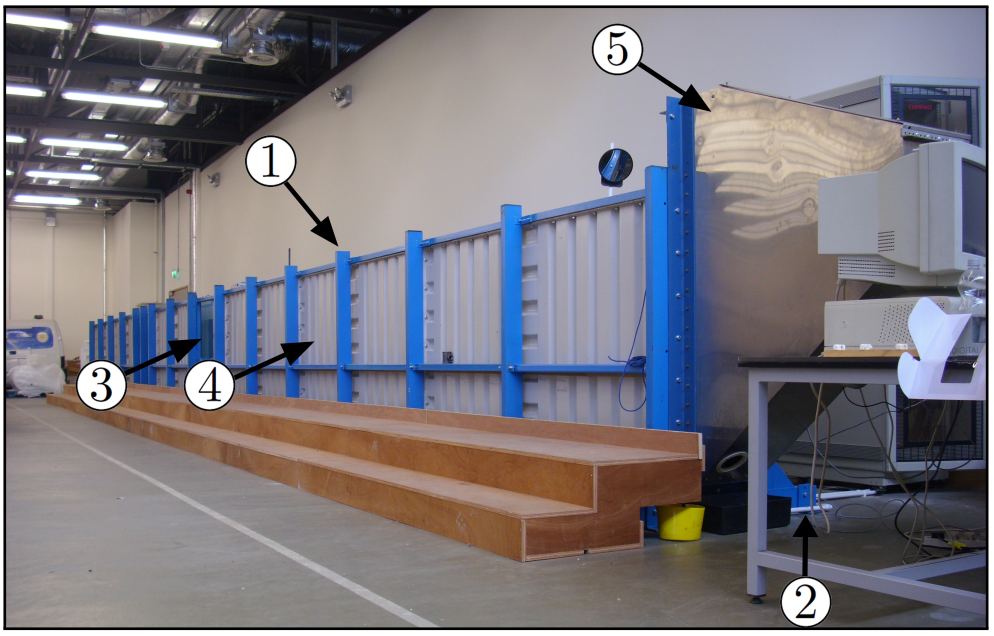

FIGURE 7.2: Narrow tank installed at DkIT

the testing at DkIT discussed herein. The interface box may also be used to generate a sinusoidal input to the control box at varying amplitudes and frequencies, allowing the wavemaker to operate without a PC if necessary, although accurate wave generation is not possible using this method. The PC, which allows a user to interface with the wave maker, communicates to the control box via the interface box. Communication between the PC and the interface box is achieved using a PCL-818L card located in the PC. For more information see [206–208].

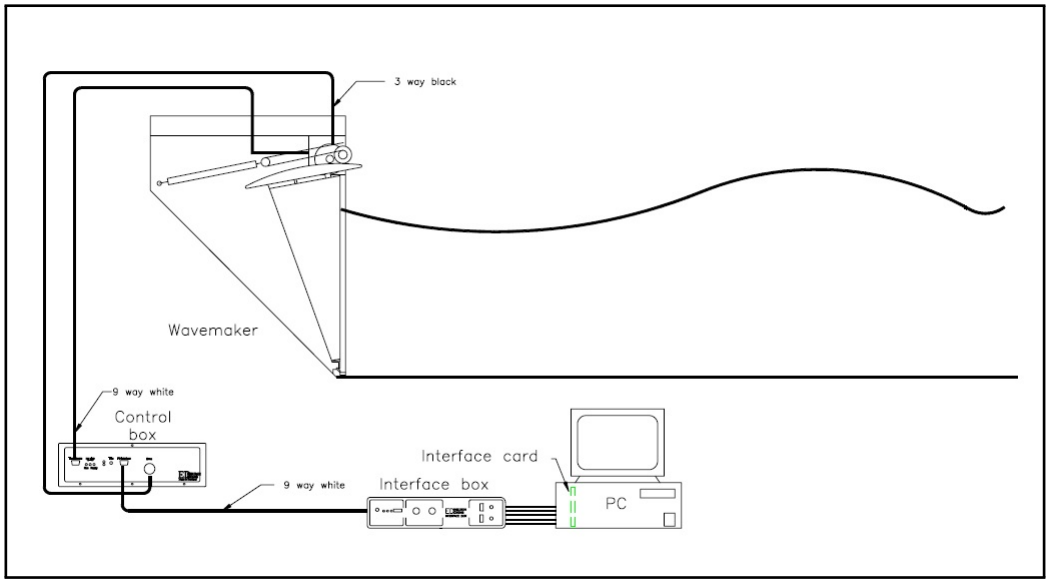

FIGURE 7.3: Schematic of the DkIT narrow tank wave generation system (adapted from [206]).

The tank may be filled from the mains water supply, which is plumbed to the tank via copper piping and a series of valves. When filling, water enters the tank from two inlets at either end of the tank. The tank may be drained to the waste water system via the inlets, which is achieved using the same piping and valve arrangement. An electric pump may be employed to speed up the draining process.

7.2.3 Wave absorbing beach

One critical component of the narrow tank system that was not present when the tank was purchased from QUB was the wave absorption beach. A beach was originally located at the opposite end of the tank from the wave maker and designed to minimise wave reflections from the beach end of the tank. A beach prevents wave reflections by absorbing whatever energy remains in the wave when it reaches the end of the tank. Should significant wave reflections from the back wall occur, the reflected wave would interfere with any tests take place in the tank before the reflections could be removed by the force feedback system of the wave maker paddle. Extensive work on the design of an optimum beach had been carried out at QUB [209], details of which are available. Figure 7.4, taken from [209], illustrates one such beach configuration.

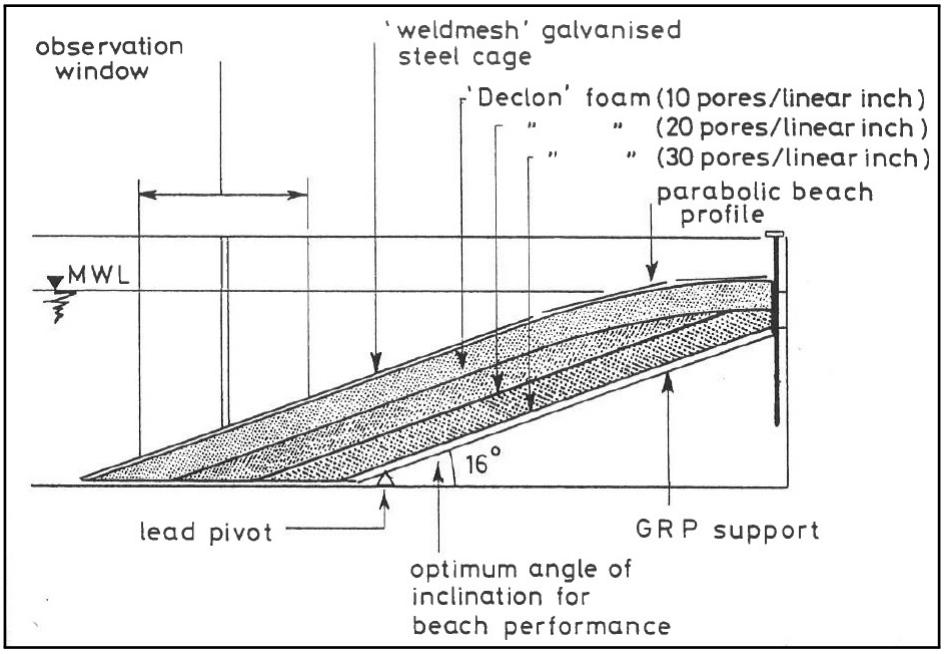

FIGURE 7.4: The beach configuration devised at QUB which was used as an exemplar for that constructed at DkIT. Source: [209].

A new beach was constructed at DkIT based on the dimensions shown in Figure 7.4. The new beach comprises a ramp-like structure that reproduced the dimensions in the QUB example. Following discussions with the technical staff at the HMRC, the ramp was then covered in layers of Enkamat. A parabolic form was given to the beach by graduating the number of thicknesses of Enkamat along the length of the beach, from 30 layers where the beach pierces the surface, to 5 layers at the tank base. Figure 7.5 illustrates a schematic of the main components of the narrow tank.

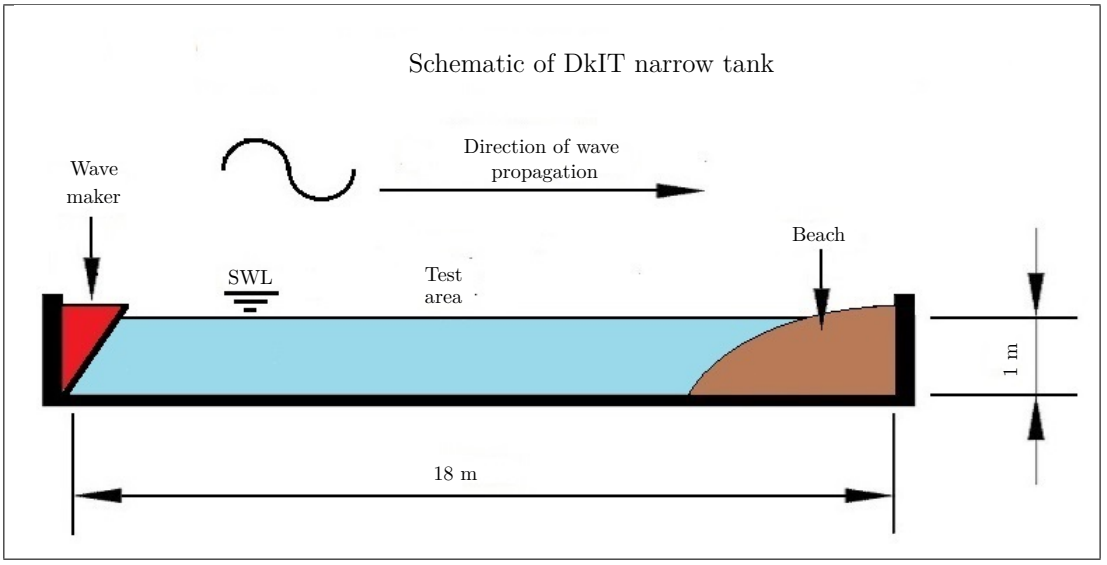

FIGURE 7.5: Schematic of the narrow tank at DkIT illustrating the main dimension and components of the tank.

All components of the tank were now physically installed.

7.2.4 Data acquisition

Before the narrow tank may be calibrated and subsequently used for model testing, a data measuring and acquisition system must be installed. In the current section, the measurement and acquisition system installed at the DkIT narrow tank is described. National Instruments LabVIEW software is used to sample and record data from the sensors used during tank calibration and model testing. LabVIEW software interfaces with the National Instruments hardware to capture sensor data. National Instruments offer a variety of data acquisition systems, and the system used with the DkIT narrow tank is the modular CompactDAQ system. The CompactDAQ system uses a generic chassis which connects to a dedicated PC (separate to the PC used to control the wave maker) which is to be used to capture and record the experimental data via either USB

or Ethernet. A large range of modules may then be 'hot swapped' in to, and out of, the chassis for use with a range of different sensor types, depending on the characteristics of the signal to be acquired. An eight-module chassis, the NI cDAQ-9178, was selected for use with the DkIT tank.

Two types of sensors were used in the work described in the current work: Honeywell 176PC14HD2 differential pressure transducers and Churchill Controls surface elevation wave resistive wave probes. The choice of measuring devices was informed by the experience gained at the HMRC, discussed in Section 7.3. Surface elevation is measured using a resistive wave probe system. Each surface elevation measurement requires two major components: the twin-wire probe, and the wave monitor module. The probe comprises two parallel stainless steel wires, which are partially submerged into the water. The wires are spaced 12.5 mm apart, have a diameter of 1.5 mm and a length of 300 mm. The conductivity between the two wires varies depending upon the immersion depth (as well as the conductivity of water). It is the task of the second component, the wave monitor module, to measure the conductivity and relate it linearly to the immersion depth. The wave monitor module is connected to the probe and excites it using a high frequency oscillator with a voltage of constant amplitude. Alternating current is used to excite the probes as direct current would result in hydrogen and oxygen forming on the probe due to electrolysis, which would effect the results from the probe. The probe current is measured by a differential amplifier, and the module outputs a voltage which varies between ± 10 volts. The variation in the voltage is linearly related to the free surface displacement and the voltage is measured and recorded by the data acquisition hardware and software. National Instruments module NI 9125 is used to acquire the wave probe data. The NI 9125 module can sample a voltage signal in the range of ± 10 volts, making the NI 9125 ideally suited to the task of acquiring the signal from the wave monitor module. Each NI 9125 module can acquire data from up to four wave monitor modules.

Before the probes can be used to acquire free surface displacement data, the exact relationship between the free surface displacement and the voltage from the wave monitor must be established, that is to say, the wave probe must be calibrated. Wave probe calibration is achieved through the 'Measurement and Automation Explore' utility supplied by National Instruments. Within the 'Measurement and Automation Explore' utility, a software entity known as a 'virtual channel' is created. Each physical probe has a unique, corresponding 'virtual channel'. The 'virtual channel' contains the information required

by the LabVIEW software to correctly read and interpret the signal from the physical probe, such as to which of the four channels on the NI 9215 module the wave monitor module is connected. In the case of a wave probe, the 'virtual channel' is configured to measure a change of voltage in the range of ±10 volts. Furthermore, it is through an array of wave monitor module signal value vs. wave probe immersion depth pairings, generated using the 'Measurement and Automation Explore' utility, that the probe is calibrated. In the case of the wave probes, calibration is achieved by mounting the wave probe in a custom-made holder. The holder positions the probe mid-way across the tank while partially submerging the probe when the tank is full. The vertical position of the holder above the free surface, and hence the level to which the wave probe is immersed, can be adjusted in increments of 10 mm. The holder was created using a Leapfrog manufactured Creatr [sic] 3-D printer, and the spacings between the centres of the holes in the holder have been confirmed to be at 10 mm spacings. The wave probe and wave probe holder arrangement can be see in Figure 7.6.

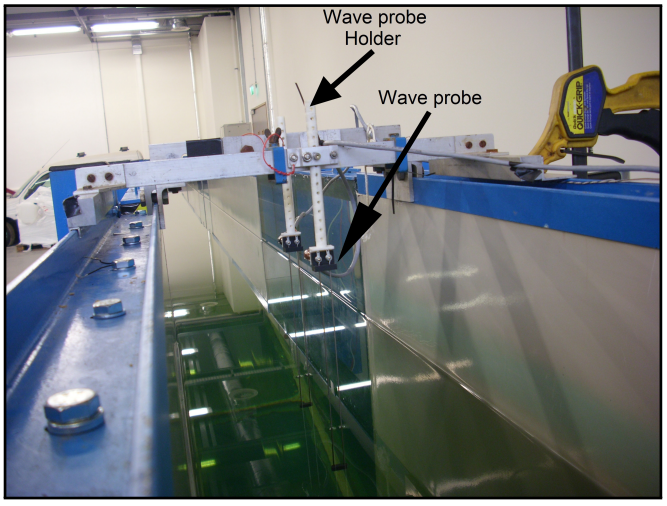

FIGURE 7.6: Wave probe and probe holder: note holes at 10 mm spacing.

The wave probe is first located at the neutral position for still-water conditions and the output from the module, which may be varied within the ±10 volt range using a control knob on the front of the probe controller, is set to zero. The probe is moved incrementally up and down in steps of 10 mm. At each increment, both the displacement from the neutral position, and the voltage from the wave monitor module are recorded, creating the required wave monitor module signal value vs. wave probe pairings, which are saved in the 'virtual channel'. During operation, LabVIEW software automatically interpolates signal values which lie between values stored in the calibration data set to

determine the corresponding free surface elevations. Figure 7.7 shows a typical calibration plot for one of the wave probes supplied by Churchill Controls. As can be seen, the plot is extremely linear, with a R^2 value of 0.9999. Once created and calibrated, a

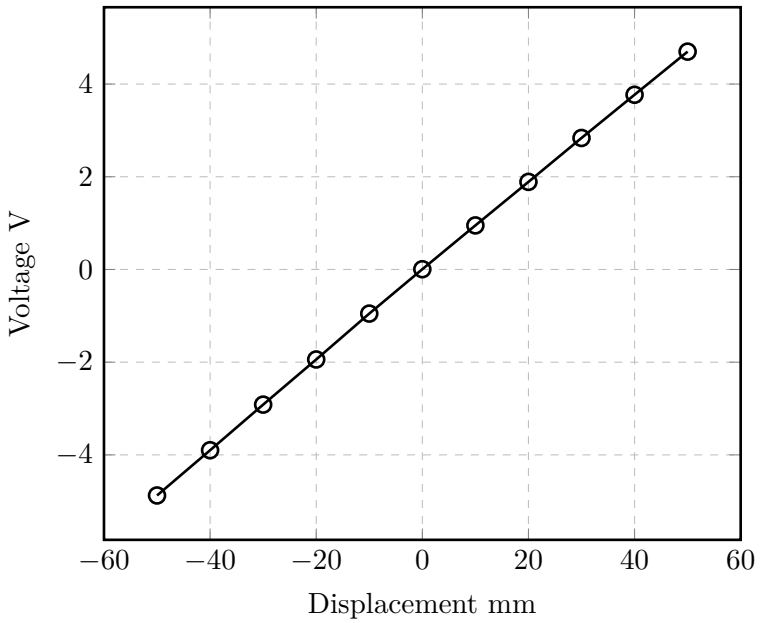

FIGURE 7.7: Calibration curve for a typical Churchill Controls wave probe at the DkIT narrow tank with a R^2 of 0.9999.

'virtual channel' is then available for use in LabVIEW. It should be noted that while the y-intercept drifts slightly for each wave probe over the time scale of days (which would, anecdotally, appear to be due to changes in water temperature), the slope of the calibration curve remains constant. Any drift in the y-intercept can either be removed by setting the probe controller output voltage to zero, for still water conditions, by adjusting the control knob on the probe controller as required, or through taking still water readings, wherein data is recorded in the absence of waves at regular intervals to establish the required offset. In practice, for all the tests performed in the narrow tank described in this thesis, the wave probes were set to zero before each set of tests, and regular still water measurements were taken to ensure the effect of any drift in the y-intercept of the probe calibration curve was accounted for. Furthermore, the calibration of the wave probes was checked on a weekly basis.

As discussed in Chapter 10, it is necessary to use a longer wave probe than was available commercially to record the motion of the water column for certain OWC models. Consequently, a custom-made wave probe was constructed following the design of the Churchill Controls probe, and can be used with the Churchill Controls controller. The necessary

mounting hardware was produced using a 3-D printer, and stainless steel welding rods of diameter 1.5 mm and of length approximately 900 mm were used for the twin wires. The custom-made probe was benchmarked against the commercial Churchill Controls probes, and, while having different calibration characteristics to the probes supplied by Churchill Controls, was shown to performed reliably. Figure 7.8 illustrates the calibration curve for the custom-made probe. As for the Churchill Controls probe, the curve is virtually linear, with a R^2 of 1.0000. Unlike the wave probes, the pressure transducers,

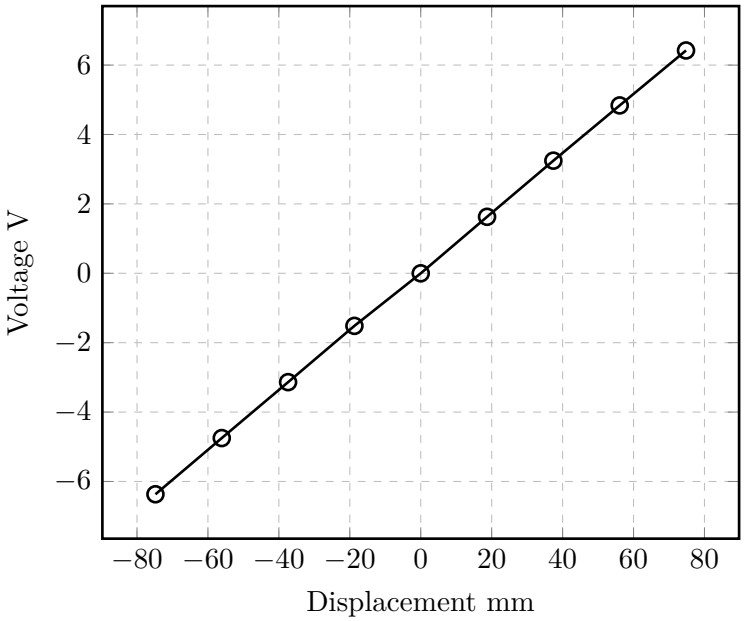

FIGURE 7.8: Calibration curve for the custom-made wave probe at the DkIT narrow tank with a R^2 of 1.0000.

which are of the bridge type, have no separate controller. They must be powered by a National Instruments module at the same time as the National Instruments module records the signal voltage. The signal voltage from the pressure transducer is in the millivolt range, and changes in the signal from the pressure transducer are amplified using a resistor bridge. The National Instrument module NI 9237 can provide exciting voltage and bridge measurement facilities for up to four pressure transducers per module, and the NI 9237 module is used with the Honeywell 176PC14HD2 differential pressure transducers to measure changes in air pressure at the DkIT tank facility. The calibration technique for the pressure transducers is similar to that used for the wave probes. The pressure transducers measure the difference in pressure between two ports of the transducer. During calibration, one port of the transducer is connected to a U-tube manometer, the other port is left open to the atmosphere. By increasing and decreasing

the pressure on the port connected to the manometer, a known pressure difference can be created which can be used to create known pressure difference/voltage pairings. As with the water level gauges, the LabVIEW software can then interpolate between the pairings. Figure 7.9 illustrates the calibration curve for one such pressure transducer. The linear nature of the curve is apparent, with an R^2 value of 0.9999.

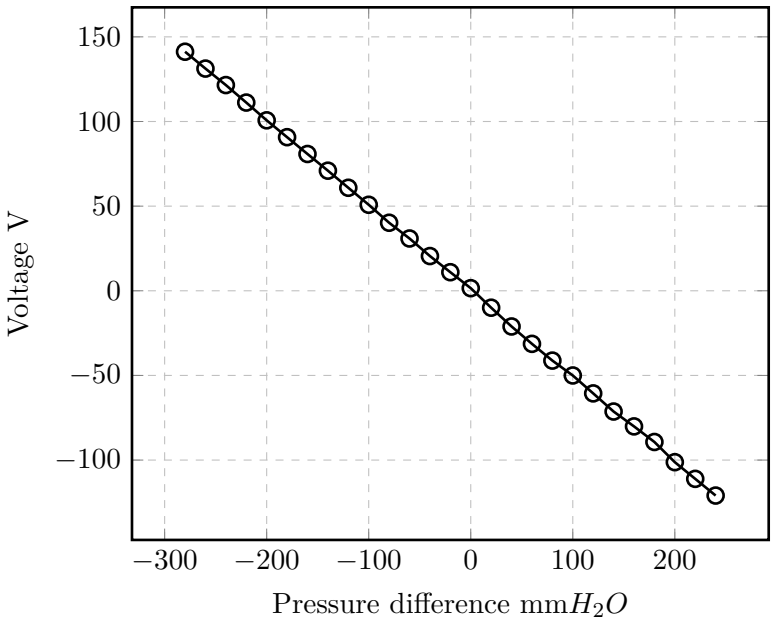

FIGURE 7.9: Calibration curve for a Honeywell 176PC14HD2 differential pressure transducer at the DkIT narrow tank with an R^2 of 0.9999.

7.2.5 Wave creation

The PC illustrated in Figure 7.3 is the primary means by which the user may control the operation of the wave maker. The designers and manufacturers of the narrow tank, Edinburgh Designs Ltd., provide a software suite to enable the user to generate both mono- and polychromatic waves in the narrow tank, which propagate parallel to the tank walls. The software suite comprises three key components:

1. the **wave** programming language (which may be written using a standard ASCII editor),
2. the **Ocean** compiler,
3. the **RUN** run-time environment.

Two types of user-generated files are required in order to create mono- or polychromatic waves in the narrow tank. The files can be categorised as experiment files, which describe the specific wave conditions to be generated during an experiment, and configuration files, which describe aspects of the tank and associated hardware. The flowchart shown in Figure 7.10 illustrates how user-generated files interact with the **Ocean** compiler and **RUN** run-time environment. The user creates the experiment file using the **wave** programming language, typically using the *.wav* extension. In Figure 7.10, the source code *.wav* is represented by *test.wav* file. Each experiment requires a unique **wave** source code file. Each experiment also requires tank transfer function information, which is contained in a user-created binary file with the extension *.ttf*, represented by *tank.ttf* in Figure 7.10. The tank transfer function file describes properties of the tank and the wave maker and does not vary between experiments, unless the water depth in the tank also changes. The information in the tank transfer function file is used to translate the output signal from the PC into actual waves in the tank. The process of creating and verifying the *.ttf* file is the subject of Section 7.2.6.

The **Ocean** compiler uses the *.wav* source code file and the *.ttf* tank transfer file to create a binary file with the extension *.sea*, represented by *test.sea* in Figure 7.10. **RUN** can then use the binary *.sea* file, together with a second configuration file with the extension *.cfg* to control the wave maker and generate the desired wave conditions in the narrow tank. The second configuration file is the tank configuration file, which is a subset of the *.ttf* file. The tank configuration file is represented by *tank.cfg* in Figure 7.10.

Both mono- and poly-chromatic waves have been used to generate the results presented in this thesis. To create mono-chromatic waves, the user specifies the desired wave frequency, in Hz, and the desired wave amplitude, in mm, in the source code, *.wav*, file. The **wave** programming language has a number of built-in functions to allow the user to create common statistical spectra with ease. For example, the user may request the tank to generate a Bretschneider spectrum using the **wave** function *bretsch*. The user specifies the peak frequency of the spectrum, f_p, as well as the zeroth spectral moment, m_0 of the required Bretschneider spectrum. The software creates the wave density spectrum, $S(f)$, based on Equation (7.1), and constructs a time series of wave elevations to match the spectrum.

$$S(f) = \frac{5m_0}{f_p}\left(\frac{f_p}{f}\right)^5 e^{-1.25(f_p/f)^4} \tag{7.1}$$

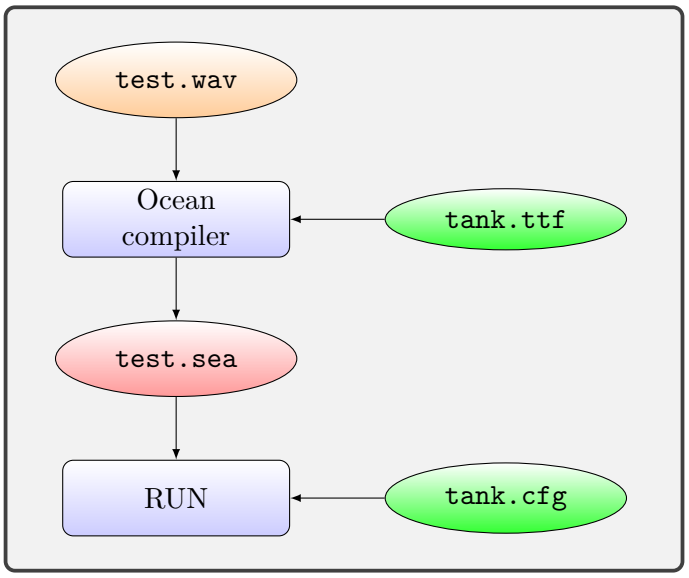

FIGURE 7.10: Flow chart illustrating the use of Edinburgh Designs Ltd. narrow tank control software.

Other spectra that may be created using built-in function in the **wave** language include the Pierson-Moskowitz, JONSWAP, Scott and the Neumann spectra [208].

7.2.6 Tank calibration

A transfer function between the input to the tank control system, in the form of the parameters specified by the user in a *.wav* file, and the desired output for the control system, in the form of a set-point force signal sent by the PC to the control box which the control box then adjusted the paddle position to follow, is necessary to generate the desired wave conditions in the narrow tank. The transfer function is stored in the 'tank transfer function' file with the extension *.ttf*. The tank calibration process creates and verifies the tank transfer function. The core of the tank transfer function is a matrix of angle, gain and phase triples, with each triple corresponding to a specific wave frequency. The gain and phase values are used to create the appropriate set-point time series signal corresponding to the force which a force transducer located on the wave-maker should experience to generate a specific wave [208, p. 101]. The system is assumed to operate linearly, and the gain and phase values for frequencies between those listed in the *.ttf* file are interpolated by the software. For a tank transfer file to be valid, there must be a minimum of two frequencies for which angle, gain and phase triples are specified.
The process of tank calibration entails the measurement of the actual frequencies and amplitudes of monochromatic waves generated in the tank and comparing the measured

values to the frequencies and amplitudes which were requested by the user. The tank transfer function triples are then adjusted until the requested wave frequencies and amplitudes for each frequency in the tank transfer file are physically generated in the tank within the required tolerances. As the tank had previously operated at a different site, an existing tank transfer function file was available from that time. The previous tank transfer file was used as a starting point when the narrow tank was calibrated at DkIT, and the triples in the previous file adjusted to suit.

A separate, but related, issue is that of reflected waves from the end of the tank opposite to the wave maker. The purpose of the beach at that end of the tank is to absorb as much of the energy in a wave that reaches the end of the tank as possible and thus reduce the reflected wave amplitude to a minimum. However, until proven otherwise, it must be assumed that some reflection occurs. In steady-state conditions, the free surface elevation recorded by a wave probe in response to user-requested monochromatic waves, at any location in the tank, will be the sum of the waves generated by the wave maker and any reflected waves. The dual objective of the tank calibration process used at DkIT is to ensure that the amplitudes and frequencies of the incident waves generated by the wave maker are repeatable and within the required tolerances matching those of the requested waves over the range of wave frequencies for which the tank is to be used and, secondly, to ensure that the energy in the reflected wave is acceptably low.

A single wave probe cannot be used to measure the generated wave *and* the reflected wave, which travel in the opposite directions, at the same time. The water elevation that the probe is measuring is the summation of the two waves. In order to decompose time series data of the surface elevation into the generated and reflected components, for each frequency and amplitude used during the calibration process, the free surface elevation is measured simultaneously at two locations in the tank using two separate resistive wave probes. Once the distance, Δl, between the probes is known (and care is taken to ensure that $\Delta l/\lambda \neq$ n/2, where λ is the wavelength of the incident wave and n is an integer) the incident and reflected wave amplitudes and frequencies can be determined. The mathematics underpinning the technique employed during the calibration of the narrow tank at DkIT were developed by Y. Goda and Y. Susuki [210]. The mathematical treatment described in Equations (7.2) to (7.6) assumes that the wavemaker is capable of removing all reflected waves which reach it, by using force feedback control. Figure 7.11 illustrates the free surface elevation in the narrow tank when an incident and reflected wave interact. Let η_I and η_R represent the free surface elevations of the incident and

reflected waves respectively. If amp_I and amp_R are the amplitude of the incident and

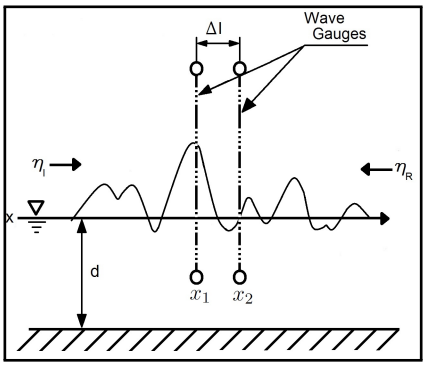

FIGURE 7.11: Illustration of interaction between incident and radiated wave and main quantities (adapted from [210]).

reflected waves respectively, k is the wave number, ω the angular frequency of the wave and ε_I and ε_R are the phase angle of the waves, then the free surface elevations due to the waves are given by:

$$\left.\begin{aligned} \eta_I &= amp_I cos\left(kx - \omega t + \varepsilon_I\right) \\ \eta_R &= amp_R cos\left(kx + \omega t + \varepsilon_R\right) \end{aligned}\right\} \tag{7.2}$$

Let the first wave probe, for which data has been recorded, be located at a reference distance x_1 and the second probe be located at a distance x_2 such that $x_2 = x_1 + \Delta l$. The free surface elevation at any point will be the sum of the elevations due to the incident wave and the reflected wave at that point. By letting:

$$\left.\begin{aligned} A_1 &= amp_I \cos\phi_I + amp_R \cos\phi_R, \\ B_1 &= amp_I \sin\phi_I - amp_R \sin\phi_R, \\ A_2 &= amp_I \cos\left(k\Delta l + \phi_I\right) + a_R \cos\left(k\Delta l + \phi_R\right), \\ B_2 &= amp_I \sin\left(k\Delta l + \phi_I\right) - a_R \sin\left(k\Delta l + \phi_R\right), \\ \phi_I &= kx_1 + \varepsilon_I, \\ \phi_R &= kx_1 + \varepsilon_R \end{aligned}\right\} \tag{7.3}$$

then:

$$\left.\begin{aligned} \eta_1 &= \left(\eta_I + \eta_R\right)_{x=x_1} = A_1 \cos\omega t + B_1 \sin\omega t, \\ \eta_2 &= \left(\eta_I + \eta_R\right)_{x=x_2} = A_2 \cos\omega t + B_2 \sin\omega t \end{aligned}\right\} \tag{7.4}$$

Assumpting that linear wave conditions exist and assuming that the dispersion relation (given by $\omega^2 = gk \tanh kd$ where d is the water depth) holds true, the above equations can be rearranged to give solutions to the incident and reflected wave amplitudes, respectively as

$$amp_I = \frac{1}{2|\sin k\Delta l|}\sqrt{(A_2 - A_1\cos k\Delta l - B_1 \sin k\Delta l)^2 + (B_2 + A_1 \sin k\Delta l - B_1 \cos k\Delta l)^2} \quad (7.5)$$

$$amp_R = \frac{1}{2|\sin k\Delta l|}\sqrt{(A_2 - A_1\cos k\Delta l + B_1 \sin k\Delta l)^2 + (B_2 - A_1 \sin k\Delta l - B_1 \cos k\Delta l)^2} \quad (7.6)$$

A Fourier analysis of the time series data from the wave probes located at x_1 and x_2 can be used to determine the amplitude of the *sin* and *cos* components in each time series, i.e., A_1, A_2, B_1 and B_2 in Equations (7.5) and (7.6), as well as being used to confirm the fundamentaly of the generated waves. Equations (7.5) and (7.6) have been implemented in MATLAB to determine the frequency and amplitude of the incident and reflected waves in the narrow tank, from time series records of the free surface displacement from two wave probes.

To create reference data against which the performance of the tank and the Enkamat beach could be compared, a series of tests were conducted with the beach uninstalled from the tank and with no other obstructions to wave propagation in the tank. The binary *.sea* files used were compiled using the tank transfer function which was accompanied the tank when it arrived at DkIT. The wave maker was requested to generate waves of amplitudes ranging from 5 mm to 35 mm in increments of 5 mm and wave frequencies ranging from 0.6 Hz to 1.4 Hz, in increments of 0.2 Hz. Wave probe data was recorded simultaneously at two known locations in the tank, ensuring that the spacing between the probes, Δl, and the wave length λ at each frequency was set so that $\Delta l/\lambda \neq$ n/2. Data was sampled at 32 Hz. The data obtained was analysed in MATLAB and Figure 7.12 illustrates the results of the analysis. In Figure 7.12, the requested wave frequency/amplitude pairings are represented by the crossing points of the dotted horizontal and vertical lines, and the achieved incident wave frequency/amplitude pairings are represented by the markers as listed in the legend. The frequency values for the generated waves were obtained from a Fourier analysis of the time series data, for the wave probe nearest the wave maker. As can be seen, the amplitudes of the incident waves quite closely match those requested, although improvements could be made, and

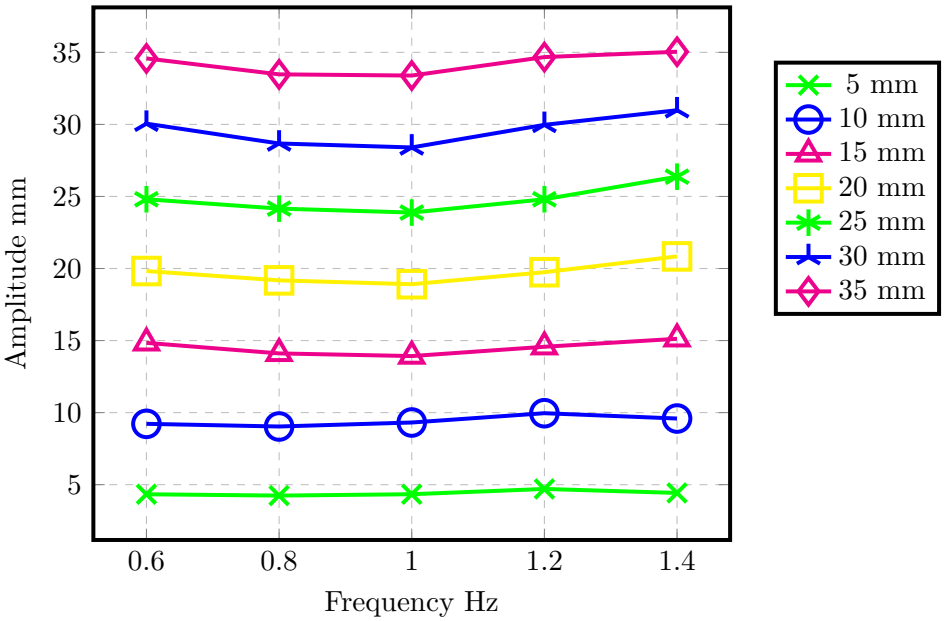

FIGURE 7.12: Amplitude and frequency of the generated waves for the DkIT narrow tank with no beach installed and prior to calibration process.

an excellent match was achieved for the frequencies. However, with no beach installed at the end of the tank, it is clear, from visual observations during the tests, that a large percentage of the energy in the waves is being reflected for each generated wave amplitude/frequency pairing. The visual observation is confirmed by Figure 7.13, which illustrates the percentage of the generated wave amplitude reflected from the end wall of the tank, for each amplitude/frequency pairing used during the test. The energy in a wave is related to the square of the amplitude, see Equation (2.29). Clearly, an unacceptable amount of energy is reflected and, indeed, for high frequency waves, the free surface variations in the tank quickly become chaotic. Once the baseline values were obtained, the beach described in Section 7.2.3 was re-installed in the tank, and the tests re-run. The values in the triples contained in the tank transfer function were adjusted until the results shown in Figure 7.14 were obtained for the same incident wave amplitudes and frequencies. Some compromise is required to achieve the best balance between the accuracy of all the amplitudes. The need for compromise is the reason why some inaccuracy in the amplitudes remains, notably at a frequency of 0.8 Hz. Efforts to improve the amplitude accuracy at 0.8 Hz resulted in larger inaccuracies at adjacent frequencies. Figure 7.15 shows the ratio of the incident wave heights to the reflected wave heights once the beach was installed and using the adjusted tank transfer function.

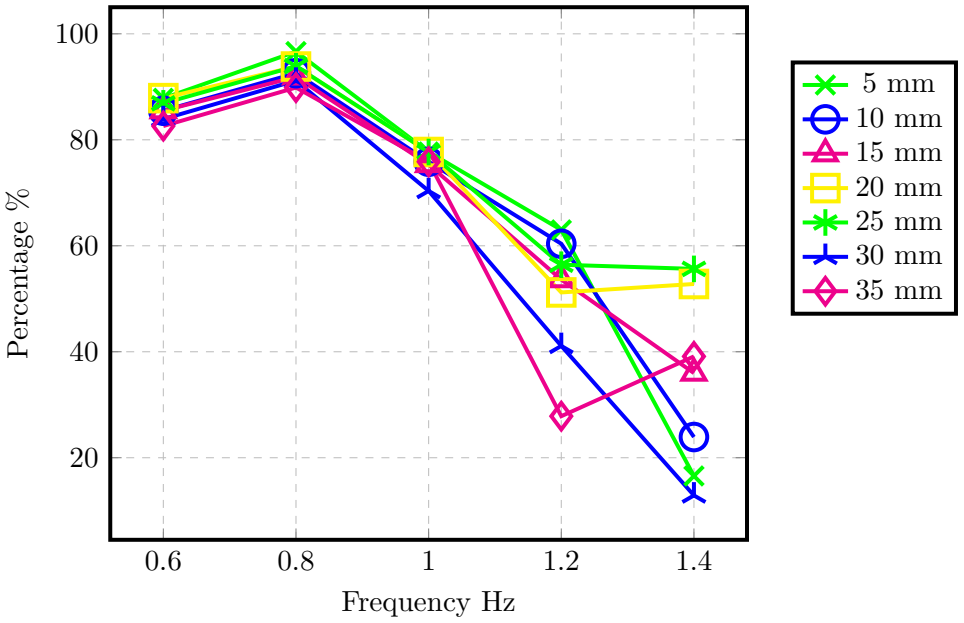

FIGURE 7.13: Percentage of generated wave amplitude reflected from tank back wall for each frequency/amplitude tested at the DkIT narrow tank prior to calibration and with no beach installed.

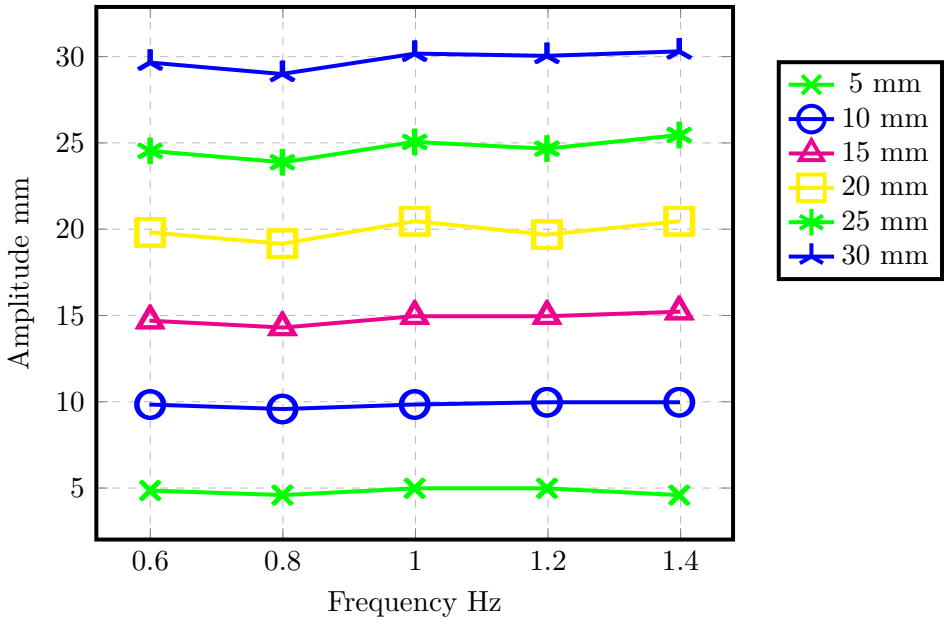

FIGURE 7.14: Amplitude and frequency of the generated waves for the DkIT narrow tank after beach installed and calibration process.

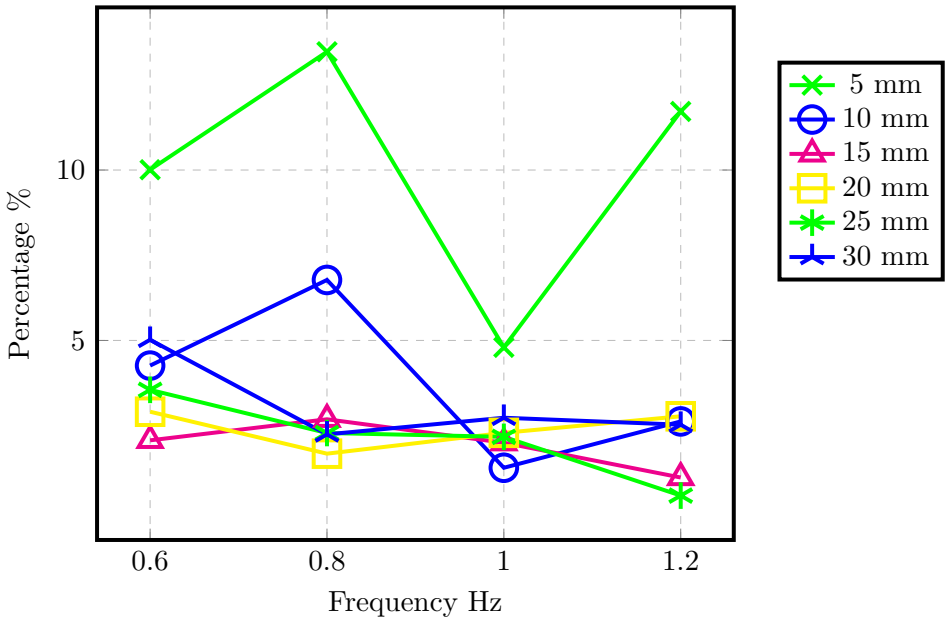

FIGURE 7.15: Percentage of generated wave amplitude reflected from tank back wall for each frequency/amplitude tested at the DkIT narrow tank after beach installed and calibration process.

A dramatic reduction in the level of wave reflection was achieved and, furthermore, it is likely that the somewhat larger levels of wave reflection seen for the 5 mm amplitude waves are due to the sensitivity of the 5 mm results to noise on the wave probes. The relative effect of any noise on the wave probe signal reduces with increasing wave amplitude. In order for a beach to be considered effective at absorbing waves, the percentage of wave amplitude reflected should be below 10% [211], and ideally below 5% over the range of wave frequencies and amplitudes the tank is capable of producing. Figure 7.15 shows that reflections of below 10% have been achieved for all amplitudes greater than 5 mm and that, for the majority of frequency/amplitude pairings, the level of reflection is below 5%. The results of the calibration process illustrated in Figures 7.15 and 7.14 demonstrate that, following the calibration process, confidence can be had that the tank accurately generates waves of the amplitude and frequency requested.

7.2.7 Issues

In general, since installation, the tank has run without major issue. A number of small leaks between the glass inspection panels and the GRP wall panels occurred, which have been repaired using Sikaflex. While leaks have not presented a significant problem to

date, the decision was taken to construct a sealed bund around the tank, which will double as a platform to improve access to the tank. The bund will open at one end only where an existing drain will receive any leakage from the tank.

A second issue that arose when the paddle drive sector, located at the top of the wave maker and which can be seen in Figure 7.1, began physically interfering with the motor drive gear. The interference between the paddle drive sector and the motor drive gear arose as insufficient care was taken in locating the paddle in the wave maker box relative to the motor gear, when the tank was being filled. Once the tank is filled, it is not possible to move the paddle transversely in the tank. It was necessary to empty the tank and readjust the paddle position within the wave maker box. Once the paddle was correctly centered within the wave maker and the tank was refilled, the paddle drive sector no longer interferred with the motor gear.

Finally, on one occasion, a curious bystander accidentally provided a ground to one side of the capacitance-based force sensor on the wave maker with an inquisitive finger. As a result, the paddle entered a run-away condition. The paddle made a number of large oscillations before the emergency machine off button was hit which resulted in the paddle coming into contact with the end stop springs, which can be seen in Figure 7.1. Following hardware checks, the calibration of the tank was rechecked, and found to have remained as shown in Figure 7.14. The point of access located by the by-stander was sealed to prevent a recurrence of the issue. While no lasting damage was done to the tank as a result of either the drive sector interferring with the drive gear, or during the run-away event, both issues are raised here for the attention of future tank users.

7.3 Ocean basin at the HMRC

Model testing was conducted on the 1 : 50 32-OWC model of the proposed WEI wave energy converter at what was, at the time, the largest wave testing facility in Ireland. At the time the testing on the 1 : 50 32-OWC model took place, the facility was located in Pouladuff, Co. Cork and was operated by what was then known as the Hydraulics and Maritime Research Centre at University College Cork. In 2015, the facility was moved to the Lir National Ocean Test Facility, and the Hydraulics and Maritime Research Centre was absorbed into the Centre for Marine and Renewable Energy (MaREI). The HMRC ocean basin wave tank, which was designed and built by Edinburgh Designs

[212], is 25 m long, 18 m wide and 1 m deep. A variety of sea states can be simulated within the basin using 40 wedge-shaped flap-type paddles, each measuring 0.75 m in height, which run along one of the 18-m sides of the basin. The paddles are driven using servomotors which are controlled using wave generation software written by Edinburgh Designs. The basin is capable of generating both mono- and pan-chromatic waves, with significant wave heights up to 180 mm and wave periods up to 2.5 s. The bulk of the testing discussed in this thesis performed at the HMRC facility was conducted using monochromatic waves, with a wave height of 60 mm, and wave periods ranging from 0.71 s to 1.98 s. The scaled wave height and wave periods correspond to a wave height of 3 m and wave periods of 5 s to 14 s, at full scale.

Two movable bridges are located across the narrow dimension of the tank. The first allows an individual to walk above the level of the tank and potentially access a model under test from above, and the second is an instrument bridge, which provides a means by which cabling from instrumentation on a model may be routed to the data acquisition system at the facility, and also a location were additional instrumentation may be mounted, such as wave probes to measure wave reflections.

A wave absorbing beach is located along the opposite side of the basin to the wave generating paddles. The beach is constructed from Enkamat[213], a wave-absorbing material used for coastal protection. The beach prevents waves from reflecting from the end of the tank and interfering with the generated waves. The paddles also incorporate an active absorption system which is based on force feedback sensors within the paddles. The force feedback system is present to cancel any waves that are reflected towards the paddles from, or generated by, a model WEC under test. The ocean basin and the narrow tank share many characteristics, as would be expected as both tanks were designed and manufactured by the same company.

Data acquisition is achieved using National Instruments LabVIEW [214] software. As discussed in Chapter 8, air pressures, in the various OWC and plenum chambers of the model under test, were measured using Honeywell 176PC14HD2 sensors, and the height of the water columns within the chambers of the model (relative to the model) were measured using resistive wave probes, supplied by Churchill Controls. The six rigid-body motions of the platform were measured using the Qualysis ProReflex motion capture system. The Qualysis system measures the location of reflective markers on the rigid body. All data acquired during testing at the HMRC facility was sampled at 32 hz. Figure 7.16 shows the scale model of the proposed WEI platform installed at the

HMRC facility prior to testing. A schematic of the layout of the 32-OWC, scale model of the proposed WEI platform can be found in Chapter 6.

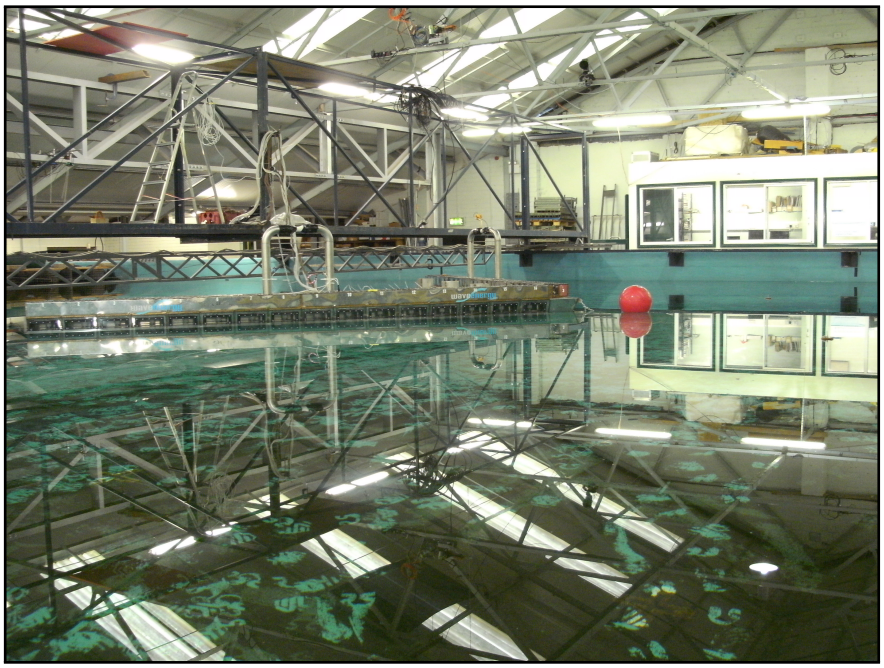

FIGURE 7.16: Large ocean Basin at the HMRC, Co. Cork, in which the scale model of the WEI 32-chamber model wind/wave platform has been installed.

Chapter 8

Scale Models for Tank Testing

8.1 Introduction

In this chapter, a 1:50 scale, physical model of the multi-chamber, floating platform is presented. This model was constructed for the frequency domain tank tests which were carried out in the ocean basin at the HMRC, as outlined in Chapter 6, the results of which are described and discussed in Chapter 9. The construction method and materials used to build the multi-chamber model, and the ancillary components required to complete the model, are described. In addition, the 1:50 scale single-chamber model that was constructed for the time domain tanks tests conducted in the narrow tank at DkIT, is also described.

8.2 Multi-chamber, stainless steel model

The multi-chamber, stainless steel model consists of 32 separate OWCs, with the OWC chamber openings at 45 degrees to the incident waves. Each OWC had a curved hull profile, and the model incorporated high- and low-pressure plenums controlled through the use of air admittance valves. This model was primarily constructed from 316-grade stainless steel of thickness 0.9 mm. A range of development drawings for use in the high-pressure water-cutting and profiling of stainless steel sheets were produced by WEI in AutoCAD, with the steel pieces joined using a combination of MIG and TIG welding.

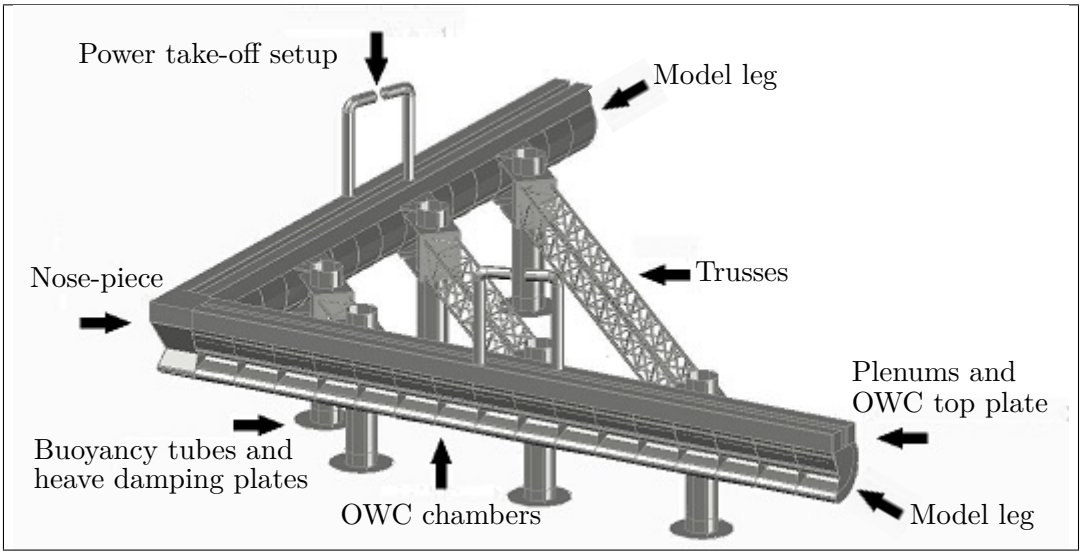

FIGURE 8.1: 3-dimensional CAD drawing of the 32-OWC chamber stainless steel model.

The model was then fitted with the air admittance valves, and a range of sensing equipment, prior to testing as discussed below. The design, detail and the development of the construction process of the model were performed by WEI together with the author. The stainless steel body of the model was constructed in several stages using a number of third party suppliers. Figure 8.1 shows a 3-dimensional CAD drawing, created by the author, of the stainless steel model illustrating the main components that were constructed, and then assembled, to create the complete model. The construction of each component of the model is discussed briefly in the next section.

8.2.1 Components of the 32-OWC model

Figure 8.2 illustrates the surface development drawing produced by WEI, which was used to manufacture the nose-piece of the stainless steel model, and an isometric view of the assembled piece. Note that, unless otherwise stated, the dashed lines in this figure (and in the remaining figures in this section) indicate where a metal piece was to be folded, once cut. As with all stainless steel pieces for the 32-OWC model, the nose-piece was cut and folded by Shortts Stainless Steel Ltd., a Limerick-based company. Once cut and folded, the component was welded by A.C. Stainless Steel Fabrication, based in Dublin, to produce the finished nose-piece.

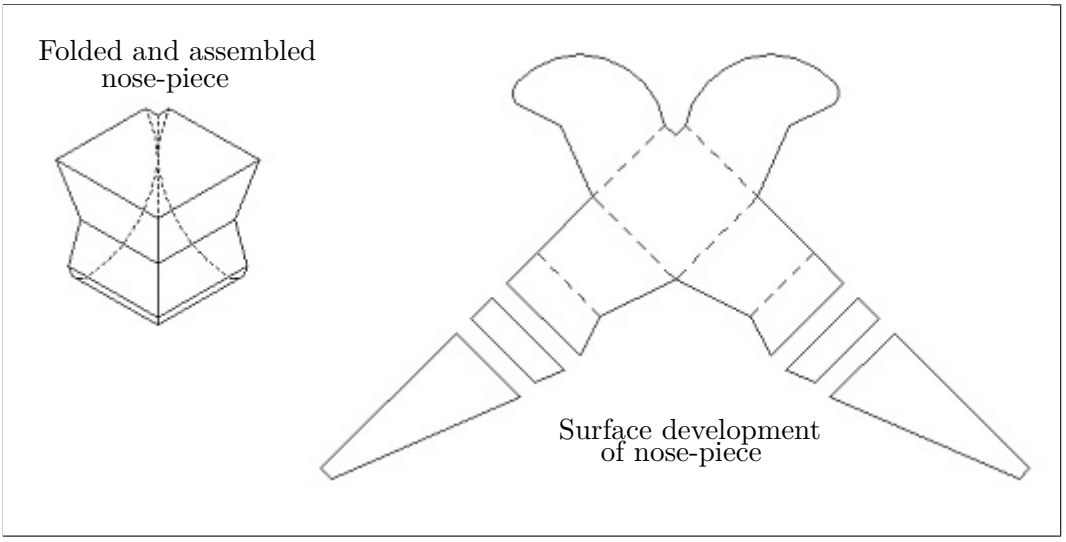

FIGURE 8.2: Nose-piece surface development and isometric view drawings.

As can be seen in Figure 8.1, the model comprises two legs. The curved back wall of each leg of the model, and hence the back walls of the OWC chambers, was constructed from two rolled stainless steel sheets, following the profile of the stencil shown in Figure 8.3.

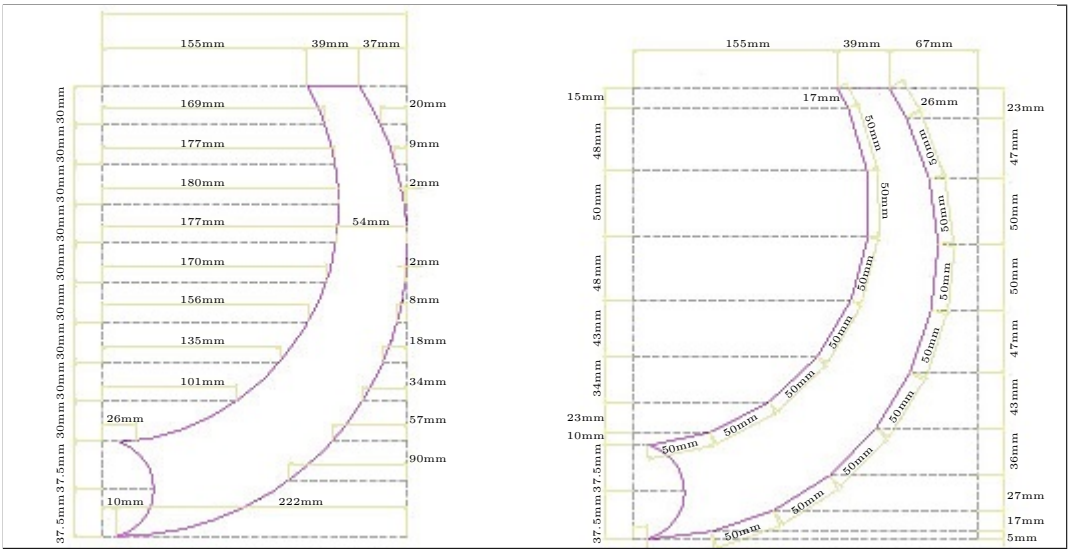

FIGURE 8.3: Stencil used to roll steel piece for hull.

Once formed, the rolled stainless steel sheets were welded to a length of 60 mm diameter stainless steel pipe. The two sheets and the 60 mm diameter pipe, which comprise the hull of the platform, are illustrated as an exploded schematic in Figure 8.4.

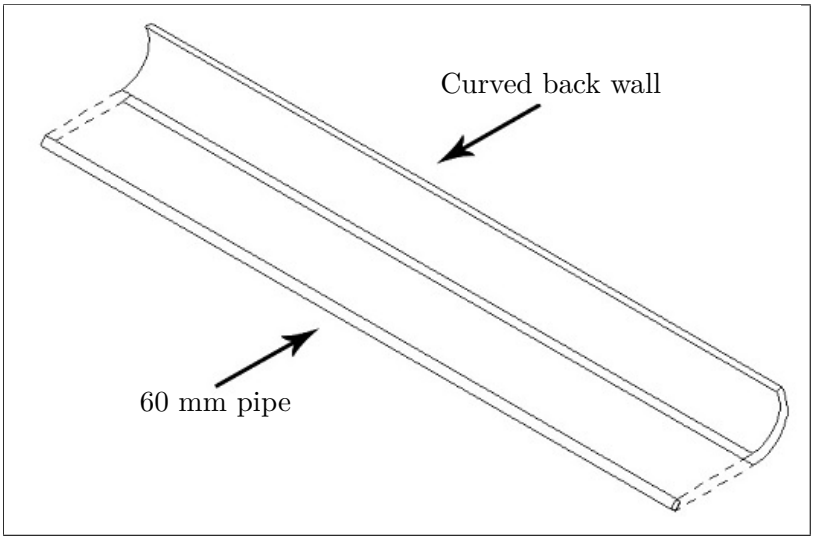

FIGURE 8.4: 3-dimensional CAD drawing of the 32-OWC chamber stainless steel model.

Separately, a total of 10 stainless steel pieces were cut to match the hull stencil and welded in place between the two steel sheets to reinforce the hull, with 5 stencil pieces used on each leg. Closed cell foam was injected into the space between the two hull plates to prevent any water ingress during testing.

The sixteen OWCs in each leg of the model were created by welding 'baffle plates' along the length of the hull plates. The development drawing for a baffle plate is shown in Figure 8.5, along with an isometric projection of the folded piece. Each baffle plate has a window, so that the motion of the water column in the chamber may be examined visually during testing. Perspex pieces, which were cut and drilled by Williaam [*sic*] Cox

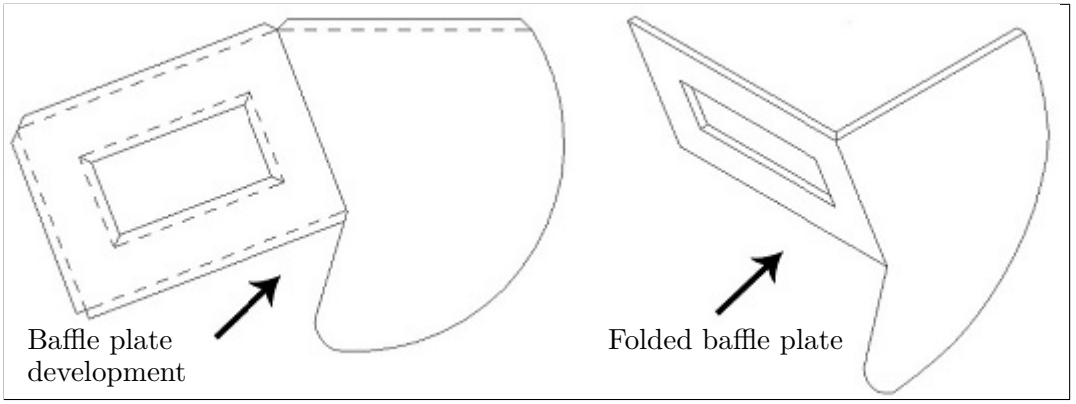

FIGURE 8.5: Baffle plate used to form the OWC chambers .

Ltd., a glazing specialist based in Dublin, were later fixed to the model over the windows using self-tapping screws. Gaskets inserted between the Perspex pieces and the models were used to create the airtight seal. These gaskets were cut by Kemtron Gaskets and

Seals Ltd., based in Cork, using drawings supplied by WEI. Figure 8.6, illustrates how these baffle plates and the hull piece are joined. A single stainless steel sheet is welded along each leg to form the top plates of the OWC chambers.

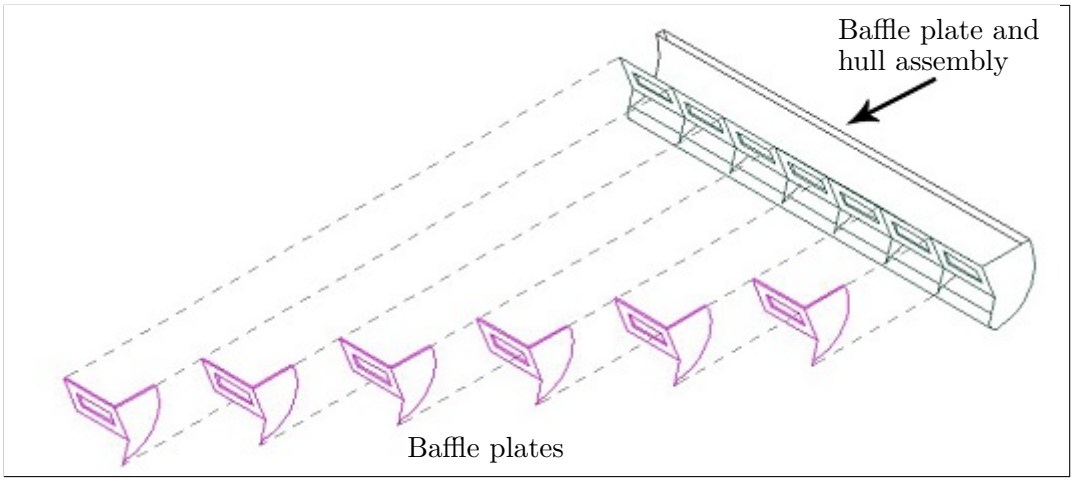

FIGURE 8.6: OWC baffle and hull assembly for one leg of the 32-OWC model .

The upper superstructure of each leg of the model consists of the high- and low-pressure plenum chambers and the power take-off arrangement. The high- and low-pressure plenums take the form of two separate boxes, which run parallel to each other along the entire length of each leg of the model, above the OWC chambers. The cross section of each plenum is rectangular. The base, outer walls and end walls of both the high- and low-pressure plenums for each leg are constructed from the same stainless steel sheet as is used to form the top of the OWC chambers. The development drawing for the plenum base/OWC top piece can be seen in Figure 8.7.

The inner walls of the plenums, which are cut separately to the base piece, are subsequently welded to the base piece. The lids of the plenums are cut from stainless steel, and were fitted to the body of the plenums using self-tapping screws. Gaskets between each lid and the body of each plenum were used to create air-tight seals. Figure 8.7 also illustrates the development drawings for both the inner plenum walls and the plenum lids. With reference to Figure 8.7, a series of holes was cut in the plenum base/OWC top piece which is positioned so that, when the model is assembled, there is a pair of identically-located holes in the top of each OWC chamber. For each OWC chamber, one of these holes will allow high-pressure air generated in the OWC chamber to flow into the high-pressure plenum as the water column moves up in the chamber, subject to control via an air admittance valve. The second hole will allow air to flow from the

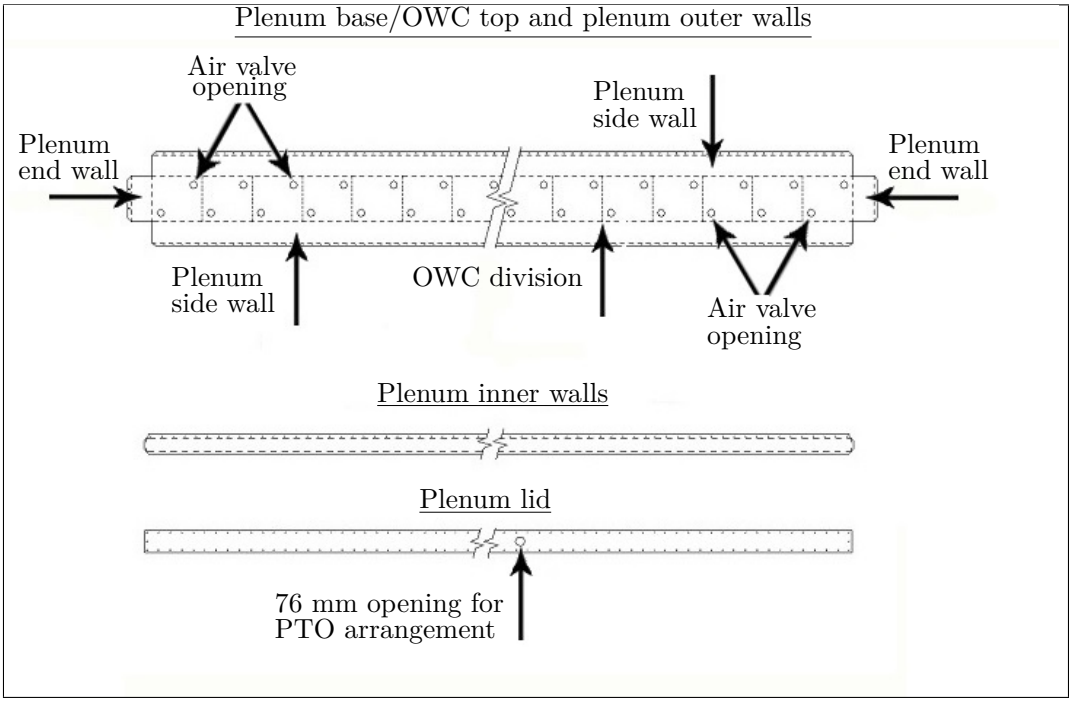

FIGURE 8.7: Development drawings of the plenum base, outer and end walls/OWC top piece, plenum inner wall piece and plenum lid piece.

low-pressure plenum back into the chamber as the water column moves down in the chamber, again subject to the control of a separate air admittance valve.

One-way air admittance valves are used to control the flow of air through the model in response to the motion of the water columns, when the model is subject to incident waves. This process is as described for the full-scale platform in Chapter 3. OsmaVent 40 Air Admittance Valves, manufactured by WAVIN Ltd., are used. For each chamber, one valve allows high-pressure air to move from the OWC chamber into the high-pressure plenum, and is located inside the OWC chamber. Conversely, the valve which allows air to flow from the low-pressure plenum into each OWC chamber is located inside the low-pressure plenum. OsmaVent valves must be kept in an upright position to function correctly. In order to locate the valves inside the OWC chambers in an upright position, U-tubes are installed connecting each chamber to the high-pressure plenum. This arrangement has the added benefit of reducing the risk of water entering the valve during the operation of the device, which would result in the valve becoming water locked. Nonetheless, the danger of water entering the U-tube remains. Thus, for each U-tube, a length of 3.2 mm Tygon laboratory tube, which has an inner diameter of 1.6 mm, was installed with one end located in the base of the U-tube, and the other routed through purpose-drilled holes in the plenum. A total of 32 lengths of Tygon tubing were

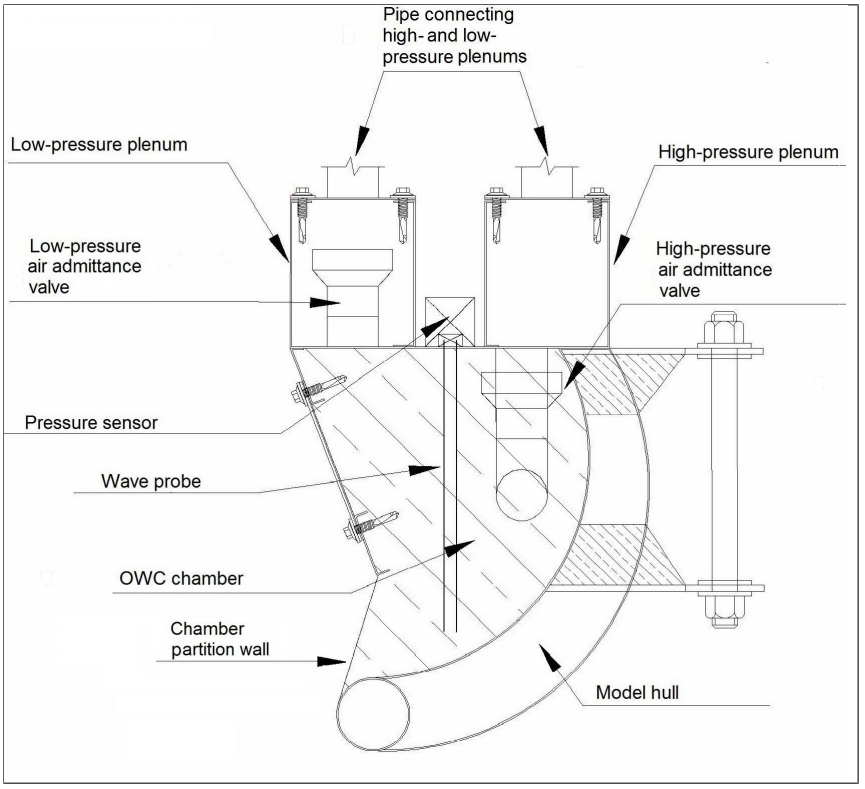

FIGURE 8.8: Section through a single OWC chamber of the 32-OWC model, showing plenum and valve arrangement

thus installed. Should water enter the U-tubes, it could then be removed using suction through these tubes, which were sealed when the model was under test. Figure 8.8 illustrates a schematic of a section through the leg perpendicular to the opening of the OWC. The U-tube, the location of the high- and low-pressure plenums and the position of the high- and low-pressure valves can be seen.

The proposed power take-off arrangement requires air to flow between the high- and low-pressure plenums. For the stainless steel model, this air flow occurs through two 76 mm diameter stainless steel pipes. One such pipe is connected to an opening in the lid of the high-pressure plenum, and the second to a corresponding opening in the lid of the low-pressure plenum. As such, each plenum lid has one 76 mm hole. This hole may be seen in Figure 8.7. The 76 mm diameter pipes are mechanically fixed to the plenums through the use of self-tapping screws and, as before, custom-cut foam gaskets are used to ensure an airtight seal between these pipes and the plenum lids. The pipes extend to a height of 600 mm above the respective plenums, at which point both pipes turn through 90 degrees to face each other. A gap of 200 mm between the upper ends of the 76 mm diameter pipes is left. Since the airflows generated in each leg of the platform

are independent, both legs have a pair of 76 mm pipes arranged as described. These pipes may be seen in Figure 8.1. At full-scale, the power take-off would comprise a uni-directional, air-driven turbine connected to an electrical generator. In order to simulate the damping that would arise from the power take-off, pairs of Venturis were fitted to the model in the 200 mm gap between the upper ends of the 76 mm diameter pipes on both legs. Varying levels of power take-off damping could thus be applied by varying the throat diameter of the Venturis. An airtight seal between the 76 mm diameter pipes and the Venturis was obtained using latex couplers and jubilee clips. A schematic of this arrangement is shown in Figure 8.9.

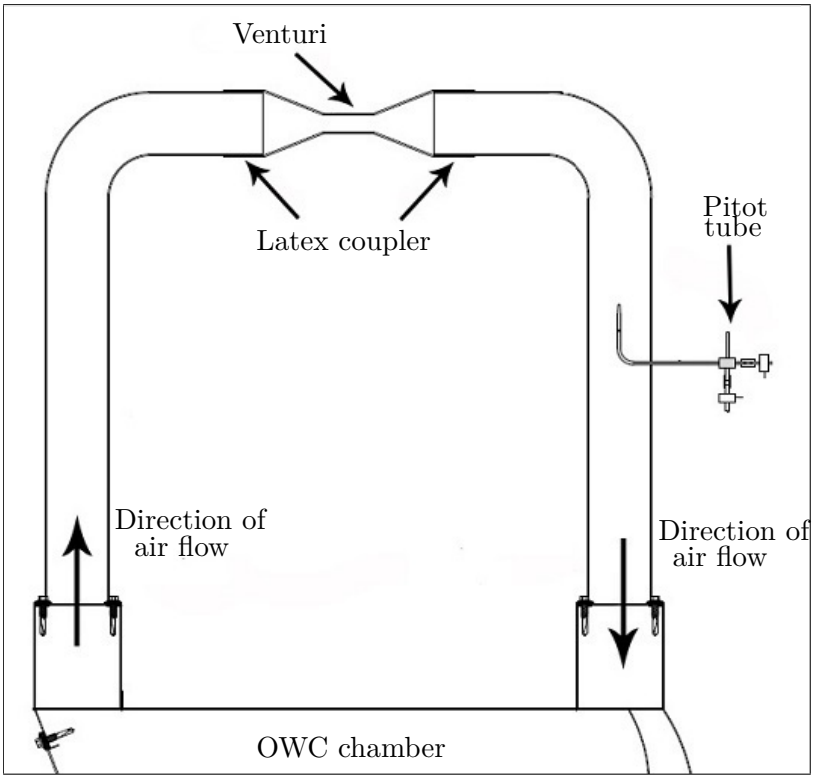

FIGURE 8.9: Power take-off arrangement.

The Venturis used to simulate power take-off damping during the tank testing of the stainless steel model were custom-made by the author from glass reinforced plastic. Initially, Venturis had been made using Isopon, a polyester-based material. However, this material proved to be porous and not air-tight, and the Venturis made from Isopon were discarded.

Three trusses, constructed from stainless steel bar, are mechanically fixed to the stainless steel model. The purpose of these trusses is threefold. Firstly, they give the model the necessary rigidity and ensure that the two legs of the model remain at the correct angle

relative to each other. Secondly, the draft of the model can be varied through the use of buoyancy tubes. These tubes mount to the model by bolting onto the trusses, one at either end of each truss. The buoyancy tubes may be moved vertically to change the overall buoyancy of the model, and hence its draft. Furthermore, the buoyancy tubes provide a convenient location to install ballast as required. Note also that heave damping plates are welded to the base of these buoyancy tubes. The buoyancy tubes/heave damping plates were constructed from 200 mm diameter, 0.9 mm thick stainless steel pipes. Two 3 mm-thick plates are welded along the length of both sides of these pipes through which an array of holes were drilled to allow the tube to be bolted to the trusses in varying vertical positions so that the overall buoyancy of the model may be varied. A 400 mm diameter plate is welded to the base of each buoyancy tube, and these 400 mm plates act as heave damping plates, as can be seen in Figure 8.10, which illustrates a plan, elevation and isometric projection of the buoyancy tubes.

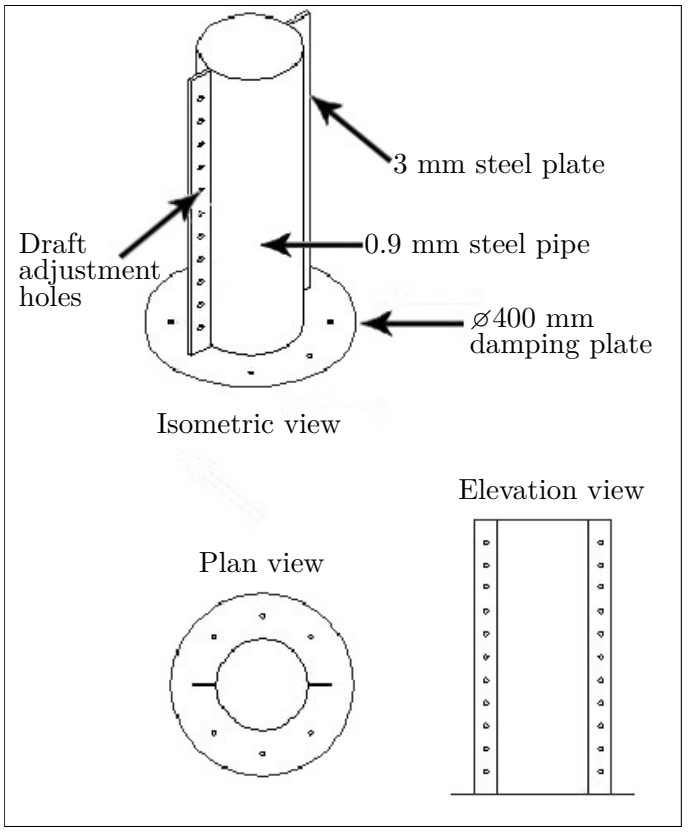

FIGURE 8.10: Buoyancy tubes.

The third purpose of the trusses is to provide a convenient and secure means by which the sensor cable train may be routed from the model to the data acquisition system. The trusses are made primarily from 8 mm and 10 mm stainless steel bar. They also

include stainless steel plate sections of thickness 0.9 mm to allow the buoyancy tubes to be mounted to the trusses, and the trusses themselves to be mounted to the model. The trusses and the buoyancy tubes can be seen in Figure 8.1.

The final stainless steel parts manufactured for the 32-OWC model were a set of stainless steel removable 'shoes', which may be bolted onto the model. The shoes are detachable wave-guide ramps designed to fit to the lower edge of the OWC chamber openings and continue into the water at an angle to a depth below the lower edge of the OWC chamber. Previous flume testing performed by WEI, on a fixed array of 3 OWCs [20], showed an improvement in the power absorbed by the OWC array through a wave run-up effect when such a shoe is installed. Each shoe is of a length equal to the width of 4 OWC openings and, as such, each leg of the stainless steel model may have four such shoes installed. Figure 8.11 shows a schematic of a shoe installed, in contrast to Figure 8.8, where no shoe is installed.

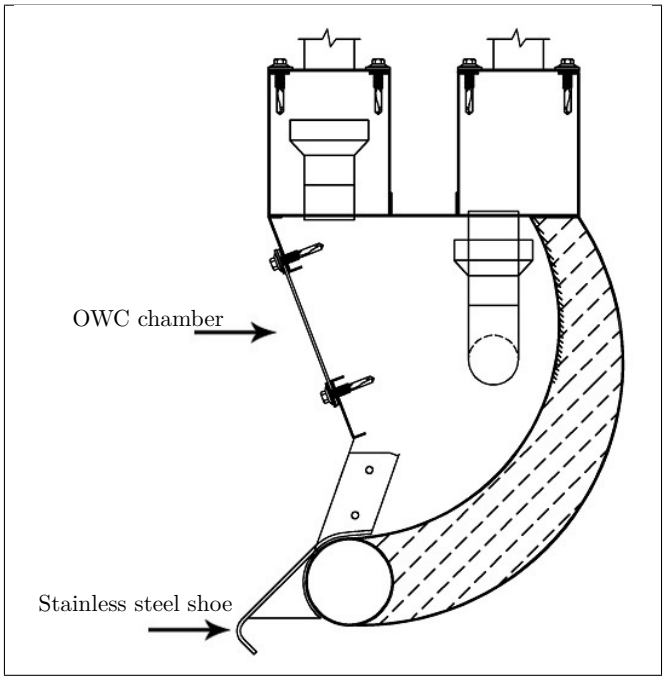

FIGURE 8.11: Section through a single OWC chamber of the 32-OWC model with stainless steel shoe installed.

8.2.2 Sensor installation

The final stage of constructing the 32-OWC stainless steel model was the installation of the sensors required to capture the data of interest during the testing. Three different types of sensing equipment were installed to record variations in pressure and water level in the OWC chambers, pressure variations in the plenums and the power take-off arrangement, and airflow through the power take-off arrangement. Honeywell 176PC14HD2 differential pressure transducers were used to measure the difference between the air pressure at various points in the model and atmospheric pressure. All 16 OWC chambers in one leg of the model were fitted with one of these pressure transducers. These transducers are located outside the chamber and connect mechanically through the top plate of each chamber using rubber grommets. The location of a pressure sensor may be seen in Figure 8.8. On this same leg of the model, three sensors were installed in both the high- and low-pressure plenums, one at each end of the plenum, and one at the lengthwise centre of the plenum. Again, on this same leg of the model, pressure transducers were fitted at the height-wise centre of both the power take-off tubes. Thus, a total of 24 transducers were installed on this leg of the model. Due to the limitation on the number of sensor channels that could be monitored during testing, the second leg was only fitted with pressure transducers at the length-wise centre of the two plenums, one at the stern end of the high-pressure plenum and one at the bow end of the low-pressure plenum, resulting in a further four transducers. Resistive wave probes were used to measure the displacement of the water columns relative to the platform during testing. Wave probes were installed in all 16 OWC chambers in one leg of the model (the same leg for which pressure transducers were installed on each OWC chamber). The wave probes were installed through the top of the OWC chambers using rubber grommets to ensure an airtight fit. Due to the limitation on the number of channels that could be recorded, only five OWC chambers had wave probes fitted on the second leg. The data gathered from the five wave probes installed in the second leg of the model could be used to ensure that both legs of the model were behaving in the same fashion, as would be expected. In total, 21 resistive wave probes were installed. The final piece of sensing equipment used was a Pitot tube, which was installed in the power take-off set-up of one leg, with the aim of measuring the airflow through the Venturi during the testing. The position of the Pitot tube can be seen in Figure 8.9. However, during testing, the Pitot tube quickly became blocked, and due to its position

in the model, it was not possible to clear the blockage. During the tests, all sensors were sampled at 32 Hz. Before the 32-OWC model was transported to the test facility, a number of tests were performed on the model. All wave probes, pressure sensors and air admittance valves were checked for functionality. That the OWC chambers, the power take-off arrangement and the plenums of each leg were all airtight was confirmed by firstly sealing the OWC chamber openings. Next, the end of the power take-off pipe from the high-pressure plenum was sealed. Both legs were pressurised in turn through the low-pressure power take-off pipe using an air pump. The configuration of the air admittance valves is such that by applying high pressure to the low-pressure side of the power take-off, air would flow into the low-pressure plenum. From there, the air could flow into the OWC chambers, and on into the high-pressure plenum, and thus pressurise the entire system. The direction of airflow during the air tightness test is essentially the opposite of that during the operation of the model. Leak spray was then used to locate any escaping air, and these leaks were stopped up through the application of silicon as required. The silicon was then allowed to cure with no pressure applied to the system. It was necessary to repeat the air tightness tests a number of times, each time smaller leaks could be detected and stopped up until such time as no further leaks could be found. Finally, the stainless steel model was tested for buoyancy in a purpose built floatation tank. The model was found to float at a draft in agreement with numerical predictions. The model was then ballasted using sandbags to determine the required ballast to set the model draft as desired. The model was subsequently transported to the testing facility at the HMRC.

8.3 Single-chamber, marine plywood model

The primary purpose of the tank testing performed on the multi-chamber model described in Section 8.2 was to determine the energy captured by the device in various configurations, when subject to monochromatic waves as described in Chapter 6 and Chapter 9. Work on characterising the hydrodynamic and thermodynamic behaviour of the device was performed, and a frequency domain model of the system developed, as described in Chapter 4. However, the large number of interacting components in the multi-chamber model resulted in difficulty in studying the behaviour of individual processes in the system. To further investigate these processes, and also characterise the individual components, and provide data for the validation of numerical models, a single-chamber, fixed OWC, model of similar dimensions to one chamber of the multi-chamber model, was constructed in marine plywood for test in a narrow tank facility located in DkIT. The single-chamber model is designed so that various control components and air volumes can be introduced to investigate the effect of, and characterise, each component in turn. The geometry of the wetted surface of this model is similar in form to that of the wetted surfaces of the individual chambers of the multi-chamber model. The single-chamber model was constructed from a single sheet of BS1088 grade marine plywood of dimensions 2400 mm $\times$ 1220 mm $\times$ 18 mm. Inspired by 3D printing techniques, the single-chamber model was constructed by 'slicing' the model width-wise into slices of thickness equal to the thickness of the sheet of marine plywood, i.e., 18 mm. All required slices were drawn in the CAD package AutoCAD as polylines and arranged so as to fit on the marine plywood sheet. This drawing was next imported into a second software package, Alphacam. Alphacam is then used to create g-code to instruct a CNC router to cut out the required pieces from the marine plywood sheet. This approach allows the complex curves of the single-chamber model to be cut as 2-dimensional sections and fixed together to form a 3-dimensional model. Figure 8.12 is an exploded diagram of the single-chamber model, illustrating the various slices required to make the model, and how the slices are combined to form the model. Note that the single-chamber model comprises 18 slices. As each slice is 18 mm thick, the total width of the model is 324 mm. The internal width of the chamber, equal to the width of the water column, is 288 mm, identical to the width of the chambers in the 32-OWC 1:50 scale model. When installed in the narrow tank, foam packing is used to fill the space

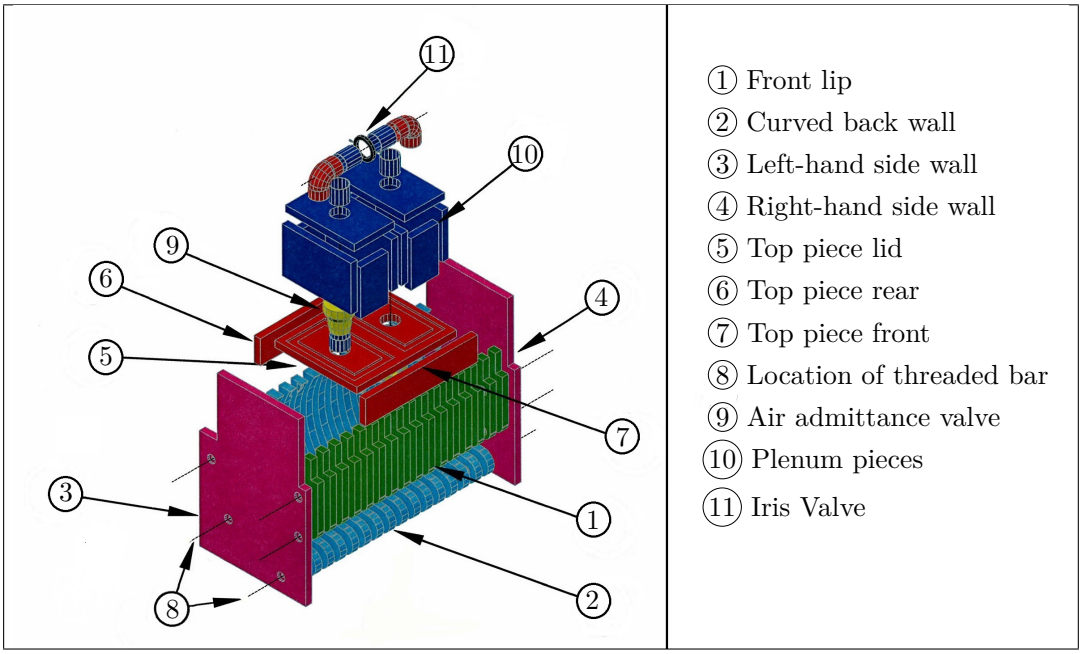

FIGURE 8.12: Exploded drawing of single-chamber OWC model.

between the model and the tank walls to prevent any water passing between the model and the tank walls.

A Masterwood Winner 2.45s CNC router was used to cut the required marine plywood pieces. Figure 8.13 shows the sheet of marine ply on the bed of the CNC router, immediately after the router has cut the required slices. Note that the depth of the router cut was set to 0.5 mm less than the thickness of the sheet of marine ply so that the pieces remain attached to the sheet until all cutting is complete. The pieces are then removed and cleaned by hand.

With reference to Figure 8.12, the single-chamber model comprises a rounded front lip ①, shown in green, a curved back wall ②, shown in cyan, two side walls ③ and ④, shown in magenta and a top piece ⑤, ⑥ and ⑦, shown in red. The model is held together using lengths of threaded bar which pass through the entire model via aligned holes cut through the model slices at the points where the dotted lines are located in Figure 8.12 ⑧. All 16 pieces of the front lip are glued together into one piece using water-proof cascamite wood glue. These pieces were aligned during gluing using threaded bar and the same holes used are then used to assemble the entire model. The same technique was used to glue all 16 pieces of the curved back wall into one piece. The three pieces, ⑤, ⑥ and ⑦, that make up the top of the single-chamber model were glued and screwed together to ensure a strong connection. These pieces make up the basic OWC

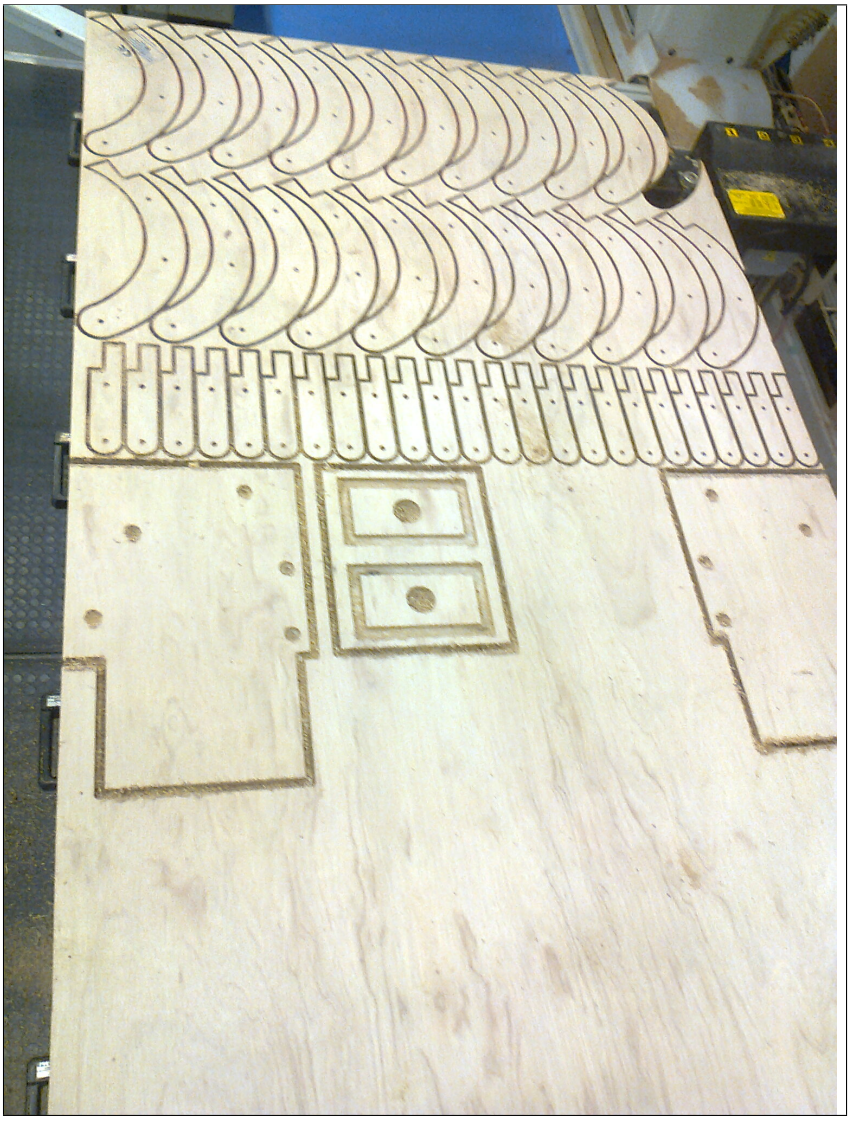

FIGURE 8.13: Marine plywood sheet with pieces cut for single-chamber model.

model. To investigate the effect of control components used during the tests performed on the 32-OWC model, the single-chamber model may be reconfigured into a number of different arrangements. Two 42 mm holes are cut in ⑤ which snugly receive a standard Wavin pipe of external diameter 42.75 mm. In one arrangement of the single-chamber model, one of the 42 mm holes is sealed, while an adjustable orifice, in the form of an iris valve ⑪, is used to apply different levels of applied damping to the motion of the water column by throttling the flow of air into and out of the OWC chamber when the single-chamber model is under test. Figure 8.14 illustrates the adjustable iris used. The opening of the iris valve may be varied between a diameter of 2 mm and 42 mm.

The 42 mm holes on the top piece, ⑤, also allow air admittance valves, ⑨, to be installed on the model during different phases of the tank testing of the single-chamber

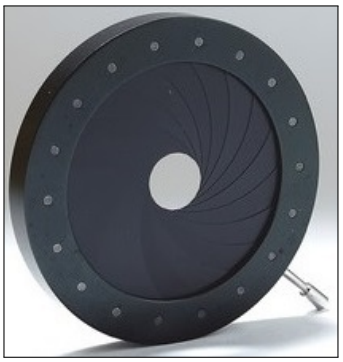

FIGURE 8.14: Iris valve used to create a variable orifice.

model. Around the 42 mm holes, rectangular tracks are routed in ⑤. The tracks allow for the installation of additional air volumes or plenums ⑩.

Chapter 9

Modelling Results

9.1 Introduction

This chapter broadly comprises two parts. The first part presents the results from the physical tank testing, and numerical modelling of the 32-OWC physical model of the proposed WEI platform, described in Chapters 4 and 6. The second part of the chapter concerns the results from the narrow tank testing and numerical modelling of the single-chamber OWC model, described in Chapters 5 and 6.

9.2 Results for the scale model of the proposed 32-OWC WEI platform

In this section, the results from the tank tests of the physical scale model of the proposed WEI platform are first presented. Time-averaged damping values for the OWC chambers are obtained from the tank testing results, and used to populate the frequency domain numerical model of the 32-OWC platform. Predictions from the frequency domain numerical model are next presented, and compared to the corresponding results obtained from tank testing.

9.2.1 Results from tank testing of the 32-OWC physical model

The focus of the tank testing of the 32-OWC physical scale model of the proposed WEI platform was on obtaining frequency domain results from monochromatic waves. In this section, some representative time domain results from the testing are first presented. Next, the frequency domain results, which form the bulk of the results from the tank testing of the proposed platform, are shown. Finally, the results from less comprehensive polychromatic testing, which was also undertaken, are illustrated.

9.2.1.1 Time domain results for the 32-OWC physical model

In Section 5.2, it was asserted that the air pressure within either the low- or high-pressure plenums of the platform, and the corresponding PTO simulating conduit, can be considered uniform at any instance in time at the scale at which the 32-OWC physical model testing was conducted. To illustrate the validity of this assertion, Figure 9.2 shows the variation in air pressure, with respect to time, of four of the installed pressure sensors. One of the sensors was located at the rear of the high-pressure plenum, and is termed P_1. Sensor P_2 was located at the front of the high-pressure plenum, and sensor P_3 was located at the horizontal midpoint of the high-pressure plenum. Sensor P_4 was located at the vertical midpoint of the corresponding high-pressure PTO conduit. The positions of the sensors is illustrated in Figure 9.1. The sample results in Figure 9.2 were taken from the test run with the model in Configuration 1, as described in Table 6.2, at an incident wave period of 1.41 s, with a Venturi diameter of 25 mm. As can be seen in Figure 9.2, a close correlation exists between the pressures recorded by these four sensors with respect to time. The cross-correlation between the four signals are given in Table 9.1. In Table 9.1, the cross-correlation between two pressure time series, $P_x(t)$ and $P_y(t)$, is termed $X_{P_xP_y}$. Two identical signals will have a cross-correlation of unity.

Cross-correlation					
$X_{P_1P_2}$	$X_{P_1P_3}$	$X_{P_1P_4}$	$X_{P_2P_3}$	$X_{P_2P_4}$	$X_{P_3P_4}$
0.9987	0.9988	0.9999	0.9961	0.9989	0.9985

TABLE 9.1: Cross-correlation between the pressure time series in Figure 9.2.

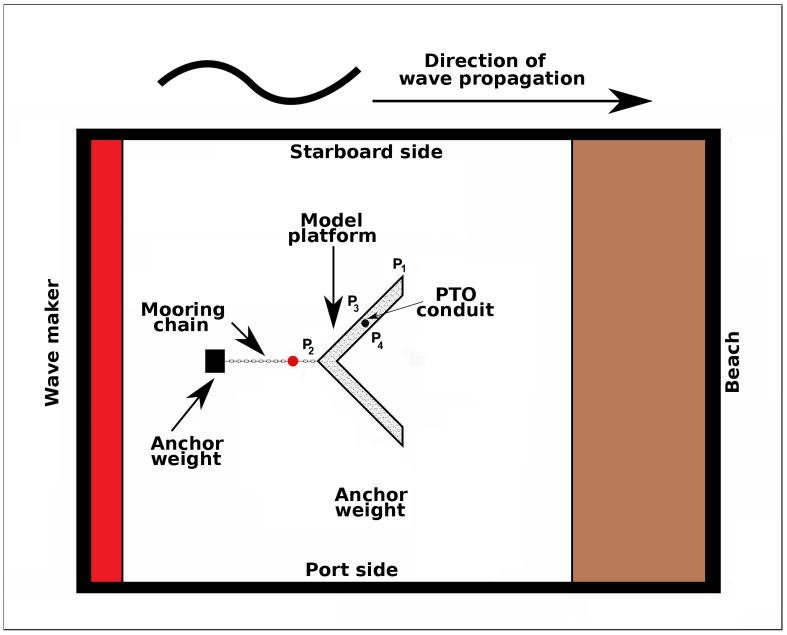

FIGURE 9.1: Location of the pressure sensors in the high-pressure plenum and PTO conduit during testing of the 32-OWC model platform.

Figure 9.3 illustrates the corresponding data for the low-pressure side for the same time frame and, again, the strong correlation between the four low-pressure sensor data sets is clear. This match exists for all model configurations and damping levels tested at this scale.

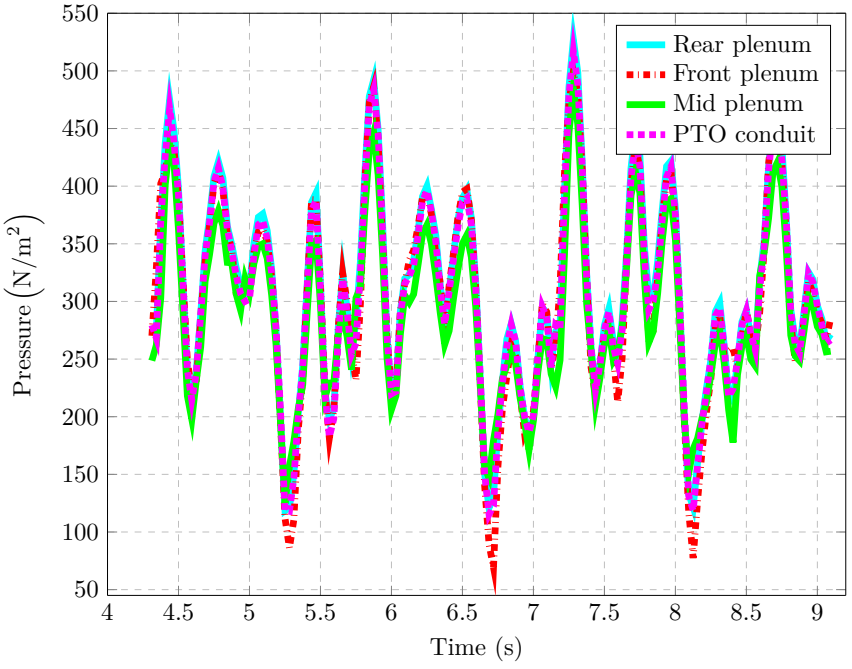

FIGURE 9.2: Time series of pressure at either end, and at the horizontal midpoint, of the high-pressure plenum, and the vertical midpoint of the high-pressure PTO conduit, illustrating the correlation between the signals.

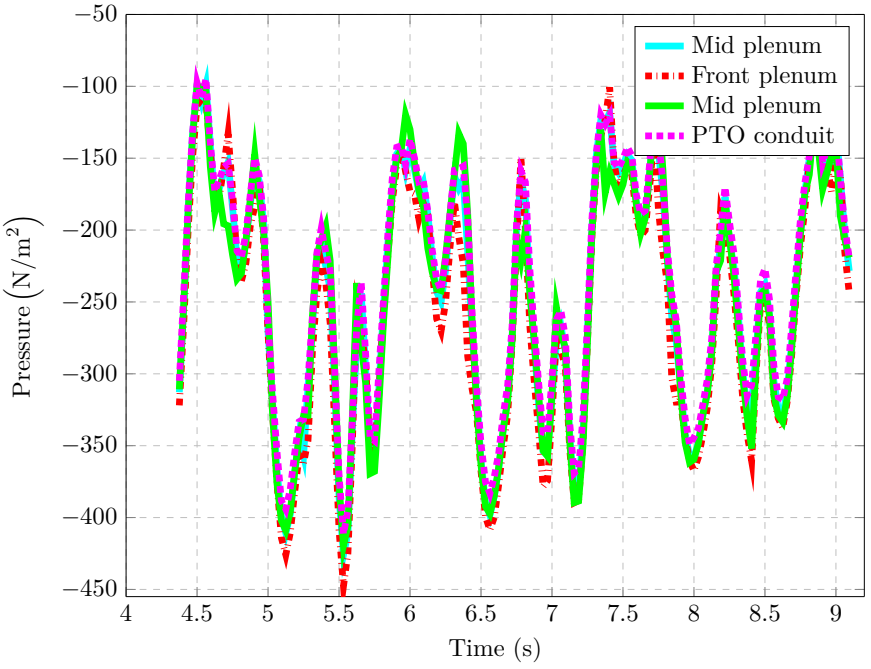

FIGURE 9.3: Time series of pressure at either end, and at the horizontal midpoint, of the low-pressure plenum, and the vertical midpoint of the low-pressure PTO conduit, illustrating the correlation between the signals.

Figure 9.4 shows the variation in air pressure, and the variation in the water column displacement, within an OWC chamber (in this instance, the ninth chamber from the stern of the platform). In addition, the variation in air pressure within the high- and low-pressure plenums with respect to time is also shown. For the results in Figure 9.4, the model was subjected to an incident wave period of 1.41 s, with Venturis of 25 mm throat diameter installed. In Figure 9.4, the green and brown dashed lines represent the pressure and water column displacement within the chamber, respectively, and the red and blue solid lines represent the variation of pressure within the high- and low-pressure plenums, respectively. In the region to the left of the point labelled 'a', it can be seen that the pressure within the chamber is below that within the low-pressure plenum, and hence the air admittance valve between the chamber and the low-pressure plenum is open. The water column at this time is moving upwards relative to the chamber. The water column motion will continue as long as the pressure within the chamber does not exceed that in the low-pressure plenum. In the region about the point labelled 'a', the pressure within the chamber exceeds that within the low-pressure plenum, and the air admittance valve connecting the chamber to the low-pressure plenum will close.

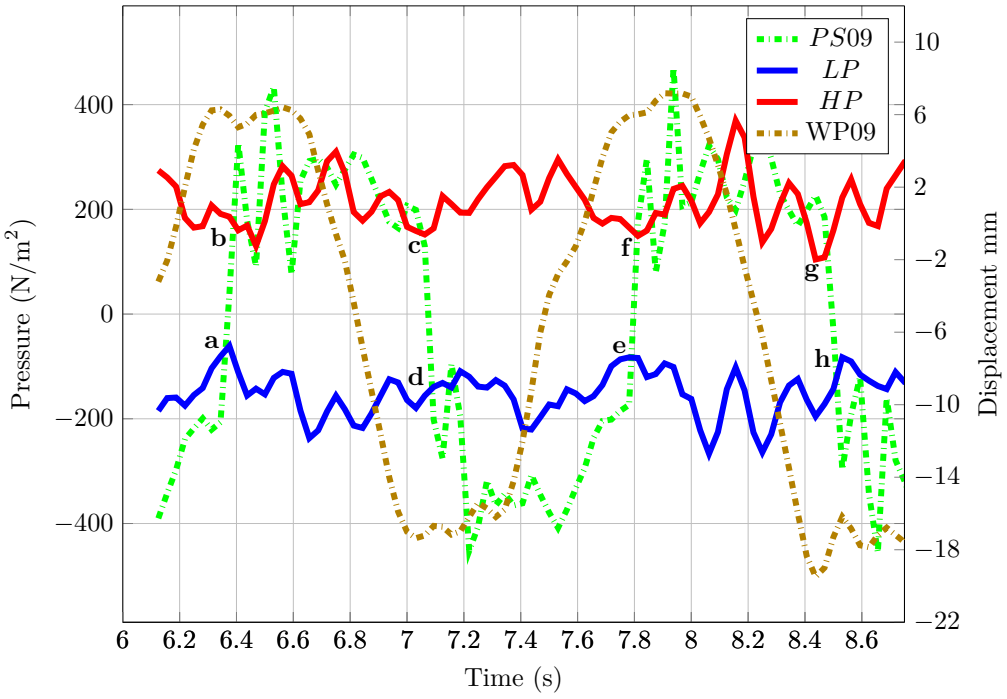

FIGURE 9.4: Variation of air pressure and water column height in the ninth OWC chamber, and the air pressure in the high- and low-pressure plenums with respect to time, illustrating the behaviour of the water column over a number of wave cycles.

Note that, at the same time, the air admittance valve between the chamber and the high-pressure plenum will also be closed, as the chamber pressure does not yet exceed that in the high-pressure plenum. The pressure within the chamber rapidly increases between point 'a' and the point labelled 'b', increasing to a value greater than the pressure within the high-pressure plenum, at which point the air admittance valve between the chamber and the high-pressure plenum will open. This rapid increase in pressure, from less than 20 mm H_2O below the initial chamber pressure to more than 30 mm H_2O, takes place over 1/16th of a second. The water column ceases to move upwards at point 'a', while the pressure within the chamber increases to that at point 'b'. Between 'b' and the point labelled 'c', the pressure within the chamber fluctuates about that in the high-pressure plenum. Before point 'c', the direction of the water column exciting force reverses, and the water column itself begins to drop in the chamber. In the reverse of the case when the pressure is below that in the low-pressure plenum before point 'a', the water column may move down relative to the platform as long as the pressure within the chamber remains above that in the high-pressure plenum, and the air admittance valve between the chamber and the high-pressure plenum remains open. The pressure within

the chamber drops below that in the high-pressure plenum for the final time in this cycle at point 'c', at which time the air admittance valve between the high-pressure plenum and the chamber will close, and the chamber pressure drops rapidly between point 'c' and 'd', in much the same fashion as it increased between points 'a' and 'b' earlier in the cycle. At point 'd', the air admittance valve between the chamber and the low-pressure plenum will re-open. Between points 'd' and 'e', the pressure within the chamber is below that in the low-pressure plenum, and is equal to the pressure in the low-pressure plenum at point 'e', completing the cycle. It can be seen, in Figure 9.4, that this cycle repeats between points 'e', 'f', 'g' and 'h'. For a full-scale platform, where the compressibility of air within the plenums would be significant, it is intended that the pressure within the high-pressure plenum would remain nearly constant with respect to time for a given sea state at a pressure above atmospheric pressure. Likewise, it is intended that the pressure within the low-pressure plenum would remain relatively constant at a pressure below atmospheric pressure. Hence the pressure across the turbine, which joins the two plenums, and the resulting electrical power generated, would be relatively constant. The plenums act in a manner analogous to a capacitor in an electrical rectifying circuit.

Figure 9.5 illustrates the displacement of the centroid of the water column surface relative to the platform with respect to time for the water column in chamber 1, located at the stern of the model (see Figure 6.1). The data was taken from a test run where the model was set up in Configuration 2 in Table 6.2, with the 25 mm throat diameter Venturi set installed, and with the model subject to an incident wave of a period of 0.99 s. Latching of the water column can be seen, for example, between a time of approximately 29.6 s and 30.1 s into the test run, and again at 30.6 s and 31.25 s. The effect of this latching on the upwards motion of the water column closely matches that as illustrated in [215].

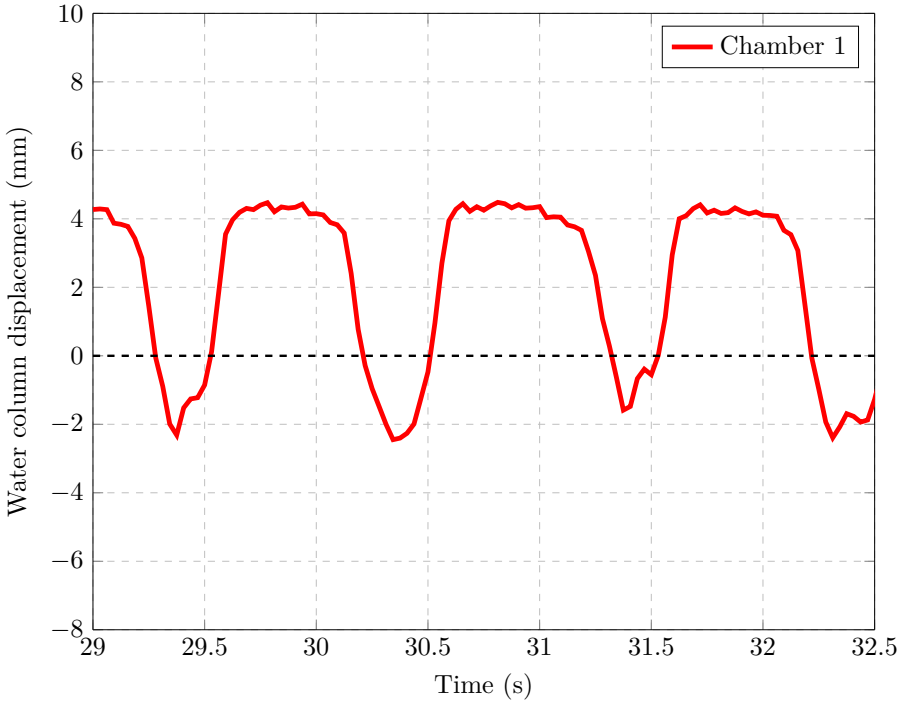

FIGURE 9.5: Time series of the variation of the relative displacement of the water column in OWC chamber 1, illustrating the latching effect.

Figure 9.6 illustrates a Pressure-Volume (pV) plot for chamber 9, with the model set up in Configuration 1, as described in Table 6.2, using the 25 mm throat diameter Venturi set and an incident wave period of 1.41 s. Figure 9.6 illustrates the relationship between the pressure in the air above the water column in the OWC chamber and the volume of that air, over one full wave period, and hence one period of oscillation, of the water column. The air pressure is the gauge pressure within the chamber as measured by the pressure transducer, and the volume of the air cavity is determined from the wave probe signal. Note how the plot forms a closed loop over a cycle and is similar in character to pV plots for reciprocating compressors as illustrated in, for example, [216]. While Figure 9.6 is a particularly good example of a pV plot from the tank tests of the 32-OWC model platform, the closed form of this curve can be found in the corresponding results for many of the chambers, and these results can be found in [23].

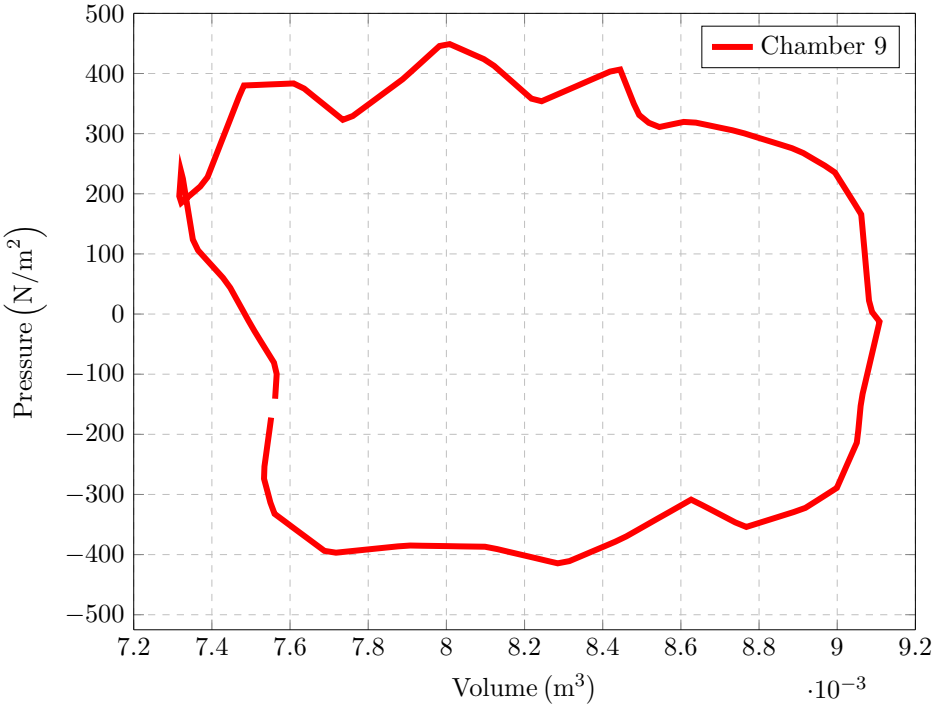

FIGURE 9.6: pV plot for chamber 9 illustrating the relationship between the volume of the air cavity and the gauge pressure of the air in the chamber over one wave cycle.

For comparison, Figure 9.7 illustrates the pV plot for a single-stage, reciprocating compressor, connected to high- and low- pressure plenums adapted from [216]. Figure 9.7 (a) illustrates the ideal pV cycle for a complete cycle of a reciprocating compressor. The ideal cycle would be obtained for a compressor travelling at an infinitely low speed if the air admittance valves could be opened by an infinitesimal pressure difference [217]. Between the points labelled 1 and 2, as the volume decreases and the pressure increases, air in the chamber undergoes compression, which, under ideal circumstances, is isothermal [218]. In reality, such a compression is likely to be polytropic. Gas flows out of the chamber between points 2 and 3 at a constant discharge pressure, before expansion takes places between points 3 and 4 at a constant inflow pressure. Gas flows into the chamber at constant pressure between points 4 and 1. Figure 9.7 (b) illustrates a more realistic cycle taking into account the inlet and outlet losses which arise due to non-ideal valve operation.

A notable difference between the modes of operation between a reciprocating compressor and one OWC in the 32-OWC model is the occurrence of latching within the OWC chamber, which will result in an increase (or decrease) in the air pressure within the

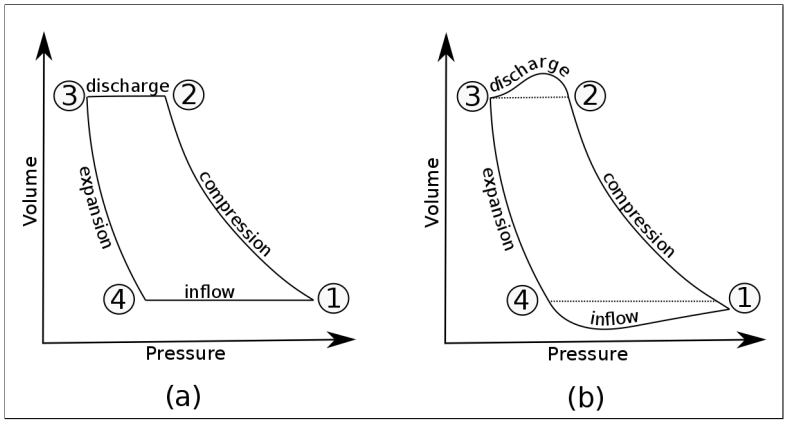

FIGURE 9.7: Typical pV plot for a reciprocating compressor, connected to high- and low- pressure plenums adapted from [216].

chamber with little or no change in volume when the water column is latched. This difference can be seen in Figure 9.6, where significant changes in the air pressure within the OWC chamber can be seen for small changes in the chamber volume while the OWC is latched.

Figure 9.8 illustrates the instantaneous power absorbed by one leg of the model platform set up in Configuration 1, in Table 6.2, with the 25 mm throat diameter Venturi set installed, while subject to an incident wave of 30 mm amplitude at a period of 1.13 s. A total of four incident wave periods would have contacted the model during the time period illustrated in Figure 9.8. Note that the frequency of oscillation of the power absorbed is twice that of the incident wave oscillation, as a result of the rectification of the airflows, and is analogous to the output voltage from a rectifier bridge in response to an input of an AC voltage. At the scale of the current model, namely 1:50, and as demonstrated by Figures 9.2 and 9.3, little compression of the air takes place within the plenums. However, at a larger scale it is envisaged that the plenums would act in a manner analogous to a capacitor in an electrical rectifying circuit by temporarily storing absorbed power as compressed air and aiding in the smoothing of the power absorption. The average power absorbed by the leg during the test run illustrated in Figure 9.8 is 4.02 W. The average power per metre wave crest in the incident wave, Pow_w, can be found from the following equation:

$$\mathrm{Pow_W} = \frac{\rho_w g^2 A^2}{4\omega} \tag{9.1}$$

where:

g = the acceleration due to gravity, m/s^2

A = the incident wave amplitude, m

ρ_w = the density of water, kg/m^3

ω = the incident wave frequency, rad/s

The model was in contact with 6.9 m of wave crest when subject to the incident wave used to generate the results shown in Figure 9.8. During the test, the platform absorbed 24% of the power in the wave. The maximum percentage of wave power absorbed by the model during these tests was achieved with the model in Configuration 4 (see Table 6.2), and was approximately 37%. As discussed in Section 9.2.1.2, numerical modelling has indicated that the 32-OWC model platform, as tested here, was over-damped, and improvements on the percentage power absorbed from the waves may be achievable. From a commercial perspective, the power absorbed by the platform from an incident wave is a key consideration, and results for this parameter in the frequency domain are presented in Section 9.2.1.2.

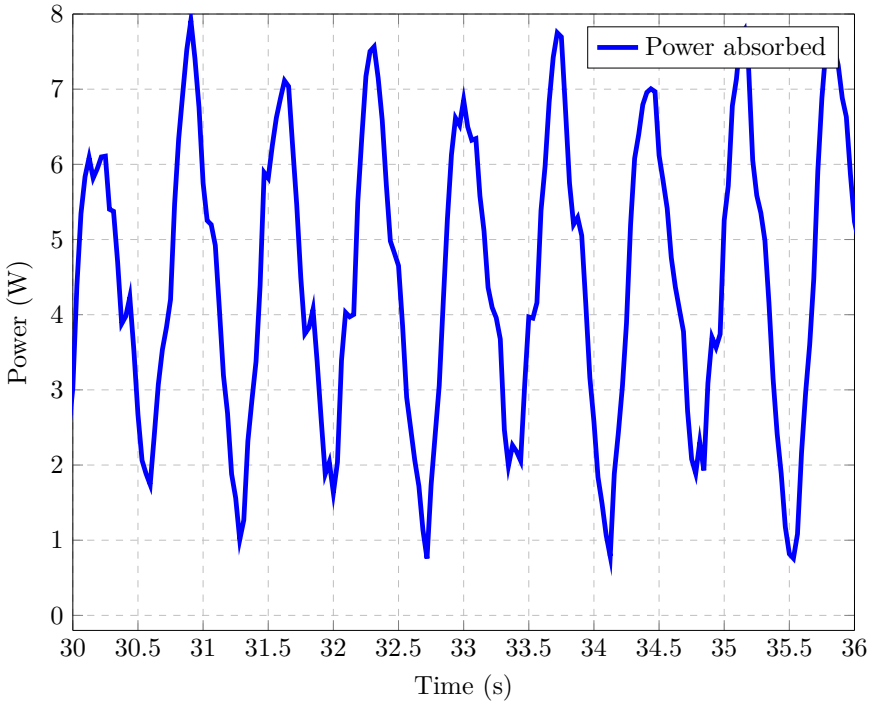

FIGURE 9.8: Time series of instantaneous power absorbed by one leg of the model in Configuration 1, with the 25 mm throat diameter Venturi set installed, while subject to an incident wave of 30 mm amplitude at a period of 1.13 s.

Consider now the rigid body motion of the platform. Concern was raised by the staff at the HMRC that, due to the single point mooring, the platform might undergo yaw motion in response to incident waves. In reality, the amount of movement the platform underwent in roll, sway and yaw, for all wave conditions tested, was minimal. (Note that only unidirectional waves were used during testing at the HMRC.) The motion in surge was limited to the platform slowly moving away from the direction of the incident waves until restrained by the mooring, with some small surge motion about that point. Thus, the modes of motion of significance to the platform were the pitch and heave motion of the platform. While such motion may be either beneficial to the power absorbed by the platform or parasitic to it, such motion will have implications for the accelerations experienced by any wind turbines that may be installed on the platform, and are thus undesirable [219]. Figure 9.9 illustrates the pitch motion of the platform for the setup which exhibited the greatest amount of pitching motion. This run occurred with the model set up in Configuration 3, in Table 6.2, with the 20 mm Venturi set installed and with the model subject to an incident wave period of 1.84 s. As can be seen from Figure 9.9, the pitch angle of the platform varied with a range of approximately $\pm 2.25^{o}$ from the neutral position. However, it should be noted that the range of pitching motion between the various configurations, for incident waves of equal periods, is not large. For example, with an incident wave of 1.98 s, the pitch motion of the platform varied between $\pm 1.5^{o}$ for the platform in Configurations 1 and 2, and $\pm 2^{o}$ with the model in Configuration 3.

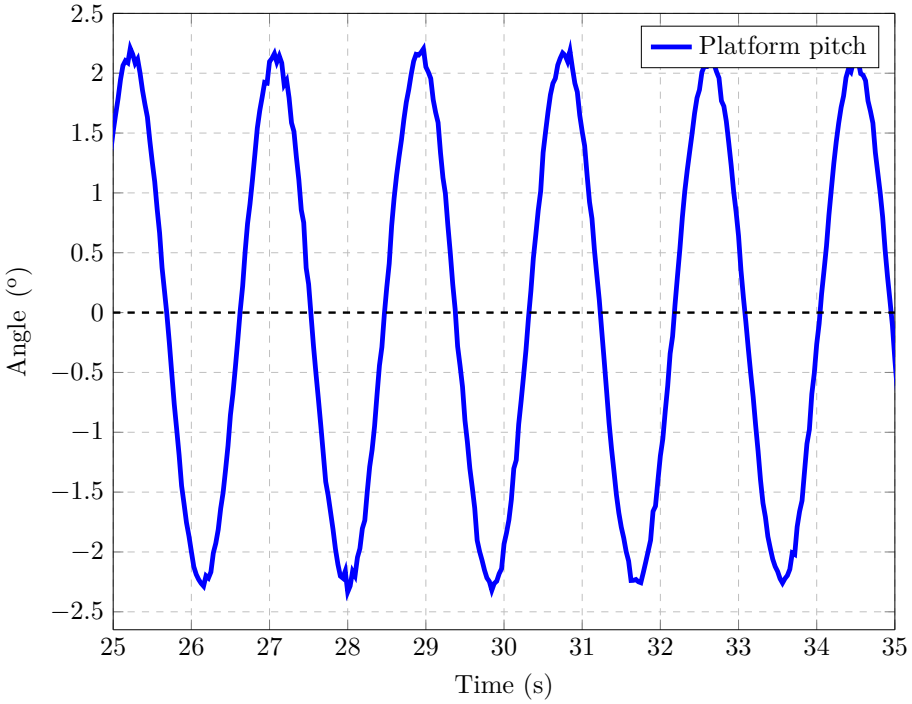

FIGURE 9.9: Pitch motion of the model platform in Configuration 3, when subject to an incident wave period of 1.84 s, using the 20 mm throat diameter Venturi set, illustrating the maximum pitching motion observed during testing.

Figure 9.10 illustrates the greatest degree of heave motion of the platform recorded, in this case for the model in Configuration 1, as described in Table 6.2, using the 15 mm throat diameter Venturi pairing, in response to an incident wave of 1.98 s. This Venturi set was not used in conjunction with any other model configuration as listed in Table 6.2, as they were found to absorb the lowest level of power during the initial testing. The heave motion in Figure 9.10 can be seen to vary between approximately ±20 mm. Typical heave motion ranges for the various remaining configurations and Venturi pairings were in the ±15 mm range for a wave frequency of 1.98 s, which resulted in the maximum heave motion in all cases. Both the pitch and heave motion of the platform reduce significantly as the incident wave period decreases and, for example, at an incident wave period of 0.99 s, the heave motion typically has a range of ±2 mm from the neutral position, and the pitch motion typically has a range of ±0.1°.

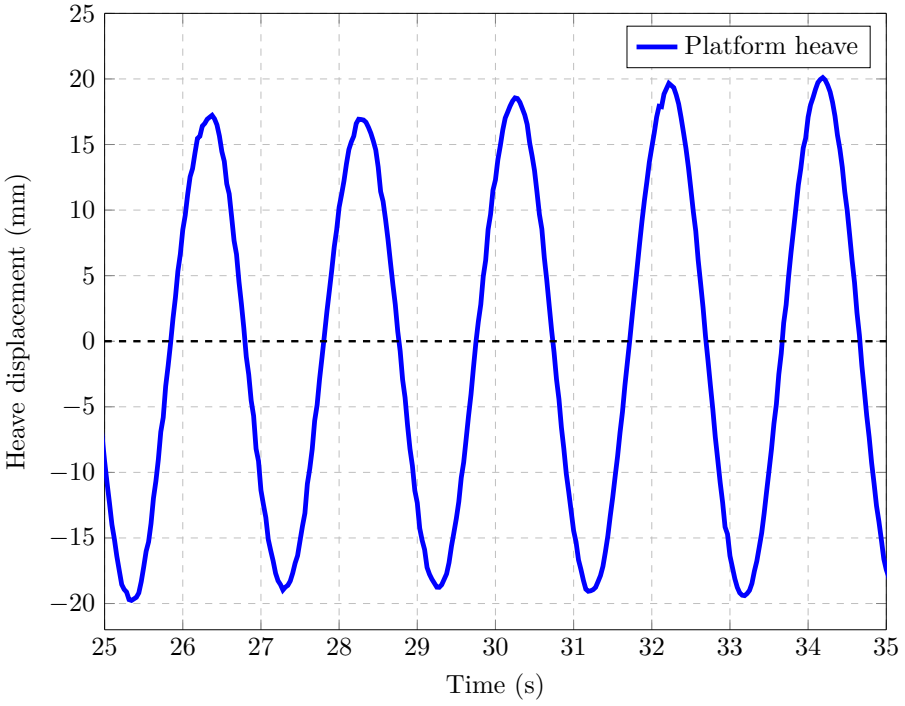

FIGURE 9.10: Heave motion of the model platform in Configuration 1, when subject to an incident wave period of 1.98 s, using the 15 mm throat diameter Venturi set, illustrating the maximum heave motion observed during testing.

While the magnitude of the pitch and heave motion does not vary significantly between configurations and damping regimes, the phase of the pitch and heave motion to each other, and the incident wave, do vary. One important consequence of this is that, under certain wave regimes, the lips of the water columns at either end of the platform pierce the surface of the water, and the OWC chamber broaches, a term used to describe the situation when the level of water at the OWC lip would drop below the lip and has been an issue in real world OWC installations [39]. This would trap more air in the system, causing the platform to rise higher in the water, exacerbating the broaching issue. The broaching issue, along with other concerns regarding the accelerations that would be experienced by a wind turbine at hub height, are two of the major drivers of current redesign work being undertaken by WEI. Both the broaching and acceleration issues can be solved by reducing the platform heave and pitch motion. Such reductions may be achieved in a number of ways, for example, through the use of larger damping plates, or by changing the platform water plane area, and hence the natural frequencies of the platform. While Figures 9.4 and 9.5 are useful in illustrating the general concept behind the intended operation of the platform, and are by no means unique, they were

specifically chosen due to their suitability for illustrating particular points. They do not, however, illustrate all of the complexity inherent in the operation of the platform. When compared to earlier, smaller-scale testing that was conducted on a three-chamber, fixed-platform model [20], it is clear that increasing the number of interacting chambers, and allowing the platform itself to operate in the standard six rigid body modes, greatly increases the complexity of the processes at work. For example, consider Figure 9.11 which illustrates the complete time series for the water column displacement in OWC chamber 17 with respect to the platform, with the model set up in Configuration 1, as described in Table 6.2, using the 25 mm throat diameter Venturi pairing with an incident wave period of 0.99 s. For much of this test run, the water column oscillates about a point approximately 10 mm above the still water level in a relatively uniform fashion. However, between approximately 25 s and 40 s into the test run, the mean level of the water column increases to approximately 20 mm above the still water level, and the amplitude of the oscillation decreases dramatically. As the period of the water column oscillations during this time is equal to that of the incident wave, such a reduction in the amplitude of oscillation is unlikely to be due to the latching effect outlined previously (although the small, higher-frequency oscillations within the main peaks may be the result of the latching effect). Once past the 25 s to 40 s time, the nature of the oscillations returns to a more regular motion.

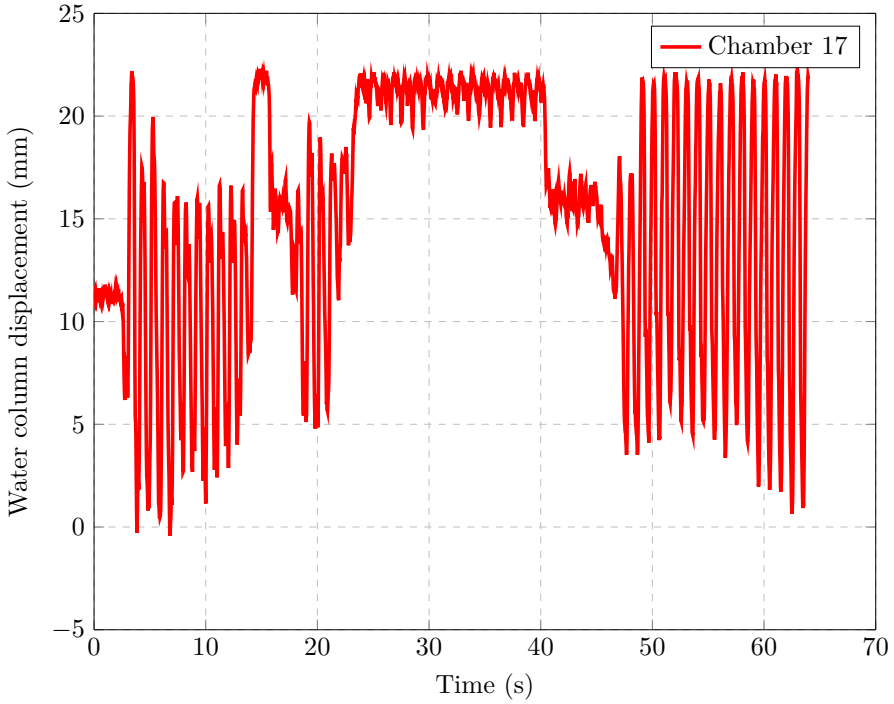

FIGURE 9.11: Complete time series of the motion of the water column in chamber 17, illustrating the complex nature of the motions of the water column.

Contrast the results presented in Figure 9.11 with the motion of the water column in OWC chamber 13, as illustrated in Figure 9.12, for the same test run. No such unusual changes in the motion of the water column are observed in this instance. There are several possible explanations for the behaviour of the relative water column motion in chamber 17 during the test run illustrated in Figure 9.11. It is possible that the coupled motion of the platform and the water column resulted in this relative motion of the water column at that time. It is also possible, however, that the air admittance valve in the low-pressure plenum became stuck, preventing the water column moving down relative to the platform during this section of the test run; see Section 9.3.2.1 for a discussion of valve stiction. A system which monitors and records the position of the valves would be a useful addition to any future testing.

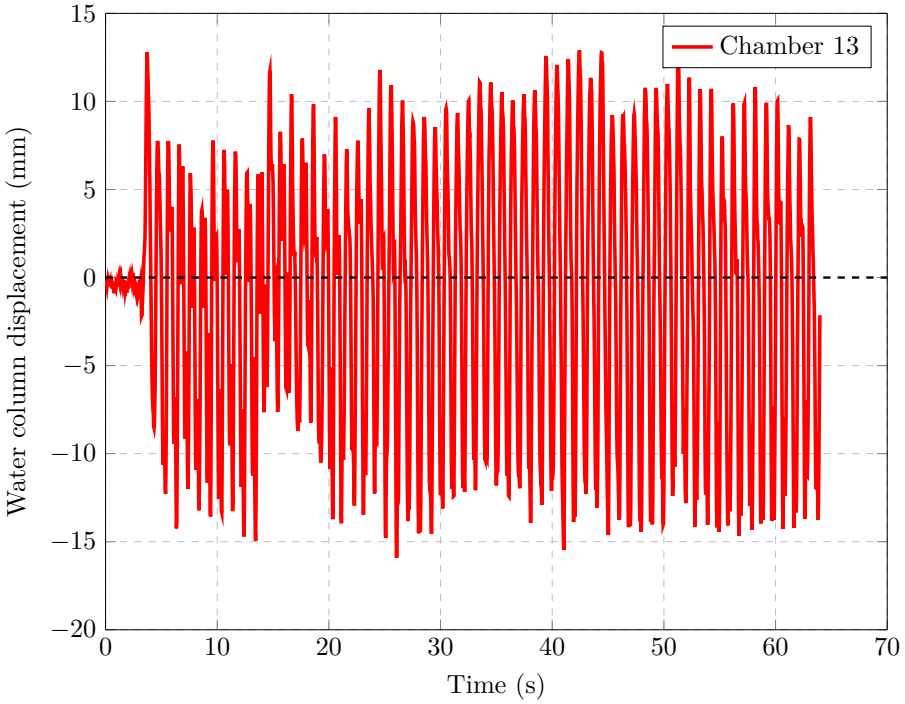

FIGURE 9.12: Complete time series of the motion of the water column in chamber 13. In contrast to the example in Figure 9.11, no unusual motions of the water column were recorded for chamber 13, demonstrating that the nature of the motion of the water column in the different chambers varied across the platform.

9.2.1.2 Frequency domain background theory

A total of 296 monochromatic wave tests were performed on the 32-OWC physical model of the proposed WEI platform, for varying wave periods and model configurations. Thus, a substantial volume of data was gathered, and it is beyond the scope of this work to present all results generated. (The complete results from the testing of the 32-OWC model may be found in [23].) In the current section, representative frequency domain results, obtained during the monochromatic wave tests performed on the 32-OWC model, are presented.

First, in order to demonstrate the effect of varying Venturi diameter on the behaviour of the platform, a total of thirty-six plots are presented in Figures 9.13 to 9.18 for the model in Configuration 1, as described in Table 6.2, for each Venturi diameter. These plots illustrate:

- Root mean square (RMS) of the gauge pressure either side of the Venturi vs. incident wave period, Figure 9.13

- RMS of the volumetric airflow through the Venturi vs. incident wave period, Figure 9.14
- RMS of selected OWC gauge pressures vs. incident wave period, Figure 9.15
- RMS of wave power absorbed by the model vs. incident wave period, Figure 9.16
- Capture width for the model vs. incident wave period, Figure 9.17
- Response amplitude operators (RAOs) of the platform motion vs. incident wave period, Figure 9.18

Next, in order to illustrate the performance of the 32-OWC model in the different configurations described in Table 6.2, the same plots, as listed above, are presented for the 32-OWC model in each of the five configuration, for a Venturi diameter of 25mm in each case. Finally, surface plots for each of the five model configurations are presented, which show the variation in absorbed wave power against both Venturi diameter, and incident wave period. The wave power absorbed by the model was determined using three different methods in order to provide confidence in the results. The three methods are described below.

Power calculation method 1

The wave power absorbed by the model may be determined by considering the airflow across the Venturi, and may be calculated as the product of the RMS of the volumetric airflow multiplied by the RMS of the pressure difference across the Venturi [220]. This calculation yields the power absorbed by one leg of the model, and since the model is symmetric, the total power absorbed is twice this figure. The pressure difference is recorded in mm H_2O, and is converted to N/m^2. The RMS of any time series, $X(t)$, comprising n values, is given by:

$$\text{RMS} = \sqrt{\sum_{i=1}^{n} \frac{(X(i))^2}{n}} \tag{9.2}$$

where $X(i)$ represents the value of the i^{th} element of the time series. The RMS of a periodic signal is related to the amplitude of the signal by:

$$\text{AMP} = \text{RMS}\sqrt{2} \tag{9.3}$$

Using standard Venturi theory [182], the mass flow rate across a Venturi can be determined once the coefficient of discharge, Cd, is known, using the following equation:

$$\dot{m}_{vent} = CdA_V\sqrt{2\rho_{air}\left|p_{pl}^{+} - p_{pl}^{-}\right|} \tag{9.4}$$

where:

$\dot{m}_{vent}$	=	the mass flow rate of air through the Venturi, kg/s
A_V	=	the cross-sectional area of the throat section of the Venturi, m^2
ρ_{air}	=	the density of air, kg/m^3
p_{pl}^{+}	=	the pressure in the conduit leading to the high-pressure plenum, N/m^2
p_{pl}^{-}	=	the pressure in the conduit leading to the low-pressure plenum, N/m^2

Typically, the measured value for Cd for a smooth Venturi ranges from 0.95 to 0.97 [182]. Note that, as one of primary purposes of the testing performed was to assess the economic viability of the WEI concept, an estimated value for Cd of 0.9 was used in conjunction with Equation (9.4), leading to conservative power estimates. Assuming that no compression of air takes place, which can be considered valid at the volumes used here and for subsonic fluid flows (Mach no. <0.3) [200], the volumetric flow rate can be determined from:

$$Q_{vent} = \frac{m_{vent}}{\rho_{air}} \tag{9.5}$$

where Q_{vent} is the volumetric flow rate of air through the Venturi in m^3/s. Combining Equations (9.4) and (9.5) allows the absorbed power to be calculated from the following equation:

$$\text{Absorbed wave power} = \frac{m_{vent}}{\rho_{air}}\left|p_{pl}^{+} - p_{pl}^{-}\right| \tag{9.6}$$

Power calculation method 2 This method of determining the power absorbed is based on the heave velocity of the water column, as determined from the derivative of

the displacement signal. The airflow from each chamber is calculated as:

$$Q_i = A^i_{OWC} v^i \tag{9.7}$$

where:

Q_i = the air flow into the i^{th} OWC chamber, m^3/s
A^i_{OWC} = the cross-sectional area of the i^{th} water column, m^2
v^i = the velocity of the water column in the i^{th} chamber, m/s

The total power is therefore:

$$\text{Total power} = \sum_{i=1}^{N} \left(\Delta p^i_{RMS} A^i_{OWC} v^i \right) \tag{9.8}$$

where:

Δp^i_{RMS} = is the pressure difference between the plenum and the i^{th} chamber, N/m^2
N = the number of OWC chambers

This method of calculating the wave power absorbed by the model assumes:

- the wave probe in each chamber is measuring the heave or pumping mode of the corresponding water column only
- the pumping mode is the only power generating mode of each water column
- the cross-sectional area of the water column chamber does not vary over the range of motion of the water column.

Therefore, this method for calculating the power absorbed by the 32-OWC model platform is considered less reliable than the approach based on the pressure drop across a Venturi using Equation (9.6).

Power calculation method 3

The final method used to estimate the power absorbed by the platform models air admittance valves as orifices, once the valve is open. The mass flow equations for these valves are given by [183]:

$$m^i_{suction} = C_v \times L_g \times h_{max}\sqrt{2\rho_{air}\,|p^{sc} - p^i|} \tag{9.9}$$

$$m^i_{comp} = C_v \times L_g \times h_{max}\sqrt{2\rho_{air}\,|p^i - p^d|} \tag{9.10}$$

where:

$m^i_{suction}$	=	the mass flow rate of air from the low-pressure plenum into the i^{th} OWC chamber, kg/s
m^i_{comp}	=	the mass flow rate of air from the i^{th} OWC chamber into the high-pressure plenum, km/s
C_v	=	the coefficient of discharge for the air admittance valves
L_g	=	the edge distance of the air admittance valves, m
h_{max}	=	the opening distance of the diaphragms in the valves, m
p^i	=	the pressure in the i^{th} chamber, N/m^2
p^d	=	the pressure in the high-pressure plenum, N/m^2
p^{sc}	=	the pressure in the low-pressure plenum, N/m^2

Equation (9.9) applies when the low-pressure plenum is discharging into a chamber, and Equation (9.10) applies when a chamber is discharging into the high-pressure plenum. The mass flow is assumed to be zero when the water column is motionless.

Regardless of which method is used to calculate the power absorbed, the geometry and orientation of the model relative to the incident waves in the ocean basin is such that the wave crest length presented to the model is 6.9 m in width, see Figure 6.1. The power per metre, Pow_w, in a monochromatic wave is given by Equation (9.1). The efficiency of the model, η_P, in converting wave energy is given by:

$$\eta_P = \frac{Pow_{ab}}{Pow_w \times L_p} \times 100 \tag{9.11}$$

where:

Pow_{ab} = the power absorbed by the model, W

L_p = the length of the wave crest presented to the model, m

Power calculation method 1, which relies on a single pressure measurement, is considered the most reliable method. Methods 2 and 3 provide a check to allow confidence be had in the results.

Platform motion

Platform translational motion was recorded by the motion capture system in mm, and the rotational motion was recorded in degrees (°). In accordance with guidelines issued by the 2005 International Towing Tank Conference [221], the heave RAO for the motion of the platform and the motion of the water columns is defined as:

$$\text{RAO} = \frac{\text{Amplitude of heave displacement}}{\text{Wave amplitude}} \tag{9.12}$$

where the amplitudes of the heave displacements and the wave amplitude are in metres. The pitch RAO for the motion of the platform is expressed non-dimensionally, in terms of the wave steepness, as:

$$\text{RAO} = \frac{\text{Amplitude of pitch displacement} \times \text{Wave length}}{360^{\text{o}} \times \text{Wave amplitude}} \tag{9.13}$$

Note that the displacements of the water columns, used to calculate the heave RAOs of the water columns, are determined as a combination of the data returned by the water column wave probes and the heave and pitch motion of the platform itself. The wave probes are fixed to the platform, therefore recording the motion of the water columns relative to the platform. Displacement (in metres) is calculated relative to a coordinate system, where the origin of the vertical axis is located at the still water level, as:

$$U^i_{rsw} = U^i_{rp} - x^i U_5 - U_3 \tag{9.14}$$

where:

U^i_{rsw} = the heave displacement of the i^{th} water column relative to the still water level, m

U^i_{rp} = the heave displacement of the i^{th} water column relative to the platform, m

x^i = the perpendicular distance from the centre of gravity of the platform to the centre of the i^{th} water column, m

U_5 = the pitch displacement of the platform, rad

U_3 = the heave displacement of the platform, m

The amplitude of the displacement signal is determined from the RMS of the displacement time signals using the formulation described in Equations (9.2) and (9.3).

9.2.1.3 Frequency domain results for the 32-OWC physical model

Having outlined the theory required to generate results for the 32-OWC scale model platform, the frequency domain results from the tank testing of the scale model are now presented. Figure 9.13 illustrates the RMS of the gauge pressure either side of the Venturi on the fully-instrumented leg of the model platform in Configuration 1, as described in Table 6.2, with respect to the incident wave period, for the Venturi throat diameters tested.

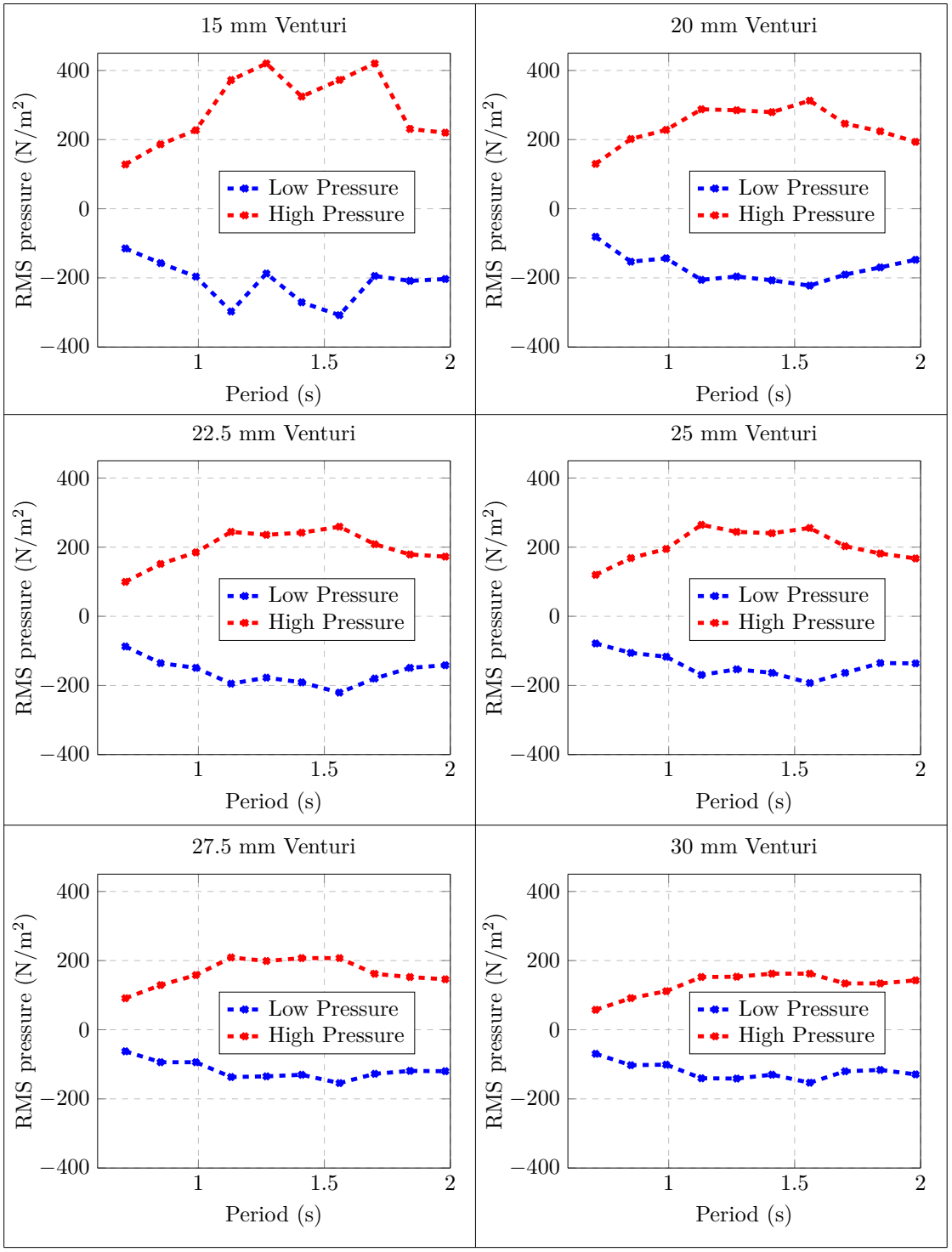

FIGURE 9.13: RMS of the gauge pressure either side of the Venturi with the model set up in Configuration 1 vs. incident wave period, illustrating the effect of varying Venturi diameter.

Figure 9.14 illustrates the RMS volumetric airflow through the Venturi on the fully-instrumented leg of the model platform in Configuration 1, as described in Table 6.2,

with respect to the incident wave period, for the Venturi throat diameters tested.

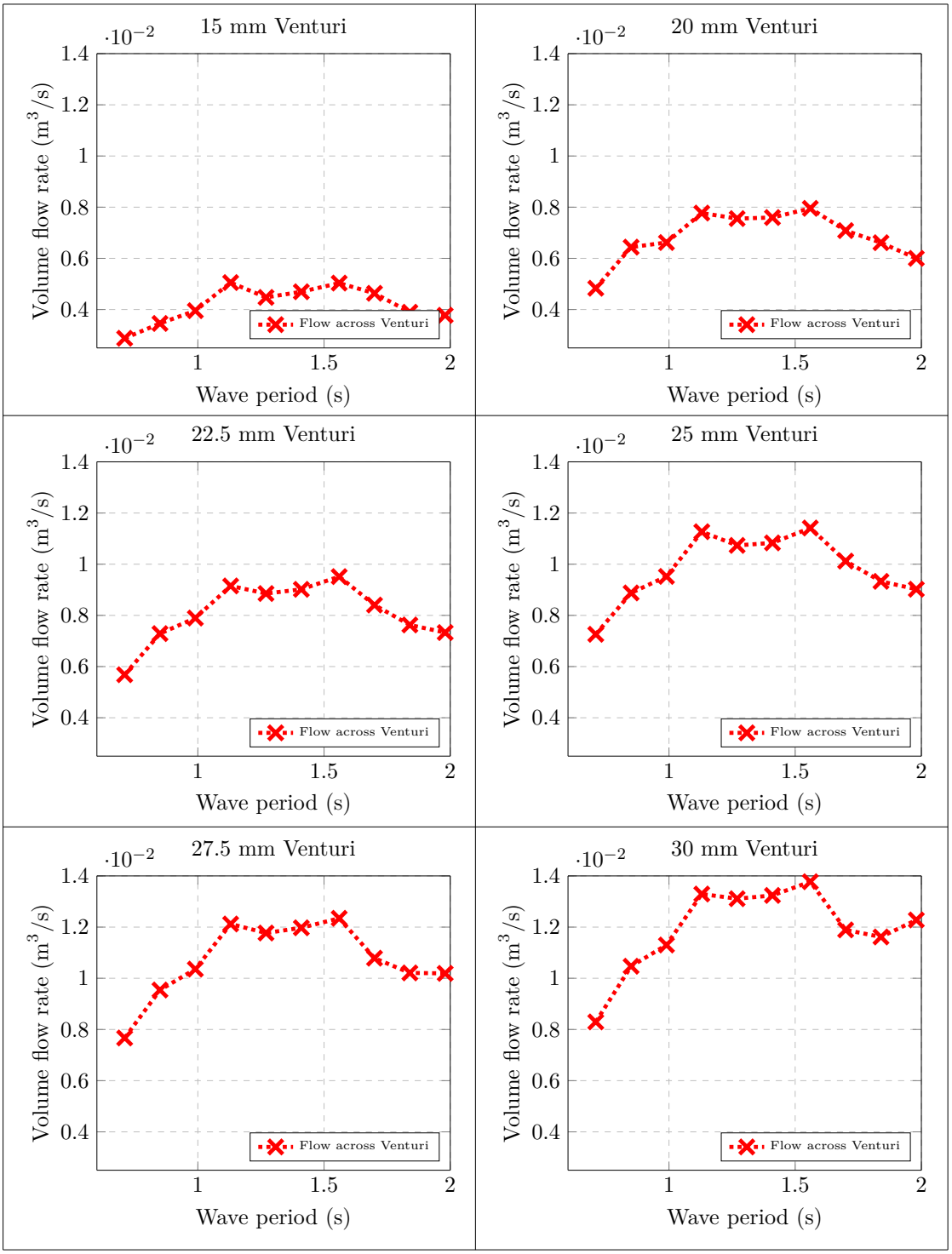

FIGURE 9.14: RMS of the volumetric airflow through Venturi with the model set up in Configuration 1 vs. incident wave period, illustrating the effect of varying Venturi diameter.

Figure 9.15 illustrates the RMS of the gauge pressure within selected OWC chambers

of the model platform in Configuration 1, as described in Table 6.2, with respect to the incident wave period, for the Venturi throat diameters tested. With reference to Figure 6.1, the pressure for Chambers 3, 5 and 11 are shown.

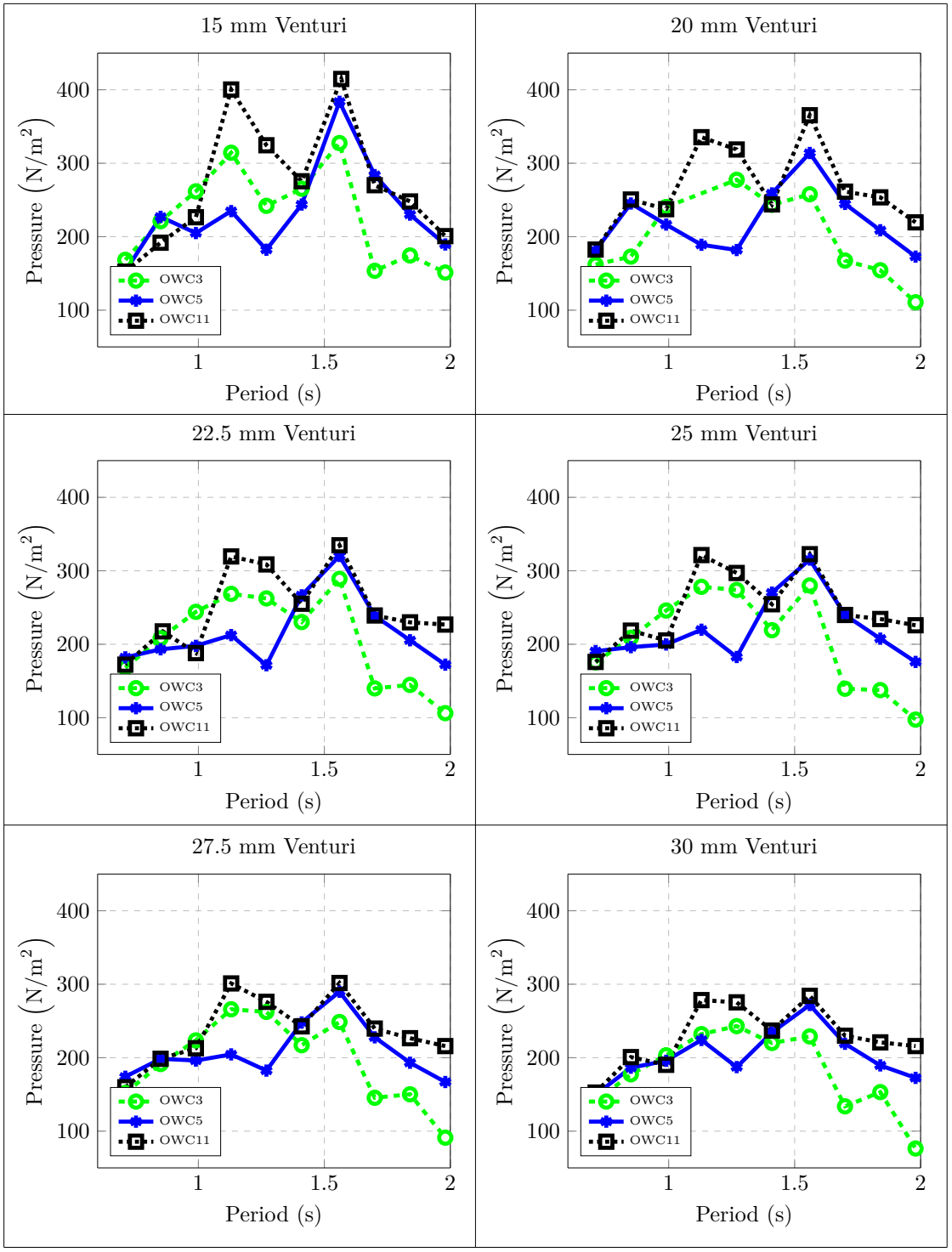

FIGURE 9.15: RMS of the gauge pressure within selected OWC chambers with the model set up in Configuration 1 vs. incident wave period, illustrating the effect of varying Venturi diameter.

Figure 9.16 illustrates the RMS wave power absorbed by the 32-OWC model platform in Configuration 1, as described in Table 6.2, with respect to the incident wave period, for the Venturi throat diameters tested, estimated using the three methods described previously, namely, the Venturi method with Equation (9.6), the method based on water column velocity using Equation (9.8) and the method where the air admittance valves are modelled as orifices.

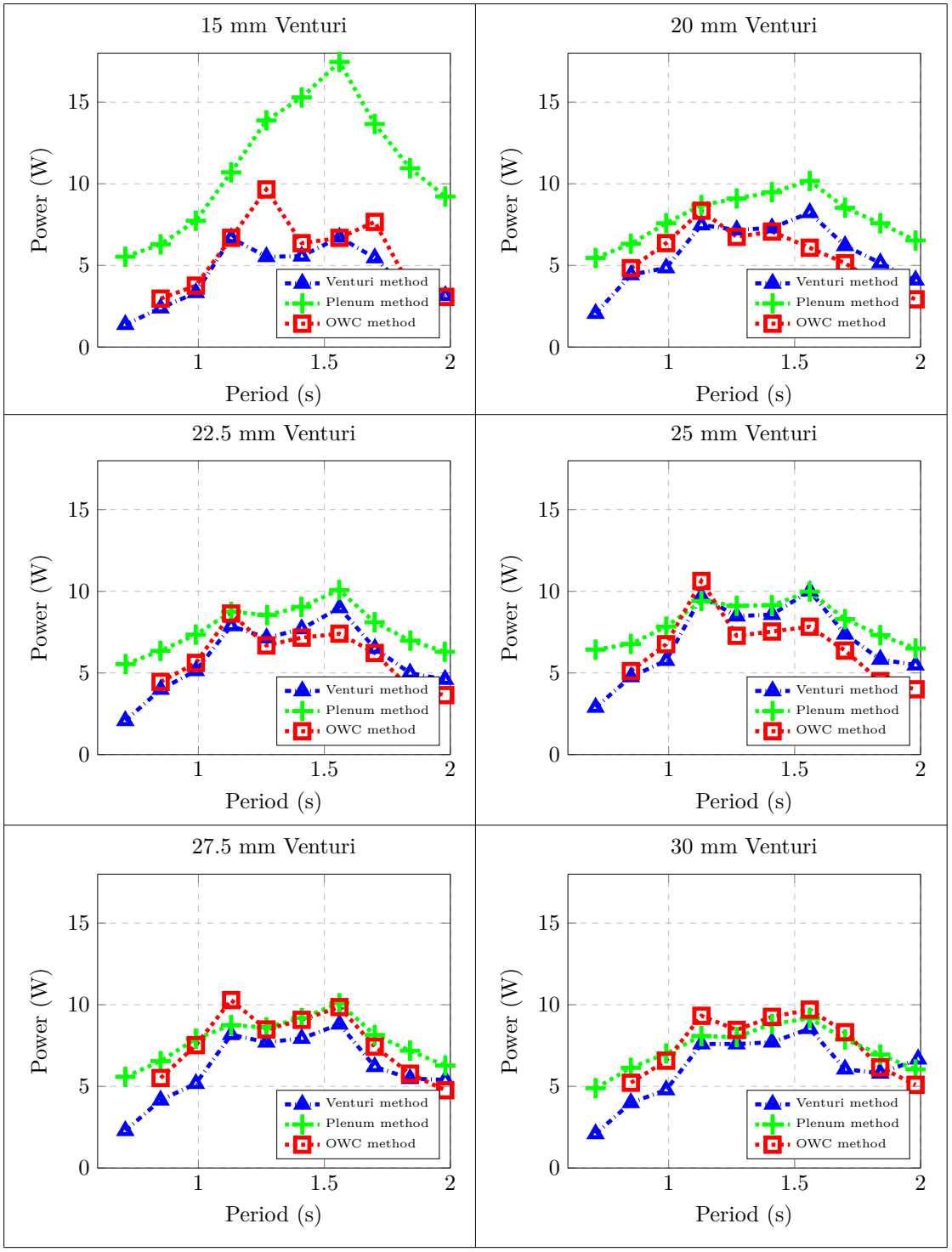

FIGURE 9.16: RMS of the wave power absorbed by the model set up in Configuration 1 vs. incident wave period, illustrating the effect of varying Venturi diameter.

Figure 9.17 illustrates the capture width for the 32-OWC model platform in Configuration 1, as described in Table 6.2, with respect to the incident wave period, for the

Venturi throat diameters tested.

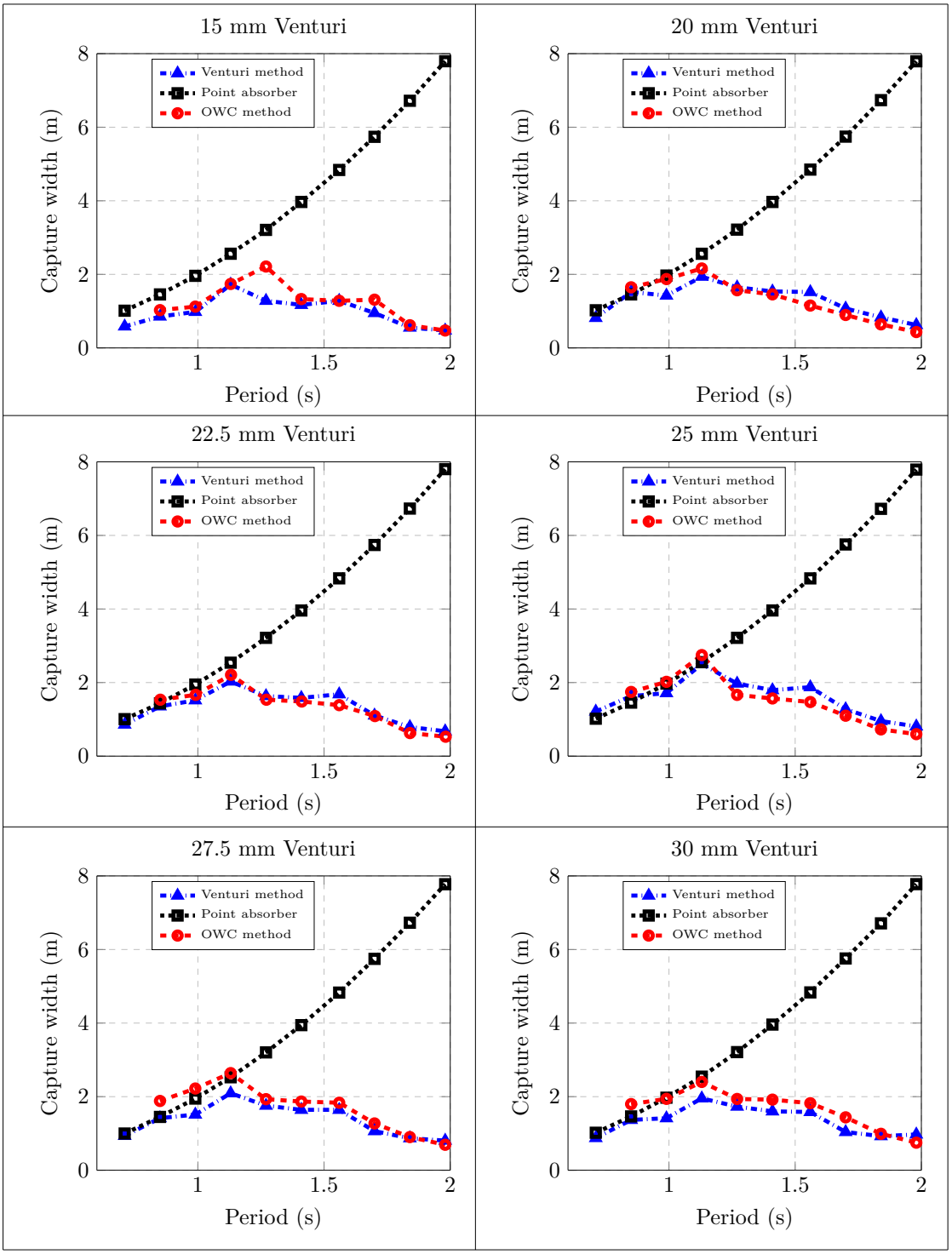

FIGURE 9.17: Capture width for the 32-OWC model platform in Configuration 1 vs. incident wave period, illustrating the effect of varying Venturi diameter.

Figure 9.18 illustrates RAOs in heave and pitch for the 32-OWC model platform in Configuration 1, as described in Table 6.2, with respect to the incident wave period, for

the Venturi throat diameters tested.

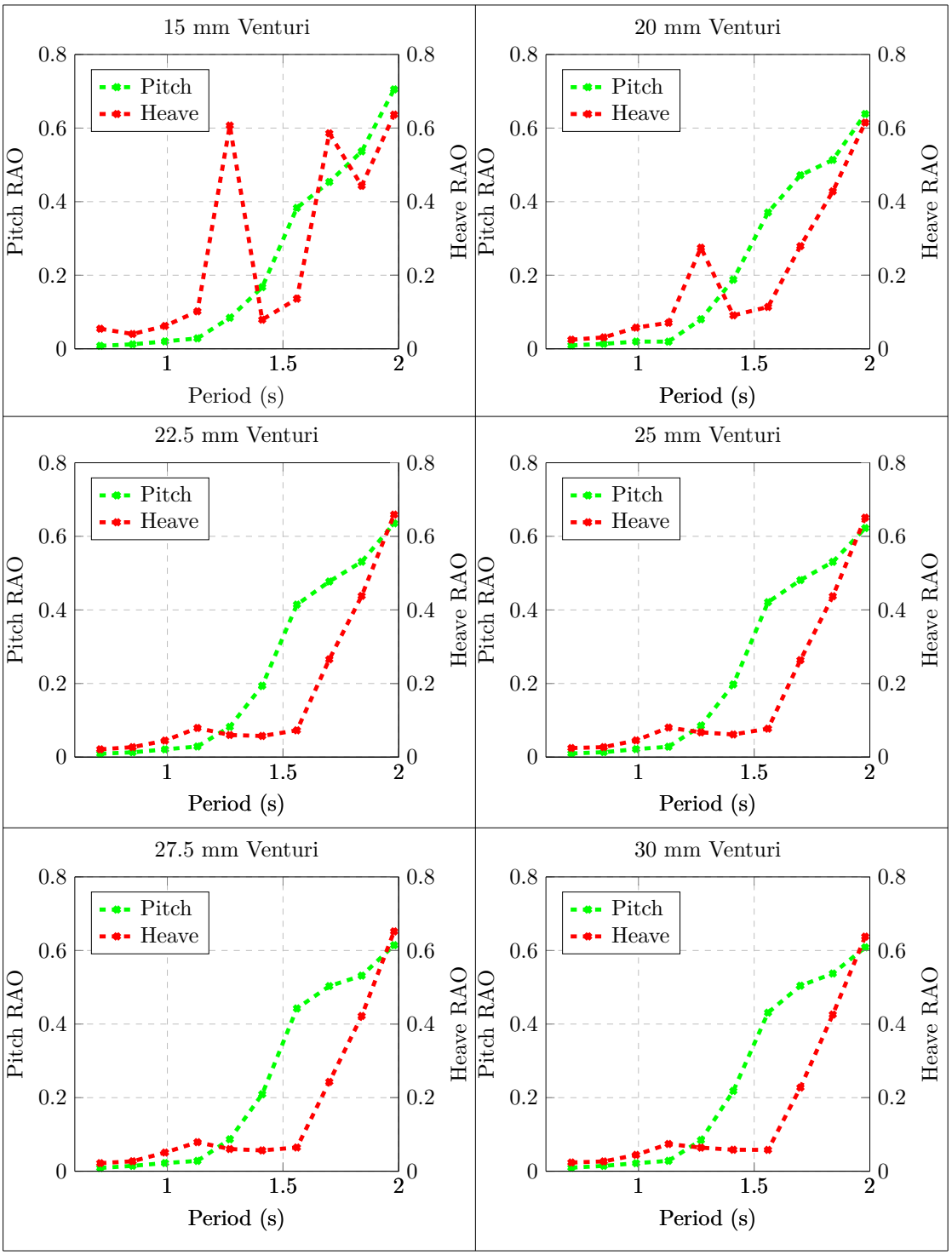

FIGURE 9.18: Heave and pitch RAOs for the 32-OWC model platform in Configuration 1 vs. incident wave period, illustrating the effect of varying Venturi diameter.

The results presented in Figures 9.13 to 9.18, for the model in Configuration 1, with various Venturi pairings installed, were also generated for the model in the remaining

four configurations (see Table 6.2) for Venturi pairings of diameters 20 mm, 25 mm, 27.5 mm and 30 mm. Comprehensive results for all model configurations and Venturi pairings may be found in [23]. As the 25 mm Venturi pairing was found to result in the greatest power absorption with the model in Configuration 1, the remaining frequency domain results, presented in Figures 9.19 to 9.24, illustrate the results obtained for the model in the remaining four configurations with the 25 mm Venturi pairings installed only. Note that the y-axis of the final plot in Figure 9.19 is to a different scale compared to the other four plots in the figure. When the low-pressure plenum is open to atmosphere, the gauge pressure in the low-pressure plenum remains at zero. Further, the pressure on the high-pressure plenum is approximately twice that when compared to the other four configurations. Similarly, the y-axis of the final plot in Figure 9.22 is to a different scale compared to the other four plots in the figure.

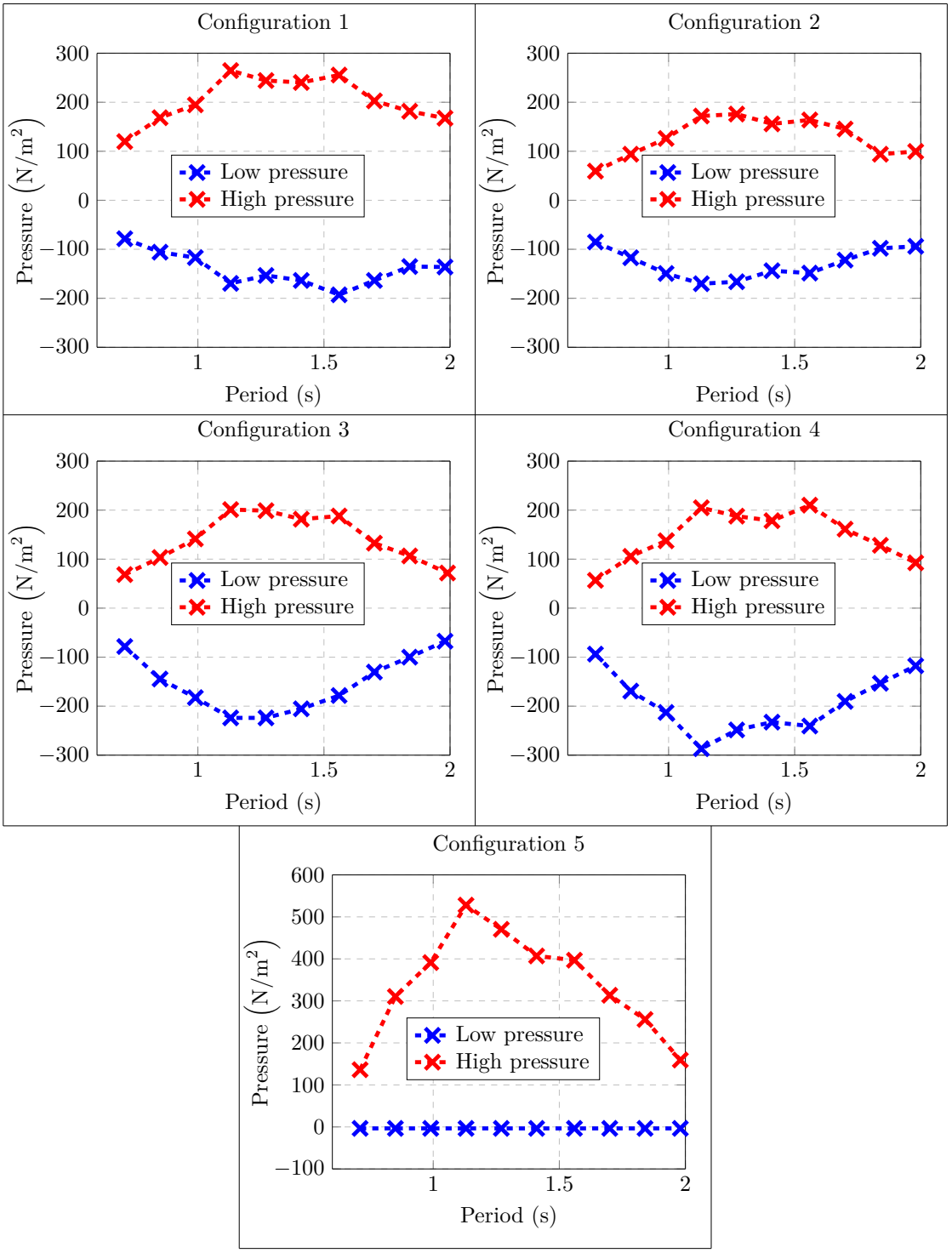

FIGURE 9.19: RMS of the gauge pressure either side of the Venturi with the 25 mm Venturi set installed vs. incident wave period for each model configuration listed in Table 6.2. Note: the y-axis of final plot is to a different scale compared to the remaining plots in this figure.

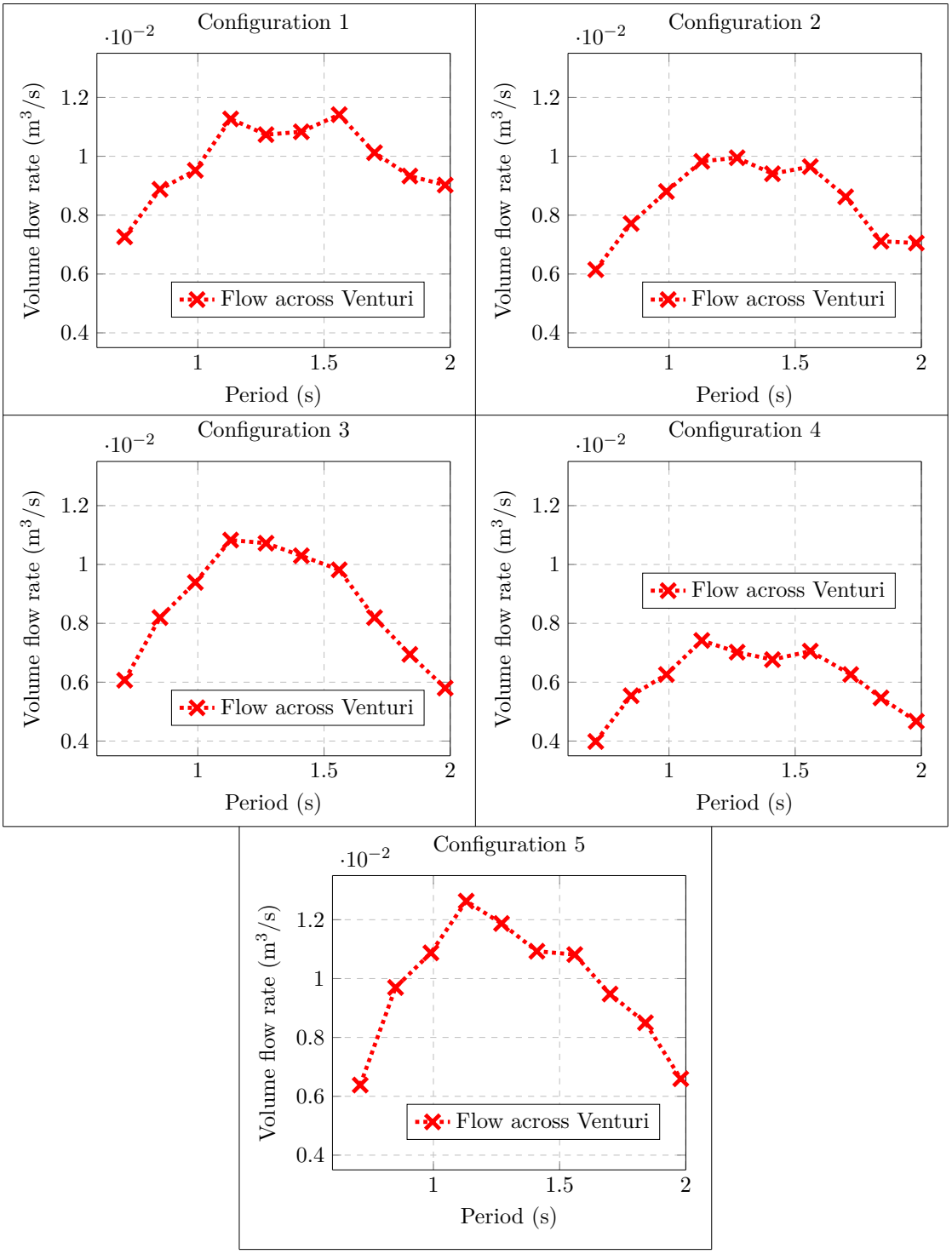

FIGURE 9.20: RMS of the volumetric airflow through the Venturi with the 25 mm Venturi set installed vs. incident wave period for each model configuration listed in Table 6.2.

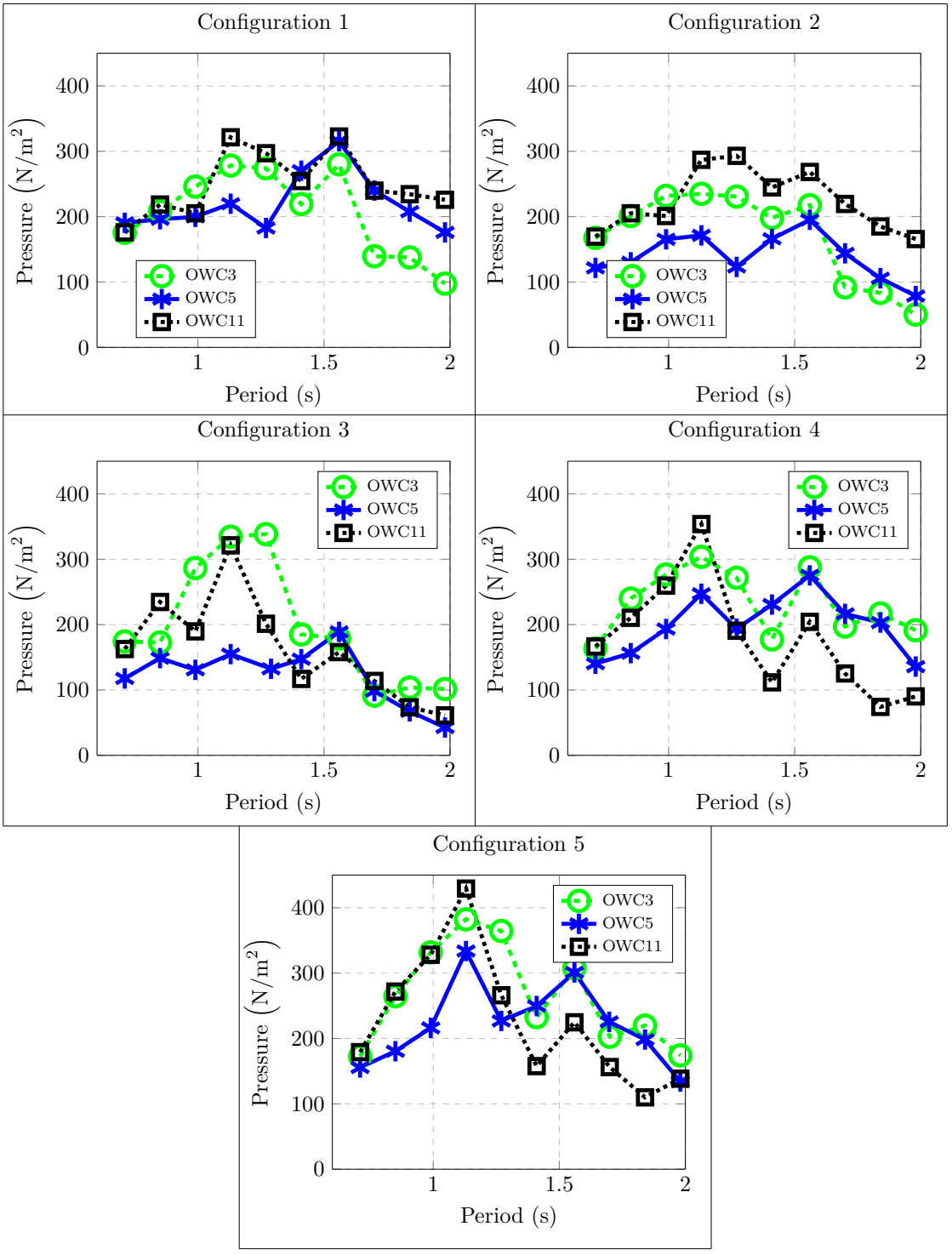

FIGURE 9.21: RMS of the gauge pressure within selected OWC chambers of the model with the 25 mm Venturi set installed vs. incident wave period for each model configuration listed in Table 6.2.

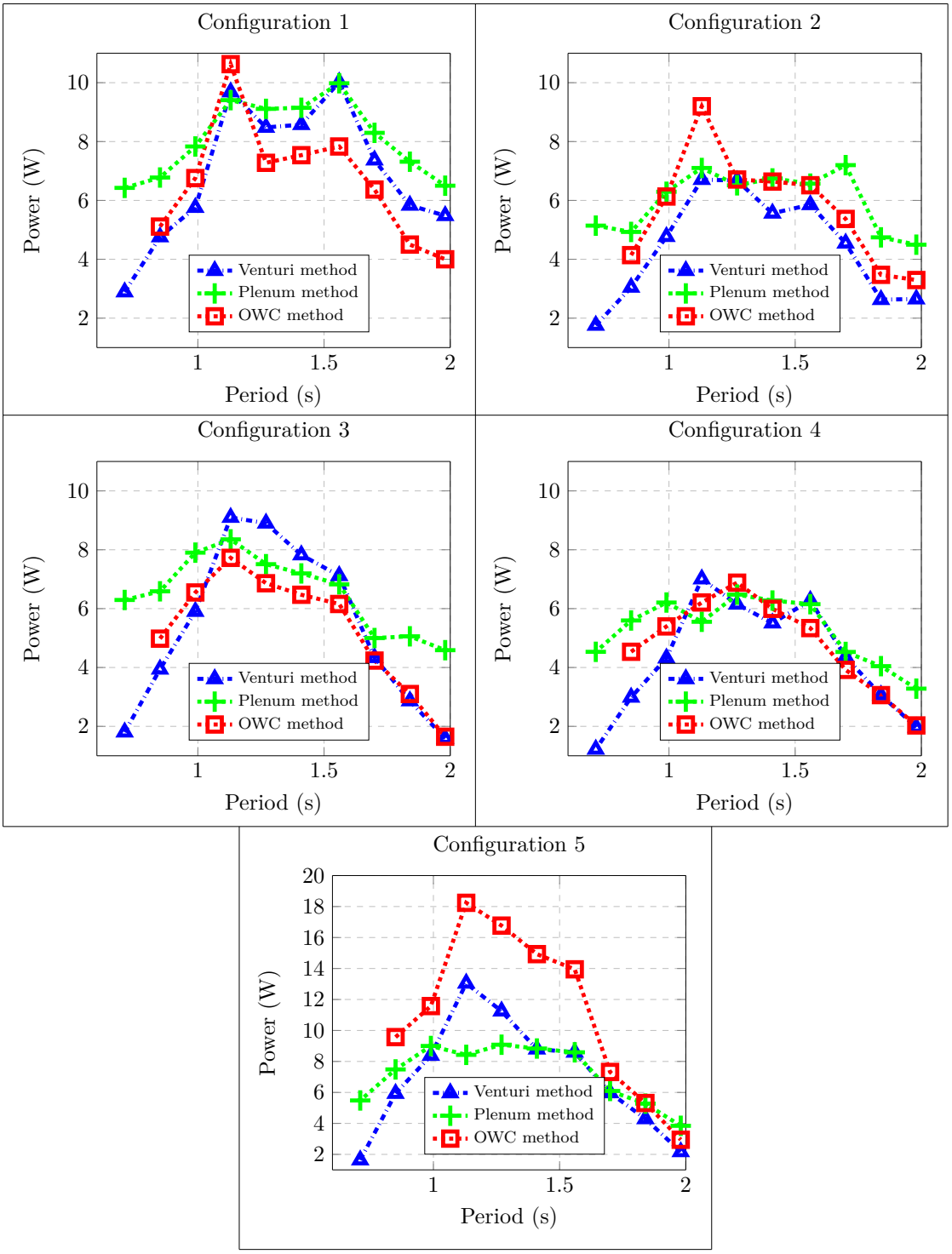

FIGURE 9.22: RMS of wave power absorbed by the model with the 25 mm Venturi set installed vs. incident wave period for each model configuration listed in Table 6.2. Note: the y-axis of final plot is to a different scale compared to the remaining plots in this figure.

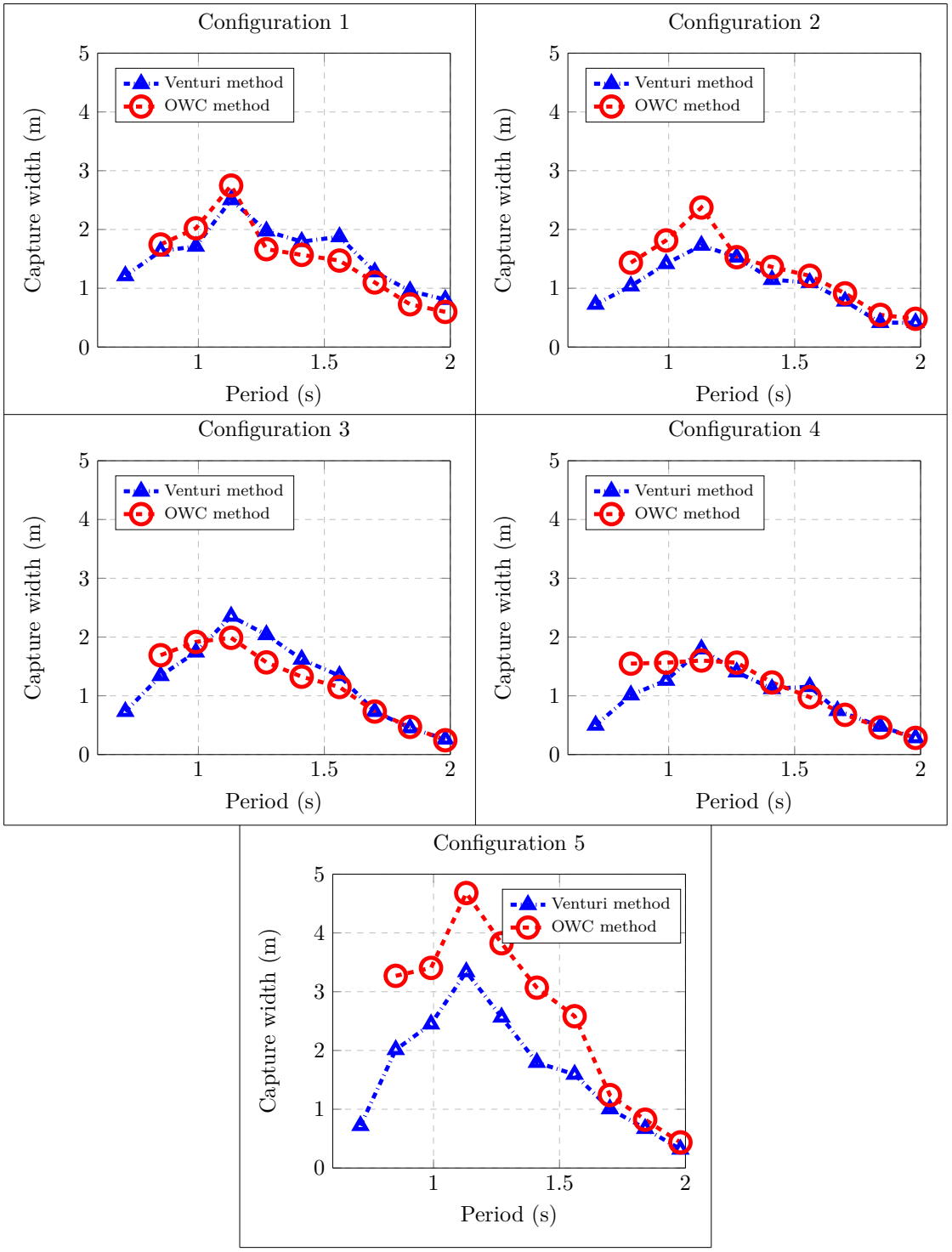

FIGURE 9.23: Capture width for the 32-OWC model with the 25 mm Venturi set installed vs. incident wave period for each model configuration listed in Table 6.2.

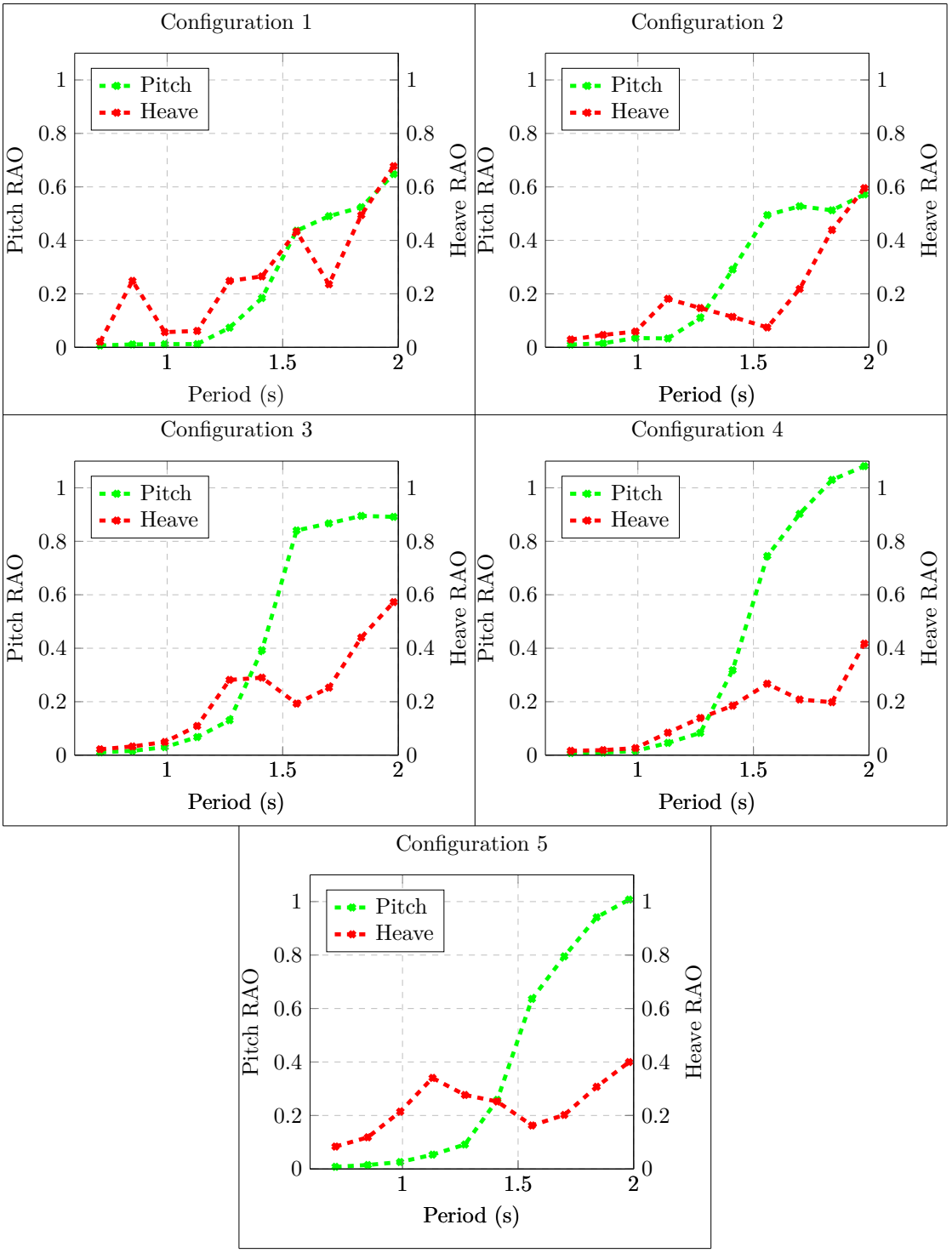

FIGURE 9.24: Heave and pitch RAOs for the 32-OWC model with the 25 mm Venturi set installed vs. incident wave period for each model configuration listed in Table 6.2.

The final set of power-related results, presented in Figure 9.25, illustrates the variation in the power absorbed by the model platform, as calculated using Equation (9.6), for each configuration and for each Venturi pairing tested versus wave period.

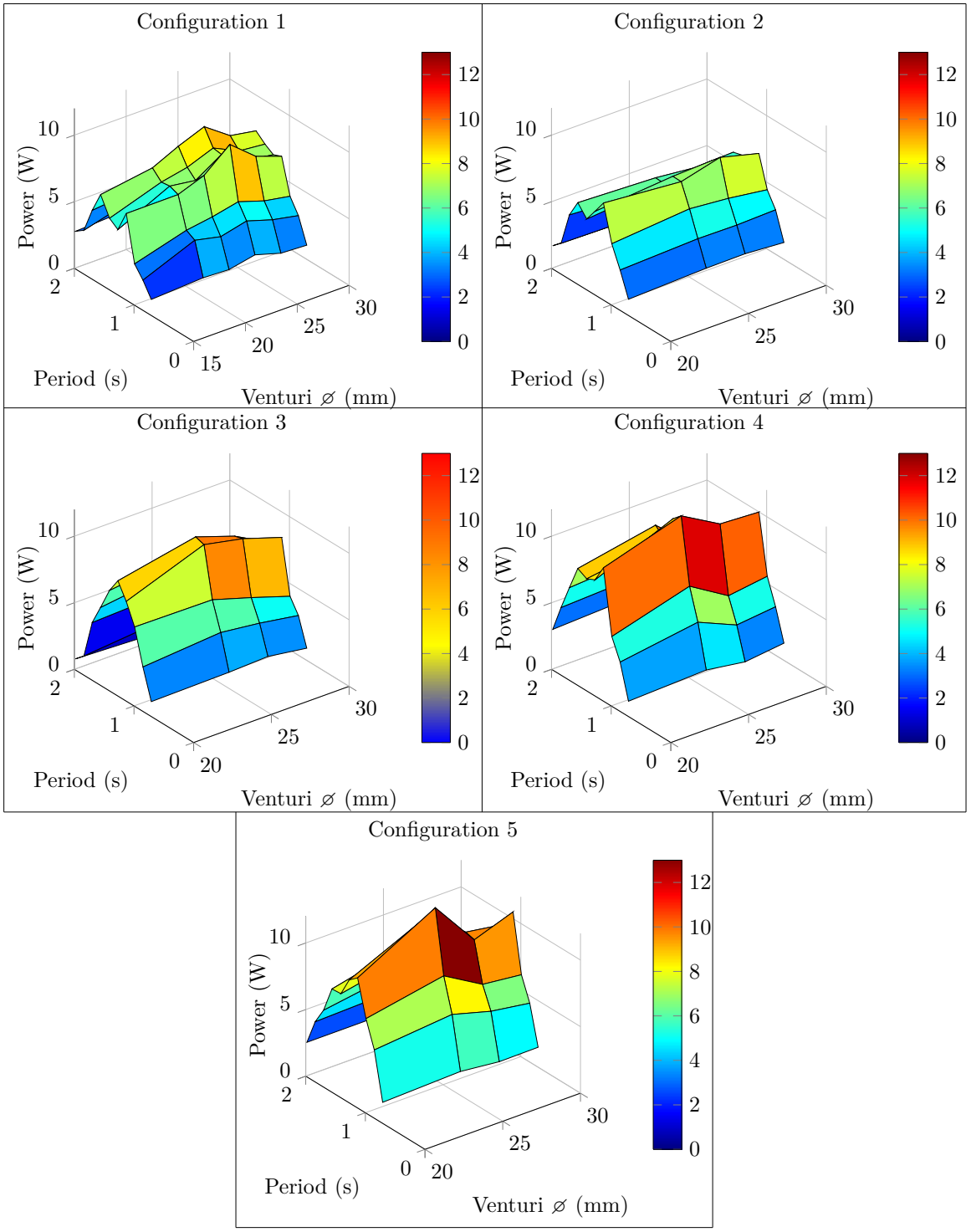

FIGURE 9.25: Variation in the power absorbed by the model platform for each model configuration listed in Table 6.2 and for each Venturi pairing tested vs. incident wave period.

9.2.1.4 Uncertainty in frequency domain results

In any measurement, a degree of uncertainty exists. Such uncertainty may arise from signal noise, instrument calibration, resolution errors environmental errors etc. [202]. In the current section, consideration is given to the precision uncertainty associated with the measurements used to generate the results presented in Section 9.2.1.3. As the same sensing and data acquisition equipment was used for all tests performed on the 32-OWC model platform, the degree of uncertainty in the results is consistent for the different model configurations and Venturi diameters. Hence, a representative set of figures,with the model set up as in Configuration 1, when the 27.5 mm Venturi pairing was installed, is used to illustrate the level of measurement uncertainty associated with:

- The pressure measured on one side of the Venturi on one leg of the model vs. incident wave frequency
- The volumetric flow rate of air through the Venturi on one leg of the model vs. incident wave frequency
- The power absorbed by the flow vs. incident wave frequency

Figure 9.26 illustrates the RMS of the gauge pressure on the high-pressure side of the Venturi vs. incident wave period. The results shown in Figure 9.26 are indentical to the corresponding results shown in Figure 9.13, but include error bars based on the standard deviation of the noise in the pressure sensor as obtained from the still water tests. Error propagation [222] has been used to convert the measurement error, in mmH_2O, to N/m^2.

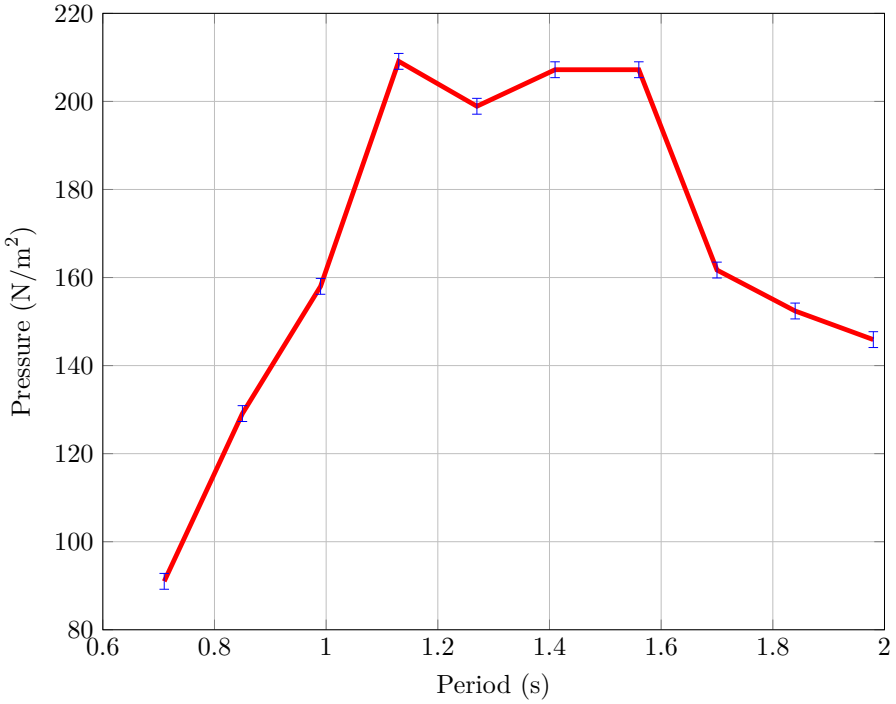

FIGURE 9.26: RMS of the gauge pressure on the high-pressure side of the Venturi vs. incident wave period, including error bars showing measurement uncertainty, for the model as in Configuration 1 with the 27.5 mm-diameter Venturi pairing installed.

Figure 9.27 shows the volumetric flow rate of air through the Venturi on one leg of the model vs. incident wave frequency. These values are calculated using Equation (9.5), and depends on the square root of the pressure difference across the Venturi, as well as the coefficient of discharge, and the cross-sectional area of, the Venturi. Using error propagation, the error bars take into account the uncertainty in the two pressure readings, the coefficient of discharge of the Venturi, and the measurement of the diameter of the throat of the Venturi.

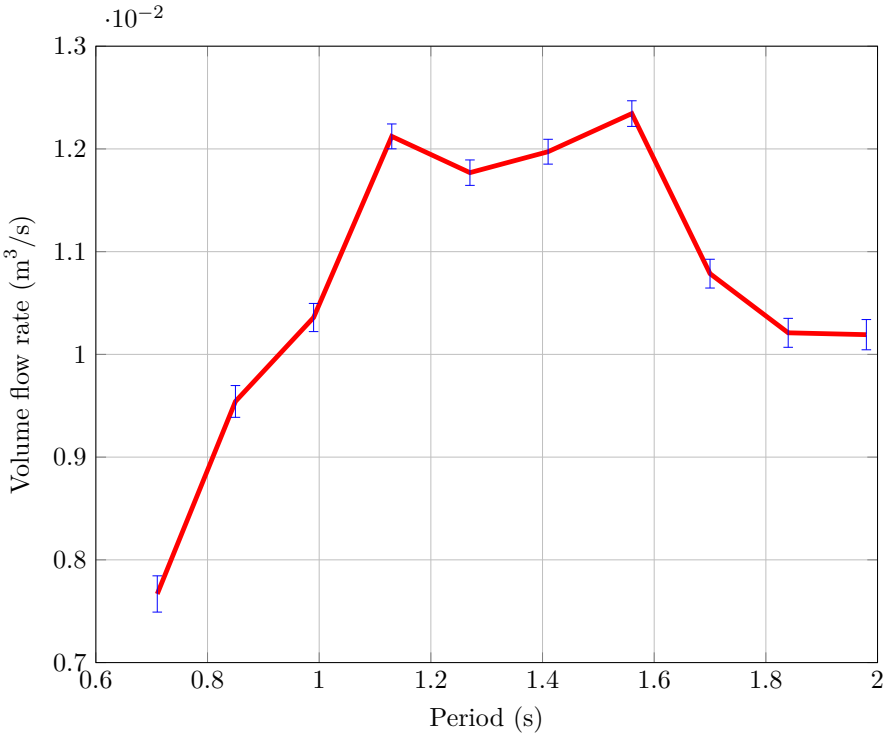

FIGURE 9.27: RMS of the volumetric airflow through Venturi vs. incident wave period, including error bars showing measurement uncertainty, for the model as in Configuration 1 with the 27.5 mm-diameter Venturi pairing installed.

The final plot in this section, Figure 9.28, illustrates the power absorbed by the model platform based on the Venturi method, based on Equation (9.6). Power is based on the volumetric flow rate of air through, and the pressure drop accross, the Venturi, and again error propagation is used to generate the error bars in Figure 9.28

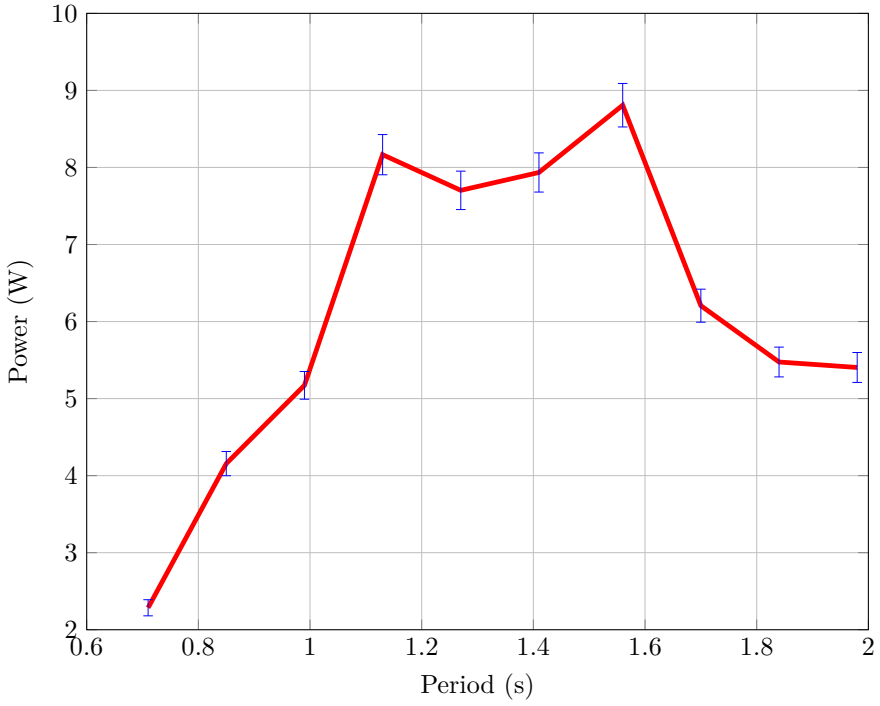

FIGURE 9.28: RMS of the wave power absorbed by the model using Equation (9.6) vs. incident wave period, including error bars showing measurement uncertainty, for the model as in Configuration 1 with the 27.5 mm-diameter Venturi pairing installed.

9.2.1.5 The effect of chamber broaching on platform motion

An issue that arose during the testing of the 32-OWC platform, which would particularly effect the results calculated for the heave RAO of the platform, was that of chamber broaching, as described in Section 9.2.1.1. In some monochromatic tests conducted, the draft of the model platform changed due to air entering what was intended to be a closed system, comprising the chamber OWCs and plenums, due to broaching of the OWC chambers. As a result, the mean vertical position of the platform changed during some test runs. The effect of broaching on the heave motion of the platform, subject to a wave period of 1.27 s, with the 25 mm Venturi pairing installed, with the model in Configuration 1, as described in Table 6.2, is illustrated in Figure 9.29.

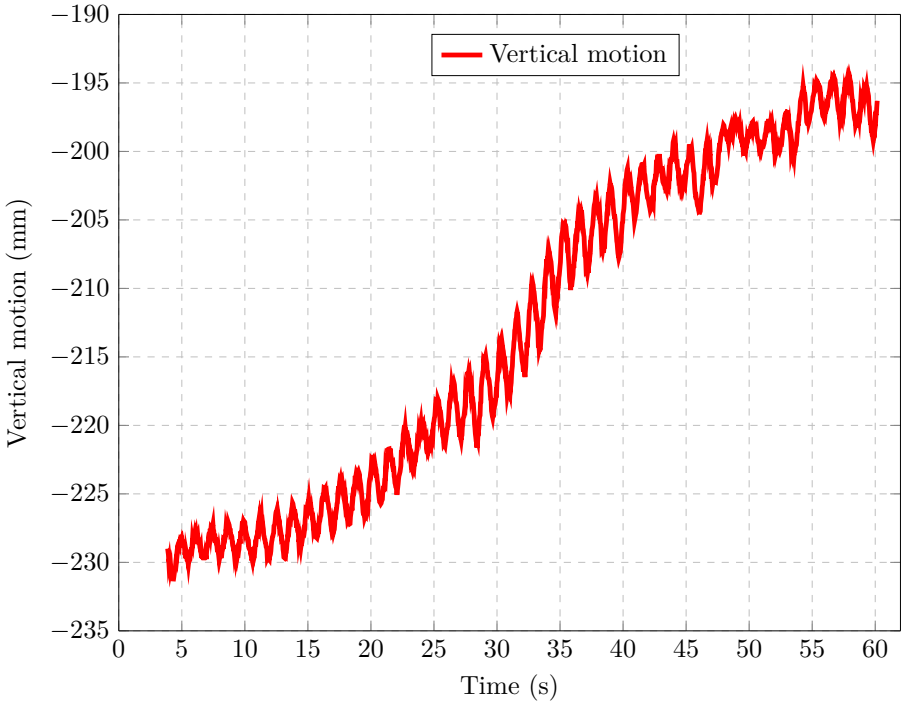

FIGURE 9.29: Time series of the vertical motion of the model platform, for a wave period of 1.27 s, with the 25 mm Venturi pairing installed, with the model in Configuration 1, illustrating the effect of chamber broaching.

The RMS of the time series shown in Figure 9.29 will not be the RMS of the heave oscillations of the platform alone, as the RMS will include the effect of the gradual increase in the platform vertical position due to broaching. When the vertical displacements of the platform were initially used to calculate heave RAOs, any potential non-zero offset, which existed in the measurement of the vertical position of the platform in stillwater conditions, was removed from the test results using data obtained during a stillwater run, which took place before any other tests were carried out. During the stillwater run, data for all sensors used was recorded in stillwater conditions. The mean stillwater value for each sensor is assumed to be the offset of that sensor, and the value is subtracted from the corresponding values for subsequent tests in a process known as 'zero-ing'. However, analysis of the time domain results of the vertical motion of the model platform revealed that the mean zero position of the platform changed during some tests due to the additional air entering the system during chamber broaching. Thus, direct application of the stillwater-based value for the stationary vertical position of the platform could not guarantee the removal of vertical offsets in the platform position. Therefore, without taking account of broaching, the results for the heave RAO of the platform

could not be considered valid. One method to take account of broaching is to 'zero' test data for the vertical platform displacement by using the mean vertical displacement of the model during each specific test run as the vertical offset for that test run, and subtracting the value of the mean vertical displacement from the test data for that test run. This approach was used to generate the results presented in Figures 9.18 and 9.24.

Using the mean vertical displacement of the platform to identify the vertical position of the platform in stillwater conditions is valid if the mean vertical position of the platform has changed between two tests, (and hence data from a stillwater test conducted before broaching occurred is no longer valid), but no broaching occurs during the particular test. However, if broaching does occur during the test, (and, again, the stillwater test is no longer valid), the calculated heave RAOs using the mean platform vertical displacement during that test, may still be incorrect.

However, it can be seen that the effect of the change in draft of the platform, due to broaching, occurs with a much lower frequency compared to the frequency of the incident wave, and hence the heave motion of the platform. Figure 9.30 illustrates the amplitude spectrum for the heave motion of the model platform shown in Figure 9.29, obtained through the Fourier transform. The large peak in this spectrum at 0.79 Hz (corresponding to a period of 1.27 s) occurs at the incident wave frequency.

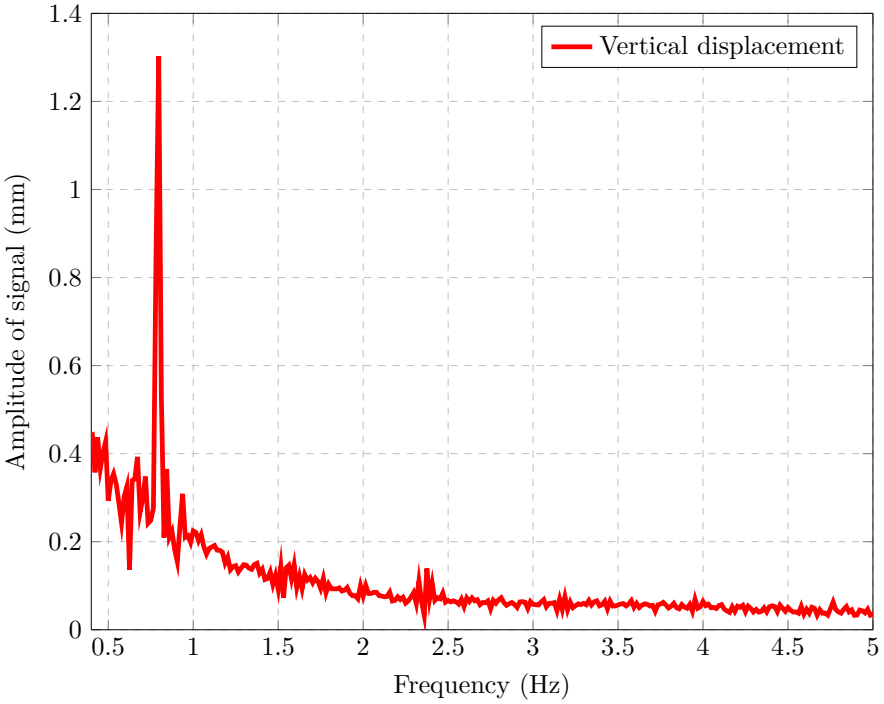

FIGURE 9.30: Single-sided Fourier transform of the heave motion of the model platform, with the 15 mm diameter Venturi set installed, in response to an incident wave of 1.27 s, illustrating the component of the platform motion at the incident wave period.

Figure 9.30 indicates that it should be possible to recover the relatively high-frequency heave motion of the platform, from the time series shown in Figure 9.29, by removing the effect of the relatively low-frequency change in platform draft. Another method that was investigated to extract the heave motion of the model at the incident wave frequency from the total vertical motion (which includes the effect of any broaching which may have occurred during a test), was to assume that the amplitude of the heave motion corresponds to the amplitude of the peak at the incident wave frequency in the amplitude spectrum of the vertical motion of the model platform. This approach has been implemented on the results for the vertical motion of the model platform, for the model in Configuration 1, as described in Table 6.2, with the 25 mm Venturi pairing installed, and the results are presented in Table 9.2. However, spectral leakage will influence the result obtained using this method. Using the magnitude of the amplitude spectrum at the frequency corresponding to the incident wave period appears to work well for certain incident wave periods, such as a wave period of 1.56 s, see Figure 9.31.

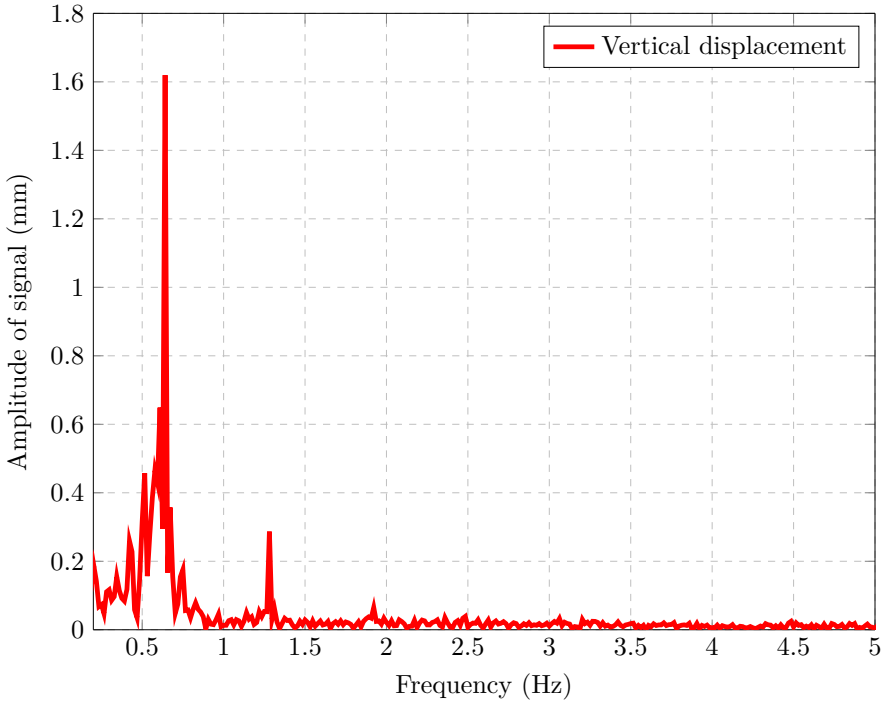

FIGURE 9.31: Single-sided Fourier transform of the heave motion of the model platform, with the 25 mm diameter Venturi set installed, with the model in Configuration 1, in response to an incident wave of 1.56 s, illustrating that the component of the platform motion at the incident wave period is dominant during the test.

However, for other periods with greater levels of reflections, such as a period of 0.71 s, the amplitude spectrum of the platform motion does not exhibit a clear peak at the corresponding frequency. Figure 9.32 illustrates the amplitude spectrum for the vertical motion of the platform for an incident wave period of 0.71 s, corresponding to a frequency of 1.41 Hz.

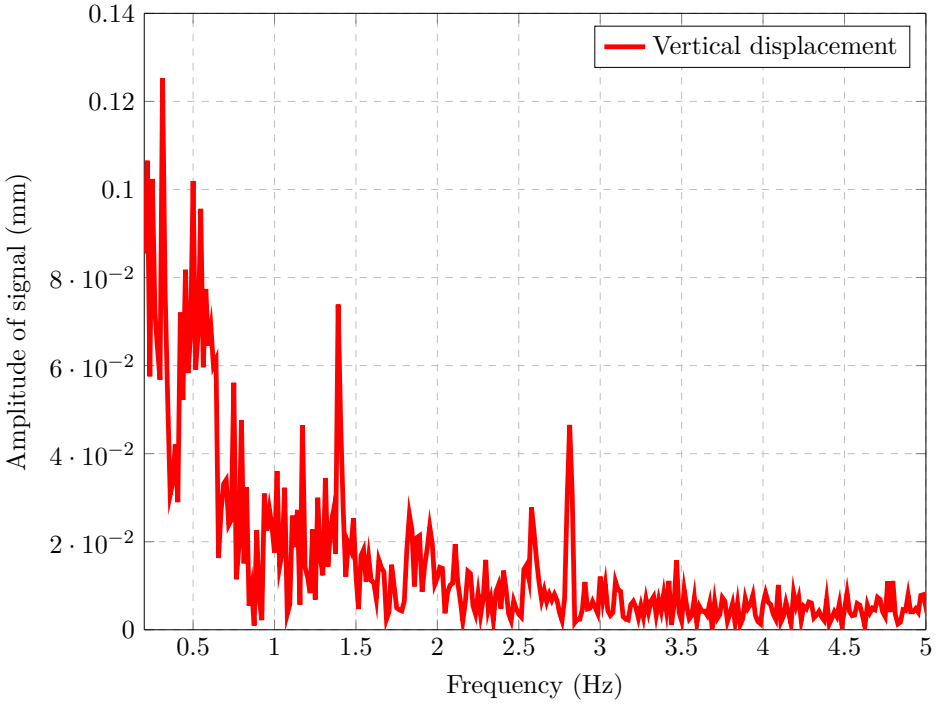

FIGURE 9.32: Single-sided Fourier transform of the heave motion of the model platform, with the 25 mm diameter Venturi set installed, with the model in Configuration 1, in response to an incident wave of 0.71 s, illustrating that the component of the platform motion at the incident wave period is not dominant during the test.

A final approach to recover the heave motion of the model platform from the total vertical motion was investigated. The approach relies on the fact that the heave motion of the model platform should have the same period as the incident wave, whereas vertical motion due to broaching or other issues will have a much longer period, as exemplified in Figure 9.29. By applying a band-pass filter, which allows periods around the region of the incident wave period to pass, but attenuates higher and lower period signals, the heave motion can, in principle, be isolated from the remaining vertical motion components (including any vertical motion due to broaching). A Butterworth band-pass filter has been applied to the vertical motion of the model platform, and the raw and filtered results are presented side by side in Figures 9.33 to 9.36, for the model in Configuration 1, with the 25 mm Venturi pairing installed. According to Butterworth [223]: "An ideal electrical filter should not only completely reject the unwanted frequencies but should also have uniform sensitivity for the wanted frequencies". Such a filter cannot be achieved [223], and all realisable filters exhibit some undesirable features. A number of filters exist in the literature, such as Chebyshev filters and Elliptic filters [224]. However, a Butterworth filter was used herein as, unlike the Chebyshev and Elliptic filters, a Butterworth filter is

designed to have a frequency response which is as flat as mathematically possible in the pass band frequency range. Other filters exhibit 'ripples' within the pass band, which would directly effect the amplitude of the signal output from the filter within the pass band, but may exhibit steeper roll-off characteristics either side of the pass band, which is a desirable feature. However, as the period of the component of the vertical motion of the model platform to be attenuated from the time series is an order of magnitude greater than the period of the heave motion of the model, the roll-off steepness is not critical in the current application. Thus, the relatively shallow roll-off characteristics of a Butterworth filter are not problematic in the current scenario. A first order Butterworth band-pass filter has been applied to the results for the vertical motion of the model in Configuration 1, with the 25 mm Venturi pairing installed, for all tested incident wave periods, and the heave RAO results are tabulated in Table 9.2. Care must be taken with the selection of the upper and lower band-pass limits. If the low-frequency pass limit is too low, the large period vertical motion component due to broaching is allowed to pass through the filter. Similarly, if the high-frequency pass limit is too high, high-frequency noise is allowed to pass.

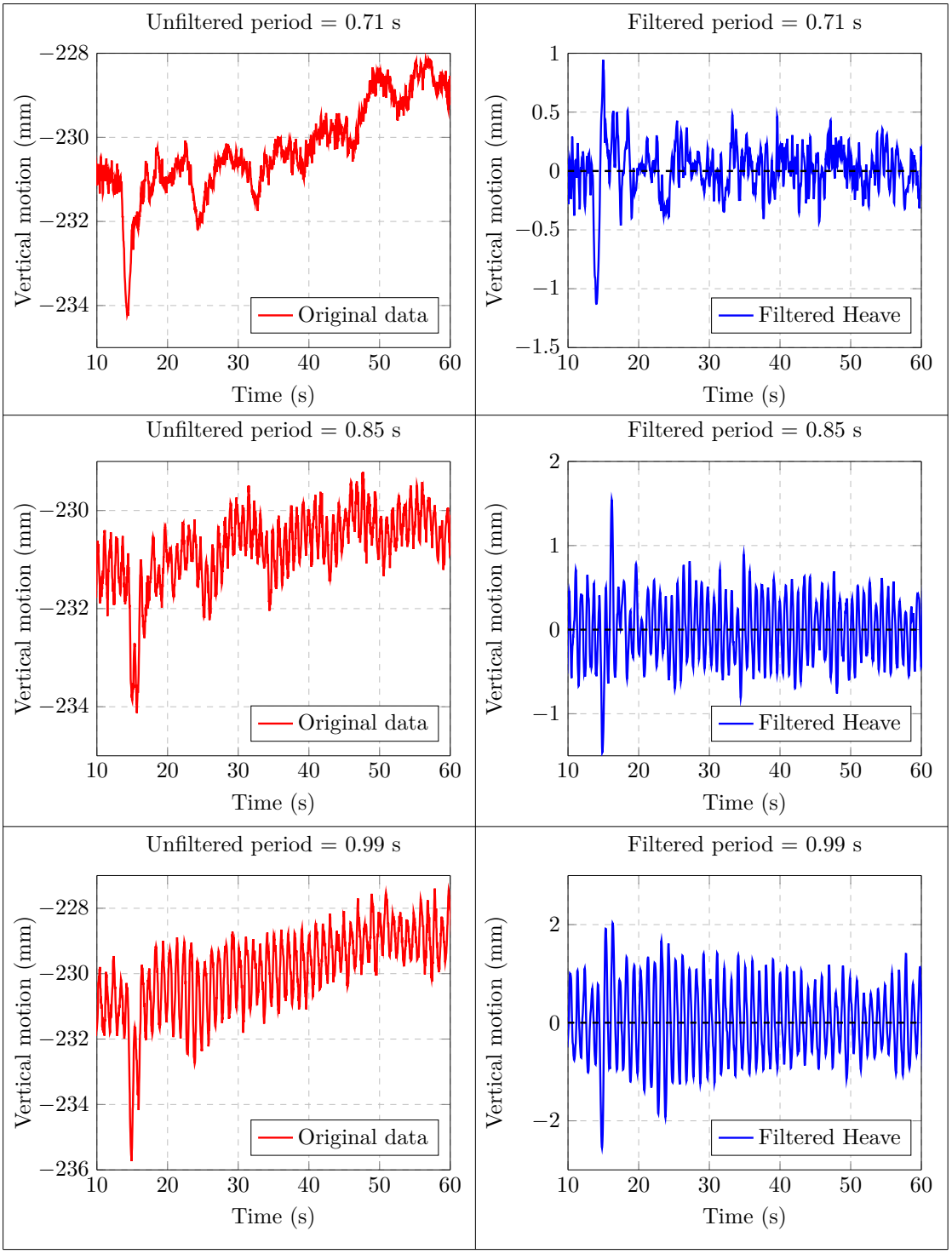

FIGURE 9.33: Vertical motion of the model platform in Configuration 1, with the 25 mm Venturi pairing installed, before and after a first order Butterworth filter is applied to the data, for incident wave periods of 0.71 s, 0.85 s and 0.99 s.

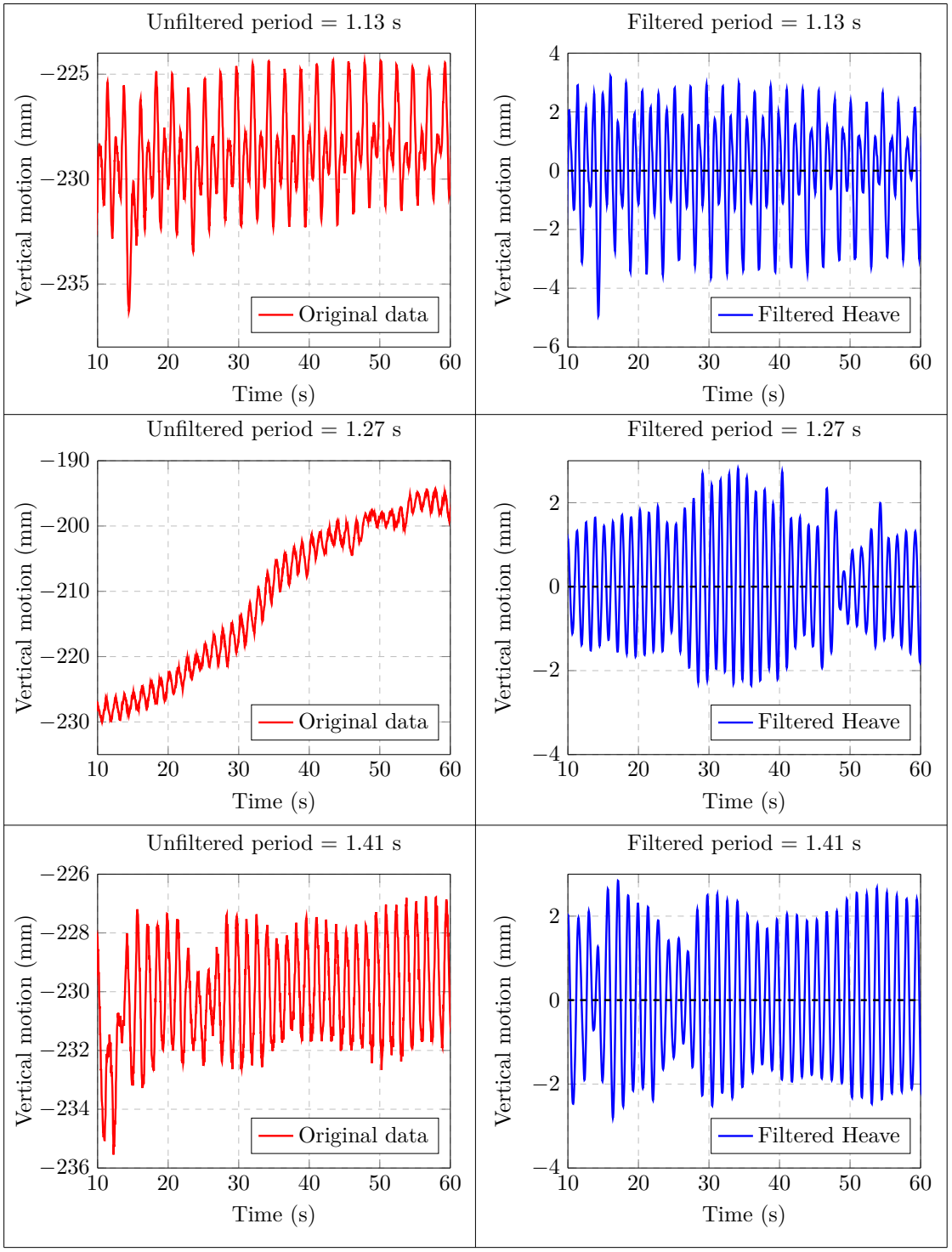

FIGURE 9.34: Vertical motion of the model platform in Configuration 1, with the 25 mm Venturi pairing installed, before and after a first order Butterworth filter is applied to the data, for incident wave periods of 1.13 s, 1.27 s and 1.41 s.

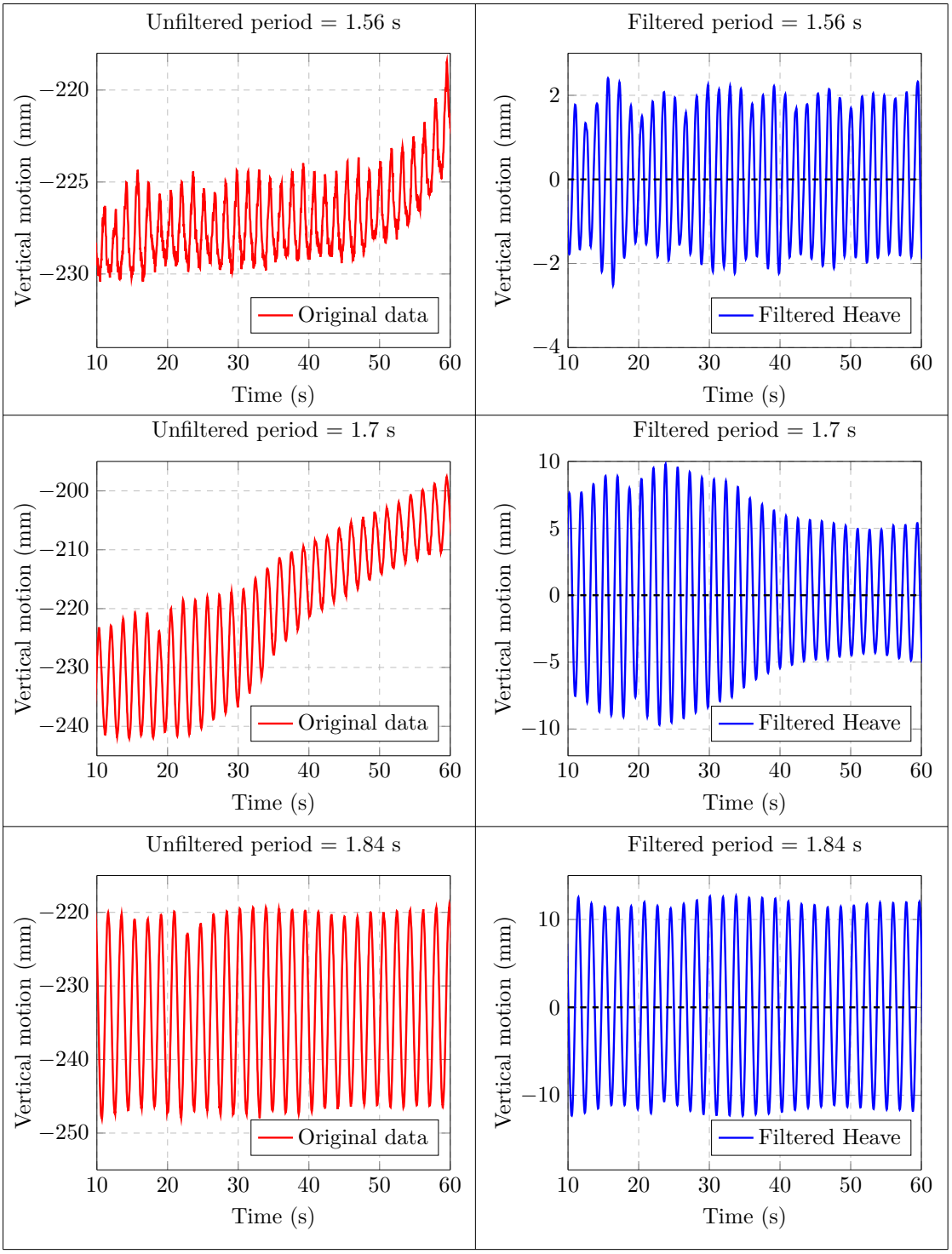

FIGURE 9.35: Vertical motion of the model platform in Configuration 1, with the 25 mm Venturi pairing installed, before and after a first order Butterworth filter is applied to the data, for incident wave periods of 1.56 s, 1.7 s and 1.84 s.

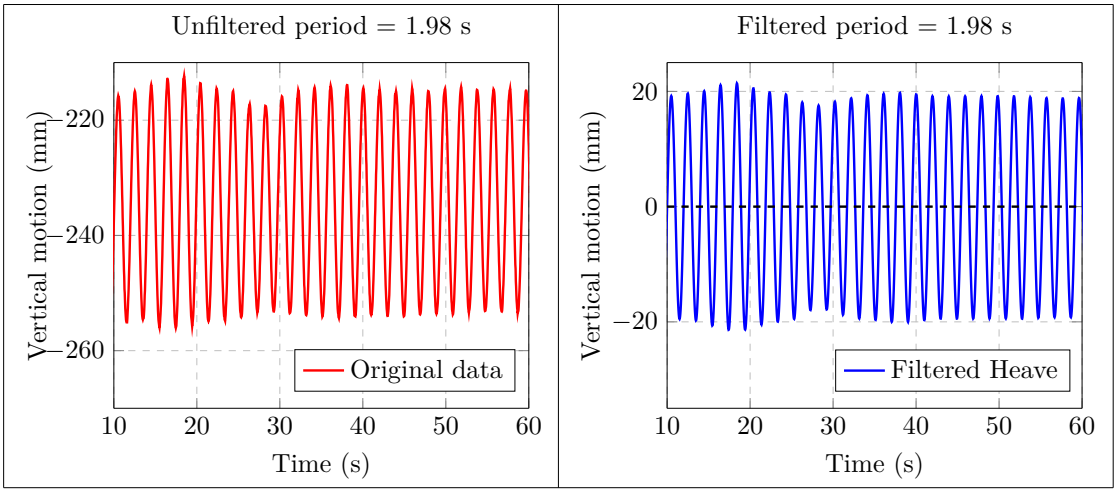

FIGURE 9.36: Vertical motion of the model platform in Configuration 1, with the 25 mm Venturi pairing installed, before and after a first order Butterworth filter is applied to the data, for incident wave periods of 1.98 s.

Table 9.2 presents the estimated RAOs for the heave motion of the platform as calculated by each method summarised below:

- Method 1: RAO estimated using the stillwater file to 'zero' the vertical displacement time series data
- Method 2: RAO estimated using the mean vertical displacement value to 'zero' the vertical displacement time series data
- Method 3: RAO estimated from amplitude spectrum of the vertical displacement time series data
- Method 4: RAO estimated using a band-pass Butterworth filter to isolate vertical displacement occurring at the incident wave period.

Method / Period (s)	RAO Method 1	RAO Method 2	RAO Method 3	RAO Method 4
1.98	0.6311	0.6366	0.4512	0.6108
1.84	0.4590	0.4432	0.3056	0.4230
1.70	0.9030	0.5858	0.1932	0.2499
1.56	0.4305	0.1361	0.0665	0.0647
1.41	0.2661	0.0791	0.0547	0.0658
1.27	1.2058	0.6069	0.0434	0.0542
1.13	0.3352	0.1019	0.0674	0.0752
0.99	0.2608	0.0621	0.0263	0.0332
0.85	0.2315	0.0403	0.0148	0.0171
0.71	0.2698	0.0545	0.0036	0.0288

TABLE 9.2: RAOs of the heave motion of the model platform in Configuration 1 with the 25 mm Venturi pairing installed as calculated using Methods 1 to 4.

Figure 9.37 illustrates the results in Table 9.2 in graph form. In this plot, it can be seen that the RAOs found using the stillwater runs to remove a vertical offset, and the RAOs found using the mean vertical motion to remove the vertical offset match in form, both showing peaks at wave periods of 1.27 s and 1.7 s. As can be seen from Figures 9.33 and 9.34, these wave periods are those where the change in model draft due to broaching was most significant, and zero-ing the vertical motion data by either technique will not eliminate this effect. The remaining methods show broad agreement in both trend and magnitude, with the RAOs estimated using the Fourier transform-based method having the smallest magnitude, possibly due to spectral leakage. By removing the low-frequency vertical movement of the model platform due to chamber broaching, while at the same time resulting in minimal attenuation of higher frequency heave motion of the platform, Method 4 should provide the most accurate means by which the heave RAO can be determined from the data recorded, provided the low-frequency vertical movement occurs at a much lower frequency than the incident wave frequency, as was the case during the testing on the 32-OWC physical scale model.

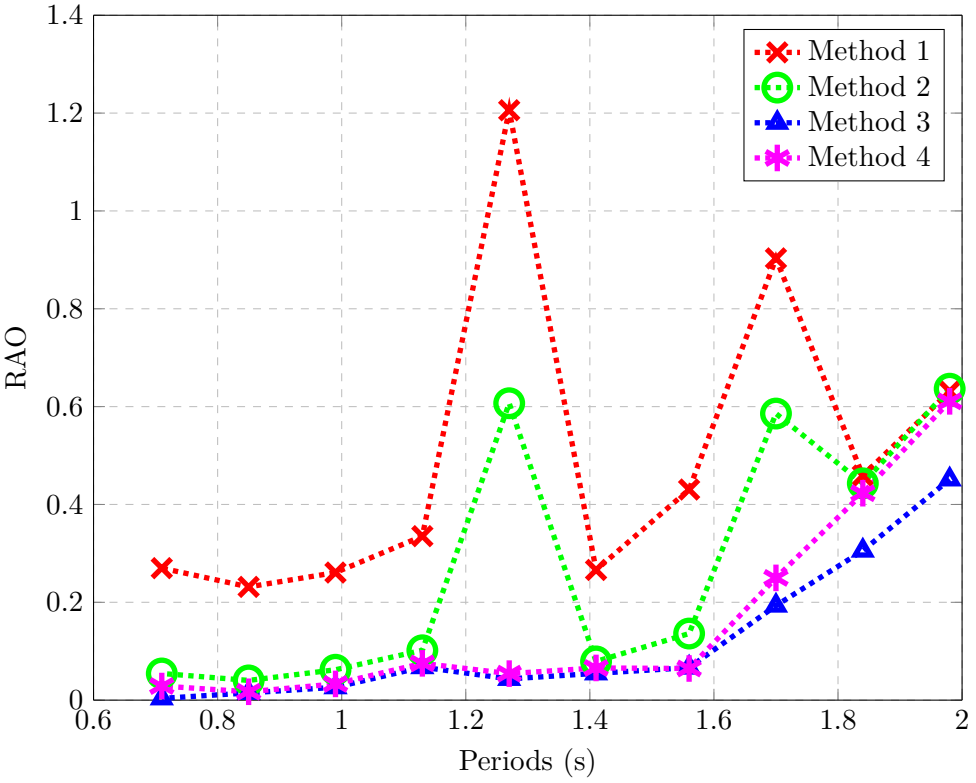

FIGURE 9.37: Graph of the RAOs of the heave motion of the model platform in Configuration 1, with the 25 mm Venturi pairing installed, as calculated using Methods 1 to 4.

Two further issues arise when considering the heave RAO of the platform, namely, reflections from the side walls of the tank and snatch loads from the mooring chain. With regard to reflections, the beach was effective at removing any waves which passed the model or were radiated by the model towards the rear of the basin and the force feedback system used to control the wave makers was effective in cancelling waves reflected or radiated by the model towards the wave makers, [225]. However, waves which radiated from the model towards the side walls of the basin were not absorbed or cancelled, and would have reflected from the side walls and interacted with the model during the tests. The second issue relates to the effect of the mooring chain, which would reach full extension under certain wave and damping conditions, causing highly non-linear, snatch loads which impacted the motion of the platform in a manner that cannot be captured by an RAO in the frequency domain. Figure 9.38, which shows the vertical motion of the platform in response to a 1.13 s incident wave period, illustrates the effect on the model platform displacement of the non-linear forces due to the mooring.

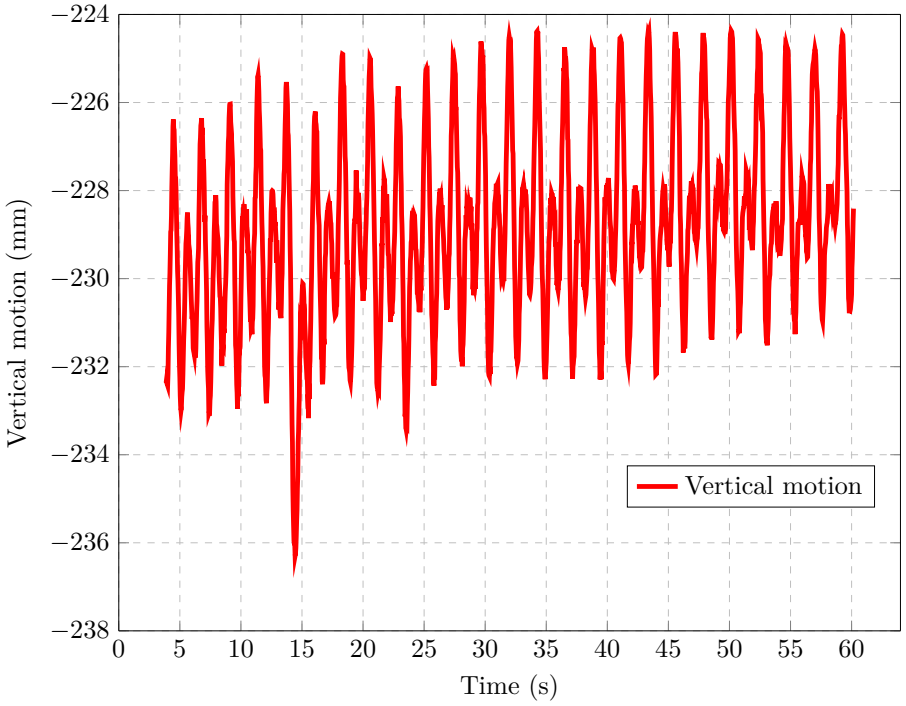

FIGURE 9.38: Time series of the vertical motion of the model platform, for a wave period of 1.13 s, with the 25 mm Venturi pairing installed, illustrating the effect on the model platform displacement of the non-linear forces due to the mooring.

9.2.1.6 Discussion of frequency domain results

In this section, the frequency domain results from the tank testing of the physical model of the 32-OWC platform, for the model in each configuration described in Table 6.2, are discussed.

Configuration 1

Consider first the results for the model in Configuration 1. Figure 9.14 illustrates the variation in pressure on either side of the Venturi, for all Venturi diameters used in testing the model in the first configuration. The power absorbed by the model is related to the pressure drop across the Venturi, as given in Equation (9.6), and Figure 9.13 illustrates a relatively smooth pressure drop for all wave periods tested. The highest value of the high-pressure side of the Venturi and the lowest point of the low-pressure side occur at the same periods for most Venturi diameters tested. Equation (9.7) shows that the power absorbed by the model is also dependent on the volumetric airflow through the Venturi, when using the Venturi method to estimate the power absorbed. Figure 9.14

presents the airflow across the Venturi as calculated by the pressure difference across the Venturi, as given in Equation (9.5). The volumetric airflow through a Venturi increases as the Venturi diameter increases. Two peaks in the RMS value of the airflow with respect to wave period can be seen for all Venturi diameters, occurring at wave periods of 1.13 s and 1.56 s. Figure 9.16, which shows the power absorbed by the model for each Venturi pairing, illustrates that the 25 mm Venturi pairing absorbed the most power, while the 22.5 mm and 27.5 mm pairings also absorbed relatively large amounts of power when compared to the remaining Venturi pairings tested.

Figure 9.18 presents the heave and pitch RAOs of the model platform versus wave period for each Venturi pairing in Configuration 1. The heave motion shows a peak at an incident wave period of 1.27 s for low Venturi diameters, which might suggest that there is an air spring effect at these diameters. The peak in the heave RAO disappears from 22.5 mm onwards, and the maximum heave response is pushed out to higher wave periods. Although not shown here, this effect occurs for the model in all configurations listed in Table 6.2. The maximum pitch response, which occurs for wave periods of 2 s or greater for the low Venturi diameters, moves to 1.6 s as the Venturi diameter increases, and is remarkably consistent in its qualitative behaviour for all higher Venturi diameters. Figure 9.15 illustrates the RMS of the variation in the gauge pressure in the air above the water column for selected OWC chambers, namely Chambers 3, 5 and 11 as shown in Figure 6.1. The variation in the RMS of the gauge pressure with respect to incident wave period for each chamber is consistent for all Venturi diameters. With respect to variations in the Venturi diameter, the pressures tend to increase up to the 25 mm Venturi diameter and fall off thereafter, reflecting the fall off in damping as the Venturi diameter increases from 25 mm to 27.5 mm and 30 mm. Furthermore, the maximum pressure occurs at periods of 1.13 s and 1.27 s, as might be expected, as the maximum airflow across the Venturi also occurs at these periods (see Figure 9.14). Figure 9.16, which illustrates the power absorbed by the model estimated, using three methods, namely, the Venturi method with Equation (9.6), the method based on water column velocity using Equation (9.8) and the method where the air admittance valves are modelled as orifices, shows reasonably good agreement across all Venturi diameters between the power estimated using Equation (9.6) (based on the airflow through the Venturi), and the power estimated using Equation (9.8), (based on the velocity of the water columns), which gives confidence in the results obtained. It should be noted that the estimation method based on Equation (9.8) requires summing over 16 chambers

with 16 wave probes and 16 pressure transducer readings, compared to the Venturi method which is based on two pressure transducer readings and Venturi flow theory. The agreement between the estimates for the power absorbed using the plenum method, based on Equation (9.10), and the estimates for the power absorbed using the above two methods, is poorer. However, the order and trend of the estimated power absorbed obtained using the plenum method match the order and trend of the estimated power absorbed obtained using the previous methods. The estimated power absorbed based on Equation (9.6) is considered the most accurate as it relies on the fewest measurements and least assumptions, and was adopted as the primary method to estimate the power absorbed. The other two methods used to estimate the power are, nevertheless, useful to provide a double check on the primary method. In order to visually represent the effect on the power absorbed, as both the Venturi diameter and the incident wave period vary, Figure 9.25 illustrates surface plots which show the variation in absorbed power for the model in each configuration with respect to Venturi diameter and incident wave period. As can be seen in Figure 9.25, for monochromatic incident waves with the model in Configuration 1, the maximum power was absorbed using a Venturi diameter of 25 mm. Two peaks in the power absorbed of roughly equal magnitude exist for this Venturi diameter at wave periods of 1.13 s and 1.56 s, equivalent to wave periods of 8 s and 11 s at full scale. This Venturi diameter also resulted in the best capture period bandwidth characteristics. While the 25 mm diameter Venturi pairing has resulted in the maximum power absorption for a wave amplitude of 30 mm, it is possible that for different wave amplitudes, different Venturi diameters would result in the optimum power absorption, and further tank testing would be required to establish the optimum diameter for each different wave amplitude.

Other configurations

As the Venturi diameter and incident wave periods change, the results for the physical model for the remaining configurations described in Table 6.2 largely follow the trends for the model in Configuration 1, as described in the previous section. The current section thus describes only the differences between the results obtained for the model in Configuration 1 and the remaining configurations. Figure 9.24 illustrates the RAOs in heave and pitch of the model platform versus wave period for each configuration with the 25 mm diameter Venturi pairing installed in each case. The removal of the heave damping plates and buoyancy tubes between Configuration 1 and Configuration

2 resulted in a surprisingly slight decrease in the heave RAO, while the pitch RAO increased somewhat, which is more in line with expectations. In fact, the removal of the wave guide shoes between Configurations 2 and 3 had a greater effect on the heave RAO, which increased noticeably, particularly at shorter wave periods, suggesting that, at shorter wave periods, the added mass due to the shoes was more significant than the added mass due to the damping plates. It should be noted that the motion of the model platform was significantly effected by the presence of the mooring chain. Under certain wave conditions, the mooring chain would reach full extension and restrain further motion of the model platform. The restraining effect was more pronounced at higher wave periods, where the model platform pitching response is greater. The additional damping plates which are added to the model platform between Configurations 3 and 4, and which were significantly larger than the original plates, have the effect of reducing the heave response, at the cost of some increase in the pitching motion. Removing the effect of the low-pressure plenum, by removing the lid of the plenum, has a very slight decreasing effect on the pitch RAO, while the heave RAO increases for lower periods. The trend of the RMS pressure within the selected OWC chambers with respect to varying incident wave periods is consistent for all configurations and Venturi diameters, with peak pressures occurring at wave periods of 1.17 s and 1.6 s in virtually all cases. However, some variation in the peak pressure values occurs. Figure 9.22 shows the power absorbed by each model configuration with the 25 mm diameter Venturi pairing installed. For all configurations, except Configuration 4, the 25 mm diameter Venturi pairing resulted in the maximum wave power absorbed by the model platform based on Equation (9.6). For Configuration 4, the 27.5 mm diameter Venturi pairing resulted in the highest absorbed power. For all configurations, except Configuration 4, the model absorbs most power in the range of periods from 0.99 s to 1.56 s, typically exhibiting two peaks at 1.13 s and 1.56 s. In Configuration 4, the highest absorbed power occurs over a slightly broader range of periods, from 0.99 s to 1.7 s. Of Configurations 1 to 4, Configuration 1 absorbs the most power, although the power absorbed in Configuration 3 is quite similar. Of all the configurations, Configuration 5 absorbs the greatest power, which would tend to confirm the observation that the current design is over-damped, (see Section 9.2.2). Both the power and the capture width plots for the model platform, as set up in Configuration 5 (Figures 9.22 and 9.23), show large discrepancies between the results obtained using the airflow-through-the-Venturi method, (Equation

(9.6)), and the results obtained using the velocity-of-the-water-column method (Equation (9.8)). When set up as in Configuration 5, the device is only absorbing power on the discharge side. The suction valves do not contribute to the absorbed power. The power and capture width plots for Configuration 5, however, use the same velocity-of-the-water-column method as was used for the earlier configurations. As such, the OWC method shows the total power in each oscillating water column as in discharge or suction mode. Only the discharge element of this power is reflected in the Venturi method calculation. This explains the large discrepancies between the results obtained using the two methods for this configuration. As illustrated in Figure 9.13, the gauge pressure in the low-pressure plenum is zero through testing of Configuration 5, as the plenum is now open to atmosphere. A word of caution is required, however. As can be seen in Section 9.2.1.5, the platform responses can be quite non-linear, notably at shorter wave periods, so the results of frequency domain analysis must be taken with care.

9.2.2 Comparison between results from tank testing and numerical predictions for the 32-OWC model

In this section, the predictions for the motions of the model platform and the OWCs, and the predicted power absorbed by the model platform obtained from the numerical model of the platform described in Chapter 4, are compared to the equivalent results obtained from the tank testing of the physical model described in Chapter 6. The model platform was numerically modelled as set up in Configuration 3 described in Table 6.2, with the 25 mm Venturi pairing installed. The required hydrodynamic parameters described in Equation (4.9) are found using the BEM solver WAMIT, in conjunction with the CAD package MultiSurf, and the mass matrix is populated using the CAD package AutoCAD. However, the power take-off matrix, D, described in Equation (4.17) must be populated, and the required entries are obtained from the implementation of Equation (4.21) using data obtained from the tank tests. Figure 9.39 illustrates the time-averaged applied damping for each chamber of the model in Configuration 3.

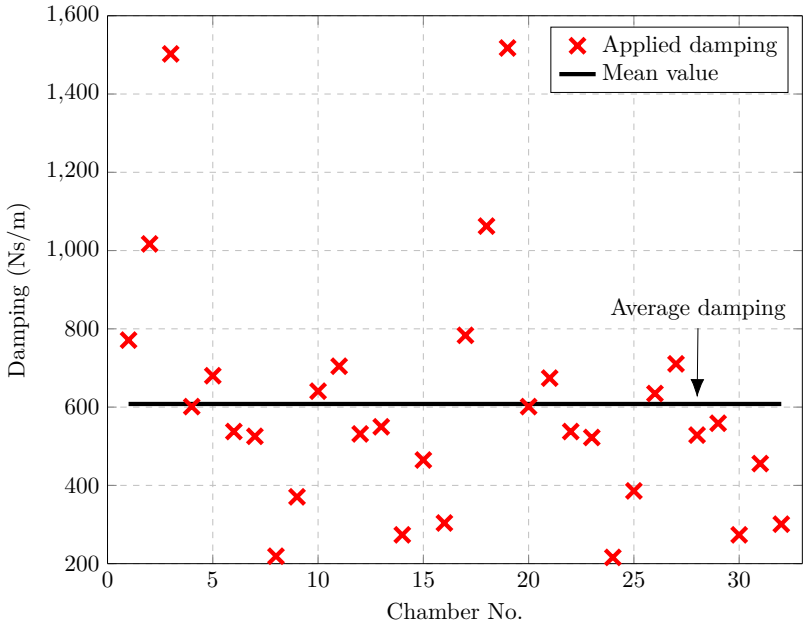

FIGURE 9.39: Time-averaged experimental applied damping determined from Equation (4.21), with the platform model in Configuration 3 and the 25 mm Venturi pairing installed.

The average damping value is 608 Ns/m, and this value is used for d_i in Equation (4.17). There is, however, some variation in damping levels about the average value, and there are very large values associated with some chambers. This would suggest that chambers with high damping levels are virtually permanently locked, since the airflow is low. By comparison, the LIMPET plant, operating at full scale, has a damping value of 1,608,768 Ns/m, as measured by Wavegen [175]. By following the guidelines for Froude scaling outlined in [199], this leads to a value of 91 Ns/m at a scale of 1:50. While any comparison between the LIMPET and the WEI platform must be treated with caution as the water column geometries, orientation and mode of excitation differ between the two devices, the significantly higher damping levels apparent in the WEI model suggests that the model platform may be over-damped. This assertion, it will be shown, is supported by the results of the numerical model of the model platform. Figures 9.40 and 9.41 illustrate the predicted RAOs for the pumping mode of the OWCs versus wave period for OWCs 1 to 16 as shown in Figure 6.1, comparing the results obtained during the testing with those from the numerical model.

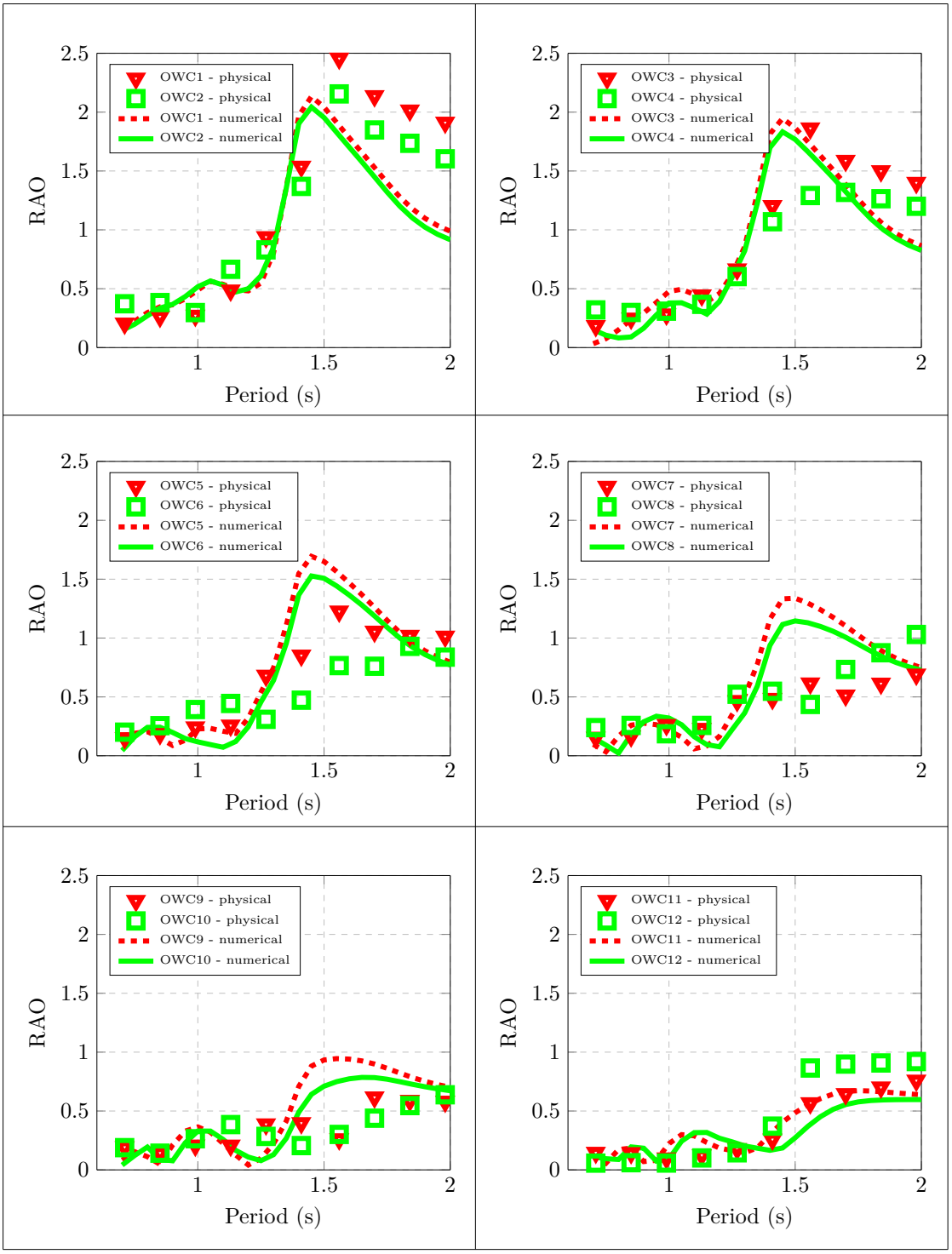

FIGURE 9.40: Comparison between the RAOs of the pumping mode of the water columns in chambers 1 to 12 in the model platform as predicted by the numerical model and as measured during tank tests.

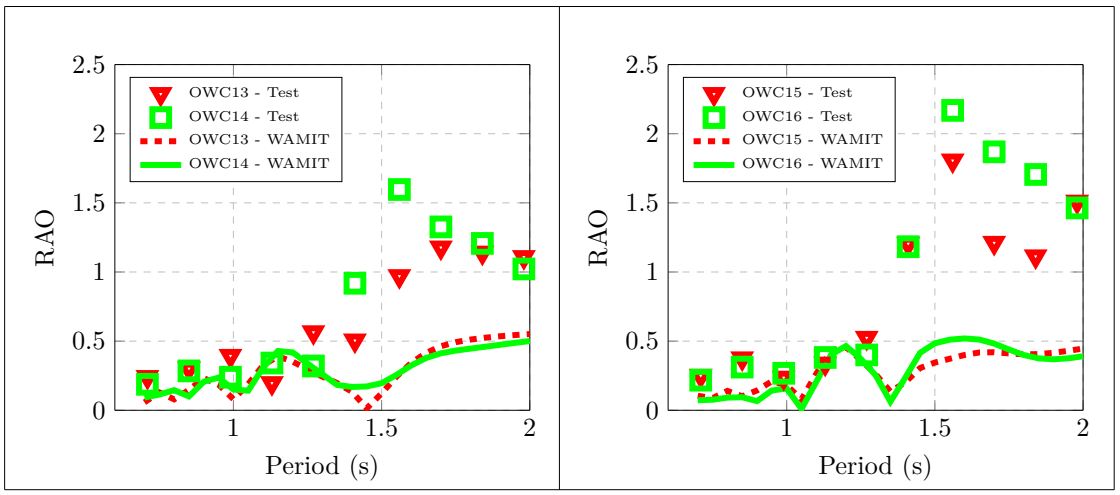

FIGURE 9.41: Comparison between the RAOs of the pumping mode of the water columns in chambers 13 to 16 in the model platform as predicted by the numerical model and as measured during tank tests.

Figure 9.42 compares the numerical predictions for the heave and pitch RAOs for the model platform to those obtained experimentally for the model in Configuration 3 with the 25 mm Venturi pairing installed.

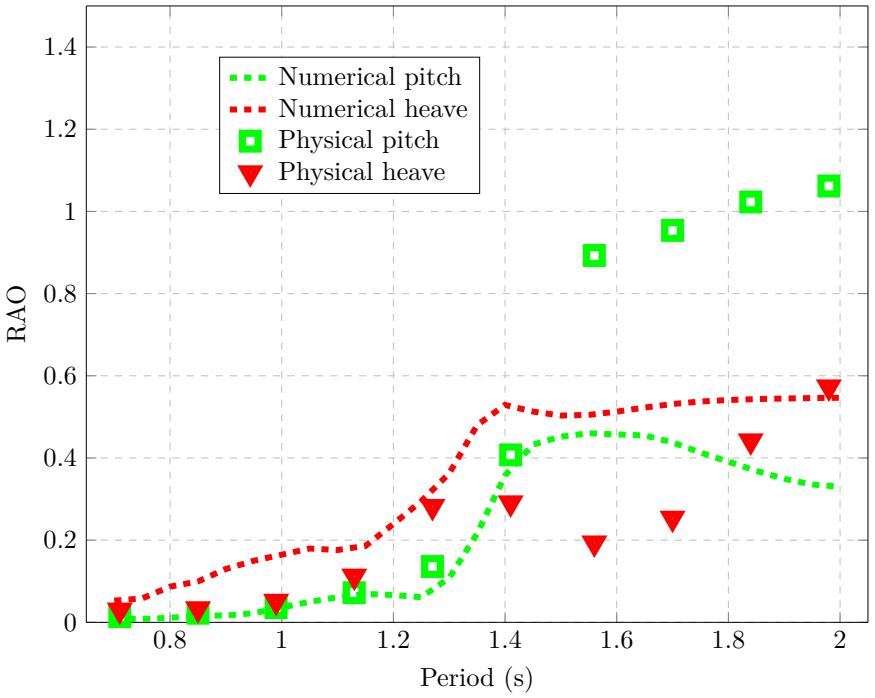

FIGURE 9.42: Comparison between the pitch and heave RAOs for the model platform as predicted by the numerical model and as measured during tank tests with a Venturi throat diameter of 25 mm, for the model in Configuration 3.

Figure 9.43 illustrates the comparison between the power absorbed as predicted by the numerical modeling and as measured from tank tests of the model platform with a Venturi throat diameter of 25 mm, for the model in Configuration 3.

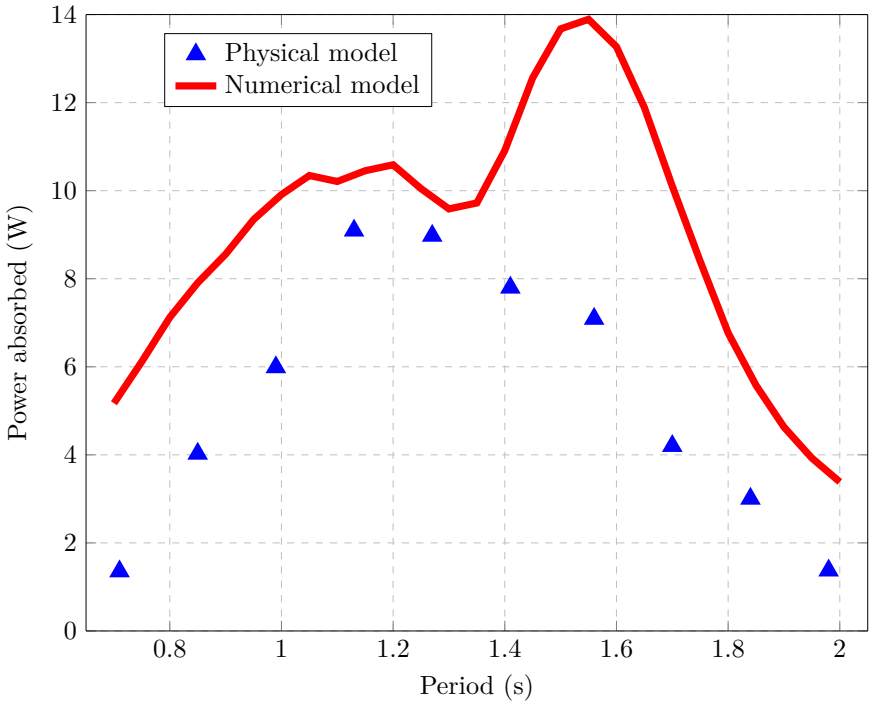

FIGURE 9.43: Comparison between the power absorbed as predicted by the numerical modelling and as measured from tank tests of the model platform with a Venturi throat diameter of 25 mm, for the model in Configuration 3.

Significantly, the experimental RAOs of the water columns appear to be dominated by the platform pitch motions at, and close to, the platform pitch resonant period. The water columns furthest away from the centre of gravity of the platform show the largest RAOs around this period of approximately 1.56 s. With respect to any proposed wind turbines to be mounted on the full scale platform, the extent of the pitching motion around this period is undesirable. However, the pitch mode of the platform is not the only one through which the platform absorbs wave power. This can be seen in Figure 9.43, where the power absorbed by the model in the physical test is shown. Significant power is also absorbed by the model at around the heave resonant period of the water columns, between wave periods of 1.3 s and 1.4 s. This shows that the relative motion of the water columns to the platform is resulting in significant power absorption at these periods.

9.2.2.1 Efforts to reconcile numerical and experimental results

In this section, the efforts made to reconcile numerical and experimental results, where significant differences occur, is discussed. Initially, consider Figure 9.42, which illustrates the rigid body heave and pitch RAOs of the platform with the 25 mm Venturi throat diameter damping level. As can be seen, a significant difference exists between the experimental and numerical results in the region of an incident wave period greater than 1.4 s. Figure 9.44 illustrates the variation in the amplitude of the pitch displacement of the model platform, with respect to incident wave period, obtained from the numerical model and the tank tests. Note that, while the amplitudes of the pitch motions obtained from the numerical model and those obtained from the physical model vary significantly for a wave period of 1.56 s and higher, the trend between the two sets of results with respect to wave period is similar.

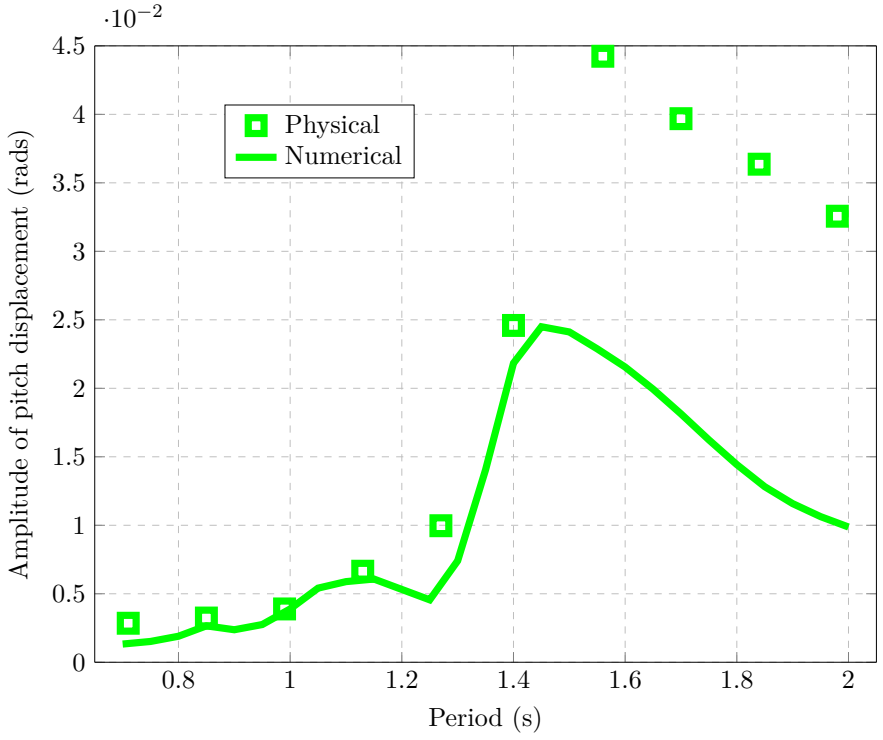

FIGURE 9.44: Variation in the amplitude of the pitch displacement of the model platform with respect to incident wave period as obtained from the numerical model and the tank tests.

The largest pitch angular displacement occurs at an incident wave period of approximately 1.5 s for both data sets (during the testing, the maximum pitch displacement

occurred at a wave period of 1.56 s), as can be seen in Figure 9.44. The experimental data shows a significantly larger pitch displacement and a lower heave displacement compared to the numerical prediction in this range of incident wave periods. However, experimental and numerical results converge once the incident wave period is less than the pitch resonant period, as can be seen in Figure 9.44. This might suggest a transfer of energy between the heave and pitch modes at incident wave periods close to the resonant period of the platform pitching mode, perhaps due to the effect of the mooring arrangement, as discussed below. Consider now the correlation between the predicted and recorded RAOs of the water columns. The results for Chambers 1 to 4, closest to the stern of the model, can be seen in Figure 9.40. Overall, good general agreement for both the RAO magnitudes and periods at which these magnitudes occur has been achieved for Chambers 1 to 4. However, where divergence does occur, it is for wave periods close to the platform pitch resonance period. The match between the experimental and predicted RAOs for water columns 5 to 8 in Figure 9.40 follows the same pattern. Overall, the magnitudes are of a similar order, with some divergence again at wave periods close to the platform pitch resonant period. The comparison between the results for OWCs 9 to 12 are also shown in Figure 9.40. These plots follow the trend of diverging at periods close to the platform pitch resonant period. The numerical results over-predict the RAOs for Chambers 9 and 10, while under-predicting the results for Chambers 11 and 12. The final water column RAOs for Chambers 13 to 16, are shown in Figure 9.41. While the plots for the RAOs for OWCs 13 to 16 exhibit the same pattern, divergence occurs at the same point as before, the divergence in these two plots is greater when compared to those for the other chambers. Chambers 13 to 16 are at the bow of the model platform and closest to the mooring point. Note that a single, averaged value, of damping was applied herein to all the OWC chambers. By fine tuning the individual chamber damping levels, better agreement could likely be achieved between the experimental and predicted results. However, as discussed below, the primary use of the numerical model as currently implemented in the frequency domain is to investigate the overall suitability of the total level of platform PTO damping. Figure 9.43 illustrates the effect that the difference in the actual and predicted RAOs of the platform has on the experimentally-determined and numerically-derived power absorbed by the platform. For incident wave periods up to the pitch resonant period at approximately 1.56 s, the predicted and measured power curves are in general agreement. However, a large spike in the numerically-predicted power occurs at the pitch

resonance. This would suggest that the real-world pitch motion of the platform may be parasitic to the power absorbed at these wave frequencies. It is interesting to note that the numerical model does predict the two peaks shown in the experimental results, at incident wave periods of approximately 1.3 s and 1.5 s. These periods correspond to the resonant heave period of the water columns, and the resonant pitch period of the platform. Peaks in the amplitude of the heave motions of the water columns can been seen at the two periods above when the relative motion of the water columns to the platform is examined, although these peaks are not apparent in Figures 9.40 and 9.41, which illustrate the RAOs of the water columns referenced to the stillwater level. Efforts were made to reconcile the results obtained from the numerical model and from the tank testing where divergence exists. The effect of the mooring chain and buoy arrangement on the behaviour of the numerical model of the platform was investigated, according to the approach suggested by [226]. The physical model mooring arrangement can be seen in Figure 6.1. The possibility that the combined heave and pitch motions at the pitch resonant period were sufficient to fully extend and tension the mooring chain was investigated. This may have had the effect of transferring energy between modes resulting in the larger-than-predicted pitch and lower-than-predicted heave experimental RAOs. However, examination of the test data showed that this was not occurring. Such an effect would be expected to manifest as a 'jerking' action. In Figure 9.45, which illustrates the time series of the pitch displacement at the pitch resonant wave period of 1.56 s, no such 'jerking' action can be observed. The inclusion of the behaviour of the mooring on the system is thus unlikely to explain the large divergence in the rigid body RAOs at the pitch resonance.

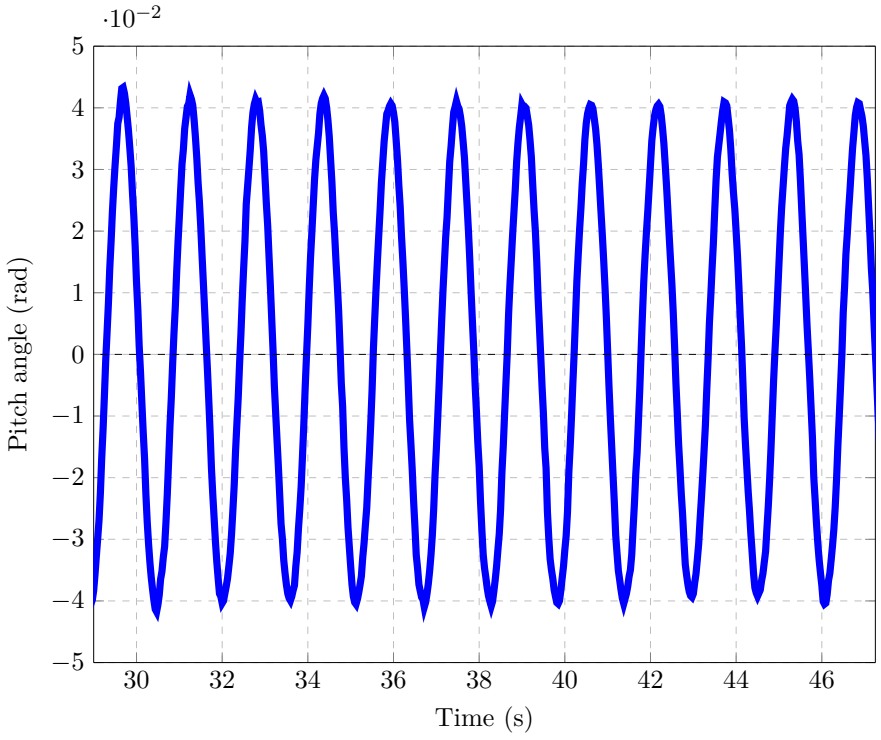

FIGURE 9.45: Time series of the platform pitch motion with the 25 mm diameter Venturi set installed, and with the model subject to an incident wave amplitude of 30 mm at an incident wave period of 1.56 s. Note, no 'jerking' action can be observed.

The most successful method employed to date to reconcile the physical and numerical results focussed on the power curves, as illustrated in Figure 9.43. This method involved increasing the rigid body pitch radiation damping at frequencies around the pitch resonance by a factor of two. Figure 9.46 illustrates the effect on the numerically-predicted power absorbed of this relatively simplistic change in the numerical model compared to the actual power absorbed. Figure 9.47 shows the resulting predicted pitch RAOs compared to the experimental values.

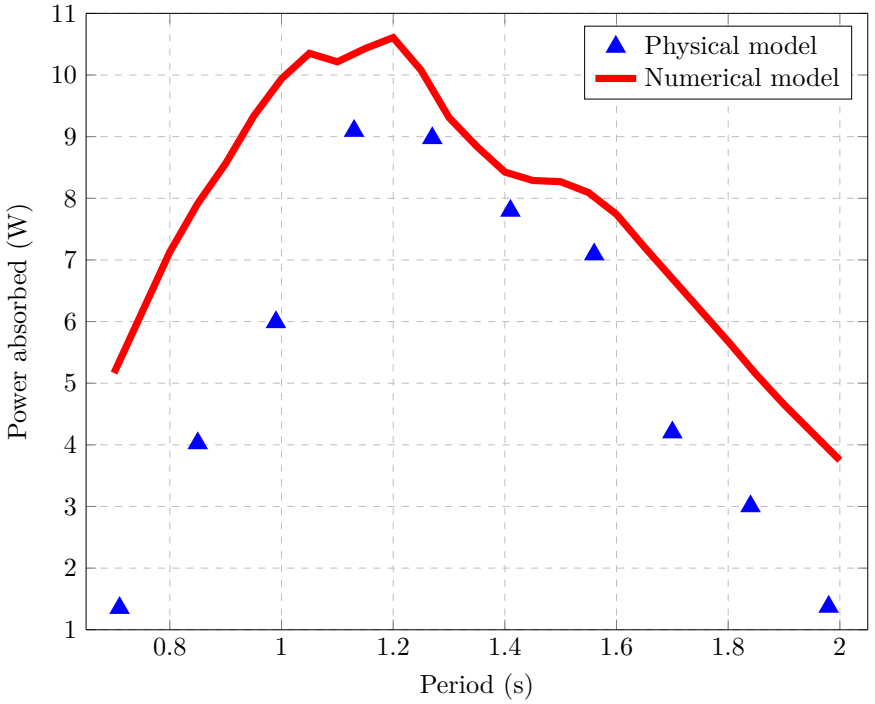

FIGURE 9.46: Comparison between the power absorbed as predicted by the numerical modelling and as measured from tank tests of the model platform with a Venturi throat diameter of 25 mm, for the model in Configuration 3, when the rigid-body pitch radiation damping for the platform at frequencies around the pitch resonance has been increased by a factor of two.

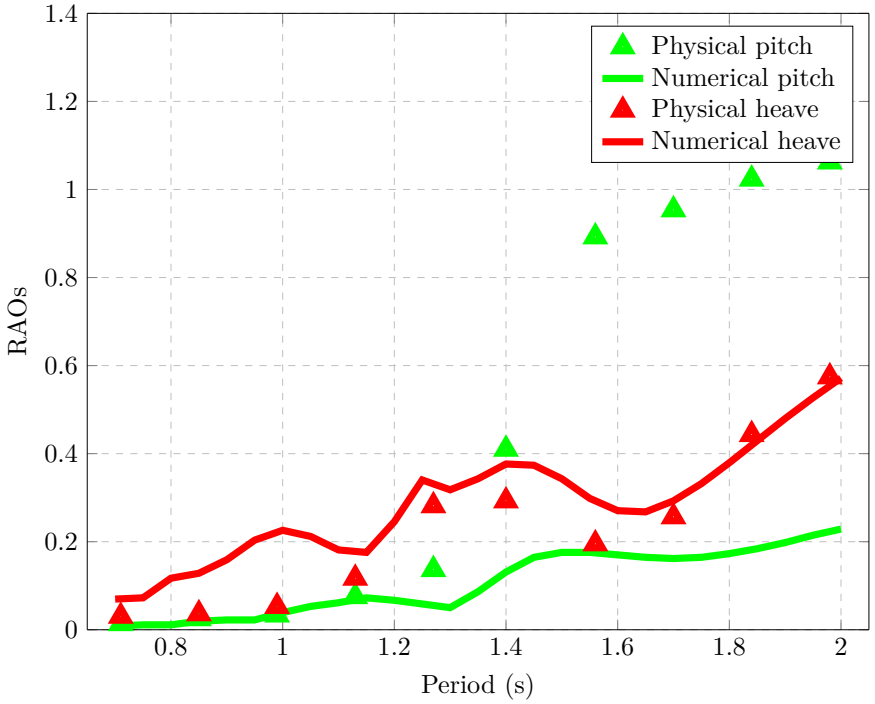

FIGURE 9.47: Comparison between the pitch and heave RAOs for the model platform as predicted by the numerical model and as measured during tank tests with a Venturi throat diameter of 25 mm, for the model in Configuration 3, when the rigid-body pitch radiation damping for the platform at frequencies around the pitch resonance has been increased by a factor of two.

The power absorption plots now show reasonably close agreement. Both the experimental and numerical results show two regions of relatively high power absorption, with respect to incident wave period, corresponding to the heave resonant period of the water columns and the pitch resonant period of the platform. Significantly, the predicted platform heave RAO plot now closely matches the experimental results, showing the same dip in values around the platform pitch resonant frequency. However, the predicted platform pitch RAO plot does not show good agreement. One further possible method to fine tune the numerical model is to include a coupling term between the heave and pitch modes in Equation (4.9). The aim of this approach is to transfer energy between these modes as the numerical model under-predicts the platform pitch RAO and over-predicts the heave RAO at the same periods. It was found that the numerically-predicted rigid body motions were highly sensitive to small changes in both the mass matrix, M, and the stiffness matrix, C in Equation (4.9). Differences in values of a few percent in these matrices have a dramatic influence on the platform RAOs. For example, the effect of the additional mass due to the cable train, which connects the onboard sensors to the

DAQ system, is hard to quantify in situ, but yet may be significant. It seems likely, due to the highly non-linear nature of the platform, along with the time-dependent latching action, that the frequency domain modelling approach discussed in Chapter 4 will be of limited use. However, while the numerical model is far from perfect, it is informative to examine the effect of varying the linear damping used in the solution of Equation (4.23) to determine the predicted power absorbed. As discussed above, the value of applied damping for the LIMPET, when scaled by 1:50 using Froude scaling, is significantly lower than the damping value calculated for each OWC during the testing outlined here. This suggests that the model of the proposed WEI platform is over-damped, reducing its energy capturing ability. To investigate if the model was over-damped, Equation (4.23) has been solved using various levels of applied damping. Figure 9.48 illustrates the effect that varying the value of PTO damping applied to each OWC chamber in the numerical simulation has on the predicted converter efficiency. This efficiency is determined using Equation (9.11). For comparison, the power absorbed for the range of Venturi throat diameters used during the tank tests is also shown in Figure 9.48. Figure 9.48 supports the contention that the model platform is significantly over-damped as currently configured and is the most useful output of the frequency domain model as currently implemented.

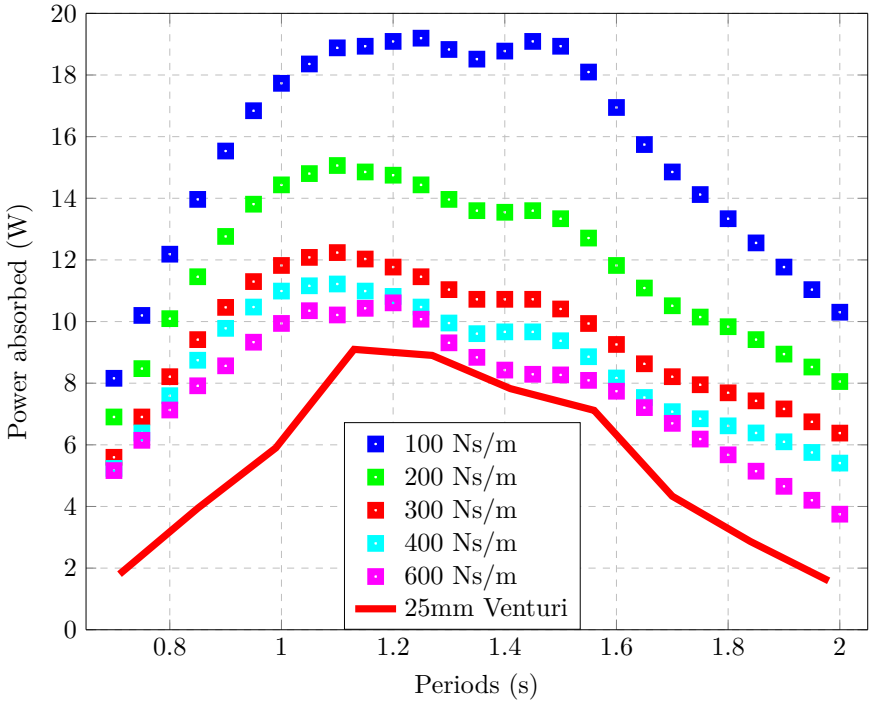

FIGURE 9.48: Comparison of power absorbed by the model platform in Configuration 3 obtained experimentally and the predicted power absorbed obtained from the numerical model, where PTO damping levels lower than those calculated for the tank tests are used in the numerical model.

9.2.3 Multiple chamber polychromatic wave test results

A set of polychromatic wave tests, which were more representative of real sea states, were conducted with the model in Configuration 4, using the 25 mm Venturi pairing. Each test run in this phase lasted 256 s, which is sufficient time for the complete range of wave heights and frequencies within each spectrum used to develop. A total of 10 tests using Bretschneider spectra were performed. Table 9.3 lists the significant wave heights and mean periods, T_p, used to generate the Bretschneider spectra. The choice of mean period, T_p, was informed by the typical range of mean period experienced at the Atlantic Marine Energy Test site (AMETS) [203]. Due to the limited time available for polychromatic testing, a wide range for the mean period was used to capture the extremes of mean period experienced at the test site.

The mean period, T_p, and zero-crossing period, T_z, are related by $T_p = 1.4T_z$ [203]. Thus, at full scale, the range of zero-crossing periods used ranges from approximately 5.5 s to 13.75 s. It can be seen from Table 2.1 that approximately 99 % of Atlantic sea

Significant Wave Height (H_s)	Mean Period (T_p)	Equivalent Full-scale T_p	Equivalent Full-scale T_z
60 mm	1.08 s	7.64 s	5.45 s
60 mm	1.52 s	10.75 s	7.68 s
60 mm	2.03 s	14.35 s	10.25 s
60 mm	2.50 s	17.68 s	12.63 s
60 mm	2.72 s	19.23 s	13.74 s
90 mm	1.08 s	7.64 s	5.45 s
90 mm	1.52 s	10.75 s	7.68 s
90 mm	2.03 s	14.35 s	10.25 s
90 mm	2.50 s	17.68 s	12.63 s
90 mm	2.72 s	19.23 s	13.74 s

TABLE 9.3: Range of significant wave heights and mean periods tested with the model set up as Configuration 4 and with the 25 mm Venturi pairing installed.

states exhibit zero-crossing periods in this range. However, due to the limited number of sea states tested, the polychromatic results presented in the current thesis may only be taken as indicative, and further polychromatic tank testing would be required to fully characterise the behaviour of the WEI platform under polychromatic conditions. The power was averaged by determining the instantaneous power absorbed at each time step, and calculating the RMS of the resulting vector. The results of the power absorbed by the model set-up in Configuration 4, with the 25 mm Venturi pairing installed and subject to the wave spectra given in Table 9.3, as determined using the RMS of the instantaneous power as outlined above, are presented in graph form in Figure 9.49 and tabulated in Table 9.4.

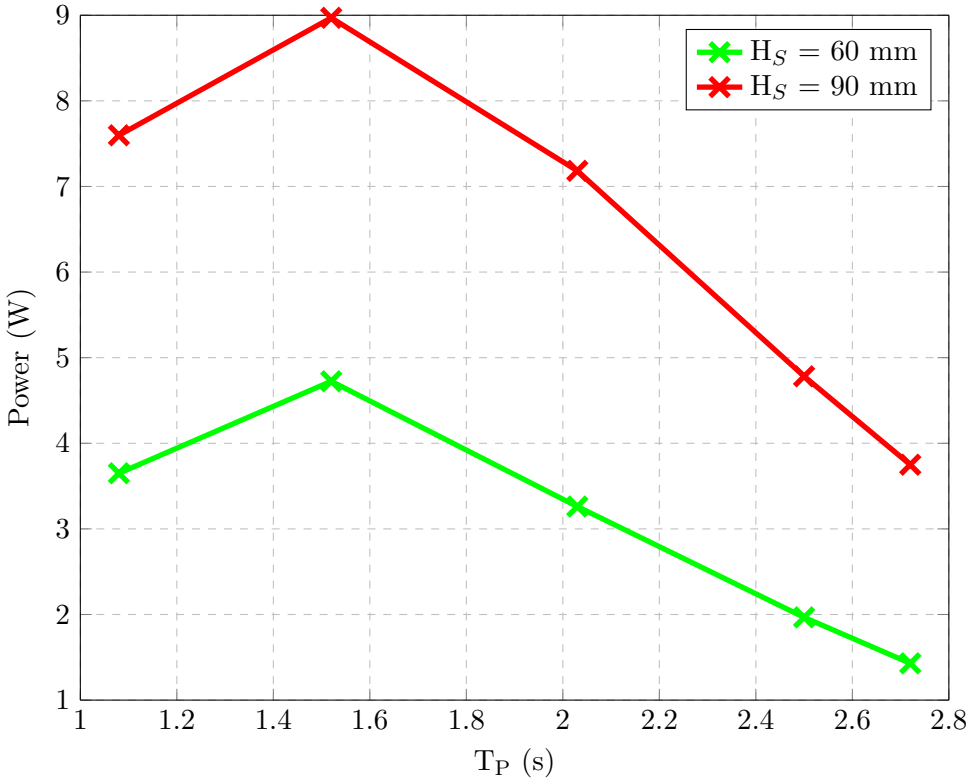

FIGURE 9.49: RMS of the power absorbed by the model platform set up in Configuration 4 with the 25 mm Venturi pairing installed and subject to the wave spectra given in Table 9.3.

H_s \ T_p	1.08 s	1.52 s	2.03 s	2.50 s	2.72 s
60 mm	3.65 W	4.72 W	3.26 W	1.97 W	1.43 W
90 mm	7.60 W	8.97 W	7.18 W	4.78 W	3.75 W

TABLE 9.4: Tabulated RMS of the power absorbed by the model platform set up in Configuration 4 with the 25 mm Venturi pairing installed and subject to the wave spectra given in Table 9.3.

Figure 9.50 illustrates the capture factor for Configuration 4, with the 25 mm Venturi pairing installed, when the model was subjected to the wave spectra described in Table 9.3. The power per metre crest in the wave spectra is calculated based on the formula for the energy density in a Bretschneider spectrum given by [227], which is given in Equation (9.15).

$$J = 0.42 H_s^2 T_p \text{ kW/m} \tag{9.15}$$

where:

J = the power per metre wave crest, W

H_s = the significant wave height, m

T_p = the mean wave period, s

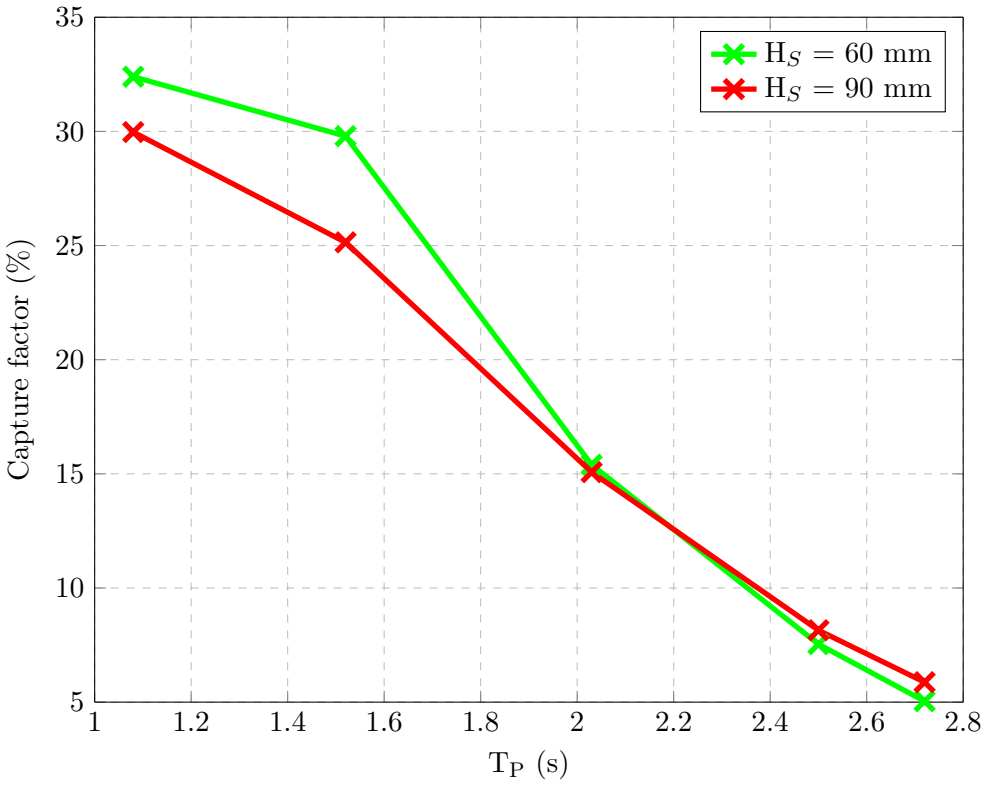

FIGURE 9.50: Capture factor for the model platform set up in Configuration 4 with the 25 mm Venturi pairing installed and subject to the wave spectra given in Table 9.3.

9.3 Results for the single-chamber OWC

In this section, test results obtained for the single-chamber OWC model, described in Chapter 6, are presented and compared to predictions obtained from the corresponding numerical models, described in Chapter 5. Firstly, the single-chamber OWC with an orifice is considered. The iris valve, used to create an adjustable orifice, is characterised using the results from narrow tank testing. Next, the numerical model of the single-chamber OWC with an orifice is used to predict the water column motion, and the air

pressure variation in the OWC chamber, for further tests conducted with a wide range of incident wave frequencies, amplitudes and orifice diameters. The predictions from the numerical model for the single-chamber OWC with an orifice are then compared to the corresponding results from narrow tank testing. Secondly, the single-chamber OWC with air admittance valves is considered. The air admittance valves are characterised from results obtained from narrow tank testing, and predictions from the numerical model of the single-chamber OWC with air admittance valves are compared to the corresponding results from further narrow tank testing. Note that all tests performed on the single-chamber OWC described in this thesis were conducted under monochromatic wave conditions.

9.3.1 Single-chamber OWC model with an orifice

Before the numerical model for the single-chamber OWC with an orifice may be implemented, the parameters in Equation (5.45) must be determined. The hydrodynamic and hydrostatic parameters are obtained from the WAMIT model, described in Section 5.4.1. The state-space approximation of the convolution term in the Cummins equation is obtained using the radiation damping values from WAMIT and the reconstructed added mass values as input to the FDI toolbox in MATLAB, as described in Section 5.4.2.3. Once an orifice diameter has been chosen for analysis, the only term in Equation (5.45) yet to be modelled or determined is the coefficient of discharge for the orifice, Cd_o. The mass flow rate of air into (and out of) the chamber is related to Cd_o, as shown in Table 5.1. Typical values for the coefficient of discharge for an orifice plate are of the order of 0.5 [185].

9.3.1.1 Orifice characterisation

A photograph of the adjustable orifice may be seen in Figure 8.14. The value for Cd_o for the iris valve may be measured experimentally from the equations presented in Table 5.1, if the difference in the air pressure within the chamber and the surrounding atmosphere is recorded when the model is subjected to incident waves. A method for measuring the volumetric flow of air between the chamber and atmosphere, which is independent of Cd_o, is also required. Equation (9.7) describes a method whereby the flow rate of air may be measured without knowledge of Cd_o. The volumetric flow rate of air may be

found if the velocity of the water column at any time step is multiplied by the cross-sectional area of the water column. This method assumes that the OWC has a uniform cross section over the range of motion of the surface of the water column, and that the water column operates in a pumping mode only. The velocity may be obtained as the first derivative of the water column displacement. The water column displacement may be measured using a resistive wave probe located in the OWC chamber. The volumetric flow rate of air is then given by:

$$Q_{air} = A_{owc} \times V_{owc} \tag{9.16}$$

where:

Q_{air} = the volumetric flow rate of air, m^3/s

A_{owc} = the cross-sectional area of the water column surface, m^2

V_{owc} = the velocity of the water column, m/s.

The mass flow rate is related to the volumetric flow rate by:

$$Q_{air} = \frac{\dot{m}_{air}}{\rho_{air}} \tag{9.17}$$

where:

$\dot{m}_{air}$ = the mass flow rate of air, kg/sec

ρ_{air} = the density of air, kg/m^3.

From the mass flow rate equations, presented in Table 5.1, Equation (9.17) may be re-written as:

$$Q_{air} = \frac{Cd_o A_o \sqrt{2\rho_{air} |\Delta p|}}{\rho_{air}} \times sign\,|\Delta p| \tag{9.18}$$

Thus,

$$A_{owc} \times V_{owc} = Cd_o \frac{A_o \sqrt{2\rho_{air} |\Delta p|}}{\rho_{air}} \times sign\,|\Delta p| \tag{9.19}$$

The pressure difference across the orifice, and the velocity of the water column, are measured at the same instances in time while the single-chamber OWC model is subject to incident waves.

If:

$$A_{owc} \times V_{owc} \tag{9.20}$$

is plotted against:

$$\frac{A_o\sqrt{2\rho_{air}\,|\Delta p|}}{\rho_{air}} \times sign\,|\Delta p| \tag{9.21}$$

a straight line should result, and the slope of the line should equal Cd_o.

However, the process to determine Cd_o depends heavily on the assumption that the motion of the water column is piston-like. A resistive wave probe, located at the centroid of the free surface, is used to measure the displacement of the water column. Additional sloshing modes within the chamber will affect the reading from the wave probe, and will also affect the mass flow rate in a non-linear fashion, potentially invalidating the process outlined above. To illustrate this concept, Figure 9.52 shows the motion of the single-chamber OWC water column for one wave period with an incident wave of frequency 0.4 Hz and an amplitude of 30 mm, with the orifice set to a diameter of 20 mm. The images in Figure 9.52 were taken from a video made of the water column motion during tank testing. The water column may be seen through the glass wall of the tank, and the Perspex side wall of the OWC. The video was recorded at 30 frames per second.

Note that the free surface of the water column, shown in Figure 9.51, remains largely flat and moves in a piston-like fashion. By contrast, Figure 9.52 illustrates the motion of the water column over the course of one wave period with the single-chamber OWC model subject to an incident wave of frequency 0.8 Hz and an amplitude of 30 mm, with the orifice set to a diameter of 30 mm. The water column moves in the most piston-like manner for waves of low frequency, i.e., for waves with relatively long wave lengths. The water column free surface in Figure 9.52 clearly shows the effect of sloshing modes. The wave probe will measure the sum of all modes of the water column, assuming linear superposition. A further issue, seen in Figure 9.52, is the effect of the jet of air entering the OWC when the water column is moving in a downward direction. This jet impinges on the water surface, and will effect the reading of the wave probe. The effect is particularly pronounced at 0.233 s, where the effect of the jet on the free surface around the wave probe can be seen in Figure 9.52. (Note that in both Figure 9.51 and Figure 9.52, the free surface of the water column has been highlighted with a blue outline for clarity.)

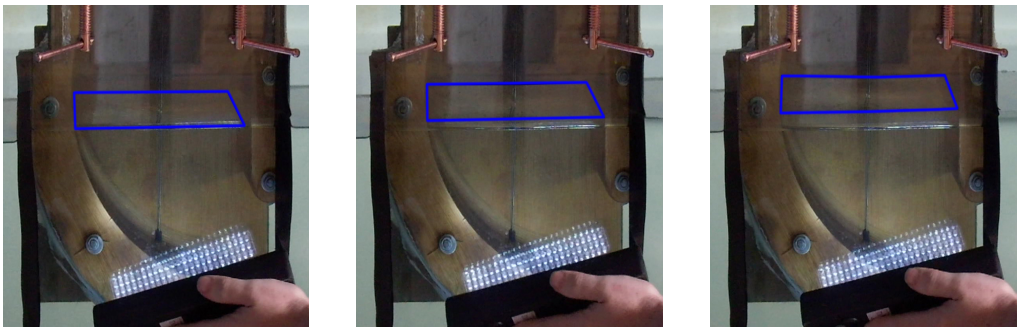

(A) 0.033 s (B) 0.2 s (C) 0.367 s

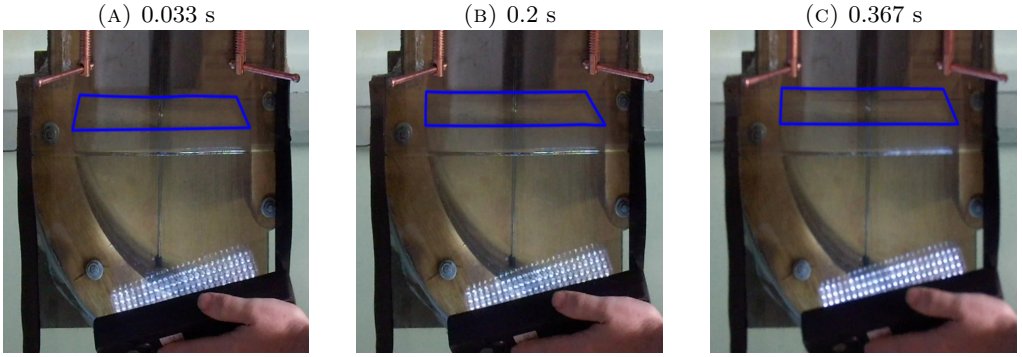

(D) 0.533 s (E) 0.7 s (F) 0.867 s

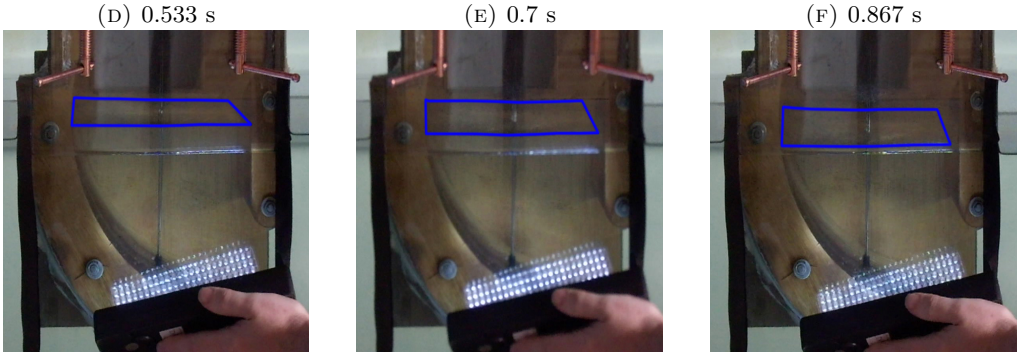

(G) 1.033 s (H) 1.2 s (I) 1.367 s

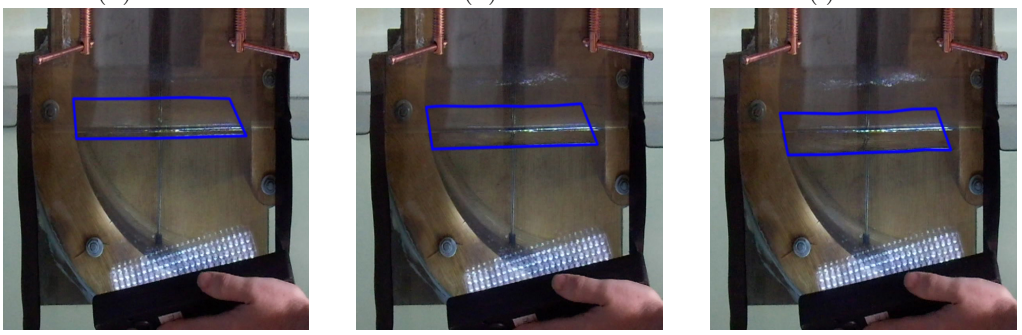

(J) 1.533 s (K) 1.7 s (L) 1.867 s

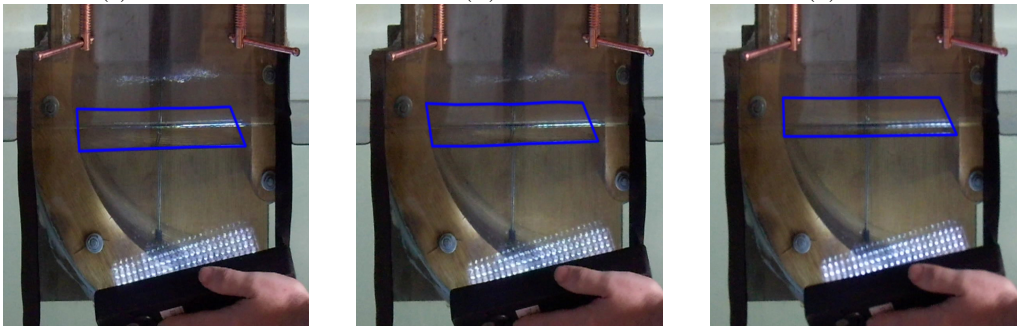

(M) 2.033 s (N) 2.2 s (O) 2.367 s

FIGURE 9.51: Motion of the single-chamber OWC water column for one wave period with an incident wave of frequency 0.4 Hz and an amplitude of 30 mm, with the orifice set to a diameter of 20 mm. Note the piston-like motion of the water column.

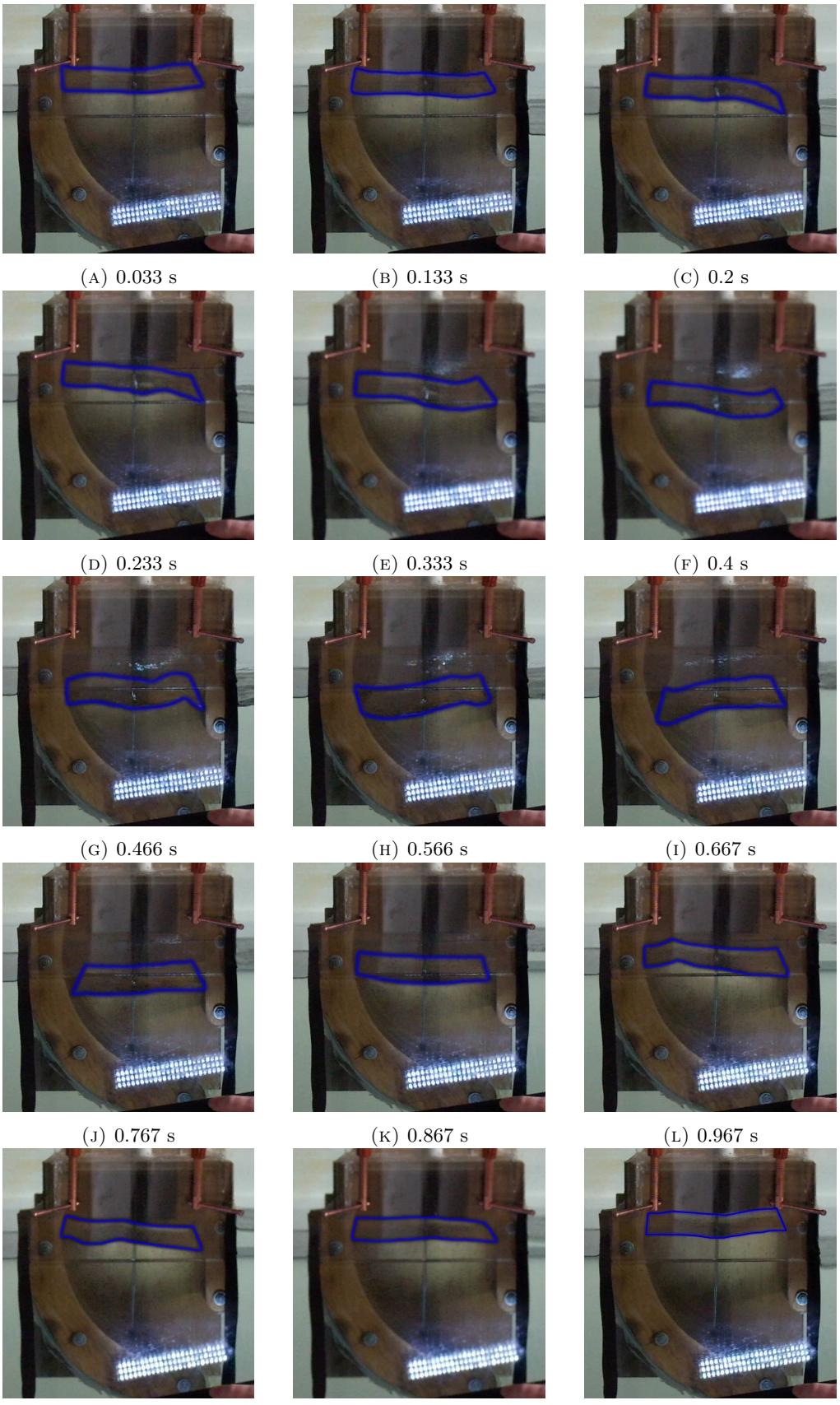

(A) 0.033 s (B) 0.133 s (C) 0.2 s

(D) 0.233 s (E) 0.333 s (F) 0.4 s

(G) 0.466 s (H) 0.566 s (I) 0.667 s

(J) 0.767 s (K) 0.867 s (L) 0.967 s

(M) 1.067 s (N) 1.133 s (O) 1.267 s

FIGURE 9.52: Motion of the single-chamber OWC water column for one wave period with an incident wave of frequency 0.8 Hz and an amplitude of 30 mm, with the orifice set to a diameter of 30 mm. Note the presence of sloshing modes.

Before Cd_o may be found using the technique outlined above, the displacement signal of the water column must be differentiated to obtain the corresponding time series of the velocity of the water column. The displacement time series was initially processed by approximating the derivative using the difference between adjacent time series entries. However, the using the difference approach to approximate the derivative of a signal is susceptible to noise, and the susceptibility increases as the data sampling rate increases. The susceptibility results in large spikes in the output of the differencing process, which would adversely effect the estimation for Cd_o, if applied directly to the data obtained from narrow tank testing. Thus, the displacement signal was first filtered using a low-pass filter before being numerically differentiated. Figure 9.53 shows the scatter plot of Expression 9.20 against Expression 9.21, for a 60 s test run, for the model subject to an incident wave of 30 mm in amplitude, and a frequency of 0.4 Hz for an orifice diameter of 20 mm. The green line has been fitted using a 'least squares' fitting routine in MATLAB. The R^2 value for the line fitted to the data in Figure 9.53 is 0.9797. The slope of this line yields the coefficient of discharge for the orifice.

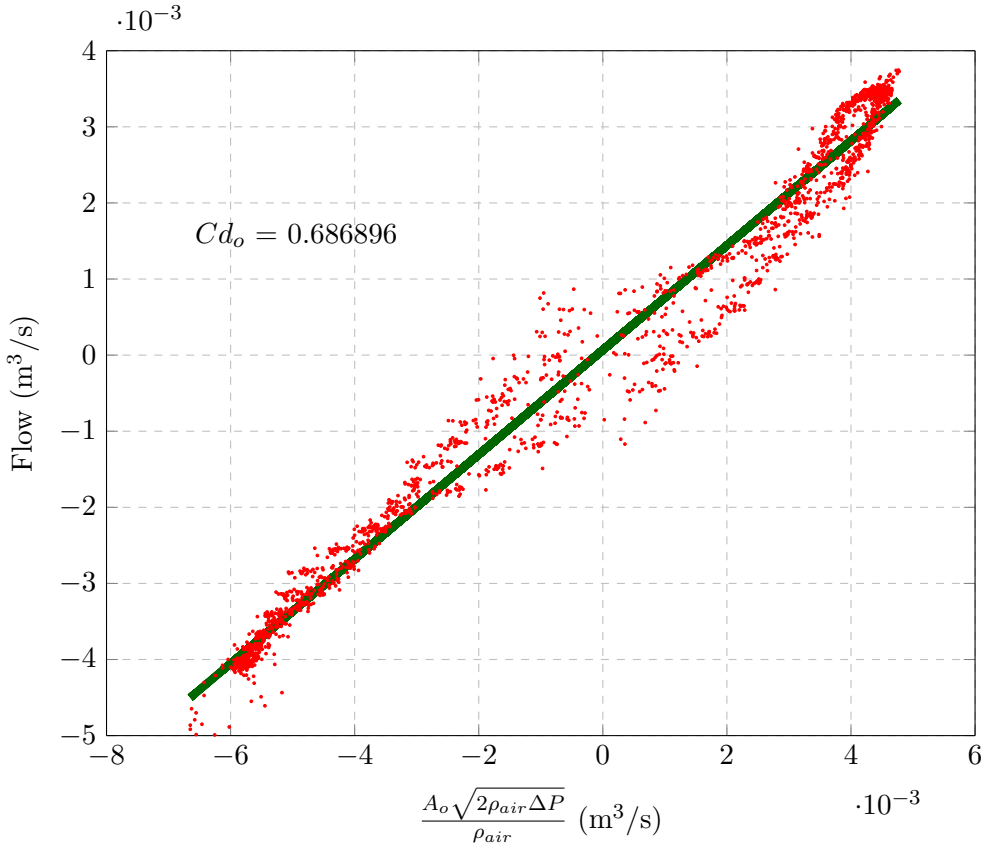

FIGURE 9.53: Plot of airflow through the orifice calculated using the Expression (9.20) based on the velocity of the water column vs. the Expression (9.21) for an incident wave of 30 mm and a frequency of 0.4 Hz for an orifice diameter of 20 mm. Note this figure illustrates a useful set of data for determining Cd_o for the orifice.

In contrast to Figure 9.53, Figure 9.54 illustrates similar data, but for a 60 s test run for the model subject to an incident wave of 30 mm in amplitude and a frequency of 1.4 Hz for an orifice diameter of 30 mm. As before, the green line in Figure 9.54 has been fitted using a least squares fitting routine. It is clear that, due to the effect of slosing, a linear correlation does not exist in Figure 9.54, and the R^2 value is 0.3021. For this reason, the Cd_o value used to produce the numerical predictions in the current work is obtained from the results acquired using the longest wave the narrow tank is capable of generating, which occurs at a frequency 0.4 Hz. The value of Cd_o for a number of different wave amplitudes, with the iris valve configured to generate a range of different orifice diameters, is presented in Table 9.5.

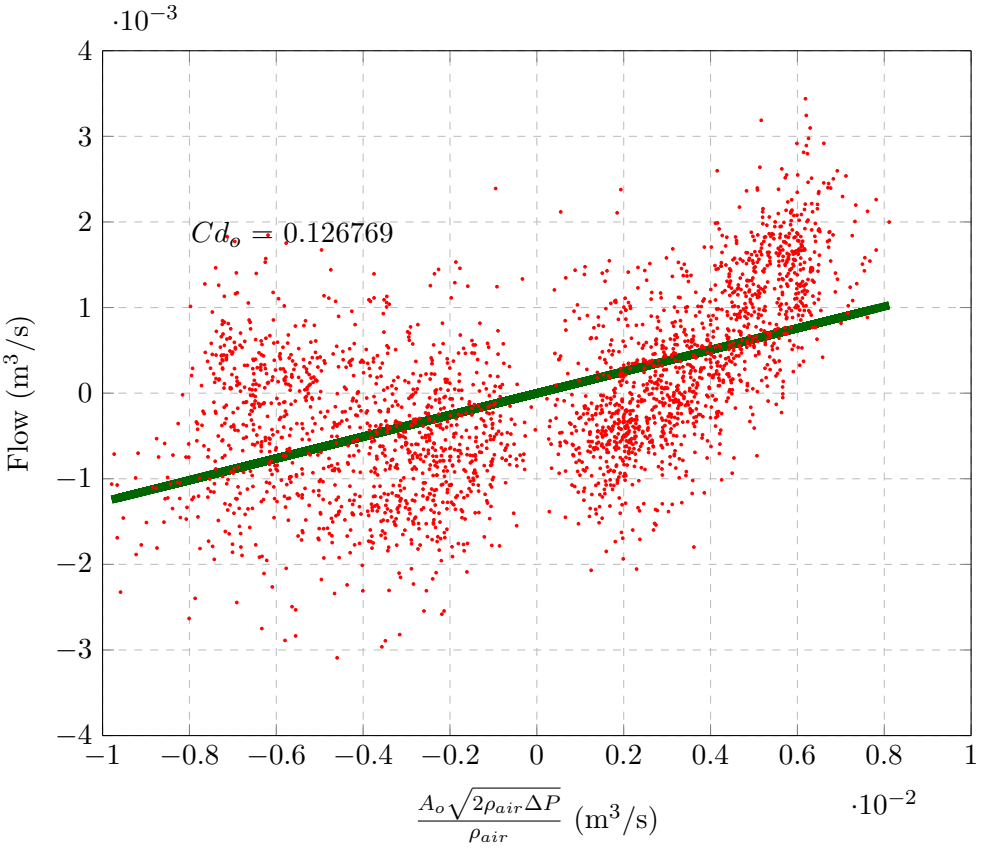

FIGURE 9.54: Plot of airflow through the orifice calculated using the Expression (9.20) based on the velocity of the water column vs. the Expression (9.21) for an incident wave of 30 mm and a frequency of 1.4 Hz for an orifice diameter of 30 mm. Note this figure illustrates a set of data which is not suitable for determining Cd_o for the orifice.

Wave Amplitude \ Orifice Diameter	20 mm	25 mm	30 mm
15 mm	0.683	0.640	0.637
20 mm	0.693	0.666	0.645
25 mm	0.694	0.672	0.664
30 mm	0.687	0.674	0.671

TABLE 9.5: Cd_o for the adjustable orifice as determined for varying orifice diameters and incident wave amplitudes, all with a frequency of 0.4 Hz. Note the consistency of the result for Cd_o obtained across the range of wave amplitudes and orifice diameters.

The values for Cd_o, presented in Table 9.5, show good consistency, but are higher than would be normally expected for an orifice plate [185]. The larger-than-expected values for Cd_o can, perhaps, be explained by the nature of the iris valve. For the 20 mm orifice tests, if the value for the diameter of the orifice used to estimate Cd_o in Equation (9.19) is increased by 2.8 mm during the calculation of Cd_o, the estimated value of Cd_o decreases

to 0.5 or lower, illustrating the sensitivity of the calculation to the orifice diameter. The overlapping leaves from which the valve is constructed are lightweight, and will deform under pressure, which will allow the orifice diameter to change slightly with time. Air may also escape between the leaves, as well as through the central opening of the valve. Further, air may potentially escape between the iris valve and the coupler. Any factor which allows air to flow into, or out of, the chamber, other than through the central opening of the valve, would result in an over-estimation of the value of Cd_o. In effect, such factors would have the same influence on the airflow into, or out of, the chamber as would increasing the orifice diameter.

9.3.1.2 Comparison between results from tank testing and numerical predictions for the single-chamber OWC with orifice

In this section, the results from narrow tank testing of the single-chamber OWC model with an adjustable orifice, as described in Section 6.4.2, are compared to the predictions made by the numerical model, presented in Section 5.3.1. Figures 9.55 and 9.56 illustrate the comparison for the motion of the water column and the variation of gauge pressure within the OWC chamber when the model was subject to an incident wave of 20 mm at a frequency of 0.4 Hz with the adjustable orifice set to a diameter of 20 mm.

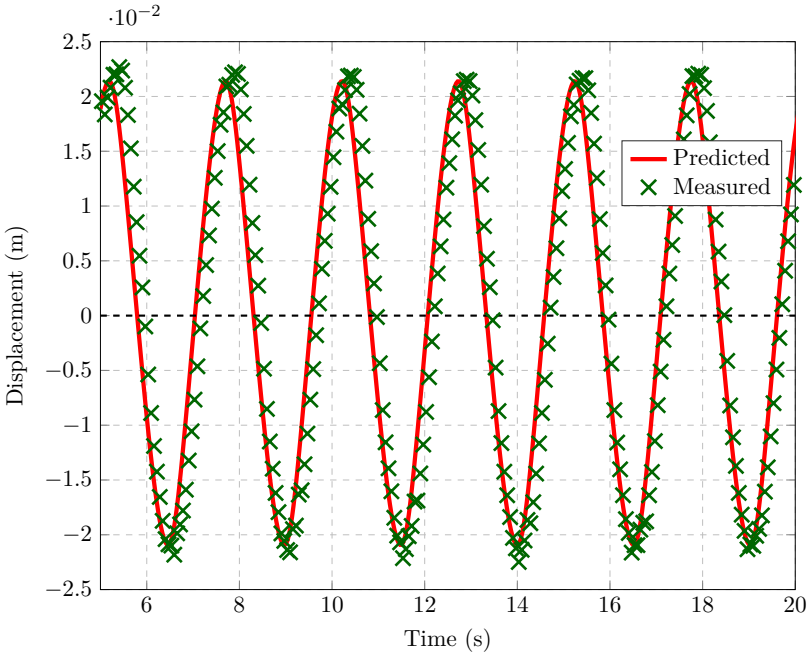

FIGURE 9.55: Comparison between the predicted results and the test results, for the displacement of the water column in response to an incident wave of 20 mm and a frequency of 0.4 Hz for an orifice diameter of 20 mm in steady-state conditions for the single-chamber OWC model with an orifice.

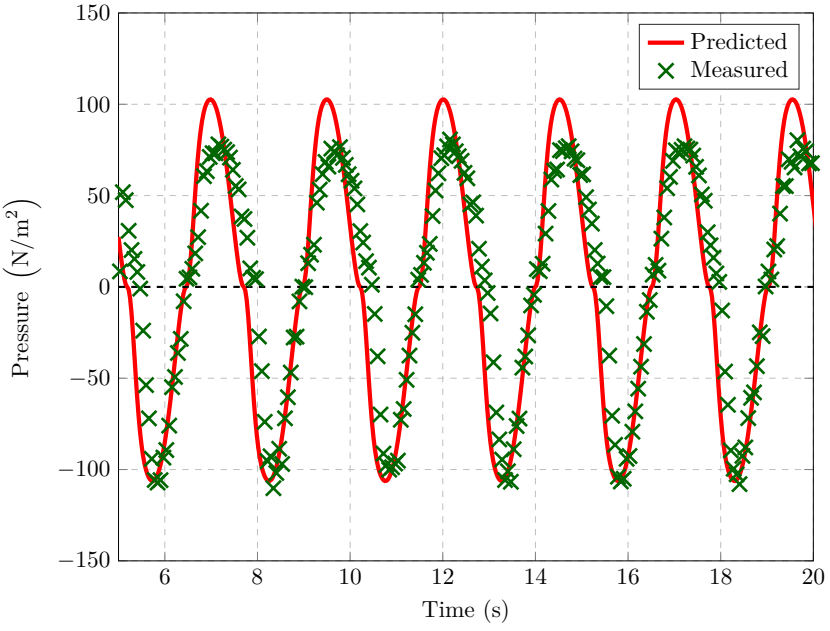

FIGURE 9.56: Comparison between the predicted results and the test results, for the air pressure above the water column in response to an incident wave of 20 mm and a frequency of 0.4 Hz for an orifice diameter of 20 mm in steady-state conditions for the single-chamber OWC model with an orifice.

Figures 9.55 and 9.56 show good agreement between the predicted and measured results, for one specific set up. A large number of set ups were tested and numerically modelled, and a cross-section of results are now presented. Firstly, to illustrate the accuracy of the numerical model with respect to frequency, Figures 9.57 to 9.62 show the comparison between the predicted results and the test results for the complete range of frequencies tested, when the adjustable orifice was set to a diameter of 25 mm, and the single-chamber OWC model was subject to waves of 15 mm amplitude. Subsequently, to illustrate the accuracy of the numerical model with respect to variations in incident wave amplitude and orifice diameter, Figures 9.63 to 9.68 illustrate the comparison between the predicted results and the test results, for an incident wave frequency of 0.4 Hz, while the orifice diameter varies between 10 mm and 30 mm, and the wave amplitude varies between 10 mm and 30 mm. Each plot illustrates approximately 5 wave periods, hence, the duration of the time series varies as the incident wave frequency varies.

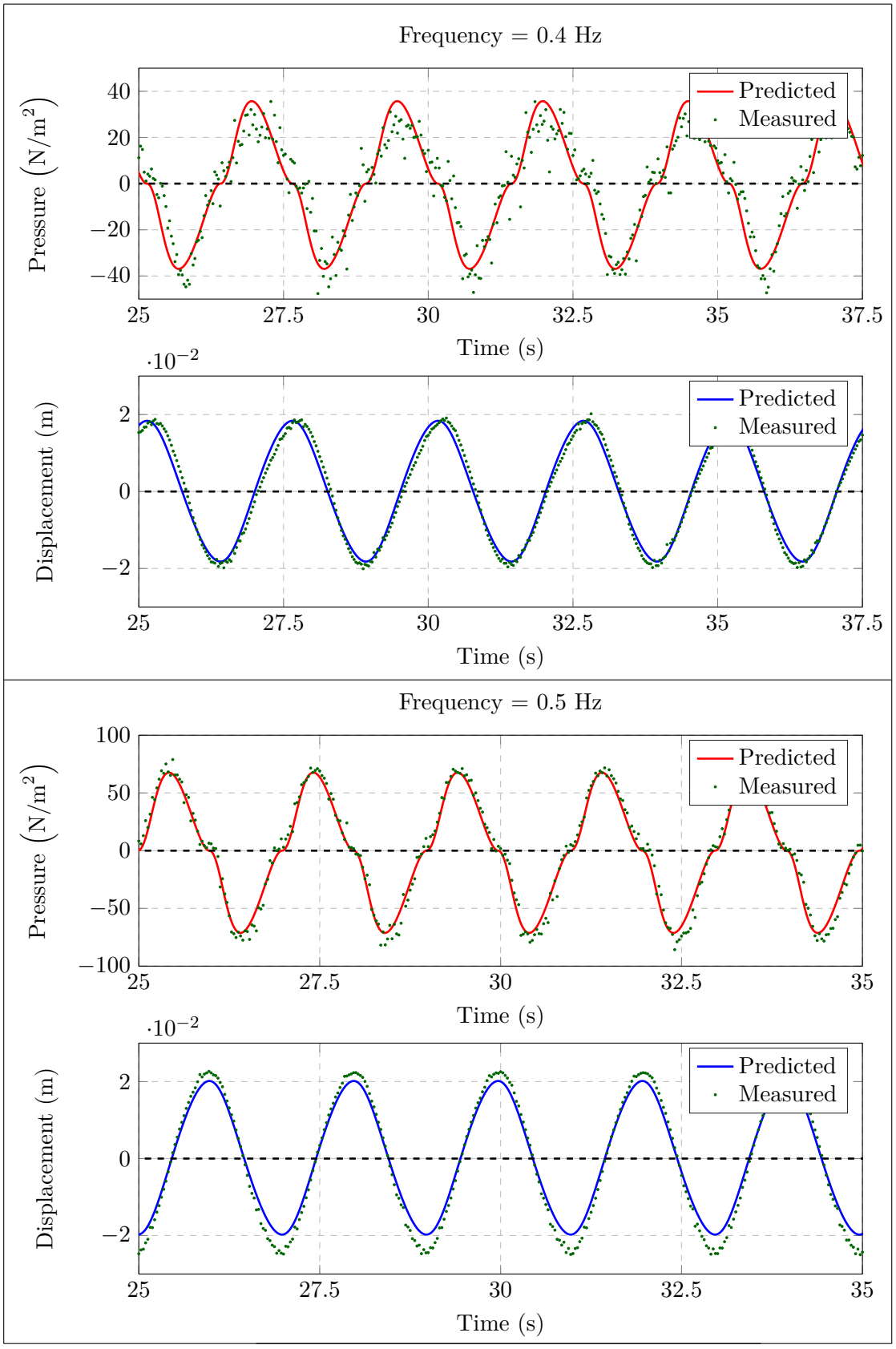

FIGURE 9.57: Comparison between the gauge pressure and the motion of the water column in the single-chamber OWC model obtained experimentally and as predicted by numerical model, with the adjustable orifice diameter set to 25 mm and subject to incident waves of 15 mm amplitude for wave frequencies of 0.4 Hz and 0.5 Hz.

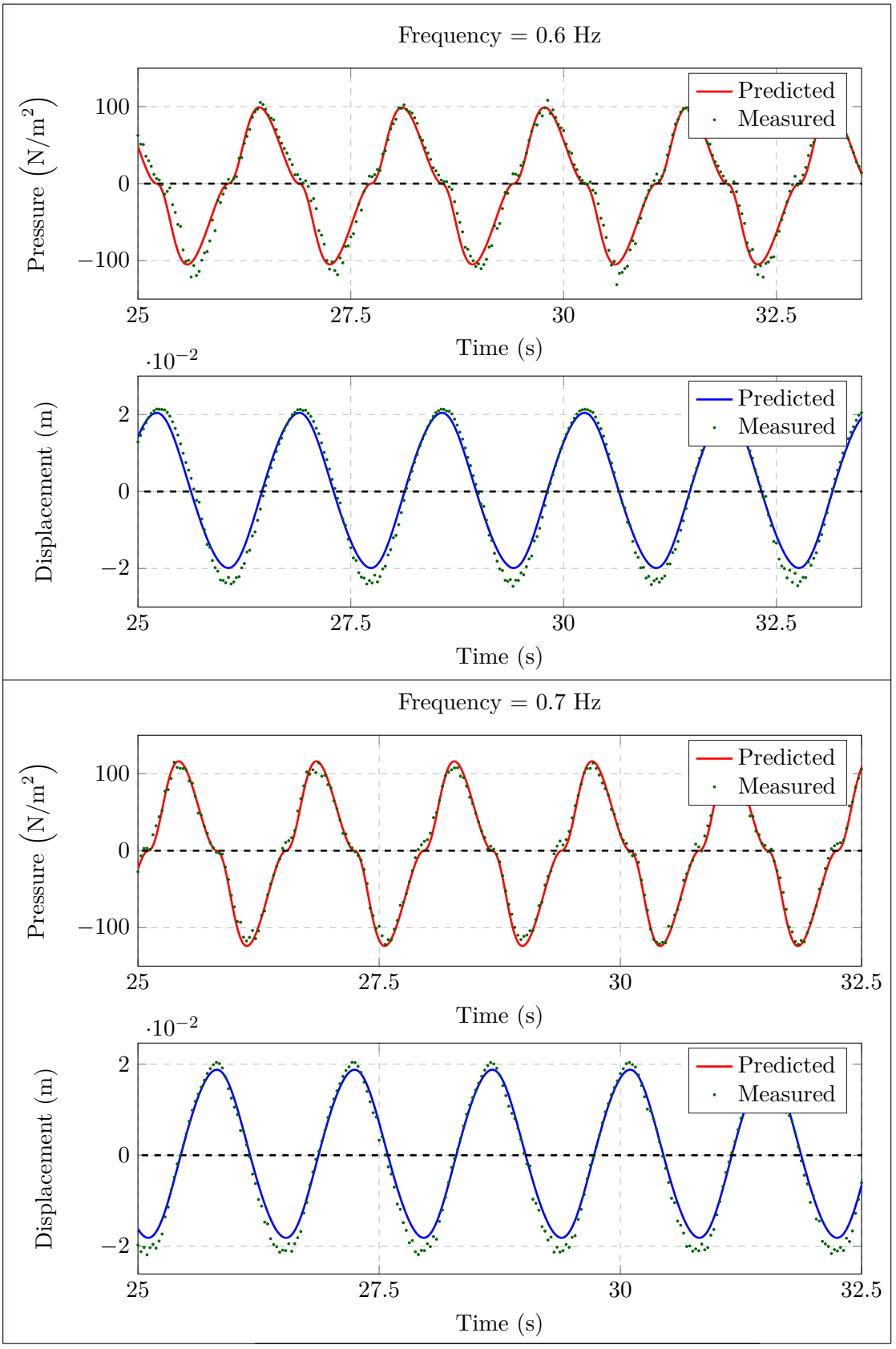

FIGURE 9.58: Comparison between the gauge pressure and the motion of the water column in the single-chamber OWC model obtained experimentally and as predicted by numerical model, with the adjustable orifice diameter set to 25 mm and subject to incident waves of 15 mm amplitude for wave frequencies of 0.6 Hz and 0.7 Hz.

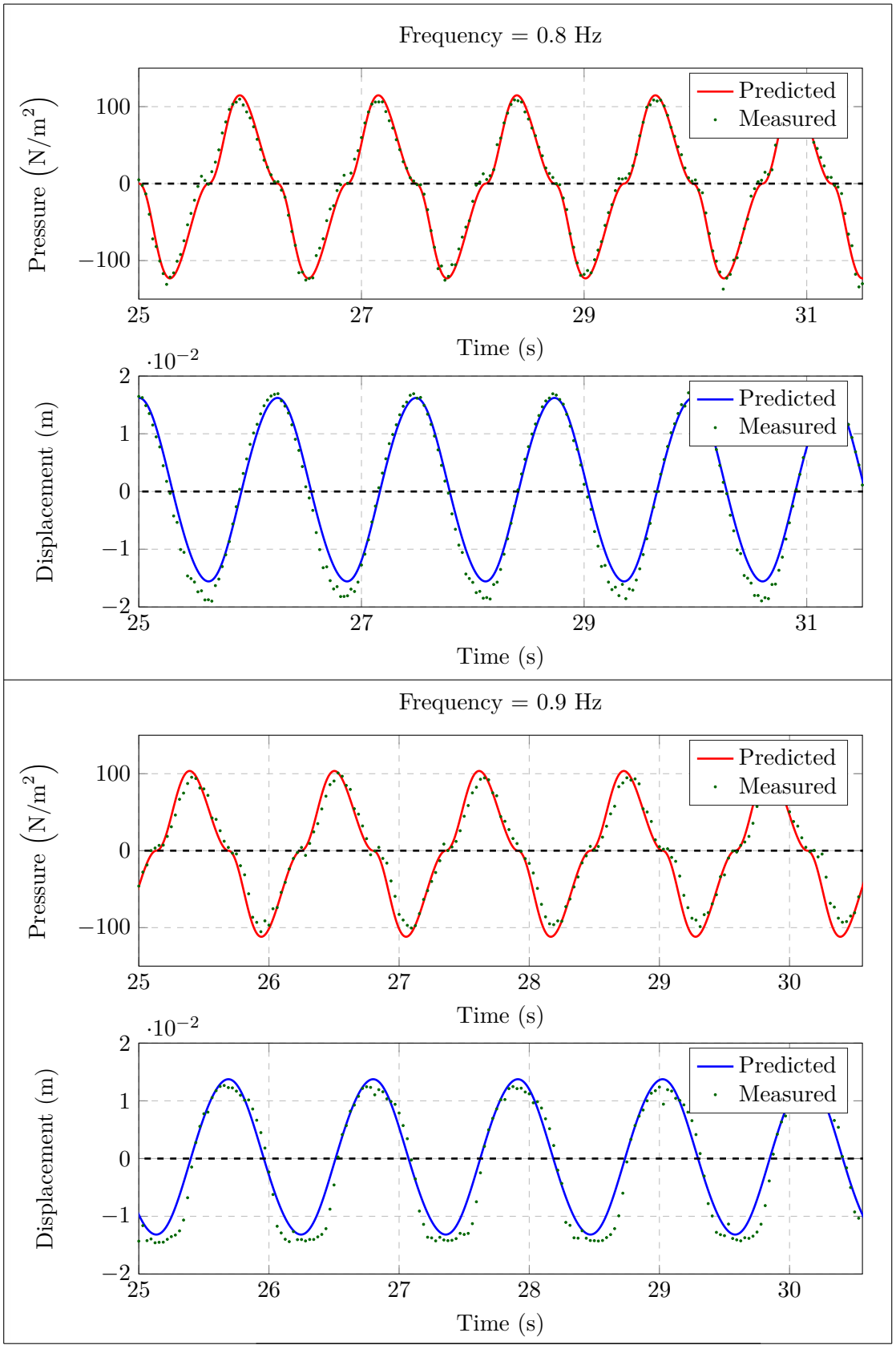

FIGURE 9.59: Comparison between the gauge pressure and the motion of the water column in the single-chamber OWC model obtained experimentally and as predicted by numerical model, with the adjustable orifice diameter set to 25 mm and subject to incident waves of 15 mm amplitude for wave frequencies of 0.8 Hz and 0.9 Hz.

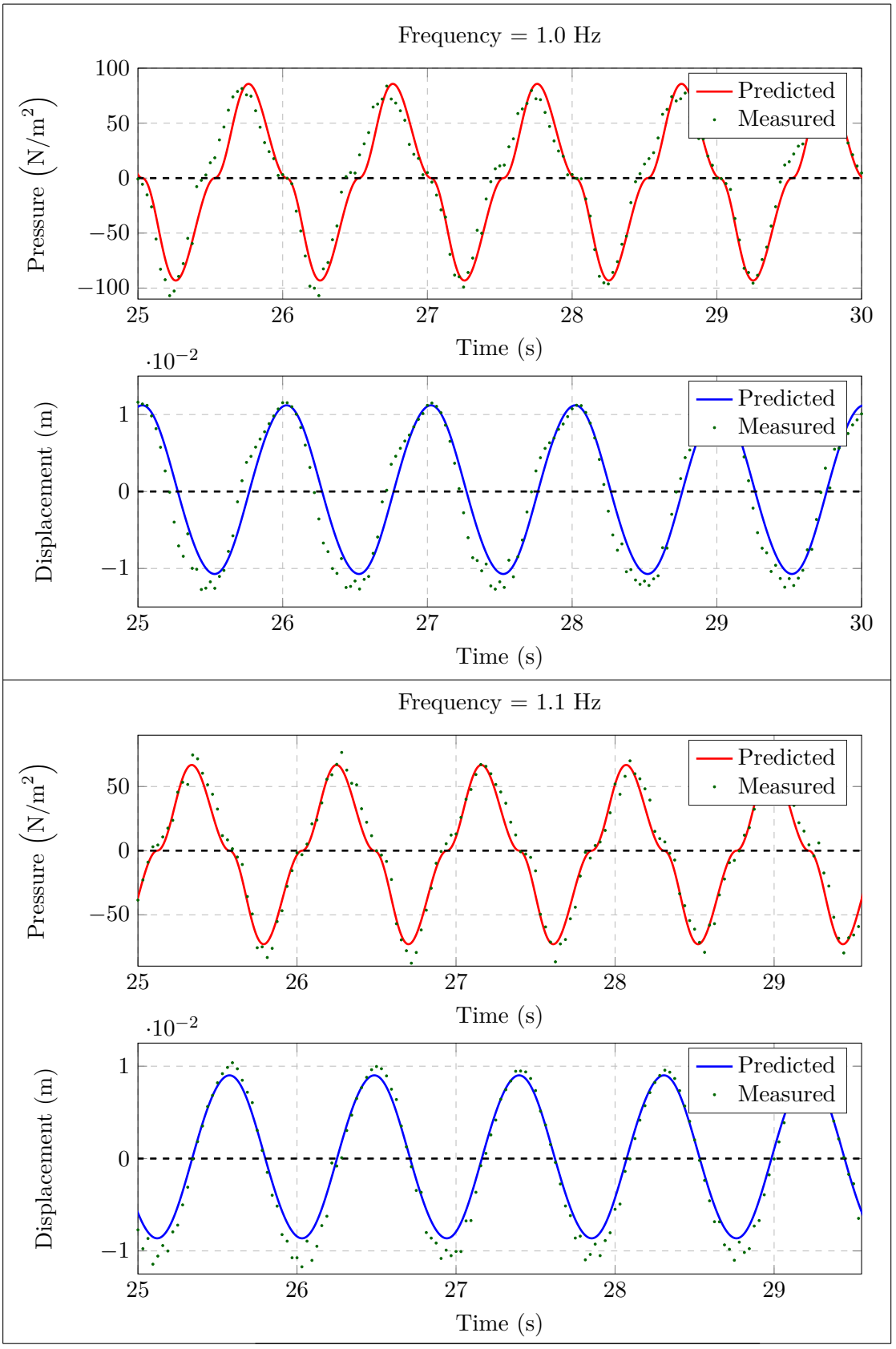

FIGURE 9.60: Comparison between the gauge pressure and the motion of the water column in the single-chamber OWC model obtained experimentally and as predicted by numerical model, with the adjustable orifice diameter set to 25 mm and subject to incident waves of 15 mm amplitude for wave frequencies of 1.0 Hz and 1.1 Hz.

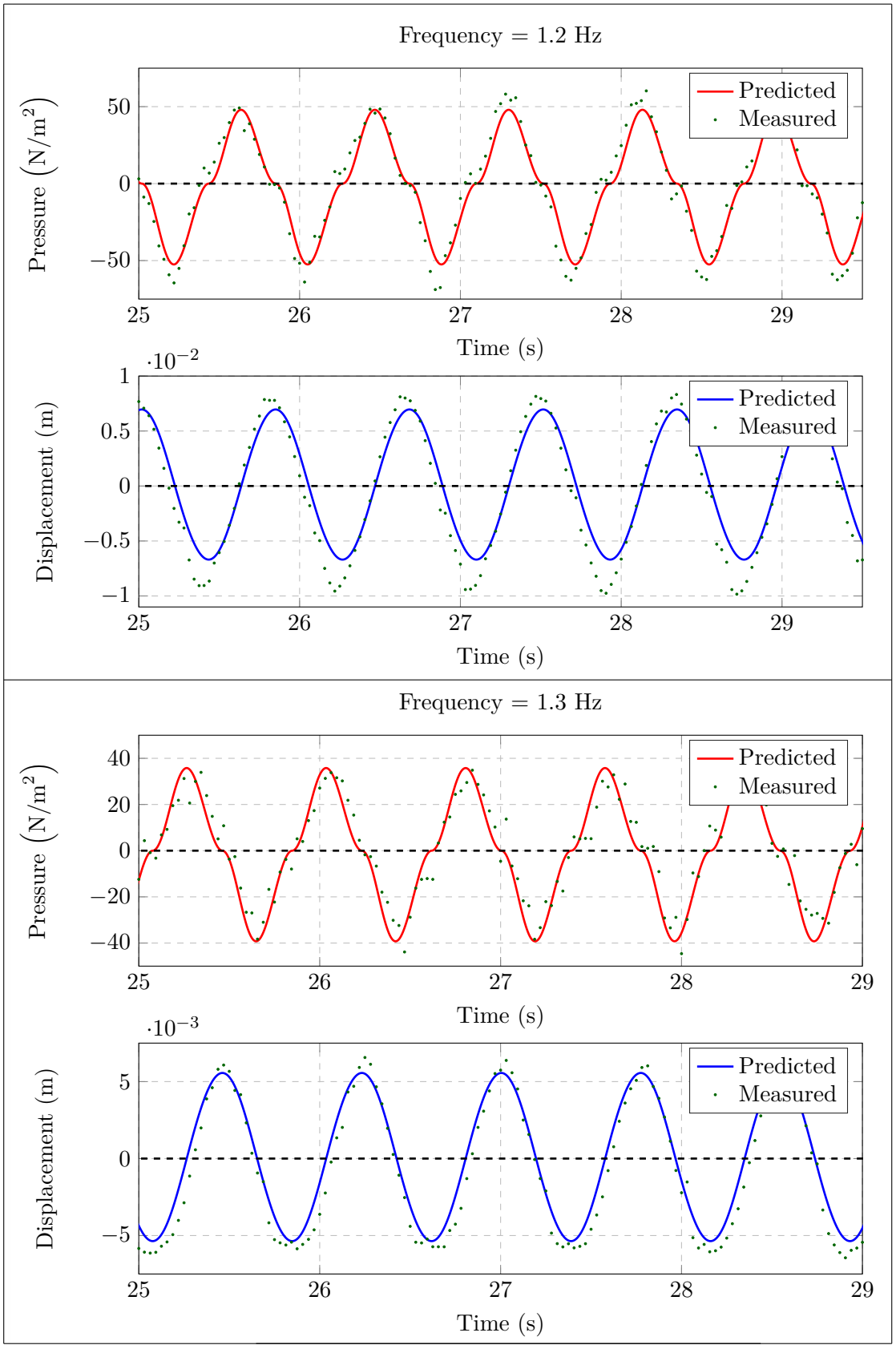

FIGURE 9.61: Comparison between the gauge pressure and the motion of the water column in the single-chamber OWC model obtained experimentally and as predicted by numerical model, with the adjustable orifice diameter set to 25 mm and subject to incident waves of 15 mm amplitude for wave frequencies of 1.2 Hz and 1.3 Hz.

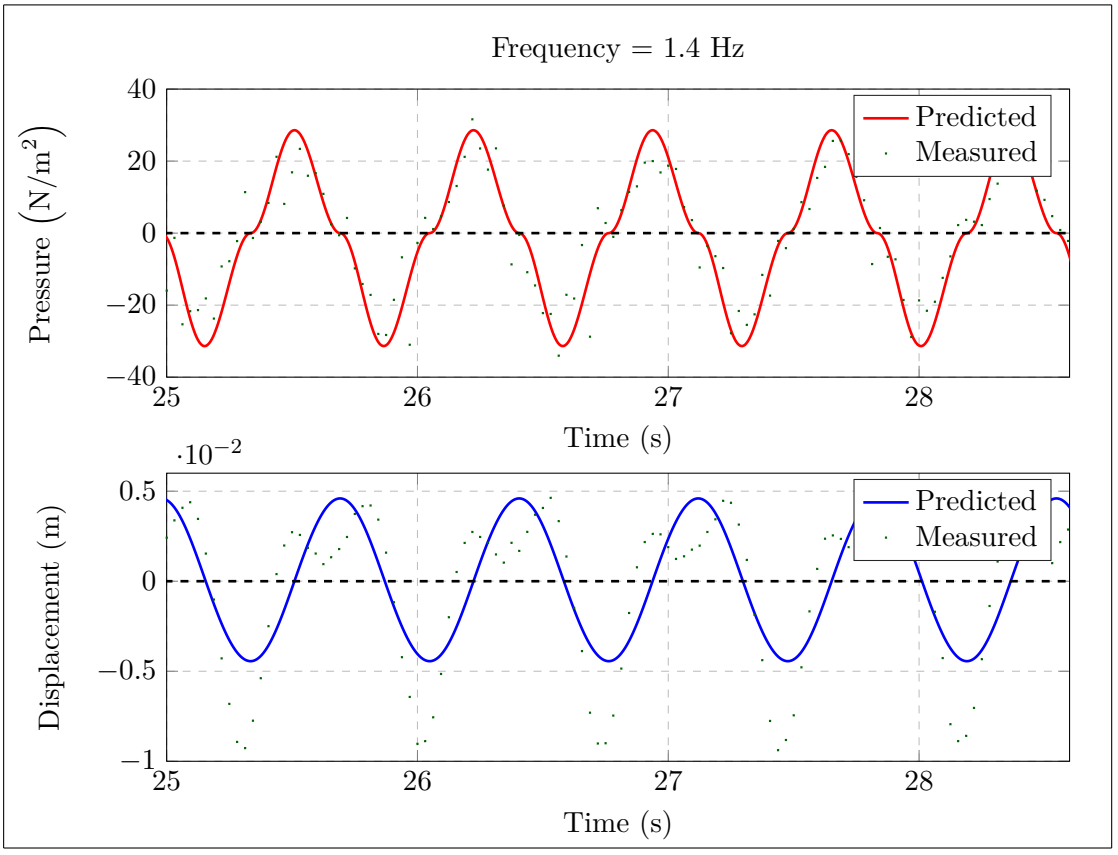

FIGURE 9.62: Comparison between the gauge pressure and the motion of the water column in the single-chamber OWC model obtained experimentally and as predicted by numerical model, with the adjustable orifice diameter set to 25 mm and subject to incident waves of 15 mm amplitude for a wave frequency of 1.4 Hz.

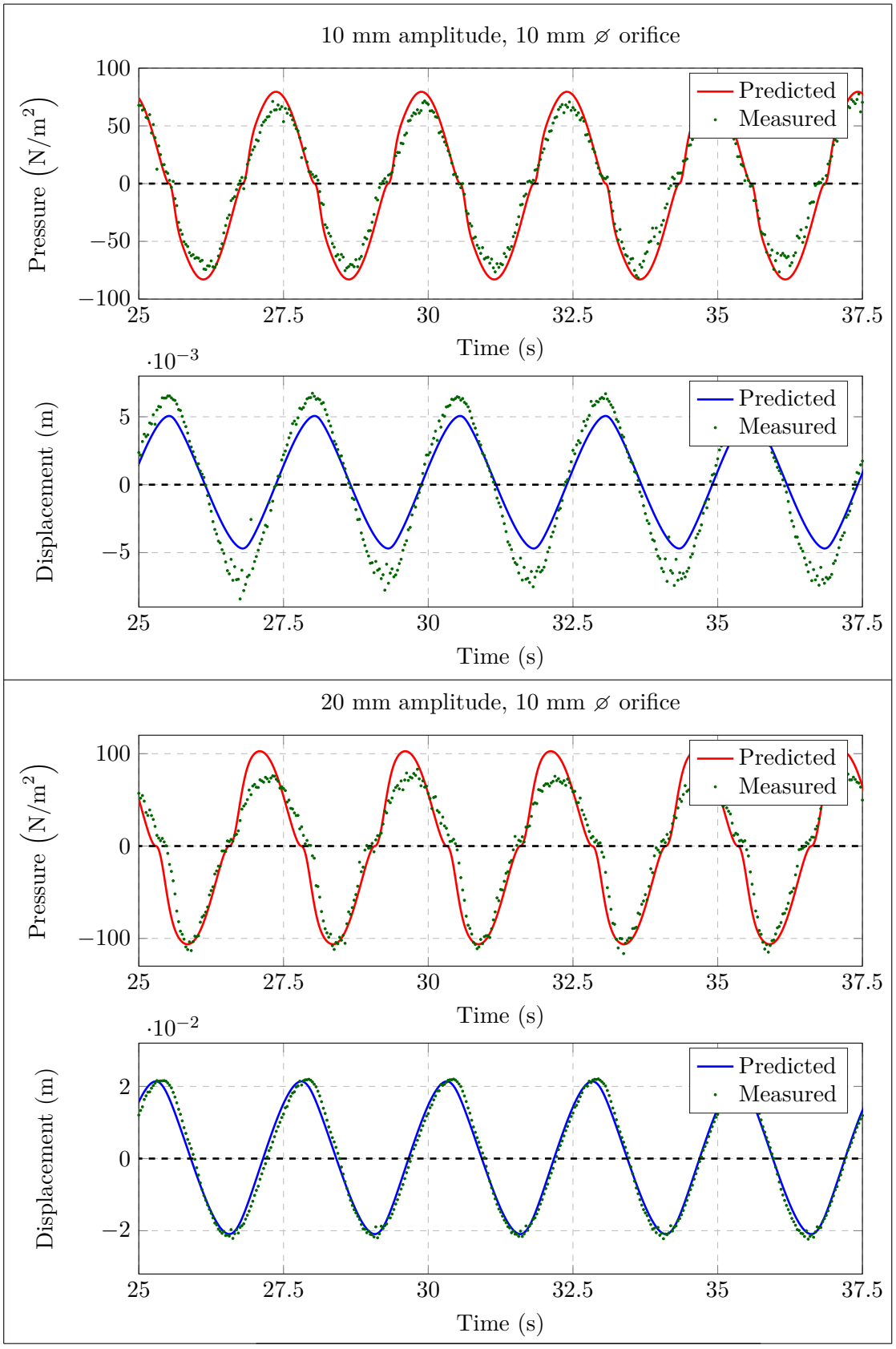

FIGURE 9.63: Comparison between the gauge pressure and the motion of the water column in the single-chamber OWC model obtained experimentally and as predicted by numerical model, with the adjustable orifice diameter set to 10 mm and subject to incident waves of a frequency of 0.4 Hz with amplitudes of 10 mm and 20 mm.

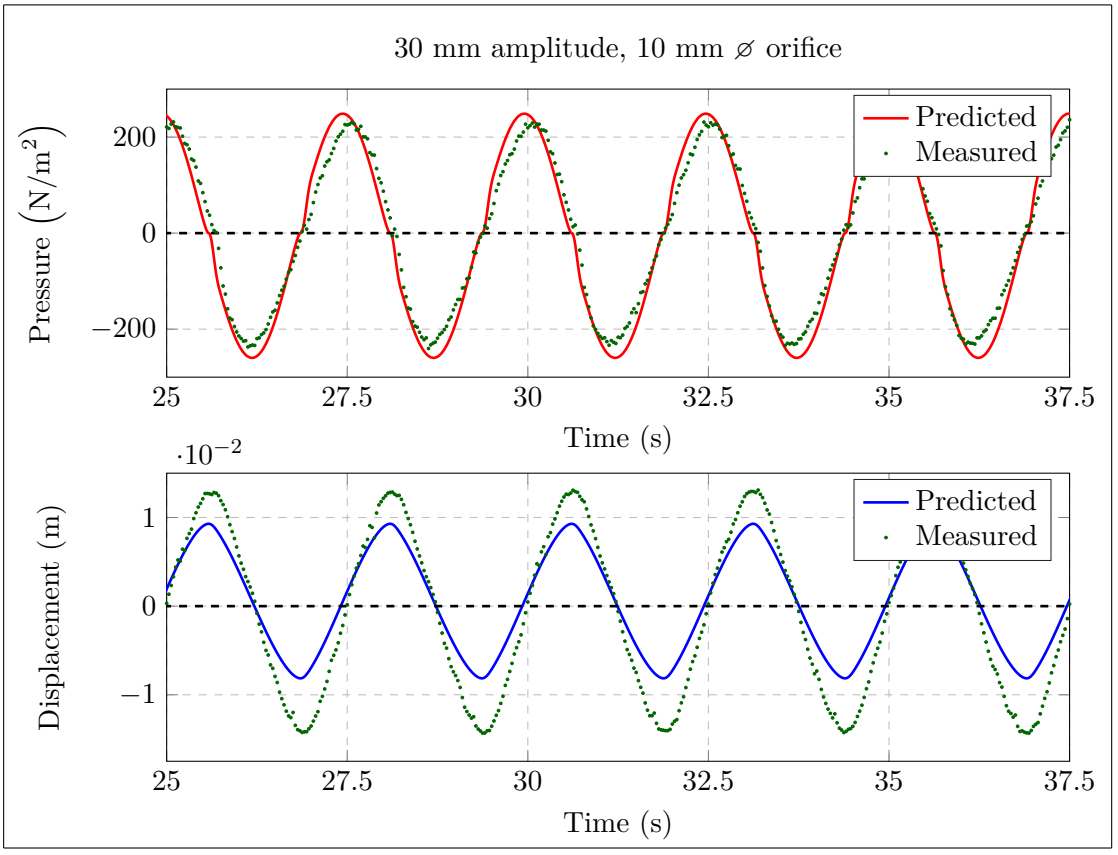

FIGURE 9.64: Comparison between the gauge pressure and the motion of the water column in the single-chamber OWC model obtained experimentally and as predicted by numerical model, with the adjustable orifice diameter set to 10 mm and subject to incident waves of a frequency of 0.4 Hz with amplitude of 30 mm.

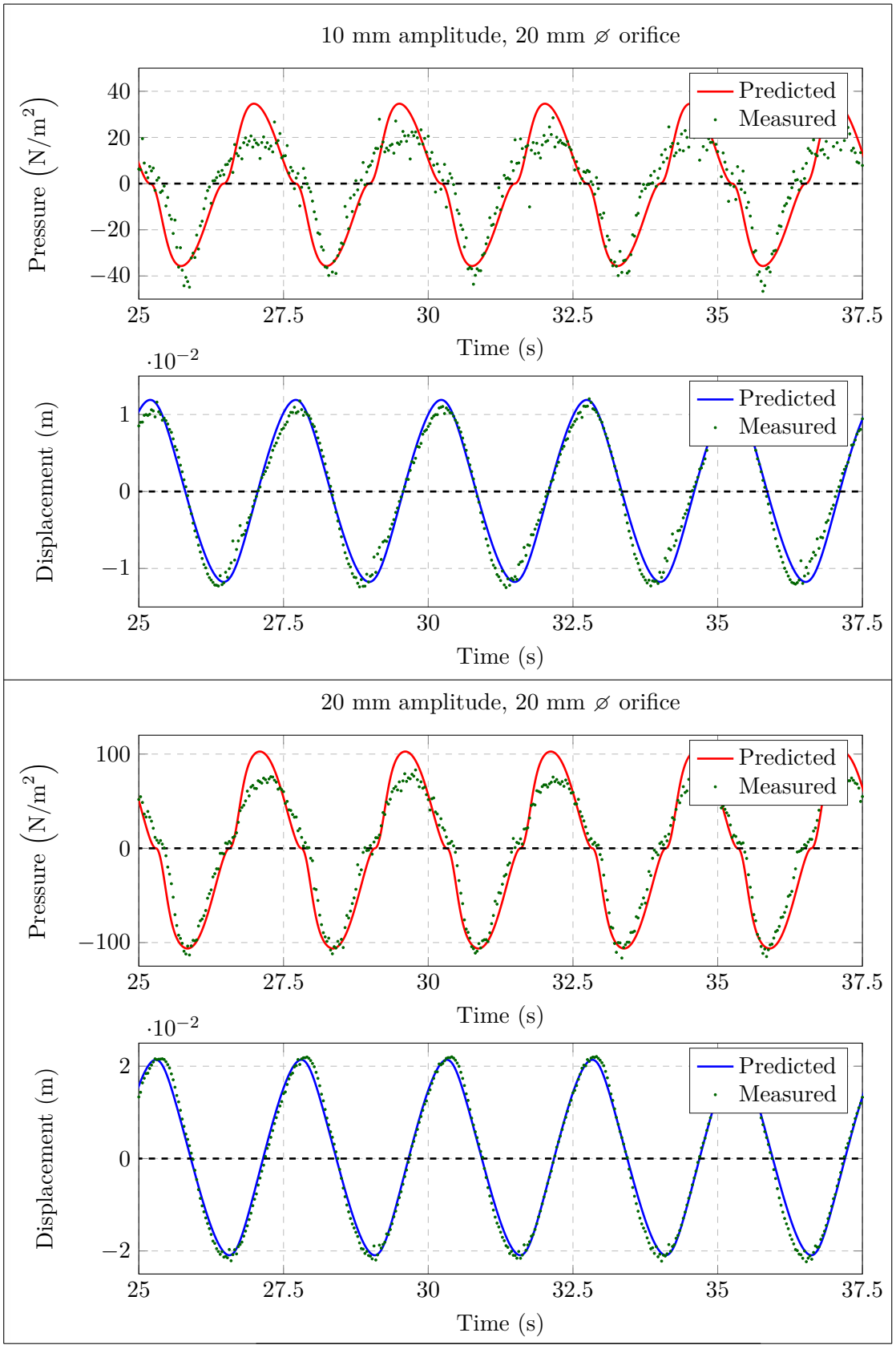

FIGURE 9.65: Comparison between the gauge pressure and the motion of the water column in the single-chamber OWC model obtained experimentally and as predicted by numerical model, with the adjustable orifice diameter set to 20 mm and subject to incident waves of a frequency of 0.4 Hz with amplitudes of 10 mm and 20 mm.

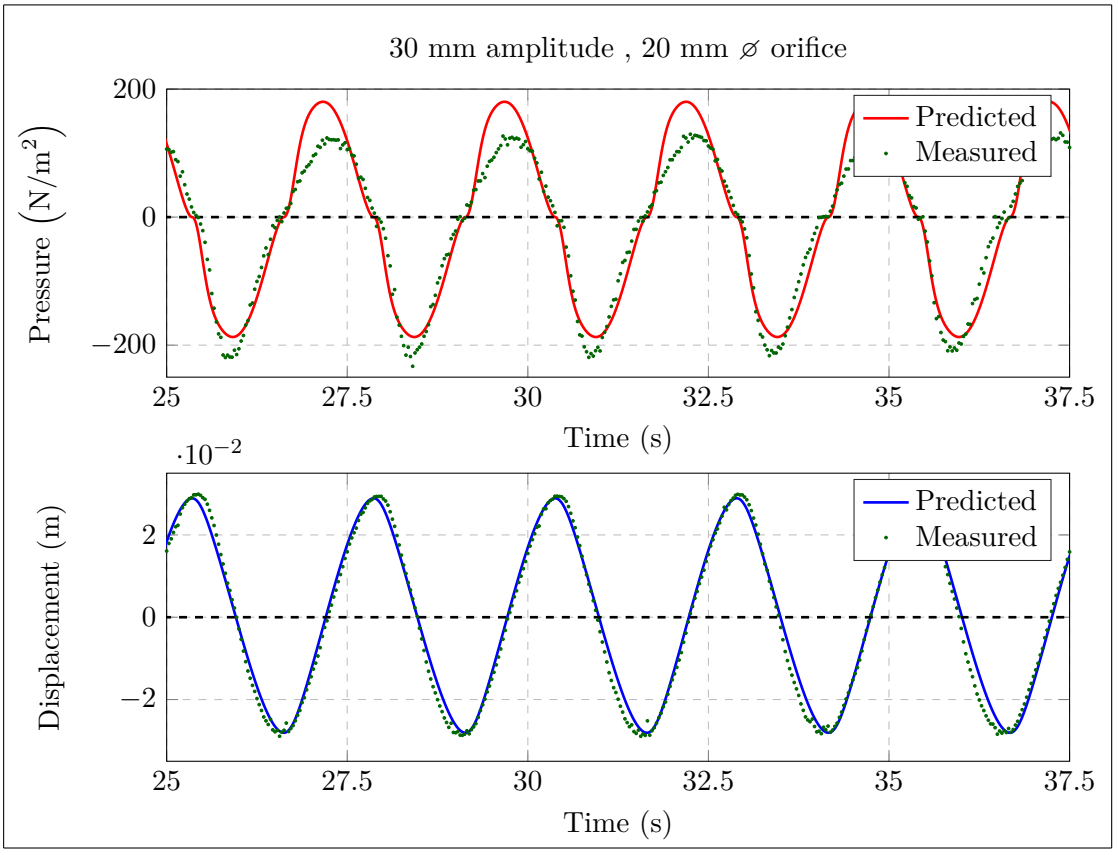

FIGURE 9.66: Comparison between the gauge pressure and the motion of the water column in the single-chamber OWC model obtained experimentally and as predicted by numerical model, with the adjustable orifice diameter set to 20 mm and subject to incident waves of a frequency of 0.4 Hz with amplitude of 30 mm.

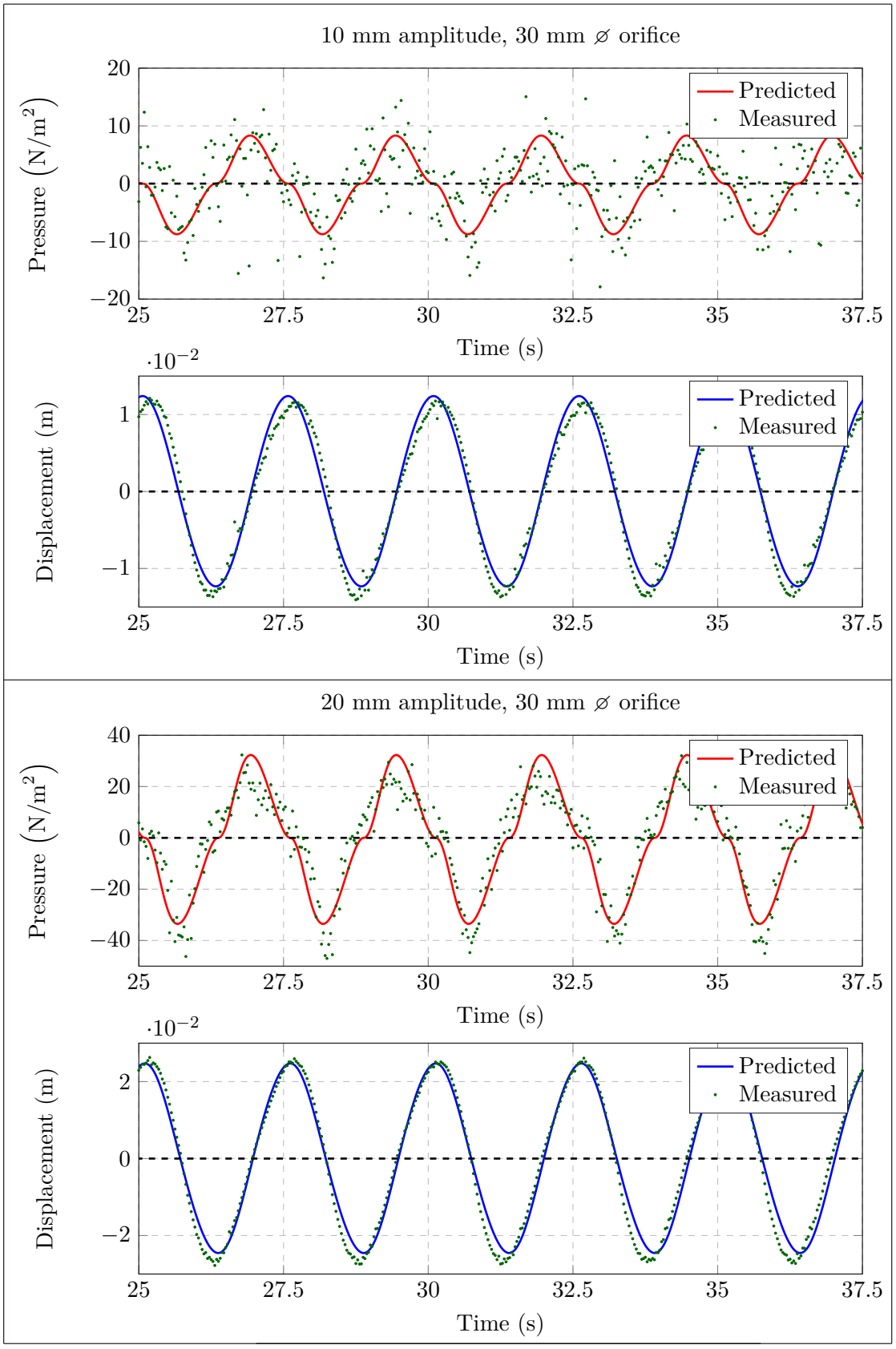

FIGURE 9.67: Comparison between the gauge pressure and the motion of the water column in the single-chamber OWC model obtained experimentally and as predicted by numerical model, with the adjustable orifice diameter set to 30 mm and subject to incident waves of a frequency of 0.4 Hz with amplitudes of 10 mm and 20 mm.

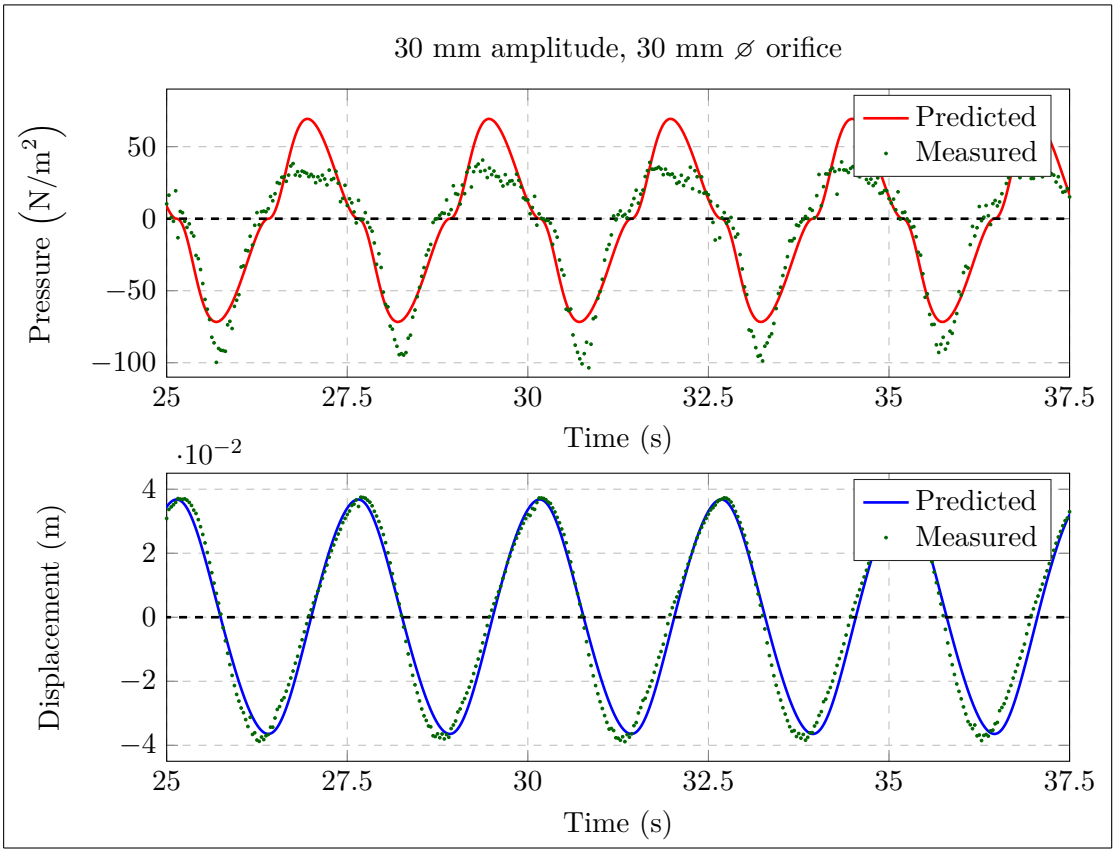

FIGURE 9.68: Comparison between the gauge pressure and the motion of the water column in the single-chamber OWC model obtained experimentally and as predicted by numerical model, with the adjustable orifice diameter set to 30 mm and subject to incident waves of a frequency of 0.4 Hz with amplitude of 30 mm.

9.3.1.3 Discussion of results for the single-chamber OWC model with an orifice

In this section, a number of observations on the predictions of the numerical model for the single-chamber OWC model with an orifice, and the corresponding results obtained from tank testing, are presented. It can be seen in Figure 9.57 to Figure 9.68 that, in general, a good fit has been obtained for the predictions for the gauge pressure and the water column displacement made by the numerical model and the results obtained from tank testing for the range of frequencies, wave amplitudes and orifice diameters modelled. One parameter upon which the numerical model depends is the coefficient of discharge, Cd_o, and the results presented in Section 9.3.1.2 would appear to justify the decision to use a singe value for Cd_o, obtained as described in Section 9.3.1.1, for all test conditions. The numerical model further depends on the quality of the hydrodynamic parameters obtained from WAMIT, as well as the reconstructed added

mass parameters as described in Section 5.4.3 and, based on the comparison between numerical and physical modelling results obtained to date, the numerical model has been quite successful. While the numerical results for the single-chamber OWC model presented herein were obtained with a non-linear hydrostatic stiffness, as described in Section 5.20, examination of the models has shown that the difference between such results, and the results obtained if a linear hydrostatic stiffness at stillwater conditions is used, is minimal.

At wave frequencies below 1.2 Hz, the numerical model tends to slightly over-predict the variation in the motion of the water column with time, while predicting the variation in gauge pressure within the chamber well. The results presented in Section 9.3.1.2 show that, for the longest wave to which the model was subjected, which occurs at 0.4 Hz, the magnitude of the maximum positive measured gauge pressure is greater than the magnitude of the maximum negative measured gauge pressure, an effect which is not captured by the model, and which is not apparent at higher wave frequencies in the test data.

For wave frequencies of 1.2 Hz to 1.4 Hz, the match between the predicted and measured displacement results is less good, see Figures 9.61 and 9.62, although the fit between the predicted and measured gauge pressure results is still quite good. This is due to the presence of sloshing modes which are not included in the numerical model. However, the fact that the fit between the two sets of gauge pressure results remains good suggests that the sloshing modes do not significantly effect power absorption at the frequencies tested herein.

The single-chamber OWC model was intended to represent one chamber of the 1:50 scale 32-OWC model. However, for a number of reasons, including the dimensions of the narrow tank and model construction methods, the single-chamber OWC model does not have exactly the same physical dimensions as one cell of the 32-OWC scale model. Thus, the natural frequency of the pumping mode of the water column in the single-chamber OWC model will not necessarily match the natural frequency of the pumping mode of the water column in one of the chambers which the 32-OWC scale model comprises. From the results in Figures 9.57 to 9.62, an increase in the amplitude of the displacement of the water column can be seen between 0.4 Hz and 0.5 Hz. The amplitude of the displacement remains almost constant up to 0.6 Hz before dropping for higher frequencies. This would

indicate that the natural frequency of the pumping mode of the water column in the single-chamber OWC model lies around a frequency of 0.5 Hz, and has been captured during the testing of the single-chamber OWC model. Finally, there is no clear reduction in the goodness of fit between the results from the numerical and the physical models, as the motion of the water column increases. Compare, for example, Figures 9.65 and 9.66, which illustrate the results with constant wave frequency and orifice diameter, but where the incident wave amplitude increases from 10 mm to 30 mm. This suggests that, for the range of incident wave amplitudes, incident wave frequencies and levels of applied damping used in this thesis, the velocity of the water column is such that non-linear viscous forces do not play a significant role in the behaviour of the system.

9.3.2 Single-chamber OWC model with air admittance valves

In the previous section, the results for the single-chamber OWC model with an orifice, obtained from tank testing, were compared to the predictions made by a numerical model. In this section, test results obtained for the single-chamber OWC model with two air admittance valves installed in place of the adjustable orifice are presented and compared to predictions obtained from the corresponding numerical model described in Chapter 5. It had been intended that the same air admittance valves as were used on the 32-OWC scale model would be employed during the testing of the single-chamber OWC model; however, the manufacturer had discontinued the production of the 'OsmaVent 40' valves used in the 32-OWC model. Two other air admittance valves were considered as replacements. The first replacement valve investigated was the 'W151' valve, manufactured by Multikwik Ltd., and the second was the 'HypAir Balance' valve, manufactured by Capricorn S.A. The advantage of the W151 valve is that the direction of air flow permitted by the valve may be easily reversed, thus both the discharge and the suction valves may be located outside the OWC chamber in the atmosphere. However, when the W151 valve was tested, it was found that the flow rate of air through the valve is significantly lower than that for the original OsmaVent 40 valve, and, upon inquiry, it was discovered that the rated flow for the W151 vavle is 0.7 l/s, compared to 7.6 l/s for the OsmaVent 40 valve. As a result, very little motion of the water column would take place when the W151 valves were installed. By contrast, the HypAir Balance valve has the same rated flow of 7.6 l/s as the OsmaVent 40 valve. When the single-chamber OWC model was tested with the HypAir Balance valve installed, significant motion of

the water column did take place, and the results presented in this section were obtained with the HypAir Balance valves installed. Note that it was necessary to install the discharge HypAir Balance valve inside the chamber on the inner surface of the top piece lid, (see Figure 8.12), and to ensure it did not become flooded during testing. The suction valve was located outside the chamber on the outer surface of the top piece lid.

9.3.2.1 Valve characterisation

Two parameters of the air admittance valves are required to implement the numerical model. The first parameter required is the relationship between the pressure drop across a valve, Δp, and the mass flow rate though the valve, $\dot{m}$, which can be considered analogous to the coefficient of discharge for an orifice. The second parameter which must be established is the pressure required to overcome valve stiction. Firstly, in order to determine the relationship between the pressure drop across a valve, Δp, and the volumetric flow rate though the valve, Q_{air}, consider Equations (9.9) and (9.10), which illustrate that the relationship between the mass flow rate and the pressure drop takes the same form as that for an orifice. Hence, the volumetric flow rate, Q_{air} through the valve is given by:

$$Q_{air} = Cd_v \frac{\sqrt{2\rho_{air}\,|\Delta p|}}{\rho_{air}} \times sign\,|\Delta p| \tag{9.22}$$

where Cd_v is a constant. Equation (9.22) is analogous to Equation (9.18) for the orifice case. For a valve, the constant, Cd_v, is given by $C_d L_g h_{max}$ in Equations (9.9) and (9.10), and can be measured experimentally following the same approach used to find Cd_o for the orifice, as described in Section 9.3.1.1. Cd_v for the air admittance valves was determined from a test with an incident wave of frequency 0.4 Hz and amplitude 30 mm. Note that, as was the case when Cd_o was determined for the orifice, a low frequency incident wave was used to determine Cd_v to minimise the effect on the water column displacement readings of sloshing in the chamber. For reasons relating to valve stiction, discussed below, the data obtained during testing on the model with air admittance valves was sampled at 1 kHz. Data was filtered using a low pass filter, and the results of plotting the volumetric airflow rate, based on the velocity of the water column, against $\frac{\sqrt{2\rho_{air}\,|\Delta p|}}{\rho_{air}} \times sign\,|\Delta p|$ is shown in Figure 9.69. A line has been fitted to the data, and

the slope of this line is the value used for Cd_v in the numerical model of the single-OWC with air admittance valves.

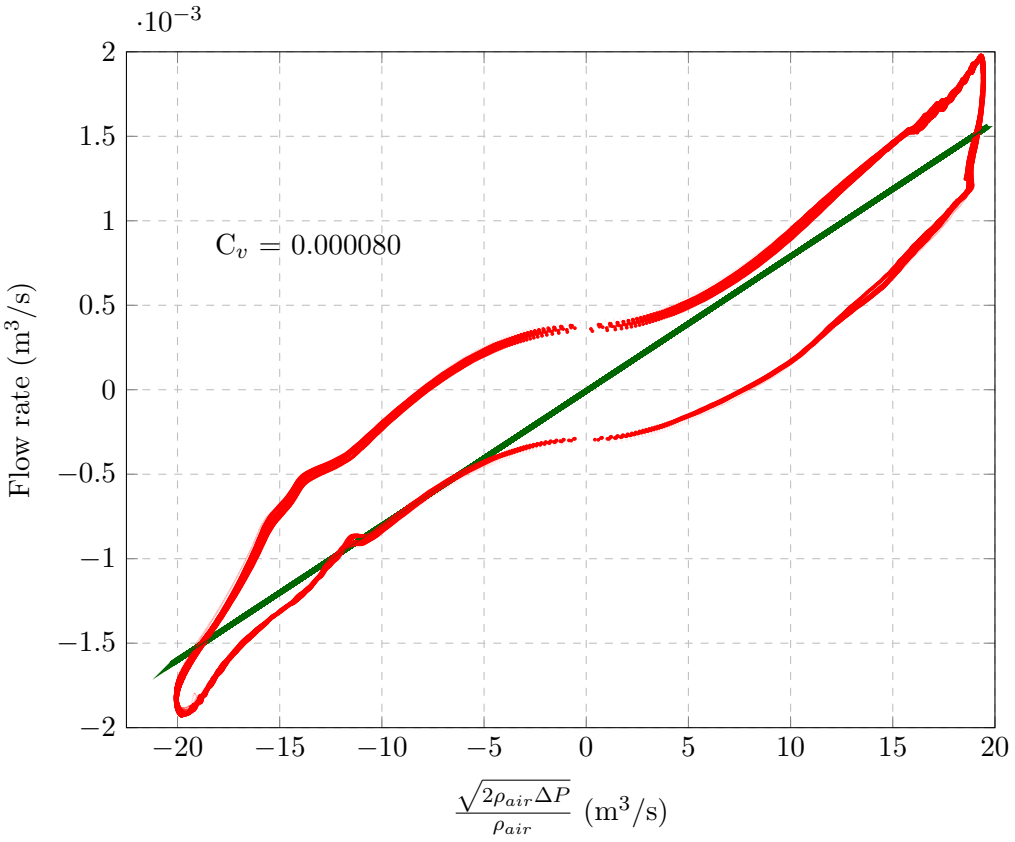

FIGURE 9.69: Plot of airflow through the air admittance valves calculated using the Expression (9.20) based on the velocity of the water column vs. $\frac{\sqrt{2\rho_{air}\,|\Delta p|}}{\rho_{air}} \times sign\,|\Delta p|$, for an incident wave of 30 mm and a frequency of 0.4 Hz using filtered pressure and displacement signals.

The slope of the fitted line is equal to 0.000080, and this value is used for $C_d L_g h_{max}$ in the numerical model of the single-chamber OWC model with air admittance valves. The second parameter of the air admittance valves which must be established before the numerical model of the single-chamber OWC model with air admittance valves may be implemented is the pressure required to overcome valve stiction. Data was sampled at 1 kHz during the testing of the model with air admittance valves. When the first sets of data recorded at 32 Hhz during this round of testing were initially examined, the time traces of the pressure signal demonstrated some unexpected behaviour. Short-lived, sudden increases in pressure were observed when the gauge pressure in the OWC chamber was increased from a negative value to a positive value and, similarly, a rapid, short-lived, decrease in pressure was observed within the air chamber when the gauge

pressure was decreased from a positive value to a negative value, over the course of a single wave cycle. The dramatic increases and decreases in pressure took place over very short time periods, of the order of hundredths of a second. The effect was not observed for every wave cycle, when data was sampled at 32 Hz. Further tests confirmed that a sampling rate of 32 Hz was sufficiently low that entire instances of the short-lived high- or low-pressure events could take place between samples and, as a result, the events could go entirely unrecorded. The sampling period was increased to 1 kHz for all subsequent testing, and it was seen that these events occurred for every wave period. The cause of the rapid increases and decreases in gauge pressure appears to be what is termed 'valve stiction' [187]. Valve stiction occurs when the valve member (which is a movable obstruction inside the stationary body that restricts flow through the valve) bonds or 'sticks' to the seat of the valve. As a result, more pressure is required to open a valve to overcome the bond than is required to keep the valve open. Figure 9.70 illustrates an example of the time trace of the pressure signal within the OWC chamber showing the effect of stiction.

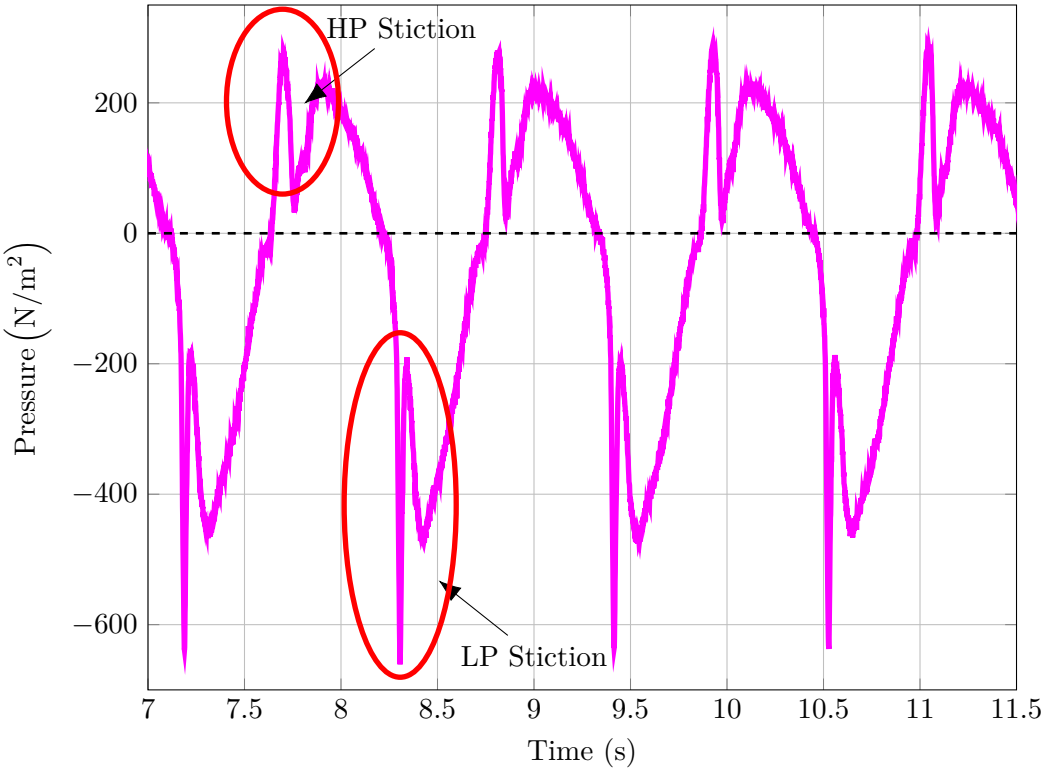

FIGURE 9.70: Time series of the variation in gauge pressure in the single-chamber OWC model with air admittance valves illustrating the short-lived, high-and low-pressure events which arise due to valve stiction.

The pressure required to overcome valve stiction is referred to in the current work as the threshold pressure. It can be seen in Figure 9.70 that, at approximately 7.7 s, a rapid increase in pressure occurs as the gauge pressure in the chamber transitions from a positive to a negative value as the stiction in the discharge valve is overcome. This rapid increase in pressure is repeated every time the gauge pressure transitions from a negative to a positive value, as can be seen at approximately 8.8 s, 9.9 s and 11.1 s. A similar effect can be seen at approximately 8.85 s, 9.45 s and 10.05 s as the chamber gauge pressure transitions from positive to negative values as the stiction in the suction valve is overcome. However, the drop in gauge pressure required to overcome the stiction in the suction valve would, at first glance, appear significantly greater than the increase required to overcome the stiction in the discharge valve. This difference is apparent for all wave conditions. However, a number of observations would call such a conclusion into question. Firstly, the large difference between the pressure drop required to overcome the stiction between the two valves occurs regardless of which valve type, or which the valve arrangement (as described in Section 9.3.2) is used. Secondly, the maximum pressure drop across the suction valve varies for different tests with different incident wave conditions, ranging from approximately 420 N/m^2 to 640 N/m^2. While it is possible that the pressure within the chamber may continue to drop after the suction valve opens, leading to a recorded maximum pressure drop greater than that required to overcome stiction, the rate of this change would alter once the valve opened. Finally, and most conclusively, the maximum magnitude of the negative gauge pressure which appears to be required to overcome the stiction in the suction valve in Figure 9.70 is of the order of 550 N/m^2 to 600 N/m^2. This is larger than the magnitude of the negative gauge pressure experienced in the chamber when the model is entirely sealed from atmosphere (see Chapter 11). Thus, it seems likely that the large pressure drop which is recorded as the gauge pressure transitions from positive to negative may be either the result of a localised pressure drop within the chamber not captured by the thermodynamic model, or an artefact of the pressure sensor itself. A test which could be performed in future to identify if the effect is an artefact of the sensor would be to simply reverse the orientation of the sensor and repeat the test. Under such conditions, the sign of the gauge pressure recorded will be the opposite of that actually occurring in the chamber. If the form of the pressure time series then becomes the mirror image about the time axis of the pressure time series shown in Figure 9.70, i.e., the recorded positive pressure spikes are now significantly larger in magnitude than the recorded negative

pressure spikes, this would suggest the valves are responsible for the difference in the magnitudes. If the form of the pressure time series is not mirrored about the time axis, this would suggest that an artefact of the pressure sensor is responsible for the effect.

A further effect of valve stiction is that, for lower amplitude waves, which produce lower gauge pressures within the OWC chamber, the valves would fail to open reliably, and, in some cases, fail to open entirely as the gauge pressure is never high enough (or low enough) to overcome valve stiction. For all valve arrangements where were fully tested, stiction would prevent the valve reliably opening for incident wave amplitudes of less than 20 mm for all wave frequencies tested. Thus it is clear that valve stiction would reduce power absorbed by a device in low energy sea states and must be considered in the design of any proposed WEC device which is to make use of air admittance valves. In order to incorporate the effect of valve stiction in the numerical model presented in the current work, it is first assumed that the threshold pressures for the suction and discharge valves are equal in magnitude. Next, the logical states under which the model may operate are identified, and tabulated as shown in Table 9.6. In Table 9.6, the valve threshold pressure is termed 'pthresh', and the gauge pressure within the OWC chamber is termed 'Δp'. The terms 'flag 1 in' and 'flag 2 in' refer to the open/closed status of the suction and discharge valves at the end of the previous time step, a value of '1' corresponding to an open valve, and a value of '0' corresponding to a closed valve. Similarly, 'flag 1 out' and 'flag 2 out' refer to the open/closed status of the suction and discharge valves at the end of the current time step, again, a value of '1' corresponds to an open valve, and a value of '0' corresponds to a closed valve. For example, logic state 17 states that, if the gauge pressure in the chamber is positive, while at the same time less than the discharge threshold pressure, and the discharge valve is currently closed, no air flows out of, or into the chamber during the proceeding time step, and both valves remain closed. Logic state 21 states that, if the gauge pressure in the chamber is positive and the threshold pressure has been reached, the discharge valve will open if closed, air will flow from the chamber to atmosphere during the time step, and the discharge valve will remain open. Logic state 19, which states that if the gauge pressure in the chamber is positive, while at the same time less than the discharge threshold pressure, but the discharge valve is currently open, air will flow from the chamber to atmosphere during the time step, and the valve will remain open. Note that a number of logic states that cannot arise physically are not included in Table 9.6; for example, it is not possible that

the gauge pressure in the chamber be simultaneously greater than the threshold pressure to open the discharge valve while at the same time being less than the threshold pressure to open the suction valve.

Logic State	Δp	Δp:pthresh	flag 1 in	flag 2 in	$\dot{m}$	flag 1 out	flag 2 out
1	$\Delta p = 0$	-pthresh $\leq \Delta p \leq$ pthresh	0	0	0	0	0
2	$\Delta p = 0$	-pthresh $\leq \Delta p \leq$ pthresh	1	0	0	0	0
3	$\Delta p = 0$	-pthresh $\leq \Delta p \leq$ pthresh	0	1	0	0	0
4	$\Delta p = 0$	-pthresh $\leq \Delta p \leq$ pthresh	1	1	0	0	0
5	$\Delta p < 0$	$\Delta p >$ -pthresh	0	0	0	0	0
6	$\Delta p < 0$	$\Delta p >$ -pthresh	1	0	0	0	0
7	$\Delta p < 0$	$\Delta p >$ -pthresh	0	1	$C_v\sqrt{2\rho\Delta p}$	0	1
8	$\Delta p < 0$	$\Delta p >$ -pthresh	1	1	$C_v\sqrt{2\rho\Delta p}$	0	1
9	$\Delta p < 0$	$\Delta p =$ -pthresh	0	0	$C_v\sqrt{2\rho\Delta p}$	0	1
10	$\Delta p < 0$	$\Delta p =$ -pthresh	1	0	$C_v\sqrt{2\rho\Delta p}$	0	1
11	$\Delta p < 0$	$\Delta p =$ -pthresh	0	1	$C_v\sqrt{2\rho\Delta p}$	0	1
12	$\Delta p < 0$	$\Delta p =$ -pthresh	1	1	$C_v\sqrt{2\rho\Delta p}$	0	1
13	$\Delta p < 0$	$\Delta p <$ -pthresh	0	0	$C_v\sqrt{2\rho\Delta p}$	0	1
14	$\Delta p < 0$	$\Delta p <$ -pthresh	1	0	$C_v\sqrt{2\rho\Delta p}$	0	1
15	$\Delta p < 0$	$\Delta p <$ -pthresh	0	1	$C_v\sqrt{2\rho\Delta p}$	0	1
16	$\Delta p < 0$	$\Delta p <$ -pthresh	1	1	$C_v\sqrt{2\rho\Delta p}$	0	1
17	$\Delta p > 0$	$\Delta p <$ pthresh	0	0	0	0	0
18	$\Delta p > 0$	$\Delta p <$ pthresh	0	1	0	0	0
19	$\Delta p > 0$	$\Delta p <$ pthresh	1	0	$-C_v\sqrt{2\rho\Delta p}$	1	0
20	$\Delta p > 0$	$\Delta p <$ pthresh	1	1	$-C_v\sqrt{2\rho\Delta p}$	1	0
21	$\Delta p > 0$	$\Delta p =$ pthresh	0	0	$-C_v\sqrt{2\rho\Delta p}$	1	0
22	$\Delta p > 0$	$\Delta p =$ pthresh	1	0	$-C_v\sqrt{2\rho\Delta p}$	1	0
23	$\Delta p > 0$	$\Delta p =$ pthresh	0	1	$-C_v\sqrt{2\rho\Delta p}$	1	0
24	$\Delta p > 0$	$\Delta p =$ pthresh	1	1	$-C_v\sqrt{2\rho\Delta p}$	1	0
25	$\Delta p > 0$	$\Delta p >$ pthresh	0	0	$-C_v\sqrt{2\rho\Delta p}$	1	0
26	$\Delta p > 0$	$\Delta p >$ pthresh	1	0	$-C_v\sqrt{2\rho\Delta p}$	1	0
27	$\Delta p > 0$	$\Delta p >$ pthresh	0	1	$-C_v\sqrt{2\rho\Delta p}$	1	0
28	$\Delta p > 0$	$\Delta p >$ pthresh	1	1	$-C_v\sqrt{2\rho\Delta p}$	1	0

TABLE 9.6: Possible logic states of the single-chamber OWC model with air admittance valves which exhibit stiction.

It is not necessary to create 28 separate routines in the numerical model of the single-chamber OWC model with air admittance valves to capture each condition presented in Table 9.6. Numerous logic states with common output conditions may be grouped

together if a suitable and unique set of input conditions may be found to identify such states. For example, the output flag conditions of states 1 to 4 match, and the input conditions for states 1 to 4 are met when $\Delta p = 0$. The condition that $\Delta p = 0$ further excludes states 5 to 28. A total of 7 logic states were identified to cover all the possible conditions presented in Table 9.6, and the reduced set of logic states are presented in Table 9.7.

Logic states	Input conditions	$\dot{m}$	flag 1 out	flag 2 out
1 - 4	Δp = 0	0	0	0
5 - 6	Δp <0, Δp >-pthresh, flag 2 = 0	0	0	0
7 - 8	Δp <0, Δp >-pthresh, flag 2 = 1	$C_v\sqrt{2\rho\Delta p}$	0	1
9 - 16	Δp $\leq$-pthresh	$C_v\sqrt{2\rho\Delta p}$	0	1
17 - 18	Δp <0, Δp <pthresh, flag 1 = 0	0	0	0
19 - 20	Δp <0, Δp <pthresh, flag 1 = 1	$-C_v\sqrt{2\rho\Delta p}$	1	0
21 - 28	Δp $\geq$pthresh	$-C_v\sqrt{2\rho\Delta p}$	1	0

TABLE 9.7: Reduced set of logic states of the single-chamber OWC model with air admittance valves which exhibit stiction.

In order to illustrate the predicted effect of the air admittance valves with stiction, as implemented using the logic states described in Table 9.7, Figure 9.71 presents a comparison of the predicted and measured variation in gauge pressure within the single-chamber OWC model with air admittance valves. The magnified section shows one instance of the discharge valve opening as the gauge pressure within the chamber increases. Considering first the measured gauge pressure (shown in green), the rapid increase in the gauge pressure in the chamber, until the threshold pressure is reached, can be seen at approximately 29.3 s. Once the threshold pressure has been reached, the chamber pressure drops for a short time as air flows from the chamber to atmosphere. However, a second spike in the gauge pressure occurs at approximately 29.45 s, when the decrease in pressure due to the mass flow of air out of the chamber is less than the increase in pressure due to the action of the incident wave. After the second spike, the form of the measured gauge pressure curve returns to one similar to the gauge pressure curve that would be expected for an OWC model with an orifice, see, for example, Figure 9.57. This pattern of gauge pressure spikes is repeated throughout the pressure time series whenever the discharge valve opens. Consider now the predicted gauge pressure (shown

in red). As can be seen in Figure 9.71, the variation in the predicted gauge pressure from the numerical model, which includes the relatively simplistic valve modelling described herein, reflects the phenomenon of valve stiction as occurs in the measured data. Two spikes also occur in the predicted gauge pressure, albeit over a somewhat faster time frame than occurs for the measured data.

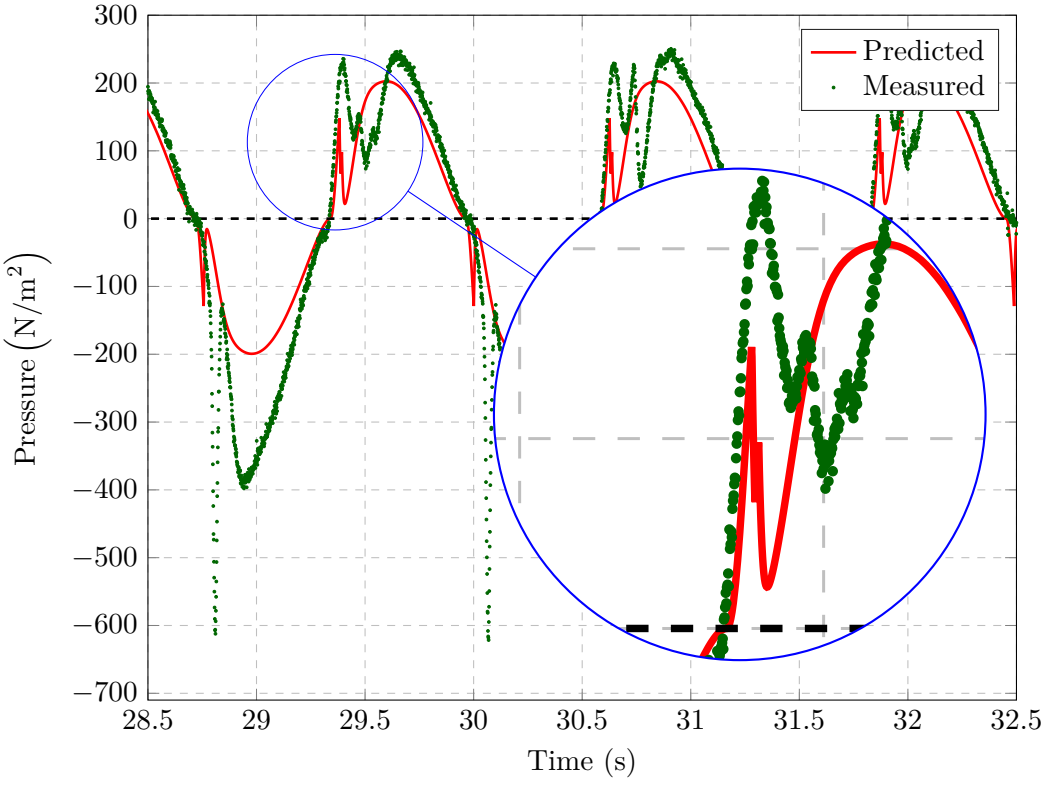

FIGURE 9.71: Time series of the variation in gauge pressure in the single-chamber OWC model with air admittance valves, illustrating the short-lived, high-pressure events which arise due to stiction of the discharge valve. Note the comparison between the measured and predicted pressure behaviour.

9.3.2.2 Comparison between results from tank testing and numerical predictions for the single-chamber OWC with air admitance valves

In this section, the results from narrow tank testing of the single-chamber OWC model with air admittance valves, as described in Section 6.4.3, are compared to the predictions made by the numerical model, presented in Section 5.3.2. Figures 9.72 to 9.77 show the comparison between the predicted results and the test results for the complete range of frequencies tested, when the single-chamber OWC model with air admittance valves was subject to waves of 30 mm amplitude.

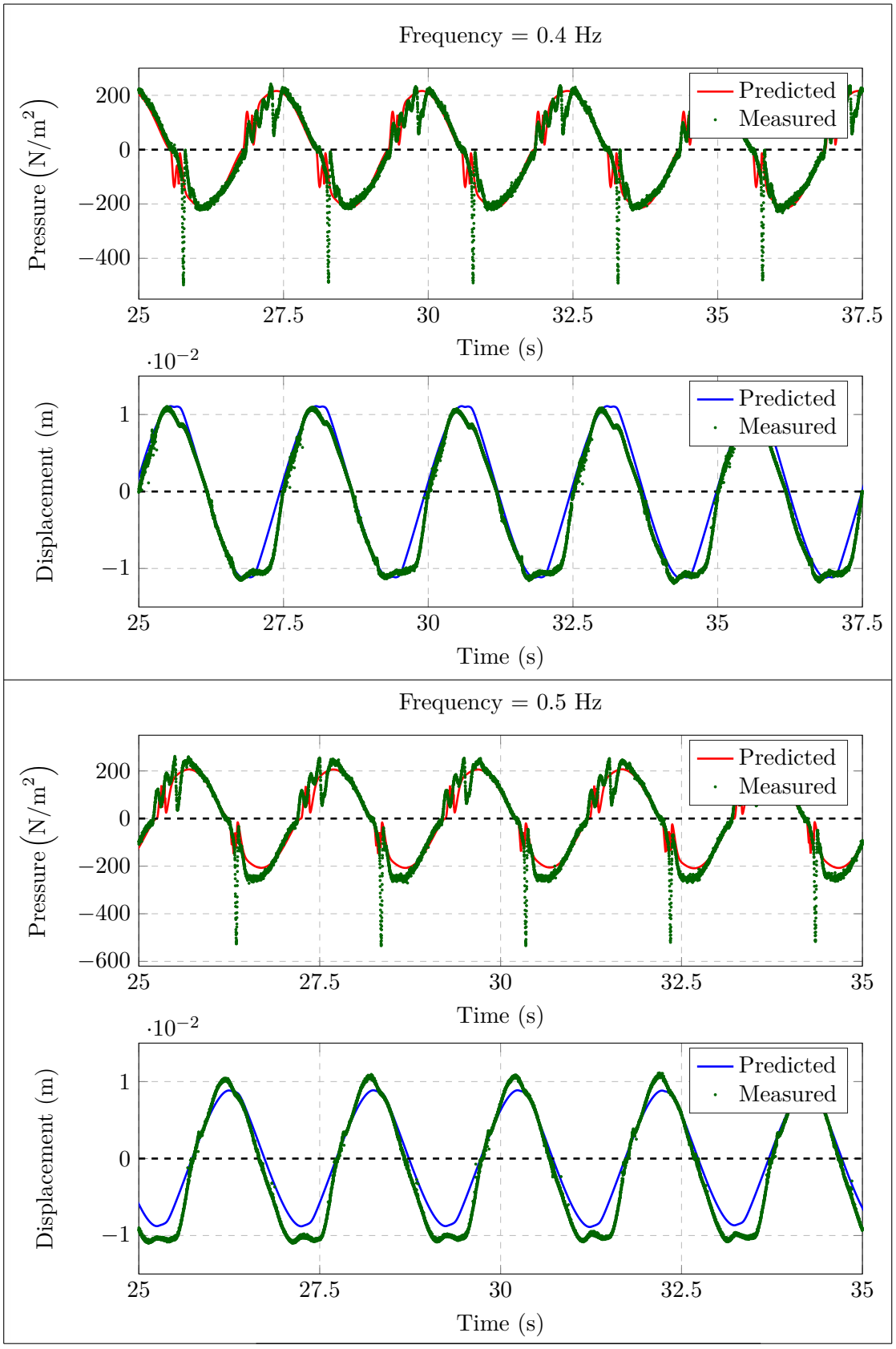

FIGURE 9.72: Comparison between the gauge pressure and the motion of the water column in the single-chamber OWC model with air admittance valves obtained experimentally and as predicted by numerical model, subject to incident waves of 30 mm amplitude for wave frequencies of 0.4 Hz and 0.5 Hz.

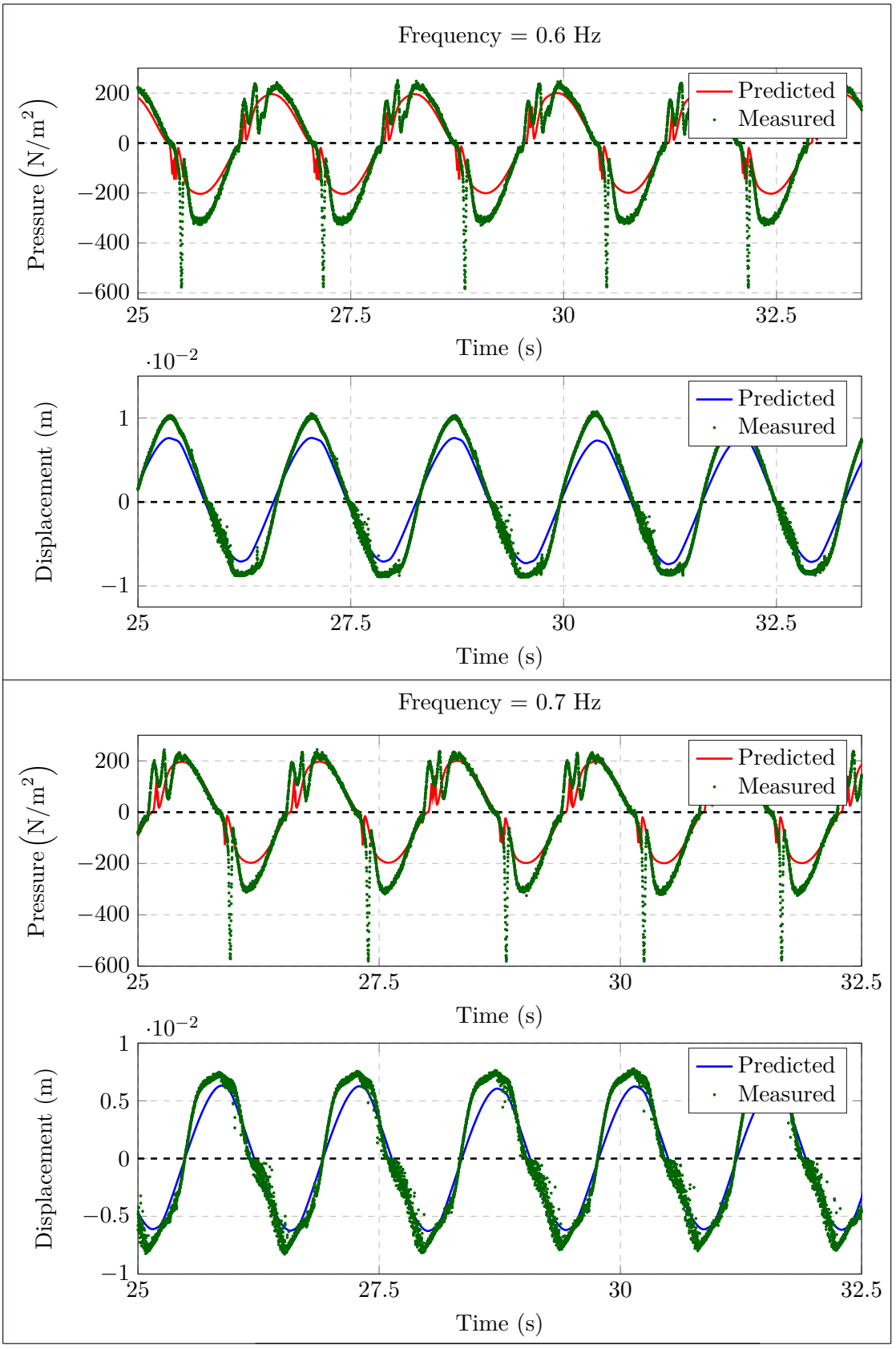

FIGURE 9.73: Comparison between the gauge pressure and the motion of the water column in the single-chamber OWC model with air admittance valves obtained experimentally and as predicted by numerical model, subject to incident waves of 30 mm amplitude for wave frequencies of 0.6 Hz and 0.7 Hz.

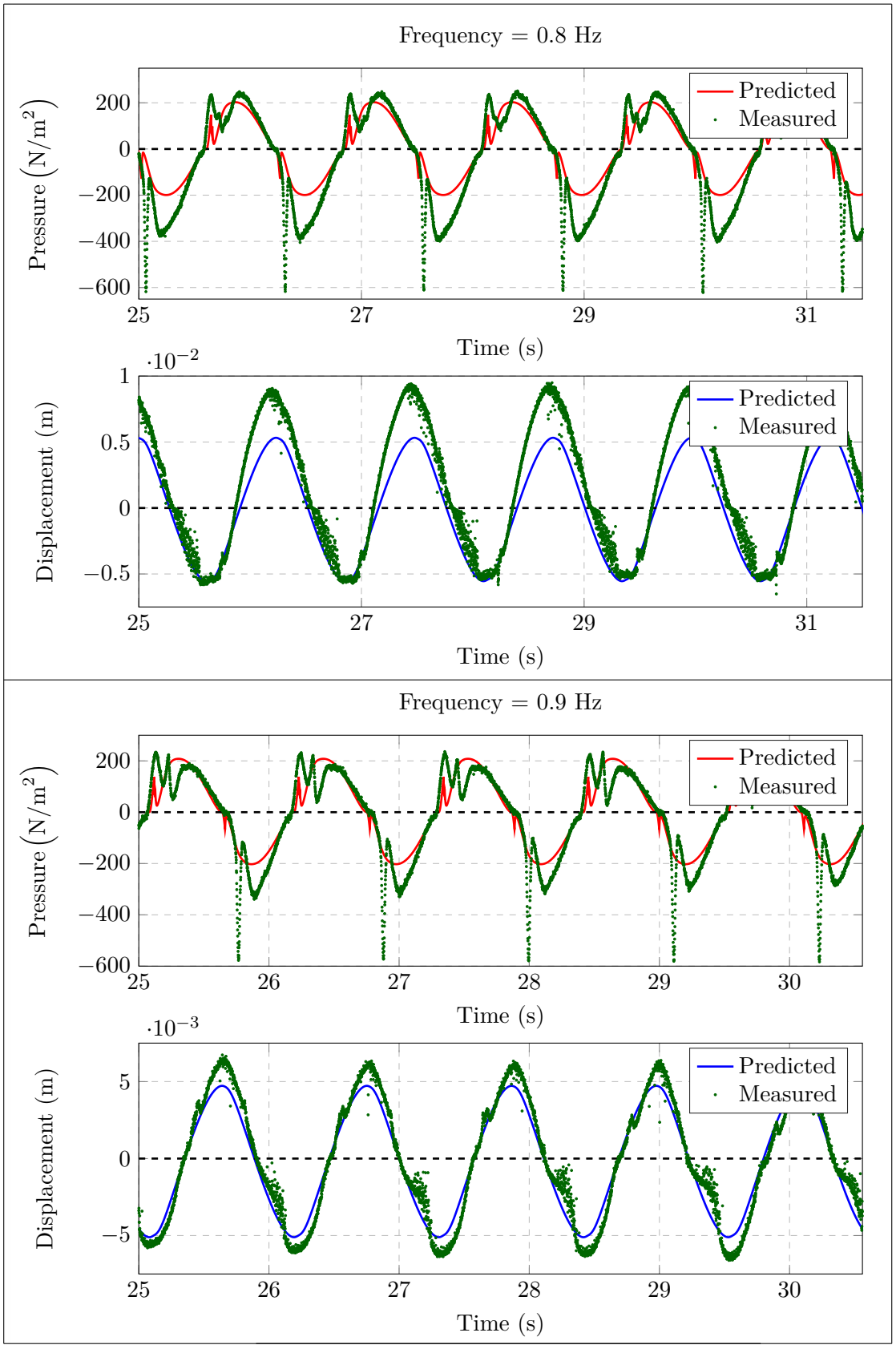

FIGURE 9.74: Comparison between the gauge pressure and the motion of the water column in the single-chamber OWC model with air admittance valves obtained experimentally and as predicted by numerical model, subject to incident waves of 30 mm amplitude for wave frequencies of 0.8 Hz and 0.9 Hz.

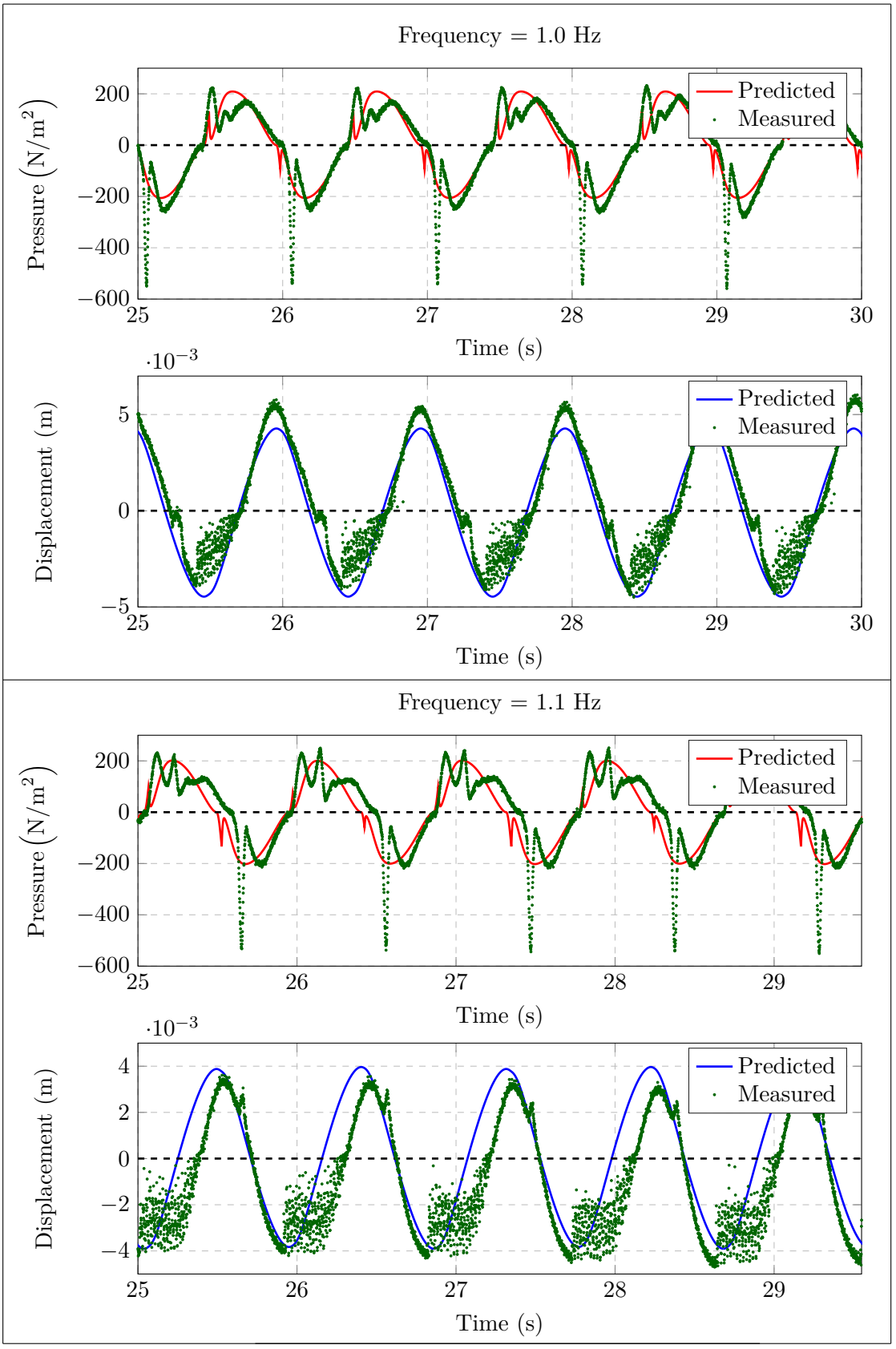

FIGURE 9.75: Comparison between the gauge pressure and the motion of the water column in the single-chamber OWC model with air admittance valves obtained experimentally and as predicted by numerical model, subject to incident waves of 30 mm amplitude for wave frequencies of 1.0 Hz and 1.1 Hz.

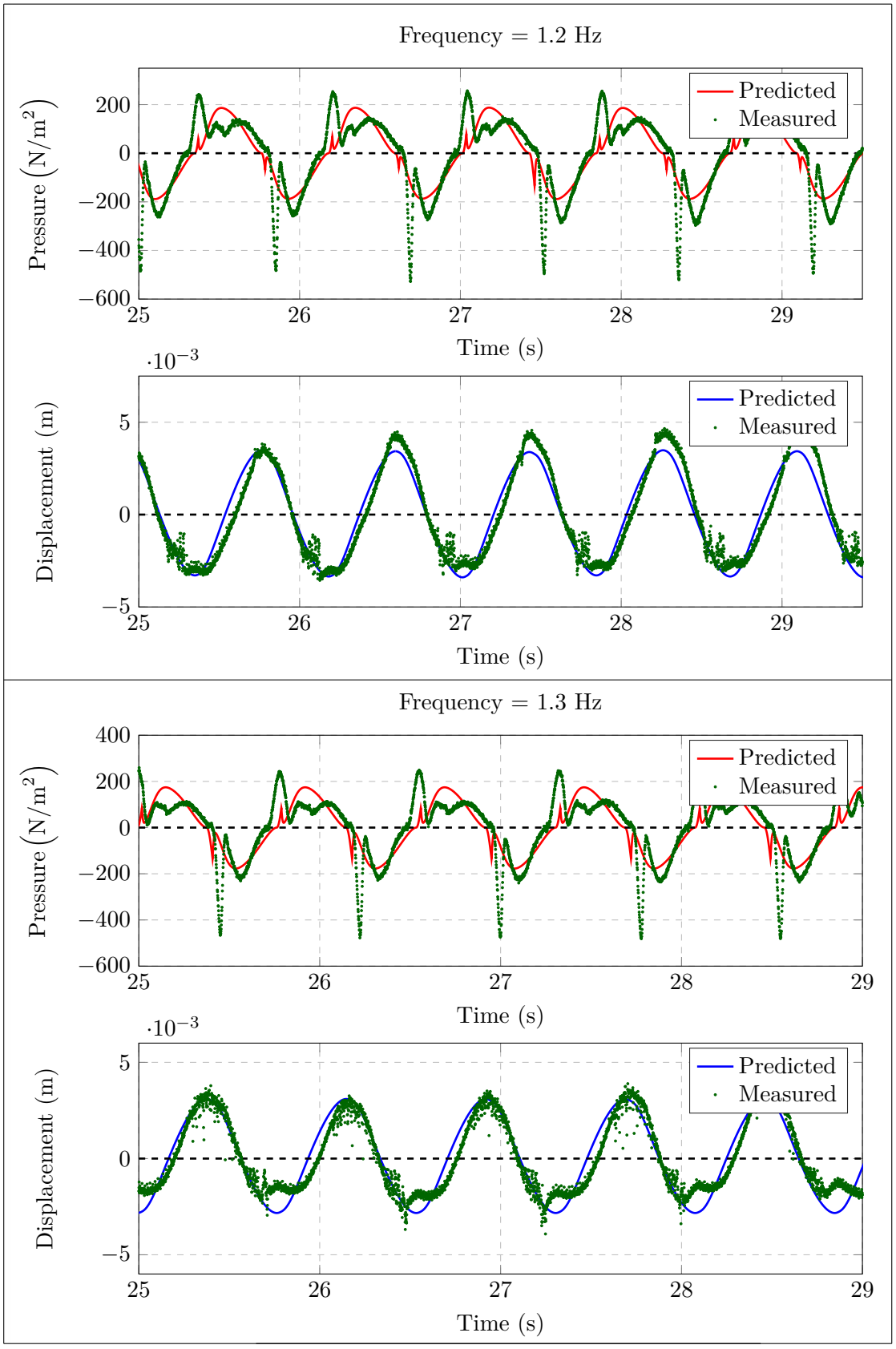

FIGURE 9.76: Comparison between the gauge pressure and the motion of the water column in the single-chamber OWC model with air admittance valves obtained experimentally and as predicted by numerical model, subject to incident waves of 30 mm amplitude for wave frequencies of 1.2 Hz and 1.3 Hz.

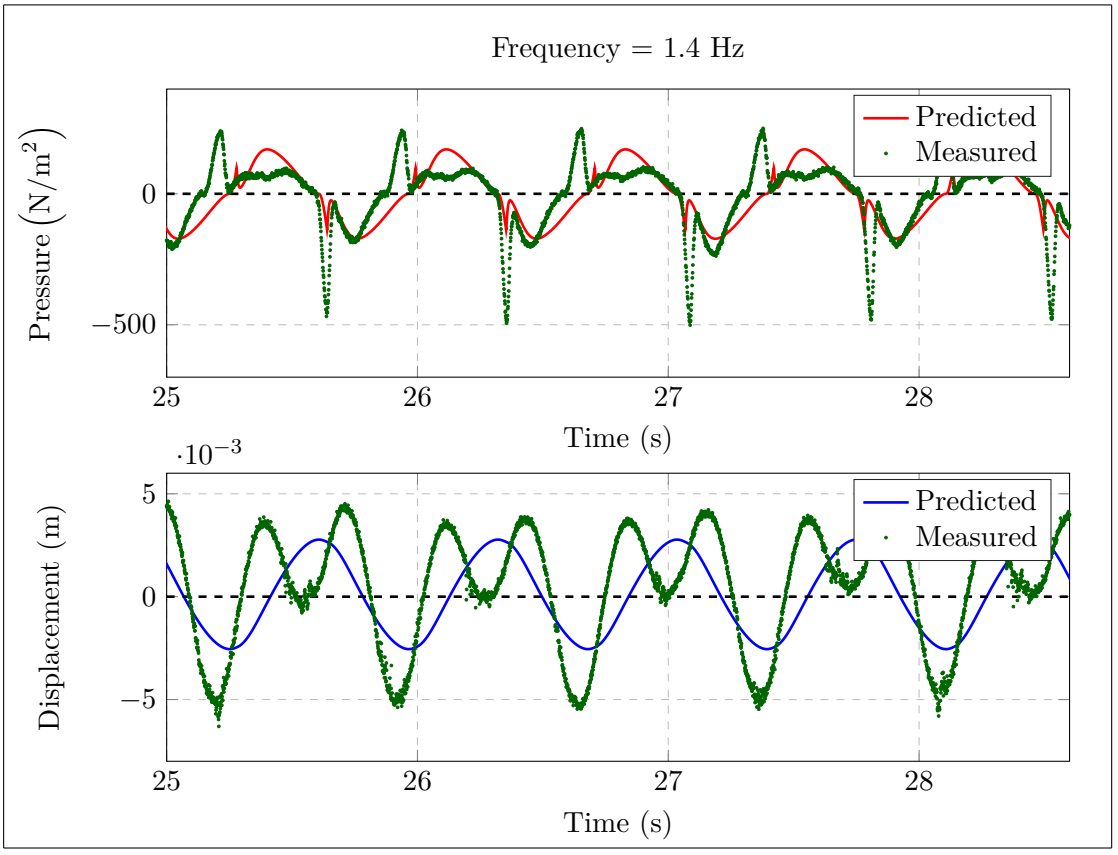

FIGURE 9.77: Comparison between the gauge pressure and the motion of the water column in the single-chamber OWC model with air admittance valves obtained experimentally and as predicted by numerical model, subject to incident waves of 30 mm amplitude for wave frequency of 1.4 Hz.

9.3.2.3 Discussion of results for the single-chamber OWC model with air admittance valves

In this section, a number of observations on both the predictions of the numerical model, and the results obtained from tank testing for the single-chamber OWC model with air admittance valves, when compared to the corresponding predictions of the numerical model, and the results obtained from tank testing for the OWC model with an orifice, are presented.

A significant difference between the orifice-based model and the air admittance-based model is the effect of stiction on the air pressure in the OWC chamber in the air admittance valve case, which is not present for the orifice-based model. While the valves are modelled numerically, somewhat simplistically, as orifices which open at a threshold pressure, the general effect of valve stiction on the behaviour of the system is captured,

and numerically modelling the open valve as an orifice with a coefficient of discharge, Cd_v, as found using the technique described in Section 9.3.2.1, has been quite successful. However, when considering the fit between the measured and predicted gauge pressures for the model with air admittance valves, a trend does emerge that, while the match between the predicted and measured pressures for an incident wave of 0.4 Hz is good, for higher frequencies, the numerical model under-predicts the magnitude of the negative pressure, while predicting the magnitude of the positive pressure well. Note that the magnitude of the measured negative pressure is, in fact, larger than the corresponding magnitude of the measured positive pressure for all tested frequencies higher than 0.4 Hz, whereas the magnitude of the negative and positive pressure for the numerical model is equal in all cases.

Another difference between the tank testing results for the model with an orifice and the corresponding results for the model with air admittance valves is apparent in the water column displacement. For example, contrast the displacement for an incident wave of 0.5 Hz, shown in Figure 9.72, when the air admittance valves are installed, with the displacement for the same frequency when an orifice is used, as shown in Figure 9.57. A distinct flattening in the troughs of the time series for the water column displacement can be seen, for example, at 27 s in Figure 9.72, an effect which occurs while the air admittance valve is opening, and is thus presumably related to valve stiction. Although not as pronounced as for the physical model, this effect does also appear in the predicted displacements (and can be seen most clearly on the displacement plot in Figure 9.72 for incident waves of frequency 0.4 Hz). Furthermore, the numerical model tends to somewhat under-predict the motion of the water column, in general, up to a frequency of 1.2 Hz. For the 1.3 Hz and 1.4 Hz results, the effects of sloshing modes can be seen in the measured data, and, as for the model with an orifice, the numerical model does not consider sloshing modes.

The non-symmetric nature of the measured pressure suggests that the suction and discharge air admittance valves have slightly different characteristics, and that the model could be improved by replacing the single value for Cd_v currently used with a more accurate representation of the valves. Future numerical modelling could introduce a complete dynamic model of the valves, based on the mass, spring and damping properties of the valves, such as that described in [217], which may capture more of the subtleties of the relationship between the airflow through a valve and the pressure drop across it.

Chapter 10

Air Compressibility

10.1 Introduction

The physical models described thus far in the current work have been constructed to achieve geometric similarity, that is to say, the ratio of any length of the model system to the corresponding length of the full-scale system is the same throughout. Froude scaling was used during the tank testing, as discussed in Chapter 6. Froude scaling may be considered appropriate for modelling hydrodynamic interactions for the wetted part of a WEC, [228]. However, as well as comprising a wetted part, an OWC also comprises an air volume above the free surface of the water column, and this air volume is subject to oscillating variations in pressure. The pressure variations give rise to changes in the density of the air (see Section 5.20), which result in a spring-like effect on the motion of the water column. A number of studies have shown that the spring effect due to air compression, which will influence the behaviour of, and the power absorbed by, an OWC, does not scale geometrically. The magnitude of the spring effect was examined, and linearised expressions for the spring constant with respect to the motion of the water column, were derived in [229], and in [22], resulting in the following linearised expression for the air spring, k:

$$ks = \frac{\gamma A_{owc}^2 p_o}{V_o} \tag{10.1}$$

where:

γ = heat capacity ratio
A_{owc} = cross-sectional area of the air chamber, m^2
p_o = air pressure in the air chamber at stillwater conditions, N/m^2
V_o = volume of the air chamber at stillwater conditions, m^3.

To maintain similarity of the air spring effect between a physical scale model and the corresponding full-scale device, the initial air pressure inside OWC chamber at model scale, and the air pressure outside the OWC chamber in the testing facility, would need to be reduced by the scaling factor. However, for small scale models, this is clearly not practical. Studies [229] and [22], both show that, in order to accurately incorporate the effect of the air spring on the motion of the water column in the physical scale model of the OWC when air pressures are not reduced by the scaling factor, the volume of air in the chamber may be scaled by the square of the scaling factor, as opposed to the cube of the scaling factor, as is the case for geometric scaling. Using dimensional analysis, [230] established the relationship between the ratio of the model-scale to full-scale air volume in terms of the scaling factor and the ratio between the density of the fluids used during tank testing, which is required to maintain similarity of the air spring effect between model and full scale. The relationship is given as:

$$\frac{V_m}{V_f} = \alpha^2 \delta^{-1} \tag{10.2}$$

where:

V_m = volume of air in chamber at model scale, m^3
V_f = volume of air in chamber at full scale, m^3
α = geometric scaling factor
δ = ratio of density of fluids between model and full scale.

A full-scale device would, of course, be deployed in sea water. However, it is common to use fresh water in wave tanks, and fresh water has a slightly lower density than sea water. All testing described herein was performed using fresh water. Nonetheless, δ may reasonably be approximated to 1. For non-floating OWC models, it is possible to maintain similarity of the air spring effect between the model- and full-scale devices by scaling the horizontal dimensions of the air chamber geometrically, while constructing the vertical dimension to the full-scale measurement. However, such an approach is clearly unsuited to floating OWCs, where the additional mass and moments of inertia

of an airbox scaled to satisfy Equation (10.2) would have a dramatic effect on the rigid body modes of the floating OWC.

While the need to scale the air volume appropriately is included in some testing described in the literature, for example, [231], it is common that this requirement is ignored, and testing be conducted with the air chamber scaled geometrically, as indeed has been the case in the current work to this point. [230] includes a numerical example, performed in the frequency domain, where the power available to a turbine in two model OWCs is compared. The volume of air above the water column in the first model is scaled to the cube of the scaling factor. The volume of air above the water column in the second model is scaled to the square of the scaling factor. The wetted surface of both models is identical. The effect of the additional air volume was realised by including a linearised model of the air spring effect. The numerical example shows that, by not including the additional air volume, significant errors in the predictions for the power absorbed by a full-scale device are introduced, which may over- or under-estimate the power absorbed by a full-scale device at different frequencies. [180] shows that, provided the appropriate volume of air is present, the tall air chamber may be replaced by a more conveniently-shaped air volume. This has led to the use, in some instances, of flexible hoses to connect the air chambers of both floating and fixed OWC models to conveniently-located, stationary air volumes. Such a set-up is illustrated for a physical model of a fixed OWC in [230]. However, as discussed in [180], undesirable effects on the dynamics of a floating OWC may be introduced by such flexible hoses. Furthermore, such flexible hoses can be considered a pressure transmission system. Pressure changes will propagate at the speed of sound, and air pressure changes will take a non-zero time to travel through ducting. Pressure losses will occur through the transmission system, for example, due to sudden changes in pipe diameter which may arise. Such time delays and pressure losses may be insignificant over relatively short pipe runs, but may become significant if longer lengths of ducting are required [232].

10.2 Experimental investigation

In order to quantify the effect of geometrically scaling the air volumes above the water columns of the model of the proposed WEI platform, a second, single-chamber OWC

physcial model was constructed. For the second, single-chamber model, the air volume above the water column was scaled to the scale factor (1:50) squared. The new model was then subjected to tank testing, described in Section 10.2.2, and in Section 10.2.3 the results obtained are compared to the corresponding results for the geometrically scaled model.

10.2.1 Model building

The new, single-chamber OWC model was constructed from marine plywood using the same techniques as described for the original, single-chamber OWC model outlined in Chapter 8. The original, single-chamber OWC Model is henceforth referred to as Model 1. The front lip and curved back wall pieces of Model 1 (pieces ① and ② in Figure 8.12) were re-used in the new model, henceforth referred to as Model 2, to ensure that the wetted part of Model 2 was consistent with that of Model 1. The volume of air above the water column of Model 1, in the absence of waves, is equal to the air volume above each water column in each chamber of the 32-chamber model, described in Chapter 8. When constructing Model 2, it was not practical to construct the model so that the height of the air chamber matched the full-scale chamber height, so, as proposed in [180], an airbox of volume equal to the full-scale volume, divided by the scale factor squared, was installed instead. This box was placed directly above the air chamber. The cross section of the air chamber was gradually increased in the manner of a diffuser until sufficiently large that an additional cuboid box results in the appropriate air volume. This design for the airbox eliminated any potential losses that might arise due to sudden changes in the cross-sectional area of the air box, or due to pressure flow through ducting. Figure 10.1 presents a comparison between the 3-dimensional CAD drawings of Model 1 and Model 2.

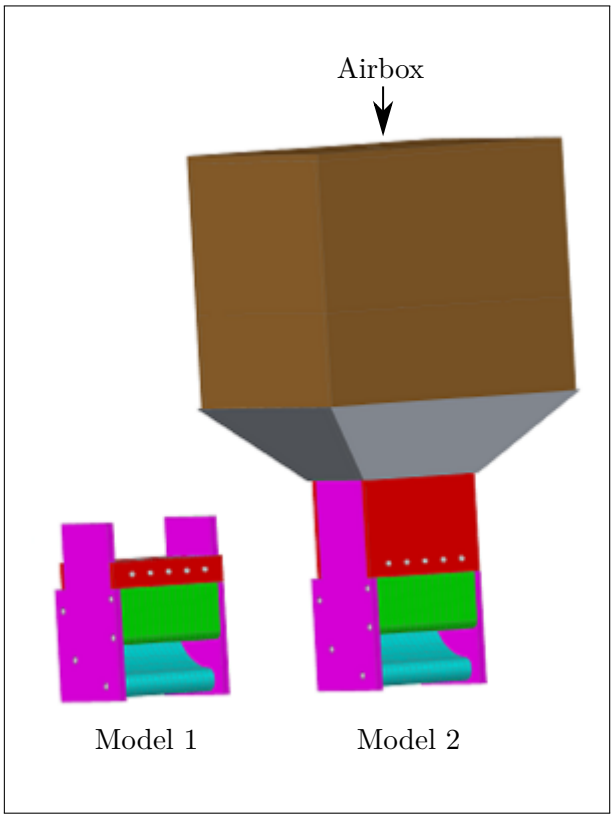

FIGURE 10.1: Comparison between CAD drawings of Model 1 (left) with airbox so that ratio of air volume to full scale is the square of the scaling factor and Model 2 (right), scaled geometrically.

For both models, a resistive wave probe was used to measure the motion of the water column when the model was under test. For Model 1, a wave probe was passed through the top of the air chamber, and the probe could be calibrated when the model was completed. However, the height of the airbox used with Model 2 prevents this approach, and the wave probe was located fully within the air volume of Model 2. A mount for the wave probe was constructed, which can be seen in Figure 10.2. The mount was positioned so that the wave probe records the vertical motion of the water column at the centroid of the still water free surface of the water column.

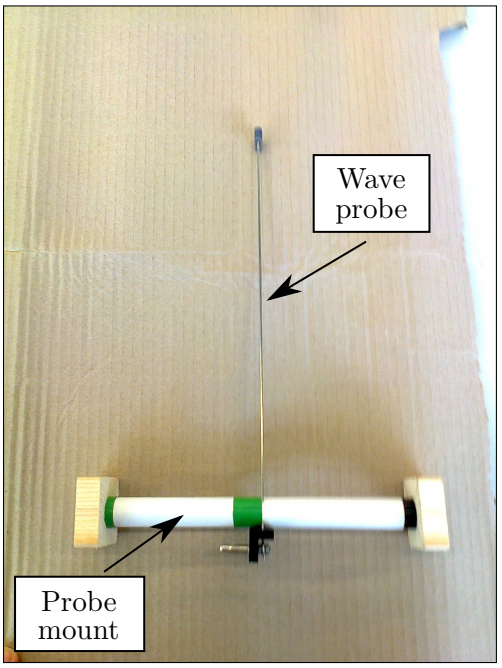

FIGURE 10.2: Wave probe mount, to be located within the air volume of Model 2 during testing.

Model 2 was constructed in a number of stages to allow the wave probe be installed and calibrated before being sealed in the air volume prior to testing. The photograph, shown in Figure 10.3, is taken from above Model 2, and shows the wave probe mounted in place ready for calibration, before the airbox was installed.

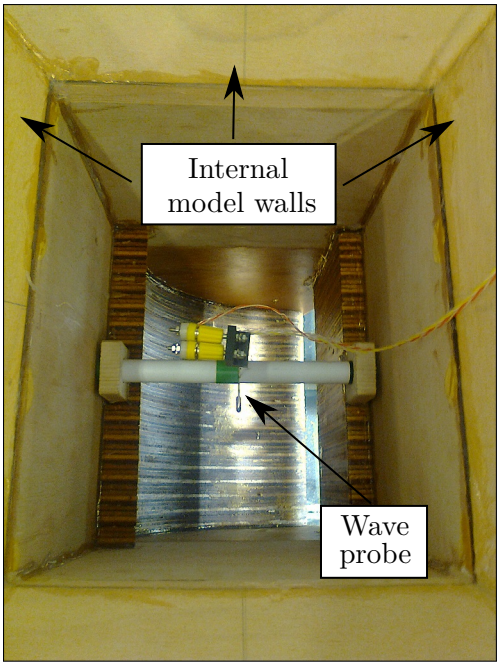

FIGURE 10.3: View from above into Model 2, showing the wave probe mounted and ready for calibration. (Note, the wave probe cable runs through an opening in the airbox, which is sealed during testing.)

Figure 10.4 illustrates Model 2 in the narrow tank at DkIT, before the final stage of construction during which the large airbox was placed on top of the 'diffuser'.

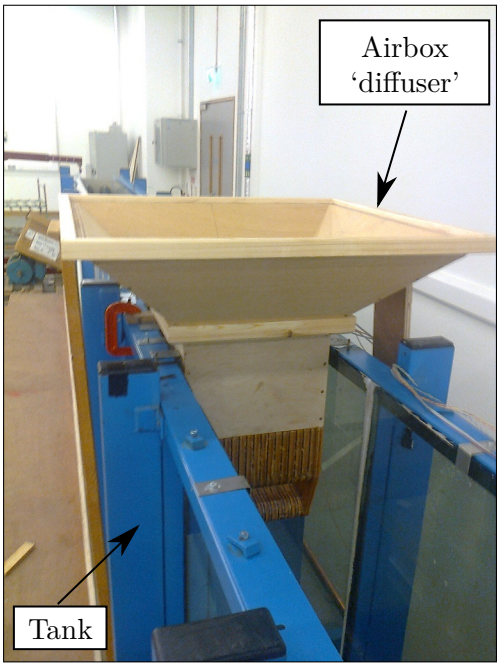

FIGURE 10.4: Model 2 installed in tank prior to the final stage of model construction, during which the large airbox was installed.

Figure 10.5 illustrates the completed Model 2, with airbox installed, ready for testing in the narrow tank at DkIT. Note the pair of supports at the front of the model. A similar pair of supports are present at the rear of the model. These supports not only transfer the weight of the airbox to the frame of the tank, but are also of adjustable height, allowing accurate positioning and levelling of Model 2.

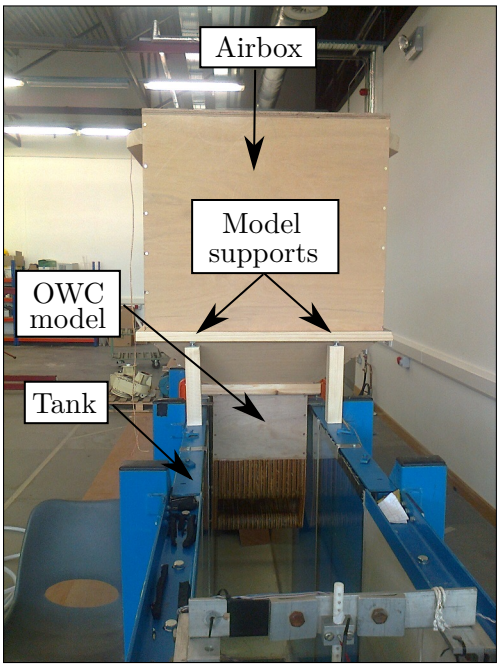

FIGURE 10.5: Completed Model 2 in narrow tank at DkIT ready for testing.

10.2.2 Test programme

In order to compare and contrast the effect of varying the incident wave frequency, incident wave amplitude and applied damping on the behaviour of, and the power absorbed by, both Model 1 and Model 2, Model 2 was subjected to a series of tests to match a number of those already performed on Model 1, as described in Chapter 6. The same variable orifice as was used for the testing of Model 1 was used to vary the level of applied damping between the tests performed on Model 2, see Figure 8.14. The orifice was installed using the same coupler used for Model 1. Tests were performed on Model 2 with orifice diameters of 10 mm, 15 mm, 20 mm, 25 mm and 30 mm. For each orifice diameter, the model was subject to incident monochromatic waves of amplitude 10 mm, 20 mm and 30 mm. Each pairing of orifice diameter and incident wave amplitude was tested for wave frequencies of 0.4 Hz, 0.6 Hz, 0.8 Hz, 1.0 Hz and 1.2 Hz. Thus, a total of 75 tests were performed.

10.2.3 Results

In this section, a representative set of results obtained from the testing described in Section 10.2.2 are presented. A comprehensive set of time and frequency domain results

can be found in [233]. It was found, during testing, that the relative behaviour of the water column motion and pressure with respect to frequency within Model 1 and Model 2 did not vary significantly as the wave amplitude increased. Hence, in the current section, only results for the 20 mm amplitude wave tests are presented as a representative sample

Consider first Figures 10.6 and 10.7, which illustrate a comparison between the air pressure in the chambers of, and the water column displacement for, Model 1 and Model 2 versus time, when the models were subject to incident waves of amplitude 20 mm and a frequency of 1 Hz, with the adjustable orifice set to 20 mm. Figure 10.6 illustrates the variation in air pressure versus time in Model 1 and Model 2, while Figure 10.7 illustrates the variation in the water column displacement versus time in both models. Note that the pressure signals in Figure 10.6 have been temporally aligned, and that the water column displacement signals in Figure 10.7 are temporally aligned to the corresponding pressure signals in Figure 10.6. This allows the difference in the phase angle between the pressure and water column motion for Model 1, when compared to Model 2, to be seen. Furthermore, a direct comparison between the amplitudes of the air pressures and the water column motions in Model 1 and Model 2 may be made. It can be seen that the phase angle between the motion of the water column, and the chamber pressure as measured at the top of the airbox differs between the two cases. Also, the displacement of the water column is greater for Model 2 when compared to Model 1. In addition, what would appear to be a sloshing mode can be seen in the water column motion in Model 2.

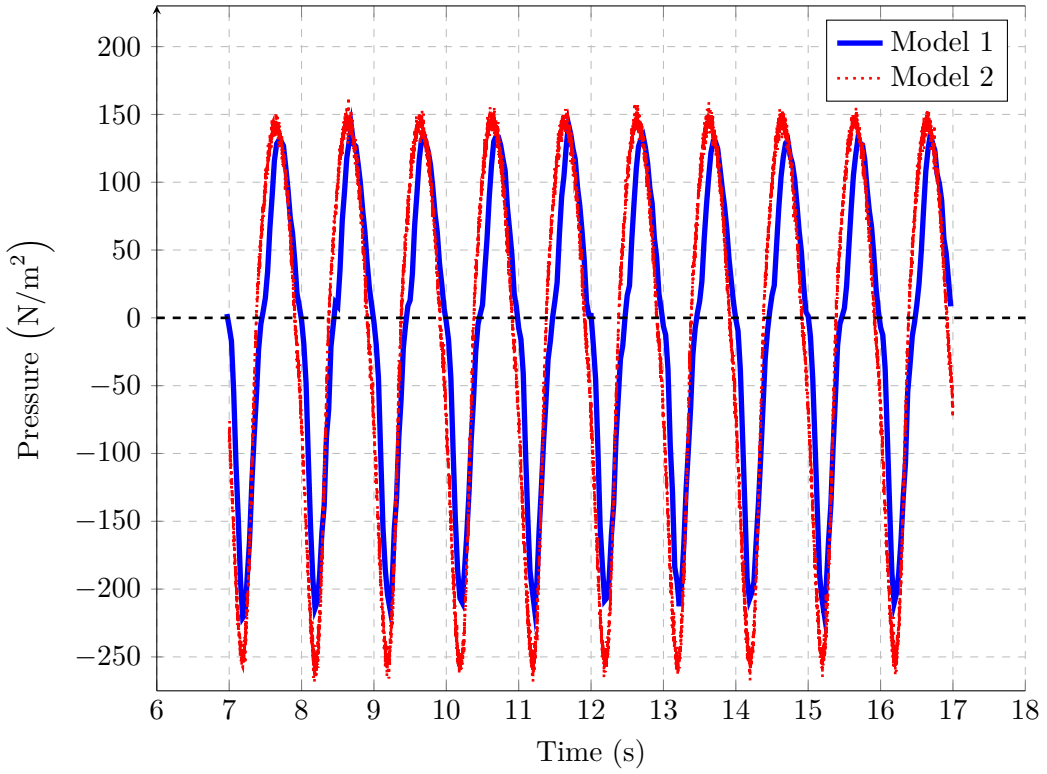

FIGURE 10.6: Comparison between the chamber pressure vs. time for a 20 mm orifice and incident wave of amplitude 20 mm at 1 Hz for Model 1 and Model 2.

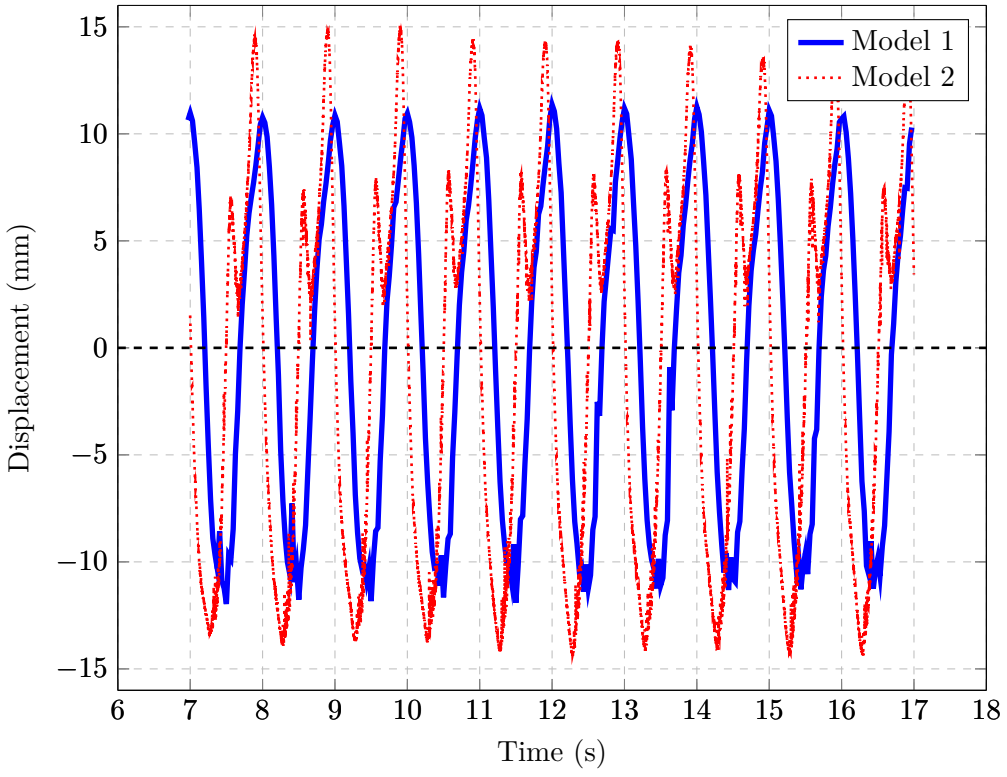

FIGURE 10.7: Model 2 chamber pressure and water column displacement vs. time for a 20 mm orifice and an incident wave of amplitude 20 mm and a frequency of 1 Hz.

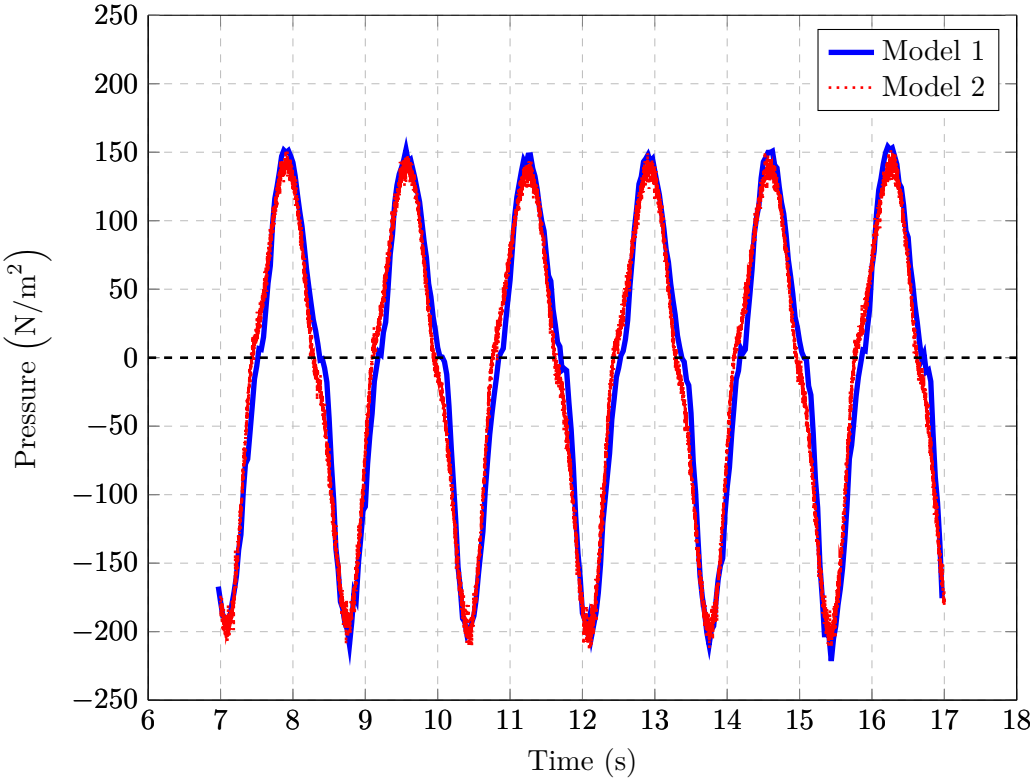

FIGURE 10.8: Comparison between the chamber pressure vs. time for a 20 mm orifice and incident wave of amplitude 20 mm at 0.6 Hz for Model 1 and Model 2.

Figures 10.8 and 10.9 compare the results when Model 1 and Model 2 were subject to incident waves of amplitude 20 mm and a frequency of 0.6 Hz, with the adjustable orifice set to 20 mm. In this case, the pressure is approximately the same for both models, while the displacement of the water column is greater for Model 1 than for Model 2.

Figures 10.10 and 10.11 present the test results for an incident wave of 20 mm at a frequency of 1.2 Hz for an orifice diameter of 10 mm. The results illustrate characteristics that are manifest for a number of tests with relatively high damping levels (corresponding to small orifice diameters) and at frequencies of 1 Hz and above. Here, the displacement and pressure signals for Model 2 are significantly higher in amplitude than those for Model 1. Futher, while a phase difference between the pressure and displacement exists for Model 1, the corresponding signals are virtually in phase for Model 2.

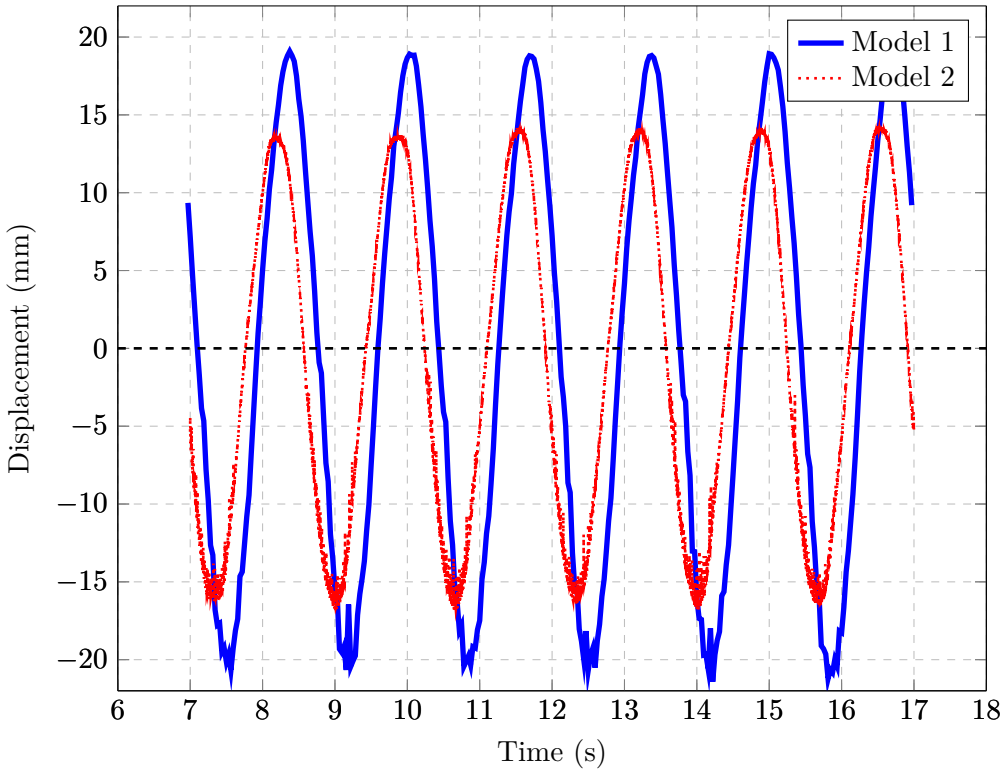

FIGURE 10.9: Comparison between the water column displacement vs. time for a 20 mm orifice and incident wave of amplitude 20 mm at 0.6 Hz for Model 1 and Model 2.

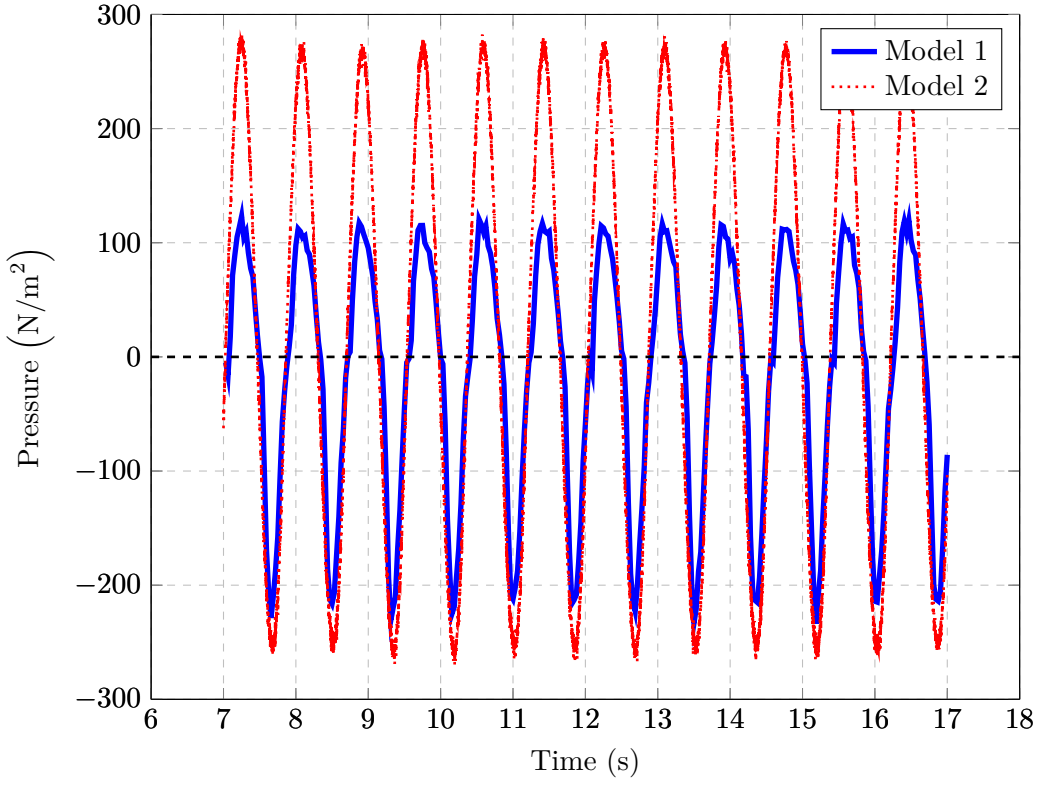

FIGURE 10.10: Comparison between the chamber pressure vs. time for a 10 mm orifice and incident wave of amplitude 20 mm at 1.2 Hz for Model 1 and Model 2.

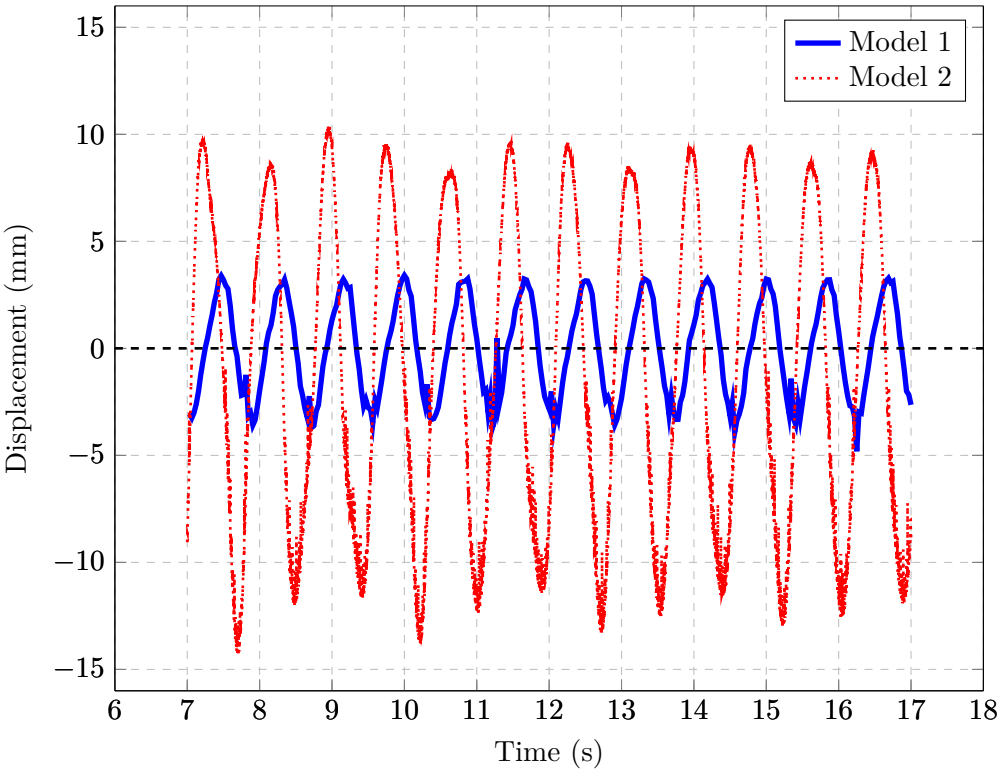

FIGURE 10.11: Comparison between the water column displacement vs. time for a 10 mm orifice and incident wave of amplitude 20 mm at 1.2 Hz for Model 1 and Model 2.

However, the effect of the additional air volume appears to be less significant as the level of applied damping decreases, which occurs when the orifice diameter is increased. Figures 10.12 and 10.13, which show results obtained with the orifice diameter set to 30 mm (for an incident wave of amplitude 20 mm and a frequency of 0.8 Hz) shows less difference between the results obtained for Model 1 compared to Model 2, and little change in phase between the pressure and displacement signals, for the two models. Furthermore, the effect illustrated in Figure 10.11, where the pressure and water column displacements are in phase, does not occur for lower damping levels.

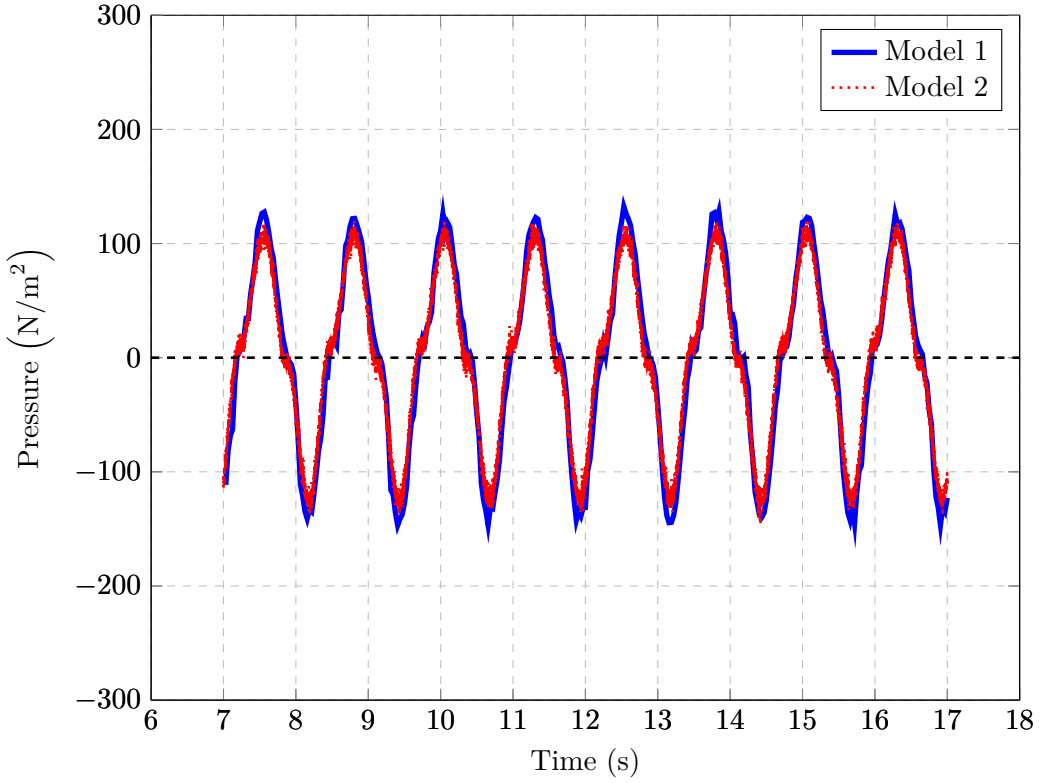

FIGURE 10.12: Comparison between the chamber pressure vs. time for a 30 mm orifice and incident wave of amplitude 20 mm at 0.8 Hz for Model 1 and Model 2.

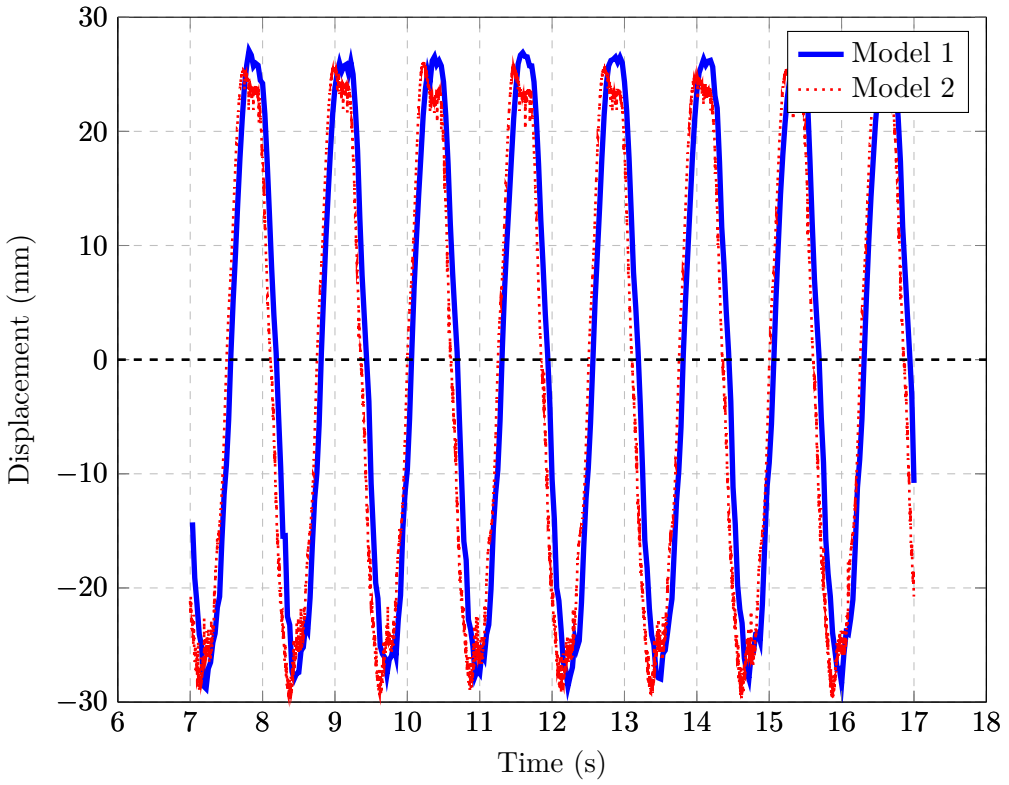

FIGURE 10.13: Comparison between the water column displacement vs. time for a 30 mm orifice and incident wave of amplitude 20 mm at 0.8 Hz for Model 1 and Model 2.

A complete set of time series results can be found in [233].

Figure 10.14 illustrates the RMS of the vertical motion of the water column at the centroid of the water column with respect to incident wave frequency for Model 1 and Model 2, when both models were subject to an incident wave of 20 mm with an orifice diameter of 10 mm. Figure 10.15 illustrates the RMS of the pressure within the air chamber above the water column for both models from the corresponding tests.

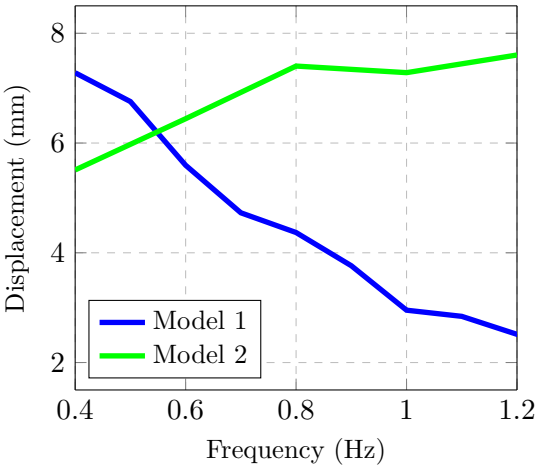

FIGURE 10.14: RMS of the water column motion vs. incident wave frequency for an incident wave of amplitude 20 mm with a 10 mm orifice.

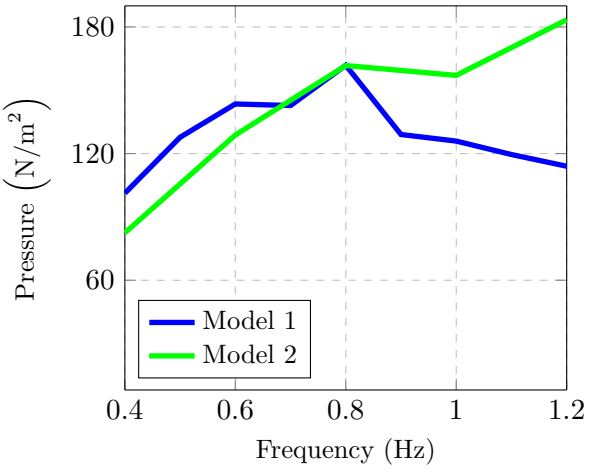

FIGURE 10.15: RMS of the pressure in the chamber vs. incident wave frequency for an incident wave of amplitude 20 mm with a 10 mm orifice.

Figures 10.16 and 10.17 illustrate the variation in the RMS of the water column displacement and the RMS of the chamber pressure with respect to frequency, for an incident wave of amplitude 20 mm with a 10 mm orifice, while Figures 10.18 and 10.19, Figures 10.20 and 10.21, and Figures 10.22 and 10.23 illustrate the corresponding results for orifice diameters of 20 mm, 25 mm and 30 mm, respectively.

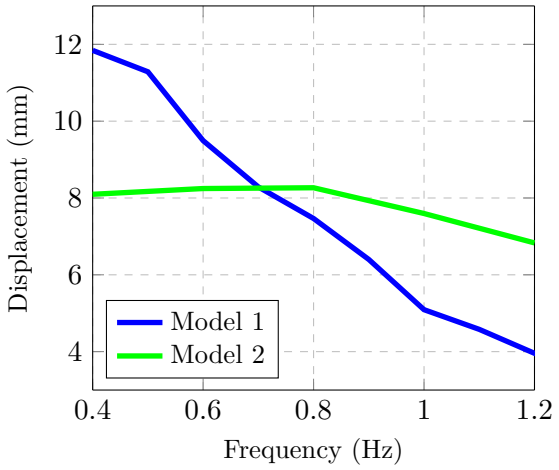

FIGURE 10.16: RMS of the water column motion vs. incident wave frequency for an incident wave of amplitude 20 mm with a 15 mm orifice.

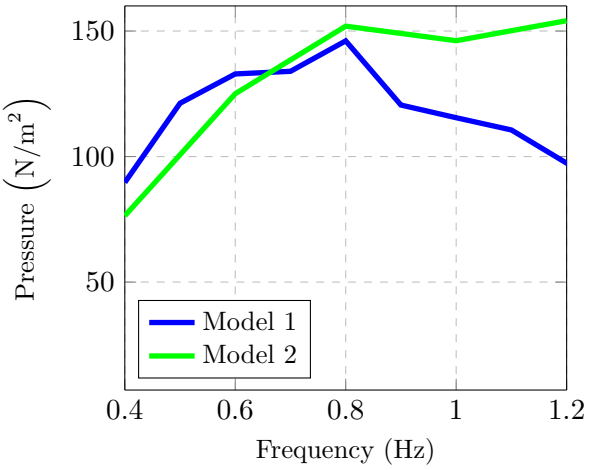

FIGURE 10.17: RMS of the pressure in the chamber vs. incident wave frequency for an incident wave of amplitude 20 mm with a 15 mm orifice.

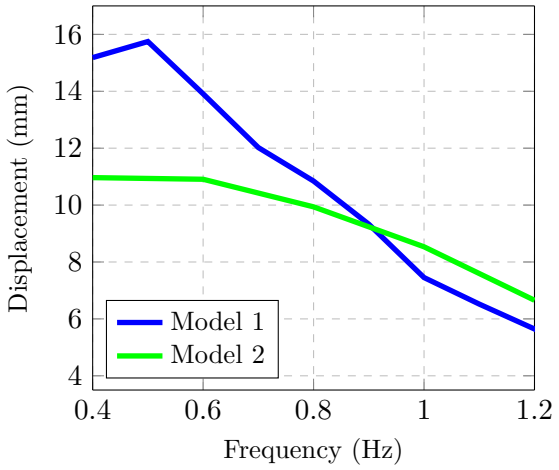

FIGURE 10.18: RMS of the water column motion vs. incident wave frequency for an incident wave of amplitude 20 mm with a 20 mm orifice.

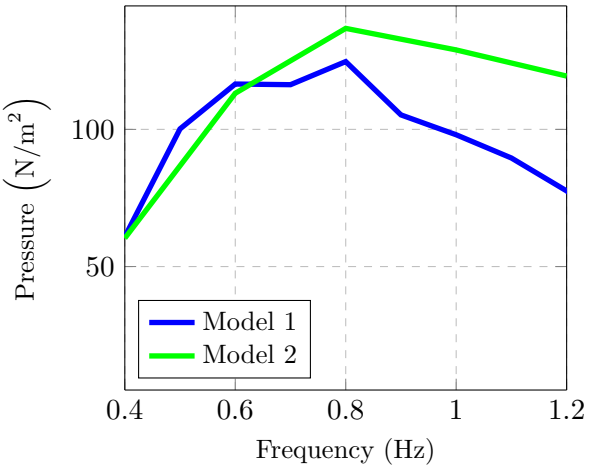

FIGURE 10.19: RMS of the pressure in the chamber vs. incident wave frequency for an incident wave of amplitude 20 mm with a 20 mm orifice.

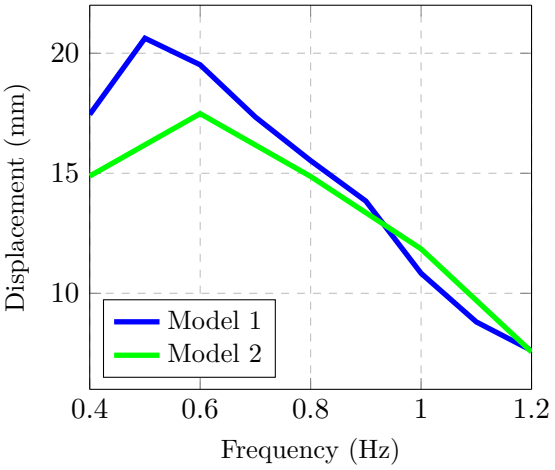

FIGURE 10.20: RMS of the water column motion vs. incident wave frequency for an incident wave of amplitude 20 mm with a 25 mm orifice.

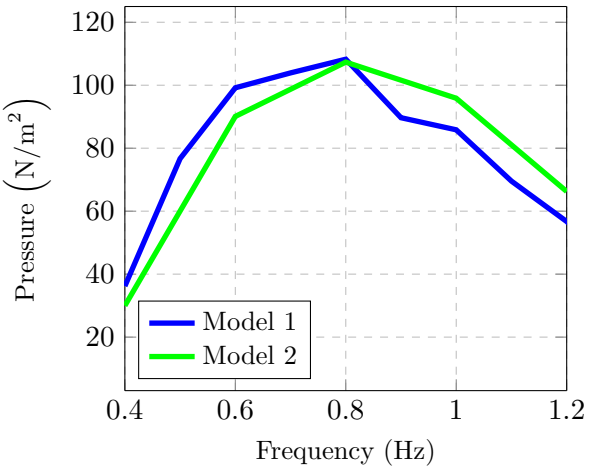

FIGURE 10.21: RMS of the pressure in the chamber vs. incident wave frequency for an incident wave of amplitude 20 mm with a 25 mm orifice.

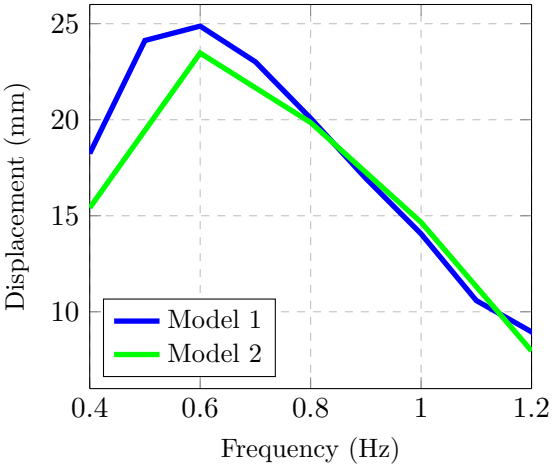

FIGURE 10.22: RMS of the water column motion vs. incident wave frequency for an incident wave of amplitude 20 mm with a 30 mm orifice.

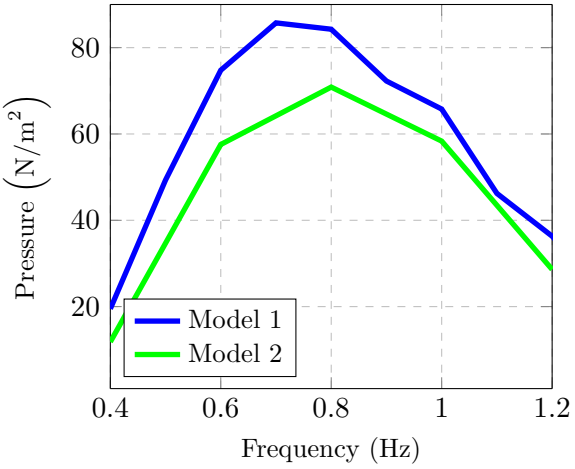

FIGURE 10.23: RMS of the pressure in the chamber vs. incident wave frequency for an incident wave of amplitude 20 mm with a 30 mm orifice.

The effect of the airbox at higher levels of applied damping (i.e., when the orifice diameter is smaller) is to reduce the pressure and displacement in Model 2 compared to Model 1 for wave frequencies below 0.8 Hz, while increasing the corresponding pressures and displacements for higher wave frequencies. It can be seen in Figures 10.14 to 10.21, that the effect decreases with increasing orifice diameter until the effect disappears entirely for the largest orifice diameter. Figures 10.22 and 10.23 support the assertion made with respect to Figures 10.12 and 10.13, which is that the effect of the additional air volume decreases as the level of applied damping decreases (i.e., as the orifice diameter

is increased). Unsurprisingly, the RMS of the pressure is the lowest for the test where the orifice diameter is greatest, and thus the degree to which the air is compressed is reduced compared to tests with greater levels of damping.

A complete set of frequency domain results for the tests described herein can be found in [233].

10.2.4 Effect on absorbed power

The key commercial concern relating to the issues of air compressibility is the impact of the air spring effect on the power which may be absorbed by the device. Tables 10.1 to 10.5 present the difference between the time-averaged power absorbed by Model 1 and the corresponding power absorbed by Model 2 as a percentage of the power absorbed by Model 1. The absorbed power was calculated using orifice theory. Negative percentages result from test runs where Model 2 absorbed less power than Model 1, and positive percentages result from test runs where Model 2 absorbed more power than Model 1.

Amplitude / Frequency	10 mm	20 mm	30 mm
0.4 Hz	-27.7%	-28.4%	-32.2%
0.6 Hz	-15.4%	-13.6%	-13.1%
0.8 Hz	0.3%	2.5%	-0.6%
1.0 Hz	42.0%	42.0%	37.4%
1.2 Hz	92.4%	111.6%	109.9%

TABLE 10.1: Percentage difference between the time-averaged power absorbed by Model 1 and Model 2, with the 10 mm orifice installed.

Amplitude / Frequency	10 mm	20 mm	30 mm
0.4 Hz	-6.4%	-22.7%	-28.3%
0.6 Hz	0.0%	-7.2%	-13.6%
0.8 Hz	28.3%	7.6%	-9.4%
1.0 Hz	100.5%	44.5%	39.0%
1.2 Hz	147.9%	112.8%	91.6%

TABLE 10.2: Percentage difference between the time-averaged power absorbed by Model 1 and Model 2, with the 15 mm orifice installed.

Amplitude / Frequency	10 mm	20 mm	30 mm
0.4 Hz	29.0%	-4.0%	-19.3%
0.6 Hz	16.1%	-3.4%	-13.3%
0.8 Hz	55.7%	17.0%	5.0%
1.0 Hz	106.7%	52.8%	44.1%
1.2 Hz	138.8%	99.2%	103.9%

TABLE 10.3: Percentage difference between the time-averaged power absorbed by Model 1 and Model 2, with the 20 mm orifice installed.

Amplitude / Frequency	10 mm	20 mm	30 mm
0.4 Hz	-22.9%	-28.1%	-29.0%
0.6 Hz	-10.4%	-13.5%	-16.2%
0.8 Hz	4.0%	0.1%	-6.8%
1.0 Hz	22.1%	19.5%	22.6%
1.2 Hz	2.8%	35.8%	31.7%

TABLE 10.4: Percentage difference between the time averaged power absorbed by Model 1 and Model 2, with the 25 mm orifice installed.

Amplitude / Frequency	10 mm	20 mm	30 mm
0.4 Hz	-27.4%	-51.67%	-54.9%
0.6 Hz	-34.2%	-31.9%	-31.6%
0.8 Hz	-23.4%	-22.2%	-23.3%
1.0 Hz	-25.2%	-15.9%	-16.6%
1.2 Hz	-30.3%	-26.5%	-26.4%

TABLE 10.5: Percentage difference between the time averaged power absorbed by Model 1 and Model 2, with the 30 mm orifice installed.

10.3 Future work

As the results presented in Section 10.2.3 confirm, geometric scaling of the air chamber above a water column in an OWC physical sale model can result in significant errors in the estimation of the likely power absorbed by a corresponding full-scale OWC. Clearly, scaling air volumes to the square of the scaling factor is not practical in many applications, and the use of flexible hoses to connect models to static air volumes introduces other issues. [180] suggests that the fixed additional air volume required to model the spring effect may be replaced by a smaller variable volume, the pressure in which acts in opposition to a mechanical or an electro-mechanical force. It is intended that the data obtained to generate the results presented in Section 10.2.3 may be used as validation data for future investigations into using such a variable volume to replicate the effect of air compressibility.

Figures 10.14 to 10.19 show a significant increase in the pressure in the air chamber, and hence the power absorbed, in Model 2 compared to that for Model 1 for incident wave frequencies greater than 0.8 Hz. This effect disappears for tests conducted with lower levels of applied damping. It is possible that the effect is due to the reduced ability of the wave maker to absorb reflected and radiated waves at higher frequencies. If similar tests to those carried out in the narrow tank described herein, were performed in a larger, 3-dimensional tank, it would be possible to investigate whether the increase in pressures in Figures 10.14 to 10.19 is due to a tank effect.

The testing described in the current chapter investigated the effect of air compression in

the air chamber above the water column. The proposed WEI wind/wave platform comprises 32 such chambers, but each leg of the platform also includes two large plenums. The plenums of the scale model of the proposed platform, described in Chapter 8, have been scaled geometrically, and thus the effect of air compression in the plenums is not fully included. One consequence of not fully modelling air compressibility in the plenums is that a smoothing effect on power absorbed by the entire system is not manifesting to an appreciable degree, as can be seen in Figure 9.8. Airflow rectification is clearly taking place (note that the power oscillates at twice the frequency of the incident wave). However, greater air compressibility would smooth out the peaks in Figure 9.8, potentially delivering higher-quality power. Future physical scale models could include a variable volume connected to the plenums, as described in [180], which could capture the effect of air compressibility within the plenums without excessively changing the rigid body dynamics of the platform itself.

Chapter 11

Experimental Measurement of Hydrodynamic Parameters of a Single OWC

11.1 Introduction

In Chapter 5, a numerical model of a single OWC was described and simulated using hydrodynamic parameters obtained from WAMIT. Chapter 9 compared the predictions made by the numerical model with the results obtained from narrow tank testing, in the time domain, of a physical model of the same OWC. In general, predictions from the numerical model are in good agreement with the results obtained experimentally. To further explore the validity of the numerical model, consideration was then given to how the hydrodynamics of a single OWC might be measured experimentally. In the current chapter, an experimental method to measure the hydrodynamic properties of the single OWC chamber is proposed. The method is based on existing methods, but eliminates the need for apparatus to force-oscillate the water column. The results from an initial implementation of the proposed method are then presented. The proposed method arose from the work described in Chapter 10.

11.2 Background to measuring hydrodynamic parameters

The process by which the hydrodynamic parameters, of rigid, semi-submersible bodies reacting in response to incident waves, may be measured through the use of 'fixed-body', 'free-decay' and 'forced-oscillation' tests is described in, for example, [234]. Such a process seeks to identify system parameters, and is commonly referred to as system identification.

A fixed-body test is used to measure the exciting force acting on a body due to an incident wave. During a fixed-body test, a semi-submersible body is held fixed in a wave tank at the draft at which the body would naturally lie in still-water conditions. The body is then subjected to incident waves, and the force acting on the body is measured using force transducers. A fixed-body test may be performed using either monochromatic or polychromatic waves.

In a free-decay test, the body is displaced from the still-water position by a known amount. The body is then released and the motion of the body is allowed to decay freely while being recorded. The free-decay test allows the added mass and the radiation damping coefficients of the body to be determined, but only at the natural frequency of the body.

During a forced-oscillation test, the body is driven about the still-water position in the absence of waves. The motion of the body is known, and the force acting on the body may be recorded. This information may be used to determine the added mass and radiation damping coefficients for the frequency of oscillation at which the test is performed. A forced-oscillation test to measure the added mass and radiation damping coefficients may be conducted for any frequency of interest by driving the body at that frequency.

The hydrodynamic parameters of an OWC may therefore be experimentally measured by adapting these three tests, as described in [235] and [236]. When performing a fixed-body test on an OWC, the water column is held fixed by completely sealing the air chamber above it. The OWC is then subject to incident waves, and the exciting force may be determined by measuring the pressure in the air above the water column using a pressure transducer. The force acting on the water column is obtained by multiplying the measured chamber pressure by the area of the water column at the free surface. Some motion of the water column can occur due to the compressibility of the air above it. This compression will also absorb and return some of the force in a manner analogous

to a spring in a mass-spring system. However, as discussed in Chapter 10, both these effects are negligible at the model scales used during this work. Great care must be taken to ensure the air chamber is fully sealed during fixed-body tests.

Free-decay tests may be conducted by displacing the water column using either a positive or negative pressure within the air chamber. By subsequently instantaneously removing this pressure, the water column will oscillate freely, and the free surface elevation may be recorded using a wave probe within the chamber.

Forced-oscillation tests can be conducted by connecting an air hose to the chamber and using this to drive the water column through the application of positive and negative pressure. The force acting on the water column may be measured, as for the fixed-body tests, using a pressure transducer, and the free surface elevation measured using an internal wave probe using equipment such as that described in Chapter 6. Unlike the fixed-body tests, it is not necessary to seal the OWC chamber during a forced-oscillation test.

The experimental method for measuring the hydrodynamics of the single OWC used in this work differs from the method described in, for example, [235, 236], in the manner in which the water column is excited during the forced-oscillation tests. The wave maker is used to excite the water column, while allowing water column motion to take place due to the compressibility of a large volume of air contained within the sealed, enlarged chamber above the water column, as described in Section 11.3.2. This method evolved from the investigation into air compressibility described in Chapter 10, and was adopted as no forced-oscillation apparatus, such as that described in [236], is available at DkIT, and so an alternative method was explored.

A second variant of forced-oscillation test, which eliminates the need for the enlarged air box, is also proposed for a single OWC, and is described in Section 11.5.

11.3 Determining hydrodynamic parameters using monochromatic waves

Both variants of the forced-oscillation test, the first utilising the large airbox and the second utilising linear damping, were first implemented using monochromatic waves, and subsequently implemented using polychromatic waves. In this section, the theory for measuring the hydrodynamic parameters of a single OWC, in monochromatic waves,

for the first variant of the forced-oscillation test, utilising the large airbox, is developed. The method by which this theory is implemented to measure hydrodynamic parameters is then described. The results obtained using this method for the single OWC are then presented.

11.3.1 Theory for the measurement of the hydrodynamic parameters of a single OWC using monochromatic waves

Fixed-body tests

For a fixed, single OWC, a fixed-body test is used to measure the exciting force acting on the water column. The single OWC model described in Chapter 8, Model 1, is an example of such an OWC, see Figure 10.1. The equation of motion in the frequency domain for the water column in Model 1, assuming linear conditions and that the water column is acting in a pumping mode only, is given in Equation (11.1). Note the similarity of Equation (11.1) to the frequency domain equation of motion for the platform model, Equation (4.9), in Chapter 4. In Equation (11.1), the applied damping term, D, of Equation (4.9) is replaced by the force acting on the water column due to the pressure within the air chamber above the water column. Note that the subscript 7 refers to the piston, or pumping, mode of the water column.

$$fe_7(\omega) = \left[c_{77} - \omega^2 (m_{77} + a_{77}(\omega)) + j\omega(b_{77}(\omega))\right] u_7 + \Delta p(\omega) \times A_{owc} \tag{11.1}$$

Using the massless disc approach [145], $m_{77} = 0$. Note that, therefore, the term m_{77} is henceforth omitted. It can be seen from Equation (11.1), that, if the water column height may be held fixed when the OWC is subject to an incident wave, that is to say $u_7 = 0$, then:

$$fe_7 = \Delta p \times A_{owc} \tag{11.2}$$

By sealing the air chamber above the water column of Model 1 from the surrounding atmosphere in an airtight fashion, the height of the water column may be held fixed, provided no compression or expansion of the air above the water column can take place. For small air volumes at low Mach numbers, air may be assumed incompressible [200]. A time series of fe_7 can thus be found by multiplying the time series of Δp, which may be measured using a pressure transducer, by A_{owc}. The time series of fe_7 can

be transformed into the frequency domain by applying a Fourier transform. Equation (11.2), which underpins the fixed-body test, is identical to that described elsewhere in the literature, [235, 236].

Forced-oscillation tests

The experimental method used to measure the hydrodynamics of the single OWC described herein varies from that described elsewhere in the literature in the manner in which a forced-oscillation test is conducted. In Chapter 10, the second model of the single OWC, Model 2 (see Figure 10.1), was described and used to investigate the effects of air compression on the behaviour of the OWC. When installed in the narrow tank, as described in Chapter 10, the geometry of the wetted surfaces of both Model 1 and Model 2 are identical, and hence both water columns have identical hydrodynamic parameters. In an OWC, in which an orifice has been installed, which is subject to incident waves, the pressure in the air above the water column, Δp, does not vary linearly. However, Equation (11.1) is only valid under linear, steady-state conditions. In order to generate linear pressure variations in the air above the water column, while still allowing motion of the water column, a large air volume, which may be sealed from atmosphere may be installed above the water column. Model 1 and Model 2 differ in the volume of air within the OWC chamber above the water column. Recall that the volume of air in Model 2 is fifty times the volume of air in Model 1. In Model 2, due to air compressibility, water column motion may take place with no airflow into, or out of, the large airbox.

If the air chamber of Model 2 is made airtight, and Model 2 is then subject to incident waves, with reference to Equation (11.1), $u_7 \neq 0$. The water column may now move due to the compressibility of air in the large airbox even though no airflow takes place into, or out of, the air box. u_7 may be recorded using a wave probe located at the centroid of the free surface of the water column. Δp may also be recorded using a pressure transducer, and then multiplied by A_{owc} in order to determine the force acting on the water column due to the compression of air in the airbox. In effect, the wave maker is being used to force-oscillate the water column. Both the force and displacement signals can be transformed into the frequency domain using Fourier transforms. With knowledge of the coefficient of buoyancy, c_{77}, of the water column (determined as described in Chapter 5), and using fe_7 measured during the fixed-body test, the only remaining unknown terms in Equation (11.1) are a_{77} and b_{77}, which may be found for each frequency tested

as follows:

$$a_{77} = \frac{c_{77} - \Re\left[\frac{fe_7 - \Delta p \times A_{owc}}{u_7}\right]}{\omega^2} \tag{11.3}$$

$$b_{77} = \frac{\Im\left[\frac{fe_7 - \Delta p \times A_{owc}}{u_7}\right]}{\omega} \tag{11.4}$$

Equations (11.3) and (11.4) may be used to find the added mass and radiation damping for the water column once the phases between fe_7 (as determined from the fixed-body test on Model 1), u_7 and $\Delta p \times A_{owc}$ (as measured in the tests on Model 2), are known.

11.3.2 Experimental method for the measurement of the hydrodynamic parameters of a single OWC using monochromatic waves

In this section, the method by which the theory described in Section 11.3.1 is implemented to measure the hydrodynamic parameters of the water column is described.

Fixed-body test

Model 1 was first installed in the narrow tank and the air chamber above the water column was carefully sealed using silicone. The airtight seal was verified by subjecting the model to large monochromatic waves. Leak spray was used to locate any openings in the air chamber, which were then sealed, again using silicone.

Fixed-body tests were then preformed for wave frequencies of 0.4 Hz to 1.2 Hz, in increments of 0.05 Hz. These tests were run for wave amplitudes of 5 mm, 10 mm and 15 mm, so that the effect of nonlinearities, such as viscous damping, could be observed; viscous damping should manifest itself as increased damping levels as the amplitude of motion increases. Thus, a total of 51 frequency/amplitude pairings were examined.

During the fixed-body tests, the variation in pressure within the air chamber, the motions of the water column and the free surface elevation at a point up-wave of the OWC chamber were recorded, using a sampling rate of 128 Hz. This relatively high sampling rate was used to allow the results of multiple tests be combined as described below. In all tests, data was only recorded once steady-state conditions had been reached. Figure 11.1 is a schematic of the fixed-body test set-up.

During the tests, the signal from the wave probe located in the chamber was monitored to ensure no movement of the water column took place and confirm not only that the

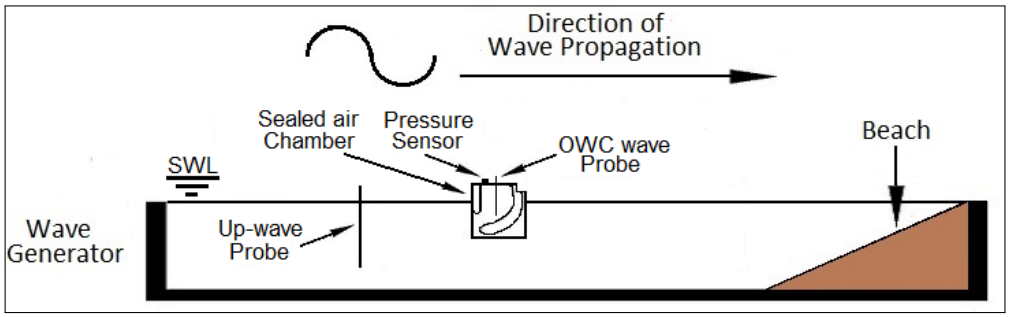

FIGURE 11.1: Schematic of Model 1 installed in the narrow tank at DkIT.

chamber remained airtight, but also confirm that the small volume of air within the chamber was effectively incompressible.

Forced-oscillation test

Once the fixed-body tests were complete, Model 1 was removed from the tank, and Model 2 was installed. Care was taken to ensure that Model 2 was positioned so that the location of the water column relative to the wave maker was the same as for Model 1 during the fixed-body tests. A custom-made locator jig was constructed for this purpose. Care was also taken to ensure that the up-wave wave probe remained in the same location relative to both the wave maker and the water column. Model 2 was then subject to the identical tests to those to which Model 1 was subject during the fixed-body tests, while the same signals were recorded, at the same sampling rate. Figure 11.2 is a schematic of Model 2 installed in the narrow tank.

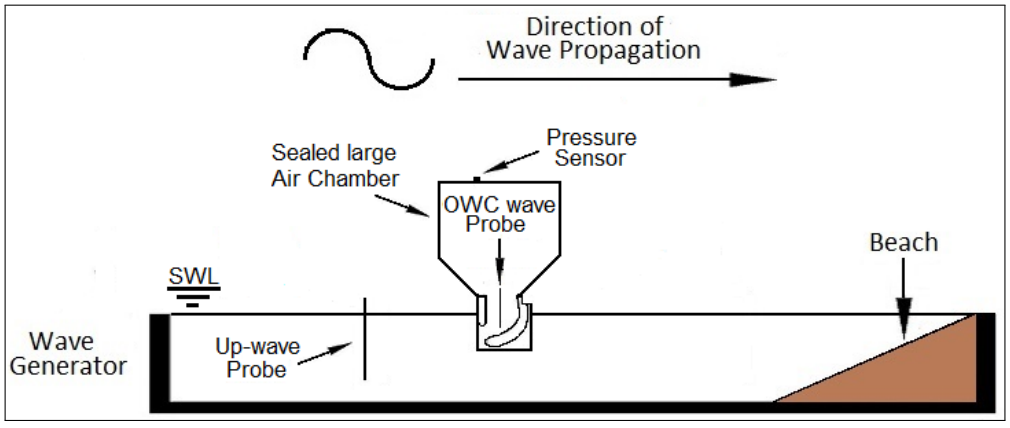

FIGURE 11.2: Schematic of Model 2 installed in the narrow tank at DkIT.

The results obtained from the fixed-body tests, using Model 1, and the forced-oscillation tests, using Model 2, were then combined to determine the hydrodynamic parameters of the water column. The purpose of the up-wave free surface measurements, made using the wave probe which may be seen in Figures 11.1 and 11.2, was to allow the results from

the fixed-body and the force-oscillation test of the same amplitude/frequency pairing to be combined. Once the up-wave probe remained in the same relative location to the wave maker and the water column for a pair of fixed-body and forced-oscillation tests, the time series of the wave elevation at the location of the wave probe may be used to align the phases of the results from the two separate tests.

A number of methods to align data sets were explored, including the cross-correlation of the signals, using the Hilbert transform of the signals and using the Fast Fourier transform (FFT) of the signals. The FFT technique, described below, was selected as the FFT is required elsewhere by the method employed herein to determine the hydrodynamic parameters of the OWC. An FFT was performed on the free surface elevation time series data from the up-wave probe for the fixed-body test. By selecting the frequency bin with the greatest amplitude, the magnitude and phase of the dominant frequency within the time series of the surface elevation measured by the up-wave probe was found. These correspond to the magnitude and frequency of the incident wave during the fixed-body test. Likewise, an FFT was performed on the up-wave free surface elevation for the forced-oscillation test, and the magnitude and frequency of the incident wave during the forced-oscillation test found. The angle between the up-wave free surface elevation during the fixed-body test, and the corresponding signal during the forced-oscillation test, may now be found, once the frequency of the incident wave is known. Terming this angle β, the time offset between the phases of the incident wave during the fixed-body test and the incident wave during the forced-oscillation test for a given amplitude/frequency pairing may now be found using Equation (11.5):

$$\text{Time Offset} = \frac{\beta \times \text{ Wave Frequency}}{2\pi} \tag{11.5}$$

Data from the forced-oscillation test was then offset by the appropriate number of time steps so that the phase of the incident wave for both the fixed-body and forced-oscillation tests were equal. The data obtained from both tests could then be considered temporally aligned, and Equations (11.3) and (11.4) used to determine the hydrodynamic parameters of the OWC.

11.3.3 Results for hydrodynamic parameters using monochromatic waves

The results for the hydrodynamic parameters for the single-chamber OWC are now presented. The results were generated following the analysis in MATLAB of results obtained using the procedure described in Section 11.3.2. Figure 11.3 illustrates the variation in the exciting force acting on the water column as determined from the fixed-body tests. The exciting force has been normalised by the incident wave amplitude to allow direct comparison of the results for the three different wave amplitudes. The results for each amplitude are shown separately, along with error bars to account for measurement uncertainty. The final plot overlays the normalised results with error bars removed for all three wave amplitudes to allow for direct comparison.

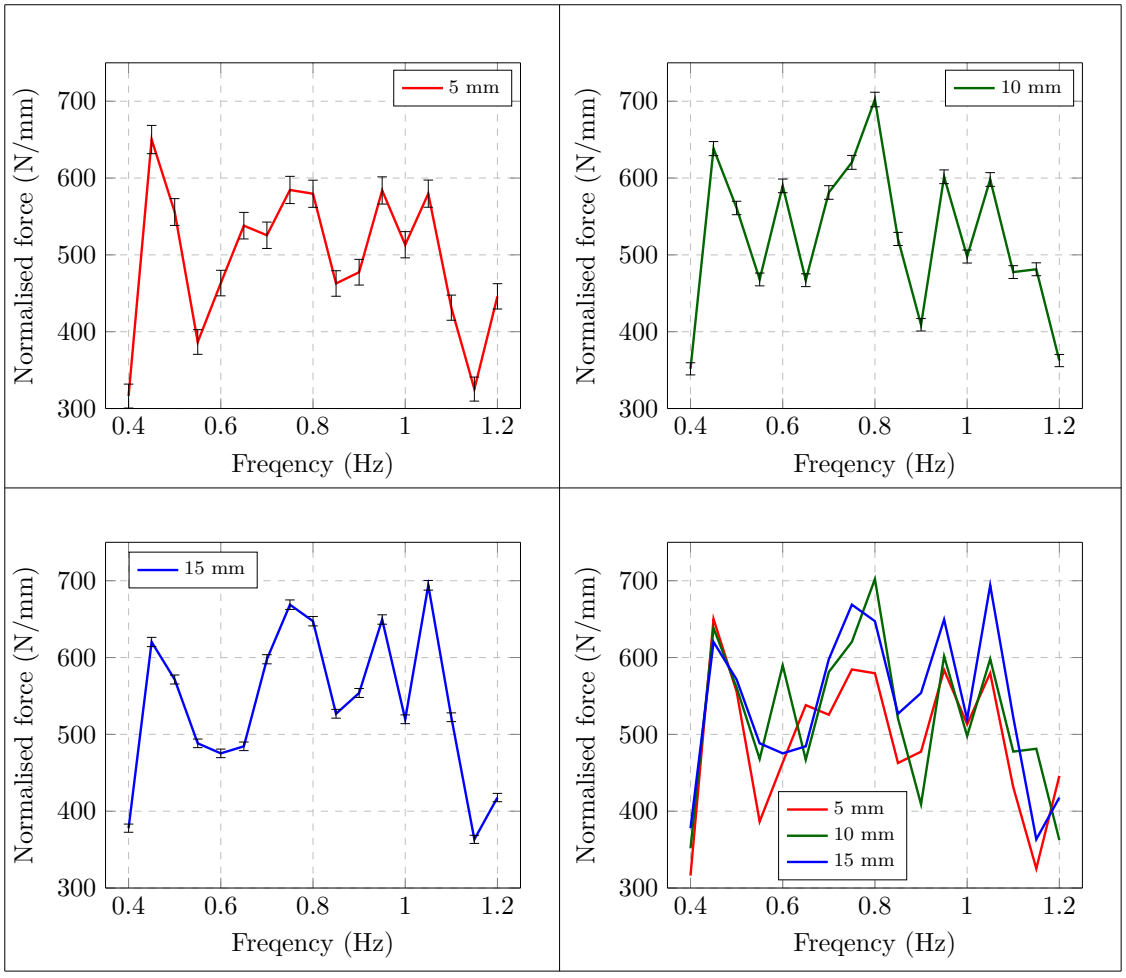

FIGURE 11.3: Normalised amplitude of the measured exciting force vs. frequency for the fixed-body tests using monochromatic waves obtained using three wave amplitudes.

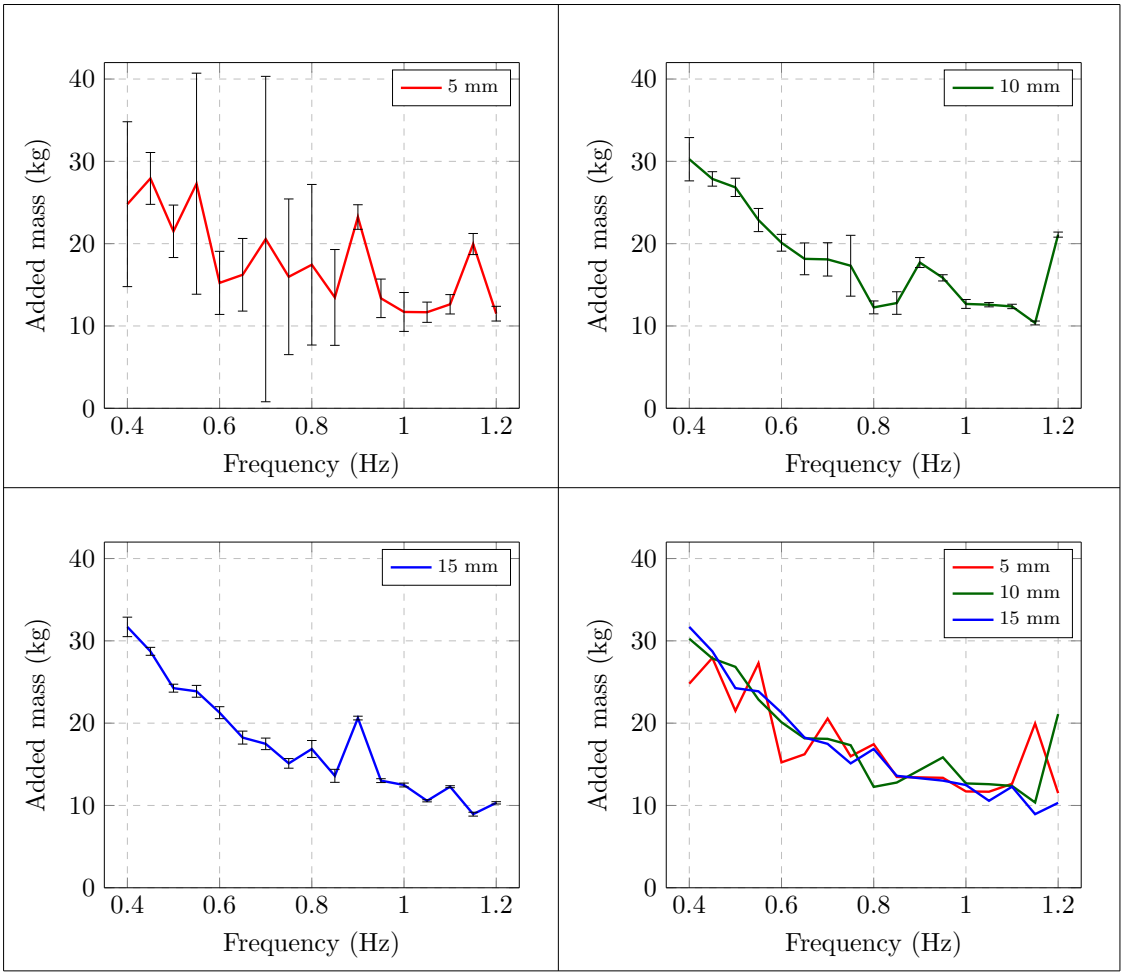

FIGURE 11.4: Added mass vs. frequency for the single OWC determined using monochromatic waves obtained using three wave amplitudes.

Figure 11.4 illustrates the added mass parameter, and Figure 11.5 illustrates the radiation damping parameter, determined by combining the fixed-body and forced-oscillation test results using monochromatic waves. In a manner similar to how the results for the normalised exciting force were presented, the results for the added mass and radiation damping obtained for each wave amplitude are shown separately, along with error bars to account for measurement uncertainty. The final plot in each set overlays the added mass results in Figure 11.4, and the radiation damping results in Figure 11.5, with error bars removed, for all three wave amplitudes to allow for direct comparison.

The error bars shown in Figures 11.3 to 11.5, have been estimated in accordance with Deliverable D3.4 of Equimar [237] using and error propagation. The error bars account for the uncertainty in the pressure transducer and wave probe measurements. The large error bars apparent in Figure 11.4 for the measurements made with an incident wave

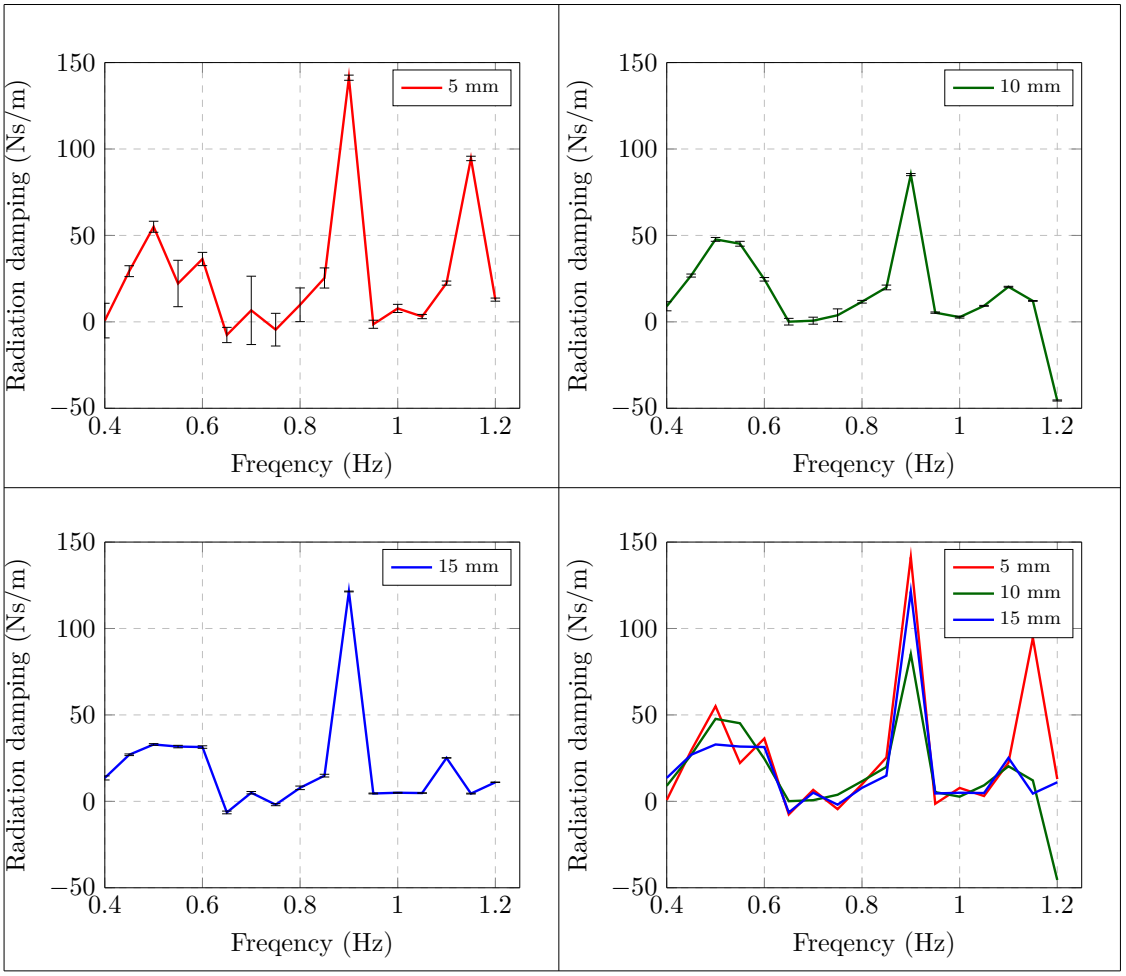

FIGURE 11.5: Radiation damping vs. frequency for the single OWC determined using monochromatic waves obtained using three wave amplitudes.

amplitude of 5 mm reflect the relatively low water column motions in Model 2 compared to the uncertainty in the measurement for this wave amplitude.

In order to provide a check on the implementation of the theory presented in Section 11.3.1 on data obtained as described in Section 11.3.2, Equation (11.1) was solved for u_7 for each frequency for which measurements were performed using the values for fe_7, a_{77} and b_{77} illustrated in Figures 11.3, 11.4 and 11.5 respectively.

Figure 11.6 compares the measured results for the amplitude of u_7 obtained from the forced-oscillation tests with the values for u_7 obtained from solving Equation (11.1), for the range of frequencies and amplitudes tested. In Figure 11.6, the '5 mm', '10 mm' and '15 mm' labels refer to the measured amplitudes of u_7 during the forced-oscillation tests, and the '$\hat{5}$ mm', '$\hat{10}$ mm' and '$\hat{15}$ mm' labels refer to the corresponding amplitudes of u_7 found by solving the equation of motion using the measured hydrodynamic parameters,

for the different incident wave frequencies and amplitudes pairings tested. As can be seen, the predicted and measured results for the amplitudes of the displacement are in agreement.

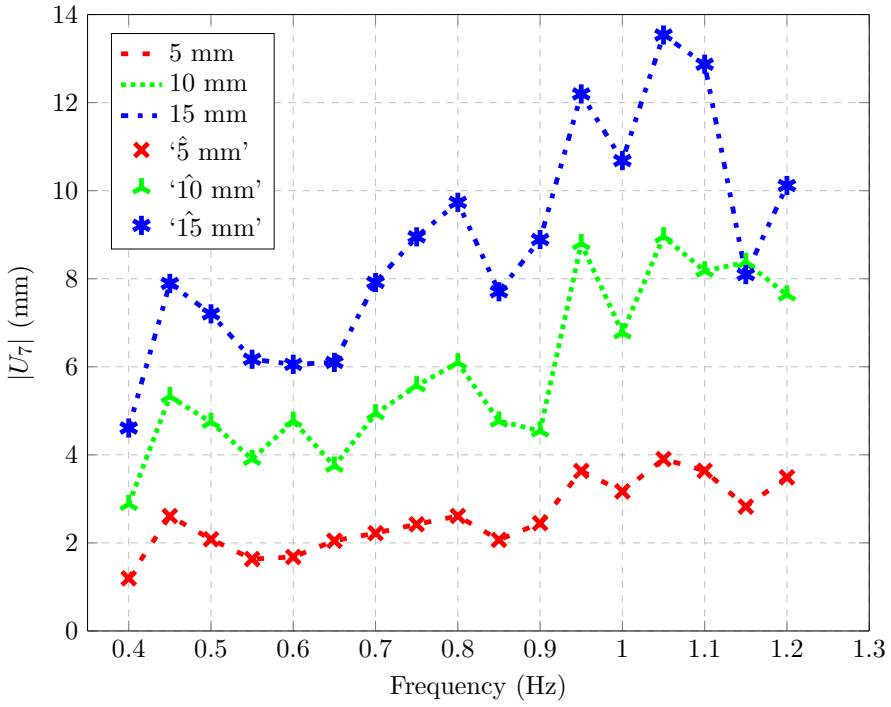

FIGURE 11.6: Comparison of the amplitude of the water column displacement vs. frequency for the single OWC as measured from the forced-oscillation test and predicted by solving Equation (11.1) using measured hydrodynamics

11.4 Determining hydrodynamic parameters using polychromatic waves

System identification of linear systems may be performed based on spectral analysis, as described in [238, 239]. In Chapter 7, the capability of the narrow tank at DkIT to generate polychromatic waves to model random sea states, as well as monochromatic waves, is described. Polychromatic waves in the DkIT narrow tank are generated in accordance with standard spectra, such as Pierson-Moskovitz, JONSWAP and Bretschneider spectra. In principle, the frequency-dependent parameters of a linear system can be identified from a single set of tests for the range of frequencies used to excite the system. In the current section, the approach to system identification for an OWC described in Section 11.3 is developed so that system identification can be performed using polychromatic waves.

11.4.1 Theory for the measurement of the hydrodynamic parameters of a single OWC using polychromatic waves

Spectral analysis may be applied to linear systems subject to random, stationary and ergodic inputs. A stationary input is one for which the statistical properties of the input, such as the mean and variance, are unchanging with time. An ergodic input is one where the time average of a sufficiently long sample of the process is the same as the time average over the probability space. This average is known as the ensemble average [238]. The output of a linear system subject to stationary and ergodic input is also stationary and ergodic. Ocean waves can be considered stationary and ergodic over the time scale of a few hours (see, for example, [148]), and the pseudo-random sea states generated by the narrow tank are stationary and ergodic once the system is run for a sufficiently long period of time. The ratio between the input to a frequency-dependent linear system, and the output of the same system, is termed the transfer function of the system. Spectral analysis allows for the determination of the transfer function for a such a system when the system is excited by a random, stationary and ergodic input, once both the input and output of the system are known. However, this is only true for frequencies that are contained within the spectrum of the input signal.

An OWC in which the water column moves in response to an incident wave can be considered a single-input/single-output (SISO) system, with the exciting force, fe_7, as the input, and the water column displacement, u_7, as the output. The frequency-dependent hydrodynamic parameters of the system may be found from the transfer function between fe_7 and u_7, once the system is linear. A SISO system can be represented graphically in the time domain and the frequency domain as shown in Figure 11.7.

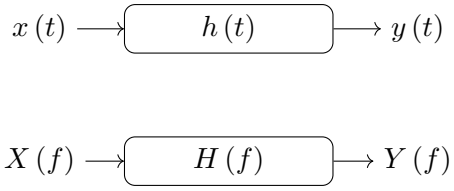

FIGURE 11.7: A single-input/single-output system in the time domain and the frequency domain.

In Figure 11.7:

$x(t)$ = the stationary input
$y(t)$ = the output
$h(\tau)$ = the impulse response of the system
$X(f)$ = the Fourier transform of $x(t)$
$Y(f)$ = the Fourier transform of $y(t)$
$H(f)$ = the frequency-dependent, Fourier transfer function between $X(f)$ and $Y(f)$

$H(f)$ is the Fourier transform of $h(\tau)$, which is given by:

$$H(f) = \int_0^\infty h(\tau)\, e^{-j2\pi f\tau} \tag{11.6}$$

The output of a linear system may be found through the convolution of the input and the impulse response of the system, hence:

$$y(t) = \int_0^\infty x(t)\, h(t-\tau)\, d\tau \equiv x(t) * h(t) \tag{11.7}$$

where $h(\tau) = 0$ for $\tau < 0$.

If $x(t)$ is of the form of a stationary, ergodic process, then, after transient effects have decayed, $y(t)$ is also stationary and ergodic, and from Equation (11.7), $y(t)\,y(t+\tau)$ may be written as:

$$y(t)\,y(t+\tau) = \int_0^\infty \int_0^\infty h(\alpha)\,h(\beta)\,x(t-\alpha)\,x(t+\tau-\beta)\,d\alpha d\beta \tag{11.8}$$

The expected value, E, of a function, $g(x)$, is given by:

$$E[g(x)] = \int_{-\infty}^{\infty} g(x)\,p(x)\,dx \tag{11.9}$$

where:

$g(x)$ = a single-valued function

$p(x)$ = the probability density function

Taking the expected value of both sides of Equation (11.8) yields the autocorrelation function, $R_{yy}(\tau)$:

$$R_{yy}(\tau) = \int_0^\infty \int_0^\infty h(\alpha)\,h(\beta)\,R_{xx}(\tau)\,(\tau+\alpha-\beta) \tag{11.10}$$

Likewise, from Equation (11.7), the product $x(t)\,y(t+\tau)$ is given by:

$$x(t)\,y(t+\tau) = \int_0^\infty h(\alpha)\,x(t)\,x(t+\tau-\alpha)\,d\alpha \tag{11.11}$$

Taking the expected values of both sides of Equation (11.11), the cross-correlation function, $R_{xy}(\tau)$, is obtained:

$$R_{xy}(\tau) = \int_0^\infty h(\alpha)\,R_{xx}(\tau-\alpha)\,d\alpha \tag{11.12}$$

The two-sided, cross-spectral density function, $S_{xy}(f)$, of two time signals, $x(t)$ and $y(t)$, can be defined in terms of the cross-correlation function, $R_{xy}(\tau)$, as follows:

$$S_{xy}(f) = \int_{-\infty}^{\infty} R_{xy}(\tau)\,e^{-j2\pi f\tau}d\tau \tag{11.13}$$

Similarly, the two-sided autospectral density function, $S_{xx}(f)$, for a time signal, $x(t)$, can be expressed in terms of the autocorrelation function as:

$$S_{xx}(f) = \int_{-\infty}^{\infty} R_{xx}(\tau)\, e^{-j2\pi f\tau} d\tau \tag{11.14}$$

Taking the Fourier transform of Equations (11.13) and (11.14), and with reference to Equations (11.6), (11.10) and (11.12), yields:

$$S_{yy}(f) = |H(f)|^2 S_{xx}(f) \tag{11.15}$$

and:

$$S_{xy}(f) = H(f) S_{xx}(f) \tag{11.16}$$

In Equations (11.15) and (11.16), the frequency may be either positive or negative, and both $S_{yy}(f)$ and $S_{yy}(f)$ are two-sided. In terms of one-sided spectral density functions, which are defined for positive frequencies only, Equations (11.15) and (11.16) become:

$$G_{xy}(f) = H(f) G_{xx}(f) \tag{11.17}$$

$$G_{yy}(f) = |H(f)|^2 G_{xx}(f) \tag{11.18}$$

where:

$G_{xy}(f)$ = the one-sided cross power spectral density of $x(t)$ and $y(t)$
$G_{xx}(f)$ = the one-sided power spectral density of $x(t)$
$G_{yy}(f)$ = the one-sided power spectral density of $y(t)$

The one-sided spectral density functions are related to the two-sided spectral density functions as follows:

$$\begin{aligned} G_{xx}(f) = 2S_{xx}(f) &= 2\int_{-\infty}^{\infty} R_{xx}(\tau) e^{-j2\pi f\tau} d\tau && f > 0 \\ &= S_{xx}(f) = \int_{-\infty}^{\infty} R_{xx}(\tau) e^{-j2\pi f\tau} d\tau && f = 0 \\ &= 0 && f < 0 \end{aligned} \tag{11.19}$$

and:

$$\begin{aligned} G_{xy}(f) = 2S_{xy}(f) = 2\int_{-\infty}^{\infty} R_{xy}(\tau)e^{-j2\pi f\tau}d\tau \qquad & f > 0 \\ = S_{xy}(f) = \int_{-\infty}^{\infty} R_{xy}(\tau)e^{-j2\pi f\tau}d\tau \qquad & f = 0 \\ = 0 \qquad & f < 0 \end{aligned} \tag{11.20}$$

The frequency-dependent transfer function of a SISO system may thus be written:

$$H(f) = \frac{G_{xy}(f)}{G_{xx}(f)} \tag{11.21}$$

For a full treatment of spectral analysis theory as applied to a SISO system, see, for example, Chapter 4 of [239].

Spectral analysis may be used to determine the frequency-dependent hydrodynamic parameters of an OWC based on Equation (11.1). Equation (11.1) may be recast into the form of a SISO system as follows:

$$[fe_7(f) - \Delta p(f) \times A_{owc}] = \left[c_{77} - \omega^2(a_{77}(f)) + j\omega b_{77}(f)\right] u_7(f) \tag{11.22}$$

The SISO system in Equation (11.22) may be represented graphically as shown in Figure 11.8.

$$[fe_7(f) - \Delta p(f) \times A_{owc}] \longrightarrow \boxed{H(f)} \longrightarrow u_7(f)$$

FIGURE 11.8: The SISO system representation of the relationship between $[fe_7(f) - \Delta p(f) \times A_{owc}]$ and $u_7(f)$ for a single-chamber OWC

In Figure 11.8, $H(f)$ is the frequency-dependent, Fourier transfer function between $[fe_7(\omega) - \Delta p(\omega) \times A_{owc}]$ and $u_7(\omega)$. Equations (11.3) and (11.4) may then be recast in terms of $H(f)$ and used to determine the added mass and radiation damping for each frequency component in $[fe_7(\omega) - \Delta p(\omega) \times A_{owc}]$ as follows:

$$\Re\{H(f)\} = c_{77} - \omega^2(a_{77}(f)) \tag{11.23}$$

$$\Im\{H(f)\} = \omega b_{77}(f) \tag{11.24}$$

and hence:

$$b_{77}(f) = \frac{\Im\{H(f)\}}{\omega} \tag{11.25}$$

$$a_{77}(f) = \frac{c_{77} - \Re\{H(f)\}}{\omega^2} \tag{11.26}$$

Note that in practice, $fe_7(f)$ is obtained from a fixed-body test, while $\Delta p(f)$ and $u_7(f)$ are obtained from a forced-oscillation test.

It is also possible to determine the hydrodynamic parameters of an OWC using the wave elevation at the location of the centroid of the water column free surface, ζ. This is achieved by first considering the SISO system between $u_7(f)$ and $\zeta_7(f)$ for a forced-oscillation test. This system is illustrated in Figure 11.9.

$$\zeta(f) \longrightarrow \boxed{H_1(f) = \frac{u_7(f)}{Amp}} \longrightarrow u_7(f)$$

FIGURE 11.9: The SISO system representation of the relationship between $\zeta(f)$ and $u_7(f)$ for a single-chamber OWC for a forced-oscillation test.

In Figure 11.9:

$\zeta(f)$ = the Fourier transform of the time series, $\zeta(t)$

$H_1(f)$ = the Fourier transfer function between $\zeta(t)$ and $u_7(t)$

Amp = the amplitude of the incident wave

Next consider the SISO between fe_7 and ζ during the fixed-body test, which is illustrated in Figure 11.10.

$$\zeta(f) \longrightarrow \boxed{H_2(f) = \frac{fe(f)}{Amp}} \longrightarrow fe_7(f)$$

FIGURE 11.10: A SISO system representation of the relationship between ζ and fe_7 for a single-chamber OWC for a fixed-body test

In Figure 11.10:

$H_2(f)$ = the Fourier transfer function between $\zeta(f)$ and $fe_7(f)$.

Finally, the SISO system between $\zeta(f)$ and $\Delta p(t)$ for a forced-oscillation test is illustrated in Figure 11.11.

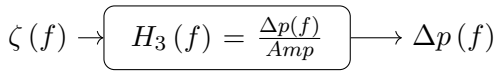

FIGURE 11.11: A SISO system representation of the relationship between ζ and $\Delta p(f)$ for a single-chamber OWC for a forced-oscillation test.

In Figure 11.10:

$$\begin{aligned} H_3(f) &= \text{the Fourier transfer function between } \zeta(f) \text{ and } \Delta p(f) \\ \Delta p(f) &= \text{the Fourier transform of the pressure signal, } \Delta p(t) \end{aligned}$$

Equation (11.22) may now be rewritten as follows:

$$\frac{fe_7(f)}{Amp} - A_{owc}\frac{\Delta p(f)}{Amp} = \left[c_{77} - \omega^2\left(a_{77}(f)\right) + j\omega b_{77}(f)\right]\frac{u_7(f)}{Amp} \tag{11.27}$$

In terms of the Fourier transfer functions described in Figures 11.8, 11.10 and 11.10, Equation (11.27) is written as:

$$H_2(f) - A_{owc}H_3(f) = \left[c_{77} - \omega^2\left(a_{77}(f)\right) + j\omega b_{77}(f)\right]H_1(f) \tag{11.28}$$

$a_{77}(f)$ and $b_{77}(f)$ for each frequency for which the Fourier transfer functions, $H_1(f)$,$H_2(f)$ and $H_3(f)$, have been measured may thus be determined as follows:

$$a_{77}(f) = \frac{\frac{\Re\{H_2(f)\} - A_{owc} \times \Re\{H_3(f)\}}{\Re\{H_1(f)\}}}{\omega^2} - c_{77} \tag{11.29}$$

$$b_{77}(f) = \frac{\frac{\Im\{H_2(f)\} - A_{owc} \times \Im\{H_3(f)\}}{\Im\{H_1(f)\}}}{\omega} \tag{11.30}$$

In order to gain confidence in the use of spectral methods, before applying such methods to the single OWC model, a case study was undertaken whereby a time domain simulation of a heaving cylinder in polychromatic waves was created using hydrodynamic parameters obtained from WAMIT. A time series of the heave motion of the cylinder was generated. The time series of the heave motion was then successfully used, in conjunction with the time series of the exciting force, to recover the real and imaginary parts of the equation of motion of the cylinder, demonstrating the suitability of using

spectral methods to measure the hydrodynamic parameters of a WEC over a range of incident wave frequencies. Details of the case study may be found in Appendix A.

11.4.2 Experimental method for the measurement of the hydrodynamic parameters of a single OWC using polychromatic waves

The experimental method for measuring the hydrodynamic parameters for an OWC using polychromatic waves is similar to the method used for monochromatic waves, as described in Sections 11.3. A total of three tests were required: a fixed-body test using the sealed, single-OWC model (Model 1), a forced-oscillation test using the sealed, modified OWC model with airbox (Model 2) and a test to measure the free surface elevation at the location of the OWC in the tank, but with no model is installed.

The tests were performed using a Bretschneider spectrum as input with an energy period, T_e, of 1.53 s, and a significant wave height, H_s, of 0.03 m. All tests ran for three hours. Care was taken to ensure the water columns were located at the same point in the tank during the fixed-body and forced-oscillation tests, and also that the wave probe measurements were taken at the same location in the tank for all three tests. As for the monochromatic wave tests, fe_7 is obtained from the fixed-body test. Δp and u_7 are obtained from the forced-oscillation test. The final test, run with no model in the tank, is performed to determine the transfer function between ζ at the centroid of the water column free surface and fe_7. During all three tests, the wave elevation was recorded using a second wave probe at a point between the test location and the wave maker. As for the monochromatic wave tests, the purpose of the probe located between the test location and the wave maker was to allow the data obtained from different tests to be aligned. For spectral analysis to be valid, all measurements involved in the analysis should be taken simultaneously [238]. It is not possible to measure fe_7 , Δp and u_7 simultaneously, as they are measured during two separate tests. However, if the narrow tank is capable of reliably reproducing the same pseudo-random wave elevation time series, and the results from the two tests can be aligned, the results from a fixed-body test and a forced-oscillation test may be combined into a 'pseudo-simultaneous' result. The ability of the tank to reliably reproduce a free surface elevation at a given point in the tank is the subject of Section 11.4.3 (below).

Unlike the monochromatic wave tests, data from polychromatic wave tests cannot be

aligned based on the phase of a signal. For polychromatic wave tests, the initial time series of the free surface elevation measured by the upstream probe, before reflected or radiated waves from the model begin to manifest at the upstream probe location, were cross-correlated to find the temporal offset between the wave maker starting and the beginning of data recording. This offset was then used to align the data set obtained from the fixed-body test and the forced-oscillation test so that the measurements recorded during the fixed-body and the forced-oscillation tests might be considered as simultaneous.

11.4.3 Tank repeatability

In order to investigate if the tank is capable of reproducing pseudo-random wave elevation time series, a Bretschneider spectrum with $Te = 0.85$ s and $Hs = 0.03$ m was created. The wave maker ran the Bretschneider spectrum for three hours with no model installed, and the free surface elevation was recorded at a point midway between the wave maker and the beach. The spectrum was run three times to create three time series of the free surface elevation at the same point in the tank. Figure 11.12 illustrates the power density spectrum of the time series of the free surface elevation recorded during one of the 3-hour test runs when no model was installed in the tank, compared to a theoretical Bretschneider spectrum with $Te = 0.85$ s and $Hs = 0.03$ m.

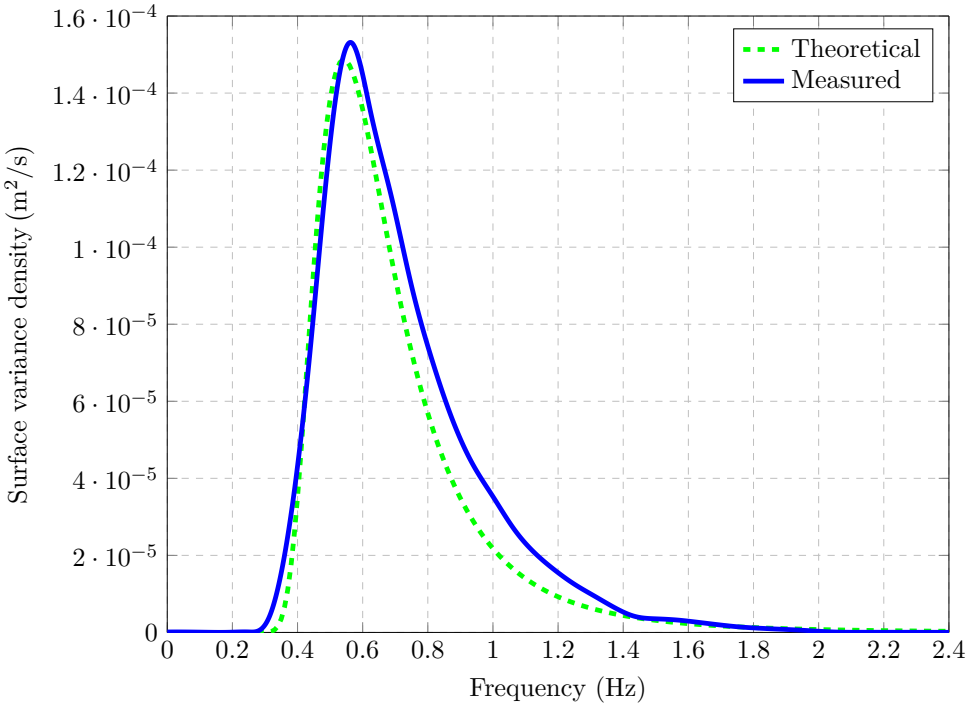

FIGURE 11.12: Bretschneider spectrum used to verify repeatability of pseudo-random wave generation of the narrow tank at DkIT.

The cross-correlation function was used to find the best fit between the time series measured by the wave probe midway between the wave maker and the beach for the length of the three series with no model in the tank, and two of the time series were offset as appropriate so as to temporally align the signals. A sample of the aligned signals is illustrated in Figure 11.13.

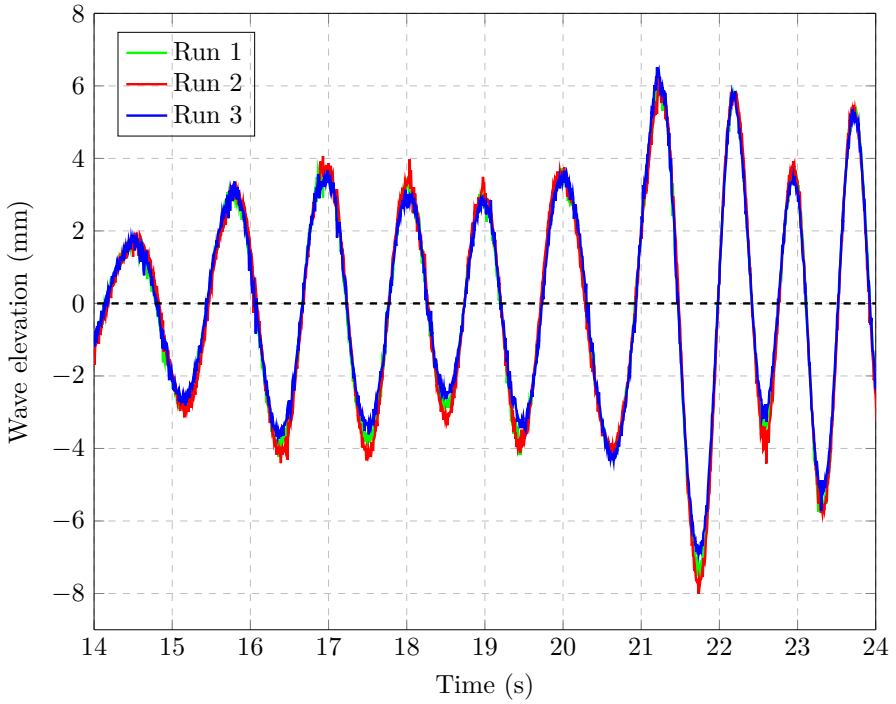

FIGURE 11.13: Three time series of free surface elevation in the narrow tank at DkIT with no model installed.

Once aligned, two measures were used to assess the repeatability of the signal: the cross-correlation factor and the RMS of the signal. The cross-correlation factor between each pair of 3-hour signals was calculated. A value of 1 indicates a total positive correlation, a value of -1 indicates a total negative correlation and a value of 0 indicates no correlation between two signals [240]. Table 11.1 lists the cross-correlation factor between all possible pairings of the three signals. The cross-correlation factor between the first and the second time series of free surface elevation is termed X_{12}, the cross-correlation factor between the first and the third time series of free surface elevation is termed X_{13}, and the cross-correlation factor between the second and the third time series of free surface elevation is termed X_{23}.

Cross-Correlation Factor		
X_{12}	X_{13}	X_{23}
0.9976	0.9955	0.9964

TABLE 11.1: Cross-correlation factor between three polychromatic time series in the DkIT narrow tank with no model installed.

As can be seen, there is a very high level of correlation between the three signals, in excess of 99%, and this could possibly be improved further with a higher sampling rate, which would allow for more precise alignment of the signals. However, the cross-correlation factor alone is insufficient to ensure the wave spectrum generated by the narrow tank is repeatable. Consider a time series,$y_1 = x(t)$, and a second time series which comprises of the first scaled by a linear factor, $y_2 = Ax(t)$, where A is the linear factor. The cross-correlation between y_1 and y_2 is 1, but the magnitudes of the two signals are clearly different. The high cross-correlations in Table 11.1 show that the time series of the free surface elevation for the three tests are very similar in form, but are not necessarily the same magnitude. To check that the magnitude of the free surface elevation is also repeatable, the root mean square value of the free surface elevation recorded in the three tests was calculated, and the results are presented in Table 11.2.

RMS of wave elevation		
Run 1	Run 2	Run 3
5.3090 mm	5.3104 mm	5.2082 mm

TABLE 11.2: Root mean square of the wave elevation recorded during three polychromatic tests in the DkIT narrow tank with no model installed.

As can be seen, the root mean square value of the wave elevation remains relatively consistent throughout the three tests. Note that, since the tank was required for other testing, some time elapsed between the first two runs and the third run described here. While the position of the wave probe was not altered, the probe was re-calibrated during this time, which may explain the slight difference in the root mean square value for the third run when compared to the first two.

Based on the cross-correlation factor and the RMS value, it can be seen that the tank is capable of repeatedly generating pseudo-random wave elevations at different times. Once tank repeatability had been demonstrated, the experimental method to measure the hydrodynamic parameters of the OWC, described in Section 11.4.2, could be implemented.

11.4.4 Results

In this section, the results for the experimentally measured added mass and the radiation damping, using the methods describe in Section 11.4.2, are presented. Figure 11.14 illustrates the measured results for the added mass based on $H(f)$ illustrated in Figure 11.8 and Equation (11.25). Overlaid on Figure 11.14 is a second set of added mass results based on the Fourier transfer functions $H_1(f)$, $H_2(f)$ and $H_3(f)$, illustrated in Figures 11.9, 11.10 and 11.11, and Equation (11.29). Figure 11.15 illustrates the measured results for the added mass and radiation damping of the OWC based on Equation (11.25), overlaid with a second set of radiation damping results based on Equation (11.30). As can be seen, the results obtained for the added mass, shown in Figure 11.14, are virtually identical. The same is true for the radiation damping results, shown in Figures 11.15.

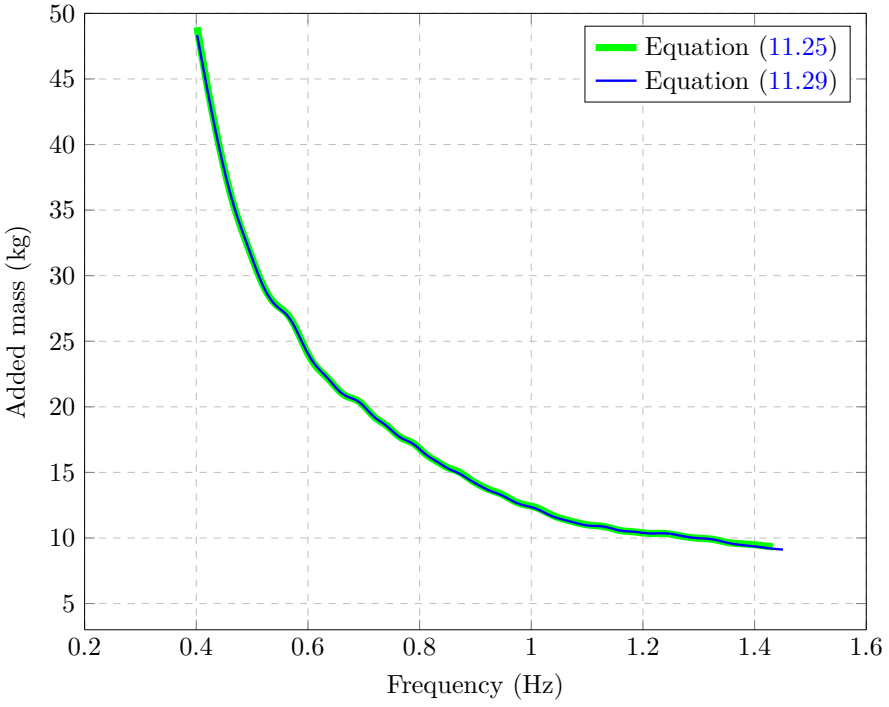

FIGURE 11.14: Added mass vs. frequency for single-chamber OWC using spectral analysis based on Equations (11.25) and (11.29).

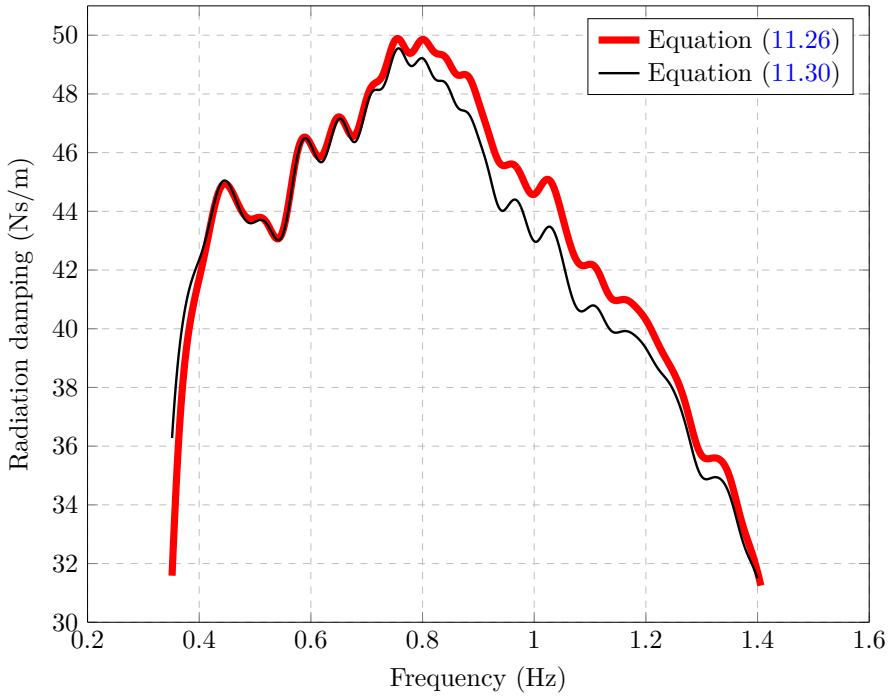

FIGURE 11.15: Radiation damping vs. frequency for single-chamber OWC using spectral analysis based on Equations (11.26) and (11.30).

As can be seen, the results obtained for the added mass, shown in Figure 11.14, are virtually identical. The same is true for the radiation damping results, shown in Figure 11.15.

11.5 Proposed method for using linear damping to determine hydrodynamic parameters

The rationale for performing forced-oscillation tests on the modified single-OWC model with the large, sealed airbox, is that the compressibility of air allows motion of the water column to take place in response to an incident wave while the air pressure in the OWC chamber varies in a linear fashion. In order to perform a frequency domain analysis, on time domain data to determine the added mass and radiation damping of the water, the time series involved must vary linearly. The variation in the air pressure in an OWC with an orifice is not linear, as discussed previously, and as illustrated in, for example, Figure 11.16. Figure 11.16 shows the variation in the air pressure in the OWC chamber

of Model 1 for a monochromatic wave of 0.8 Hz and 15 mm amplitude for an orifice of 10 mm in diameter, demonstrating the non-linear variation of the air pressure.

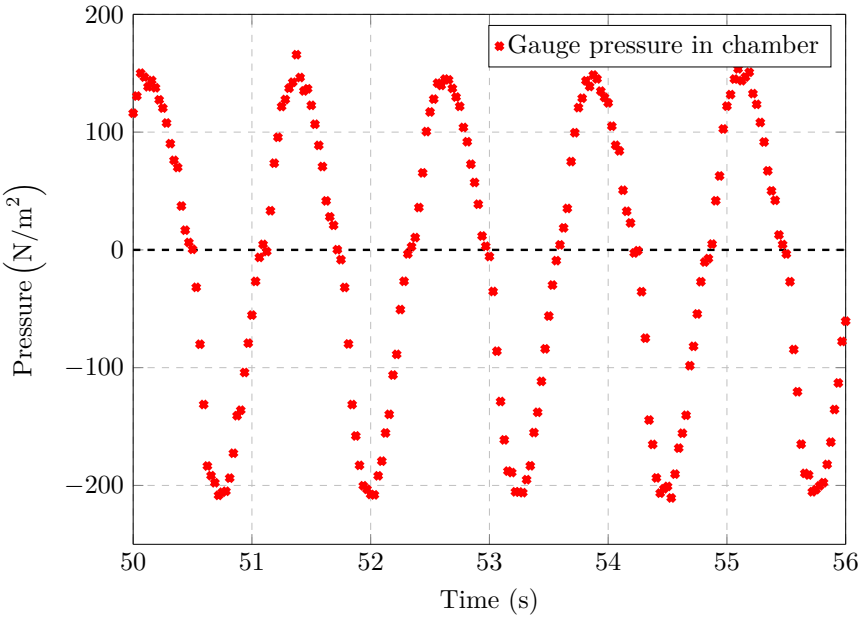

FIGURE 11.16: Pressure variation vs. time within the single-chamber OWC model with orifice (note the non-linear nature of the variation).

However, it is possible to configure an OWC so that the pressure varies in a close to linear manner while still allowing airflow into and out of the chamber (and, thus, satisfying Equation (5.1), see Chapter 5). Airflow into, and out of, the chamber can take place, while achieving linear air pressure variations within the OWC chamber, by covering an orifice with a permeable membrane. Such an arrangement will result in close to linear pressure variations in the air chamber above the water column. This approach has been used in previous work to model the damping characteristics of a Wells Turbine on an OWC [241], and carpet tiles are one form of permeable membrane that have been used. In the current work, the orifice, located at the top of the air chamber of Model 1, was covered with a face dust mask to create a permeable membrane. The variation of the pressure within the single-chamber OWC, for the same monochromatic wave of 0.8 Hz and 15 mm amplitude, with the membrane installed, is illustrated in Figure 11.17.

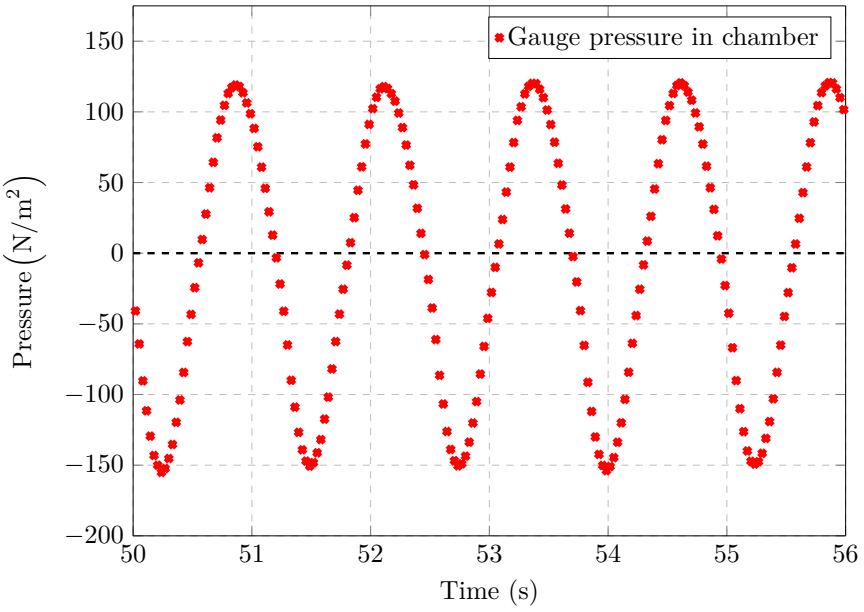

FIGURE 11.17: Pressure variation vs. time within the single-chamber OWC model using permeable dust mask (note the linear nature of the variation).

Figure 11.18 illustrates the amplitude spectrum of the pressure time series shown in Figure 11.17, showing a strong, single peak at the incident wave frequency of 0.8 Hz, although two small harmonics can be seen at 1.6 Hz and 2.4 Hz.

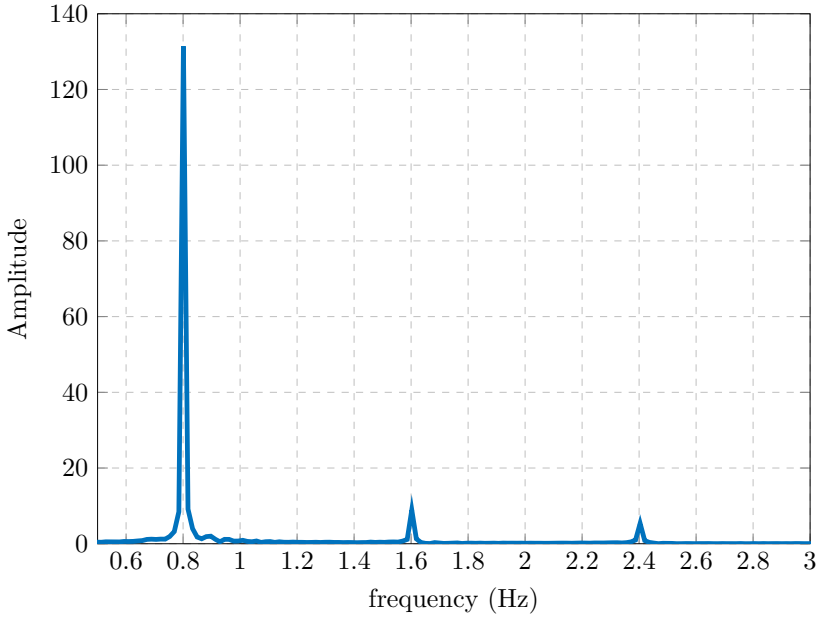

FIGURE 11.18: Amplitude spectrum of the pressure time series shown in Figure 11.17 (note the large peak at the incident wave frequency of 0.8 Hz).

Figure 11.18 would appear to demonstrate that installing a permeable membrane over the orifice of Model 1 produces near-linear air pressure variations. The near-linear air pressure variations, which could now be generated, allowed for a series of tests to be performed to carry out initial investigations into a proposed method for measuring the hydrodynamic parameters of the single-OWC model, without the need for a large airbox.

The proposed process to measure the hydrodynamic parameters of the OWC chamber is virtually identical to that used in Sections 11.3 and 11.4. However, two advantages over that process were anticipated. The first advantage is that it is only necessary to use a single model, so there is no need to replace one model (used for the fixed-body tests) in the tank, with a second, modified model (used for the forced-oscillation tests). Thus, both the water column, and the wave probe required to record the motions of the column, are guaranteed to be in the same location relative to the wave maker and the upstream wave probe for all tests required, removing a potential source of error. Furthermore, the expense of building a second model with a large airbox is removed.
The second expected advantage is that, by allowing airflow into and out of the chamber, the water column motion for the forced-oscillation tests would be greater using this technique when compared to those resulting from the methods described in 11.3 and 11.4. The signal to noise ratio would therefore increase. However, the reduced damping levels, which allow for greater motion of the water column, may also results in increased sloshing and distort results, as discussed further in Section 11.6.

11.5.1 Implementation of proposed method of determining hydrodynamic parameters of an OWC using linear damping

Model 1 was used to implement the technique proposed in the current section to measure hydrodynamic parameters of the OWC. For the fixed-body tests, the air chamber of Model 1 was sealed from atmosphere. For the forced-oscillation tests, the permeable membrane was installed on Model 1. (Note that Model 2 is not required for this technique.)

During the monochromatic wave tests, incident waves of amplitudes 5 mm, 10 mm and 15 mm, with frequencies ranging from 0.4 Hz to 1.2 Hz, in increments of 0.1 Hz, were used. The reduced number of frequencies used, compared to the number used in earlier tests, was due to the limited availability of the tank. Three separate Bretschneider wave

spectra were used to perform the polychromatic wave tests, the significant wave heights and energy periods of which are listed in Table 11.3, below.

Spectrum	Energy period	Significant wave height
1	0.85 s	0.20 m
2	1.27 s	0.30 m
3	1.53 s	0.30 m

TABLE 11.3: Bretschneider spectra used for linear damping tests to determine hydrodynamics.

11.5.2 Results of the measurement of the hydrodynamic parameters of an OWC with linear damping

Figure 11.19 illustrates the results obtained for the added mass, and Figure 11.20 the results obtained for the radiation damping, determined for the single-chamber OWC using the linear damping method with monochromatic waves.

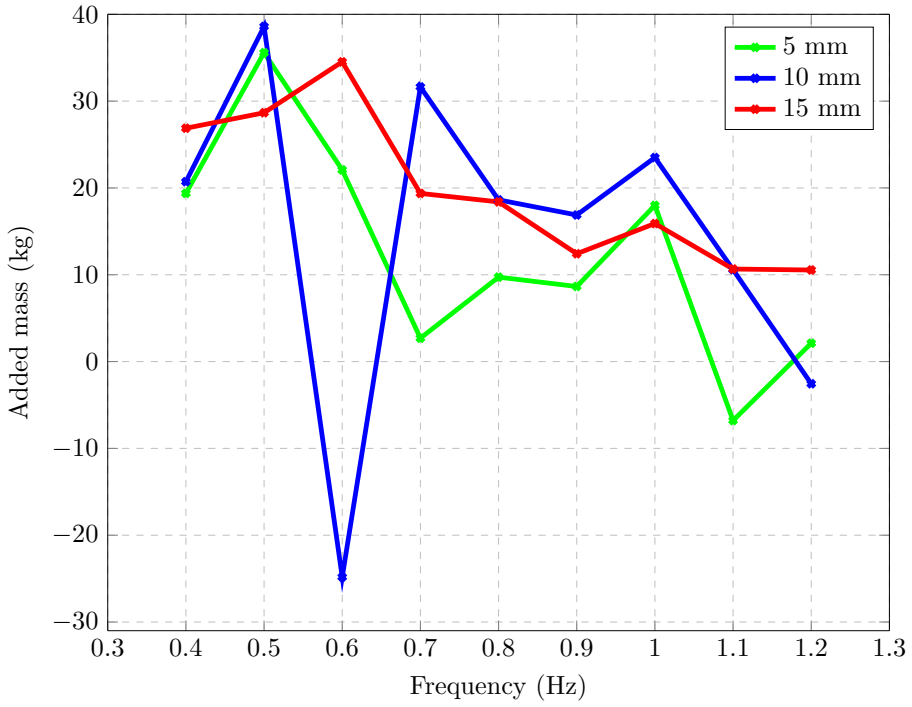

FIGURE 11.19: Added mass vs. frequency for single-chamber OWC obtained using the linear damping technique with monochromatic waves.

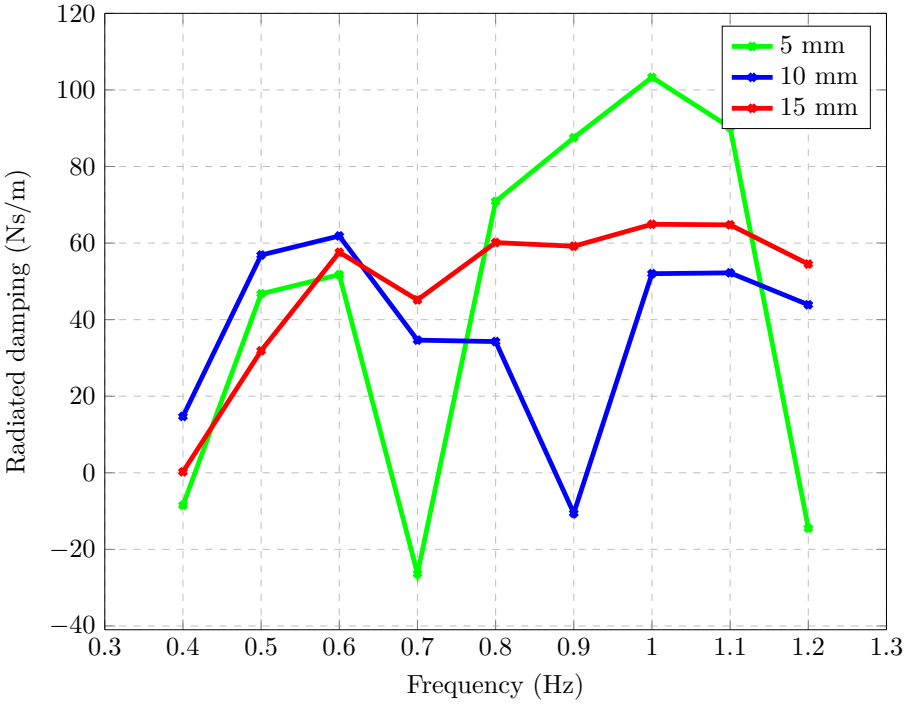

FIGURE 11.20: Radiation damping vs. frequency for single-chamber OWC using the linear damping technique with monochromatic waves.

The added mass, as determined using the three polychromatic wave spectra listed in Table 11.3, is illustrated in Figure 11.21. Note that the three plots are almost, although not entirely, identical.

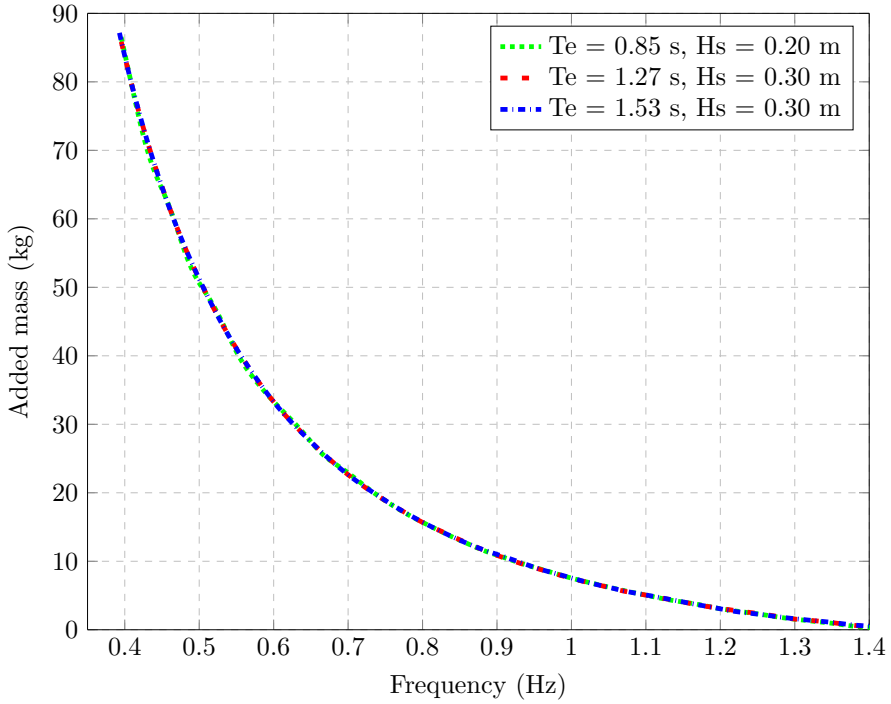

FIGURE 11.21: Added mass vs. frequency for single-chamber OWC using the linear damping technique with polychromatic waves.

The radiation damping, as determined using the three polychromatic spectra listed in Table 11.3, is illustrated in Figure 11.22.

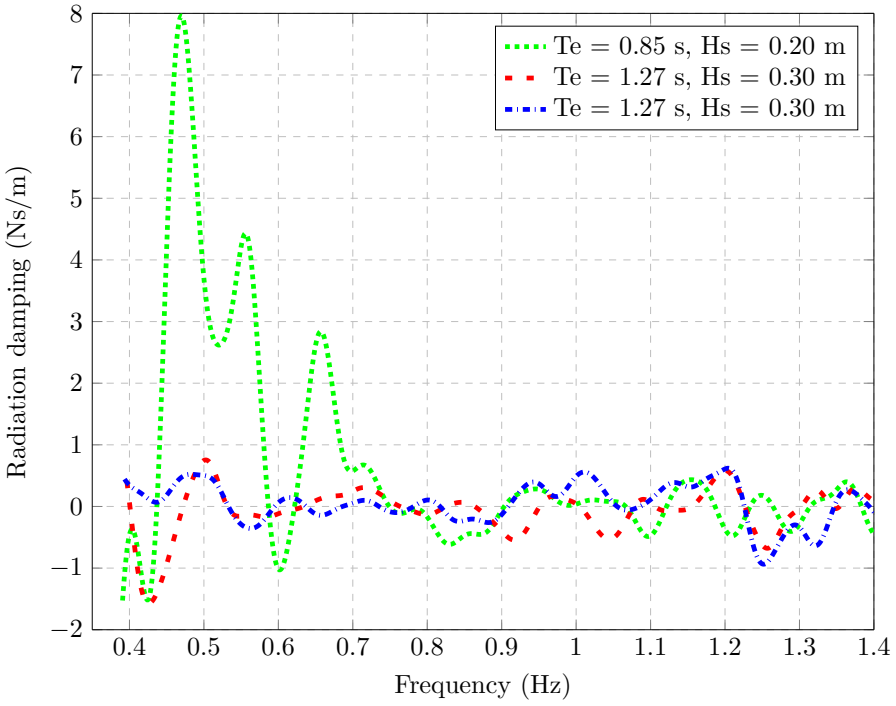

FIGURE 11.22: Radiation damping vs. frequency for single-chamber OWC using the linear damping technique with polychromatic waves.

11.6 Discussion of results

The results obtained using the method proposed for measuring the hydrodynamic parameters of an OWC suggest that the method has potential, but also raise some issues which could be investigated further in future work. Consider first the added mass results obtained using the methods described in Sections 11.3 and 11.4. As can be seen in Figure 11.4, for monochromatic waves, a strong level of consistency has been obtained between the added mass results obtained for the three different incident wave amplitudes used across the range of wave frequencies. Large error bars, based on measurement uncertainty, are present for the added mass results at 5 mm, however the error bars for the results obtained using wave amplitudes of 10 mm and 20 mm are significantly smaller. Furthermore, close agreement has also been obtained for the added mass obtained using both monochromatic and polychromatic waves, as can been seen in Figure 11.23, where the results for the added mass as measured using monochromatic waves with an amplitude of 15 mm are overlaid on the added mass as measured using

polychromatic waves. For comparison, Figure 11.23 also illustrates the corresponding added mass values predicted by WAMIT for the water column.

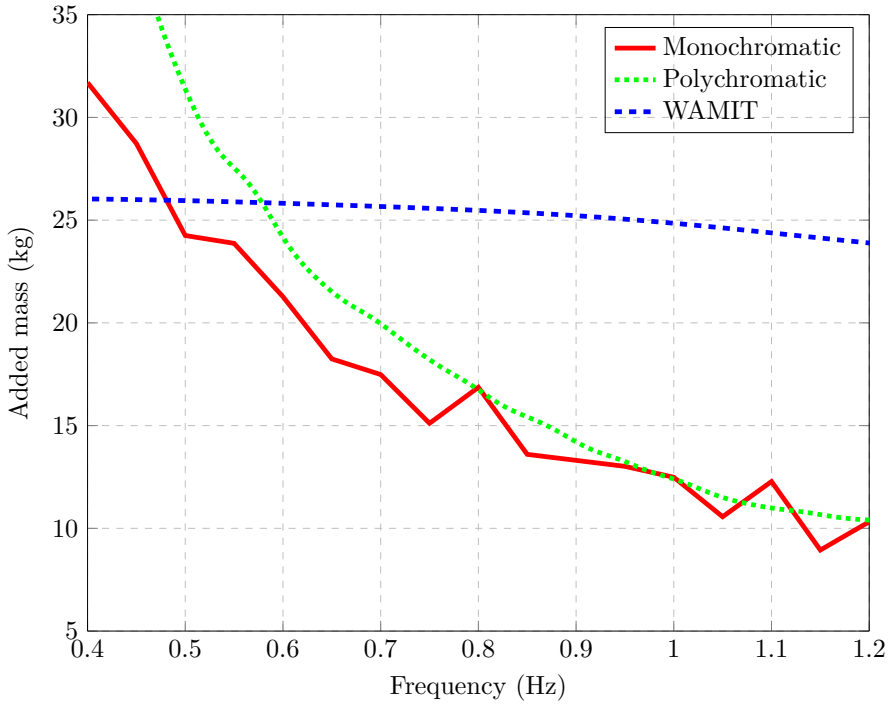

FIGURE 11.23: Comparison between the added mass for a single OWC determined using mono- and polychromatic waves, as described in Sections 11.3 and 11.4, and the corresponding results from WAMIT.

The consistency in the added mass results, combined with the demonstration of the effective use of polychromatic waves to determine the hydrodynamic parameters of a floating cylinder in simulation (see Appendix A, would suggest that the proposed measuring technique has merit. The comparison between the measured added mass for the OWC with the added mass predicted by WAMIT, illustrated in Figures 11.23, shows that, while the form of the added mass versus frequency curves obtained numerically and experimentally do not agree, the magnitudes of the experimental results are of the expected order.

The results illustrated in Figure 11.5, for the radiation damping found using monochromatic waves, show good agreement between the different amplitudes of incident waves used to perform the tests, suggesting that the motion involved was not sufficient for viscous damping to have a significant effect. Also, what appears to be an outlier can be seen for each amplitude at 0.9 Hz in Figure 11.5. Furthermore, the radiation damping curves in Figure 11.5 dip below zero, which is not realistic.

Figure 11.24 compares the results obtained for the radiation damping using mono- and polychromatic waves, and the radiation damping predicted by WAMIT. Note that the outlier at 0.9 Hz, which is not present in the polychromatic waves, has been removed from the monochromatic example in this figure. As for the added mass, the order of magnitude for the radiation damping values obtained numerically and experimentally are the same. However, the agreement between the results obtained using monochromatic waves and those using polychromatic waves is not strong. A number of possible explanations for the anomaly at 0.9 Hz, and for the difference in the radiation damping results for the mono- and polychromatic waves, are suggested later in this section.

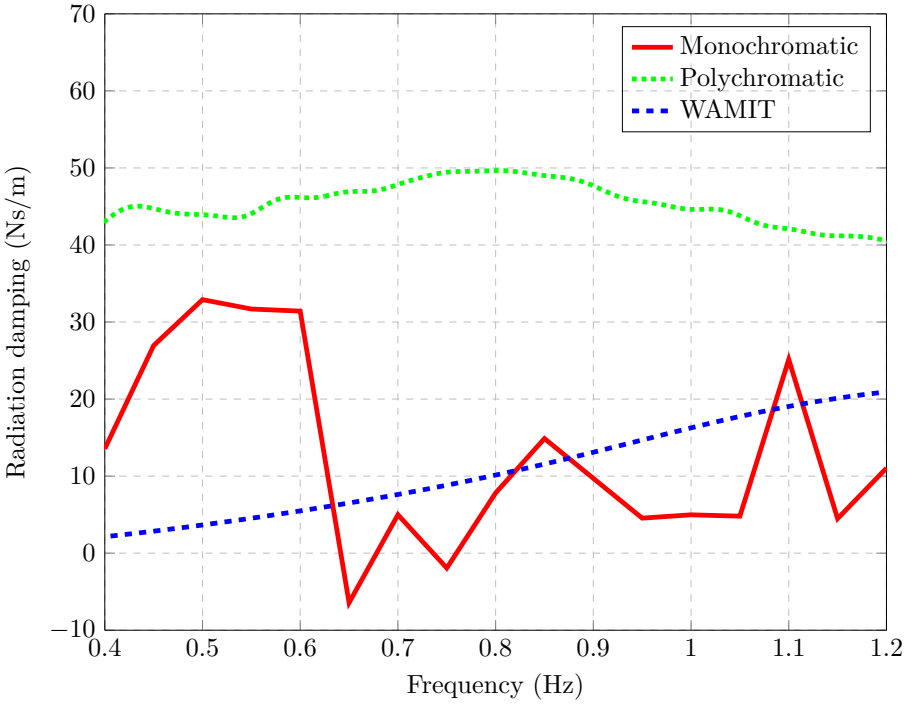

FIGURE 11.24: Comparison between the radiation damping for a single OWC determined using mono- and polychromatic waves, as described in Sections 11.3 and 11.4, and the corresponding results from WAMIT.

Figure 11.25 compares the results obtained for the exciting force using mono- and polychromatic waves, and the exciting force predicted by WAMIT. As might be expected, closer agreement has been achieved between the measured and predicted results for the exciting force than has been achieved for the added mass or the radiation damping. The exciting force depends on a single measurement, and is unaffected by any alignment issues.

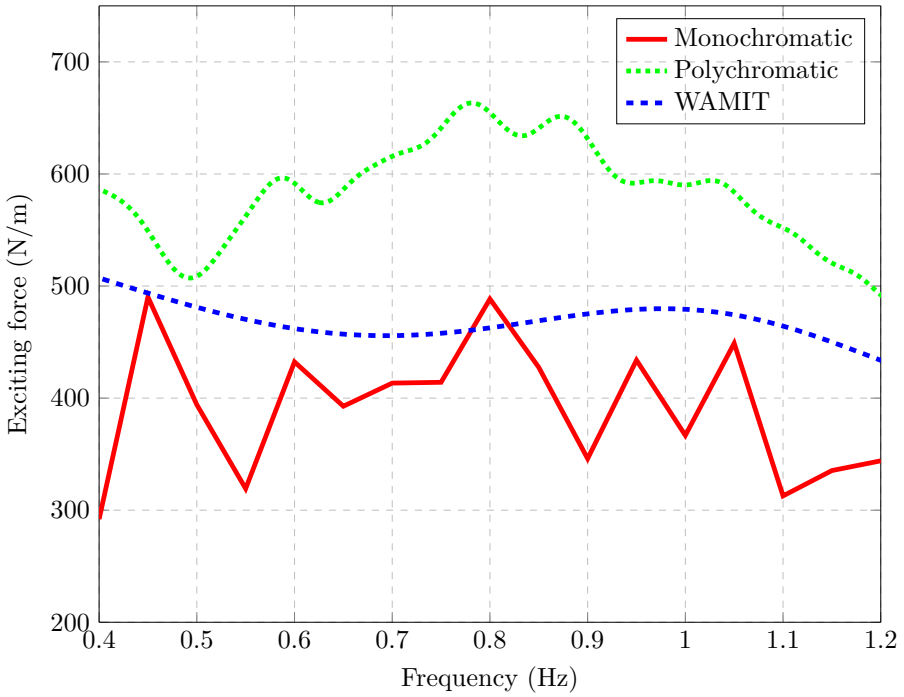

FIGURE 11.25: Comparison between the exciting force for a single OWC determined using mono- and polychromatic waves, as described in Sections 11.3 and 11.4, and the corresponding results from WAMIT.

Considering now the results obtained using the method described in Section 11.5 using monochromatic waves with near-linear damping. The results obtained using monochromatic waves with linear damping, in Figure 11.19, show less consistency compared to those in Figure 11.4. The removal of what appears to be an outlier at 0.6 Hz for the 10 mm amplitude wave yields the plot shown in Figure 11.26. With this outlier removed, the results can be seen to be generally in agreement with those shown in Figure 11.23, both in magnitude and trend. The results obtained for the added mass using polychromatic incident waves (shown in Figure 11.21), show a large degree of consistency for the three different spectra used, but differ from the results shown in Figures 11.23 and 11.26 in that added mass values, at low frequencies, are higher than in the previous cases, and the curve appears to tend to zero for higher frequencies. The shape of the curves in Figure 11.19 is not dissimilar to the shape of the curves in Figures 11.19 and 11.23, but given the inverse quadratic form of Equation (11.3), this profile is not surprising.

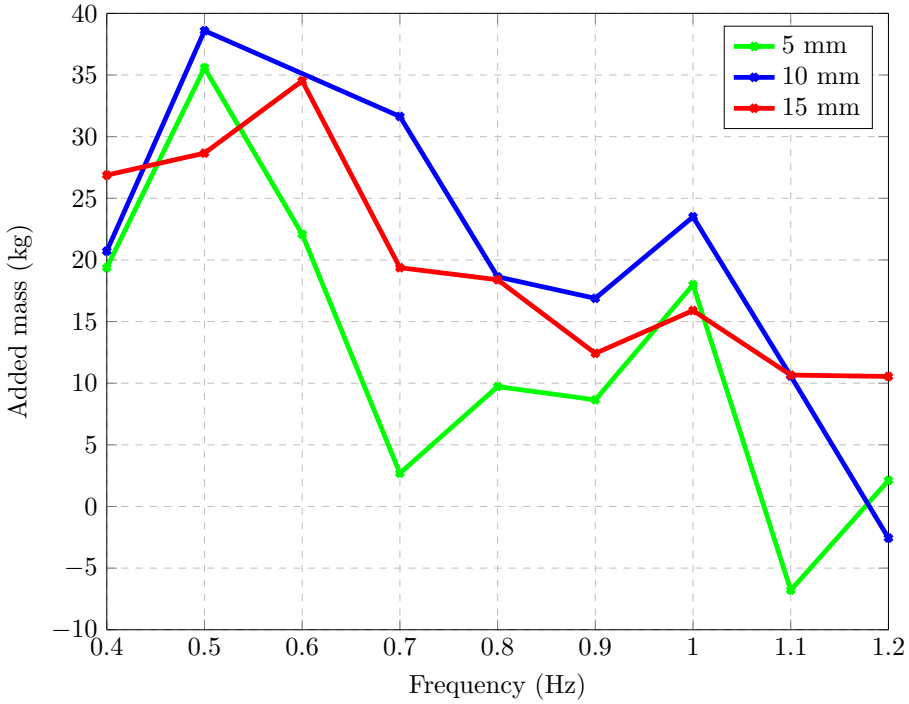

FIGURE 11.26: Added mass measured using monochromatic waves with near-linear damping vs. frequency for single-chamber OWC with outlier removed.

The radiation damping values for the polychromatic waves obtained from the near linearly-damped tests shown in Figure 11.22 are, however, surprising. These damping values are unexpectedly low and inconsistent with those found using the methods described in Sections 11.3 and 11.4.

11.6.1 Issues with the proposed technique

While the proposed technique for measuring the hydrodynamic parameters of an OWC shows promise, a number of issues arose during the implementation of the technique, including apparent outliers and discrepancies in the results obtained. There are a number of possible explanations for these outliers and discrepancies. First and foremost is the assumption that the OWC moves only in a piston-like fashion, analogous to a heaving body. This neglects sloshing modes. However, such modes are clearly present in reality. During the testing that was performed using Model 2, a camera, focussing on the water surface, was installed in the airbox, which clearly showed the presence of sloshing modes similar to those which can be seen in Figure 9.52 of Chapter 9. Such sloshing will obviously manifest itself on the readings from the wave probe located within the OWC

chamber. Sloshing will also occur to an even greater degree during the linearly-damped test, as the water column is freer to move. Figure 11.27 shows samples of the time series from the internal wave probe, for each frequency tested, during the linearly-damped tests with amplitudes of 5 mm. In each case, the series is dominated by the incident wave frequency resulting in a piston-like motion of the water column. Nonetheless, the effect of the sloshing modes is also clearly visible in the results. Run-up of the incident wave on the curved surface of the back wall of the chamber may have exacerbated the effect of the sloshing modes.

Potential sources for error may also have arisen when the single-chamber OWC model in the tank was replaced with the modified version. Care was taken to ensure the water columns were positioned as close to identically in the tank as possible, and that the location of the internal wave probes within the chambers was the same. However, slight positioning differences can effect the outcome of the analysis, particularly given how small the phase difference between signals, such as the pressure signal for the fixed-body tests and the equivalent signal during the forced-oscillation tests, can be. Related to this is the need to temporally align data from different tests. The potential for error here is clear, and the best fit can only be achieved to a precision of one sample time step.

Another possible source of error is that it is not known how effective the narrow tank paddle is at absorbing wave reflections, in particular those at higher frequencies. In Chapter 7, it was shown that the narrow tank beach is effective at absorbing waves, and that, when no other obstruction is present in the tank, the wave maker is calibrated to accurately generate the requested waves. However, for high frequency waves, where the energy in the wave is located towards the top of the water column, much of the energy in the wave can be reflected by a model in the tank back towards the wave maker. If the wave maker is not effectively removing the reflected energy, the energy may be partially reflected back again towards the model by the wave maker. This reflected energy may thus potentially interfere with the incident wave, as experienced by the model.

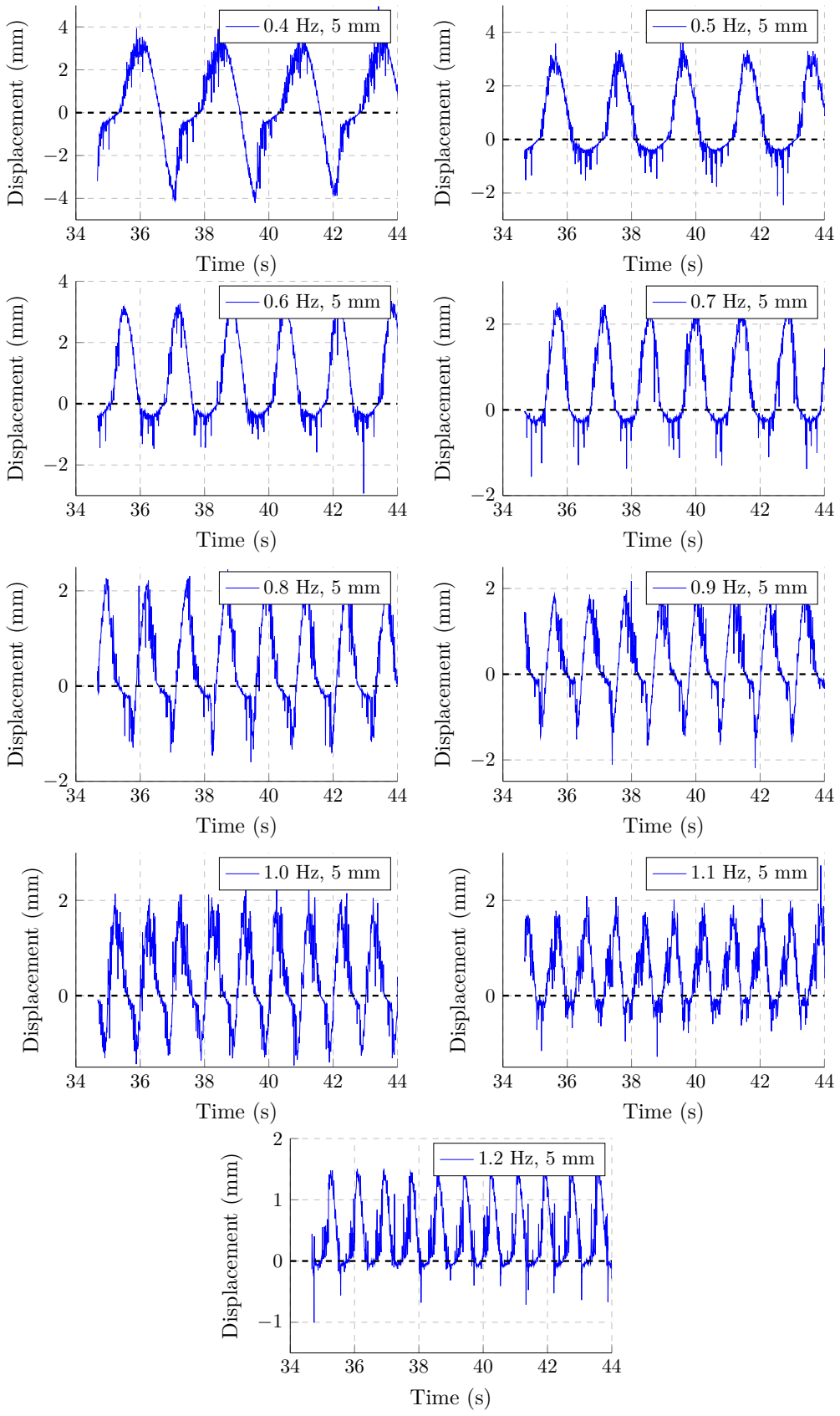

FIGURE 11.27: Time series extracts for 5 mm amplitude wave forced-oscillation test with the porous membrane installed on Model 1.

11.6.2 Potential improvements and further work

The issues discussed above suggest ways in which, in the absence a dedicated forced-oscillation rig, the technique for measuring the hydrodynamics of an OWC might be improved, and further follow up work that could be carried out on the topic.

Improve free surface motion capture

Firstly, to address the issue of sloshing within the OWC chamber, the technique could be perfected using a simple, box-like OWC designed so as to minimise sloshing mode resonances over the range of frequencies of interest. For such an OWC, the assumption that the water column acts in a piston-like mode only would be more valid. Once the technique was perfected for a single mode water column, it could potentially be developed further to include sloshing modes. The use of multiple wave probes, to record the motion of the water column at several points within the chamber, in the direction of wave travel, would allow the motion of the free surface to be better captured, and the different sloshing modes of the water column could be decomposed from the time series measured by the multiple wave probes.

Explore effect of wave reflections

To explore whether waves are being reflected from the wave maker during a test, experiments could be performed in a large, 3-dimensional tank. Such a setting would minimise the effect of any wave energy reflected, rather than absorbed, by the wave maker, although different results would be expected for the hydrodynamics in the 3-dimensional case when compared to the 2-dimensional case [242].

Synchronise testing and data acquisition

The ability of the wave maker to create virtually identical free surface elevation time series has been demonstrated. Thus, the need to align data sets could be eliminated if the same action used to start the wave maker was also used to start the data acquisition system, which is not currently implemented at the DkIT narrow tank, where the wave maker and data acquisition system are currently entirely isolated from each other. A system to begin recording at the same moment the wave maker is initiated would seem a sensible improvement to the current setup.

Employ numerical reconstruction of added mass/radiation damping

It has been noted above that the phase difference between some signals, notably the air pressure signals obtained during the fixed- and forced-oscillation tests, is small, and thus any error in measurement would have a large effect on the results obtained for the hydrodynamic parameters. However, if confidence can be had in either the added mass or radiation damping, the other could be found using the Ogilvie relations [139], derived from the Kramers-Kronig transform or the Hilbert transform [243], in a process similar to that used to reconstruct the added mass from the radiation damping for the numerical model, as described in Chapter 5.

Use admittance approach

Another possible avenue of investigation is to use the admittance approach to modelling an OWC based on susceptance and conductance. The fixed-body test would be replaced by a fully-open, undamped OWC, although sloshing could be a significant issue with this approach which has not been explored at this time.

At this time, the results obtained for the hydrodynamics of a single-OWC using the methods described in the current chapter must be treated with great caution, and a number of questions remain to be answered. Further testing is required to refine, and establish the usefulness of, the techniques described.

Chapter 12

Conclusions

A number of conclusions may be drawn from the work described in this thesis. In this chapter, the conclusions are presented in order of academic significance. There then follows an outline of the progress of the commercial objectives. Finally, some suggestions for further work are presented.

12.1 Single-chamber OWC modelling

A coupled, non-linear, hydrodynamic/thermodynamic numerical model of the single-chamber OWC, based on BEM, orifice theory and the laws of thermodynamics, has been successfully implemented using a state-space representation. It has been demonstrated through rigorous tank testing that the time domain numerical model, and the techniques developed to propagate the parameters in that numerical model, may be used to effectively predict the behaviour of a physical model of the single-chamber OWC both with, and without, control components installed, over a range of incident wave amplitudes and frequencies, and with the water column subject to a range of damping conditions. The modular nature of the state-space framework allows the numerical model to be easily adapted to predict the behaviour of different, complex OWC geometries. As a consequence of the successful predictions made by the numerical model, it can be further concluded that the technique employed to reconstruct the frequency-dependent added mass for the water column from the radiation damping predictions from BEM is valid. The work described herein numerically modelled systems which included either an orifice

or air admittance valves. From the comparison between the predictions made by the numerical model and the results obtain for the physical model (see Chapter 9), it may be concluded that a relatively simple numerical model of an air admittance valve with stiction can capture key characteristics of the behaviour of the physical valve.

Furthermore, other arrangements, for example, systems where airflow may take place into, and out of, an OWC chamber through a porous membrane or through a turbine, can be readily implemented in the numerical model developed here. The numerical model may be easily adapted once a mathematical description of the relationship between the mass flow of air into, or out of, the OWC chamber, and the pressure difference between the air in the chamber and atmosphere, is known. Modification of the numerical model may be achieved by adjusting the appropriate terms in the state-space representation. It is intended that the non-linear, time domain model of the single-chamber, fixed OWC be extended to numerically model a floating platform comprising an array of interacting OWCs, such as that proposed by WEI, using the theory outlined in Chapter 5. It is further intended that, by being freely available in the public domain, the time domain numerical model may serve as a basis for any future time domain numerical models of an array of manifolded OWC devices which may be developed by other researchers in this area.

12.2 Measurement of hydrodynamic parameters

The results for the measured frequency-dependent parameters obtained using the method proposed in Chapter 11, which arose from an investigation into the effect of air compressibility on the behaviour of, and power absorbed by, a single-chamber OWC device have been presented. While the results must be treated with caution, for the reasons discussed in Section 11.6.1, the proposed method has shown some promise, and the use of spectral methods can save considerable time when experimentally measuring frequency-dependent parameters, as demonstrated by a case study, which may be found in Appendix A. More refined measurement of the free surface elevation, and a method by which the data acquisition system and the wave generator may be started simultaneously, should lead to more accurate results for the added mass and the radiation damping using the proposed technique.

12.3 Investigation into the effect of air compressibility

The investigation into the effect of air compressibility, presented in Chapter 10, compared the results obtained for two single-chamber OWC physical models with identical wetted areas, but different volumes of air contained within the air chamber. The volume of air in Model 1 was scaled using Froude scaling, i.e., by the cube of the scaling factor, whereas the volume of air in Model 2 was scaled to the square of the scale factor. Previous studies into the effects of air compression in physical scale models of OWCs have employed secondary air volumes which were connected to the air volume above the water column using flexible hoses. However, such an arrangement introduces further, undesirable dynamics to the thermodynamic system. By employing an air volume situated directly above the free surface of the water column, and thus obviating the need for any kind of connecting arrangement to a secondary air volume, the arrangement used in the current thesis eliminates such undesirable dynamics.

The investigation has shown that neglecting the effect of air compression can have a significant effect on the power absorbed by a scale physical model of an OWC. The effect may be to either increase or decrease the power absorbed by the scale model, depending, amongst other things, on the incident wave frequency, which may be, in part, understood as a change in the natural frequency of the water column system. Such a result is in line with theory, and with the results obtained in other studies which include secondary air volumes and flexible hoses. As was expected, the difference between the pressure within the air chambers of Model 1 and Model 2 is less significant when the orifice diameter is increased, and hence the pressure within the air chambers is lower.

It has been proposed in the literature that the effect of air compressibility on the behaviour of an OWC might be replicated at model scale by using a secondary air volume which is significantly smaller than that used in previous studies which make use of secondary air volumes. The variations of pressure within this small secondary air volume would work against a mechanically-generated force, such as may be provided by a linear spring, which would replicate at model scale the air spring effect arising from air compressibility at full scale. Employing a small secondary air volume would facilitate the testing of floating (as opposed to fixed) physical scale OWC models. A data set, which may be used to assess the success of using such a small secondary air volume to replicate

the air spring effect, has been generated as part of the work carried out in this thesis, and is available in the public domain.

12.4 Progression of proposed WEI platform to TRL 3

The conclusions presented above are chiefly of academic significance. The WEI platform was conceived as a commercial project, and the remaining conclusions are both commercial and academic in nature. Through physical and numerical modelling, the proposed WEI wind/wave platform has been progressed to TRL 3. The technical feasibility of the concept has been demonstrated. It may be concluded that it is possible to manifold and harvest pneumatic power from a large number of OWCs, while rectifying such pneumatic power so that air is directed in a uni-directional manner through valves and plenums, allowing for the use of uni-directional turbines to drive electrical generation. The manifolding of the air can reduce the required number of turbines and thus reduce costs.

Monochromatic wave testing has allowed the frequency-dependent wave power absorption characteristics of the platform to be determined. As can be seen in Figure 9.25 in Chapter 9, which illustrates the power absorbed by the platform in various configurations versus incident wave period, the platform absorbs significant power between 1 s and 1.7 s. At full scale, these wave periods correspond to approximately 7 s and 12 s. Comparing these periods to those in the North Atlantic scatter matrix in Figure 2.1, it can be concluded that the platform is tuned to absorb wave power in the frequencies which dominate the Atlantic wave spectrum.

Initial estimates suggested a nameplate generator rating of 500 kW per chamber for the full-scale platform. Based on the results presented herein, it can be concluded that the rating is appropriate, and is in line with the rating of similarly-sized OWC devices. For a full-scale, 32-chamber platform, and assuming no destructive interference between OWC chambers, it can be inferred that a total nameplate rating for the wave energy converting element of the proposed WEI platform of 16 MW would be appropriate.

From the analysis of the results from the tank testing of the physical scale models, and the results from the numerical modelling, it may be concluded further that a number of areas for improvements to the WEI platform design exist, in respect to the wave power absorbed by, and the pitching motion of, the platform. With reference first to

the wave power absorbed by the model platform, it has been demonstrated that useful levels of wave energy have been absorbed by the scale model platform during testing. However, the maximum power absorbed by the physical scale model of the platform occurred with the model in Configuration 5 (i.e., when the buoyancy tubes with larger damping plates were installed, the wave guide shoes were removed and with the suction plenum was open to atmosphere), when the platform absorbed a maximum of ~50% of the power in the wave front presented to the model. In Configuration 4, when the model was configured as for Configuration 5 with the difference that the suction plenum was not open to atmosphere, the platform absorbed a maximum of ~37% of the power in the waves. Note that the power absorbed when the model was set up as in Configuration 4 was smoother with respect to time than the power absorbed when the model was in Configuration 5. The increase in power absorbed when the suction plenum lid was removed in Configuration 5 suggests that the current configuration of the 32-OWC platform is over-damped for maximum wave energy absorption. The frequency domain numerical model of the platform further suggests that reducing the PTO damping would improve the wave energy absorbed. An average level of PTO damping for each chamber of 204 Ns/m was obtained from the tank testing of the model platform in Configuration 4. Numerical simulations suggest a damping level of the order of 65 Ns/m per chamber would be the optimum level of damping.

A second potential area for improvement in the design of the WEI platform concerns the pitch motion for the model platform. The economic viability of a full-scale platform, based on the WEI concept, requires that one or more wind turbines be installed on the platform. One of the main results obtained from the tank testing of the 1:50, 32-OWC physical scale model platform was the determination of the amplitude of the pitch motion of the platform under certain wave conditions. The greater the pitch motion of the platform, the higher the levels of nacelle axial acceleration a wind turbine on the platform would experience. While no explicit standard for nacelle axial acceleration currently exists, industry practice is to limit such acceleration to between 0.2 g and 0.3 g [244]. The maximum pitch displacement recorded during the monochromatic wave testing of the 1:50, 32-OWC physical scale model of the platform, with an amplitude of approximately 2.75 degrees, occurred with the model set up as in Configuration 3, when the damping plates and wave guide shoes were removed from the model platform (see Chapter 6), and the model was subject to an incident wave period of 1.56 s, with the 20 mm Venturi pairing installed. Assuming a wind turbine tower height of 125

m located at the prow of a full-scale platform with mooring similar to the arrangement used during the tank testing, this would lead to nacelle accelerations in excess of 0.3 g, and the effect of snatching would potentially exacerbate the issue. Thus, a significant conclusion is that there is a need to modify the current platform design to reduce the pitch motion if offshore wind turbines are to be installed. As a result, WEI are currently designing changes to the platform to reduce pitch motion in the range of operational incident frequencies, and have proposed a novel, gravity-based mooring arrangement, which is to be investigated in planned future rounds of testing. A secondary benefit of reducing the pitch response of the platform would be to ameliorate the chamber broaching issue described in Chapter 9. Further tank testing of scale models will be required to determine if the redesign has reduced the pitch motion of the platform, and to establish the effect of any reduction in the pitch motion on the wave power absorbed.

12.5 Further work

A number of validated software design tools have been developed as part of this thesis, and the next step in the development of the tools is to build upon the time domain numerical model of the single-chamber OWC. The time domain numerical model can be readily adapted to model the behaviour of the OWC device when subject to polychromatic waves, and the predictions compared to the results of tank testing.

Once a successful polychromatic numerical model has been validated, the numerical model can be extended to create a non-linear time domain model of the complete floating platform. Such a model would need to account for the hydrodynamic interactions between all the water columns, and the thermodynamic interactions within the chambers and the plenums. The results of the testing, shown in Section 9.2.1.1, demonstrate that the air pressure within a plenum can be considered constant throughout the plenum at model scale, which would considerably simplify a time domain model of the full model-scale platform. However, it is unlikely that the pressure could be considered constant in the plenums of a full-scale platform. One approach that could be used to account for the thermodynamic interactions in the plenums is to consider the plenums as comprising a number of smaller control volumes, the pressure in each of which is considered constant, and with airflow taking place between the volumes.

The valves installed on the 1:50, 32-OWC physical scale model platform were commercially-available air admittance valves. Such valves allow air to flow only through an annular section, located at the outer edge of the valve, when a diaphragm is lifted by a positive pressure difference across the valve. The damping acting on the water columns due to the valves is related to the discharge area of the valves. The discharge area for the valves used herein is the outer circumference of the annular section in the valve, multiplied by the height of the lift of the diaphragm. WEI are undertaking work on new valve designs to increases the discharge area. Increasing the discharge area would increase the flow and hence reduce the applied damping. Optimisation of valve design is critical to the long-term success of the proposed platform.

The importance of the compressibility of air cannot be neglected in the scale modelling of OWCs. Further work is planned to model this effect using a small secondary air volume, the pressure in which acts against a mechanical force such as that provided by a spring. The data obtained during the investigation into the effect on the behaviour of the single-OWC model with, and without, a large secondary air volume to incorporate the effect of air compression (see Section 10.2.3) will be used as validation data for future investigations into using such a small secondary, variable air volume to replicate the effect of air compressibility.

12.6 Concluding remarks

This thesis describes the development of a non-linear, time-domain numerical model of a single-chamber OWC with control components, which has been validated with tank tests for a range of monochromatic wave frequencies and amplitudes, while subject to a range of damping conditions. The numerical model itself, and the means by which the parameters within the model may be determined, has been detailed, and may be applied by researchers to any profile of OWC. Further, the viability, from a technical standpoint, of the proposed WEI wind/wave energy floating offshore platform has been demonstrated. However, economic viability is marginal, and further design work is required, notably to stabilise the platform if one or more wind turbines are to be installed, and to optimise the wave energy extraction potential. A number of improvements have been proposed, and a number of tools to progress design work have been developed. WEI remains a going concern and is preparing work to continue development of the

wind/wave platform concept which, it is hoped, can provide jobs, contribute to energy security and independence, and help curb environmental pollution into the future.

Appendix A

Case Study

Determining the hydrodynamic parameters of a heaving cylinder using spectral methods

The use of spectral analysis to identify hydrodynamic parameters has not been extensively used in the area of ocean energy in the past. In this Appendix, the results of a simulation of a numerical model of a cylinder, oscillating in heave, are used to demonstrate the applicability of spectral identification methods to WECs. The numerical model of the cylinder is described in [188], and the model solves the Cummins equation, using hydrodynamic parameters modelled obtained from WAMIT using the built-in cylinder routine, and a state-space approximation of the convolution term. In order to generate suitable data for spectral analysis, a random exciting force was used as input to the numerical model of the cylinder. The output from the numerical model is the displacement of the cylinder, in a single degree of freedom. Spectral analysis may be used to determine the real and imaginary parts of the equation of motion of the heaving cylinder from knowledge of the exciting force acting on the cylinder, combined with the resultant displacement of the cylinder. As the real and imaginary parts of the equation of motion of the cylinder are known from WAMIT, the results obtained for the real and imaginary parts of the equation of motion from spectral analysis of the displacement from the numerical model can be validated.

In the absence of external damping, the frequency domain equation for the cylinder is

given by:

$$fe_3(f) = \left[c_{33} - \omega^2 (m_{33} + a_{33}(f)) + j\omega(b_{33}(f))\right] u_3(f) \tag{A.1}$$

Note for a rigid body, $m_{77} \neq 0$. The subscript 3 is used to denote the heave mode of the cylinder. The SISO system for the cylinder is illustrated in Figure A.1.

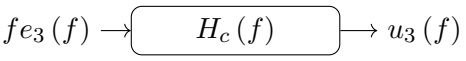

FIGURE A.1: A SISO system representation of the relationship between $fe_3(f)$ and $u_3(f)$ for a cylinder.

In Figure A.1, which is analogous to Figure 11.8 in Section 11.4.1, the Fourier transfer function between $fe_3(f)$ and $u_3(f)$ is termed $H_c(f)$, and this is given by:

$$H_c(f) = \left[c_{33} - \omega^2 (m_{33} + a_{33}(f)) + j\omega(b_{33}(f))\right] \tag{A.2}$$

From Equation (A.2), the real part of the transfer function between $fe_3(f)$ and $u_3(f)$ is given by:

$$\Re\{H_c(f)\} = c_{33} - \omega^2 (m_{33} + a_{33}(\omega)) \tag{A.3}$$

The imaginary part of the transfer function between $fe_3(f)$ and $u_3(f)$ is given by:

$$\Im\{H_c(f)\} = \omega(b_{33}(\omega)) \tag{A.4}$$

Equation (11.21) may also be applied to the heaving cylinder, thus:

$$H_c(f) = \frac{G_{fe_3u_3}(f)}{G_{fe_3fe_3}(f)} \tag{A.5}$$

where:

$H_c(f)$ = the Fourier transfer function between fe_3 and u_3

$G_{fe_3u_3}(f)$ = the one-sided cross power spectral density between fe_3 and u_3

$G_{fe_3fe_3}(f)$ = the one-sided power spectral density of fe_3

It is now possible to use Equations (A.3) and (A.4), in conjunction with Equation (A.5), to demonstrate the use of spectral methods to identify the hydrodynamic parameters of

WECs. In order to create random input for the numerical model of the cylinder, the Wave Analysis for Fatigue and Oceanography (WAFO) [245] toolbox for MATLAB was used to generate a three-hour time series of pseudo-random data to fit a Bretschneider spectrum. While WAFO is intended to create time series of wave height, the data created using WAFO was used directly as a force input to the numerical model of the cylinder, and subsequently as the force input in the spectral analysis. Figure A.2 illustrates the Fourier transform of the time series of the force input to the numerical model of the cylinder.

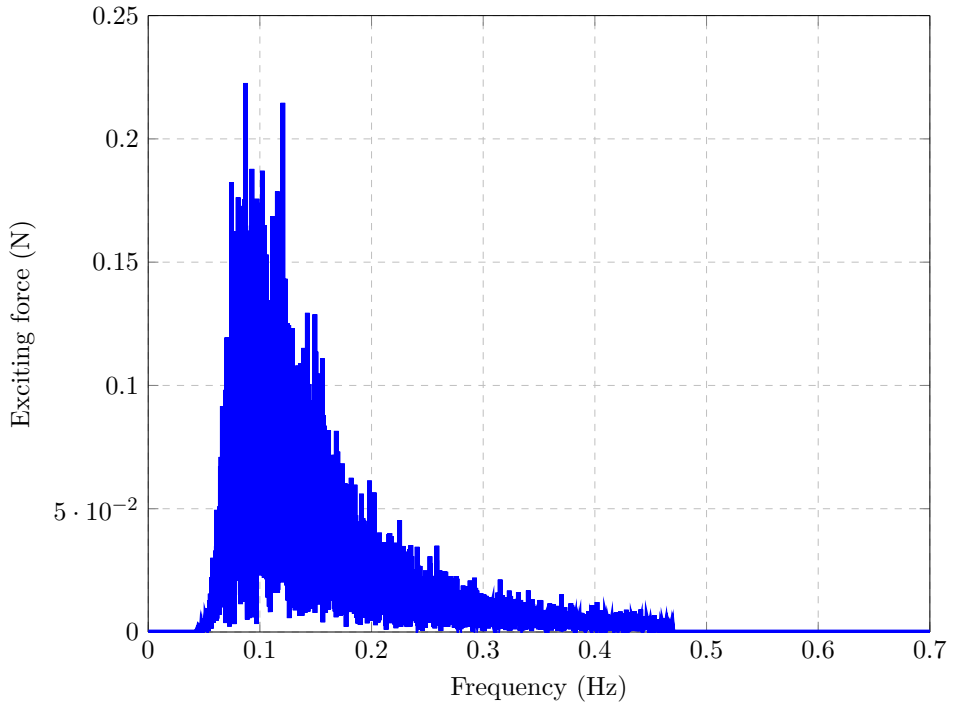

FIGURE A.2: Fourier transform of the force time series generated in WAFO as used as input to the numerical model of a cylinder.

Figure A.3 shows the Fourier transform of the displacement of the cylinder as predicted by the numerical model of the cylinder.

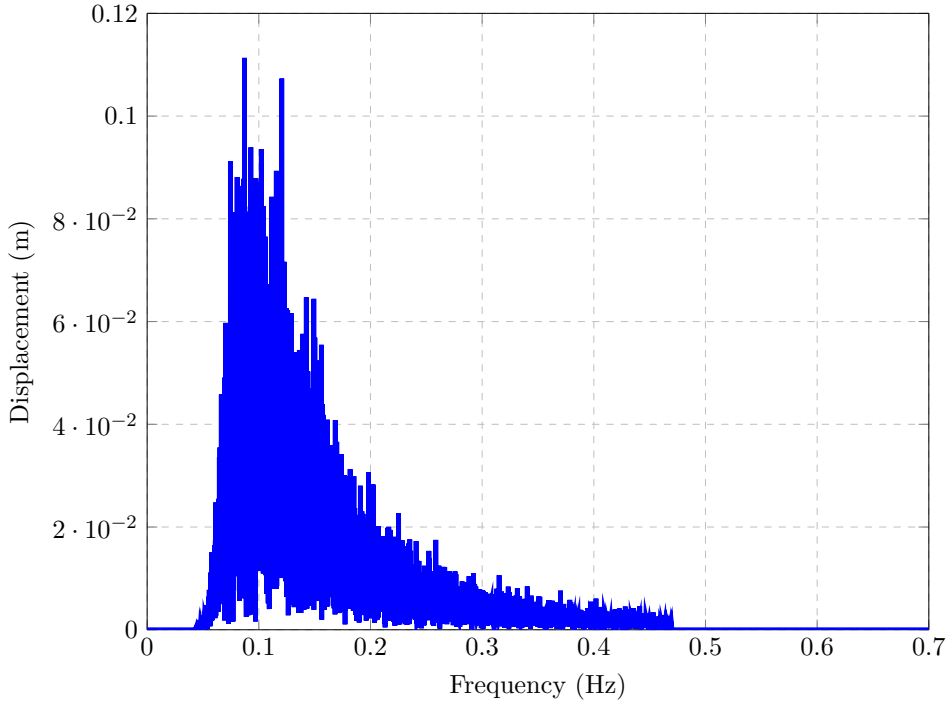

FIGURE A.3: Fourier transform of the heave displacement time series generated using the numerical model of a cylinder with a force time series created using WAFO.

The frequency-dependent transfer function between fe_3 and u_3 is found by solving Equation (A.5). Welch's averaged periodogram method with windowing [246] is used to determine $G_{fe_3u_3}$ and $G_{fe_3fe_3}$. The calculations required to find $H_c(f)$ are performed in MATLAB using the *tfestimate* command available in the *Signal Processing Toolbox* [247].

The real and imaginary parts of $H_c(f)$ may be found from directly substituting the values for a_{33}, $b_{33}$and c_{33} obtained from WAMIT along with m_{33} into Equations (A.3) and (A.4). The same hydrodynamic parameters are used to create the time-domain model of the cylinder. A direct comparison may then be made between the real and imaginary parts of the transfer function from the direct application of Equations (A.3) and (A.4) using the hydrodynamic parameters for the cylinder from WAMIT, and the results obtained from Equation (A.5).

Figure A.4 illustrates the comparison between the results for the real part of $H_c(f)$ obtained from Equations (A.3) and (A.4) using the hydrodynamics parameters for the cylinder from WAMIT and from the results obtained from Equation (A.5) for the real

part of the transfer function, while Figure A.5 illustrates the comparison between the imaginary part of $H_c(f)$, obtained from WAMIT and Equation (A.5).

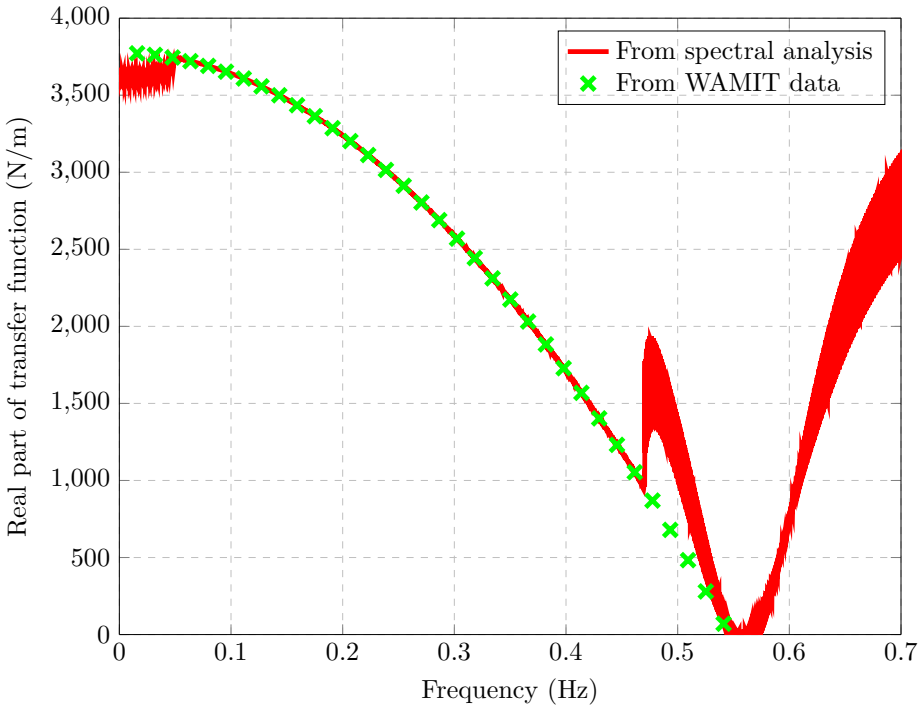

FIGURE A.4: Comparison between the real part of the transfer function found by direct application of WAMIT hydrodynamic parameters and the real part of the transfer function found by using spectral analysis on fe_3 and u_3 for a cylinder.

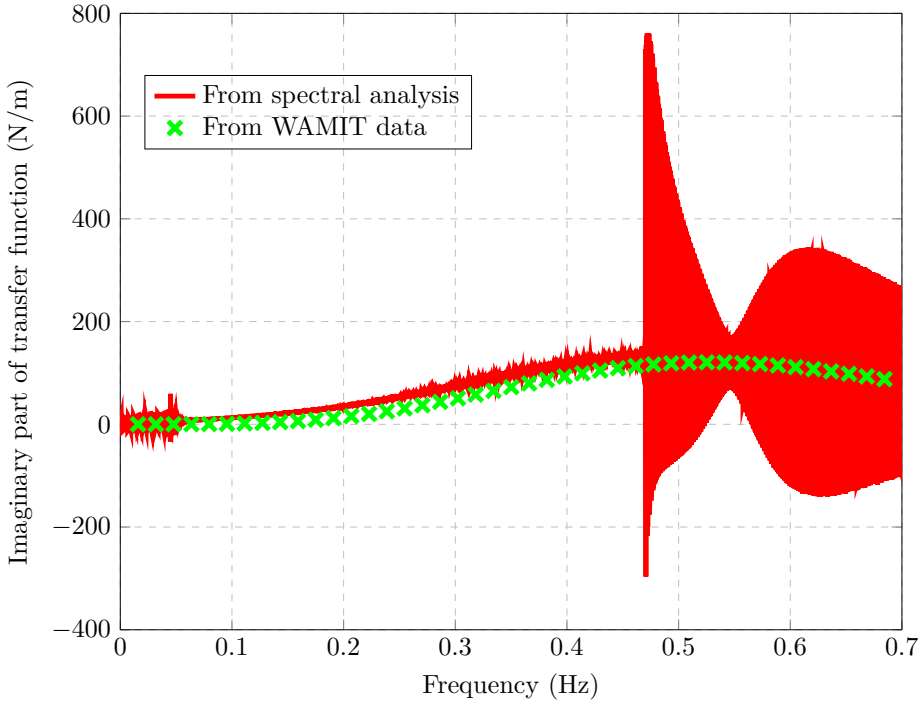

FIGURE A.5: Comparison between the imaginary part of the transfer function found by direct application of WAMIT hydrodynamic parameters and the imaginary part of the transfer function found by using spectral analysis on fe_3 and u_3 for a cylinder.

Figures A.4 and A.5 show good agreement between the real and imaginary parts of $H_c(f)$ as obtained from the direct substitution of hydrodynamic parameters obtained from WAMIT into Equations (A.3) and (A.4), and the results obtained from Equation (A.5), in the range of frequencies of 0.04 Hz to 0.46 Hz. Outside of 0.04 Hz to 0.46 Hz, the agreement is poor, with a notable divergence occurring in both Figures A.4 and A.5 at 0.46 Hz. The spectrum of fe_3, illustrated in Figure A.2, shows that fe_3 only has frequency components in the range of frequencies of 0.04 Hz to 0.46 Hz. For frequencies outside the range 0.04 Hz to 0.46 Hz, fe_3 does not excite the cylinder. For spectral analysis to produce meaningful results at a frequency, the input and output must contain information at that frequency. No information is contained within the input or the output signals outside of the range of frequencies between 0.04 Hz to 0.46 Hz, hence spectral analysis fails to determine the hydrodynamic parameters for frequencies outside the 0.04 Hz to 0.46 Hz range.

Bibliography

[1] IEA, *World Energy Balances 2017*. International Energy Agency, 2017.

[2] IEA, *World Energy Outlook 2016*. International Energy Agency, 2016.

[3] K. R. Smith *et al.*, "Joint CO_2 and CH_4 accountability for global warming," *Proceedings of the National Academy of Sciences*, vol. 110, no. 31, pp. 2865–2874, 2013.

[4] SEAI, "Energy in Ireland 1990–2015," Tech. Rep. 2016, Sustainable Energy Authority of Ireland, November 2016.

[5] Nuclear Energy Agency, *Uranium 2016*. Organisation for Economic Co-operation and Development, 2016.

[6] IRENA, *Renewable Capacity Statistics 2018*. International Renewable Energy Agency, 2018.

[7] J. Falnes, "A review of wave-energy extraction," *Marine Structures*, vol. 20, no. 4, pp. 185–201, 2007.

[8] P. Murtagh, "Bord na Móna signals end of peat harvesting by 2030," *The Irish Times*, 5 October 2015.

[9] Marine Institute, "Accessible wave energy resource atlas: Ireland," Tech. Rep. 4D404A-R2, Sustainable Energy Ireland, December 2005.

[10] SQWenergy, "Economic study for ocean energy development in Ireland: A report to Sustainable Energy Authority Ireland and Invest Northern Ireland," Tech. Rep. 2010, Sustainable Energy Authority Ireland and Invest Northern Ireland, London, July 2010.

[11] Department of Communications, Energy and Natural Resources, "Offshore renewable energy development plan: A framework for the sustainable development of Ireland's offshore renewable energy resource," Tech. Rep. 2014, DCENR, 2014.

[12] "2020 Climate and Energy Package (contains Directive 2009/29/EC, Directive 2009/28/EC, Directive 2009/31/EC and Decision no. 406/2009/EC of the Parliament and the Council)," vol. L 140/63, 23 April 2009.

[13] CCAC, *Annual Review 2017*. Climate Change Advisory Council, November 2017.

[14] EPA, *Ireland's Final Greenhouse Gas Emissions*. Environmental Protection Agency, April 2018.

[15] A. F. O. Falcão, "Wave energy utilization: A review of the technologies," *Renewable and Sustainable Energy Reviews*, vol. 14, no. 3, p. 899–918, 2010.

[16] C. Pérez-Collazo, D. Greaves, and G. Iglesias, "A review of combined wave and offshore wind energy," *Renewable and Sustainable Energy Reviews*, vol. 42, pp. 141–153, 2015.

[17] F. Fusco, G. Nolan, and J. V. Ringwood, "Variability reduction through optimal combination of wind/wave resources – an Irish case study," *Energy*, vol. 35, no. 1, pp. 314–325, 2010.

[18] T. Dooley and T. Kelly, "Initial assessment of WEI floating wind platform," Tech. Rep. EI RV IV-2010-1069, Centre for Renewable Energy at Dundalk IT, July 2011.

[19] J. Fitzgerald and B. Bolund, "Technology readiness for wave energy projects; ESB and Vattenfall classification system," in *Proceedings of the 4th International Conference on Ocean Energy (ICOE), 17-19 October*, (Dublin), 2012.

[20] T. Dooley, "Analysis of wave flume testing of WEI models at HMRC, Cork," Tech. Rep. 2010, WEI Ltd., November 2010.

[21] T. Kelly, "Numerical analysis of WEI models tested in wave flume at HMRC," Tech. Rep. 2010, Centre for Renewable Energy at Dundalk IT on behalf of WEI Ltd., 2010.

[22] R. Jefferys and T. Whittaker, "Latching control of an oscillating water column device with air compressibility," in *Hydrodynamics of Ocean Wave-Energy Utilization*, pp. 281–291, Berlin: Springer Verlag, 1986.

[23] T. Dooley *et al.*, "Analysis of testing of Cúnamara model in ocean basin, report to Sustainable Energy Authority of Ireland," Tech. Rep. 2012, WEI Ltd., May 2012.

[24] D. Ross, *Energy from the Waves*. Elsevier Science, 2nd ed., 2012.

[25] J. Falnes, *Ocean Waves and Oscillating Systems: Linear Interactions Including Wave-Energy Extraction*. Cambridge University Press, 1st ed., 2002.

[26] J. Cruz, *Ocean Wave Energy: Current Status and Future Prespectives*. Berlin: Springer Verlag, 1st ed., 2010.

[27] A. F. S. Pecher and J. P. Kofoed, *Handbook of Ocean Wave Energy*, vol. 7. Berlin: Springer Verlag, 2017.

[28] B. Drew, A. R. Plummer, and M. N. Sahinkaya, "A review of wave energy converter technology," in *Proceedings of the Institution of Mechanical Engineers, Part A: Journal of Power and Energy*, vol. 223, pp. 887–902, 2009.

[29] B. Czech and P. Bauer, "Wave energy converter concepts : Design challenges and classification," *IEEE Industrial Electronics Magazine*, vol. 6 (2), pp. 4–16, June 2012.

[30] K. H. Mohamed, N. C. Sahoo, and T. B. Ibrahim, "A survey of technologies used in wave energy conversion systems," in *2011 International Conference on Energy, Automation and Signal*, pp. 1–6, December 2011.

[31] F. Farley, "Wave power converters 2008," in *ECOR Symposium*, 2008.

[32] "CorPower Ocean AB." http://www.corpowerocean.com/. Accessed: 2 June 2018.

[33] "OPT - Ocean Power Technologies." https://www.oceanpowertechnologies.com/. Accessed: 2 June 2018.

[34] G. Dalton, R. Alcorn, and T. Lewis, "Case study feasibility analysis of the Pelamis wave energy convertor in Ireland, Portugal and North America," *Renewable Energy*, vol. 35, no. 2, pp. 443–455, 2010.

[35] A. Poullikkas, "Technology prospects of wave power systems," *Electronic Journal of Energy and Environment*, pp. 47–69, 2014.

[36] "Wave Energy Conversion Corporation of America - Technology." https://weccamerica.com/technology/. Accessed: 2 June 2018.

[37] F. Neumann, A. Brito-Melo, E. Didier, and A. Sarmento, "Pico OWC recovery project: Recent activities and performance data," in *Proceedings of the 7th European Wave and Tidal Energy Conference, Porto, Portugal, 11-13 September*, 2007.

[38] G. Ibarra-Berastegi *et al.*, "Electricity production, capacity factor, and plant efficiency index at the Mutriku wave farm (2014–2016)," *Ocean Engineering*, vol. 147, pp. 20–29, 2018.

[39] The Queen's University Belfast, "Islay LIMPET Wave Power Plant," Tech. Rep. 2002, QUB, 2002.

[40] J. P. Kofoed *et al.*, "Prototype testing of the wave energy converter Wave Dragon," *Renewable Energy*, vol. 31, no. 2, pp. 181–189, 2006.

[41] D. Vicinanza *et al.*, "The SSG wave energy converter: Performance, status and recent developments.," *Energies*, no. 5, pp. 193–226, 2012.

[42] E. Lejerskog *et al.*, "Experimental results on power absorption from a wave energy converter at the Lysekil wave energy research site," *Renewable Energy*, vol. 77, pp. 9–14, 2015.

[43] J. Frandsen, M. Doblaré, and P. Rodriguez, "Preliminary technical assessment of the Wavebob energy converter concept," Tech. Rep. 2012, Abengoa Seapower, 2012.

[44] E. Renzi *et al.*, "How does Oyster work? The simple interpretation of Oyster mathematics," *European Journal of Mechanics - B/Fluids*, vol. 47, pp. 124–131, 2014.

[45] "Resolute Marine Energy - Clean Water from Ocean Waves." http://www.resolutemarine.com/about/technology/. Accessed: 2 June 2018.

[46] l. Erselcan and A. Kukner, "A review of power take-off systems employed in wave energy converters," *Journal of Naval Science and Engineering*, vol. 10, pp. 32–44, 2014.

[47] J. Brooke, *Wave Energy Conversion*. Elsevier Ocean Engineering Series, Elsevier Science, 2003.

[48] D. Valério, P. Beirão, and J. S. da Costa, "Optimisation of wave energy extraction with the Archimedes Wave Swing," *Ocean Engineering*, vol. 34, no. 17, pp. 2330–2344, 2007.

[49] J. Chaplin *et al.*, "Development of the Anaconda all-rubber WEC," in *Proceedings of the 7th European Wave and Tidal Energy Conference, 11-14 September, Porto, Portugal*, 2007.

[50] "Wello OY - The Penguin." https://wello.eu/the-penguin/. Accessed: 2 June 2018.

[51] L. Cameron *et al.*, "Design of the next generation of the Oyster Wave Energy Converter," in *Proceedings of the 3rd International Conference on Ocean Energy*, ICOE, October 2010.

[52] J. Falnes and P. Lillebekken, "Budal's latching-controlled-buoy type wave-power plant," in *Proceedings of the 5th European Wave Energy Conference*, pp. 233–244, 2003.

[53] S. H. Salter, J. R. M. Taylor, and N. J. Caldwell, "Power conversion mechanisms for wave energy," in *Proceedings of the Institution of Mechanical Engineers, Part M: Journal of Engineering for the Maritime Environment*, vol. 216, pp. 1–27, 2002.

[54] T. V. Heath, "A review of oscillating water columns," *Philosophical Transactions of the Royal Society of London A: Mathematical, Physical and Engineering Sciences*, vol. 370, no. 1959, pp. 235–245, 2012.

[55] A. F. O. Falcão, J. C. C. Henriques, and J. J. Cândido, "Dynamics and optimization of the OWC Spar Buoy wave energy converter," *Renewable Energy*, vol. 48, pp. 369–381, 2012.

[56] Y. Masuda *et al.*, "Study of Backward Bent Duct Buoy," in *Oceans '87 Proceedings, 28 September-1 October, Halifax, Canada*, pp. 384–389, 1987.

[57] E. R. Jefferys, "Simulation of wave power devices," *Applied Ocean Research*, vol. 6, no. 1, pp. 31–39, 1984.

[58] K. Fukuda, "Behavior of water in vertical well with bottom opening of ship, and its effects on ship-motion," *Journal of the Society of Naval Architects of Japan*, vol. 1977, no. 141, pp. 107–122, 1977.

[59] A. F. O. Falcão and J. C. C. Henriques, "Oscillating-water-column wave energy converters and air turbines: A review," *Renewable Energy*, vol. 85, pp. 1391–1424, 2016.

[60] D. V. Evans, "The oscillating water column wave-energy device," *J. Inst. Maths. Applics.*, vol. 22, pp. 423–433, 1978.

[61] A. A. Hopkins, ed., *Scientific American Reference Book: a Manual for the Office, Household and Shop.* New York: Scientific American Publishing Co., 1921.

[62] A. Palme, "Wave motion turbine," *Power*, vol. 52 (18), p. 200–201, November 1920.

[63] Y. Masuda, "An experience of wave power generator through tests and improvement," in *Hydrodynamics of Ocean Wave Energy Utilization IUTAM Symposium, Lisbon, Portugal* (D. V. Evans and A. F. O. Falcão, eds.), pp. 445–452, 1986.

[64] J. C. C. Henriques *et al.*, "Design of oscillating-water-column wave energy converters with an application to self-powered sensor buoys," *Energy*, vol. 112, pp. 852–867, 2016.

[65] T. Whittaker, A. G. Barr, and F. A. McPeake, "The development and testing of a wave-activated navigation buoy with a Wells turbine," *J. Energy Resour. Technol.*, vol. 107 (2), pp. 268–273, 06 1985.

[66] "Ryokuseisha Corporation - Energy Power Source (Clean Energy)." http://www.ryokuseisha.com/eng/product/power_supply/index.html. Accessed: 2 June 2018.

[67] J. Butterworth, "The Kaimei project," in *Proceedings of the Wave Energy Conference*, (London-Heathrow), pp. 45–48, November 1978.

[68] A. E. Long and T. J. Whittaker., "The Belfast Device," in *Proceedings of the Wave Energy Conference*, (London-Heathrow), pp. 61–62, November 1978.

[69] R. Meir, "The development of the oscillating water column," in *Proceedings of the Wave Energy Conference*, (London-Heathrow), pp. 35–42, Novemeber 1978.

[70] Rendel Palmer and Tritton Consulting Engineers and Kennedy and Donkin Consulting Engineers, "United Kingdom wave consultants' 1981 assess wave energy

programme," Tech. Rep. 1981, Department of Energy Wave Energy Steering Committee, 1981.

[71] G. Retief *et al.*, "Detailed design of a wave energy conversion plant.," in *Proceedings of 19th Conference on Coastal Engineering*, vol. 1, September 1984.

[72] R. D. Bolding, "Wave power pneumatic system for power generation," September 1974. US Patent No. 4013379.

[73] J. Conroy *et al.*, "Stochastic modelling and data analysis of wave energy device Kaimei," final report to the Electricity Supply Board, International Energy Agency, 1982.

[74] J. Kelly *et al.*, "Challenges and lessons learned in the deployment of an offshore oscillating water column," *COMPEL: Int. J. for Computation and Maths. in Electrical and Electronic Eng.*, vol. 33, pp. 1678–1704, 2014.

[75] "Wave energy conversion pioneer, Ocean Energy, inks major deal for deployment at US Navy wave energy test site in Hawaii." http://www.oceanenergy.ie/oe-usa. Accessed: 2 June 2018.

[76] R. W. Robinson and A. Murray, "Geometric wavefield influences on the behaviour of an oscillating water column," in *International Symposium on Hydrodynamics in Ocean Engineering, Trondheim, Norway, 24-28 August*, 1981.

[77] M. Ravindran and P. M. Koola, "Energy from sea waves — the Indian wave energy programme," *Current Science*, vol. 60, no. 12, pp. 676–680, 1991.

[78] J. Butterworth, "A review of the Islay shoreline wave power station," in *Proceedings of the 1st European Wave Energy Symposium*, (Edinburgh), pp. 283–286, 1993.

[79] "Joule II - Economy/energy/environment models." https://cordis.europa.eu-/news/rcn/5622_en.html. Accessed: 2 June 2018.

[80] A. F. O. Falcão, "The shoreline OWC wave power plant at the Azores," in *Proceedings of the 4th European Wave Energy Conf., Aalborg, Denmark*, pp. 42–47, 2000.

[81] "Joule II - Economy/energy/environment models." Press Release: Read the latest news about the Pico Wave Power Plant., April 2018. Accessed: 2 June 2018.

[82] Wavegen, "Research into the further development of the LIMPET shoreline wave energy plant.," Tech. Rep. 2002, Department of Trade and Industry UK, 2002.

[83] F. Neumann, A. Brito-Melo, and A. J. N. A. Sarmento, "Grid connected OWC wave power plant at the Azores, Portugal," in *Proceedings of the Int. Conf. Ocean Energy: from innovation to industry, OTTI*, pp. 53–60, 2006.

[84] T. Lewis, "Review of ocean energy projects within the European Union," Tech. Rep. ERK5-CT-1999-20001, The Energy, Environmental and Sustainable Development Programme, 2003.

[85] Entec UK Ltd., "Cost estimation methodology - the marine energy challenge approach to estimating the cost of energy produced by marine energy systems," Tech. Rep. 2006, The Carbon Trust, May 2006.

[86] A. F. O. Falcão and L. M. C. Gato, *Comprehensive Renewable Energy*, vol. 8, ch. Air Turbines, pp. 111–149. Elsevier, 1st ed., 2012.

[87] J. Trinnaman and A. Clarke, *2004 Survey of Energy Resources*. Elsevier Science, 2004.

[88] D. Zhang, W. Li, and Y. Lin, "Wave energy in China: Current status and perspectives," *Renewable Energy*, vol. 34, no. 10, pp. 2089–2092, 2009.

[89] J. C. C. Henriques *et al.*, "A comparison of biradial and Wells air turbines on the Mutriku breakwater OWC wave power plant," in *International Conference on Offshore Mechanics and Arctic Engineering*, pp. 19–22, ASME, 2017.

[90] M. A. Mustapa *et al.*, "Wave energy device and breakwater integration: A review," *Renewable and Sustainable Energy Reviews*, vol. 77, pp. 43–58, 2017.

[91] H. Hotta *et al.*, "R&D on wave power device 'Mighty Whale'," *Renewable Energy*, vol. 9, no. 1, pp. 1223–1226, 1996.

[92] R. P. F. Gomes *et al.*, "Hydrodynamic optimization of an axisymmetric floating oscillating water column for wave energy conversion," *Renewable Energy*, vol. 44, pp. 328–339, 2012.

[93] R. P. F. Gomes *et al.*, "Testing of a small-scale floating OWC model in a wave flume," in *Proceedings of the 4th International Conference on Ocean Energy, 17-19 October*, (Dublin), 2012.

[94] Wavegen Ltd, "Near shore oscillating wave column - prototype development of power take off systems," Tech. Rep. V/06/00202/00/00, The Department of Trade and Industry, 2006.

[95] Renewable Energy World, "Construction completed on AquaBuOY 2.0 wave energy converter." https://www.renewableenergyworld.com/articles/2007/09/construction-completed-on-aquabuoy-2-0-wave-energy-converter-49827.html, September 2017. Accessed: 2 June 2018.

[96] "PolyWEC - New mechanisms and concepts for exploiting electroactive polymers for wave energy conversion." http://www.polywec.org/. Accessed: 2 June 2018.

[97] S. R. e Silva, R. P. F. Gomes, and A. F. O. Falcão, "Hydrodynamic optimization of the UGEN: Wave energy converter with U-shaped interior oscillating water column," *International Journal of Marine Energy*, vol. 15, pp. 112–126, 2016.

[98] S. Raghunathan, "The Wells air turbine for wave energy conversion," *Progress in Aerospace Sciences*, vol. 31, no. 4, pp. 335–386, 1995.

[99] R. A. Davey and W. K. Tease, "CFD simulation of the Wells turbine," in *5th International CFX Users Conference, Friedrichschafen, June*, 1999.

[100] A. Thakker and R. Abdulhadi, "The performance of Wells turbine under bi-directional airflow," *Renewable Energy*, vol. 33, no. 11, pp. 2467–2474, 2008.

[101] S. Raghunathan and O. O. Ombaka, "Effect of frequency of air flow on the performance of the Wells turbine," *International Journal of Heat and Fluid Flow*, vol. 6, no. 2, pp. 127–132, 1985.

[102] M. Folley, R. Curran, and T. Whittaker, "Comparison of LIMPET contra-rotating Wells turbine with theoretical and model test predictions," *Ocean Engineering*, vol. 33, no. 8, pp. 1056–1069, 2006.

[103] R. Curran, "Ocean wave energy systems design: conceptual design methodology for the operational matching of the wells air turbine," in *Collaborative Product and Service Life Cycle Management for a Sustainable World* (R. Curran, S.-Y. Chou, and A. Trappey, eds.), Advanced Concurrent Engineering, pp. 601–615, Springer London, 2008.

[104] A. F. O. Falcão and P. A. P. Justino, "OWC wave energy devices with air flow control," *Ocean Engineering*, vol. 26, no. 12, pp. 1275–1295, 1999.

[105] V. Jayashankar *et al.*, "A twin unidirectional impulse turbine topology for OWC based wave energy plants," *Renewable Energy*, vol. 34, no. 3, pp. 692–698, 2009.

[106] M. E. McCormick, J. G. Rehak, and B. D. Williams, "An experimental study of a bidirectional radial turbine for pneumatic wave energy conversion," in *OCEANS 92 Proceedings: Mastering the Oceans Through Technology*, vol. 2, pp. 866–870, 1992.

[107] B. Pereiras *et al.*, "An improved radial impulse turbine for OWC," *Renewable Energy*, vol. 36, no. 5, pp. 1477–1484, 2011.

[108] A. F. O. Falcão, L. M. C. Gato, and E. P. A. S. Nunes, "A novel radial self-rectifying air turbine for use in wave energy converters," *Renewable Energy*, vol. 50, pp. 289–298, 2013.

[109] J. C. C. Henriques *et al.*, "Air turbine and primary converter matching in Spar-Buoy oscillating water column wave energy device," in *32nd International Conference on Offshore Mechanics and Arctic Engineering*, ASME, 2013.

[110] T. K. Das, P. Halder, and A. Samad, "Optimal design of air turbines for oscillating water column wave energy systems: A review," *International Journal of Ocean and Climate Systems*, vol. 8(1), pp. 37–49, 2017.

[111] T. Setoguchi *et al.*, "A review of impulse turbines for wave energy conversion," *Renewable Energy*, vol. 23, no. 2, pp. 261–292, 2001.

[112] D. G. Dorrell, M. F. Hsieh, and C. C. Lin, "A multichamber oscillating water column using cascaded Savonius turbines," *IEEE Transactions on Industry Applications*, vol. 46, no. 6, pp. 2372–2380, 2010.

[113] T. Setoguchi and M. Takao, "Current status of self rectifying air turbines for wave energy conversion," *Energy Conversion and Management*, vol. 47, no. 15–16, pp. 2382–2396, 2006.

[114] "Chapter 4 - Non-return valves," in *Handbook of Valves and Actuators* (B. Nesbitt, ed.), pp. 131–141, Oxford: Butterworth-Heinemann, 2007.

[115] J. C. C. Henriques *et al.*, "Peak-power control of a grid-integrated oscillating water column wave energy converter," *Energy*, vol. 109, pp. 378–390, 2016.

[116] L. Martinelli, P. Pezzutto, and P. Ruol, "Experimentally based model to size the geometry of a new OWC device, with reference to the Mediterranean sea wave environment," *Energies*, vol. 6, pp. 4696–4720, 2013.

[117] J. P. Kofoed and P. Frigaard, "Hydraulic evaluation of the Leancon wave energy converter," Tech. Rep. 45, Dept. Civil Engineering, Aalborg University, Denmark, October 2008.

[118] M. Vicente *et al.*, "Tupperwave: Preliminary numerical modelling of a floating OWC equipped with a unidirectional turbine," in *Proceedings of the 12th European Wave and Tidal Energy Conference*, 2017.

[119] K. Mala *et al.*, "A twin unidirectional impulse turbine topology for OWC based wave energy plants – experimental validation and scaling," *Renewable Energy*, vol. 36, no. 1, pp. 307–314, 2011.

[120] European Commission Community Research and Development Service, "ORECCA summary report." https://cordis.europa.eu/result/rcn/54046_en.html, December 2012. Accessed: 2 June 2018.

[121] European Commission Community Research and Development Service, "Marine Renewable Integrated Application Platform." https://cordis.europa.eu/project/rcn/93425_en.html, May 2017. Accessed: 2 June 2018.

[122] K. O'Sullivan, "Techno-economic optimisation of an oscillating water column array wave energy converter," in *Proceedings of the 10th European Wave and Tidal Energy Conference*, 2013.

[123] Y. Masuda, "Apparatus for generating electrical power by wave energy and dissipating waves," March 1975. UK Patent No. 1492427.

[124] N. Barltrop, "Multiple unit floating offshore wind farm (MUFOW)," *Wind Engineering London*, vol. 17, no. 4, pp. 183–188, 1993.

[125] A. Wells, "Combined wind and wave power generator," April 1994. International Patent No. WO/94/09272.

[126] L. Christensen, E. Friis-Madsen, and J. P. Kofoed, "The wave energy challenge: The Wave Dragon case," in *PowerGen 2005 Europe conference*, 2018.

[127] E. Friis-Madsen, "Offshore wind/wave-energy converter," January 1996. International Patent No. WO/96/00848.

[128] K. D. Rasmussen, "Wave energy converter comprising pressure and suction pipes," May 2007. International Patent No. WO/2007/057013.

[129] P. Griffin, B. Kirke, and P. D. Parter, "Energy extraction method and apparatus," February 2008. International Patent No. WO/2008/019436.

[130] J. I. Edwards and P. T. Diver, "Wave and wind power generation," April 2008. International Patent No. WO/2008/044065.

[131] B. S. Kallesøe *et al.*, "Prototype test and modeling of a combined wave and wind energy conversion system," in *Proceedings of the 8th European Wave and Tidal Energy Conference*, EWTEC, 2009.

[132] A. Pecher, J. P. Kofoed, and T. Larsen, "Design specifications for the Hanstholm WEPTOS wave energy converter," *Energies*, vol. 4, no. 5, pp. 1001–1017, 2012.

[133] K. S. Banister, A. Weinstein, and D. Roddier, "WindWaveFloat: Combining offshore wind turbines and WEC in a single structure," in *Proceedings of the 9th European Wave and Tidal Energy Conference*, EWTEC, 2011.

[134] J. E. Hanssen *et al.*, "Design and performance validation of a hybrid offshore renewable energy platform," in *2015 Tenth International Conference on Ecological Vehicles and Renewable Energies (EVER)*, pp. 1–8, 2015.

[135] G. B. Airy, "Tides and waves.," *Encyclopedia Metropolitana, Mixed Sciences*, vol. 3, 10 1841.

[136] T. Sarpkaya and M. Isaacson, *Mechanics of wave forces on offshore structures*. London: Van Nostrand Reinhold Co., 1981.

[137] A. D. D. Craik, "The origins of water wave theory," *Annual Review of Fluid Mechanics*, vol. 36, no. 1, pp. 1–28, 2004.

[138] T. A. A. Adcock and P. H. Taylor, "The Mulberry Harbours: A review of an early example of offshore engineering," in *International Conference on Offshore Mechanics and Arctic Engineering*, vol. 6, pp. 567–574, ASME, 2009.

[139] T. Ogilvie, "Recent progress towards the understanding and prediction of ship motions," in *6th Symposium on Naval Hydrodynamics*, 1964.

[140] W. E. Cummins, "The impulse response function and ship motions," Tech. Rep. 1661, Navy Department, David Taylor Model Basin, DTNSRDC, October 1962.

[141] Wamit®, *WAMIT® 7.0 User manual*. The Massachusets Institute of Technology, 2012.

[142] J. M. Paixão Conde and L. M. C. Gato, "Numerical study of the air-flow in an oscillating water column wave energy converter," *Renewable Energy*, vol. 33, no. 12, pp. 2637–2644, 2008.

[143] J.-R. Nader *et al.*, "A finite-element study of the efficiency of arrays of oscillating water column wave energy converters," *Ocean Engineering*, vol. 43, pp. 72–81, 2012.

[144] D. V. Evans and R. Porter, "Hydrodynamic characteristics of an oscillating water column device," *Applied Ocean Research*, vol. 17, no. 3, pp. 155–164, 1995.

[145] D. V. Evans, "Wave-power absorption by systems of oscillating surface pressure distributions," *Journal of Fluid Mechanics*, vol. 114, p. 481–499, 1982.

[146] J. Falnes and P. McIver, "Surface wave interactions with systems of oscillating bodies and pressure distributions," *Applied Ocean Research*, vol. 7, no. 4, pp. 225–234, 1985.

[147] L. H. Holthuijsen, *Waves in Oceanic and Coastal Waters*. Cambridge University Press, 2010.

[148] S. K. Chakrabarti, *Hydrodynamics of Offshore Structures*. Berlin: Springer Verlag, 1987.

[149] International Association of Classification Societies, *No. 34 Standard Wave Data*. Guidelines and recommendations, IACS, 2001.

[150] J. Marqués, L. I. López de Aguileta, and Y. Torre-Enciso, "Mutriku. Lessons learnt," in *Proceeedings of the 3rd International Conference on Ocean Energy*, (Bilbao), October 2010.

[151] Government of Ireland, *Sustainable Energy Act, 2002.* Dublin: The Stationery Office.

[152] Det Norske Veritas, *DNV Offshore Standard: Structural Design of Offshore Units (WSD Method): DNV-OS-C201.* DNV offshore services, DNV, 2014.

[153] Det Norske Veritas, *DNV Recommended Practice: Environmental Conditions and Environmental Loads: DNV-RP-C205.* DNV offshore services, DNV, 2014.

[154] Det Norske Veritas, *DNV Offshore Standard: Offshore Concrete Structures: DNV-OS-C502.* DNV offshore services, DNV, 2012.

[155] Det Norske Veritas, *DNV Rules for Classification of Ships: Offshore Concrete Structures: Part 3. Chapter 1. Hull Structural Design, Ships with Length 100 metres and above.* DNV offshore services, DNV, 2012.

[156] A. F. O. Falcão, "Modelling and control of oscillating-body wave energy converters with hydraulic power take-off and gas accumulator," *Ocean Engineering*, vol. 34, no. 14–15, pp. 2021–2032, 2007.

[157] A. F. O. Falcão, "Phase control through load control of oscillating-body wave energy converters with hydraulic PTO system," *Ocean Engineering*, vol. 35 , no. 3-4, pp. 358–366, 2008.

[158] A. Arapogianni *et al.*, "Deep water - The next step for offshore wind energy," Tech. Rep. 2013, European Wind Energy Association, July 2013.

[159] "Adwen 8MW Offshore Wind Turbine." http://www.adwenoffshore.com/products-services/products/8-mw-turbines/, 2015. Accessed: 3 January 2017.

[160] T. Kelly, J. Campbell, and A. Sancraian, "Report for J. J. Campbell & Associates in association with Wave Energy Ireland," Tech. Rep. Grant no. OC/OC/2014/201414903, J. J. Campbell & Associates Wave Energy Ireland, Centre for Renewable Energy at DkIT, June 2014.

[161] K. O'Sullivan, "Technical review of CÚNAMARA hydrodynamic model testing and technology development plan," Tech. Rep. 122388, Black and Veatch Limited, 2015.

[162] T. Stallard *et al.*, "Project assessment," in *Protocols for the Equitable Assessment of Marine Energy Converters*, pp. 241–264, University of Edinburgh, 2011.

[163] T. Kelly *et al.*, "Report into works carried out as part of SEAI grant OCN/00031," Tech. Rep. Grant no. OCN/00031, J. J. Campbell & Associates in partnership with WEI Ltd. and the Centre for Renewable Energy at Dundalk IT, June 2017.

[164] European Union Horizon 2020 Research and Innovation Programme, "Marine renewables infrastructure network." http://www.marinet2.eu/, April 2017. Accessed: 2 June 2018.

[165] R. Atan *et al.*, "Assessment of wave characteristics and resource variability at a 1/4-scale wave energy test site in Galway Bay using waverider and high frequency radar (CODAR) data," *Ocean Engineering*, vol. 117, pp. 272–291, 2016.

[166] Kishorn Port Limited, "About Kishorn - dry dock facilities." https://www.kishorn-port.co.uk/services/dry-dock-facilities/, 2015. Accessed: 2 June 2018.

[167] R. Atan, J. Goggins, and S. Nash, "A detailed assessment of the wave energy resource at the Atlantic Marine Energy Test Site," *Energies*, no. 9, p. 967, 2016.

[168] International Towing Tank Conference, "ITTC Recommended Guidelines. Wave Energy Converter Model Test Experiments," Tech. Rep. 2014, International Towing Tank Conference, 2014.

[169] Sustainable Energy Authority Ireland, "Prototype Development Fund." http://www.seai.ie/Renewables/Ocean-Energy/Prototype-Development-Fund/, 2015. Accessed: 6 June 2017.

[170] R. Aasen and B. Hays, "Method for finding min and max values of error range for calculation of moments of inertia.," in *Proceedings of the 69th Annual Conference of the Society of Allied Weight Engineers*, 2010.

[171] Autodesk, *AutoCAD® 2013 User Guide*, 2012.

[172] K. A. Stroud, *Engineering Mathematics*. Hampshire and London: Macmillan Press, 4th ed., 1995.

[173] Aerohydro Inc., *Aerohydro Multisurf® User Manual*. Aerohydro Inc., Southwest Harbor, Maine, 2011.

[174] C.-H. Lee *et al.*, "Integration of geometry definition and wave analyis software," in *Proceedings of 21st OMAE Conference*, 2002.

[175] T. Heath, "Full-scale WECs," in *Ocean Wave Energy: Current Status and Future Perspectives* (J. Cruz, ed.), (Berlin), pp. 287–296, Springer Verlag, 2008.

[176] M. F. P. Lopes *et al.*, "Experimental and numerical investigation of non-predictive phase-control strategies for a point-absorbing wave energy converter," *Ocean Engineering*, vol. 36, no. 5, pp. 386–402, 2009.

[177] R. Joel, *Basic Engineering Thermodynamics*. Harlow, UK: Longman, 5th ed., 1996.

[178] C. Josset and A. Clément, "A time-domain numerical simulator for oscillating water column wave power plants," *Renewable Energy*, vol. 32, no. 8, pp. 1379–1402, 2007.

[179] W. Sheng, R. Alcorn, and A. Lewis, "On thermodynamics in the primary power conversion of oscillating water column wave energy converters," *Journal of Renewable and Sustainable Energy*, vol. 5, 2013.

[180] J. Weber, "Representation of non-linear aero-thermodynamic effects during small scale physical modelling of OWC WECs," in *Proceedings of the 4th International Conference on Ocean Energy*, 2012.

[181] H. I. Ali *et al.*, "Mathematical and intelligent modeling of electropneumatic servo actuator systems," *Australian Journal of Basic and Applied Sciences*, vol. 3, no. 4, pp. 3663–3671, 2009.

[182] ISO, "Measurement of fluid flow by means of pressure differential devices inserted in circular cross-section conduits running full – Part 4: Venturi tubes," standard, International Organization for Standardization, Geneva, CH, 2003.

[183] R. A. Habing, *Flow and plate motions in compressor valves*. PhD thesis, Twente University Holland, 2005.

[184] R. L. Willans II and D. A. Lawrence, *Linear state-space control systems*. Hoboken, New Jersey: John Wiley & Sons, Inc., 2007.

[185] ISO, "Measurement of fluid flow by means of pressure differential devices inserted in circular cross-section conduits running full – Part 2: Orifice plates," standard, International Organization for Standardization, Geneva, CH, 2003.

[186] D. N. Brughes and A. Graham, *Introduction to control theory, including optimal control*. Ellis Horwood series in mathematics and its applications, E. Horwood, 1980.

[187] M. A. A. Shoukat Choudhury, N. F. Thornhill, and S. L. Shah, "Modelling valve stiction," *Control Engineering Practice*, vol. 13, no. 5, pp. 641–658, 2005.

[188] Z. Yu and J. Falnes, "State-space modelling of a vertical cylinder in heave," *Applied Ocean Research*, vol. 17, no. 5, pp. 265–275, 1995.

[189] T. Perez and T. I. Fossen, "Joint identification of infinte-frequency added mass and fluid-memory models of marine structures," *Modeling, Identification and Control*, vol. 29, no. 3, pp. 93–102, 2008.

[190] T. Perez and T. I. Fossen, "Identification of dynamic models of marine structures from frequency-domain data enforcing model structure and parameter constraints," Tech. Rep. 2009, University of Newcastle, Australia Norwegian University of Science and Technology, 2009.

[191] R. Taghipour, T. Perez, and T. Moan, "Time-domain hydroelastic analysis of a flexible marine structure using state-space models," *Journal of Offshore Mechanics and Arctic Engineering*, 2009.

[192] T. Perez and T. I. Fossen, "A MATLAB Toolbox for Parametric Identification of Radiation-Force Models of Ships and Offshore Structures," *Modeling, Identification and Control*, vol. 30, no. 1, pp. 1–15, 2009.

[193] J. A. Armesto *et al.*, "Comparative analysis of the methods to compute the radiation term in Cummins' equation," *Journal of Ocean Engineering and Marine Energy*, vol. 1, no. 4, pp. 377–393, 2015.

[194] D. Vandenberg, "Mathematical Survey and Application of the Cross-Ambiguity Function," Master's thesis, Indiana University South Bend, U.S.A., 2012.

[195] M. Rahman and D. D. Bhatta, "Evaluation of added mass and damping coefficient of an oscillating circular cylinder," *Applied Mathematical Modelling*, vol. 17, no. 2, pp. 70–79, 1993.

[196] J. N. Newman and J. Grue, *Marine Hydrodynamics*. MIT Press, 2018.

[197] M. Penalba, T. Kelly, and V. Ringwood, "Using NEMOH for modelling wave energy converters: A comparative study with WAMIT," in *Proceeedings of the 12th European Wave and Tidal Energy Conference*, EWTEC, 2017.

[198] L. F. Shampine and M. W. Reichelt, "The MATLAB ODE suite," *SIAM Journal on Scientific Computing*, vol. 18, no. 1, pp. 1–22, 1997.

[199] G. Payne, "Guidance for the experimental tank testing of wave energy converters," Tech. Rep. 2008, University of Edinburgh, 2008.

[200] B. S. Massey and J. Ward-Smith, *Mechanics of Fluids*. CRC Press: London, UK, 1998.

[201] Hydraulics and Maritime Research Centre, "Ocean energy: development and evaluation protocol," Tech. Rep. 2003, Hydraulics and Maritime Research Centre, University College Cork, 2003.

[202] D. M. Ingram *et al.*, eds., *Protocols for the equitable assessment of marine energy converters*. University of Edinburgh, 1st ed., 2011.

[203] B. G. Cahill and T. Lewis, "Wave energy resource characterisation of the Atlantic Marine Energy Test Site," *International Journal of Marine Energy*, vol. 1, pp. 3–15, 2013.

[204] T. Whittaker *et al.*, "The development of Oyster - a shallow water surging wave energy converter," in *Proceedings of 7th European Wave and Tidal Energy Conference, Porto, Portugal*, 2007.

[205] M. Folley, T. Whittaker, and M. Osterried, "The oscillating wave surge converter," in *Proceedings of 14th International Offshore and Polar Engineering Conference, Toulon, France*, 2004.

[206] Edinburgh Designs, *Narrow tank wavemaker hardware manual*. Edinburgh Designs Ltd., United Kingdom, 1st ed., 1995.

[207] D. Rodgers and G. B. King, *Wave generation using the Ocean system*. Edinburgh Designs Ltd., United Kingdom, 1st ed., 1995.

[208] D. Rodgers and G. B. King, *Wave Generation using Ocean and Wave*. Edinburgh Designs Ltd., United Kingdom, 3.62 ed., 1997.

[209] H. M. Brian, *The hydrodynamics of single and multiple moonpools*. PhD thesis, The Queen's University Belfast, 1991.

[210] Y. Goda and S. Suzuki, "Estimation of incident and reflected waves in random wave experiments," in *Proceedings of 15th International Conference on Coastal Engineering*, pp. 828–845, ASCE, 1976.

[211] W. W. Jamison and E. P. D. Massard, "An efficient upright wave absorber," in *Proceeedings on Coastal Hydrodynamics*, (Newark, Delaware), pp. 124–139, ASCE, 1987.

[212] "Edinburgh designs - the perfect wave." http://www.edesign.co.uk/, 2016. Accessed: 1 November 2016.

[213] Bonar Civil Products, *Enkamat 7010*, 2014. Datasheet.

[214] "National instruments: Test, measurement and embedded systems." http://www.ni.com/, 2016. Accessed: 1 November 2016.

[215] J. Falnes, "Principles for capture of energy from ocean waves. Phase control and optimum oscillation," Tech. Rep. 1995, NTNU, 1995.

[216] A. Tramschek and J. F. T. MacLaren, "Simulation of a reciprocating compressor accounting for interactions between valve movement and plenum pressure chamber," in *International Compressor Engineering Conference Paper 356* (P. U. e-Publications, ed.), (West Lafayette, IN. USA), 1980.

[217] M. Costagliola, *Dynamics of a reed type valve*. PhD thesis, Massachusetts Institute of Technology, 1942.

[218] M. Heidari, M. Mortazavi, and A. Rufer, "Design, modeling and experimental validation of a novel finned reciprocating compressor for isothermal compressed air energy storage applications," *Energy*, vol. 140, pp. 1252–1266, 12 2017.

[219] P. Sclavounos, C. Tracy, and S. Lee, "Floating offshore wind turbines: responses in a seastate; pareto optimal designs and economic assessment," Tech. Rep. 2007, Massachusetts Institute of Technology, 2007.

[220] A. Fleming and G. Macfarlane, "In-situ orifice calibration for reversing oscillating flow and improved performance prediction for oscillating water column model test experiments," *International Journal of Marine Energy*, vol. 17, no. Supplement C, pp. 147–155, 2017.

[221] International Towing Tank Conference, "ITTC recommended procedures and guidelines. Testing and extrapolation methods, loads and responses, sea keeping - sea keeping experiments," Tech. Rep. 2005, International Towing Tank Conference, 2005.

[222] J. Taylor, *Introduction To Error Analysis: The Study of Uncertainties in Physical Measurements*. University Science Books, 1997.

[223] S. Butterworth, "On the theory of filter amplifiers," *Wireless Engineer*, vol. 7, 1930.

[224] R. W. Daniels, *Approximation methods for electronic filter design: with applications to passive, active, and digital networks*. University of Michigan: McGraw-Hill, 1974.

[225] S. Draycott *et al.*, "Application of complex wave and current conditions in a laboratory environment," in *Proceedings of the Twelfth European Wave and Tidal Energy Conference* (A. Lewis, ed.), (University College Cork, Ireland), pp. 890-1–890-8, EWTEC, Aug 27–Sep 1 2017.

[226] J. Fitzgerald and L. Bergdahl, "Including moorings in the assessment of a generic offshore wave energy converter: A frequency domain approach," *Marine Structures*, vol. 21, no. 1, pp. 23–46, 2008.

[227] G. Hagerman and R. Bedard, "Guidlines for preliminary estimation of power production, by offshore wave energy conversion devices," Tech. Rep. 297213, Electric Power Research Institute, California, USA, 2003.

[228] M. E. McCormick, *Ocean Wave Energy Conversion*. Dover Publications, 2007.

[229] A. J. N. A. Sarmento and A. F. O. Falcão, "Wave generation by an oscillating surface-pressure and its application in wave energy extraction," *J. Fluid Mech.*, vol. 150, pp. 111–149, 1985.

[230] A. F. O. Falcão and J. C. C. Henriques, "Model-prototype similarity of oscillating-water-column wave energy converters," *International Journal of Marine Energy*, vol. 6, pp. 18–34, 2014.

[231] A. J. N. A. Sarmento, "Model-test optimization of an OWC wave power plant," *Int. J. Offshore Polar Eng.*, pp. 66–172, 1993.

[232] M. Carello, A. Ivanov, and L. Mazza, "Pressure drop in pipe lines for compressed air: comparison between experimental and theoretical analysis," *J. Fluid Mech.*, 1998.

[233] T. Kelly, "Experimental investigation into the effects of scaling air compression in physical models of oscillating water wolumns - a technical report," Tech. Rep. 2018, Maynooth University, 2018.

[234] J. M. J. Journee and W. W. Massie, *Offshore Hydrodynamics*. Delft University of Technology, 2001.

[235] A. B. Aalbers, "The water motions in a moonpool," *Ocean Engineering*, vol. 11, no. 6, pp. 557–579, 1984.

[236] T. P. Stewart, *The Influence of Harbour Geometry on the Performance of Oscillating Water Column Wave Power Converters*. PhD thesis, The Queen's University of Belfast, 1993.

[237] EquiMar, "Equitable testing and evaluation of marine energy extraction devices (equimar)," tech. rep., 03/12 2012.

[238] J. S. Bendat and A. G. Piersol, *Engineering Applications of Correlation and Spectral Analysis*. New York: Wiley, 2nd ed., 1980.

[239] J. S. Bendat and A. G. Piersol, *Random Data: Analysis and Measurement Procedures*. New York: Wiley, 2011.

[240] D. J. Sheskin, *Handbook of Parametric and Nonparametric Statistical Procedures*. London: CRC Press, 3rd ed., 2003.

[241] Y. M. C. Delaure and A. Lewis, "3D hydrodynamic modelling of fixed oscillating water column wave power plant by a boundary element method," *Ocean Engineering*, vol. 30, no. 3, pp. 309–330, 2003.

[242] N. W. Newman, "The exciting forces on fixed bodies in waves," *Journal of Ship Research*, vol. 6, no. 3, pp. 423–433, 1963.

[243] F. W. King, *Hilbert Transforms*. Cambridge University Press, 2009.

[244] A. Rasekhi Nejad, E. E. Bachynski, and T. Moan, "On tower top axial acceleration and drivetrain responses in a spar-type floating wind turbine," in *International Conference on Offshore Mechanics and Arctic Engineering*, vol. 9, ASME, 2017.

[245] WAFO-group, *WAFO - A Matlab Toolbox for Analysis of Random Waves and Loads - A Tutorial*. Math. Stat., Center for Math. Sci., Lund Univ., Lund, Sweden, 2000.

[246] P. D. Welch, "The use of fast Fourier transform for the estimation of power spectra: A method based on time averaging over short, modified periodograms," *IEEE Transactions on Audio and Electroacoustics*, vol. 15, pp. 70–73, 1967.

[247] "Signal processing toolbox documentation - transfer function estimate." https://uk.mathworks.com/help/signal/ref/tfestimate.html, 2016. Accessed: 6 October 2010.